Application of Semi-Automated Strain Analysis Techniques and Anisotropy of Magnetic Susceptibility in Fold and Thrust Belts

Dave J. McCarthy

A thesis submitted for the degree of
Doctor of Philosophy
April 2014

Research Supervisors:
Dr. P. Meere
and
Dr. K. Mulchrone

National University of Ireland, Cork

School of Biological, Earth and Environmental Sciences (Discipline of Geology)

College of Science, Engineering and Food Sciences

Head of School: Prof. John O'Halloran

Declaration

This thesis is the candidates own work and has not been submitted for another degree either at University College Cork or elsewhere.

Signed: 

Table of Contents **Page No**

“Because in the end, you won’t remember the time

you spent working in the office or mowing your lawn.

Climb that goddamn mountain.”

Jack Kerouac

Abstract

Quantitative analysis of penetrative deformation in sedimentary rocks of fold and thrust belts has largely been carried out using clast based strain analysis techniques. These methods analyse the geometric deviations from an original state that populations of clasts, or strain markers, have undergone. The characterisation of these geometric changes, or strain, in the early stages of rock deformation is not entirely straight forward. This is in part due to the paucity of information on the original state of the strain markers, but also the uncertainty of the relative rheological properties of the strain markers and their matrix during deformation, as well as the interaction of two competing fabrics, such as bedding and cleavage. Furthermore one of the single largest setbacks for accurate strain analysis has been associated with the methods themselves, they are traditionally time consuming, labour intensive and results can vary between users. A suite of semi-automated techniques have been tested and found to work very well, but in low strain environments the problems discussed above persist. Additionally these techniques have been compared to Anisotropy of Magnetic Susceptibility (AMS) analyses, which is a particularly sensitive tool for the characterisation of low strain in sedimentary lithologies.

Acknowledgments

Writing a PhD has probably been one of the most miserable things I have done, while being a PhD student is a thoroughly enjoyable and rewarding experience. This would not have been possible without the considerable friendship, support and advice that has been furnished from more people than it is possible to thank individually. Thank you all! That said there are several groups of people that I have to thank in particular.

My principal supervisor Dr. Pat Meere is deserving of more thanks than I can offer, he has been a constant source of reassurance, knowledge and sound advice on avoiding snakes in the field. Dr. Kieran Mulchrone has also been of great assistance as a secondary supervisor, he has tried to convince me of the usefulness of mathematics and has certainly matched my own cynicism. I would also like to thank my official-unofficial supervisor, Prof. Mike Petronis, for many things, particularly for providing use of his lab and for keeping me on track in all things magnetic, but also for providing a friendly face and showing a pasty white boy around the badlands of New Mexico! Despite their efforts any errors or shortcomings found here are mine only.

I would not have been convinced to continue academic pursuits if it had not been for the solid background I received as an undergraduate in Geology at UCC, but also for the friendly atmosphere and inspiration that permeates the building, the many students, masters students and my fellow research students have certainly contributed, but the staff are ultimately responsible and for that they are all thanked: John Gamble, Andy Wheeler, Alistair Allen, Pat Meere, John Reavy, Ed Jarvis, Ken and Bettie Higgs, Ivor MacCarthy, Richard Unitt, Mary Lehane, Stuart Warner, Maria McNamarra and especially Mary McSweeney for finding all of the right paperwork all of the time. In particular I have to thank my ‘grandfather in research’, Alistair, for superb supervision and encouragement during my Bachelors research project and for pushing me further. Also John Reavy has certainly contributed to my understanding of the Caledonian, but I’m still not sure how it all works, possibly due to the ‘shear’ number of morale boosters that were imbibed. Long may the “Work hard, play harder” ethos of this great ‘department’ carry on.

Speaking of ‘carrying on’, I have had the fortune to share an office with some good friends and colourful characters. Drilly-Willy, now Professor McCarthy, has shared with me his insights on magnets, feldspars and drilling, but has also brought more than his fair share of terrible music, random chair dancing and general mayhem to the office. I have no idea how the benevolent Jo Mackey and virtuous Caroline Jepson forbearingly shared an office with myself and Willy for so long.

I think we have all lived vicariously through the salty sea dog that is Mark Coughlan. He has been a constant source of camaraderie, banter and general mayhem since

the early days, and a great friend to boot, but watch your beer and women when he's about. Aaron 'junior' Lim is no longer the new kid, but I'm sure he will still be treated as such. Cora McKenna acted as a mother to us all and showed us how the internet worked, amongst other things, I still don't understand how she was the most sober one that night. I don't know where to start with the indescribable Marian McGrath… I'm sure the dis-reputation of geology postgrads is in good hands with David, Aidan, Brenton and Mohit.

All of the IFG students provided beds, couches, floor space and banter at times when they were in short supply, but in particular Stephen McLaughlan and Katie Quinn helped me stray from the path and back on again. Likewise the postgrads of NMHU geology, Adam, Rhonda and Danni eased the passing of time in a windowless room in the middle of a science building.

Many friends and fellow climbers have been responsible for distractions in the form of good times and great routes climbed and have regularly reminded that there is a lot more to life than finishing a thesis.

My family have always supported me, put up with me and have constantly asked when will it be finished! My father has usually encouraged me to do the things I've wanted to do, when he didn't I did them anyway, and like all great fathers he can fix most things! Kelly and Peter deserve a special mention for sharing a house with me, especially towards the end when nights were long and tempers short.

Finally, Alex has certainly made much of this easier, she has lived with me, suffered loss of use of all working surfaces all at the same time, endured endless one-sided discussions on how the earth works. More importantly she has shared my passion for the mountains and has even taught a science geek a few things about culture.

I'm sure I've forgotten someone!

Daithí

As an addendum I would like to thank Dr. John Reavy and Dr. Mark Cooper for examining and ultimately considering this tome worthy of a doctorate, I am rather grateful. In particular I would like to thank John for ensuring that I learnt some grammar throughout this process, his command of the English language is intimidating! I would also like to thank Mark for his insights into the structural geology of Munster, Montana and Wyoming, his breadth and depth of knowledge is an inspiration.

Chapter 1.

Introduction

1. Introduction

The Earth's lithosphere is deformed as a consequence of global-scale plate tectonic interactions. In order to fully understand these processes it is necessary to accurately characterise and quantify deformation patterns from past mountain building events. This typically involves analysis of the geometric changes that the rock bodies being studied have undergone due to deformation.

The characterisation of these geometric changes or strain in the early stages of rock deformation is not entirely straight forward, for a truly accurate measurement of strain the 3D geometries of objects of known original shape need to be recorded then a relationship between the pre-deformed shape and deformed shape can be established. Unfortunately objects that have a known original shape are far from ubiquitous and a variety of strain analysis techniques have been developed to account for this paucity. These techniques are typically based on the behaviour of populations of approximately ellipsoidal objects such as sedimentary clasts. This allows strain analysis to be carried out in almost all rock types. The major drawback of these methods is that they are not capable of accurately constraining weak deformation and they cannot account for non-passive behaviour.

In samples with very weak deformation the original fabric can dominate the overall rock fabric more so than the developing strain fabric. This can lead to some difficulties when attempting to characterise deformation. Additionally most methodologies for strain analysis rely on the assumption that the strain markers acted passively during deformation, i.e. the marker and surrounding matrix material respond identically to the deformation. In reality, there is a contrast in competency between strain markers and their surrounding matrix, which means that they react

differently during deformation. Neglecting this leads to a significant underestimation of strain estimates. Analysis of magnetic fabrics is used in this study to identify the geometries and relative strength of these weak tectonic fabrics. The magnetic susceptibility of a rock relates the induced magnetisation to the magnetic field in which the rock is immersed and typically defines an ellipsoid that allows imaging of the rock fabric. AMS ellipsoid geometries are sensitive to finite-strain and stress directions in tectonised rocks (Borradaile and Jackson, 2010) and is a particularly sensitive tool for the characterisation of low strain in these lithologies.

1.1. Aims and objectives

The purpose of this thesis is threefold:

1) To determine the accuracy of recently developed geological strain analysis techniques, the Delaunay Triangulation Nearest Neighbour (DTNNM) and Mean Radial Length (MRL) methods that have been incorporated into a Mathematica package (Appendix 1; Mulchrone et al., 2013)

2); To evaluate the relationship between the results determined from the strain analysis techniques and the magnetic fabric of the samples determined from Anisotropy of Magnetic Susceptibility (AMS) measurements and

3); To relate both the strain estimate results and the AMS results to regional deformation in each study area.

To this extent the thesis can be split in to two main sections:

I Theory and analysis methods (Chapters 2 & 3)

Chapter 2. Theory and Development of Strain Analysis Methods

Chapter 3. Theory of Anisotropy of Magnetic Susceptibility

II Field Applications (Chapters 4, 5 & 6)

Chapter 4. Analysis of The Deformation of a Carbonate Platform Incorporated into the Sevier Fold and Thrust Belt, Northwest Montana.

Chapter 5. A comparison of Anisotropy of Magnetic Susceptibility Studies to Clast Based Strain Analysis in Sandstones from the Outer Margin of the Sevier Fold and Thrust Belt, Western Wyoming.

Chapter 6. Application of Strain and AMS Studies to the Irish Variscides of the eastern Munster Basin.

These are the followed by a discussion and conclusion in Chapter 7.

1.2. Previous Studies

The study of rock deformation, strain analysis and petrofabric techniques, such as AMS, is often a large component of structural geology studies. To this extent a large amount of research has been dedicated to this field. A brief literature review of the main topics is presented below, with more detailed accounts of previous work presented in each respective chapter.

The natural deformation of sedimentary rocks and the resulting formation of a tectonic fabric has been studied since the mid to late 19th century (Darwin, 1846; Harker, 1885; Haughton, 1856; Sedgwick, 1835; Sharpe, 1847; Sorby, 1849). It was not until Cloos' seminal study on oolites (1947) that quantitative strain analysis studies were truly carried out. Ramsay (1967) provided the first complete description of a variety of strain analysis methods and the following half century of research on strain analysis studies were largely spring boarded from these seminal texts.

Although the pioneering discoveries in magnetism were recorded, along with the similarities between electricity and magnetism, in 1600 by Gilbert, it was not until 1820 when Oersted discovered how an electric current induced torque in a magnetic compass (Jones and Childers, 2001). This paved the way for fundamental research on electromagnetism, including Amperes discoveries of the properties of the magnetic fields produced by electrical currents. In 1905, Einstein confirmed through quantum physics that magnetism and electricity were intrinsically linked (Einstein, 1923). Shortly after these discoveries on the effects of an electrical current on a magnetic field, research began on the effects of placing different minerals into a magnetic field and it was found that crystal orientation was related to their magnetic susceptibility and hence detectable through magnetic properties (Voight and Kinoshita, 1907). This led to the analysis of rock fabrics using magnetic properties, with both Ising (1942) and Graham (1954) noting that induced magnetism in the rock specimen being analysed was easier along bedding or schistosity planes. Graham established that the axes of Anisotropy of Magnetic Susceptibility (AMS) of a rock could be related to grain fabrics.

This was a major development in the study of petrofabrics, as AMS is capable of accurately averaging the orientation distribution and alignment intensity of all the rock components in a specimen in a quick, reproducible and objective manner. AMS has since been used to establish flow directions in igneous intrusions (Bouchez, 1997; Petronis et al., 2012; Stevenson et al., 2008, 2007), evaluation of tectonic fabrics (Bakhtari et al., 1998; Debacker et al., 2004; Imaz et al., 2000; Parés, 2004; Parés, 2002) and as a comparison to strain analysis techniques (Burmeister et al., 2009; Evans et al., 2003; Hirt et al., 1988; Lüneburg et al., 1999; for more complete

reviews of AMS and tectonic fabrics interested readers are referred to Borradaile and Jackson, 2004 & 2010).

Despite the advances in these fields, the identification and quantification of initial tectonic fabrics formed at the onset of deformation has either been elusive or unsatisfactory. This is partly due to the variety of mechanisms by which rocks deform and the complications of estimating strain in rocks that have a significant primary fabric.

1.3. Purpose of study

Strain analysis studies are a fundamental process in reconstructing pre-tectonic geometries. Strain data provides the basic information for the restoration of stratigraphic thicknesses (Ramsay, 1969) sedimentary basins and for accurately balancing cross sections (Dahlstrom, 1969). Furthermore strain estimates can be related to the rheological properties of deformed rocks and the deformation mechanisms that occur (Etheridge and Vernon, 1981; Lisle and Savage, 1983; Lisle, 1985). By analysing rocks using a suite of strain analysis techniques and fabric tools various interpretations can be made on the manner in which rocks can deform and how these mechanisms relate to regional structures.

Chapter 2.

Strain Analysis Techniques

2. Introduction to Strain Analysis

This chapter presents a brief review of the background theory of traditional strain analysis methods, the theory behind two specific methods, namely the Mean Radial Length method and the Delaunay Triangulation Nearest Neighbour Method, as well as the Intercepts method and reviews some of the problems associated with these methods. Hence this chapter provides the relevant background information for one of the primary questions addressed in this thesis; how effective are these traditional methods at detecting and accurately quantifying strain in areas of low grade deformation.

2.1. Stress and Strain

Strain is a direct result of an applied stress to a body. Stress can be simply divided into two types of forces: forces that act throughout the entire volume of a body and are proportional to its mass, and forces that act upon an internal or external surface of a body. The first, known as body forces, are seen in gravity and centrifugal forces etc., they are measured in units of force per unit volume. The second are surface forces which are seen in everyday occurrences, such as a hammer striking a surface; they are measured in units of force per measured area (for a more complete review of stress within a geological context the reader is referred to Ramsay, 1967). Structural geologists are primarily concerned with surface forces and their effects. As stress conditions within the earths lithosphere change these changes can lead to deformation or strain of the crustal rocks (Ramsay, 1967). The concept of measuring strain in rocks has had its role in geology since the seminal work on the development of cleavage by Sorby (1853) and has evolved drastically since those

early studies. To properly evaluate methods of strain analysis, it is necessary to at least define strain and characterise what features of strain can be measured.

When external forces act on a rock mass the rock is deformed, causing a change in its shape or size (Hobbs and Talbot, 1966; Nevin, 1949). Change in shape of a rock is called distortion, whereas a change in size is called dilation. Both of these usually occur during a single deformation event, resulting in strain (Hobbs and Talbot, 1966). Strain can be considered to be the geometrical expression of the amount of deformation caused by the action of a system of stresses on a body, therefore it is essentially a quantitative measure of deformation and defines the distortion and dilation components (Hobbs and Talbot, 1966). This specification does not include rigid body rotations or translations which can also be part of the deformation (Hobbs and Talbot, 1966). These distortion and dilation components result in bulk strain and are accommodated by crystal plasticity, grain boundary sliding and pressure solution (Ramsay and Huber, 1983). Consequently finite strain can be defined as the end result of a deformation history that can incorporate overlapping or sequential deformation events (Borradaile and Jackson, 2004). As a result discrete sub-fabrics may form at different stages, by different mechanisms, involving different mineral and/or grain-size fractions (Borradaile and Jackson, 2004).

Given the inhomogeneous composition of rocks and complexities of tectonic forces, most deformation and resulting strain is inhomogeneous. Although some work has been carried out on finite inhomogeneous strain, it is generally considered too complicated to yield sensible and meaningful results; instead it is customary to

divide the deformed body into regions of homogeneous strain (Ramsay, 1967). Regions of homogeneous strain are defined as those in which all initially straight lines remain straight after deformation (Hobbs and Talbot, 1966). This definition implies that an initial sphere undergoing deformation becomes an ellipsoid (Hobbs and Talbot, 1966). Natural stresses tend to act in three dimensions and the resulting strain developed is typically triaxial (Hobbs and Talbot, 1966). To calculate the degree of strain in three dimensions, three (or more) mutually perpendicular lines of known initial lengths and orientations are required (Ramsay, 1967). It is rarely possible to obtain a complete data set, additionally information is typically restricted to objects that can be recognized before and after strain (Hobbs and Talbot, 1966). Furthermore evaluations must be made as to whether these strain markers reflect bulk strain, the strain the entire rock mass is undergoing (Hobbs and Talbot, 1966). If the marker and the host rock have different rheological properties then the marker will not represent the bulk strain (Borradaile, 1987; Hobbs and Talbot, 1966; Meere et al., 2008; Treagus and Treagus, 2002; Vitale and Mazzoli, 2005). Similarly if any rigid body rotation of the strain marker has occurred it will not reflect the bulk strain (Hobbs and Talbot, 1966).

2.1.1. Measuring Strain

Various methods have been developed to quantify strain, most of which rely on objects of a known initial shape. This approach was first taken by Phillips (1843) and Sharpe (1847) who used deformed fossils, with Sharpe (1847) noting that the most deformed fossils were present in the beds with the most intense cleavage. This led to Sorby's interpretation of cleavage development (1853). Haughton (1856)

provided the first mathematical description of length changes in fossils due to strain in naturally deformed rocks. This was then followed by the introduction of the strain ellipsoid concept by Harker (1886), which established a framework for strain to be considered and compared across study areas. It was not until the quantitative studies on distorted ooids by Cloos (1947) that truly numerical and methodological strategies were fully applied to strain analysis.

By the early and mid-sixties it was generally thought that strain analysis depended solely on the presence of strain markers of known initial shape, such as fossils or reduction spots (DeSitter, 1964), until Ramsay (1967) set out strain analysis methods which allowed objects, such as sedimentary clasts, of non-spherical and fluctuating initial shape to be used for analysis as strain markers. These methods depended on clast orientation, repacking and intraclast deformation of clasts due to deformation (discussed in detail below). This was a key development in strain analysis, as it allowed estimates to be made from material that did not have any high quality strain markers such as reduction spots.

2.1.2. The Strain Ellipsoid

The clearest method of graphically displaying strain in three dimensions is the strain ellipsoid. As mentioned above any spherical object will develop an ellipsoidal geometry while undergoing homogeneous deformation (Means, 1976; Ramsay, 1967). Similarly if the object being strained is not spherical, its strain ellipsoid can be calculated by selecting three mutually perpendicular axes (the principal strain axes) x, y & z, so that they are parallel to the greatest, intermediate and least

elongation of the strained body respectively (Ramsay, 1967). The three principal axes of this ellipsoid represent the three principal longitudinal strains (Figure 2. 1; Ramsay, 1967). The geometry of these strain axes is the result of the acting principal stresses (σ1≤σ2≥σ3).

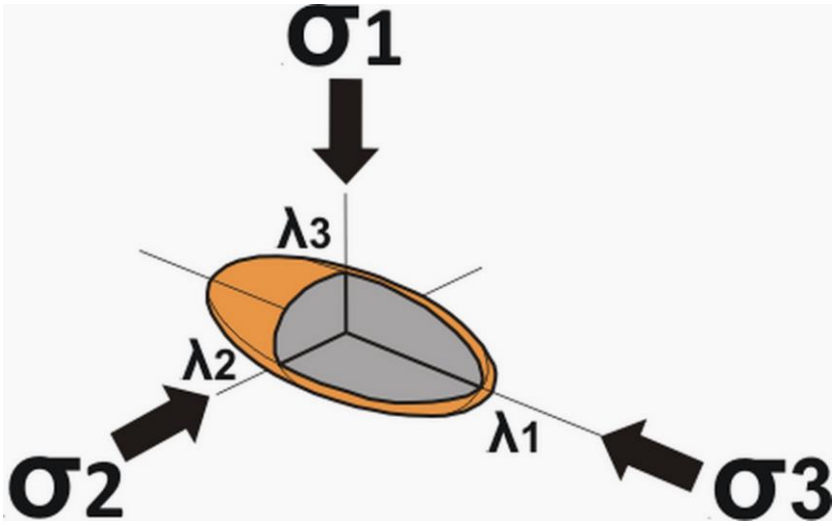

Figure 2. 1 The strain ellipsoid with principal stresses, σ, and strains, λ.

Calculating the lengths of these axes is relatively simple: each axis is equal to the unit diameter of the initial sphere plus the elongation (*e*) along each individual axis (elongation can be positive or negative), $(1+e_1)\geq(1+e_2)\geq(1+e_3)$(Ramsay, 1967). The principal strains are denoted as $\lambda_1 \geq \lambda_2 \geq \lambda_3$ with λ_1 taken as the direction parallel to the longest diameter of the ellipsoid and λ_3 as the shortest diameter (Means, 1976). The strain shape of the ellipsoid can be quantified using K, where $K= \frac{Ln(\lambda 1/\lambda 2)}{Ln(\lambda 2/\lambda 3)}$. The shape of a strain ellipsoid can range from oblate, which represents pure flattening strain, to prolate, which represents pure stretching strain. These geometries are easily plotted on a Flinn diagram (Flinn, 1962a, 1956) and will be discussed in detail below.

Under homogeneous deformation these principal directions/axes remain mutually perpendicular (Means, 1976; Ramsay, 1967). Planes through the ellipsoid containing any two of the principal directions are considered as the principal planes of strain, and their intersection of the strain ellipsoid can be traced as ellipses (Means, 1976). The axial ratio of one of these strain ellipses is termed R and the orientation of the long axis in relation to a reference orientation is termed Φ. For a complete review of the background theory interested readers should refer to the work of Ramsay (1967) and Means (1976).

2.2. Measuring Strain

As mentioned above, Ramsay (1967) developed methods whereby strain estimates could be made using parameters derived from the following: strain marker orientation, strain marker shape, position of strain marker centres, distance between centres and the angle between centres. The two main types of methods that emerged were the $R_f/Ø$ method and centre to centre or nearest neighbour method (Ramsay, 1967). The $R_f/Ø$ method determined finite strain from randomly oriented populations of deformed elliptical objects, while the centre to centre method used the distance between centres of adjacent objects, provided the objects were evenly distributed prior to deformation.

Subsequent to the initial $R_f/Ø$ method, alternative methods based on marker shape and orientation have since been developed (Borradaile, 1976; Dunnet and Siddans, 1971; Dunnet, 1969; Elliott, 1970; Lisle, 1985, 1977a, 1977b; Matthews et al., 1974; Mulchrone and Meere, 2001; Mulchrone et al., 2003; Peach and Lisle, 1979; Robin,

1977; Shimamoto and Ikeda, 1976; Yu and Zheng, 1984). Dunnet (1969) developed an $R_f/Ø$ diagram method, while Elliott (1970) applied a similar graphical approach, the shape factor grid. Dunnet and Siddans (1971) took non-random initial distributions into consideration for the $R_f/Ø$ diagram method. Unfortunately these methods are subjective and essentially non-repeatable. An algebraic method that accommodated statistical analysis of any errors produced was introduced by Matthews et al. (1974). The drawback of this method was that the orientation of the principal strain axis needed to be calculated independently prior to using the method. Similarly Robin, (1977) derived a method that allowed analysis of strain markers of any shape but required prior independent knowledge of the principal strain axes. In order to address some of the above issues with calculating strain from distributions of elliptical objects, Mulchrone et al. (2003) introduced a non-graphical and repeatable approach to strain analysis, the Mean Radial Length (MRL) method.

The second strain analysis methodology is based on using object to object separation and assumes that the marker objects are anti-clustered and that the relative position of the centres of these objects is directly related to the orientation and magnitude of the finite strain ellipse (Ramsay, 1967). Compared to the $R_f/Ø$ method the centre to centre method involves relatively complicated calculations and is particularly labour intensive. As a result has received significantly less attention then the $R_f/Ø$ method. The first major modification of the Ramsay's centre to centre method was the development of a graphical approach which used all object-object separations by Fry (1979). This was subsequently further improved

as the Normalised Fry Method (Erslev, 1988) and the enhanced Normalised Fry Method (Erslev and Ge, 1990). McNaught (1994) further extended these methods by facilitating the use of non-elliptical markers by determining best-fit ellipses for these irregular shaped objects. The Fry methods have been regularly incorporated into automated analysis tools (Ailleres et al., 1995; Launeau and Robin, 1996; Launeau et al., 2010). Despite popularity and ease of use, these methods are subjective and not entirely repeatable. Mulchrone (2002) used Delaunay triangulation, to characterise nearest neighbour separations and define object centres. This Delaunay Triangulation Nearest Neighbour Method (DTNNM) was argued to be less subjective and a more computationally efficient strain analysis technique than the Fry methods (Mulchrone, 2002).

2.2.1. Mean Radial Length (MRL)

The Mean Radial Length (MRL) (Mulchrone et al., 2003) method relies on the orientation of grains to determine strain. The premise of the MRL method is that the mean radial length of a truly isotropic distribution of ellipses is a constant, independent of orientation, and as result forms a circle (Figure 2. 2). If the population of ellipses become deformed, either by shape change or rotation, this circle becomes an ellipse (Mulchrone et al., 2003). The resulting ellipse can then be related to the finite strain ellipse in the same manner any physical circle is after deformation (Mulchrone et al., 2003). To paraphrase, a population of randomly oriented ellipses have an MRL equal to a circle, while a population of ellipses with a

preferred orientation have an MRL equal to an ellipse representative of the strain ellipse.

The MRL method can be applied accurately if the deformation being measured is homogenous and passive, and if the viscosity contrast is low between the ellipsoidal markers and the matrix (Mulchrone et al., 2003). Additionally the following assumptions are made for the ellipse populations in the unstrained state: the long axis orientation is a uniform random variable; and the distribution of axial ratios (R) is independent of orientation, (i.e. R is isotropic).

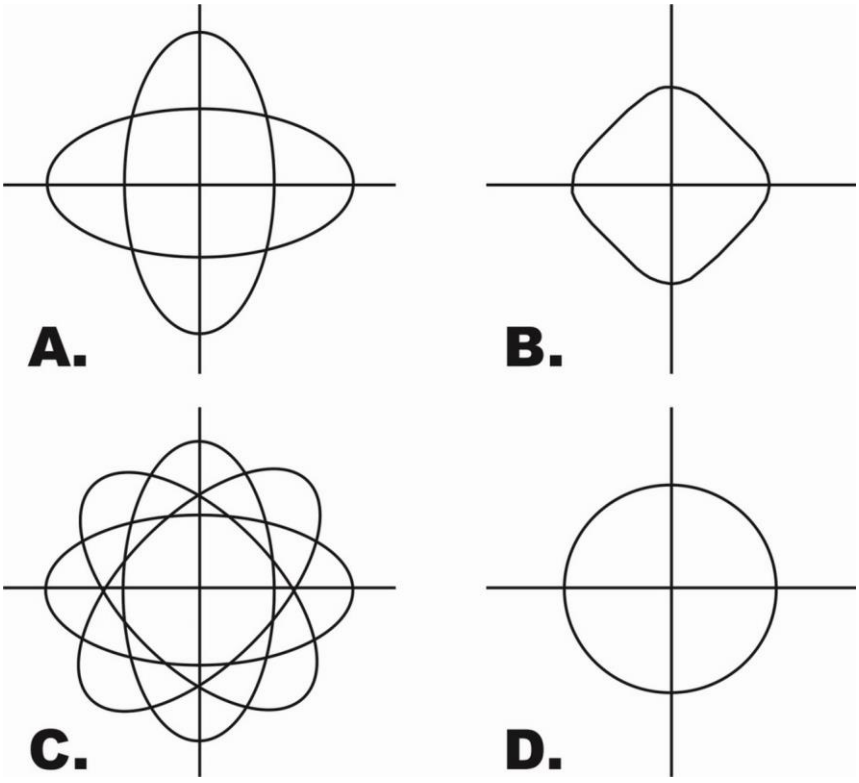

Figure 2. 2 The MRL relies on the orientation of grains to determine strain. The method requires that randomly orientated ellipses have a Mean Radial Length that equates to a circle, whereas ellipses with a preferred orientation have MRL averages that equate to an ellipse. **A.** Shows two ellipses orientated at 90° and **B.** plots their mean radial length. **C.** Shows four ellipses orientated at 45° and **D.** plots their mean radial length. Redrawn from Mulchrone et al. (2003).

2.2.2. Delaunay Triangulation Nearest Neighbour Method (DTNNM)

As mentioned above Ramsay (1967) first introduced the concept of calculating finite strain by using the distance between centres of adjacent objects. The method involves determining the centres of objects that were originally nearest neighbours, and connecting these object centres with tie lines and analysing the changes in length and orientation of these tie lines due to deformation (Ramsay and Huber, 1983). The technique is based on the assumption that the lines between nearest neighbours had a uniformally random distribution in the unstrained state. In the strained state distances between clasts become shorter in the tectonic shortening direction and longer in the tectonic stretching direction.

Therefore the tie lines can be used to calculate the shape and orientation of the strain ellipse, as line orientation and line length change with deformation (Ramsay and Huber, 1983). The centre to centre technique enables the estimation of bulk rock strain using the redistribution of rock components (ooids, grains , clasts, etc.) in the deformed rock and the distances between these points as extended line elements (Ramsay and Huber, 1983).

Implementation of this technique in two dimensions involves determining pairs of nearest neighbours, calculating the distance between their centres (d_i) and the orientation of the line joining them (α_i) (Figure 2. 3). The minimum and maximum average values of di (dmin and dmax) are estimated by plotting di against α_i in a polar plot. By dividing d_{max} by d_{min} the axial ratio is calculated and this provides an estimate of ellipticity, R (Ramsay and Huber, 1983). The orientation of the extensional axis of the strain ellipse is taken parallel the orientation of d_{max}. The Nearest Neighbour method is essentially a measure of strain due to matrix

deformation and pressure solution (Mulchrone, 2002) and as a result measures bulk rock strain and is generally closer to the true finite strain (Meere et al., 2008; Pastor-Galán et al., 2009). Despite this, the centre-centre methods are relatively unused compared to other $R_f/Ø$ methods. This is in part due to problems in objectively defining the object centres, the high number of individual calculations required and related labour intensity as well as interpretation problems (Erslev, 1988).

The application of Delaunay Triangulation to the centre-centre method removed subjectivity in measurement in defining centres (Mulchrone, 2002). The subsequent automation of the technique (Mulchrone, 2005) reduced the labour intensity associated with the large number of calculations. The more recent work by Mulchrone et al. (2013) further reduced the labour intensity by introducing a semi-automated process for identifying objects and the required parameters and combining it with a statistical analysis method.

Unfortunately problems with the validity of the estimates derived from the centre-centre method still exist. This is mainly due to the complex relationship between the original object shapes and the competency contrast between the objects and the matrix, as well as the influence of neighbouring objects (Ramsay and Huber, 1983). Furthermore the variation in tie line lengths is independent of initial line orientation and is a function of particle size and initial degree of packing (Ramsay and Huber, 1983).

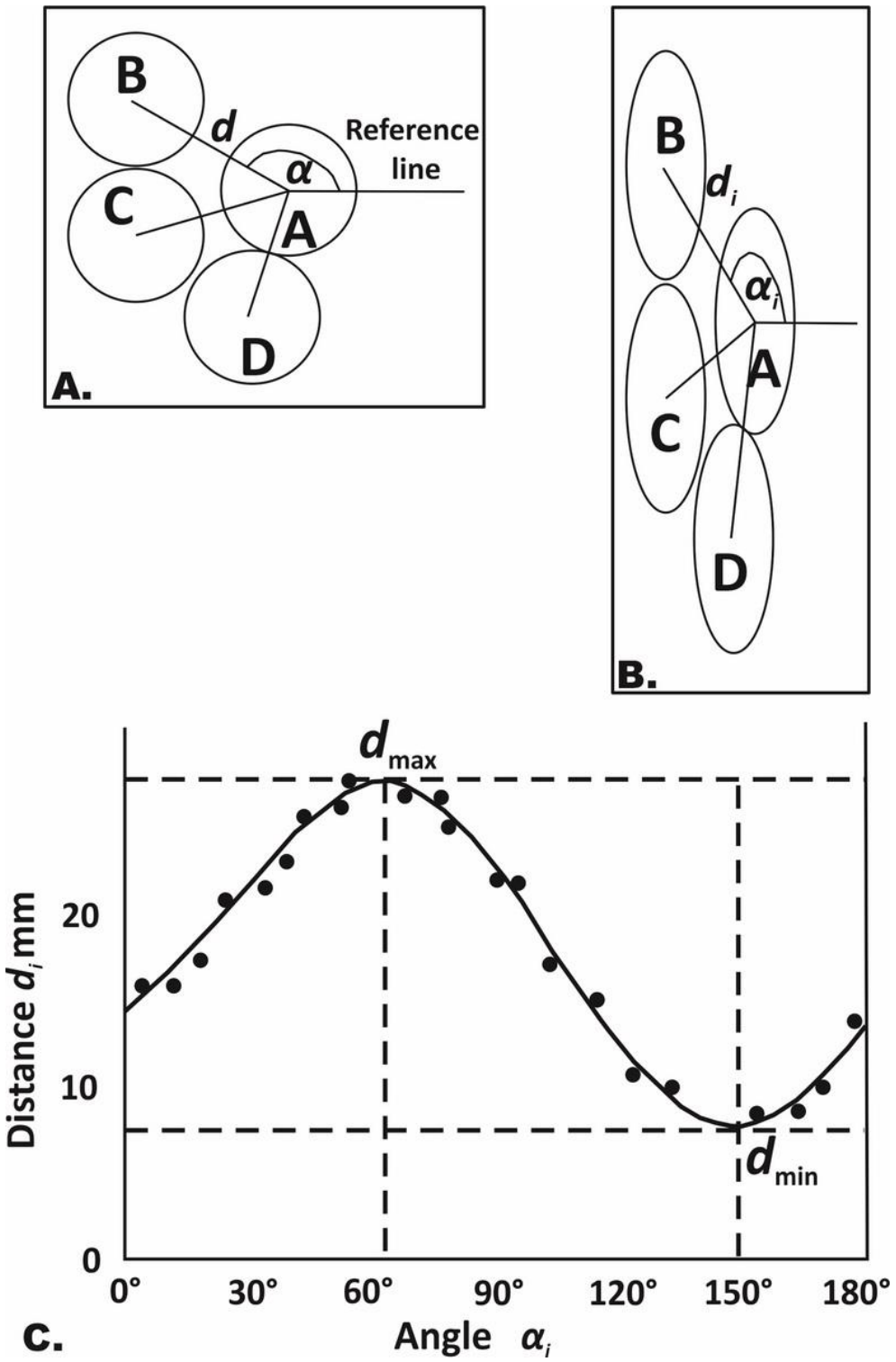

Figure 2. 3 **A.** The lengths, **d,** and orientations, **α**, of tie lines joining object centres are marked. Centre to centre techniques are based on the assumption that the tie-lines between nearest neighbours have a uniformally random distribution in the unstrained state. In the strained state distances become shorter in the tectonic shortening direction, as seen in **B**. **C.** Polar plot of **d** vs **α**, the apex of the curve shows the orientation of the longest direction and the nadir shows the orientation of the shortest direction. Redrawn from Park (1997).

2.2.3. Automation

The use of MRL and DTNNM requires the analysis of multiple parameters for at least 150 objects per calculation to maintain statistical integrity (Meere and Mulchrone, 2003). In order to reduce the labour intensity and subjectivity in determining the required parameters of the MRL and DTNNM methods Mulchrone et al. (2013) combined the MRL and DTNNM method in a Mathematica package that carries out image analysis, estimates strain and calculates statistical analysis of the errors in one work flow. This semi-automated method requires the manual tracing of grain boundaries from a microphotograph (Figure 2.4 A&B), after which the Mathematica package then identifies the grain boundaries (Figure 2. 1Figure 2.4C) and all of their morphological parameters required to calculate the DTNNM (Figure 2.4 D&E) and MRL results as well as bootstrapping the data, to provide confidence intervals (Figure 2.4 F&G).

This integration of image analysis, parameter extraction and strain analysis routines significantly reduces the time and labour intensity of geological strain analysis studies. Although automation of strain analysis techniques has received considerable attention in the past (Ailleres et al., 1995; Erslev and Ge, 1990; Heilbronner, 2000; Masuda et al., 1991; McNaught, 1994; Mukul, 1998; Mulchrone et al., 2005; Panozzo, 1984), there is still a large degree of user input into the process. The main limiting step has been the recognition and fitting of best fit ellipses to geological strain markers such as sedimentary clasts. It has been found that an initial manual identification of the boundaries of the objects to be analysed, followed by completely automated strain analysis is the most mentally bearable

and least subjective method (Mulchrone et al., 2013). The manual identification of object boundaries can be done relatively quickly with tracing paper and an ink pen. They can then be scanned and analysed using the Mathematica code developed by Mulchrone et al. (2013) with very little extra input from the user. Additionally the grain boundary maps can also be analysed for grain size, shape and sorting analysis using a similar piece of Mathematica code developed by McCarthy (in prep).

2.2.4. Statistical Analysis

The strain estimates from the MRL and DTNNM methods were analysed using the Bootstrap method to calculate errors associated with the data and provide confidence intervals for R and Φ. As mentioned above the Bootstrap method has been incorporated into the Mathematica code for strain analysis presented by Mulchrone et al. (2013). The Bootstrap method constructs approximate sampling distributions for complex statistical estimates (Efron and Gong, 1983; Efron, 1979). It generates multiple "samples" of a given dataset by repeatedly resampling the original dataset with replacement. By analysing the multiple generated samples multiple parameter estimates can be calculated. These artificial parameter estimates should closely approximate the true sampling distribution of the parameters, allowing estimation of suitable confidence intervals by calculating the 90, 95 and 99% percentiles. In higher dimensions (in 2D strain analysis that data are bivariate), elliptical regions centred on the mean are found which enclose a specified percentage of the data using the built-in EllipsoidQuantile function of Mathematica (Mulchrone et al., 2013).

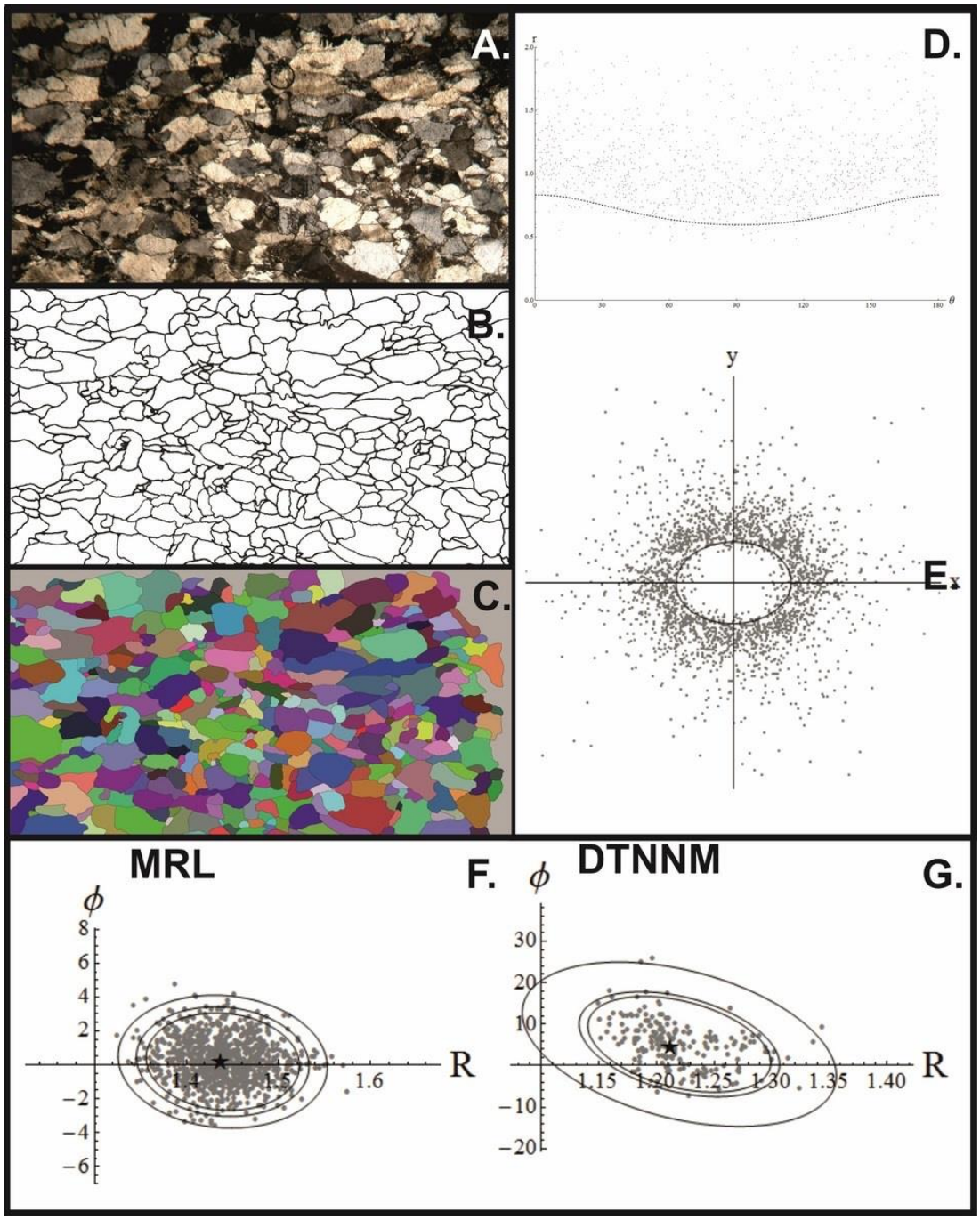

Figure 2.4 Generalised workflow for the automation of the MRL and DTNNM methods. **A**. Photograph of a sample. **B**. Manual trace of grain boundaries. **C**. Identification of grain boundaries in Mathematica. **D**. Polar plot of the nearest neighbour data, r (distance from origin) is plotted against orientation and superimposes the curve representing the best-fit ellipse. **E**. Cartesian or Fry style plot of the nearest neighbour data. **F.** Bootstrap plot of the MRL data with 90, 95 & 99% confidence intervals and the actual estimate marked by a star. **G**. Bootstrap plot of the DTNNM data.

While the Bootstrap method has been shown to be applicable to geological strain analysis (McNaught, 2002; Mulchrone et al., 2003), the complete background theory for bootstrapping strain estimate data is beyond the scope of this research (Interested readers are referred to Efron, 1979; Efron and Gong, 1983; McNaught, 2002; Mulchrone et al., 2003).

2.2.5. Intercepts

As a comparison to the clast based methods discussed above, analysis using the Intercepts software package (Launeau and Robin, 1996; Launeau et al., 2010) has been applied to the same samples. This method is a style of measuring crystal preferred orientation (CPO) and records the orientation of all the linear elements in an image. It is a quick and relatively simple way of establishing a quantitative measure of fabric strength. The intercepts can be applied to unprocessed images and applies various thresholding methods to define grain boundaries, as well as the grain boundary maps produced for the MRL and DTNNM methods.

The Intercepts method involves analysing a circular area of an image at 6° intervals along a set of parallel lines spaced with one pixel intervals (Launeau and Cruden, 1998). The intercepts between object boundaries and the analysis lines in all directions are recorded. This is the “rose of intercepts”, by dividing the total area of objects by their number of intercepts in each direction provides the “mean rose of intercept lengths” (Launeau and Cruden, 1998). This is a measure of the images’ anisotropy and similar to strain analysis studies this is represented by a ratio, R, and the orientation of the long axis Φ (Figure 2.5). The intercepts method is a measure of fabric strength rather than a method of estimating strain, therefore its R values

may represent an underestimate compared to the MRL and DTNNM, but the orientations produced should be similar. For the Intercepts analyses of the unprocessed photos and the grain boundary maps, mean tensor values are reported and for the Shape Preferred Orientation (SPO) analysis of the grain boundary maps, the mean shape results are reported.

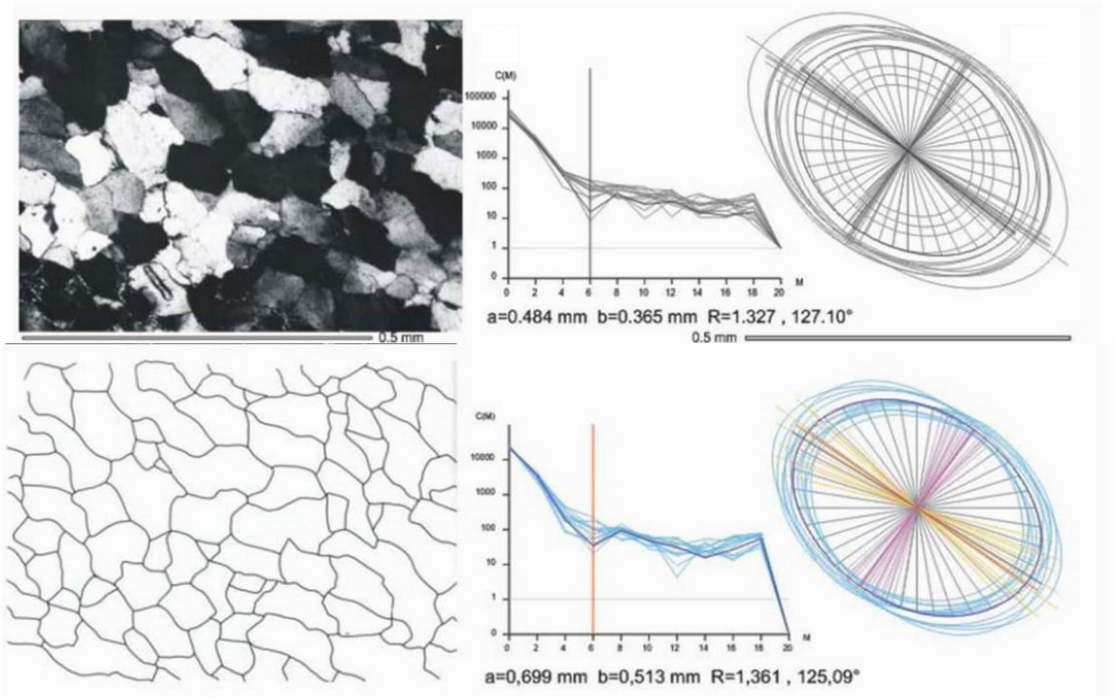

Figure 2. 5 Generalised output from Intercepts software. Both rows represent output for the sample, with the top row displaying the results for an unprocessed image and the bottom row displaying the results for an image of manually traced grain boundaries. Modified from Launeau and Robin (1996).

2.2.6. Plotting Strain Data

As mentioned above the traditional method for reporting 2D strain data typically involves R and Φ, which represent the axial ratio of the strain ellipse and the orientation of the long axis of that ellipse, respectively. The majority of 2D strain graphs in this study plot R against Φ. Additionally, in order to represent strain orientations in comparison to AMS fabrics the Φ angle is plotted as a pitch in the sampling plane on a stereonet.

Determining the orientations and magnitudes of the principal axes of the strain ellipsoid requires data from strain ellipses measured from a minimum of two planes throughout a sample. This is not a trivial calculation and as a consequence numerous attempts have been made at determining the most accurate best fit ellipsoid (Launeau and Robin, 2005; Mookerjee and Nickleach, 2011; Owens, 1984; Ramsay, 1967; Robin, 2002). Ramsay (1967) considered three mutually perpendicular planes and derived a series of equations to solve for the best-fit ellipsoid**.** Owens (1984) described a method for the calculation of the best-fit strain ellipsoid from 3 or more non-perpendicular planes using a least squares approach, as well as applying a scale factor. The Robin method (Robin, 2002; Robin & Launeau, 2005) utilised a similar algebraic approach, with or without a scale factor in the Ellipsoid application. Mookerjee and Nickleach (2011) presented a method which attempts to minimise the errors between the best-fit ellipsoid and any of the measured planes used as input data.

The most conventional and practical method of representing finite strain states is to use the strain ellipsoid. Flinn plots (Figure 2. 6; Flinn, 1956 & 1962) are used to represent all possible ellipsoid geometries in a 2D space. The standard convention is to use a logarithmic plot, where the ratio of the maximum to intermediate ellipsoid axes (lg X/Y) is plotted as ordinate and the ratio of the minimum to intermediate axes (lg Y/Z) is plotted as abscissa (Flinn, 1956, 1962; Ramsay, 1967). When plotted in this manner prolate spheroids plot along the vertical axis and oblate spheroids plot along the horizontal. As these ellipsoids become less spherical, they plot further away from the origin (Wood, 1973). The ratio *K*

((X/Y)/(Y/Z)) can be used to describe the symmetry of the ellipsoid. If *K*>1 then the ellipsoid is considered to have an axial symmetric constriction and has one long axis and two shorter axes, (Ramsay, 1967). If *K*<1 the ellipsoid is considered to be axially symmetrically flattened and has two long axes and one shorter axis (Park, 1997). Between these two fields of flattening and constriction is the field of plane strain (*K*=1) and which only occurs when strain is acting in the XZ plane. *K* represents the slope of a line from the data point to the origin at (1,1), so that $K = a - \frac{1}{b} - 1$ with $a = \frac{x}{y}$ and $b = \frac{y}{z}$. *K* on the diagram can define a series of domains, so that when $K = 0$ the finite strain ellipsoid is uniaxial oblate and has been flattened perpendicular to Z. As K tends towards 1 the ellipsoid moves away from being purely uniaxial, but remains in the oblate and flattened domain. For K values greater than 1 the ellipsoid lies in the prolate or constrictive domain, and for $K = \infty$ the ellipsoid is purely uniaxial prolate and stretched along the X axis (Park, 1997). The degree of how far removed the ellipsoid is from spherical (ellipsoid eccentricity) is calculated as $\sqrt{(\mathrm{X/Y})2 + (\mathrm{Y/Z})2}$.

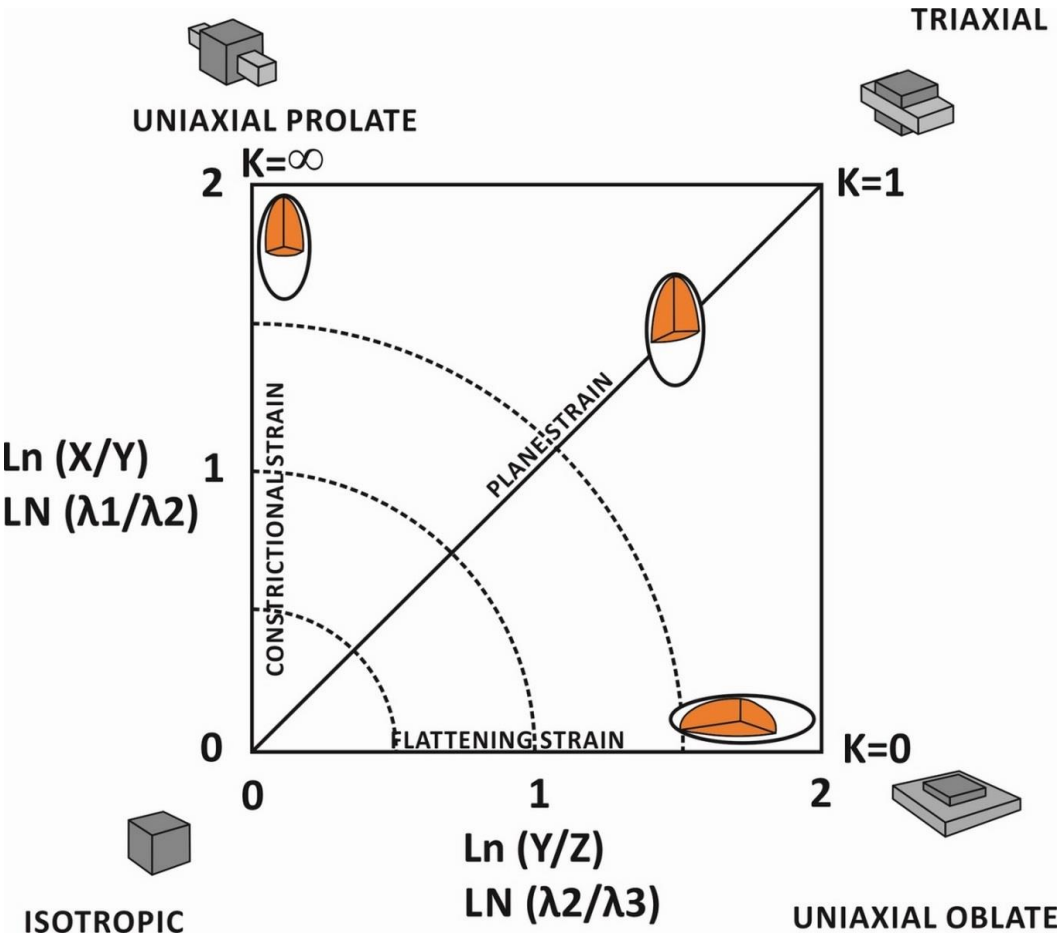

Figure 2. 6 Flinn plot, showing range of ellipsoid geometries, modified from Ramsay (1967).

2.3. Strain Markers, Progressive Deformation and Cleavage Development

Regardless of what strain markers are used to facilitate strain analysis they are all subject to deformation and the variety of mechanisms that accommodate deformation. Hence it is important to consider these deformation mechanisms and how they affect populations of strain markers.

2.3.1. Fabric Development

In order to accommodate the shape change of a rock mass undergoing deformation, individual mineral components are required to become rearranged mechanically either by rotation or internal deformation, with some components undergoing mass transfer, through mechanisms such as solution and precipitation

(Ramsay, 1967; Ramsay and Huber, 1983; Vernon, 2004). This combination of textural and chemical alteration, due to strain and mass transfer, results in a geometric organisation of the rock's various components, such as preferred orientations of minerals (Sorby, 1856; Wood, 1974). This results in a tectonic fabric or cleavage. The term fabric refers to the total sum of grain shape, grain size and grain configuration in a rock (Dennis, 1967). While fabric can refer to undeformed rocks, cleavage can be defined as a population of elements of a secondary planar fabric that impart a mechanical anisotropy to a deformed rock (Dennis, 1967). This anisotropy is essentially the result of a flow phenomenon that typically forms perpendicular to the direction of maximum shortening (Cloos, 1947; Hobbs and Talbot, 1966; Means, 1976; Ramsay, 1967; Wood, 1974). Cleavage is a set of systematic variations in mineralogy and fabric, that have been brought about by the need to accommodate distortion of the rock body (Davis and Reynolds, 1996). These systematic variations in mineralogy and fabric produce a domainal structure, or structural lamination, composed of alternating cleavage domains and microlithon domains (Davis and Reynolds, 1996). The cleaved domains are typically thin and mica rich and can be anastomosing to subparallel laminations in which the fabric of the host rock has been strongly rearranged and/or partially removed (Davis and Reynolds, 1996). The microlithon domains are typically narrow lenses in which the mineralogy and fabric of the protolith have largely been preserved (Davis and Reynolds, 1996).These tectonic fabrics can initiate mechanically during diagenesis and continue to develop by chemical-mechanical processes during low grade metamorphism (Vernon, 2004). The majority of phyllosilicate alignment and resulting cleavage development occurs by solution of old grains and

neocrystallisation as well as physical grain rotation, when dewatering and lithification processes have completed or are near completion (Vernon, 2004). Therefore cleavage formation cannot be viewed simply as a purely mechanical process, as chemical reactions are intimately involved with the later stages, additionally the compositional domains of cleavage require redistribution of chemical components (Vernon, 2004). This has serious implications for strain analysis.

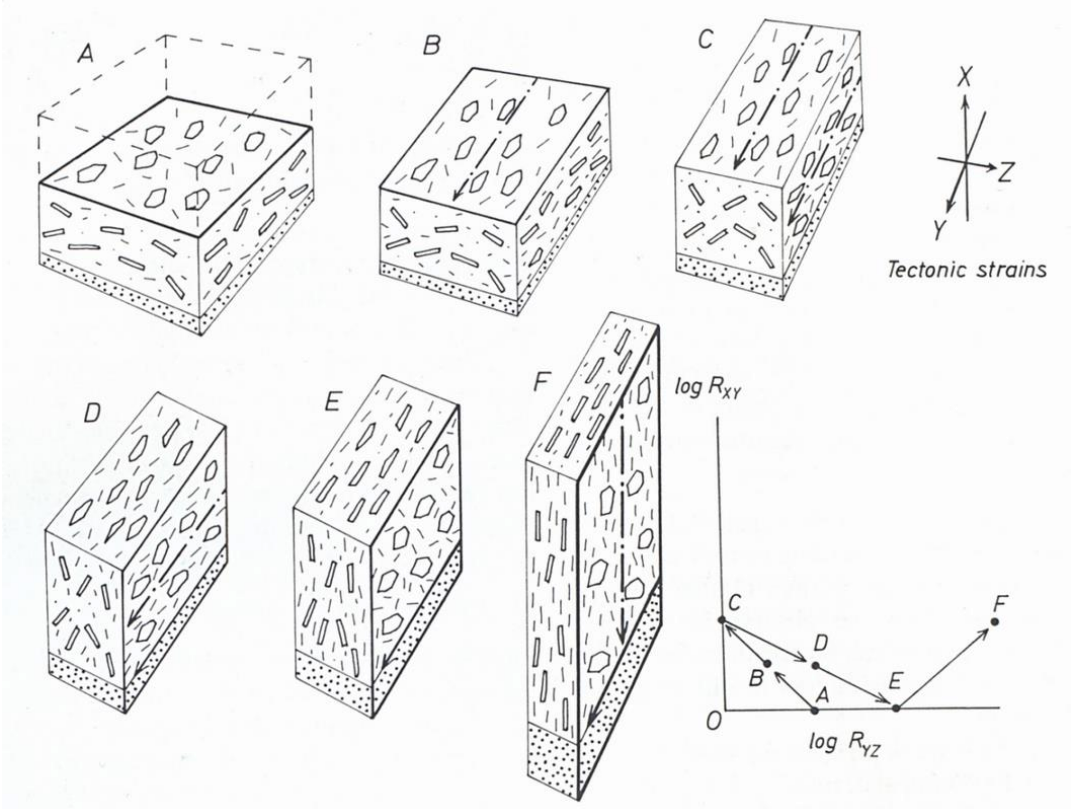

Figure 2. 7 Progressive deformation stages as discussed in the text (From Ramsay and Huber, 1983). **A.** represents an initially compacted sedimentary rock. **B**. is the earliest deformation stage and represents an extremely weak tectonic lineation. **C**. as the strength of the tectonic lineation becomes approximately equal to the strength of the bedding foliation a pencil cleavage is formed. **D**. the tectonic lineation starts to become a foliation, forming embryonic cleavage. **E**. the tectonic foliation has become the dominant fabric in the rock and a penetrative cleavage is formed. **F**. as flattening continues the rock mass undergoes stretching. The Flinn diagram illustrates this evolution form an initially oblate fabric through prolate and back into oblate.

2.3.2. Progressive Fabric Development

The reorganisation of the components of a rock mass into a tectonic fabric can be considered as a series of progressive changes or a deformation continuum (Ramsay and Huber, 1983). This progressive deformation can be viewed synchronously with changes in the strain ellipsoid. Ramsay and Huber (1983) presented this simply by defining stages of a hypothetical undeformed sedimentary rock mass featuring a primary bedding plane fissility (Figure 2.7 A) undergoing progressive deformation.

The onset of deformation starts with a contraction sub-parallel to the bedding plane (Figure 2.7 B). This can be accompanied by volume loss associated with mechanical closure of pore space and expulsion of pore water, if this process had not completed during diagenesis. The initial bedding plane fissility will become less distinct due to the rotation of platy elements and the development of weak linear orientation of acicular minerals. This first stage results in a weak bedding fabric and extremely weak tectonic lineation.

As tectonic strain increases and deformation and volume loss continues a more defined linear fabric is developed (Figure 2.7 C), usually producing a pencil cleavage. This stage is associated with 10 to 25% shortening and the strain ellipsoid takes on a prolate geometry.

With increasing strain the prolate/linear fabric tends towards a flattened or oblate fabric (Figure 2.7 D). This is brought about by progressive shortening in the tectonic Z direction and elongation in the X direction. Mineral rotations and/or new

mineral growth along the tectonic extension plane form a weak or embryonic cleavage.

When the tectonic strain has become strong enough to sufficiently overprint bedding a dominant planar cross cutting fabric or cleavage is formed. Platy and acicular minerals are well oriented in the cleavage plane (Figure 2.7 E). The resulting strain ellipsoid should have an oblate or flattened 'pancake' geometry. The development of cleavage concludes with a progressively intensifying linear structure in the cleavage surface parallel to the tectonic X direction and a strongly developed planar cleavage (Figure 2.7 F). This cleavage is inherently linked to the finite strain state, with the fabric forming perpendicular to the shortest axis (Z) of the finite strain ellipsoid and increases with intensity with the strain ratio R_{xz} (Ramsay and Huber, 1983).

2.3.3. Conditions for Cleavage Development

Tectonic fabric development is typically associated with grain or clast alignment, brought about by mechanical grain rotation, pressure solution and neocrystallisation. While slaty cleavage is typically associated with lithologies that are too fine for strain analysis techniques that require clear definition of grain boundaries and geometries, spaced cleavage in fold and thrust belts is typically associated with lithologies that display alignment of clasts big enough to allow for strain analysis studies. The presence of spaced cleavage provides some information in regards to the conditions associated with fabric development. Spaced cleavage initiates under low grade metamorphism, with approximate temperatures of 200°C and pressures of 5 kb (Engelder and Marshak, 1985; Marshak and Engelder, 1985;

Mitra and Yonkee, 1985). This typically equates to crustal depths of 5-8km depth. Spaced or disjunctive cleavage is characterised by a planar/domainal fabric with zones of less deformed microlithons, which resemble the protolith, and deformed selvage zones (Davidson et al., 1998; Holl and Anastasio, 1995). These selvages are associated with clay rich seams are fine grained, optically opaque and have straight to anastomosing geometries with straight or serrated edges (Davidson et al., 1998). These dark fine grained areas are composed of insoluble residues that have become concentrated due to dissolution of quartz or calcite, depending on the bulk chemistry of the rock (Alvarez et al., 1976, 1978; Engelder and Marshak, 1985; Marshak and Engelder, 1985; Davidson et al., 1998; Vernon, 2004; Passchier and Trouw, 2005). Pressure solution is driven by diffusive mass transfer, involving dissolution, evidenced by sutured grain boundaries, and precipitation, evidenced by fibrous overgrowths (Davidson et al., 1998; Vernon, 2004). This process initiates with strain concentrating at grain-to-grain contacts causing the dissolution and concentration of this dissolved grain material in grain boundary fluid films (Marshak and Engelder, 1985). This dissolved material then diffuses to areas of lower strain precipitates (Marshak and Engelder, 1985). Davidson et al. (1998) argue that these dissolution planes and fibrous overgrowths define the principal axes of the finite strain ellipsoid (X>Y>Z) in the same manner that slaty cleavage defines these axes (Wood, 1974).

2.4. Problems with Strain Analysis

The stark conclusions reached by Hobbs and Talbot (1966) on the limits of strain analysis seem to be the same limitations that prevail today. These limitations are summarised below:

1) the initial shapes of many geological bodies cannot be exactly measured within a small enough range to yield useful results;

2) even if the initial shapes can be measured within a tight range, not enough information can be gleaned from the rock to solve the mathematical problem unless assumptions concerning the state of strain are made;

3) the assumptions made by geologists concerning the states of strain in deformed rocks are not justified, since they are often part of the required information.

An important concern for any strain analysis is the properties of the strain markers studied. Clearly the most ideal strain markers are those that were originally spherical that deform passively with no competency contrast between the marker and the host. If this holds true then the post finite strain shape of the marker will reflect that of the finite strain ellipsoid (Ramsay, 1967). So true strain markers are those “geologic bodies within a rock which, during the deformation of that rock, have retained their identity but did not differ from their surrounding material in their mechanical behaviour" (Robin, 1977). Unfortunately these strain markers, such as reduction spots, are far from ubiquitous, leading to the development of methods based on the properties of object populations discussed above. The single most conceptual problem for these methods besides assumptions concerning the primary fabric of a rock mass, such as the initial orientation of objects and degree of

packing, is that of passive deformation. Rock particles and their surrounding matrix rarely deform in a passive or homogeneous manner, this is due to ductility contrasts between the marker and the host rock.

2.4.1. Primary Fabric

The largest problem for most strain analysis methods that employ sedimentary clasts as strain markers is that of an initial primary fabric. Most strain analysis methods, particularly the Rf/Ø style, rely on the assumption that clastic sediments have a random initial orientation fabric. This is rarely true, as most sediments have a preferred orientation prior to deformation (Holst, 1982; Paterson and Yu, 1994; Seymour and Boulter, 1979).

Even if a random depositional fabric existed, a preferred orientation would probably develop during diagenesis and compaction through active or partly rigid body rotation (Borradaile 1987). The only cross-sections that might exhibit random initial fabrics are those that are parallel to bedding. Patterson and Yu (1994) highlighted further points concerning the assumptions made by structural geologists when considering the primary fabrics of sedimentary rocks used for strain analysis. These incorrect assumptions typically made during strain analysis include (Paterson and Yu, 1994): individual grains are spherical prior to straining; orientations and shapes of grain populations define spherical, pre-strain fabric ellipsoids (i.e. grains have an initial uniform distribution); pre-strain fabric ellipsoids are symmetric around bedding; and initial fabrics are recognizable even after straining. Taking these incorrect assumptions into account clearly illustrates that the starting or pre strain fabric ellipse/ellipsoid is rarely circular/spherical. Paterson

and Yu (1994) argued that failing to take the consequences of these assumptions into account has serious implications for strain analysis, particularly due to the wide range of pre-strain ellipsoid shapes. The first major implication discussed by Paterson and Yu (1994) is that small strain ellipse principal ratios (1.5 or less) may be largely influenced by depositional fabrics. Furthermore the XY planes of the estimated strain ellipsoids may not be parallel to the foliation, except at large strains (strain ratios >3.0) (Paterson and Yu, 1994).

To resolve these implications they suggest that a correction for the existence of primary fabrics must be applied. This largely echoes earlier reports that suggested that minor deviations in the types of primary fabrics can cause significant errors in finite strain estimates (Seymour and Boulter, 1979). Multiple efforts have been made to remove the effects of primary fabrics on strain estimates (Dunnet and Siddans, 1971; Elliott, 1970; Holst, 1982; Lisle, 1977a; Matthews et al., 1974; Seymour and Boulter, 1979; Shimamoto and Ikeda, 1976), but unfortunately most of these procedures utilise one or more of the above assumptions and/or assume the existence of independent information concerning the strain ellipsoid. The algebraic approach of Wheeler (1986) involves superimposing the tectonic strain ellipsoid on a bedding symmetrical ellipsoid. Paterson and Yu (1994) contested this method on the grounds that sandstones rarely have bedding as a definite symmetry plane and that data for primary fabric ellipsoid ratios and orientations is usually non-existent. To counter this they suggested that the final strain estimate could be bracketed into a triangular area on a Flinn plot (Figure 2.8) by multiplying the estimated strain ellipsoid by an average reciprocal pre-strain ellipsoid (Paterson and Yu, 1994). The obvious problem is that of what magnitude and orientation of the

principal axes to use for the pre-strain ellipsoid. The magnitude of the principal axes can be derived by determining an average of multiple measured pre-strain ellipsoids (the averages used by Paterson and Yu (1994) are 1.31:1.14:1). While magnitude data can easily be averaged across multiple samples, unless some information is known about the primary fabrics orientation, orientation data presents a problem in that it can vary greatly across multiple samples. In order to resolve this, the estimated strain ellipsoid can be multiplied by the reciprocal pre strain ellipsoid multiple times in numerous orientations to create an error bracket. Although this seems complicated, Ramsay (1967) showed that all possible combinations of two ellipsoids result in an approximate triangular region on a Flinn plot.

The three extreme points reflect three of the six possible ways of coaxially combining two ellipsoids. Although this may seem counterproductive in terms of strain analysis, in that it might add too large an error bracket to what is already an approximate measurement, it will have a larger effect on weakly deformed samples and a much smaller effect on strongly deformed samples. The principal axial ratios of pre-strain ellipsoids tend to be small and as a result the triangular-shaped confidence bracket will be relatively small when estimated finite strain ellipsoids are combined with pre-strain ellipsoids (Paterson and Yu, 1994)

The method of Paterson and Yu (1994) can be simplified into a two-step process: calculation of a reciprocal pre-strain ellipsoid using the estimated/averaged pre-strain axial ratios and orientation; and the multiplication of this reciprocal ellipsoid

and the estimated strain ellipsoid, the resulting ellipsoid is then representative of a theoretically more correct estimate of the strain ellipsoid (Wheeler, 1986).

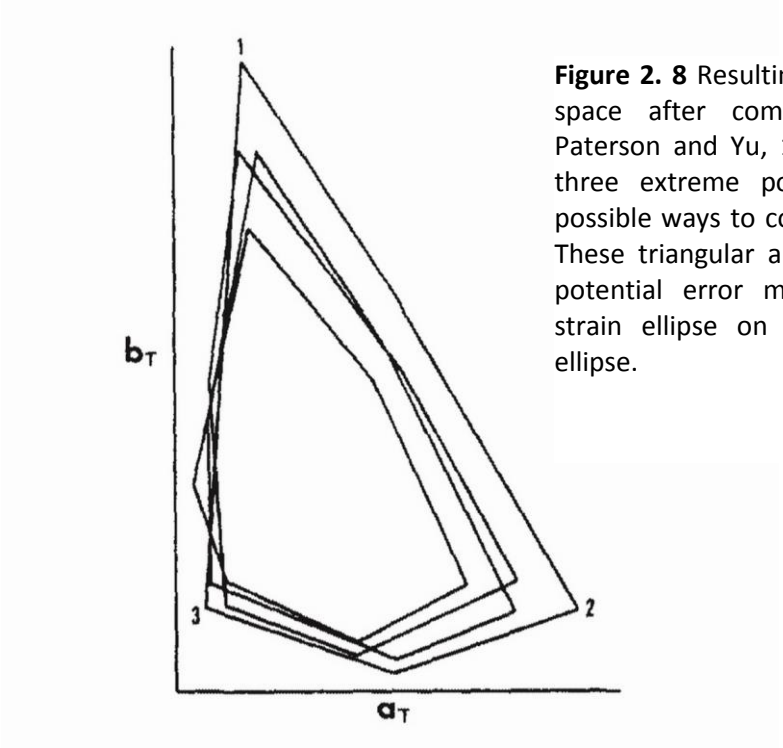

Figure 2. 8 Resulting triangular fields in Flinn plot space after combining two ellipsoids (From Paterson and Yu, 1994; after Ramsay, 1967).The three extreme points represent three of the possible ways to coaxially combine two ellipsoids. These triangular areas are representative of the potential error margin when superimposing a strain ellipse on a pre-existing bedding fabric ellipse.

2.4.2. Non-Passive Deformation

Most of the existing strain analysis techniques make the assumption that clasts used as markers deform passively, i.e. the marker and surrounding rock matrix responded to deformation identically. Meere et al. (2008) concluded that a number of existing strain analysis techniques using sedimentary clasts yield significant underestimates of finite strain when these clasts have not behaved passively. Unfortunately for these methods it has been well established that there are significant competency contrasts between sedimentary clasts and their matrix (Ramsay, 1967; Gay, 1968a,b). This competency contrast is inherently linked to the

viscosity contrast between different clast types and the matrix (Ramsay, 1967; Gay, 1968a,b). This at its most basic represents a two component system. Gay (1968a) discussed the effect the viscosity ratio between clasts and their matrix has on the style of deformation. It was found that clasts with a low viscosity deformed faster than the bulk rock strain ellipse, while clasts with high viscosities resisted deformation and deformed slower than the bulk rock strain ellipse (Gay, 1968a). Gay (1968a) concluded that the viscosity ratio between a clast and the matrix is dependent on the relative proportion of clasts and matrix. It is important to note that the viscosity of a matrix is in itself a mean viscosity. When the ratio of clasts to matrix is low there is a high ductility contrast as the clast to matrix ratio increases the ductility contrast reduces. This is arguably due to the reduced ability of the matrix to flow due to the increase in clast on clast interaction. As mentioned above, object concentration, packing and interaction clearly have a significant influence on finite strain estimates in two component systems due to the effect they have on the viscosity contrasts (Gay, 1968a; Mandal et al., 2003; Vitale and Mazzoli, 2005).

Higher object concentrations have been shown by Mandal et al. (2003) to reduce strain partitioning. Similarly Vitale and Mazzoli (2005) demonstrated that higher ooid concentrations in deformed oolites lead to higher underestimates of bulk strain with less of an effect on object strain. From this work alone it is clear that using clasts with high viscosity contrasts to matrix as strain markers, as is often the case in sandstones and conglomerates, causes significant bulk strain underestimates. Treagus and Treagus (2002) while addressing these competency contrasts found that Rf/Ø style methods (Dunnet, 1969; Ramsay, 1967)

characterised clast strain whereas centre to centre methods (Fry, 1979; Ramsay, 1967) characterised bulk rock strain. Meere et al. (2008) attributed non-passive deformation to a relatively incompetent clay-rich matrix and that this ductile matrix effectively cushioned clasts from internal deformation. This behaviour accommodated high degrees of competent clast long-axis alignment achieved by a combination of rigid body rotation, layer boundary slip and particle–particle interactions (Meere et al., 2008). Where this behaviour occurs there is typically little or no evidence of penetrative deformation, despite evidence from traditional strain markers such as reduction spots and deformed burrows (Meere et al., 2008). This non-passive deformation particularly affects the clast strain estimates and the intercepts methods of calculating strain, mainly because these methods are recording the amount of rigid body rotation and repacking of clasts achieved by grain boundary slipping during deformation. Meere et al. (2008) found that the effective bulk strain values (R_b) from centre to centre methods are generally closer to the true strain estimates, yet they still report significant underestimates and poor correlations with true strain, confirming the earlier reports from Treagus and Treagus (2002).

Chapter 3:

Anisotropy of Magnetic Susceptibility

3. Introduction to Anisotropy of Magnetic Susceptibility

3.1. Introduction

Magnetic susceptibility measures how magnetised a material can become and its anisotropy is the preferential direction of magnetisation (Jones and Childers, 2001). This essentially relates the induced magnetisation to the magnetic field in which the material is immersed through the equation K=M/H, where K is susceptibility, M is magnetisation & H is the induction field (Borradaile and Jackson, 2004). Anisotropy of Magnetic Susceptibility (AMS) can average the orientation-distribution (OD) of all rock components contributing to its magnetic susceptibility, including minerals, crystal lattices and all sub-fabrics (Borradaile and Jackson, 2010). Therefore the result is dependent on the magnetic (mineral susceptibility and anisotropy) and physical (shape, size, and preferred orientation) properties of these components (Tarling and Hrouda, 1993). Hence AMS properties can aid fabric interpretation such as preferred grain orientations, current directions and strain histories (Borradaile and Jackson, 2010).

The anisotropic response of a sample is an average of the different magnetic responses of all the mineral ODs, and is dictated by the intrinsic susceptibility of each mineral in the sample (Borradaile and Jackson, 2010). The simplest way to visualise the results is by using the AMS ellipsoid, similar to the strain ellipsoid, represented by three mutually orthogonal principal axes Kmax ≥Kint ≥ Kmin (or K1 ≥K2 ≥ K3 (Borradaile, 1988, Borradaile and Jackson, 2010). These axes are the eigenvectors and eigenvalues of K, i.e. the bulk susceptibility or kmean ($\overline{K} = \frac{K1+K2+K3}{3}$). A structurally significant magnetic foliation (the plane perpendicular to K3, defined by K1 and K2) and lineation (parallel to Kmax) can be obtained from this

ellipsoid (Borradaile and Jackson, 2004). Additionally the overall shape of the AMS ellipsoid can be useful for structural interpretations, with three main geometries being oblate (K1 ≅ K2 > K3, with K3 perpendicular to magnetic foliation), prolate (K1 > K2 ≅ K3, with K1 parallel to magnetic lineation) and triaxial (K1 ≠ K2 ≠K3). AMS is capable of recording contributions from multiple ferromagnetic (sensu lato), paramagnetic, and diamagnetic minerals that grew at different times and were deformed by different mechanisms. Consequently, AMS often represents a composite fabric related to multiple depositional, diagenetic and tectonic processes, which complicates fabric interpretation (Borradaile and Jackson, 2004). This chapter discusses the background theory of AMS and interpretations of the AMS results, and how the magnetic ellipsoid can be related to strain and petrofabric studies.

3.2. Magnetization

3.2.1. Magnetization of a Material

The magnetic properties of any substance are derived from the motion of electrically charged particles (Tarling and Hrouda, 1993). Electrons have magnetizations that are controlled by their axial spin and their orbital motion around a nucleus (Tarling and Hrouda, 1993). In order to naturally reduce the magnetostatic energy produced by these motions of electrically charged particles, electrons are organised into pairs in shells of variable electron capacity (Tarling and Hrouda, 1993). However, all materials magnetise in response to an applied magnetic field, by developing a preferred orientation in the spin and angular momentum of all electrons (Tarling and Hrouda, 1993). This results in an increase in

the magnetic moment (the measured intensity of magnetization) (Tarling and Hrouda, 1993). The strength of this magnetic response is controlled by two factors: the number of unpaired electrons in the atomic shells of an atom and the strength of the applied field. For atoms with complete atomic shells the net magnetic moment is very weak (diamagnetic), whereas atoms with increasing unpaired electrons in their atomic shells have an increasingly stronger magnetic response to an applied field (paramagnetic) (Tarling and Hrouda, 1993; Dunlop and Ozdemir, 1997). This occurs because unpaired electrons promote the alignment of angular momentum and spin of electrons, resulting in an electrostatic charge (Dunlop and Ozdemir, 1997; Tarling and Hrouda, 1993). The strength of the magnetization (M) is also related to the strength of the applied field (H) and how magnetisable the material is, i.e. the material's susceptibility (K): M=KH (Tarling and Hrouda, 1993).

Clearly susceptibility of a material is controlled by atomic configuration, but is also affected by crystal structure (Borradaile and Jackson, 2010; Tarling and Hrouda, 1993). In a well organised crystal structure the alignment of electrons due to magnetisation creates poles on the crystal surface at either end of the crystal's long axis (Dunlop and Ozdemir, 1997; Tarling and Hrouda, 1993). The anisotropy of susceptibility will therefore depend on both the composition of a material and the orientation of the crystalline axes relative to the applied field (Borradaile and Henry, 1997).

The units used in AMS studies are typically reported in *systeme internationale* (SI) units. Older publications (pre-1980) report units in CGS, which can be converted into SI units (Tarling and Hrouda, 1993). The SI units for magnetization are based

on current loops, if a current loop has a radius *r* and a current *i*, then the magnetic field, H, produced at the centre of the loop can be defined as $\mathrm{H} = \frac{i}{2r}$, which can be measured in Amperes per metre (A/M) (Moskowitz, 1991).

The magnetic moment, m, of the current loop is defined as m = *i* X Area, measured in A m^2 (Moskowitz, 1991). The intensity of magnetization, M, within that field is defined as the magnetic moment per unit volume, M =m/v, and is measured in Amperes per metre (A/M) the same unit used to measure H (Moskowitz, 1991). The susceptibility, K, is defined as the ratio of magnetization to magnetic field, K = M/H (Moskowitz, 1991) and is dimensionless.

3.2.2. Classes of Magnetic Behaviour

Materials can be classed by their responses to an applied magnetic field. The analysis of these responses is different from the study of palaeomagnetic fabrics, which are controlled by the residual magnetisation in the absence of an inducing field. Depending on the type of response to an applied magnetic field materials can be classed as magnetically disordered (diamagnetic or paramagnetic) or ordered (ferromagnetic, ferrimagnetic or antiferromagnetic) (Borradaile and Jackson, 2010; Dunlop and Ozdemir, 1997).

3.2.2.1. Diamagnetism

The weakest of these magnetic responses is a negative susceptibility called diamagnetism that is always present in all materials, but is usually masked by larger, positive effects such as ferromagnetism and paramagnetism (Borradaile and Jackson, 2010; Jones and Childers, 2001). This negative susceptibility indicates that

the direction of the induced moment is opposite to the direction of the applied field. This is caused by the change in the atomic electron orbits about the direction of the field, resulting in a magnetic field opposite to the applied field (Figure 3. 1A)(Jones and Childers, 2001).

This type of response only occurs when a magnetic field is applied to a material with complete atomic shells (Tarling and Hrouda, 1993) and is caused by a change in the atomic electron orbits about the direction of the field, resulting in a magnetic field opposite to the applied field (Jones and Childers, 2001). The resulting negative polarisation of ions disappears when the applied field is removed (Jones and Childers, 2001). More simply put the resulting magnetisation is opposite to the direction of the applied field (Tarling and Hrouda, 1993) and in terms of M=KH, M has a weakly negative, non-permanent response to increasing H (O'Driscoll et al., 2008). The most common rock forming diamagnetic components are quartz, calcite, dolomite and coal. Because they do not contain iron, nickel or chrome, so cannot form ferromagnetic minerals under metamorphic conditions (Tarling and Hrouda, 1993).The magnetic response of diamagnetic minerals only becomes significant when ferromagnetic paramagnetic minerals are practically absent (<.0001% and < 1% respectively; Tarling and Hrouda, 1993). The mean susceptibilities for quartz, calcite and dolomite are -13.4×10^{-6}, -13.8×10^{-6} and -38×10^{-6} S.I respectively.

3.2.2.2. Paramagnetism

For materials with atoms that have incomplete electron shells, a paramagnetic response is displayed when an external magnetic field is applied (Borradaile and Jackson, 2010; Dunlop and Ozdemir, 1997; Jones and Childers, 2001; Tarling and

Hrouda, 1993). Paramagnetism is characterised by the partial alignment of magnetic moments parallel to the applied field and is therefore, a much stronger positive response than diamagnetism (Dunlop and Ozdemir, 1997; Tarling and Hrouda, 1993). Like in the case of diamagnetism the orientation of each moment is independent of the orientation of its neighbouring moments, but unlike diamagnetism paramagnetism arises from atoms with permanent magnetic dipole moments that exist independently of any applied field (Jones and Childers, 2001).

As a result of this independence these moments are randomly orientated and have no net magnetisation in the absence of an applied field (Figure 3. 1B); therefore their response is non-permanent (Jones and Childers, 2001). However, when a magnetic field is applied, the moments align preferentially along the direction of the applied field causing a net magnetisation (Jones and Childers, 2001). Paramagnetic grains have a positive proportional non-permanent relationship between H and M, even at high strengths, and M is zero when H is zero (the magnetisation is not permanent) (O'Driscoll et al., 2008). Furthermore paramagnetism depends inversely on the absolute temperature in such a way that the susceptibility decreases with increasing temperature according to the Curie Law (Jones and Childers, 2001; O'Driscoll et al., 2008). Paramagnetic behaviour is predominantly displayed by iron-bearing silicates (biotite, muscovite, pyroxene and amphibole etc.) as well as some Fe-Ti oxides (ilmenite etc.) and iron sulphides (pyrite, etc.) (Tarling and Hrouda, 1993). In sedimentary rocks paramagnetic minerals are typically micas present as fine grained matrix material. Biotite rich rocks are ideal for AMS studies as the magnetic fabric of biotite populations is

similar to that of their lattice fabric and the magnetic axes of biotite are parallel to its crystallographic (shape) axes (Bouchez, 1997). The average susceptibilities of paramagnetic minerals are typically around $500x10^{-6}$ SI with biotite usually having a susceptibility of $1100x10^{-6}$ SI (Tarling and Hrouda, 1993).

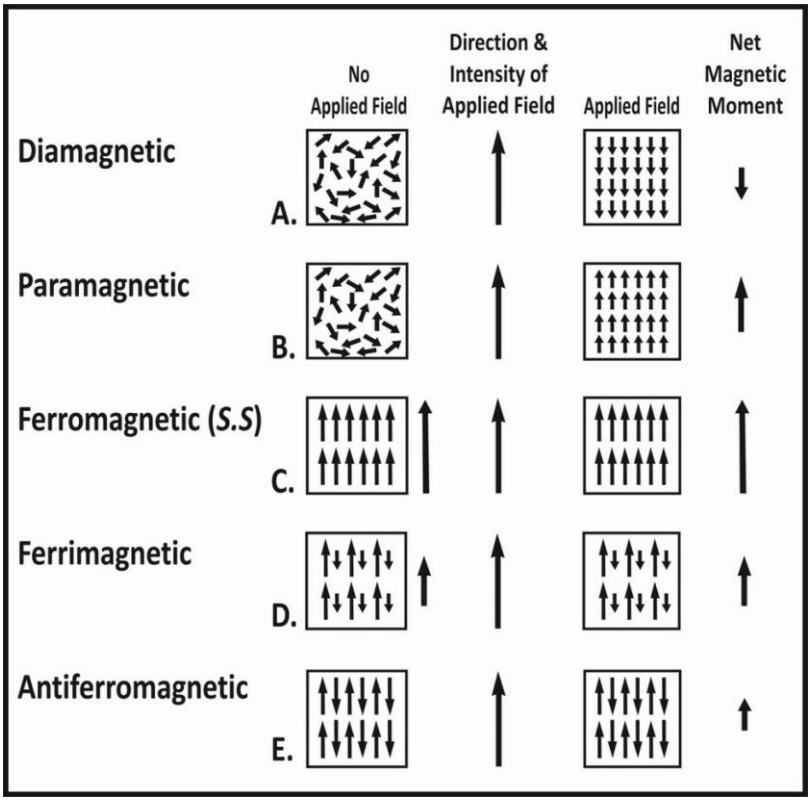

Figure 3. 1 Different types of magnetization behaviours. The left hand row illustrates the magnetic behaviour of the five main types in the absence of a magnetic field. Note that only ferromagnetic (*s.s.*) and ferrimagnetic types have a net magnetic moment when no external magnetic field is applied. The right hand row illustrates the effects of an applied magnetic field. A. Diamagnetic minerals become very weakly magnetized in the opposite direction to that of the applied field; this magnetization disappears with the removal of the applied field, as the magnetic moments become randomised. B. Paramagnetic minerals become weakly magnetized in the same direction to that of the applied field; this magnetization disappears with the removal of the applied field, as the magnetic moments become randomised. C. Ferromagnetic minerals acquire and retain a strong magnetization as their magnetic moments are all aligned. D. Ferrimagnetic minerals acquire and retain a weaker magnetization than ferromagnetic minerals as their magnetic moments are anti-parallel, but of differing magnitudes. E. Antiferromagnetic minerals become moderately magnetized in the direction of the applied field, but do not retain the magnetization as their magnetic moments are exactly anti-parallel. Redrawn and modified from Tarling and Hrouda (1993).

3.2.2.3. Ferromagnetism

The third type of magnetic response or behavior is that of ferromagnetism, this type is caused by cooperative interactions of individual ionic moments (Jones and Childers, 2001). Unlike that of diamagnetism and paramagnetism the individual moments of ferromagnetic (*sensu lato*) materials are not independent and interact strongly (Jones and Childers, 2001). Ferromagnetism only occurs when the electron spins have been coupled in an arrangement that aligns all the individual spin magnetisations without applied magnetic field (Tarling and Hrouda, 1993). This type of magnetisation is limited to the first transition elements and is a function of the unpaired electrons in their *3d* shell (Tarling and Hrouda, 1993). These domains contain aligned ionic moments, and for crystals that contain multiple domains the polarisation of these domains is normally in different directions (Jones and Childers, 2001; Tarling and Hrouda, 1993). These domains increase in size when they are preferentially aligned close to the direction of an applied field and those that are in other directions decrease, resulting in a large net magnetisation (Jones and Childers, 2001). Ferromagnetic materials possess a strong positive proportional relationship between M and H, but with a maximum value of M (O'Driscoll et al., 2008).

Ferromagnetic responses can be split into three types: ferromagnetic (*sensu stricto*; Figure 3. 1C), antiferromagnetic (Figure 3. 1 E) and ferrimagnetic (Figure 3. 1D). Ferromagnetic (*s.s*) behaviour is characterised by the alignment of all magnetic vectors in the same direction, brought about by the coupling of electron spins in adjacent cations (Tarling and Hrouda, 1993). This kind of behaviour is seen in

metallic transition elements, such as iron, nickel and cobalt. A more complicated behaviour is exhibited by oxides of these metallic elements, whereby the electron spins of cations are shared via an oxygen anion (Tarling and Hrouda, 1993). This results in the reversal of the electron spins in adjacent cations, creating oppositely magnetised lattices in the material (Tarling and Hrouda, 1993). If these lattices are of equal strength antiferromagnetic behaviour occurs, whereby there is no net magnetisation, whereas if one lattice is stronger than the other then a net magnetisation is present in that direction, this is termed ferrimagnetic behaviour (Tarling and Hrouda, 1993).

In Fe-bearing silicate dominated rocks, the magnetocrystalline anisotropy of paramagnetic silicates such as biotite or amphibole will control the AMS fabric when magnetite is absent or of very low volume percent (<0.1 Vol. % magnetite) (Tarling and Hrouda, 1993). For magnetite bearing rocks the contribution of paramagnetic minerals is negligible because of the high intrinsic magnetic susceptibility of magnetite (Tarling and Hrouda, 1993). The magnetic fabric of magnetite bearing rocks is dictated by the shape anisotropy of the magnetite grains (Tarling and Hrouda, 1993). In a magnetite bearing rock, due to the higher susceptibility of magnetite compared to other minerals, the bulk susceptibility will be much higher than for a paramagnetic rock of the same iron content (Bouchez, 1997). The other important ferromagnetic mineral in terms of sedimentary rocks is hematite. The magnetic susceptibility of hematite is controlled by its crystallography, with K1 being parallel to the basal planes (Borradaile, 1988).

Magnetite has a typical bulk susceptibility of 5 SI, while that of hematite is $6x10^{-3}$ SI (Borradaile, 1988).

The bulk magnetic susceptibility of a material is the sum of all the contributions: K = Kpara + Kferro + Kantiferro + Kdia is approximately equal to Kpara + Kferro, since Kantiferro and Kdia are almost negligible (Bouchez, 1997).

3.3. Magnetic Responses of Minerals in Sedimentary Rocks

From the above discussion on magnetization it is clear that the magnetic anisotropy of a rock depends on the degree of alignment and anisotropies of the minerals that it is composed of (Tarling and Hrouda, 1993).

If ferromagnetic minerals, such as iron oxides like magnetite or hematite, are present in proportions of more than a few percent they can dominate a rock's magnetic properties (Tarling and Hrouda, 1993). Rocks with sufficient amounts of magnetite or hematite typically have bulk susceptibilities $>5x10^{-4}$. In rocks with weak bulk susceptibility ($<5x10^{-4}$ Si) the magnetic fabric is typically controlled by the paramagnetic minerals, whereas rocks with diamagnetic minerals as the dominant components have negative bulk susceptibilities (Tarling and Hrouda, 1993).

The ferromagnetic (*S.L.*) components of sedimentary rocks can be detrital or authigenic and their presence is controlled by sediment source, sediment composition, diagenesis conditions and the composition of circulating fluids. Detrital grains are usually subject to alteration during diagenesis due to changes in the redox conditions, this is particularly true of magnetite (Tarling and Hrouda, 1993). Hematite is usually the most important ferromagnetic mineral in

sedimentary rocks, as it is chemically robust in oxidizing conditions, and furthermore it is particularly common as an authigenic growth mineral (Tarling and Hrouda, 1993). It regularly replaces magnetite and can form rims around other mineral species, such as quartz, and accentuates their shape anisotropy. It can also be found as fine grained groundmass crystals (Tarling and Hrouda, 1993).

Paramagnetic minerals become more important with low percentages of ferromagnetic minerals. The most common paramagnetic minerals in sedimentary rocks tend to be phylosillicates and their anisotropy is largely shape controlled (Tarling and Hrouda, 1993). The diamagnetic minerals, such as quartz and calcite, in a rock only become the dominant magnetic minerals if ferromagnetic and paramagnetic minerals make up less than 0.0001% and 10% respectively of the total rock composition (Tarling and Hrouda, 1993).

3.4. Determining Petrofabrics using Anisotropy of Magnetic Susceptibility

Graham (1954) first suggested that magnetic fabrics could be a valuable tool in petrofabric anlaysis and established a link between LPS and AMS. Since then there has been a flourish of research applying AMS to petrofabrics. As discussed in Chapter 2, a rock's fabric or petrofabric "includes the complete spatial and geometrical configuration of all the components that make up a rock" (Hobbs et al., 1976). This includes textures, structures and preferred orientation of a rocks components. AMS is capable of measuring an entire petrofabric and providing some information regarding the components that control that fabric. Unfortunately the parameters that are used to describe the petrofabric are far from universal. In this study Jelinek's (1981) parameters are primarily used. A brief discussion of how

these parameters are derived, what they represent and how they are presented is outlined below.

3.4.1. AMS Parameters

In order to easily represent and derive comparable results from AMS studies, the magnetic fabric is described by the magnetic susceptibility tensor. This can be presented as an ellipsoid with three principal susceptibility magnitudes and corresponding orthogonal principal axis directions (K1≥K2≥K3) (Figure 3. 2; Tarling and Hrouda, 1993), similar to the strain ellipsoid. These axes are the eigenvectors and eigenvalues of K, the bulk susceptibility ($\overline{K} = \frac{\mathrm{K1+K2+K3}}{3}$). This is the arithmetic mean, which is most commonly used in most magnetic studies. In studies where the where the magnitude of the anisotropy is correlated to strain the geometric mean has regularly been used: $K_g = \sqrt[3]{K1 * K2 * K3}$. The geometric mean is quite useful as it describes the radius of the initial undeformed sphere (Hirt and Almqvist, 2012; Hirt et al., 1988; Kligfield et al., 1981; Tarling and Hrouda, 1993).

Originally Flinn diagrams (Flinn, 1956 and 1962) were borrowed from strain ellipse theory to represent AMS ellipsoid geometries. Flinn diagrams for AMS are constructed by plotting *a* (K1/K2) against *b* (K2/K3) (Flinn, 1956 & 1962). Shape is represented by *K,* the slope of a line from the data point to the origin at (1,1), so that $K = a - \frac{1}{b} - 1$ with $a = \frac{x}{y}$ and $b = \frac{y}{z}$. When $K = 0$ the finite strain ellipsoid is uniaxial oblate and has been flattened perpendicular to Z. As K tends towards 1 the ellipsoid moves away from being purely uniaxial, but remains in the oblate and flattened domain. For K values greater than 1 the ellipsoid lies in the prolate or constrictive domain, and for $K = \infty$ the ellipsoid is purely uniaxial prolate and

stretched along the X axis. Flinn diagrams were later modified by Ramsay to include a logarithmic scale, so that Ramsay's K = ln(a)/ln(b) (1967). This handling of the AMS parameters is quite simple and is considered to oversimplify the graphical representation (Borradaile and Jackson, 2004), but despite this it is still regularly used (Weil and Yonkee, 2009). One of the advantages of Flinn's method is that magnetic lineation and foliation can be calculated quite easily: linear anisotropy degree ($a = \mathrm{L} = \frac{\mathrm{Kmax}}{\mathrm{Kint}}$), and planar anisotropy degree ($b = \mathrm{F} = \frac{\mathrm{Kint}}{\mathrm{Kmin}}$).

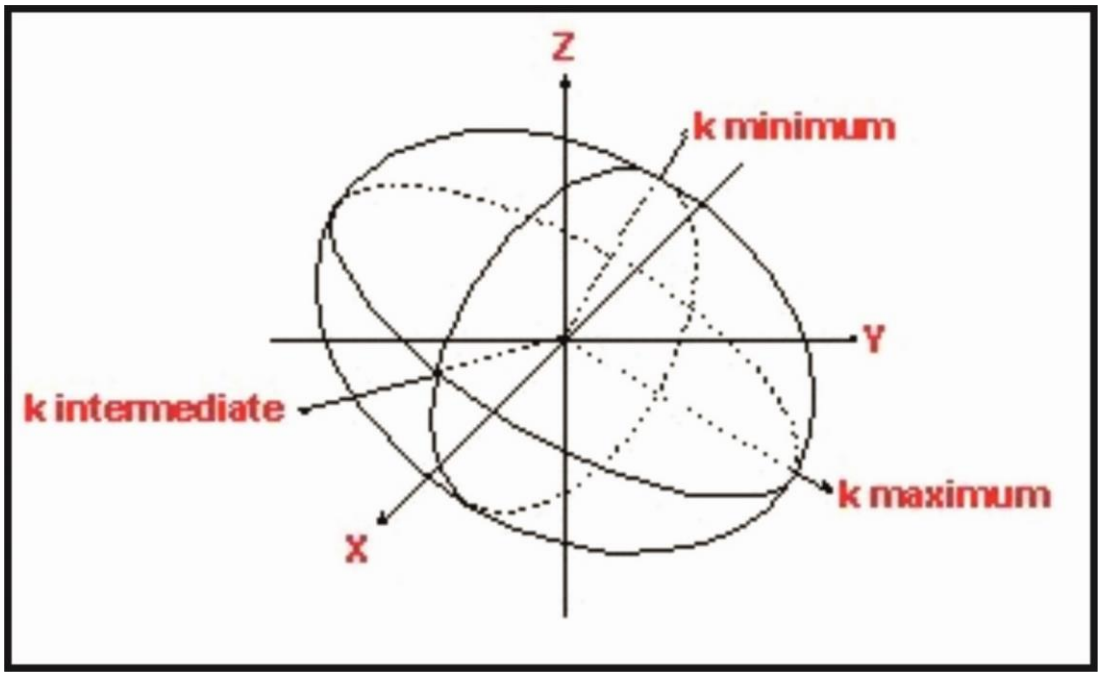

Figure 3. 2 Magnetic susceptibility ellipsoid with three mutually orthogonal axes. These axes correspond to the maximum (K1), intermediate (K2) and minimum (K3) susceptibility values, whose magnitudes and orientations can be defined in Cartesian coordinates.

Jelinek re-evaluated the statistical methods for the characterisation of anisotropy in two landmark papers (1978 & 1981). These re-evaluations are still widely preferred and also used in this research. Jelinek's shape parameter is represented by Tj = $\frac{\left[\mathrm{Ln}\left(\frac{\mathrm{K2}}{\mathrm{K3}}\right)-\mathrm{Ln}\left(\frac{\mathrm{K1}}{\mathrm{K3}}\right)\right]}{\left[\mathrm{Ln}\left(\frac{\mathrm{K2}}{\mathrm{K3}}\right)+\mathrm{Ln}\left(\frac{\mathrm{K1}}{\mathrm{K2}}\right)\right]} = \frac{[\mathrm{Ln(F)}-\mathrm{Ln(L)}]}{[\mathrm{Ln(F)}+\mathrm{Ln(L)}]}$ and the corrected anisotropy degree is commonly

represented by P' or P_j and was derived from Nagata's (1961) P= Kmax/Kmin (1961), where:

$$\mathrm{Ln}(\mathbf{P_j}) = \sqrt{2\left(\left(\ln\left(\frac{K1}{K}\right)\right)^2 + \left(\ln\left(\frac{K2}{K}\right)\right)^2 + \left(\ln\left(\frac{K3}{K}\right)\right)^2\right)^{\frac{1}{2}}} \quad \text{or}$$

$$\mathrm{Ln}(\mathbf{P_j}) = \ln(P)\sqrt{\left(1 + \frac{T^2}{3}\right)}.$$

Jelinek's K' (1984) is a less used alternative to the Kmean and depends on the deviatoric susceptibilities (K1-K)≥(K2-K)≥(K3-K), and is defined as $K' = \sqrt{\frac{(K1-K)^2+(K2-K)^2+(K3-K)^2}{3}}$. The parameters Tj and Pj can be plotted against each other in a convenient manner on separate Cartesian axes (Figure 3. 3), Tj values range from -1 (prolate) to +1 (oblate), with a Tj value of 0 representing a triaxial ellipse, whereas Pj describes degree or strength of ellipsoid shape expression. Borradaile & Jackson (2004) proposed an alternative of plotting Tj vs Pj in a polar plot (Figure 3. 4) so that slight variations in shape at lower anisotropies plot closer together.

Jelinek also proposed the use of the U-parameter as a descriptor of shape that did not depend on bulk susceptibility. The U-parameter is defined as $U = \frac{2K2-K1-K3}{K1-K3}$ and ranges from +1 to -1. Schmidt et al. (2006) in a study of calcite proposed the use of ΔK, defined as ΔK = K1-K3. These parameters are quite useful for studies of rocks that have a significant diamagnetic contribution as they do not depend on bulk susceptibility, and are not affected when the bulk susceptibility is near zero. Hirt and Almqvist (2012) argued that ΔK and U were more accurate representations of degree of anisotropy and shape of the anisotropy ellipsoid in rocks and minerals with bulk susceptibility values that approximated zero.

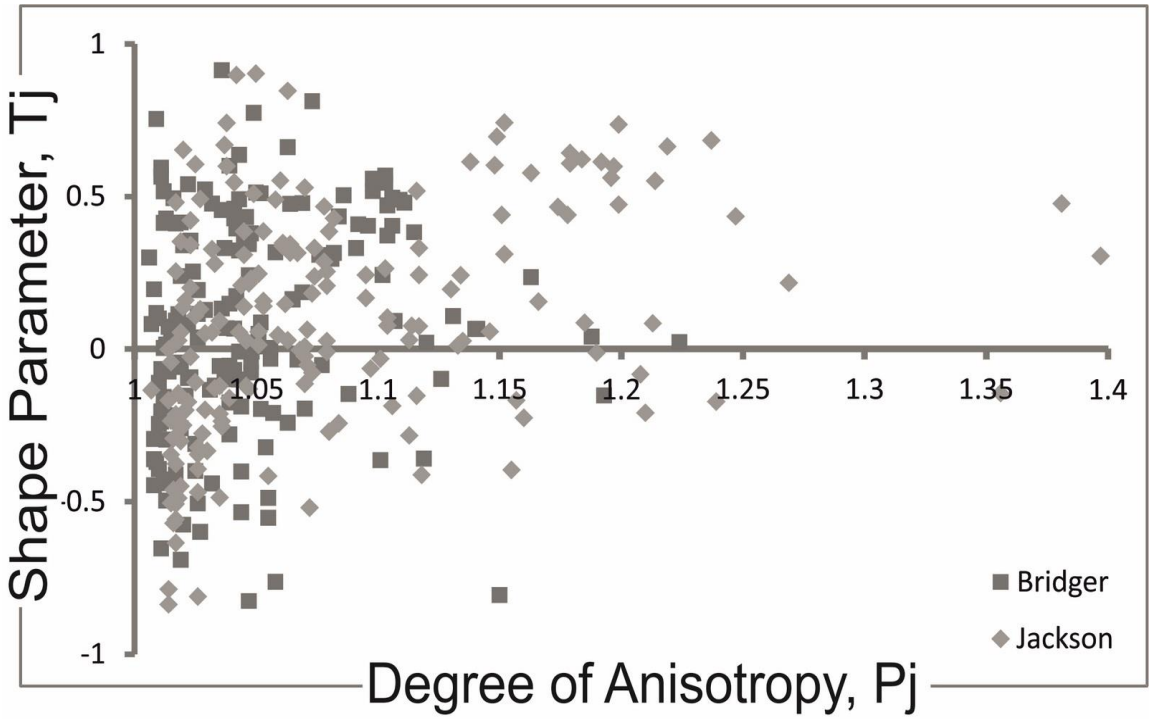

Figure 3. 3 An example plot of Tj vs Pj (P'). Oblate ellipsoids plot between 0 and +1 with prolate ellipsoids plotting between 0 and -1 on the vertical axis; purely triaxial ellipsoids plot at 0. The horizontal axis (P') represents the strength of ellipsoid shape. Data shown is from Triassic sandstones in the Rocky Mountains, Wyoming.

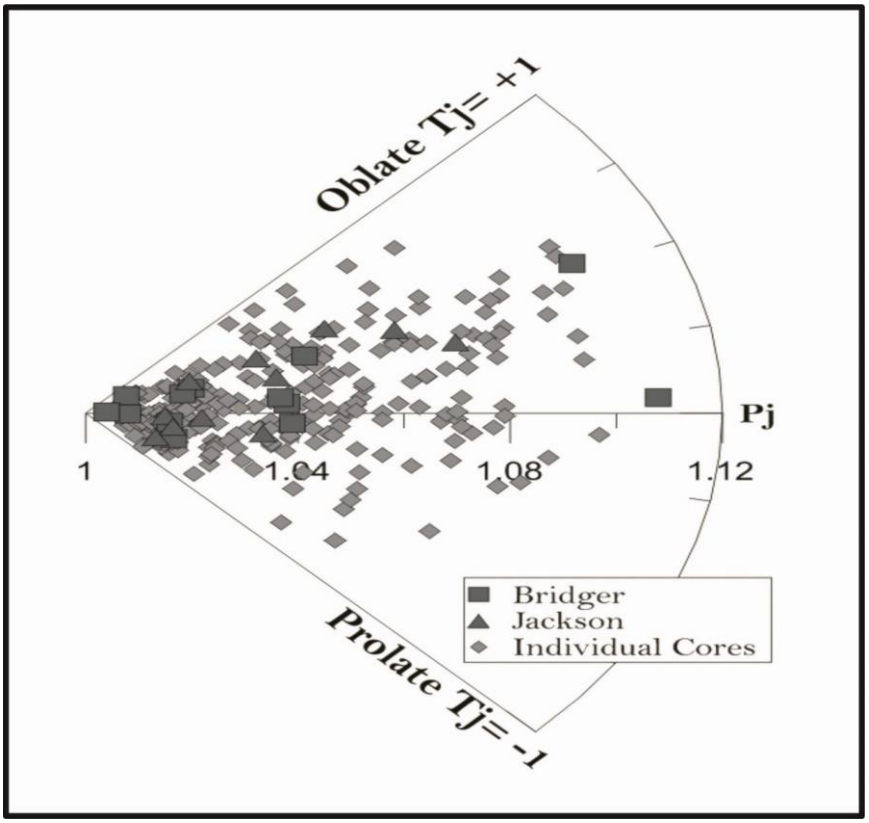

Figure 3. 4 An example of a polar plot proposed by Borradaile and Jackson (2004). This plot shows the same data as Figure 3. 3. Oblate ellipsoids between 0 and +1, prolate ellipsoids plot between 0 and -1, while purely triaxial ellipsoids plot at 0. Degree of anisotropy or strength of ellipsoid shape is plotted along the horizontal axis. The advantage of this plot is that low anisotropy ellipsoids plot closer together.

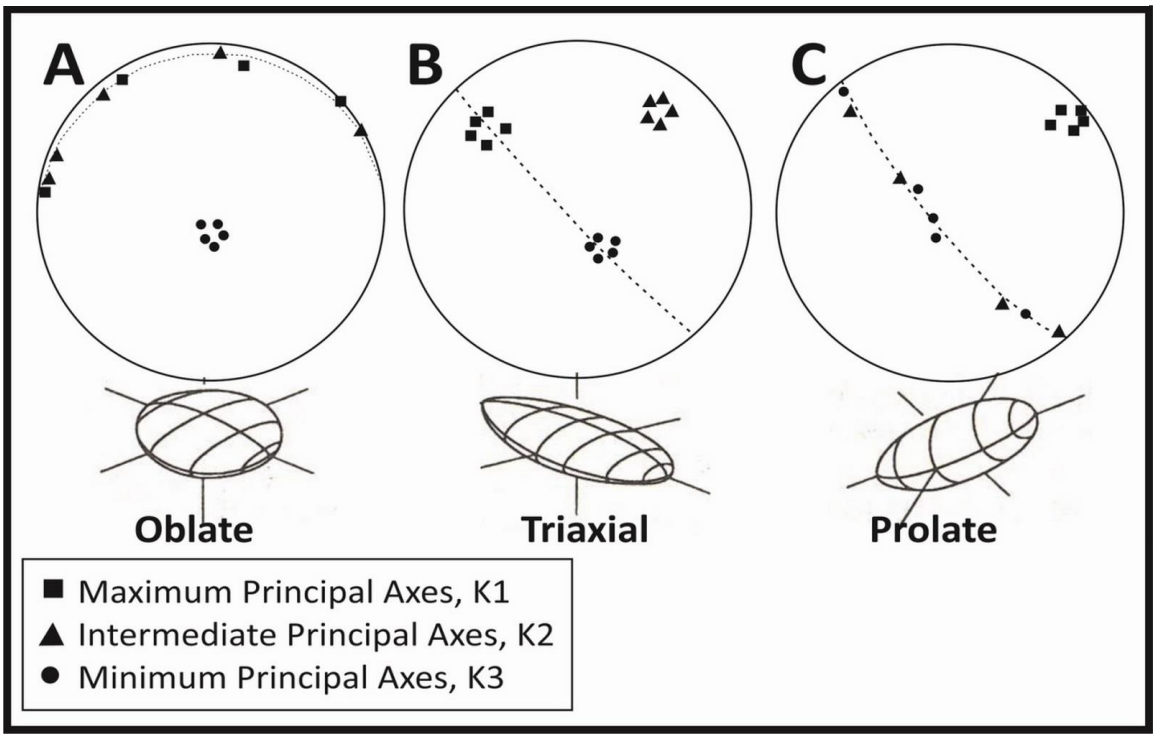

Figure 3. 5 The three main ellipsoid geometries (**A.** oblate, **B.** triaxial and **C.** prolate) and their representative stereographic projections. Stereographic representation of ellipsoid geometries, modified from Tarling & Hrouda (1993)

3.4.2. Causes of AMS Ellipsoid Geometries

Generally speaking prolate ellipsoids (3.4 C) typically result from the stretching and extension of minerals and define a linear fabric, whereas oblate ellipsoids (3.4 **Error! Reference source not found.**A) typically form due to flattening and define a planar fabric. Despite this it is important to stress that the AMS ellipsoid is the result of multiple processes and mineral contributions, furthermore multiple sub-fabrics can exist in a single sample (Hirt and Almqvist, 2012). As a result great care must be taken when making interpretations based on the geometries of the magnetic ellipsoid. It is important to note that any progressive change or evolution of an AMS fabric will depend on strain, strength of primary fabrics, mineralogy, as well as deformation mechanisms (Bakhtari et al., 1998; Borradaile and Henry, 1997; Borradaile and Jackson, 2010, 2004; Borradaile and Tarling, 1981; Parés and van der Pluijm, 2002; Parés, 2004; Parés et al., 1999a; Tarling and Hrouda, 1993). Despite these complications, systematic changes in AMS ellipsoid geometries have been observed in fold and thrust belts as primary fabrics become replaced or overprinted by tectonic fabrics as progressive deformation occurs (Bakhtari et al., 1998; Borradaile and Henry, 1997; Borradaile and Jackson, 2010, 2004; Parés and van der Pluijm, 2002; Parés, 2004; Parés et al., 1999a). This suite of AMS geometries has been characterised by the relationship of magnetic foliations and lineations to bedding. Magnetic foliation (the plane perpendicular to K3, defined by K1 and K2) can be parallel to bedding in undeformed or weakly deformed rocks and can be parallel to cleavage in strongly deformed rocks, but can also represent a composite fabric of bedding and cleavage (Bakhtari et al., 1998; Borradaile and Henry, 1997; Borradaile and Jackson, 2010, 2004; Parés and van der Pluijm, 2002; Parés, 2004;

Parés et al., 1999a). Magnetic lineation (parallel to K1) has been interpreted to represent the intersection between layer parallel shortening and bedding fabrics and is largely subparallel to regional structural trend (Bakhtari et al., 1998), but this is not always the case (Borradaile, 1991; Borradaile and Tarling, 1981; Tarling and Hrouda, 1993).

Alternatively the magnetic lineation has been interpreted to track the maximum extension direction and is sub perpendicular to structural trend (Weil and Yonkee, 2009). Mixed patterns also occur (Aubourg et al., 1991), and oblique fabrics locally develop in complex structures (Saint-Bezar et al., 2002). The magnetic lineation in deformed sedimentary rocks can be the result of two competing magnetic fabrics, essentially where the combination of two foliations produce a lineation (Borradaile and Tarling, 1981; Housen et al., 1993). These magnetic foliations can be due to bedding and tectonic controls (Borradaile and Tarling, 1981) or post tectonic mineralisations (Saint-Bezar et al., 2002).

3.5. Establishing which Minerals or Sub-Fabrics Control the AMS Ellipsoid

The single greatest drawback of AMS methodology is determining what rock components define the magnetic response of a sample. Varying temperatures, field strengths and frequencies can provide methods of establishing the magnetic response of specific components (Dunlop and Ozdemir, 1997; Tarling and Hrouda, 1993), but this is largely beyond the scope of this study. The bulk susceptibility of a sample is mainly controlled by the concentration of various minerals, as shown in Figure 3. 6.

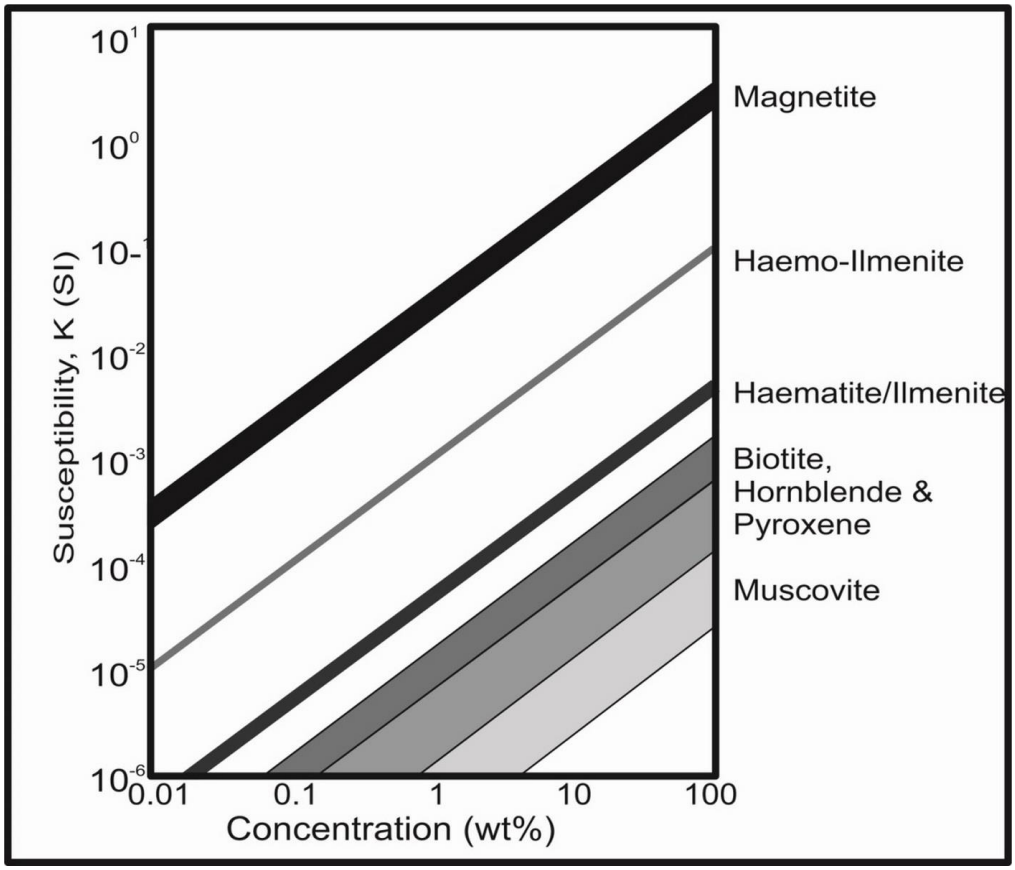

Figure 3. 6 The control of mineral contribution percentages on bulk susceptibility. Redrawn from Tarling and Hrouda (1993).

On a first principal basis it can be determined whether magnetic fabrics are dominated by diamagnetic, paramagnetic, or ferromagnetic (s.l.) phases based on the bulk susceptibility and degree of anisotropy (Hirt and Almqvist, 2012; Pierre

Rochette, 1987). When the bulk susceptibility is $<3x10^{-4}$ SI and P is <1.35, then ferromagnetic minerals are typically not dominating the anisotropy and paramagnetic minerals are the main magnetic mineral in the sample (Hirt and Almqvist, 2012; Rochette, 1987). When the susceptibility is close to zero, then diamagnetic minerals start to have a significant role on the net anisotropy (Hirt and Almqvist, 2012; Rochette, 1987). The other methods used in this study to determine the magnetic carriers are largely limited to comparisons of K with the values and orientations of the principal axes, as well as the comparison of normalized to non-normalized data (Borradaile and Jackson, 2010).

3.5.1. Comparison of Bulk Susceptibility (Km) to Principal Axes Susceptibilities (Ki)

When a paramagnetic silicate mineral and a ferromagnetic mineral appear to control susceptibility, a plot of Ki versus Kmean (Figure 3.7) can reveal relationships between the principal axes and bulk susceptibility (Borradaile and Jackson, 2010). If

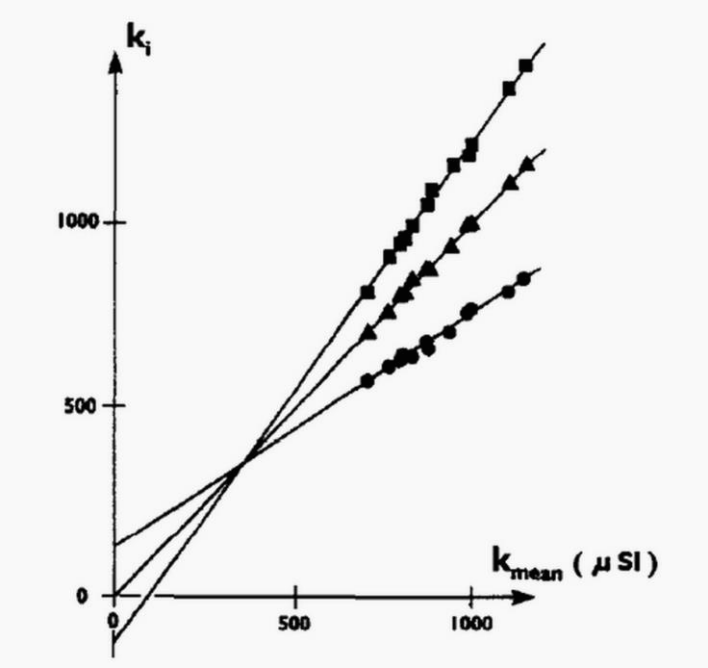

Figure 3. 7 Plot of principal axes susceptibilities versus bulk susceptibility for samples of uniform mineralogy that have undergone vary degrees of deformation. This shows that for this case susceptibilities are controlled by a petrofabric (From Borradaile and Jackson, 2010).

anisotropy increases with K and the principal axis (Ki) curves intersect at the mean matrix susceptibility then rock-AMS is controlled by the relative abundance of the high-anisotropy, lower K mineral rather than the lower anisotropy, high- K mineral (Borradaile and Jackson, 2010).

3.5.2. Comparison of Pj and Tj for specimens of different K

The bulk susceptibility, K, is the average of all magnetic contributions of minerals in a sample. Similarly Pj represents an average of mineral anisotropies while Tj is a complex sum of mineral orientation distributions.

Plotting the frequency distribution of K-values allows the identification of any sub-sample groups with significantly different bulk susceptibility (Figure 3. 8). A subsequent plot of Pj against K for these groups will illustrate any correlation between anisotropy and susceptibility (Figure 3. 9). Similarly separating these groups and plotting them on a Pj-Tj may reveal samples whose AMS ellipsoid geometries are controlled by composition rather than by tectonic history etc. (Borradaile and Jackson, 2010).

3.5.3. Comparison of Normalised vs Non-Normalised AMS Ellipsoids

Normalisation of AMS data involves dividing the magnitudes of the principal axes (K1, K2 & K3) by K (Figure 3. 10). This normalises all specimens to a bulk unit susceptibility and prevents specimens with high bulk susceptibility from dominating the results (Borradaile and Jackson, 2010). Specimens can be compared on the basis of their normalised AMS ellipsoids, allowing any sub-fabrics to be identified by comparing normalised AMS ellipsoids to non-normalised ellipsoids (Borradaile and Jackson, 2010).

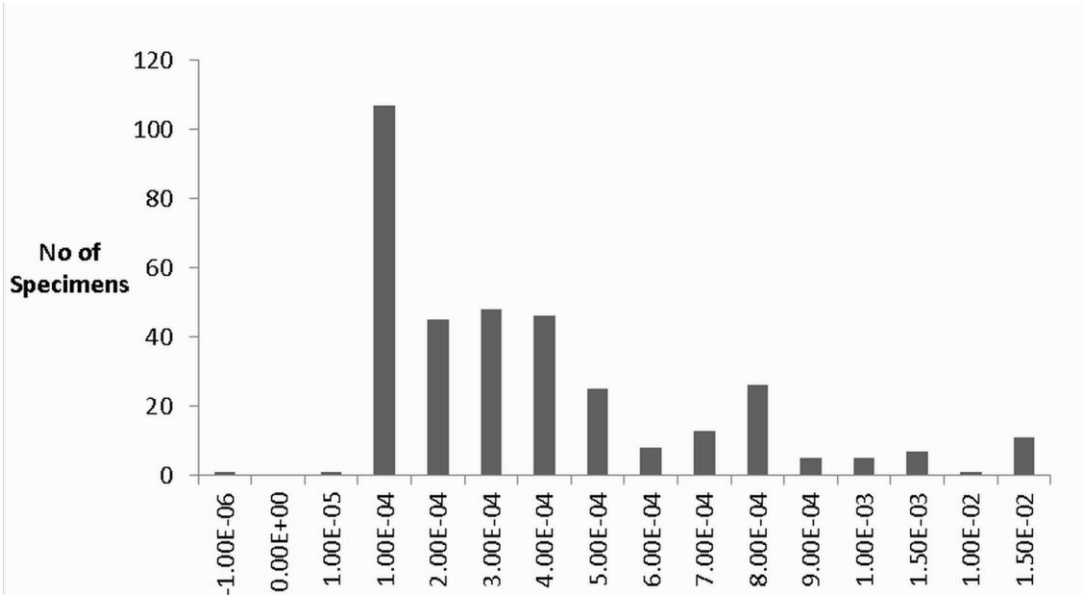

Figure 3. 8 Example histogram of the bulk susceptibility of a sample set. This allows a quick evaluation of the dominant magnetic minerals. In this case the dominant magnetic fabric is paramagnetic (<3x10^{-4} SI), although a ferromagnetic fabric is clearly present in some samples. Data is from Triassic sandstones in the Rocky Mountains, Wyoming.

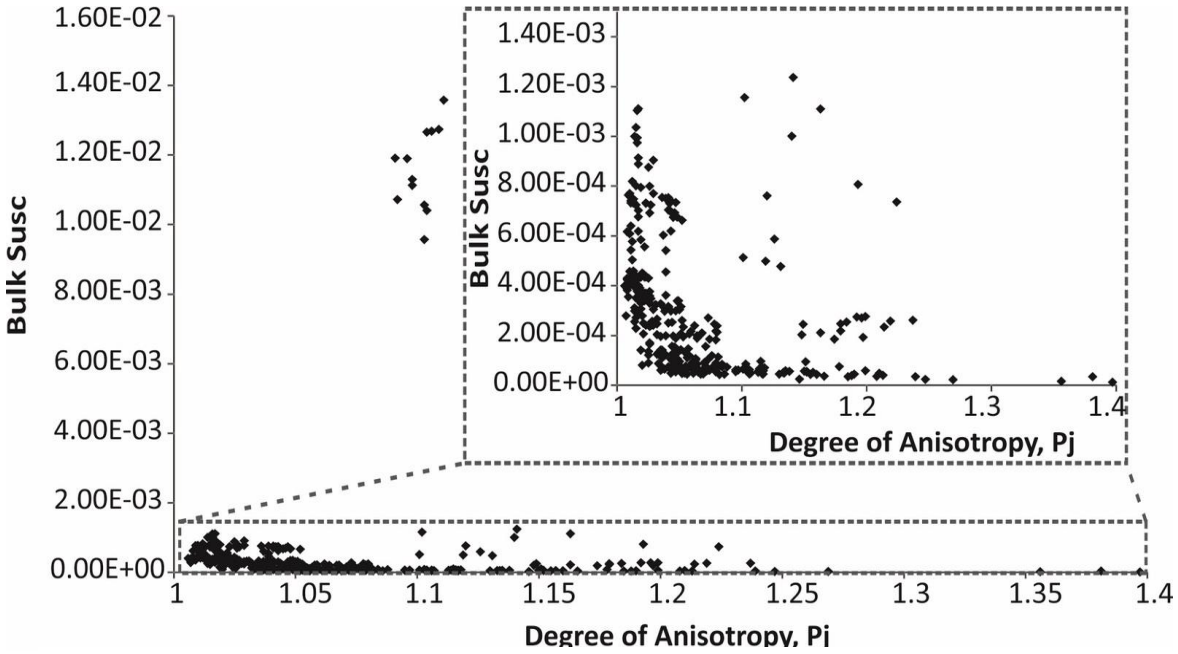

Figure 3. 9 Example plot of Km vs Pj. This plot indicates variations in anisotropy susceptibility, for this data set it suggests that variations in susceptibility or composition do not have a major control on anisotropy. The inset plot shows the same data below the range of 1.5x10^{-4}. Data is the same as shown in Figure 3. 8.

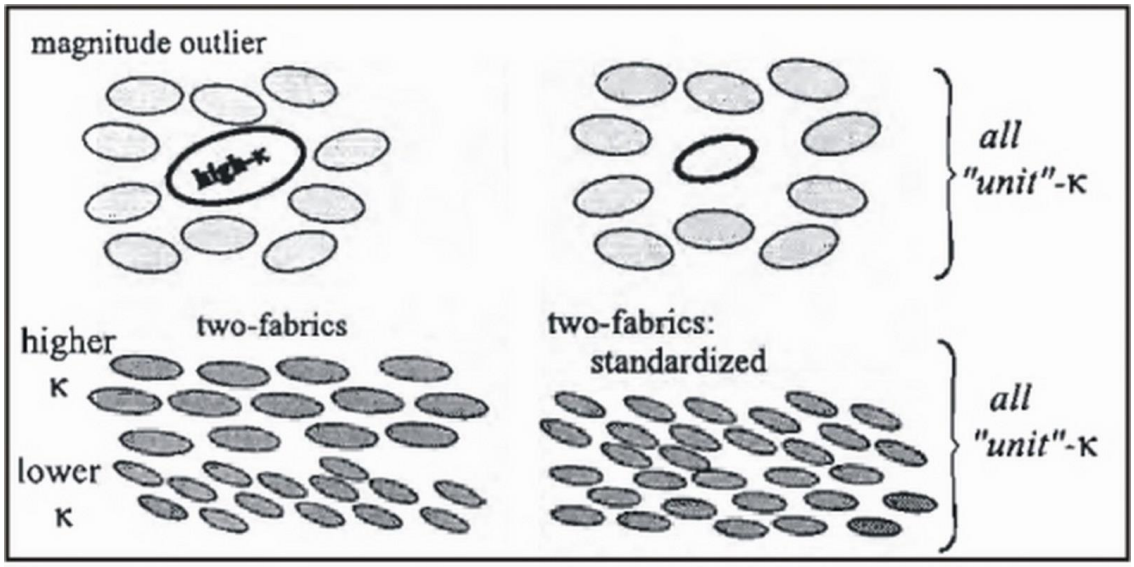

Figure 3. 10 The effects of normalisation (From Borradaile and Jackson, 2004). The top left diagram shows a fabric with a high susceptibility mineral overshadowing the fabric of the low susceptibility minerals. The top right illustrates the effects of normalisation, in that all components have the same magnitude. The lower diagrams show a similar situation for sub-fabrics.

3.6. Relationship between AMS and Strain

Graham (1954) first suggested that magnetic fabrics could be a valuable tool in petrofabric anlaysis and established a link between layer parallel shortening and AMS. Since that initial link was established a considerable amount of research into anisotropy of magnetic susceptibility and its relationship to deformation and the strain ellipse has been carried out (Amrouch et al., 2010; Averbuch et al., 1992; Bakhtari et al., 1998; Borradaile, 1991; Borradaile and Henry, 1997; Borradaile and Jackson, 2010, 2004; Borradaile and Tarling, 1981; Fuller, 1963; Graham, 1954; Hirt and Almqvist, 2012; Housen et al., 1993; Housen and Pluijm, 1991; Kissel et al., 1986; Mamtani and Vishnu, 2011; Oliva-Urcia et al., 2010; Parés, 2004; Parés and van der Pluijm, 2002; Parés et al., 1999b; Saint-Bezar et al., 2002; Tarling and Hrouda, 1993; Tripathy et al., 2009; Weil and Yonkee, 2009; Wood et al., 1976). Despite these research efforts no universally accepted relationship between the two has been determined.

Fuller (1963) described the parallel relationship of the principal axes of AMS ellipsoids and strain ellipsoids derived from the Slate Belt of North Wales (1963). This was followed by a more rigorous study that claimed to quantitatively correlate the magnitude of the AMS ellipsoid axes to the magnitudes of the strain ellipsoid axes by Wood *et al.* (1976). This was largely based on the link between preferred crystal orientation and the strain ellipsoid. Considering that AMS accurately measures the PCO of a rock's components and that that successive grain/rock component reorientation was a consequence of progressive deformation and tectonic strain (Ramsay, 1967; Ramsay and Huber, 1983) the magnetic ellipsoid can be conceptually correlated with the strain ellipsoid.

Although both Tarling (1976) and Borradaile (1991) concluded that AMS could be used as a tool to determine principal rock fabrics, the direction of the net total strain to which the fabric has been subjected leading to a possible determination of the orientation of the strain ellipsoid, they identified the problems arising from direct comparisons of the finite strain ellipsoid to an AMS ellipsoid. Tarling (1976) stated that although AMS is highly sensitive to slight changes in grain shape of the ferromagnetic minerals that can occur due to deformation being applied to undeformed rocks, the method is insensitive to these processes caused by higher strain rates. Therefore it is unlikely that magnetic fabrics could provide a reliable indicator of the magnitude of strain.

Kligfield et al. (1983) argued that AMS could effectively record changes in progressive deformation, but it was also thought that the AMS fabrics were primarily controlled by ferromagnetic components alone. Bakhtari et al. (1998)

used AMS to identify tectonic lineations and tracked a deformation gradient using magnetic fabrics. Similarly Pares et al. (1999, 2002 & 2004) used AMS to track progressive changes in deformation and to identify weak tectonic lineations and foliations that form prior to cleavage. They further confirmed that the correlation between AMS and strain required information on the magnitude and orientation of the pre-deformational ellipsoid, identification of the rock's magnetic carriers and their orientations and coaxial deformation without recrystallisation of the rocks components (Parés, 2004). Borradaile & Jackson (2004) reiterated the earlier arguments of Borradaile (1988) by concluding that AMS ellipsoid shapes rarely correlate with finite strain magnitudes and that rock composition, not strain, is a primary control on anisotropy degree, but moderate strains can affect the AMS ellipsoid shape and very high strains would affect degree of magnetic anisotropy.

3.6.1. Interpreting Magnetic Lineations and Foliations

Even the simple correlation between the orientation of the axes of the AMS ellipsoid and strain ellipsoid proposed by earlier researchers (Graham, 1954; Fuller, 1963 and Wood et al., 1976) needs to be approached with caution. This can be clearly seen by relating the magnetic lineation (Lm, defined by the long axis of the AMS ellipsoid and given by a cluster of K1 axes) of a sample to surrounding structural controls. As suggested by Borradaile and Tarling (1981) and later confirmed by Parés and van der Pluijm (2002) with field data and numerical and experimental models, the magnetic lineation is usually controlled by the interaction of two fabrics. They inferred that the magnetic lineation can parallel or track the intersection of two competing planar fabrics, such as bedding and cleavage in

sedimentary rocks undergoing deformation (Parés and van der Pluijm, 2002). This is not always the case as the magnetic lineation can also parallel the tectonic stretching direction (Parés and van der Pluijm, 2002).

On a more regional scale the magnetic lineation can also develop parallel to fold axes under very low deformation intensity (Kissel et al., 1986). Furthermore the magnetic lineation is affected by other factors besides strain. The extent to which the magnetic lineation parallels the intersection between two planar fabrics or tectonic extension direction depends on the original AMS tensor, which in turn depends on the lithology and the deformation intensity (Parés and van der Pluijm, 2002). The original AMS tensor is somewhat controlled by the rock's primary fabric and composition, therefore lithologies that have a distinct pre-deformational fabric will require relatively higher levels of deformation before the magnetic lineations track the intersection between two planar fabrics or tectonic extension direction (Parés and van der Pluijm, 2002). Likewise lithologies that have a weak pre-deformational fabric will more readily develop magnetic lineations that align with tectonically significant directions (Parés and van der Pluijm, 2002). Borradaile and Henry (1997) argued that the correlation of principal directions of the magnetic and strain ellipses, while valid in some situations is invalid in cases where the strain fabric fails to overprint the primary fabric, where inverse fabrics might be present and where deformation has not been coaxial.

This is a very similar misconception to that which is regularly ignored in structural geology and strain analysis and highlighted by Paterson and Yu (1994). The original tensor is not necessarily spherical and can have any range of geometries,

orientations or magnitudes, although they are typically weak, oblate and aligned parallel to bedding in sedimentary lithologies. These original tensor conditions need to be significantly overprinted by deformation before the AMS ellipsoid is likely to show any resemblance to the strain ellipsoid, in the same way that strain needs to overcome primary fabrics before the measured strain ellipsoid will resemble the actual strain ellipsoid. Borradaile and Henry (1997) discussed this in further detail as well as some considerations for modelling the interaction of two planar features.

Despite this, AMS can still be used effectively in the study of low grade deformation. Grouping of K1 orientations occurs under progressive deformation and is occasionally accompanied by a girdle containing K2 and K3 axes. This particular axis distribution is thought to be the first evidence for layer parallel shortening in sedimentary rocks (Parés and van der Pluijm, 2002). Similarly the relationship of the magnetic foliation (the plane containing the K1 and K2 axes or the pole to K3) to significant structures can be interpreted in numerous ways. In sedimentary rocks undergoing deformation, it can be parallel to either bedding or cleavage, alternatively there may be a weak foliation that is not necessarily structurally significant. When the magnetic foliation is parallel to cleavage, it forms perpendicular to the shortest axis of the finite strain ellipsoid (Pares, 2004). In this situation, the minimum susceptibility axis is perpendicular to cleavage and the maximum susceptibility axis or magnetic lineation is parallel to the tectonic extension or the intersection of bedding and cleavage (Pares, 2004).

From this review of previous research establishing the link between the AMS ellipsoid, preferred orientations of mineral grains, and strain, it should be clear that

the evolution of the AMS ellipsoid geometry (and magnetic lineation and foliation) in terms of its shape and shape strength is determined by the pre-deformation AMS tensor, the angle between this original AMS ellipsoid relative to the strain ellipsoid and the degree of deformation. Therefore, when making any interpretation using AMS, it is necessary to be aware that the tectonic significance of magnetic foliations and lineations can vary across lithologies, outcrops or orogenic belts. Furthermore it is not possible to derive finite strain directly from the AMS ellipsoid. Hence with that in mind AMS is used in this study to accurately and quickly quantify the petrofabric and determine the origin of that fabric (i.e. whether it is purely sedimentary, composite bedding/tectonic or dominantly tectonic etc.).

3.7. Primary Sedimentary and Diagenetic Fabrics

Primary fabrics in sedimentary rocks are typically controlled by depositional and diagenetic processes. The initial depositional fabrics are determined by the gravitational and hydrodynamic forces that are prevalent during sedimentation. These fabrics are typically weakly oblate, but can be prolate if a current was prevalent during deposition (Tarling and Hrouda, 1993). Once deposition has ceased and any active currents have been removed, gravitational loading takes over and compacts the sediments, rotating grains into a horizontal oblate fabric (Tarling and Hrouda, 1993). Subsequent early-stage diagenesis can lead to chemical alterations, that can have implications for magnetic studies, particularly the generation of sulphuric and humic fluids and gases, as well as bacterial compounds by biochemical reactions. During reduction, bacteria convert Fe^{3+} to Fe^{2+}, hence ferromagnetic grains such as magnetite, maghaemite and hematite become

reduced. This results in decrease in bulk magnetic susceptibility, but promotes the formation of paramagnetic iron sulphides (Tarling and Hrouda, 1993). Increased lithostatic overburden is typically associated with late stage diagenesis, resulting in a more pronounced flattened oblate fabric (Tarling and Hrouda, 1993).

3.8. Relationship of AMS Geometries to Bedding and Tectonic Fabrics

The development of AMS fabrics in sedimentary rocks with a primary bedding fabric undergoing LPS follows the path outlined in Figure 3. 11 (Parés et al., 1999a). The K1 axes become re-orientated so that they are normal to the principal strain axis, producing a magnetic foliation parallel to the flattening plane. As compression continues K3 forms a girdle that is parallel to the principal strain axis, and the AMS ellipsoid tends towards prolate as the tectonic fabric competes with the original fabric to produce a composite fabric. With continued compression the tectonic fabric becomes the dominant fabric and the AMS ellipsoid becomes oblate and the magnetic foliation is parallel to the cleavage plane.

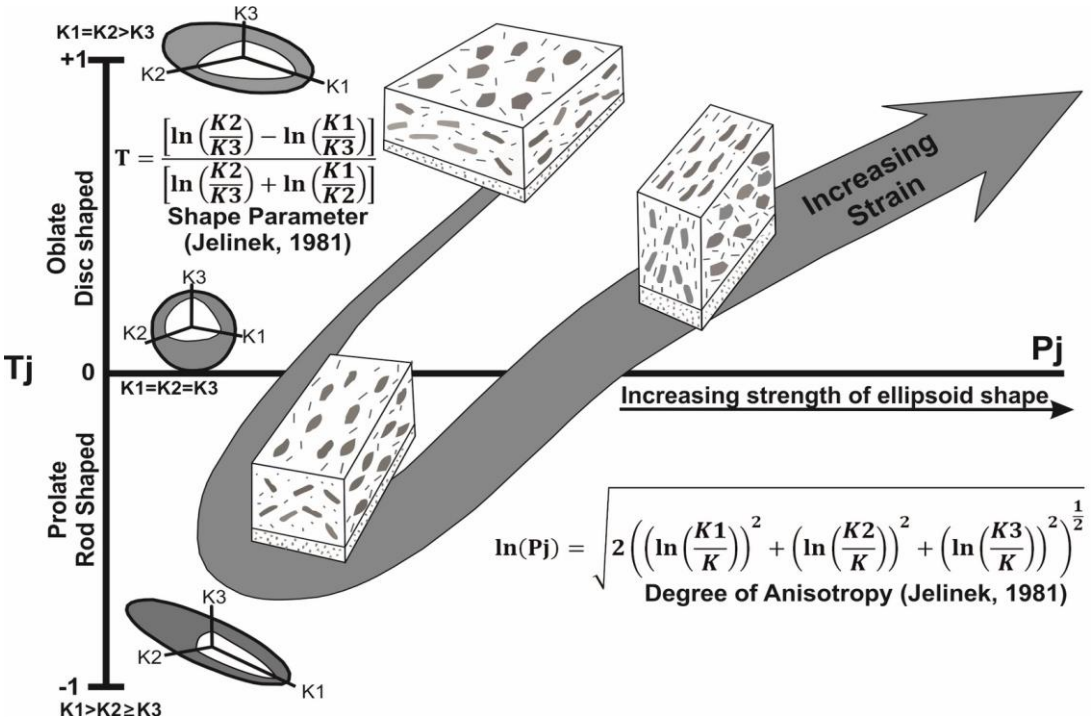

Figure 3. 11 The progression in ellipsoid shapes under progressive deformation using a Pj-Tj plot. Pj represents degree of anisotropy and increases in this imply increasing strength of the ellipsoid shape. Tj represents the shape parameter; positive numbers imply an oblate ellipsoid, whereas negative values imply a prolate ellipsoid, perfectly triaxial ellipsoids are represented by Tj values of 0. Modified from Pares (2004). The representative fabric block diagrams are from Ramsay and Huber (1983).

For ease of classification of AMS geometries and their relationship with bedding/tectonic controls, four main types of ellipsoid geometries have been designated in this study (Figure 3. 12). These classifications, which are similar to the threefold classification of Bakhtari et al. (1998) and follow the interpretations of Parés et al. (1999, 2002 & 2004), are summarised below:

Type 1: Relates to a dominantly sedimentary fabric attributed to deposition and diagenesis (compaction and cementation), which are characterized by an oblate AMS ellipsoid. The Kmax and Kint axes are scattered in a girdle roughly conforming to bedding and Kmin plots as the pole to bedding. In this case the magnetic foliation is conformable to bedding and no magnetic lineation is present as Kmax is too scattered.

Type 2: Relates to minor LPS, whereby the tectonic fabric is weaker than the primary sedimentary fabric and the AMS ellipsoid can still be weakly oblate and conformable with bedding but tends towards a triaxial geometry. Kmin remains perpendicular to bedding, Kmax and Kint although still plotting on the bedding plane become well defined, with Kmax roughly clustering parallel to the intersection of an incipient LPS fabric with bedding. The magnetic foliation remains conformable with bedding, but the magnetic lineation is typically perpendicular to the shortening direction or parallel to regional fold axes.

Type 3: Is the point at moderate LPS where the tectonic fabric starts to dominate and the AMS ellipsoid is tending towards prolate geometries. Kmax is now strongly clustered parallel to the intersection of LPS and bedding fabrics, while Kmin begins to scatter away from the bedding pole, possibly forming a girdle with Kint potentially conforming to bedding. At this stage the magnetic foliation is quite weak and the magnetic lineation becomes more defined.

Type 4: This type is characterised by flattened oblate AMS ellipsoids perpendicular or at least a high angle to bedding, that represent well defined tectonic fabrics. Kmax (Kmax may cluster either parallel to structural trend or down the dip of cleavage) and Kint define a girdle parallel to a tectonic cleavage, while Kmin clusters perpendicular to cleavage. Typically as the tectonic fabric becomes the dominant petrofabric the magnetic foliation is now at a high angle to bedding and conformable to cleavage, while magnetic lineation may still be clustered at the intersection of bedding and cleavage, but Kmax may also be scattered in the plane of cleavage.

This method of classification provides a quick and simple method of visualising the evolution of a petrofabric under continuous deformation.

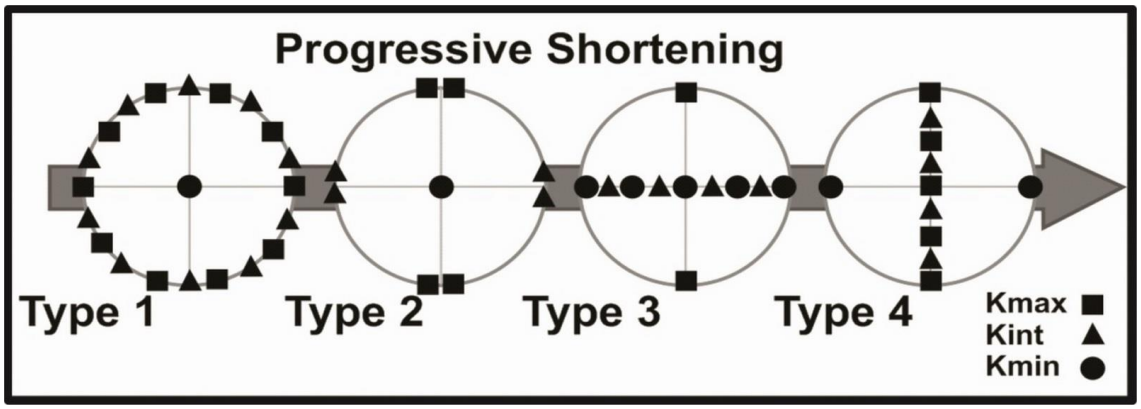

Figure 3. 12 The evolution of ellipsoid geometries by progressive deformation (LPS) of an originally horizontal bedding fabric (Type 1). As this deformation continues the AMS ellipsoid becomes triaxial and starts to resemble Type 2. The first visible stage of deformation is associated with the development of a lineation, typically represented by a prolate ellipsoid. As deformation continues this lineation becomes a foliation that is perpendicular to the original bedding plane. Modified from Bakhtari et al. (1998).

3.9. AMS Methodologies

3.9.1. Sample Selection

For this study samples were collected as orientated blocks in the field. The purpose of the study is to analyse the accuracy of strain estimates made in sedimentary rocks that have undergone low grade deformation, therefore deviation of a petrofabric from the primary bedding fabric is minimal. In order to reduce error and avoid introducing calculation problems in the analysis, samples were selected with this in mind. Samples were only selected where good control on bedding fabric orientation could be recorded, tectonic fabrics were also recorded when present. Additionally lithologies with complex sedimentary fabrics, such as syn-sedimentary deformation, burrowing, cross bedding etc. were avoided, as were coarse grained rocks such as conglomerates that had clasts that would be larger than the specimen size for the AMS analysis. Individual sampling strategies for each study area are described in their respective chapters.

For practical reasons samples with well-defined bedding planes were collected. This allows for good structural control but also provides a smooth flat drilling surface. As a result sample size was largely determined by bed thickness. Lithologies with a high degree of bedding plane or cleavage plane fissility were avoided as they would not survive drilling intact to yield a minimum of six sub-specimens. Before a selected block was removed it was orientated in the following fashion (Figure 3. 13). A strike line and dip mark were drawn on the bedding surface selected for drilling using a permanent marker. The dip mark represents the maximum inclination of the surface and the strike line was recorded using the left hand rule with an extra arrow marked at the left hand of the strike line to ensure correct reorientation. The locality information was recorded and the sample was photographed, the sample was then removed from the outcrop using a sledge hammer and chisel, and it was then ensured that the original orientation marks and labels had maintained their integrity and were duplicated for good measure.

Figure 3. 13 Block marking prior to extraction.

3.9.2. Lab Preparation

Prior to drilling, the drilling surface of each samples was cleaned and painted to ensure that any orientation mark would not wash off during the drilling process. Once the paint dried the field orientation mark was extended and duplicated with multiple dip marks per strike line. These represented targets for each core to be drilled. Samples were drilled using a table mounted drill press.

The samples to be drilled were placed on the drill-table and adjusted until the drilling surface was perfectly horizontal and perpendicular to the drill bit. This ensured that the samples were drilled perpendicular to bedding. Using the drill press 25mm diameter cores were removed from the block (Figure 3. 14). The orientation marks were then drawn vertically down the sides of each core with a downward facing tick mark on the left hand side. The drill cores were then cut into 22mm cylindrical sub samples or specimens (Figure 3. 14) using a non-magnetic, diamond tipped saw blade. The minimum number of specimens required for Jelinek statistics (1981) to be applied satisfactorily is six, therefore a minimum of seven specimens were prepared per sample and due to time constraints the maximum number of specimens prepared was usually sixteen.

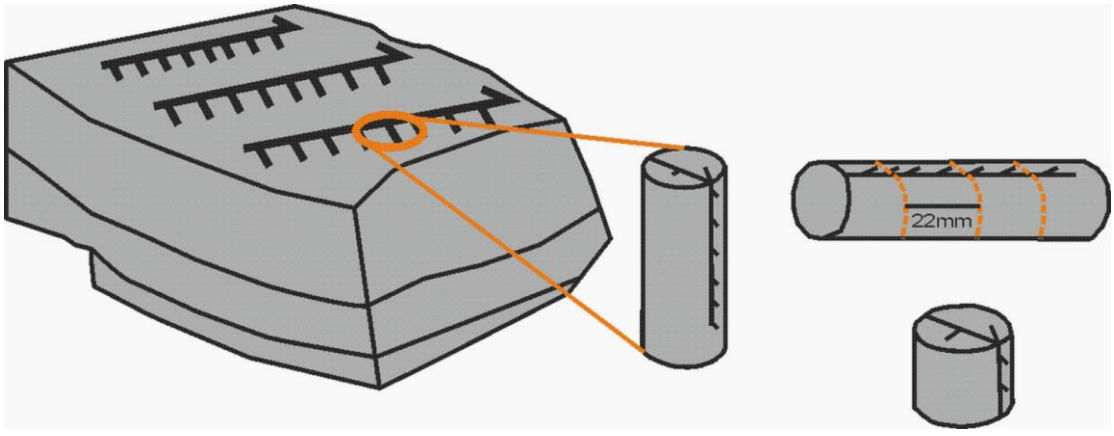

Figure 3. 14 Schematic diagram of the sample preparation process.

3.9.3. AMS Analysis

The AMS of the specimens was analysed using a MFK1-A Kappabridge (AGICO, Czech Republic) in the Rock Magnetism Lab at New Mexico Highlands University (Figure 3. 15). The MFK1-A has an operating frequency of 875Hz and an average sensitivity of ~2.0 × 10^{-8} SI. The AMS of each specimen was measured in three orientations as well as a bulk susceptibility measurement, according to the Agico user guide (see www.agico.com). The results for each specimen were combined reorientated with respect to their original field position and Jelinek statistics were evaluated using Anisoft (Figure 3. 16; version 4.2; AGICO, Czech Republic). Anisoft presents the Jelinek statistics in a table format, as well as displaying the normalised ellipsoid axes with 95% confidence ellipses on a lower hemisphere stereographic projection. Axes are deemed to be independent if the 95% confidence intervals do not overlap, i.e. not part of a girdle. The AMS results can be related back to structures seen in individual specimens (Figure 3. 17) or the whole sample.

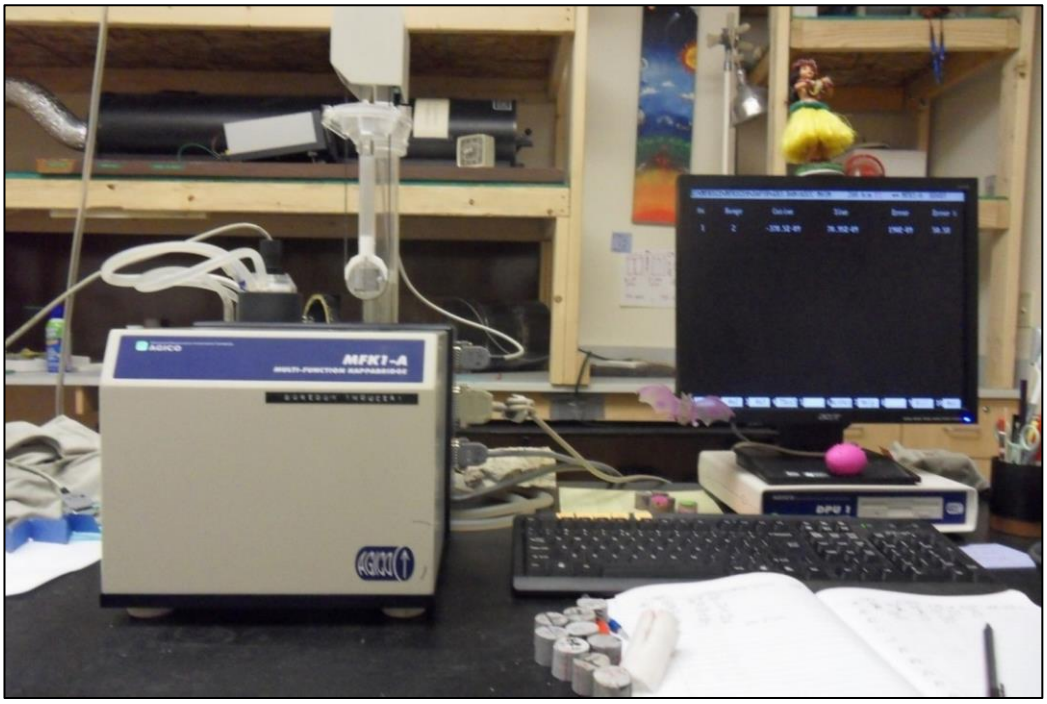

Figure 3. 15 Agico MFK1-A Kappabridge with workstation, Rock Magnetics Lab, NMHU.

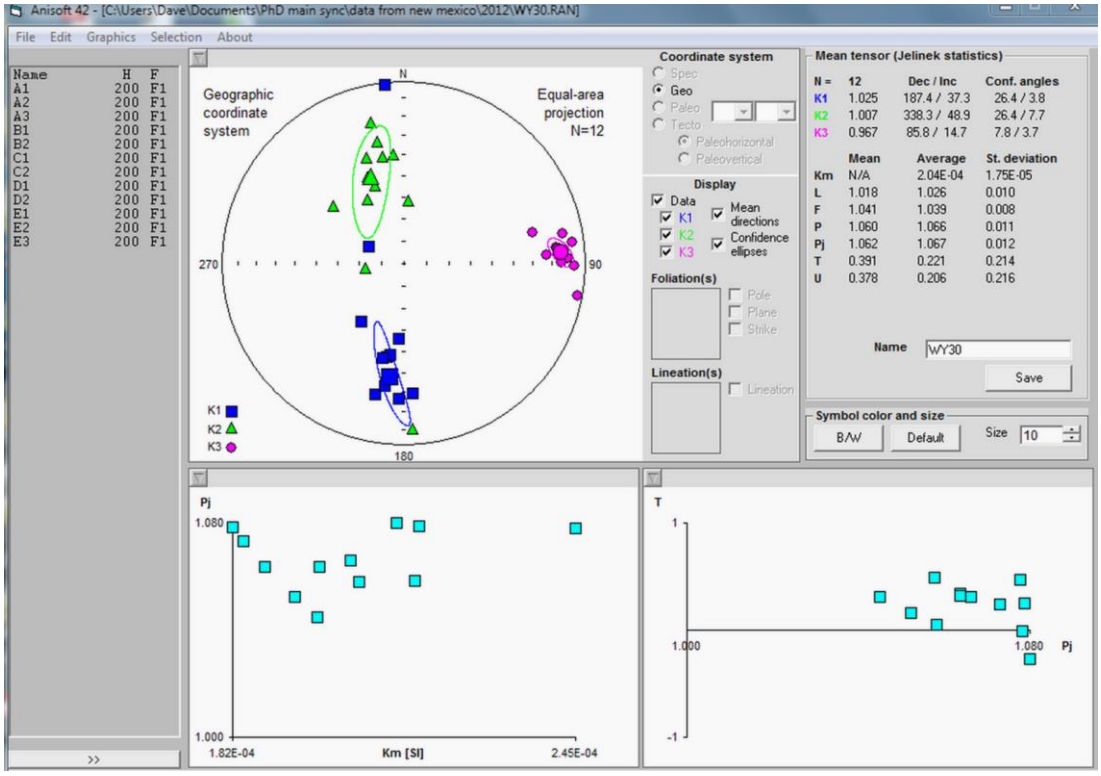

Figure 3. 16 Example of output from Anisoft. A lower hemisphere stereographic projection of the AMS tensor principal axes 1 sample is shown top left. The small symbols represent normalised measurements for individual specimens. The larger symbols represent the mean axes directions for the entire sample. 95% confidence ellipses as calculated using Jelinek statistics (1981) are also plotted. For this example the axes distribution suggest that both a magnetic foliation and lineation are present. The magnetic foliation is defined by the girdle formed by K1 and K2, while the lineation is defined by K1 alone. Also the confidence ellipses indicate that the principal axes are distinct as they do not overlap. Jelinek statistics and parameters are displayed top right. The graphs shown bottom left and bottom right, represent Pj vs Km and Pj vs Tj respectively. The Pj vs Km plot shows that anisotropy has little variation with varying susceptibility values, while the Pj-Tj plot indicates that the overall ellipsoid shape is strongly oblate.

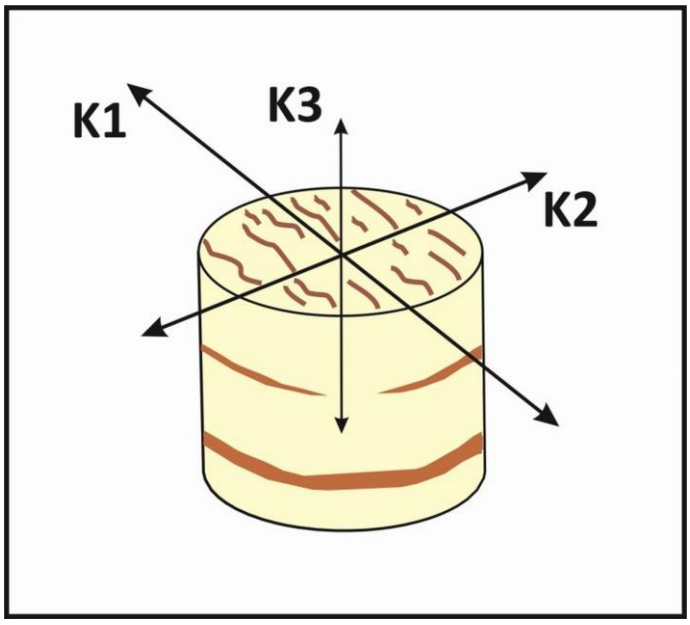

Figure 3. 17 The AMS response of a single specimen with a linear element and weak bedding planes.

Chapter 4:

Application of Anisotropy of Magnetic Susceptibility to Detect Incipient Tectonic Fabrics in the Central Sawtooth Range, NW Montana

4. Introduction

The fold and thrust Belt of Northwestern Montana (Figure 4.1) is characterised by eastward propagating thrusts that have largely placed Mississippian Madison Group carbonates as well as Cambrian and Devonian lithologies above Cretaceous and Jurassic shales and sandstones (Mudge, 1970). The Sawtooth Range (Figure 4.2) is part of the frontal imbricate thrust system of this belt, formed during the Sevier Orogeny (DeCelles, 2004). The central Sawtooth Range is an arcuate zone of north trending, closely spaced, westerly dipping, imbricate thrust sheets and associated folds. This structural regime and deformation was largely caused by the emplacement of the Lewis, Eldorado and Hoadley Thrust Slab during the Sevier Orogeny in the Late Cretaceous to Early Paleocene (Holl and Anastasio, 1992; Sears, 2001). The superb exposures of faulted Mississippian limestones in the Sun River Valley provide an Ideal location to test the ability of AMS to detect incipient tectonic fabrics.

4.1. North American Cordillera

The modern day Cordilleran belt of North America was formed by collision tectonics and resulting orogenesis (Figure 4.3), through the Mesozoic and Cenozoic (DeCelles, 2004). Throughout the early Mesozoic, the western coast of America was a large subduction zone that extended along the length of the continent (DeCelles, 2004; Park, 1988). The Farralon plate was subducted, at a shallow angle, under the North American plate creating a contractional arc (Miall, 2009). This subduction zone was accompanied by a volcanic arc to the east, represented by the Cordilleran Mesozoic

batholiths belt (Park, 1988), and the Cordilleran fold and thrust belt on the easternmost margin (Figure 4.4; DeCelles, 2004).

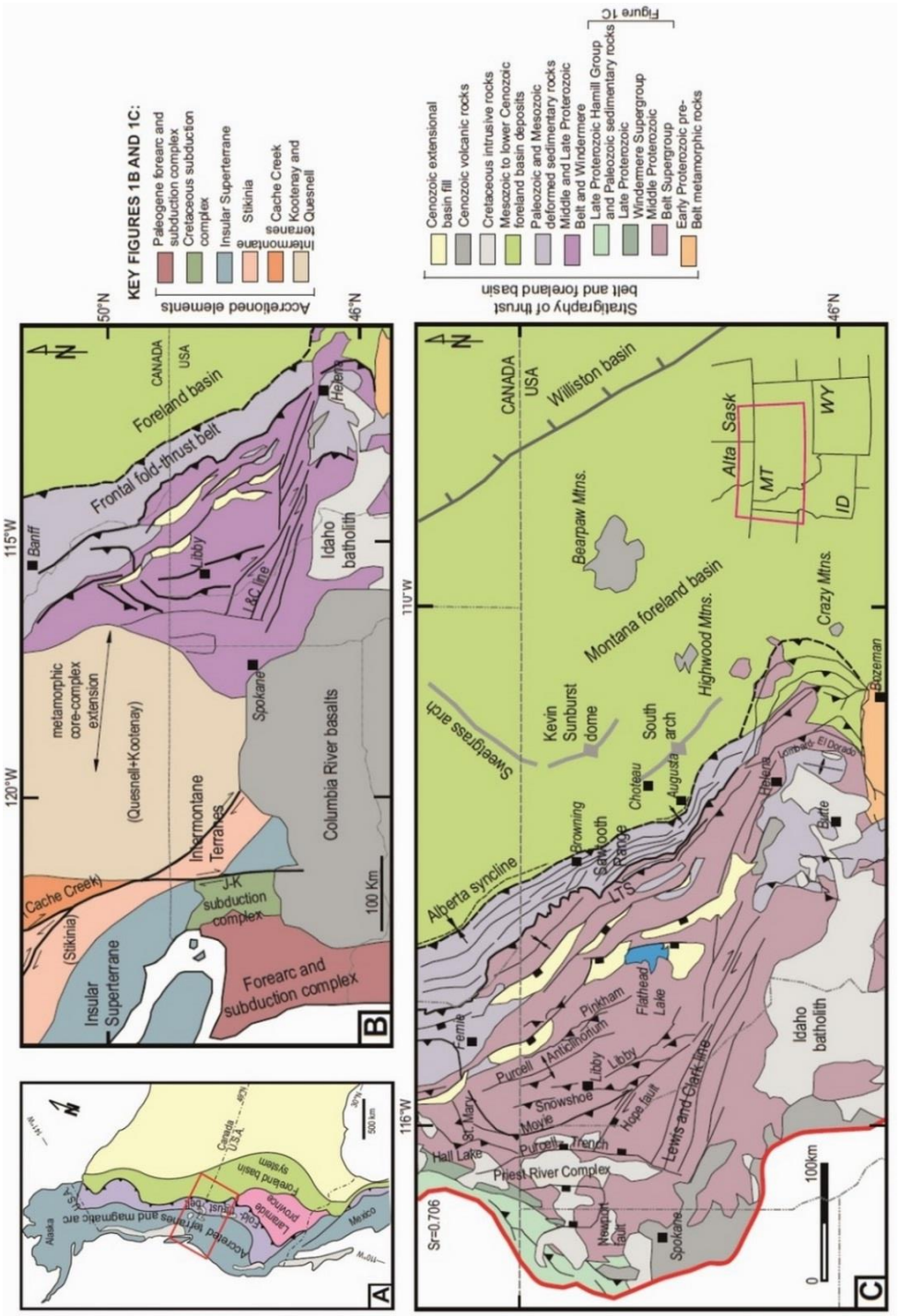

Figure 4. 1 Tectonic maps of North America. A. Simplified map of North American Cordillera. B. Terrane map of northwest America. Tectonic map of northwest Montana. Modified from Fuentes et al. 2012.

The Cordilleran orogenic system of Montana and southern Canada is composed of three main tectonic areas or regimes (Fuentes et al., 2009):

- a western complex of accreted terranes;
- the eastern fold-and-thrust belt, that features Paleozoic and Mesozoic strata, with Proterozoic strata in the hinterland;
- and a foreland basin composed of Mesozoic to early Paleogene strata that has been incorporated into the fold-and-thrust belt.

Figure 4. 2 Aerial photograph looking north across the Sawtooth Range, the Gibson Reservoir is right foreground and the Sun River extends eastward from the reservoir. Thrust geometries can be clearly seen with consistent westward dips**.**

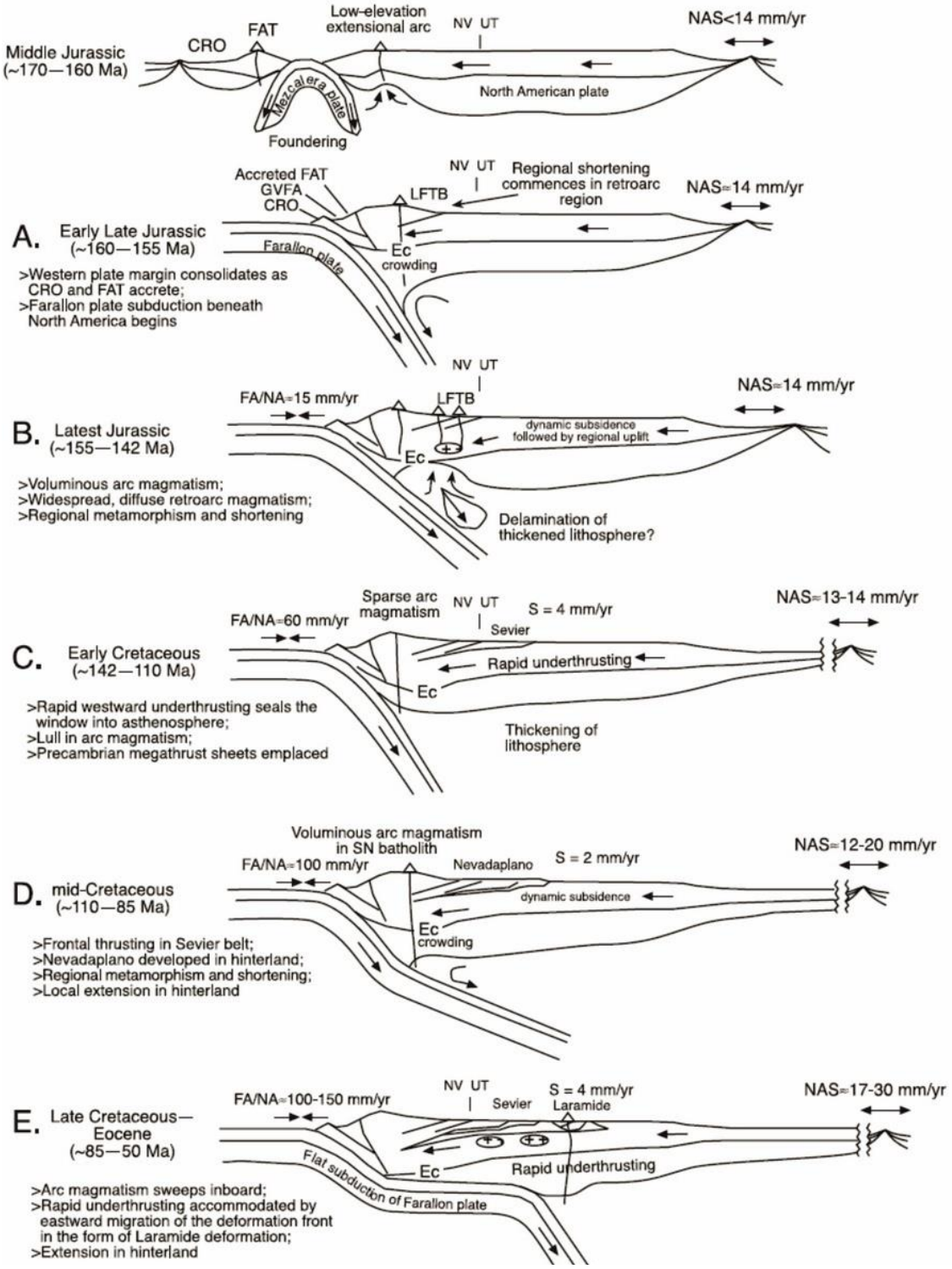

Figure 4. 3 Kinematic reconstructions of Cordilleran belt (After DeCelles, 2004). CRO, Coast Range Ophiolite; FAT, Foothills Arc Terrane; GVFA, Great Valley forearc basin; Ec, Eclogitisation; FA/NA Farallon-North American convergence rates; NAS, North Atlantic spreading rates.

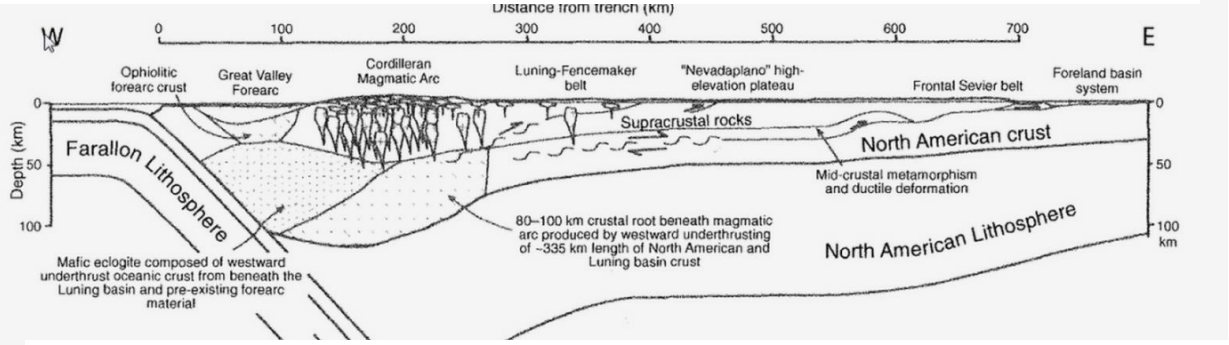

Figure 4. 4 Typical cross section across the Cordillera (From Hildebrand, 2009).

The western complex is a tectonic collage of allochthonous terranes that were emplaced largely by strike-slip deformation (DeCelles, 2004; Hildebrand, 2009). The eastern foreland thrust and fold belt (i.e. Rocky Mts. of Montana and Canada) was produced by continued convergent deformation of the western continental margin from Mesozoic to early Cenozoic time (Sears, 2001). The thrust front consists of an east directed set of thrust sheets defining a belt up to 300km wide (DeCelles, 2004; Hildebrand, 2009). This front developed on the Precambrian basement of the North American Craton (Park, 1988). Extension in the late Cenozoic has occurred across the region and has exploited the pre-existing thrust faults and reactivated them as normal faults (DeCelles, 2004; Hildebrand, 2009). This activity led to the formation of structures like the Basin-and-Range province (DeCelles, 2004; Hildebrand, 2009).

4.2. Sevier and Laramide Orogeny

Most reviews of the American Cordillera refer to the Laramide and Sevier Orogenies as separate events or more confusingly use the terms interchangeably. The two 'orogenies' (the Laramide and the Sevier) were produced by the same collision and crustal shortening event, collision of the Farrallon and North American plates (DeCelles, 2004). The Laramide Orogeny developed in the late Campanian of the Upper Cretaceous and continued into the Oligocene, this is largely synchronous with the Sevier (Late Jurrassic-Upper Cretaceous; DeCelles, 2004). Laramide deformation is characterised by basement cored uplifts, that partitioned or separated the Cordillera foreland basin (the Western Interior Basin (WIB)), into a series of smaller basins, separated by the uplifted basement blocks (Tetons, Uinta Arch, etc.; Miall 1990).

Each uplifted basement segment (or Laramide range) is bound by moderate to steep angle reverse faults that may extend into the lower crust (DeCelles, 2004). Miall (1990) argues that these segments were uplifted due to the widespread contraction caused by the low angle subduction and that the subducting slab remained mechanically coupled to the overlying crust (Miall, 1990). Sevier deformation is largely associated with the formation of a fold and thrust belt to the west of the WIB. This Sevier thrust belt is a narrow zone of regional scale thin skinned thrust faults and related folds that extends from Canada to California, the limits of its southern extent are unclear due to structural complexities (DeCelles, 2004). The Sevier belt was classically considered to be defined by thin skinned deformation, yet DeCelles (2004, and references within) show that segments of the Precambrian metamorphic rocks of the basement have been involved in faulting and that these 'thin skinned' brittle thrusts are linked with ductile shear zones to the west at a structurally lower level

The Laramide and Sevier orogens have been separated by differing styles of deformation, which seems unnecessary, misleading and confusing. The general consensus has been that the Laramide Orogeny is largely an interior orogeny that produced "basement-cored" uplifts that reactivated pre-existing Pre-Cambrian normal faults, while the Sevier Orogeny was a more western thin-skinned compressional event that exploited weaknesses in bedding planes in Paleozoic and Mesozoic strata (DeCelles, 2004). The segregation of these two differing styles of deformation into two separate orogenies seems a little unnecessary and impractical, the most sensible solution would be to accept that they are the result

of differing rheological properties in the crust. Similarly DeCelles (2004) argues that all of the thrust systems that were formed east of the Cordilleran magmatic arc and that were active from the Late Jurassic to the Eocene should be considered to be part of a coherent Cordilleran orogenic wedge.

4.3. Geological Setting

4.3.1. Regional Tectonics

The Cordilleran orogenic belt of western North America formed during Jurassic–Eocene time in response to convergence between Pacific domain plates and the North American plate (Allmendinger, 1992; Bird, 1984; Burchfiel et al., 1992; DeCelles, 2004; Dickinson, 2004; Hildebrand, 2009; Monger et al., 1982; Saleeby et al., 1992). The resulting subduction led to the accretion of fringing arcs, granitic intrusions and allochthonous terranes (Dickinson, 2004). This terrane structure in the U.S. is largely obscured by the Columbia River Basalt Group, but these structures extend into Canada and are well studied due to the excellent exposures (Fuentes et al., 2012).

The composite Intermontane Superterrane is the easternmost terrane accreted to the North American plate during the Mid-Late Jurassic (Colpron et al., 2007; Dickinson, 2004) while the westernmost terrane in the Cordillera, the Insular Superterrane, is the result of a complex accretion history that commenced in the Mid Jurassic (Colpron et al., 2007). A fold and thrust belt developed in the back arc basin region and included the sedimentary sequences of the Belt Supergroup that were carried on the North American cratonic basement (Fuentes et al., 2012). The Belt Supergroup is a 15km (approx.) thick Proterozoic succession of clastic,

carbonate, and igneous rocks deposited in an intra-continental rift (Harrison, 1972; Price and Sears, 2000; Sears, 2001). Paleozoic strata including carbonate shelf material and minor clastic rocks were deposited over the Supergroup units after the Precambrian rifting event (Fuentes et al., 2012).

These units then became incorporated into thrust sheets in the easternmost regions of the orogenic foreland while the western regions of the retroarc thrust belt are dominated by rocks of the Belt Supergroup (Fuentes et al., 2012). In the Sawtooth Range this division in the thrust belt is largely defined by the Lewis, Eldorado and Hoadley (LEH) thrusts and smaller associated thrusts, (Fuentes et al., 2012; Sears, 2001). The LEH effectively splits the Sawtooth Range into two sensible divisions, a major hangingwall or thrust sheet (LEH) in the western regions and a deformed footwall towards the east (Sawtooth). The hangingwall of the LEH consists mainly of Proterozoic strata caught up in the thrust system (DeCelles, 2004) and associated structures that have been displaced along with the thrust front, such as the Purcell Anticlinorium (Sears, 2001; DeCelles, 2004). The footwall is represented by the frontal Sawtooth Range which consists of deformed Paleozoic and Mesozoic strata incorporated into thrust sheets with detachments in Cambrian to Mississippian lithologies (Fuentes et al., 2012; Holl and Anastasio, 1992). To the east of the thrust front lies the foothills region which is characterised by weakly folded and deformed Mesozoic deposits, with more deeply buried structures in Paleozoic rocks inferred from seismic data (Fuentes et al., 2012; Holl and Anastasio, 1992).

4.3.2. Lewis Thrust System

The dominant structure in northwestern Montana is the Lewis thrust system (Figure 4.5; Fuentes et al., 2012; Sears, 2001). The hangingwall of this thrust system is referred to as the LEH Thrust slab and is composed of a thick sequence of Proterozoic and Lower Paleozoic rocks. This thrust slab overlies the deformed Paleozoic and Mesozoic strata of the Sawtooth Range in its footwall (Mudge, 1982; Sears, 2001). The Sawtooth Range is composed of closely spaced imbricated sheets of Paleozoic and Mesozoic rocks (Mudge, 1982), this imbricate sequence plunges northward beneath the Lewis thrust salient and diverges into the Flathead and Waterton duplexes (Fuentes et al., 2012). To the south of the Sawtooth Range, the thrust front is disrupted by a complex array of strike-slip faults, the Lewis and Clark line (Fuentes et al., 2012). From a 145km balanced cross sections Fuentes et al. (2012) argue that there has been approximately 135km of east-west shortening in the area. This shortening was accommodated by progressive eastward thrusting. The crustal scale LEH Thrust slab is comprised of a large allocthon, 70 -110 km wide and up to 30km thick that tapers eastward (Sears, 2001). The total displacement on this thrust sheet varies from 40km at Rogers Pass to 140km at the Montana-Alberta border (Sears, 2001). This thrust sheet is mainly composed of siliclastic Mesoproterozoic to Phanerozoic Strata.

Movement on the Lewis Thrust System has been constrained by a variety of studies. Illite dating in clay-bearing fault gouge by 40Ar/39Ar, suggest contractional periods for Lewis Thrust between 72 and 52Ma (van der Pluijm et al., 2006). Sears (2001) argued that ash-fall deposits deposited on both the footwall and hanging-wall LEH Thrust slab constrain a latest age that compression must have started by 74Ma,

similarly Fuentes et al. (2012) suggest that the ash deposits could have been deposited on moving thrust sheets and that an earlier date for initiation of contraction cannot be ruled out. Sears (2001) further constrained the age of thrust sheet movement by correlating 76Ma andesitic sills intruded in undeformed Cretaceous strata in both the LEH thrust slab and its footwall prior to thrusting. Fuentes et al (2012) have provided new dates for one of these sills west of Gibson Reservoir using U-Pb geochronology of zircons sampled by laser ablation–multicollector–inductively coupled plasma mass spectrometry (LA-MCICPMS). This analysis yielded an age of 82.8 ± 0.8 Ma for this sill sample and therefore a new maximum age of deformation of Cretaceous rocks in the footwall of the Lewis Thrust system. Similarly the data for cessation of movement of the Lewis Thrust system is constrained by undeformed intrusives cross cutting faults associated with thrusting. A monzonite intrusion that cross cuts the Steinbach Thrust in the Rogers Pass Area has a U-Pb age of 52.6 ± 0.4 Ma and limits the youngest possible movement in this area (Fuentes et al., 2012).

Thrusts in the Sawtooth Range developed as a response to movement in the Lewis Thrust system and therefore should postdate displacement on the Lewis thrust. Timing of maximum burial metamorphism temperatures have been constrained by dating illite/smectite growth in Cretaceous bentonite beds caught up in thrust sheets, yielding K/Ar ages of 72-56Ma (Hoffman et al., 1976). Additionally the youngest lithologies cut by thrust faults is the Maastrichtian Willow Creek Formation (Mudge and Earhart, 1983).

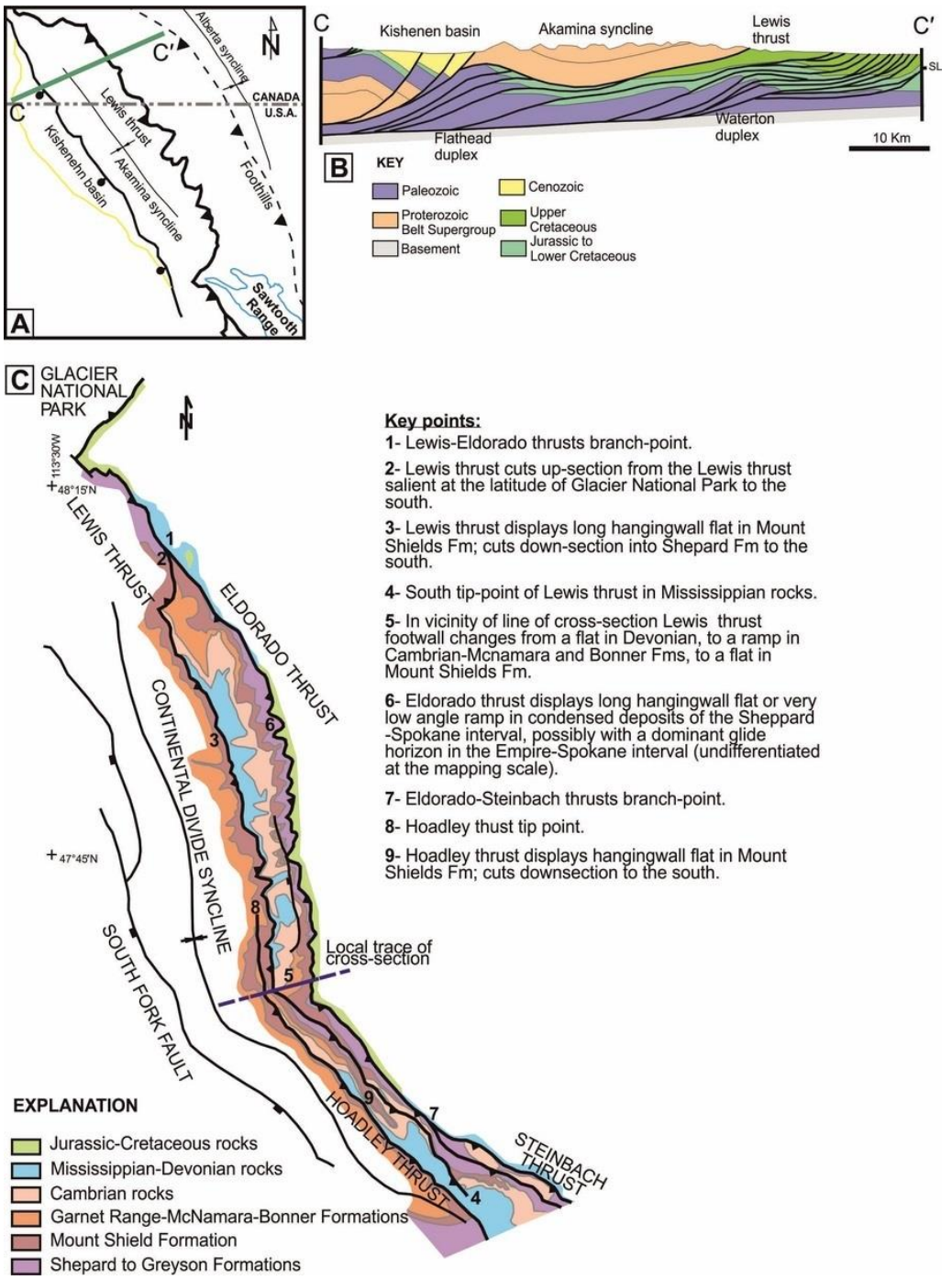

Figure 4. 5 Structural relationship between LEH and Sawtooth Range, modified from Fuentes et al. (2012). **A.** Location map of LEH and Sawtooth Range. **B.** Simplified cross section of the LEH and the structures in its footwall. Cross section is from the South Canadian Cordillera, trace indicated in A. The Waterton duplex is thought to be the northern downplunge extension of the Sawtooth Range. **C.** Map of the Lewis Thrust system in Montana. Location of Cross section in Figure 4.7 is indicated.

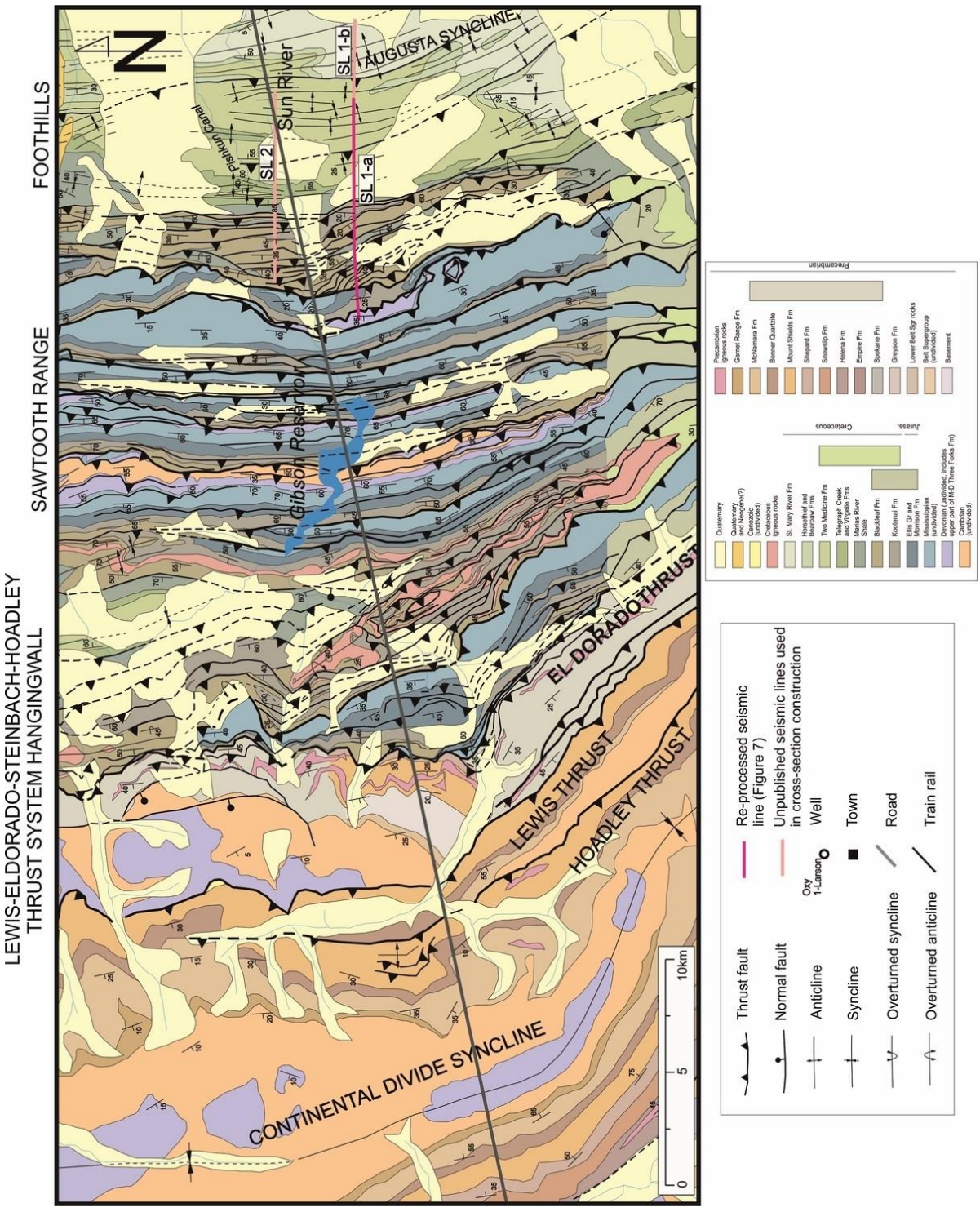

Figure 4. 6 Geological map of the Central Sawtooth Range and surrounding areas. Modified from Fuentes et al. (2012). Line of cross section in Figure 4.7 is indicated.

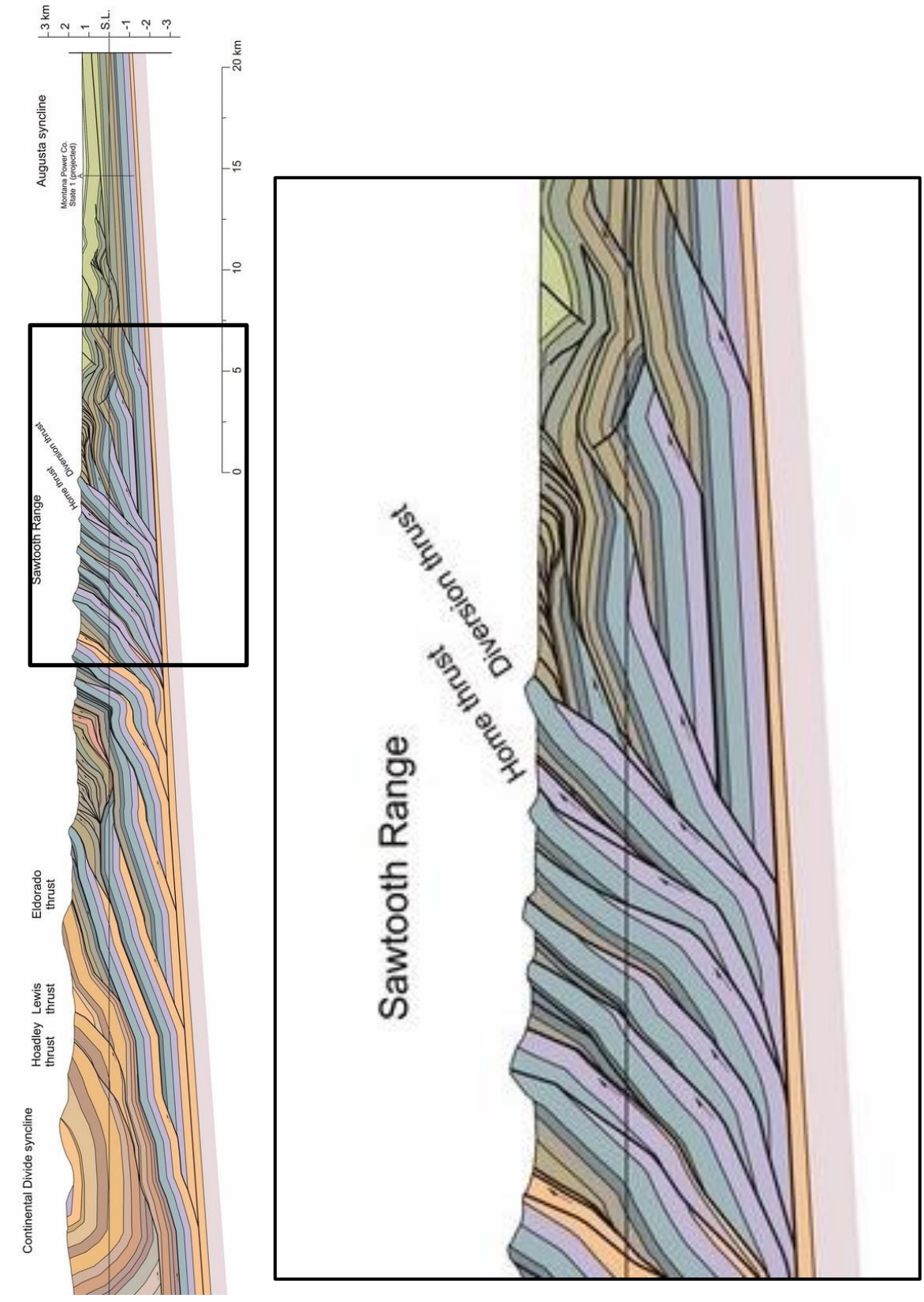

Figure 4. 7 Cross section of line indicated in Figure 4.5 (Modified from Fuentes et al., 2012). Rectangle indicates location of the Sawtooth Range Inset shows detailed cross section for the Sawtooth Range.

Figure 4. 9 View looking northeast across Diversion Lake at Home Thrust and the overlying Sawtooth Thrust.

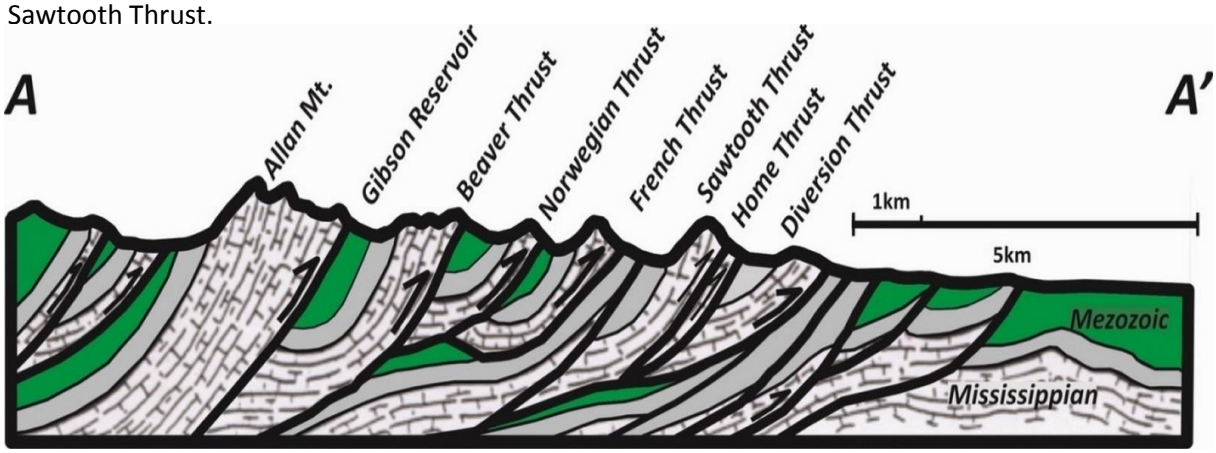

Figure 4. 8 Schematic cross section of the Sawtooth Range modified and redrawn from Alt (1984).

4.3.3. Sawtooth Range

The Sawtooth Range exposes primarily Paleozoic and Mesozoic sedimentary rocks (Figure 4. 6 and Figure 4. 7). The Mississippian carbonates of the Allan Mountain Limestone Formation and Castle Reef Dolomite Formation are the main lithologies incorporated in the thrust sequences in the eastern sections, although occasional Devonian sequences are exposed (Mudge et al., 1962). Further west Devonian and

Cambrian strata are incorporated and exposed. The carbonate units are typically interbedded limestone and dolomite, unconformably overlain by Jurassic and Cretaceous siliciclastic strata (Mudge, 1972a). The main structures of the area are characterized by thrusts that climb from a detachment in the upper Devonian and culminates in the Cretaceous, with minor detachments in the Mississippian Allan Mountain Limestone (Mitra, 1986). Close spacing of thrust surfaces led to the steep fault surface dips and sigmoidal geometries (Mitra, 1986). Although individual thrust fronts are sometimes characterised by ramp flats (Figure 4.8). Figure 4.9 illustrates the location of individual thrusts discussed in the text.

Due to the emplacement of the LEH thrust sheet the strata in its footwall experienced elevated temperature conditions. Maximum temperature conditions have been constrained between 100˚C-175˚C, from illitic mineral assemblages in Cretaceous shales (Gill et al., 2002; Hoffman et al., 1976; O'Brien et al., 2006). O'Brien et al. (2006) concluded that chemical remagnetisation associated with these temperature conditions had occurred prior to thrusting and rotation of the carbonates. This largely concurs with vitrinite reflectance studies that suggested that only very localised frictional heating was associated with large scale thrusting (Bustin, 1983). This suggests that any heating associated with the thrust related deformation of the Sawtooth Range did not exceed the temperatures associated with the prior heating event. Holl and Anastasio (1992) determined that the deformation of the strata of the Sawtooth Range accommodated a minimum bulk shortening of 60%. This shortening was primarily enabled by thrusting associated with the forward developing imbricate fan, thrusting in turn was enabled by

progressive development of mesoscopic fault arrays that allowed the base of the thrust sheets to deform by cataclastic flow (Figure 4. 10; Holl and Anastasio, 1992). The dominant structures observed at an outcrop scale are regular fractures that are typically at a high angle to bedding (Figure 4.9). Tectonic fabrics where developed are at a high angle to bedding and limited to occassional stylolitisation and cleavage.

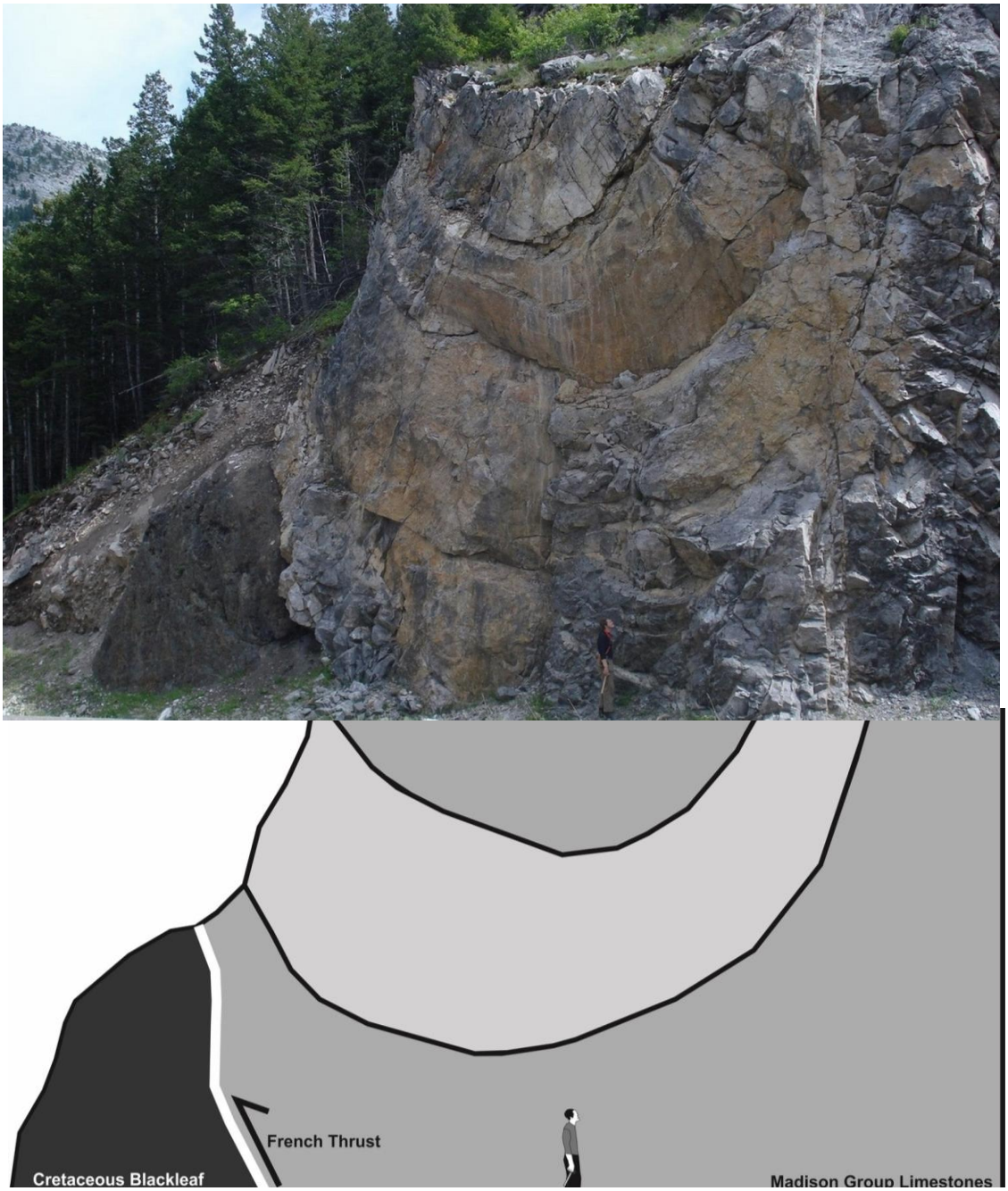

Figure 4. 10 Base of the French Thrust, with the Madison Limestone thrust over the Cretaceous Blackleaf Formation. Brittle deformation increases towards the base of the thrust sheet. Also present is an extensive fracture network.

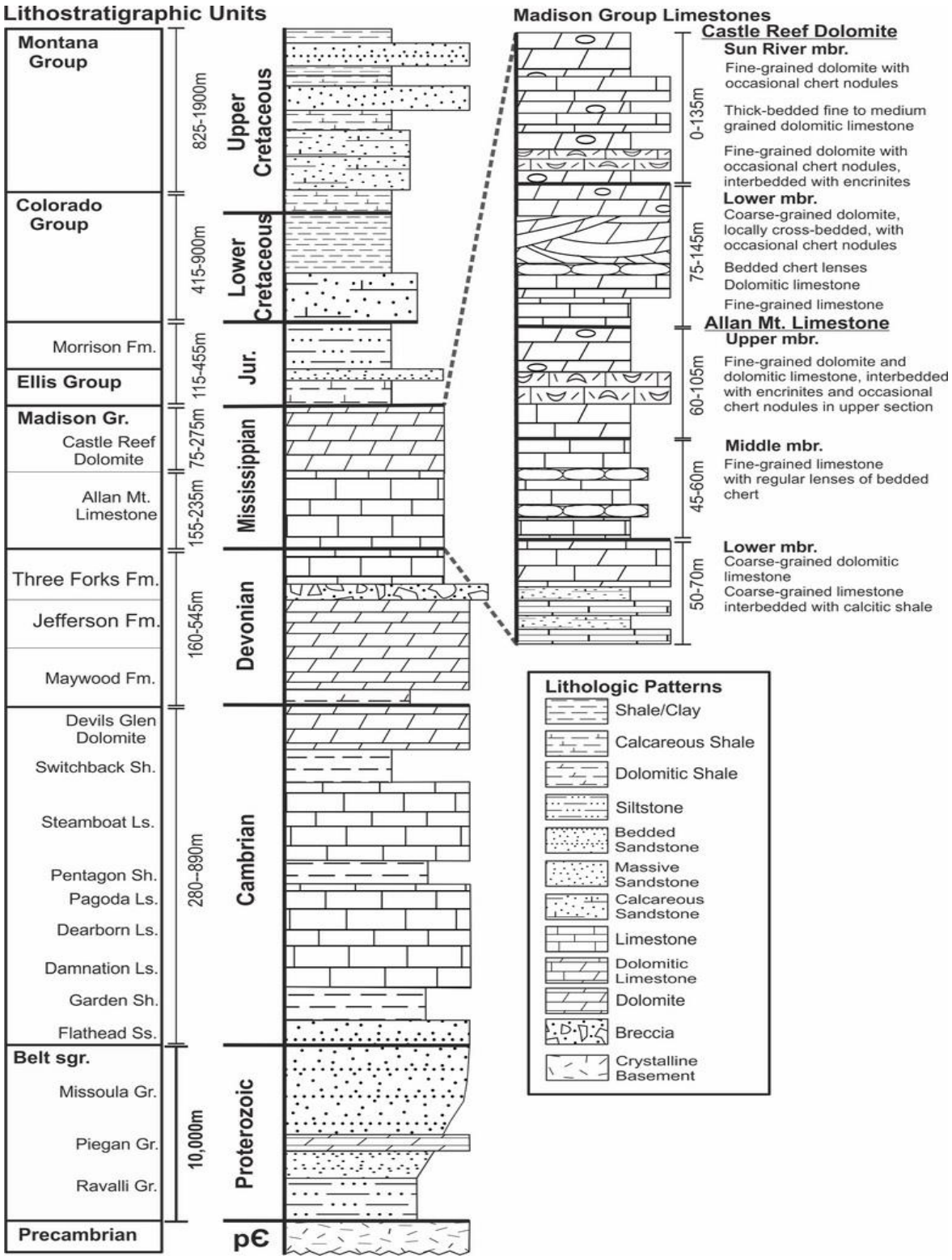

Figure 4. 11 Stratigraphic column drawn from description of Mudge (1972a).

4.3.4. Stratigraphy

4.3.4.1. Stratigraphy of the Sawtooth Range

The Sawtooth Range of the LEH footwall is comprised of Paleozoic and Mesozoic strata (Mudge, 1982) but the most prominent lithologies in the Sun River Canyon area are the Missisippian carbonates of the Madison Group. The Madison Group is divided into the Allan Mountain Limestone Formation and Castle Reef Dolomite Formation (Figure 4.11 & 4.12, Mudge, 1972). The Allan Mountain Limestone Formation is characterised by thin beds of dark-gray limestone whereas the Castle Reef Dolomite Formationis mostly thick beds of light-gray dolomite (Mudge et al., 1962). These carbonates are unconformably overlain by Mesozoic strata, and are themselves resting unconformably on Cambrian and Devonian carbonates (Mudge, 1972). The Mesozoic sequences are composed of Jurassic and Cretaceous marine and non-marine, foreland-basin, mudstones and minor sandstones (Mudge, 1972).

4.3.5. Madison Group Limestones

The boundary between Devonian and Mississippian strata has been clearly established in the Sun River Canyon by Mudge (1972a), described as a “slight disconformity at the base of a limestone sequence of the Madison Group that contains crinoidal debris and Mississippian corals in the exposure at the north end of Sawtooth Ridge. The base of the Mississippian Madison Group is represented by the Allan Mountain Limestone Formation, first named by Mudge et al. (1962) from exposures on Allan Mountain. This group is present in nearly every thrust sheet in the Sun River Canyon.

The Allan Mountain Limestone Formation is approximately 180 metres thick and is divided into three distinctive members (Mudge, 1972a). The lower member is mainly composed of argillaceous dolomitic limestone interbedded with thin shale layers. The first 15m of the member is comprised of 1m thick grey limestone beds, interbedded with 1m thick brown calcareous mudstones that thin bedded. The member is also abundant in fossils, which Mudge et al. (1962) have classified as faunal Zone A.

The middle member is a thinly bedded, fine-grained, dark limestone, with occasional dolomitic beds, and is characterised by regular occurrences of chert nodules and lenses (Mudge, 1972a). The contact between the lower member and the middle member is gradational and below the lowest occurrence of bedded chert (Mudge, 1972a).

The upper member varies from thin to thick beds of fine grained and dark gray limestone and dolomitic limestone (Mudge, 1972a). Chert while present is less abundant than in the middle member. Crystalline encrinite beds and lenses are particularly common in this member This member is also dominated by corals and brachiopods.

The upper Mississippian Madison Group is represented by the Castle Reef Dolomite Formation (Mudge et al., 1962). The Castle Reef Dolomite Formation is typically present on the crests and western slopes of the mountain ridges in the Sun River Canyon area. It varies in thickness from 200m-250m (Mudge, 1972a). The Castle Reef Dolomite Formation has been split into two members by Mudge (1972a), the lower member and the Sun River Member. The Castle Reef Dolomite Formation

overlies the Allan Mountain Limestone Formation conformably, with the contact at the base of the lowest thin (1-3m thick) fine grained dolomite bed in the Madison Group (Mudge et al., 1962). Not only is this boundary defined by the presence of this dolomite, but also by the decrease in abundance of *Homalophyllites*, a small solitary horn coral, in the Castle Reef Dolomite Formation.

The lower member varies from thick bedded crystalline dolomite, calcitic dolomite, dolomitic limestone, and limestone (Mudge, 1972a). The crystalline dolomitic beds are occasionally cross-bedded coarse grained and dominantly composed of crinoid debris (Mudge, 1972a). Approximately thirty metres above the thin dolomite unit, denoting the base of the lower member is a distinctive widespread thinly bedded dark chert (Mudge, 1972a). Additionally the lower member contains a varied fauna, mostly brachiopods and corals comprising part of the faunal Zone C from Mudge et al. (1962).

The contact between the lower member and the Sun River Member is not well defined across the area. In the east the Sun River Member base is marked by a crystalline light-grey dolomite, overlying a crystalline encrinite of the lower member (Mudge et al., 1962). In the west the basal dolomite of the Sun River Member overlies the fine grained upper dolomite of the lower member (Mudge et al., 1962). The Sun River Member, first described by Chamberlin (1955), is not as widespread or as thick as the other members probably due to extensive pre-Jurassic erosion (Mudge, 1972a). Mudge (1972a) reported thicknesses that varied from 75-135m. The Sun River Member is composed of very fine to medium-grained crystalline light grey dolomite, with occasional interbedded calcitic dolomite (Mudge, 1972a).The

lower section of this member has frequent lenses of dolomitised coarse crystalline encrinite (Mudge, 1972a). Also silicified corals and brachiopods are present in dolomite beds, implying that silicification preceded dolomitisation (Mudge et al., 1962). The coral assemblage from the Sun River member forms the fauna Zone D of Mudge et al. (1962).

	Series	Group	Formation	Member	Thickness (Metres)	Description
Mississippian	Upper Mississippian	Madison	Castle Reef Dolomite	Sun River Member	0-135	Light grey fine to medium grained crystalline dolomite, with thick bedded dolomitic limestone. Occasional chert nodules.
				Lower Member	75-145	Thin to thick bedded grey dolomite, calcitic dolomite, dolomitic limestone and magnesian limestone. Occassional chert lenses and nodules
	Lower Mississippian		Allan Mountain Limestone	Upper Member	60-106	Thin to thick bedded grey limestone, occassional dolomitic limestone and magnesian limestone. Occassional chert lenses and nodules.
				Middle Member	45-60	Dark fine grained limestone, occassional dolomitic limestone. Abundant chert lenses and nodules.
				Lower Member	50-70	Dark grey limestone and dolomitic limestone. Thin mudstone beds and thicker limestone beds near base.

Figure 4. 12 Stratigraphy of the Madison Group, modified from Mudge (1972a).

4.3.6. Faunal Zones

Mudge et al. (1962) applied the faunal zonation of Madison strata of Sandro and Dutro (1960) to the lithologies of the Sawtooth Range, this zonation scheme is largely based on corralline material. Zone A is defined by the regularly occurrence of the rugose coral *Cyathaxonia* (Carruthers, 1912), it is present at the base of the lower member of the Allan Mountain Limestone Formation and becomes less abundant upsection (Mudge et al., 1962). Zone B is largely limited to the middle member of the Allan Mountain Limestone and is characterised by various brachiopods and small horn corals (Mudge et al., 1962). Zone C is the most extensive zone and stretches from the upper member of the Allan Mountain Limestone Formation to the middle of the Sun River Member of the Castle Reef Dolomite Formation (Mudge et al., 1962). The zone is characterised by corals,

particularly *Homalophyllites*, and abundant brachiopods (Mudge et al., 1962). Zone D is restricted to the to top part of the Castle Reef Sun River Member and is characterised by silicified brachiopods and rugose corals (Mudge et al., 1962). Despite the wide range and abundance of fossils, particularly *Syringopora* and *Vesiculophyllum*, the most abundant fossils in the Madison Group are the coarse crystalline beds of crinoidal debris or encrinites (Mudge, 1972a).

The environmental reconstruction of the upper Madison Group is an important consideration for the dolomitisation and diagenetic processes that occurred after deposition. The upper Sun River Member is characterised by faunal zone D which in turn is dominated by *Perditocardinia, Faberophyllum,* and *Lithostrotion Siphonodendron* (Mudge et al., 1962). *Perditocardinia* is an epifaunal brachiopod that is typically found in shallow subtidal environments (Sepkoski, 2002). Similarly *Faberophyllum* and *Lithostrotion Siphonodendron* are rugose horn corals that are also found in shallow marine environments (Sepkoski, 2002). Mudge et al. (1962 and 1972) concluded that shoal conditions with warm shallow open marine waters was the main depositional environment controlling Madison Group sedimentation.

4.3.7. Mississippian-Jurassic Unconformity

The erosive unconformity at the top of the preserved Sun River member is significant for a number of reasons, firstly it represents a period of approximately 130ma spanning from Late Mississippian to Middle Jurassic (Mudge, 1972a), secondly it provides some information regarding the post-depositional and diagenetic conditions for the Madison Group. Some lithologies representative of the missing strata occur in some parts of Montana and Alberta (Mudge, 1972a; and

references there within), with Pennsylvanian and Permian sedimentary units widely exposed across western Montana, Triassic and Lower Jurassic units are less common in western Montana and surrounding areas. Mudge (1972a) argued that if evaporite beds were interbedded in the missing Upper Mississippian strata of the Sun River Canyon, as is the case in eastern and southern Montana, they could have accounted for the required magnesium for dolomitisation of the upper Madison by seepage refluxion. Solution widened joints and clam borings infilled with Mid-Jurassic sands, confirm that Mississippian strata was regularly exposed at the surface until Jurassic sedimentation (Mudge, 1972a). This extensive erosion led to the removal of the characteristic Karst topography of the Mississippian strata in Montana (Mudge, 1972a).

4.3.8. Dolomitisation of the Upper Madison

As previously mentioned Mudge (1972a) argued that if evaporites were present in the Sun River area, seepage refluxion from hypersaline brines may have driven dolomitisation. A more local source for the required magnesium was also suggested by Mudge (1972a), with magnesium being sourced from the abundant encrinites. A sufficient local source seems unlikely considering Mudge et al. (1962) showed that the magnesium percentage decreases downwards in the Madison strata which is suggestive of an external source located above the Madison, rather than a localised internal source. Also this implies dolomitisation occurred after deposition of the majority of the sequence and it's overlying beds. Additionally the dolomitising fluids were shown to be selective towards fine-grained argillaceous units, with these units

showing a gradual decrease in magnesium towards adjacent coarse-grained encrinites and limestones (Mudge et al., 1962).

Similar to the conclusions of Mudge (1972a), Balch (1987) summarised the post-depositional and diagenetic evolution of the Madison group in southern Montana using several phases (Figure 4.13):

1. Extensive dolomitisation of inner-shelf carbonate sediments beneath evaporites;
2. Surface exposure of dolomitised sediments, leading to desiccation and brecciation as well as circulation of groundwater during evaporite deposition;
3. Early Visean epeirogenic uplift leading to regional karstification and associated solution breccias;
4. Late Serpukhovian to Early Bashkirian sedimentation;
5. Moscovian epeirogenic uplift leading to further erosion and a second stage of karstification;
6. Continued Pennsylvanian sedimentation
7. Late Cretaceous tectonism.

Evaporites overlying Madison Group limestones in southern Montana are generally held to have formed in an arid climate marine regressions of the interior seaway (Balch, 1988). Marine regressions would have led to precipitation of gypsum and anhydrite and increased salinity of the shelf sediment pore waters (Balch, 1987). These brines were enriched in magnesium and dolomitised their host sediments (Balch, 1988). Sediments beneath the shelf were dolomitised by brines that seeped downwards through them (Balch, 1987). Mid-Visean epeirogenic uplift the Cordilleran shelf brought upper Madison carbonates above groundwater level, which would have promoted the erosion and karstification of the upper 100m of the Madison (Balch, 1987).

Diagenesis of the Madison Group units in Wyoming was described extensively by Westphal et al. (Figure 4.14; 2004). The first diagenetic alteration they identified was the development of micritic envelopes, followed by bedding normal mechanical compaction (Westphal et al., 2004). The resulting bedding parallel fabric and minor grain deformation was interpreted to indicate an absence of a widespread early cement framework prior to initial compaction (Westphal et al., 2004).

Compaction and pressure-solution related cementation developed synchronously with mechanical compaction (Westphal et al., 2004). Interestingly Westphal et al. (2004) reported that dolomitisation was restricted to the lower sequences with little preference of lithologies for the dolomitising fluids, while the upper units are preserved as limestones. Stylolite formation due to deep burial was concluded to postdate dolomitisation and cement formation, with stylolites cross-cutting cements and calcite spar (Westphal et al., 2004). Late Cretaceous tectonic activity induced subsequent fracturing and brecciation.

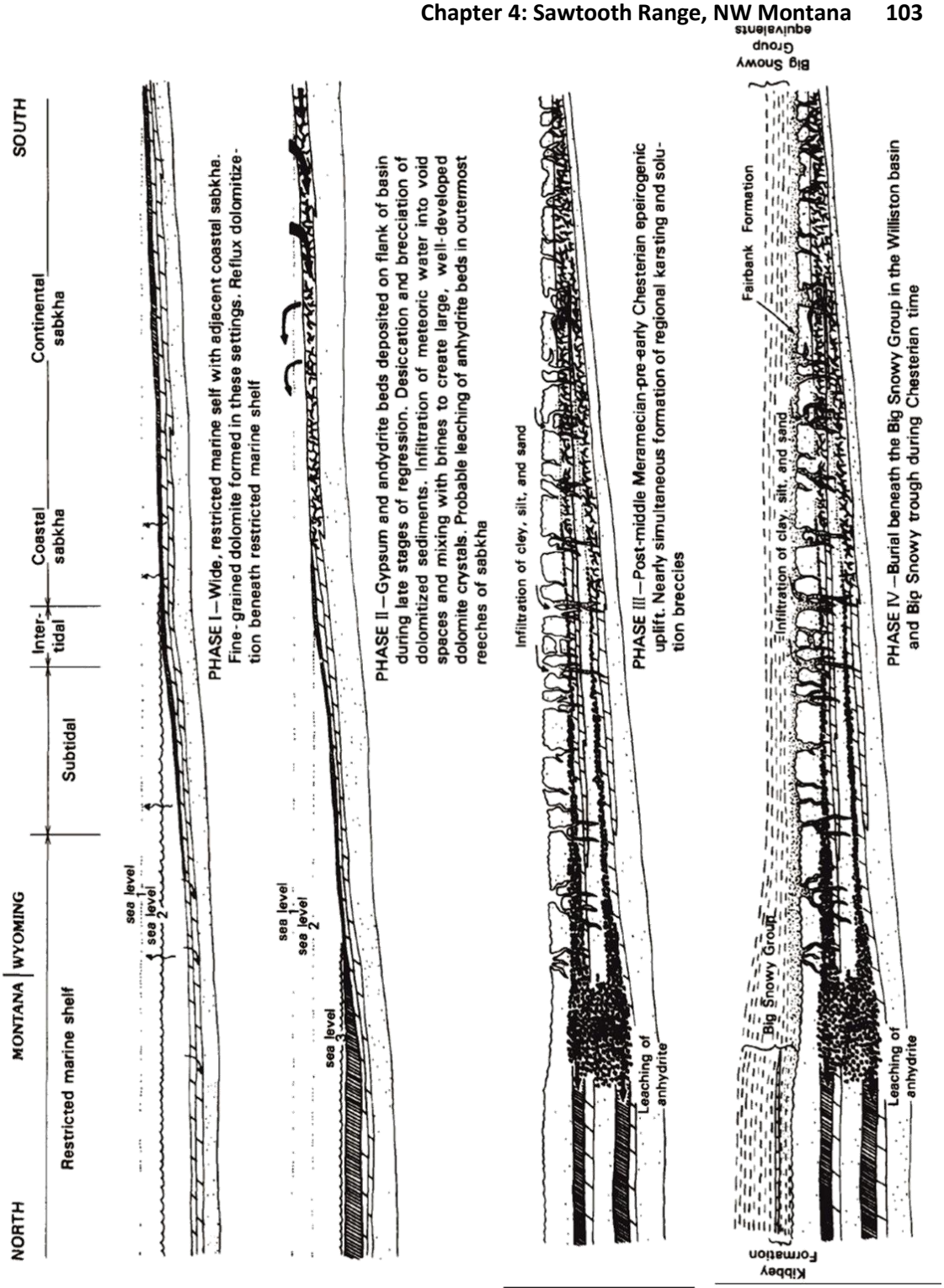

Figure 4. 13 Diagenetic and dolomitisation phases in the Madison Group, Southern Montana, continued overleaf (modified from Balch, 1988).

Infiltration of clay, silt, and sand
Leaching of anhydrite
PHASE V—Post-late Chesterian-pre-late Morrowan epeirogenic uplift of the Wyoming shelf. Erosion of Chesterian rocks except for parts of the Fairbank Formation that were preserved locally. Second stage of karsting and solution brecciation
Lower member of Minnelusa Formation
Leaching of anhydrite
PHASE VI—Burial beneath Pennsylvanian rocks and infilling of the second-stage karst surface by mud
Ground-water flow enlarging preexisting fractures and vugs
Leaching of anhydrite
PHASE VII—Late Cretaceous to Holocene post-burial modification by tectonism and ground-water flow
EXPLANATION
Nodular anhydrite
Very finely crystalline dolomite
Micritic limestone
Sandstone and siltstone
Shale
Desiccated and brecciated dolomite with well-developed dolomite crystals in vugs
Solution breccia
Karst features
Anticlinal fold with tectonic fractures

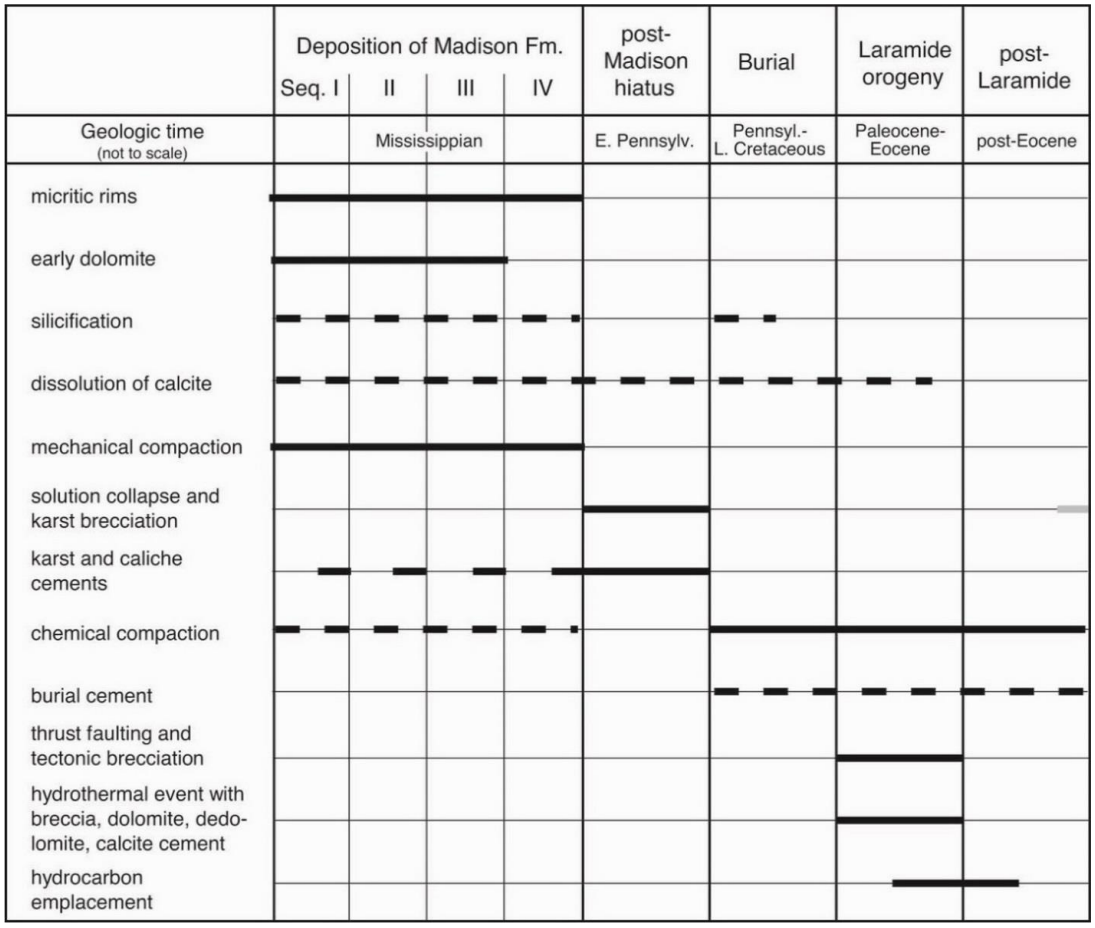

Figure 4. 14 Diagenetic sequence of the Madison Group in Wyoming (Westphal et al., 2004).

4.4. Deformation within Thrusts

As mentioned above the main structures of the Sawtooth Range are characterised by thrust faults that place Madison Limestones over Cretaceous Shales (Holl and Anastasio, 1992). The emplacement of these thrusts was enabled by progressive development of mesoscopic fault arrays that allowed the base of the thrust sheets to deform by cataclastic flow (Figure 4.15; Holl and Anastasio, 1992). This brittle deformation is the most pervasive style of deformation at the front of each thrust sheet, with little or no penetrative deformation present. Holl and Anastasio (1992) characterised the deformation at the base of each thrust sheet in the Sun River Canyon area into Brittle Deformation Zones (BDZ's) composed of arrays of mesoscopic faults. The fault spacing, attitude, and slip direction have systematic

patterns within each BDZ, additionally fault density decreases away from each main thrust surface (Holl and Anastasio, 1992).

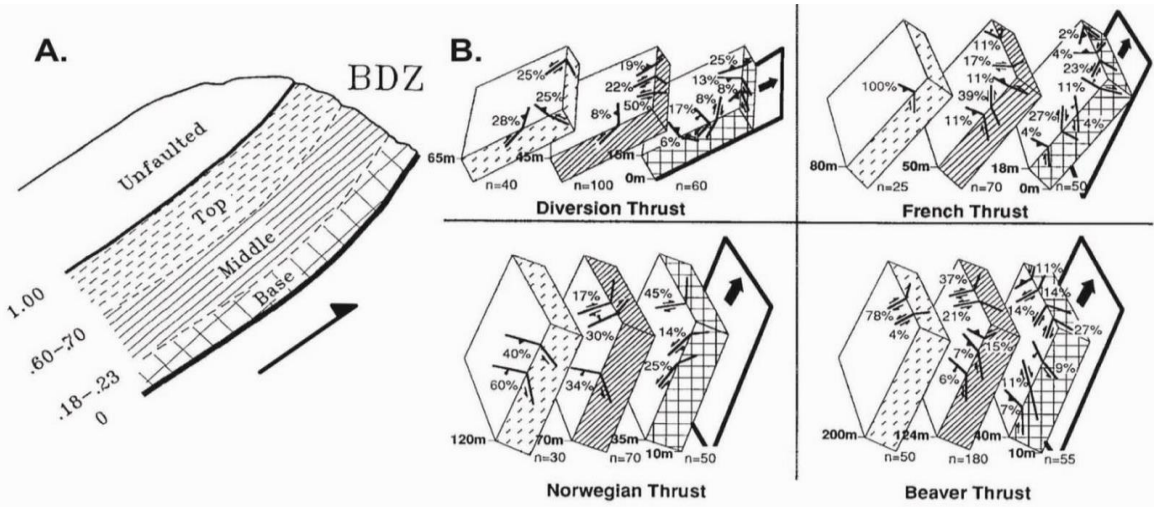

Figure 4. 15 Brittle Deformation Zones in the Sawtooth Range (Holl and Anastasio, 1992). **A.** BDZ divisions. Percentages of BDZ divisions are indicated. **B.** Distribution of minor faults in each BDZ division. Percentages relative abundance of mesoscopic faults.

Although the ratio of BDZ width to overall fault displacement was found to be constant across separate thrust sheets, Holl and Anastasio (1992) found that there was some correlation between BDZ thickness and displacement for thrust sheets in the Sun River Canyon, whereby BDZs widen uniformly with increased displacement. This is in agreement with the earlier conclusions of Wojtal and Mitra (1986), that as a thrust sheet propagates forward an array of interlocking fractures/minor faults forms and effectively splits the base of the thrust sheet into metre and sub-metre sized blocks (Figure 4.16). With continued fault movement more fractures develop until the dense network of faults can no longer accommodate the required displacement and the BDZ needs to widen (Wojtal and Mitra, 1986). Interestingly, despite this extensive brittle deformation, penetrative grain-scale deformation was reported as uniformly low across each thrust sheet studied (Holl and Anastasio, 1992). As mentioned above penetrative deformation fabrics where developed are

at a high angle to bedding and largely limited to stylolitisation and occasional spaced cleavage. The distribution of cleavage and tectonic stylolites appear to increase towards the back and away from the base of individual thrust sheets (Figure 4.17 & 4.18). Unfortunately due to the sparsity of their occurrences, it is not possible to be certain about this distribution using field data alone. The regular spaced fractures are illustrated in Figure 4.19 & 4.20.

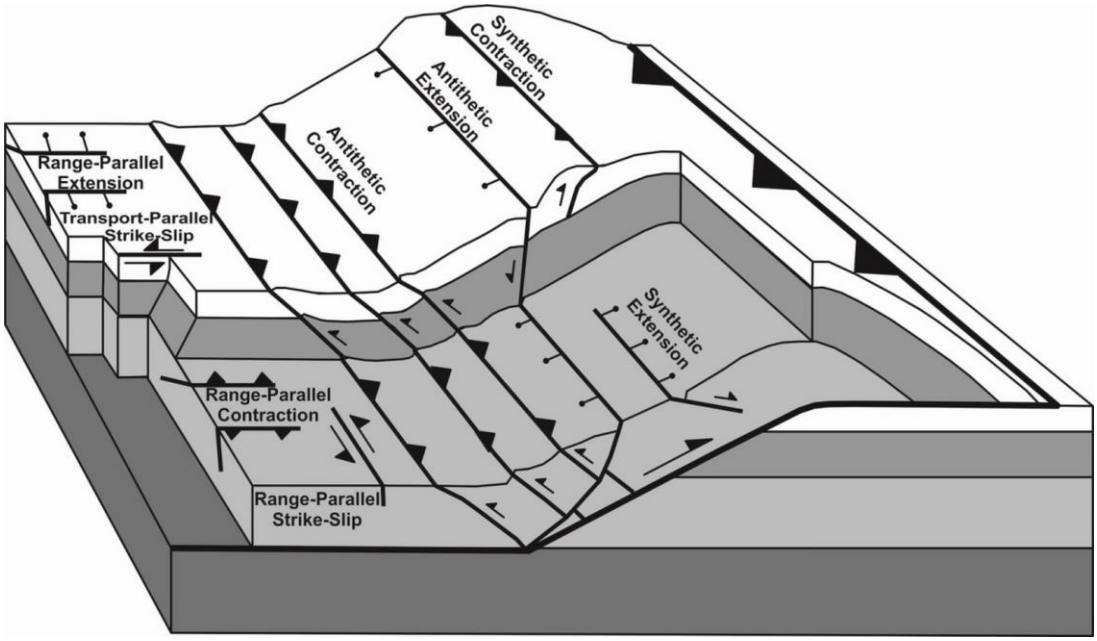

Figure 4. 17 Fault types across a schematic thrust sheet (redrawn from Holl and Anastasio, 1992).

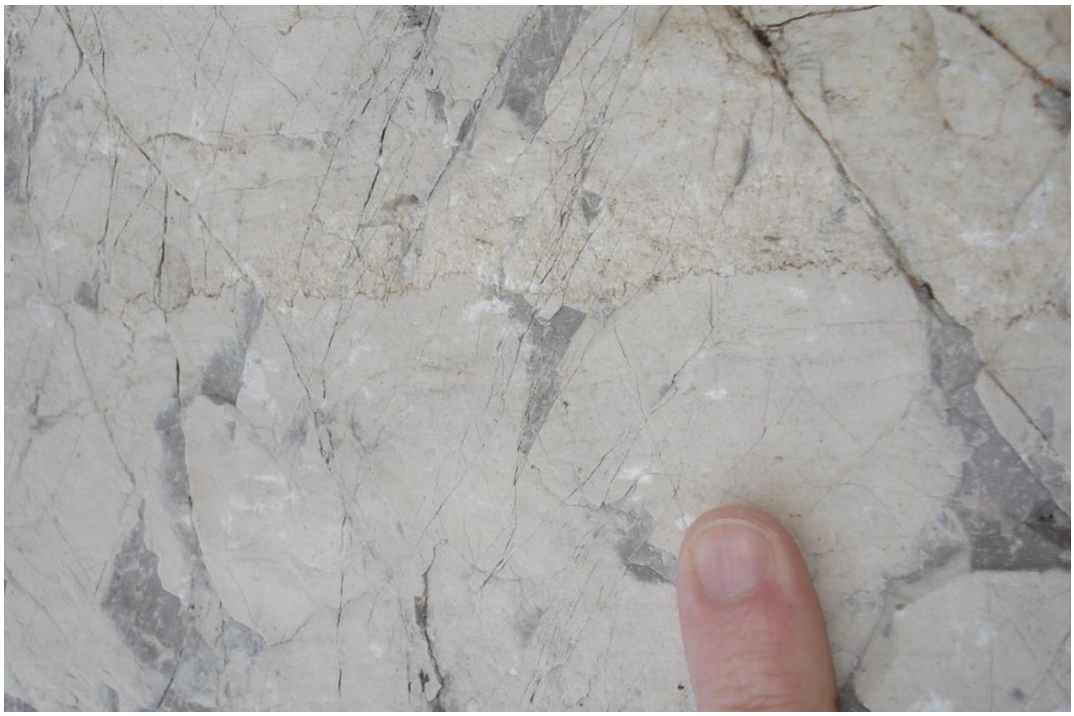

Figure 4. 16 Stylolitisation perpendicular to a bedding plane in Allan Member Limestone. Also visible are conjugate shear fractures and extension fractures.

Figure 4. 18 Vertical solution seams cross-cutting bedding and running parallel to the hammer handle. Bedding is also vertical in this case,identified by lenses of chert above the hammer.

Figure 4. 19 Fracture development in Allan Member Limestone at the back of the Norwegian Thrust.

In thin section most samples are too fine grained (Figure 4.21) for accurate strain analysis using the clast based techniques discussed in Chapter 2. Furthermore these fine grained samples do not appear to exhibit any grain scale strain. Some samples have coarser grained textures (Figure 4.22) and these also display evidence for grain scale deformation, such as type 1 calcite twinning (Ferrill et al., 2004) and grain boundary bulging (Passchier and Trouw, 2005). Both of these textures indicate deformation temperatures below 170°C.

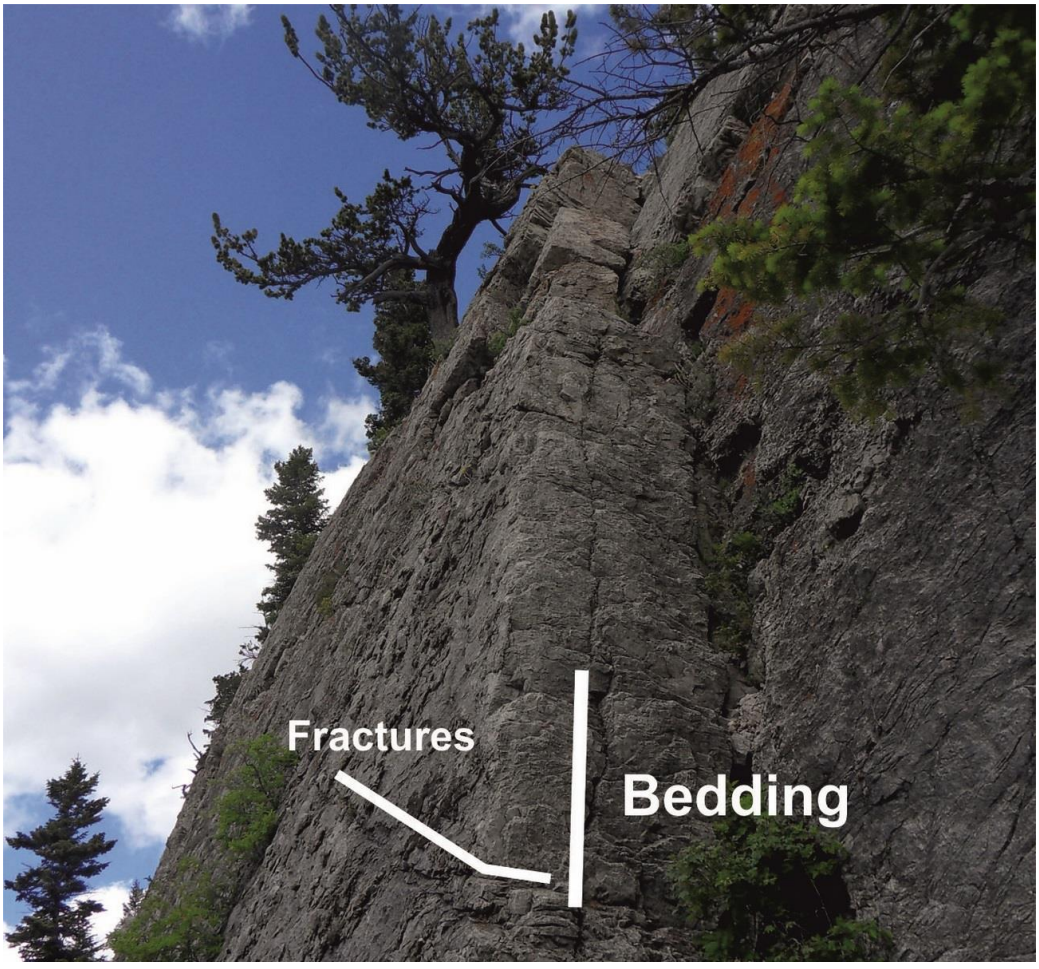

Figure 4. 20 Bedding/fracture relationships from Beaver Thrust.

Figure 4. 221 Thin section of sample Wy3. Field of view is approximately 4mm. The fine grained texture observed is typical of the Allan Mountain Limestones studied and is too fine grained for accurate strain analysis

Figure 4. 212 Thin section of sample Wy18. Field of view is approximately 4mm. The coarse grained texture while ideal for strain analysis is rarely observed. Microstructural deformation observed is mainly grain boundary bulging and calcite twinning.

4.5. Application of AMS

4.5.1. Methods

Oriented block samples for AMS analysis were collected in the Madison limestone units in a traverse along the Sun River Valley running from east to west and parallel to the direction of thrust transport. Only outcrops with well-defined structural relationships bedding, cleavage, etc. were sampled. Additionally lithologies with complex sedimentary fabrics, such as syn-sedimentary deformation, burrowing, cross bedding etc. were avoided, as these might add further complexities to the relationship between bedding and tectonic fabrics. AMS samples and structural data were obtained from 72 sites from the Diversion Thrust to the Allan Mountain Thrust. Due to the abundance of brittle deformation structures observed in the front of each thrust sheet it was difficult to extract block samples from these areas, as a result there are less samples from the front of individual sheets than there are from the middle or back of sheets. Additionally the most western thrust sheets (Allan Mountain and Big George Thrusts) had a higher abundance of brittle structures, resultingly no block samples from these thrust sheets survived drilling. The location of analysed samples is indicated in Figure 4.23.

On average 8-14 core samples, measuring 25.4mm diameter and 22mm length, were drilled from each block sample. Out of the block samples collected, 43 samples survived drilling and provided enough sub-specimens to be statistically viable (Borradaile and Shortreed, 2011). This yielded 479 individual specimens for analysis. AMS analyses were carried out using the procedures described in Chapter 3.

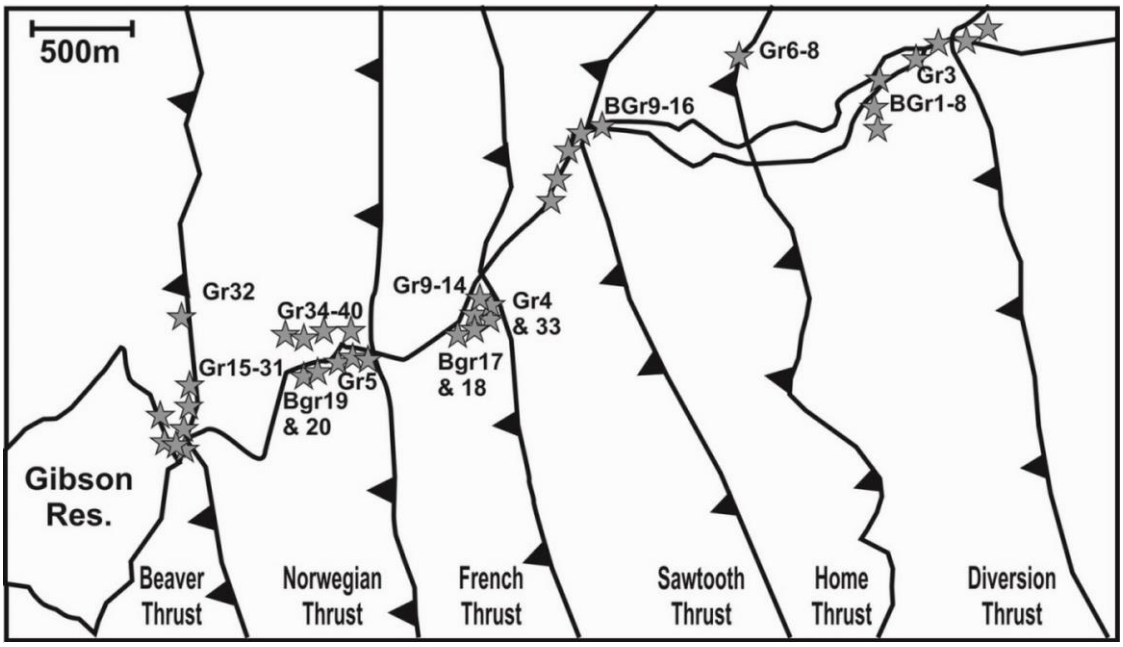

Figure 4. 23 Map of sample localities .

4.5.2. Results

Bulk susceptibility varies from -3.80E-05 to 1.90E-04 with the majority of samples yielding, a negative or extremely weak susceptibilities (Figure 4. 24A). Negative and extremely weak positive susceptibilities are common in very pure limestones. Calcite or dolomite, which are diamagnetic minerals (Hunt et al., 1995), are the dominant carrier of the AMS fabric in samples with negative bulk susceptibilities. The specimens with positive susceptibility values up to 1.90E-04 are indicative of minor amounts of paramagnetic minerals, likely phyllosilicates, but these value are too low to indicate the presence of any dominant ferromagnetic minerals (Rochette, 1987). The degree of anisotropy values (Pj) have a wide range from 1.01 to 2 (Figure 4. 24B). This variation in Pj values does not appear to be affected by changes in bulk susceptibility and, therefore, implies that Pj is controlled by either primary or tectonic fabrics rather than composition in the limestones of this study. Additionally there is no obvious correlation between the shape parameter (Tj) and bulk susceptibility (Figure 4. 24C). Pj and Tj values are plotted for all specimens

(Figure 4.25 A) and mean block samples (Figure 4.25 B) in each main thrust sheet. It is evident from these plots that all thrust sheets sampled exhibit a range of AMS ellipsoid geometries from weak oblate through prolate with some samples exhibiting strong oblate geometries.

The contribution of diamagnetic minerals in the sample suite from the Madison limestones complicates AMS interpretations. In pure calcite and dolomite, the principal susceptibility axis with the most negative magnitude is aligned along the minerals c-axis (Borradaile et al., 2012), which is typically perpendicular to schistosity or tectonic cleavage (Flinn, 1965). Therefore, the most negative susceptibility axis in calcites largely coincides with the normal to the dominant foliation (Borradaile et al., 2012). In order to compare the diamagnetic fabrics to paramagnetic fabrics, k1 is represented by the most negative axis and k3 is represented by the least negative axis for diamagnetic specimens (Borradaile et al., 2012).

To identify regional magnetic fabrics, specimens have been split into two groups, paramagnetic and diamagnetic, and plotted on stereonets with bedding and cleavage, where observed (Figure 4. 25 A&B). These plots show a considerable amount of scatter for both paramagnetic and diamagnetic samples; regardless of being corrected for bedding tilt (Figure 4. 25 C&D). Despite the scatter, there is a slight degree of clustering of K1 axes along bedding, cleavage, and particularly the bedding/cleavage intersection lineation. Similar diagrams to Figure 4. 25 are presented plotting K1 only, K1 and K2 and K3 only in Figure 4. 27, Figure 4. 26 and Figure 4. 29 respectively. Presenting the data in this fashion allows for a clearer

representation of the principal axes distribution. Contoured plots of the magnetic lineation (K1) are shown in Figure 4.30. Similar to the stereographic projections there is no obvious distinct trend in the orientation of K1 (mahgnetic lineation), regardless of whether the specimens were paramagnetic or diamagnetic.

Whilst the stereographic projections of all the data do not reveal any convincing trends or patterns the stereographic projections of the AMS ellipsoid for representative block samples for all thrust sheets sampled as shown in Figure 4.31, yields further insights into petrofabric development in the Madison limestones. In addition to the overall diagram stereographic projections of the AMS ellipsoid for all block samples for individual thrust sheet sampled are shown in Figure 4.32 to Figure 4.36. AMS fabric types in the Madison Limestones evolve from Type 1 to Type 4 and there appears to be no consistent spatial control on fabric types. Lathough there does appear to be an increase in the number of type 3 and 4 magnetic fabric types in the Castle Reef Dolomite. This distribution agrees with the increased number of observed tectonic stylolites and may be due to differences in deformation styles between the Castle Reef Dolomite Formation and the Allan Mountain Limestone Formation, rather than localisation of strain. In additioin to the full range of magnetic fabric types observed within each sheet, it is interesting to note that some samples that have been recorded as type 1 or 2 occur next to samples that have been recorded as type 4, as in the case of GR18 and GR19 in the Beaver Thrust. This is taken to be indicative of the domainal manner in which tectonic fabrics develop in limestones, with microlithons formed between areas of cleavage development. Similarly the Pj-Tj plots for each thrust sheet (Figure 4.37) exhibit the same patterns of AMS ellipsoid evolutions, from weakly oblate to

strongly oblate, through a prolate stage, with the exception of the French thrust sheet, regardless of their position in the thrust belt. The pattern observed in the French thrust sheet could be due to the lower sample count.

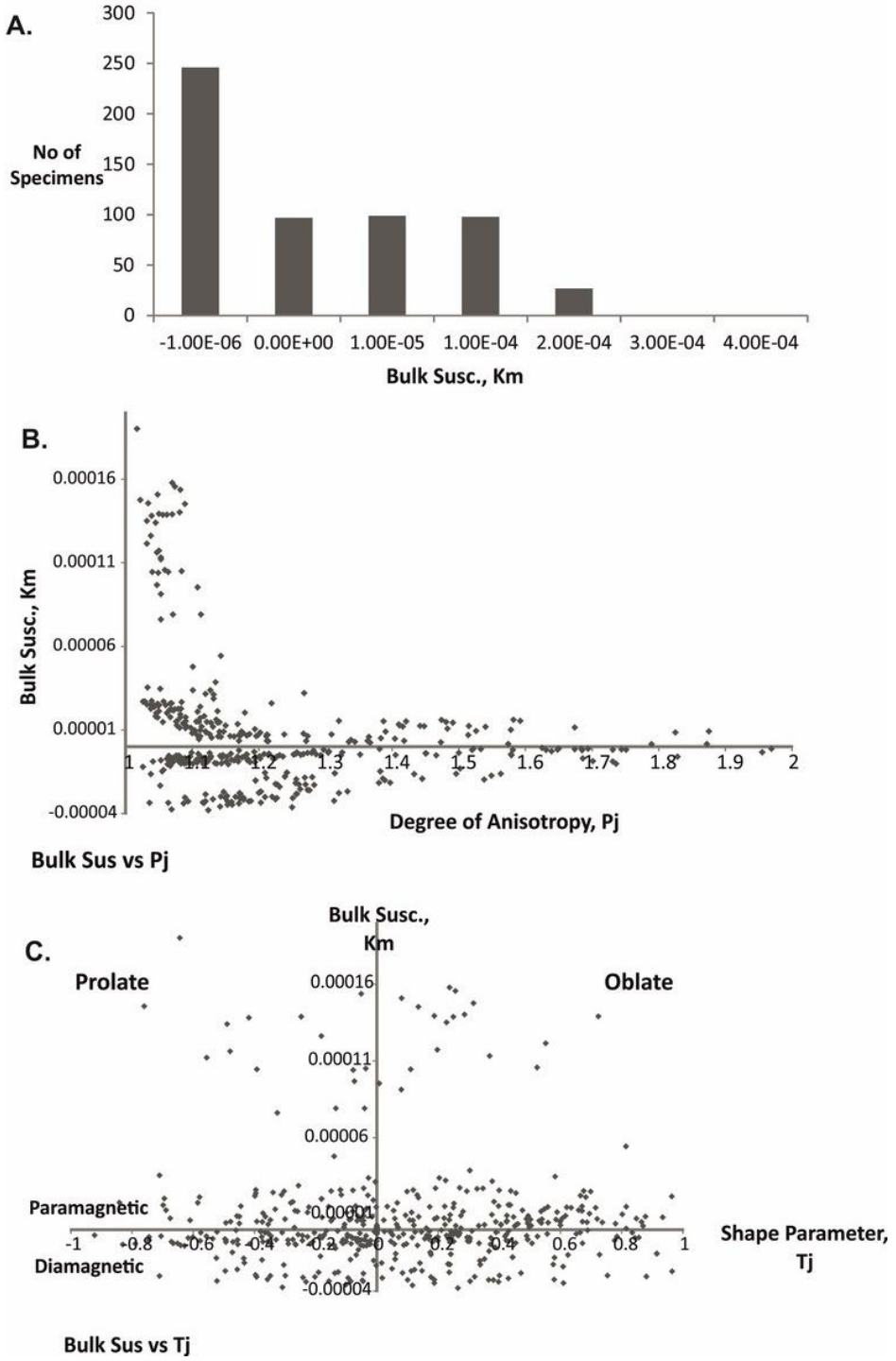

Figure 4. 24 AMS results **A.** Histogram of bulk susceptibility for all samples. **B.** Bulk susceptibility values versus corrected degree of anisotropy (Pj) **C.** Bulk susceptibility versus shape parameter (Tj).

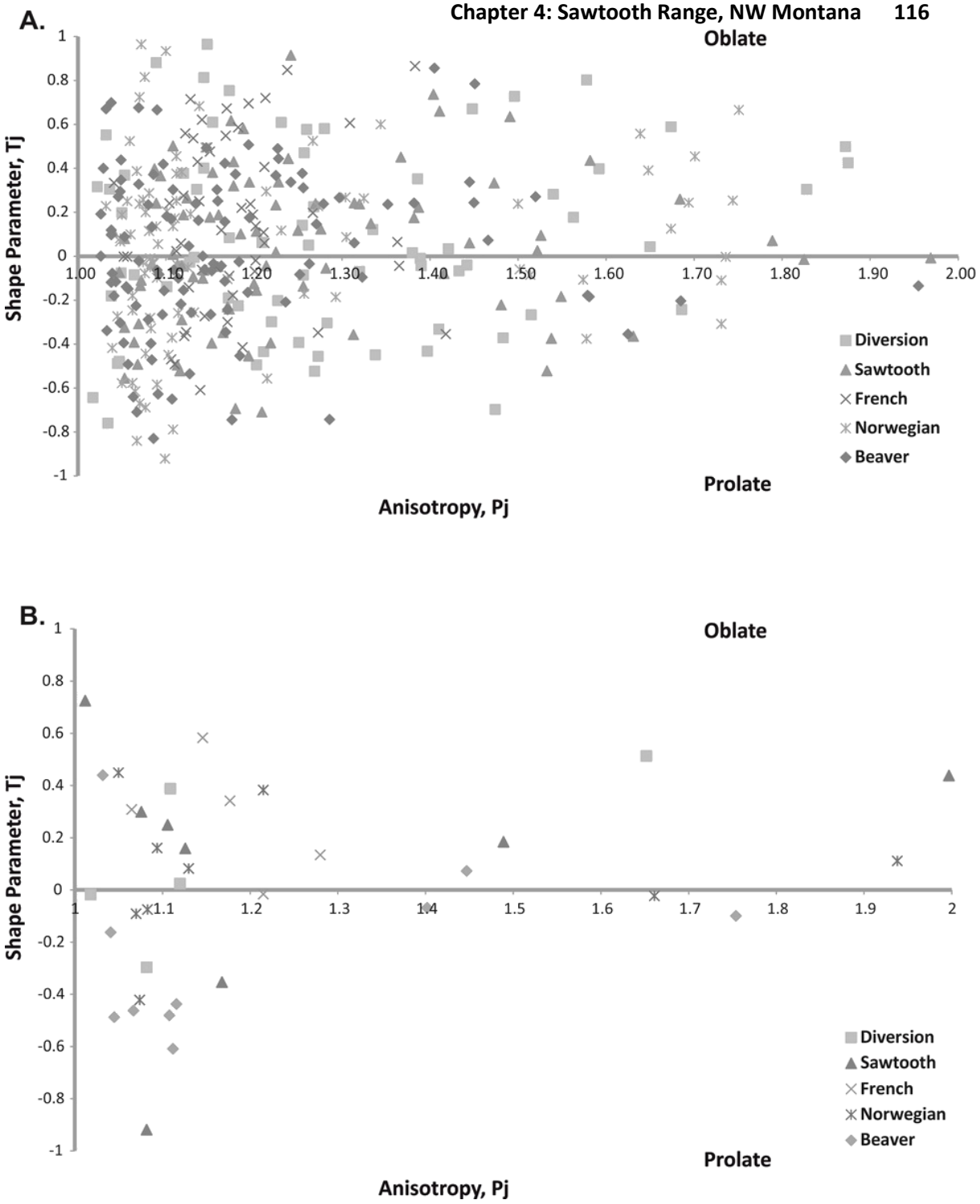

Figure 4.25 Jelinek plots. **A.** Pj versus Tj plots for all specimens collected across 5 thrust sheets. **B.** Pj versus Tj for mean samples.

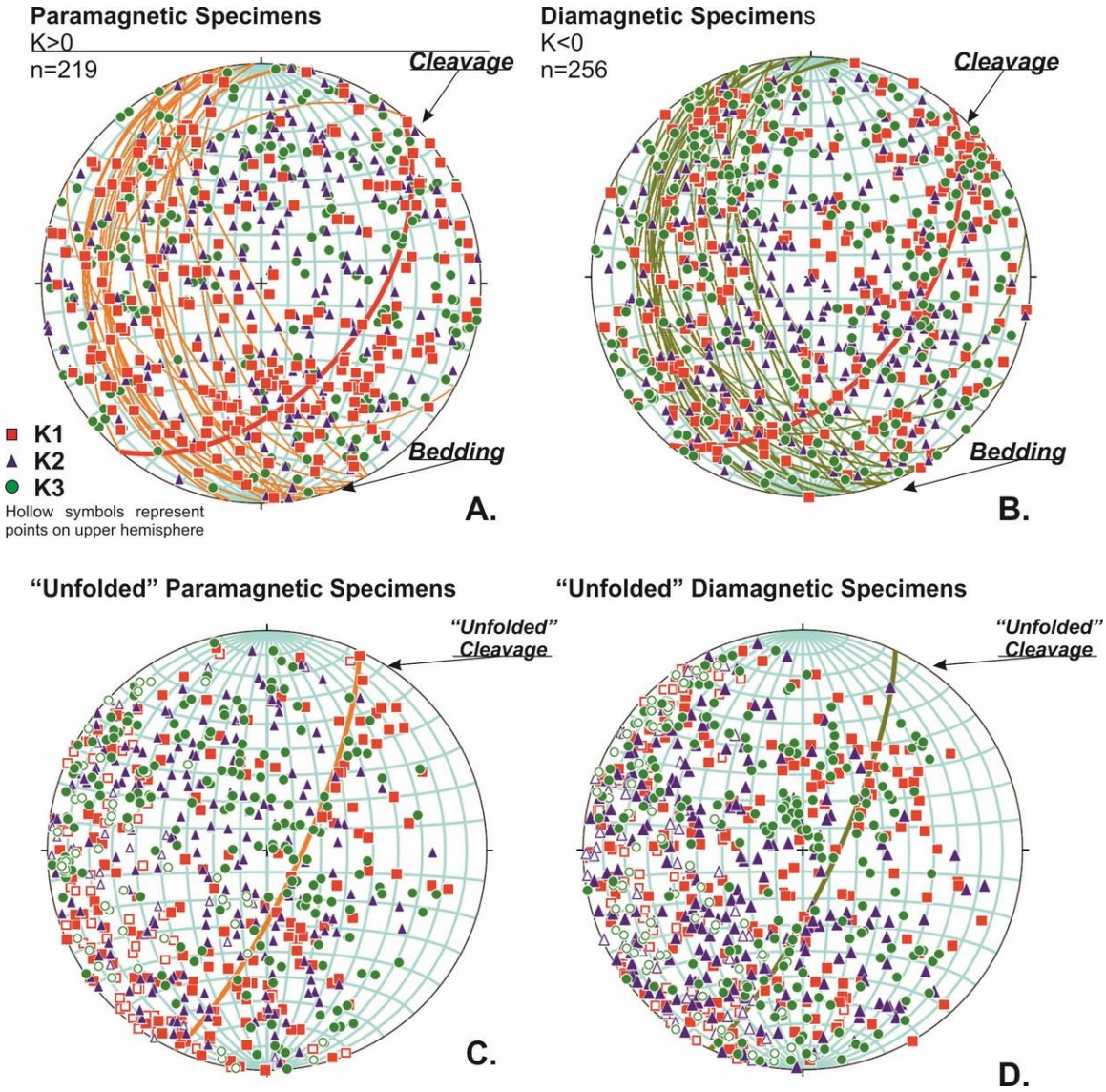

Figure 4. 25 Stereographic projections of principal axes for all specimens separated into two groups, paramagnetic (**A.**)and diamagnetic (**B.**). Individual bedding planes are indicated and primarily dip to westward. Average cleavage orientation is indicated. The second row shows the same data but corrected for bedding tilt for both paramagnetic (**C.**) and diamagnetic (**D.**) samples. Hollow symbols represent points plotting in the upper hemisphere.

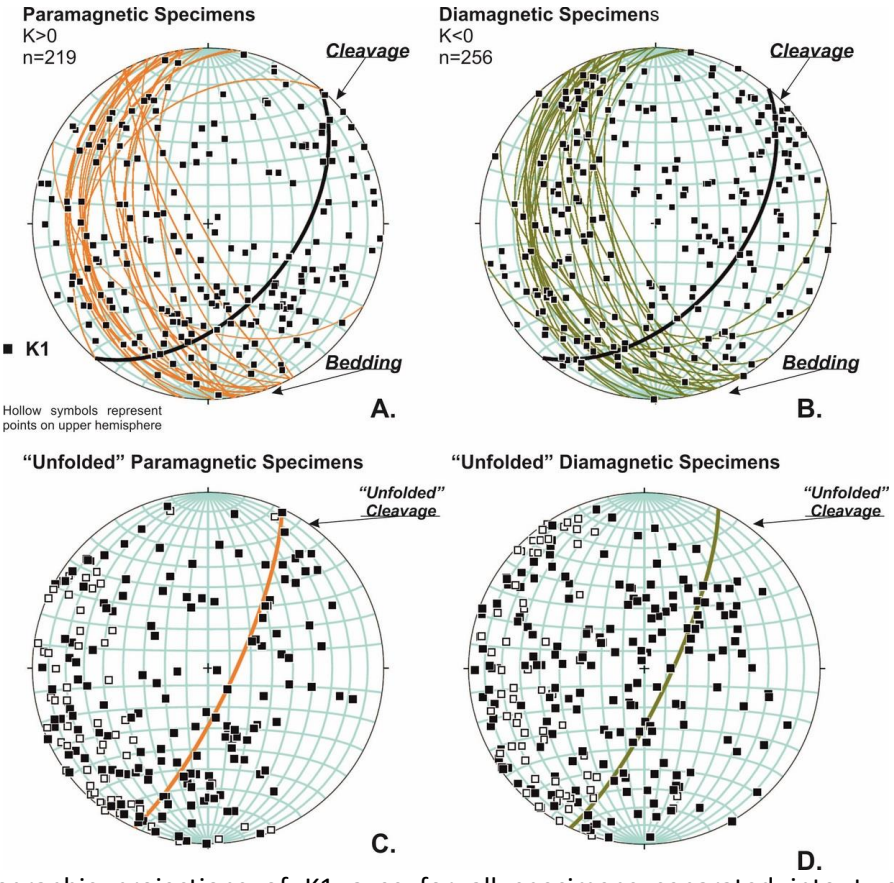

Figure 4. 27 Stereographic projections of K1 axes for all specimens separated into two groups, paramagnetic (**A.**) and diamagnetic (**B.**). Individual bedding planes and average cleavage orientation is indicated. **C.** and **D.** show the same data corrected for bedding tilt for paramagnetic and diamagnetic specimens respectively.

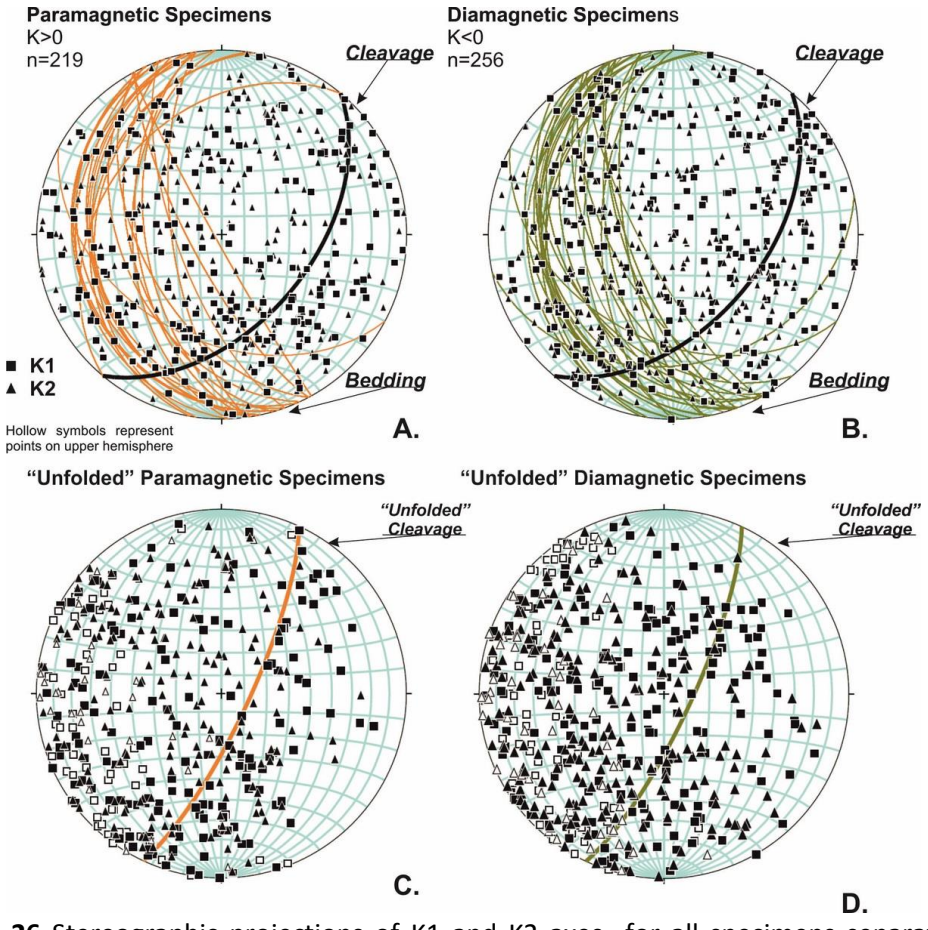

Figure 4. 26 Stereographic projections of K1 and K2 axes for all specimens separated into two groups, paramagnetic (**A.**) and diamagnetic (**B.**). Individual bedding planes and average cleavage orientation is indicated. **C.** and **D.** show the same data corrected for bedding tilt for paramagnetic and diamagnetic specimens respectively.

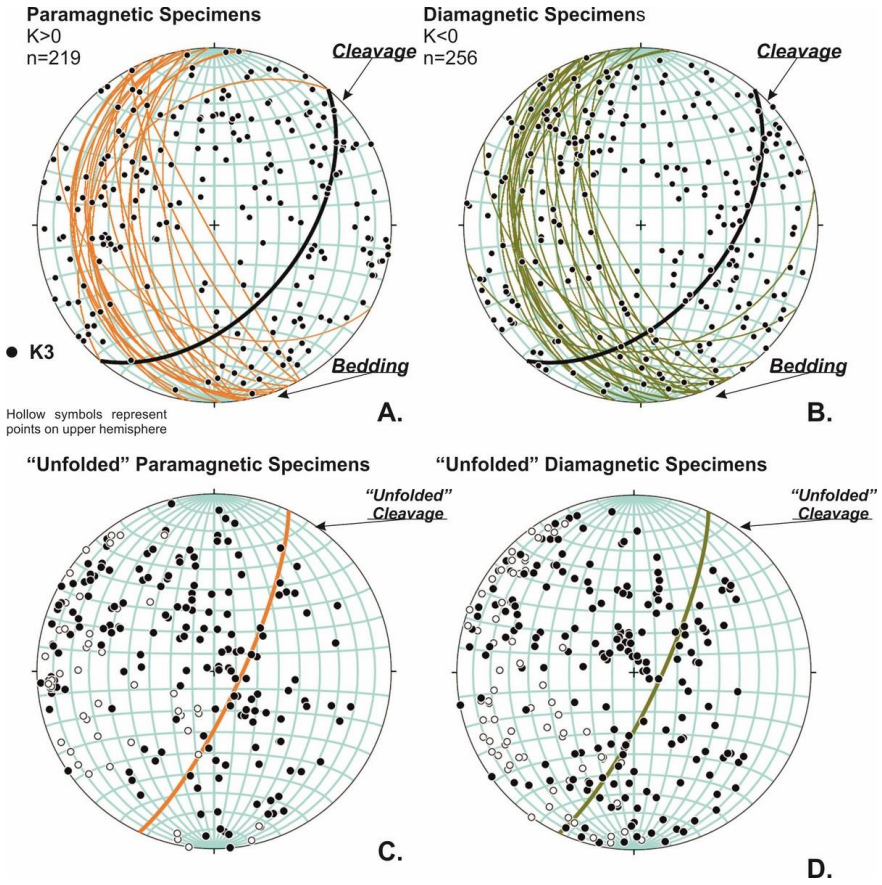

Figure 4. 29 Stereographic projections of K3 for all specimens separated into two groups, paramagnetic (**A.**) and diamagnetic (**B.**). Individual bedding planes and average cleavage orientation is indicated. **C.** and **D.** show the same data corrected for bedding tilt for paramagnetic and diamagnetic specimens respectively.

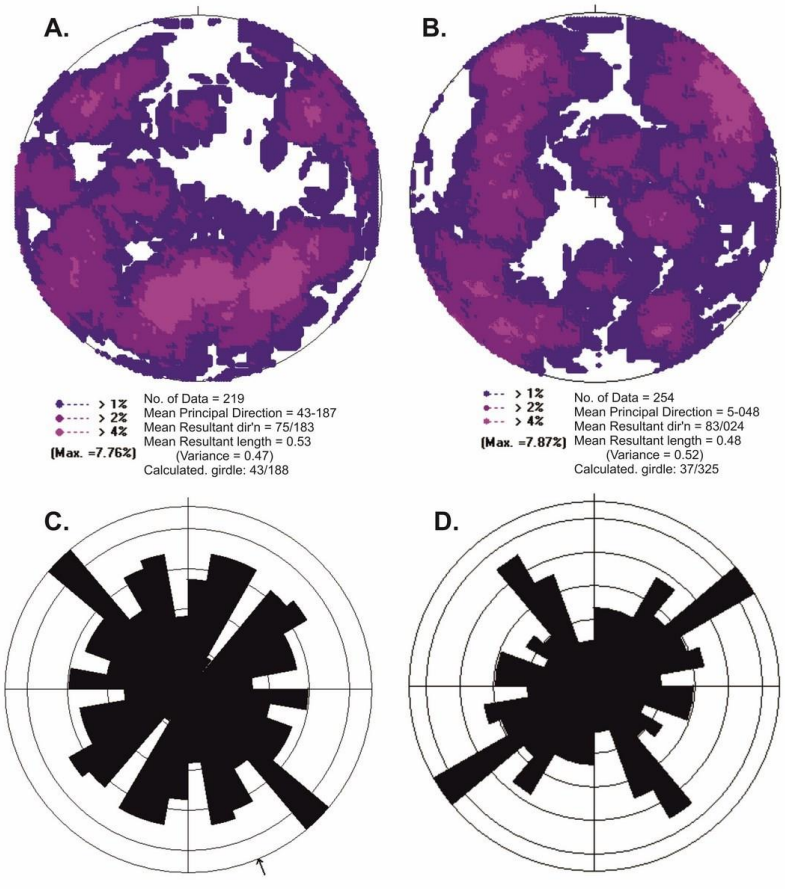

Figure 4. 28 Contoured stereonets and rose diagrams of K1 from the data in Figure 4.26. Contoured plot of K1 of paramagnetic specimens. B. Contoured plot of K1 of diamagnetic specimens. C. Rose diagram of K1 for paramagnetic specimens. D. Rose diagram of K1 for diamagnetic specimens.

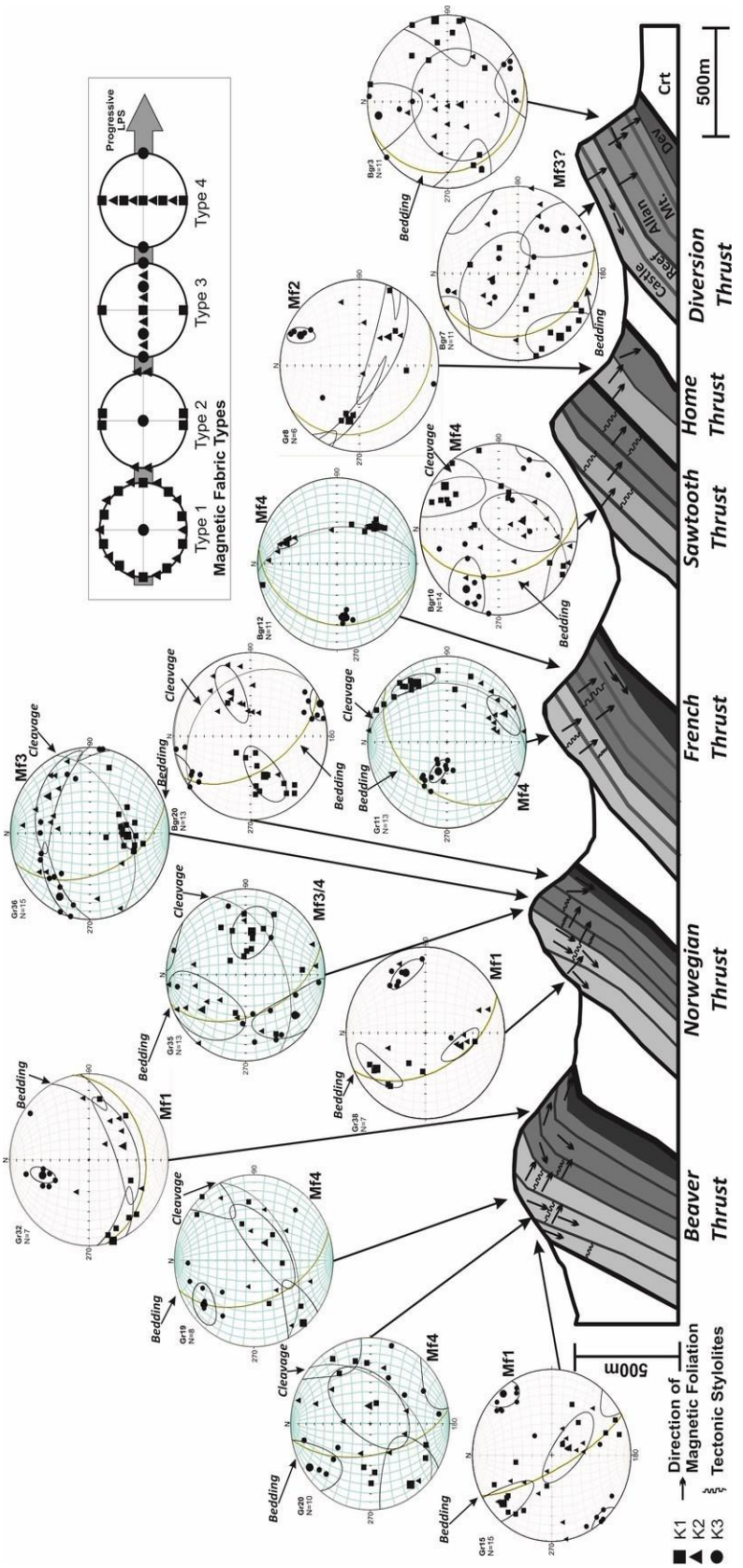

Figure 4. 30 Stereographic projections of principal susceptibility axes for representative block samples across the the sampled thrust sheets. Also shown is the inclination of magnetic foliation relative to bedding and tectonic stylolites. Magnetic fabric types are indicated. Inset illustrates evolution of magnetic fabric types assuming horizontal bedding.

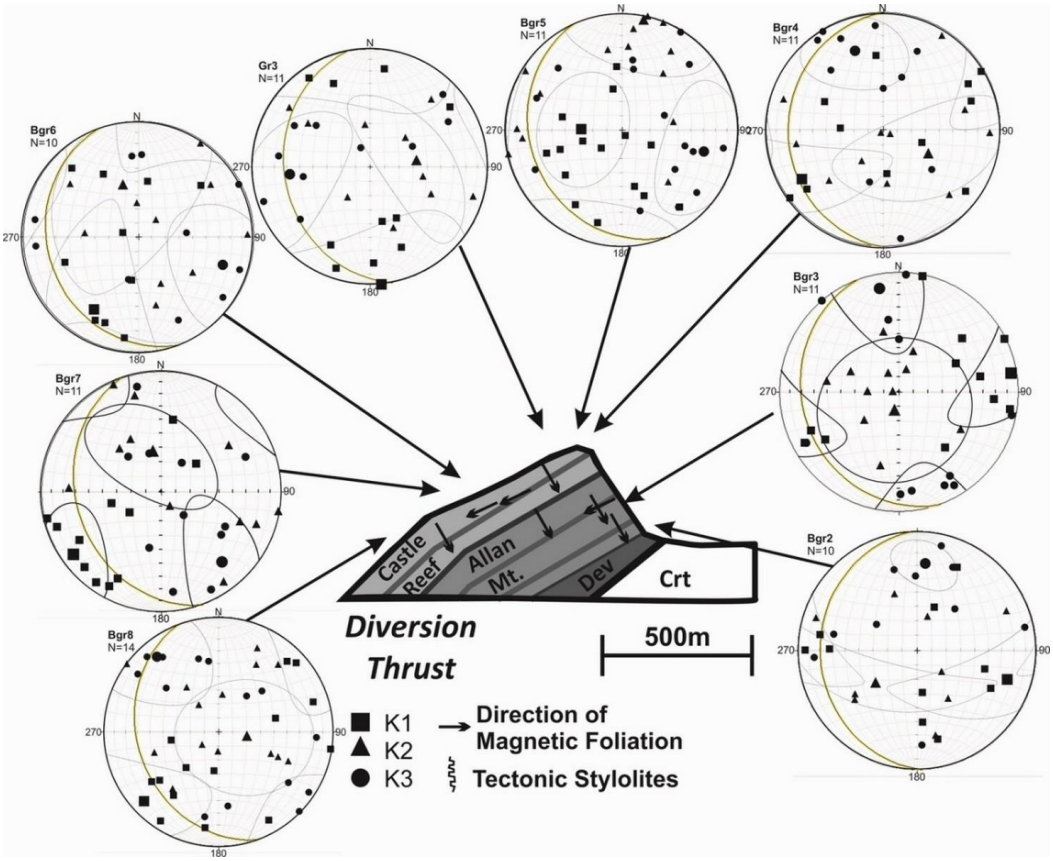

Figure 4. 31 Stereographic projections of principal susceptibility axes for block samples across the Diversion thrust sheet. Also shown is the inclination of magnetic foliation relative to bedding and tectonic stylolites. Larger symbols indicate mean principal axes.

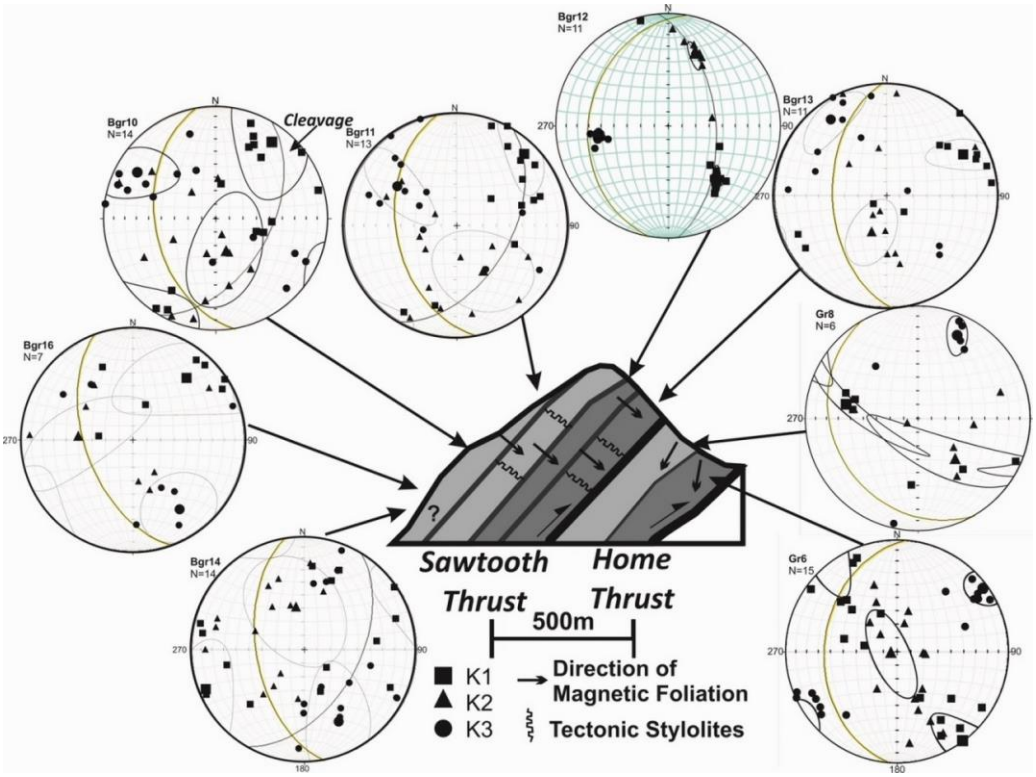

Figure 4. 32 Stereographic projections of principal susceptibility axes for block samples across the Sawtooth and Home thrust sheets. Also shown is the inclination of magnetic foliation relative to bedding and tectonic stylolites.

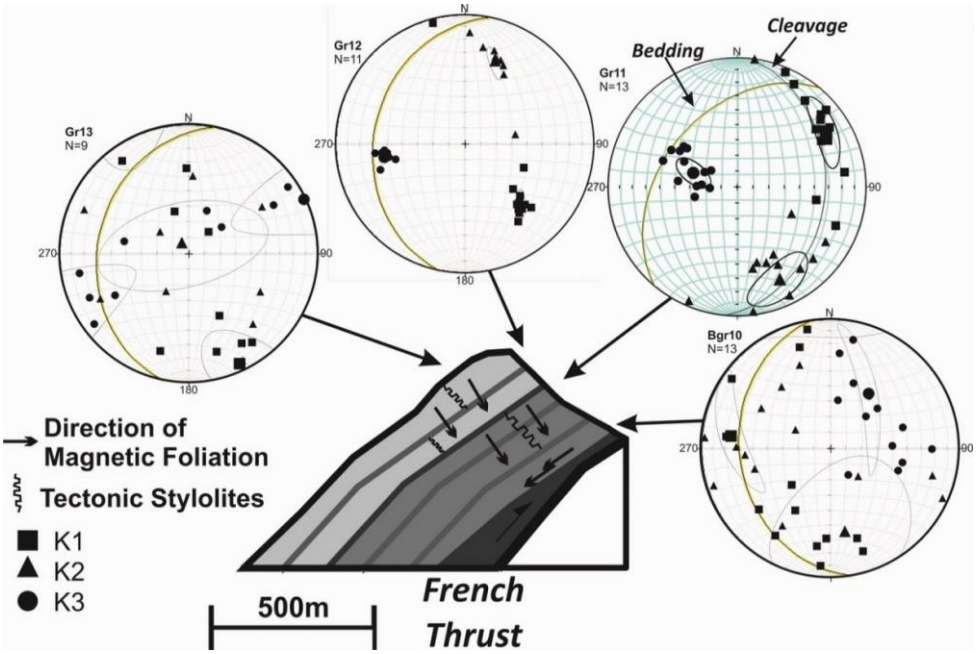

Figure 4. 33 Stereographic projections of principal susceptibility axes for block samples across the French thrust sheet. Also shown is the inclination of magnetic foliation relative to bedding and tectonic stylolites.

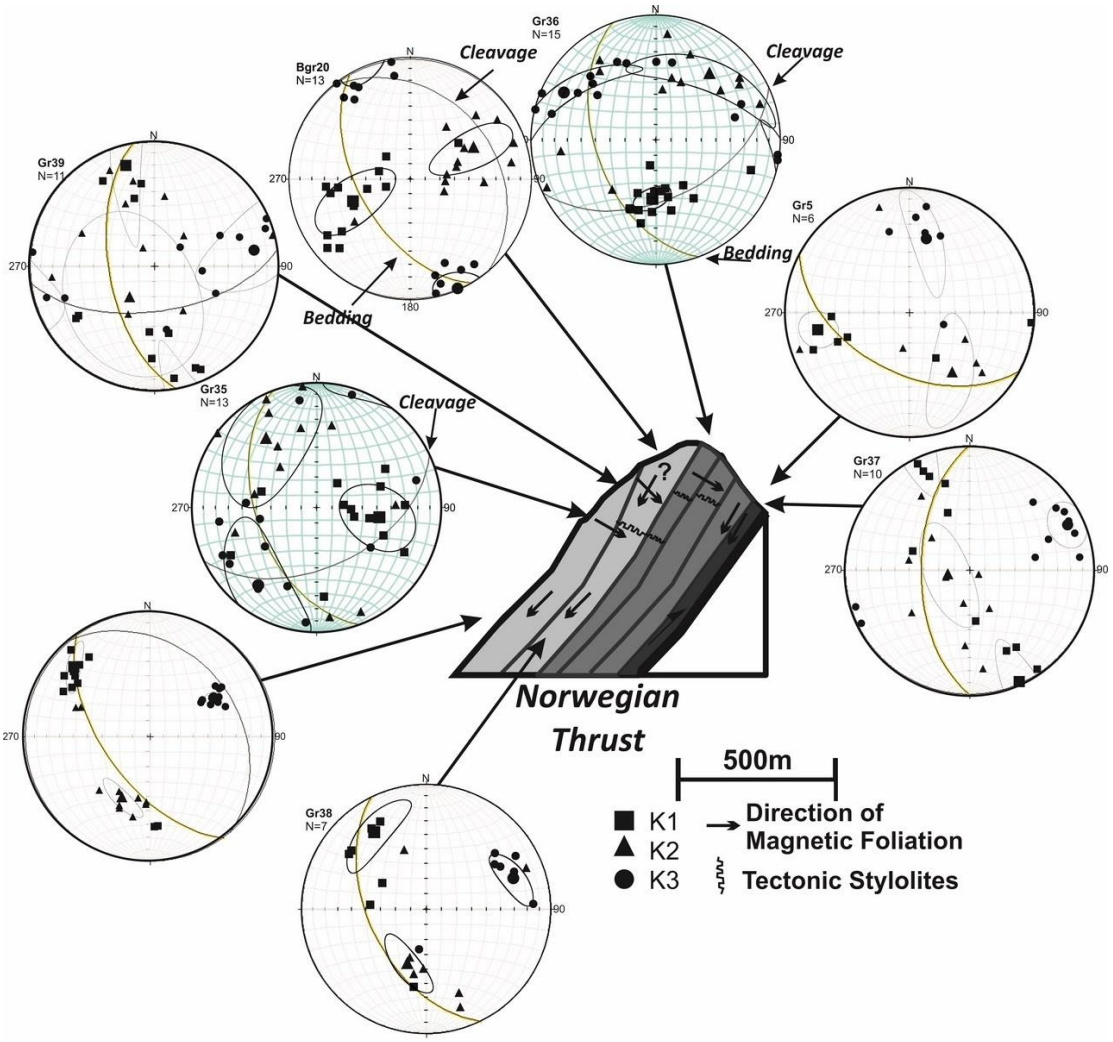

Figure 4. 34 Stereographic projections of principal susceptibility axes for block samples across the Norwegian thrust sheet. Also shown is the inclination of magnetic foliation relative to bedding and tectonic stylolites.

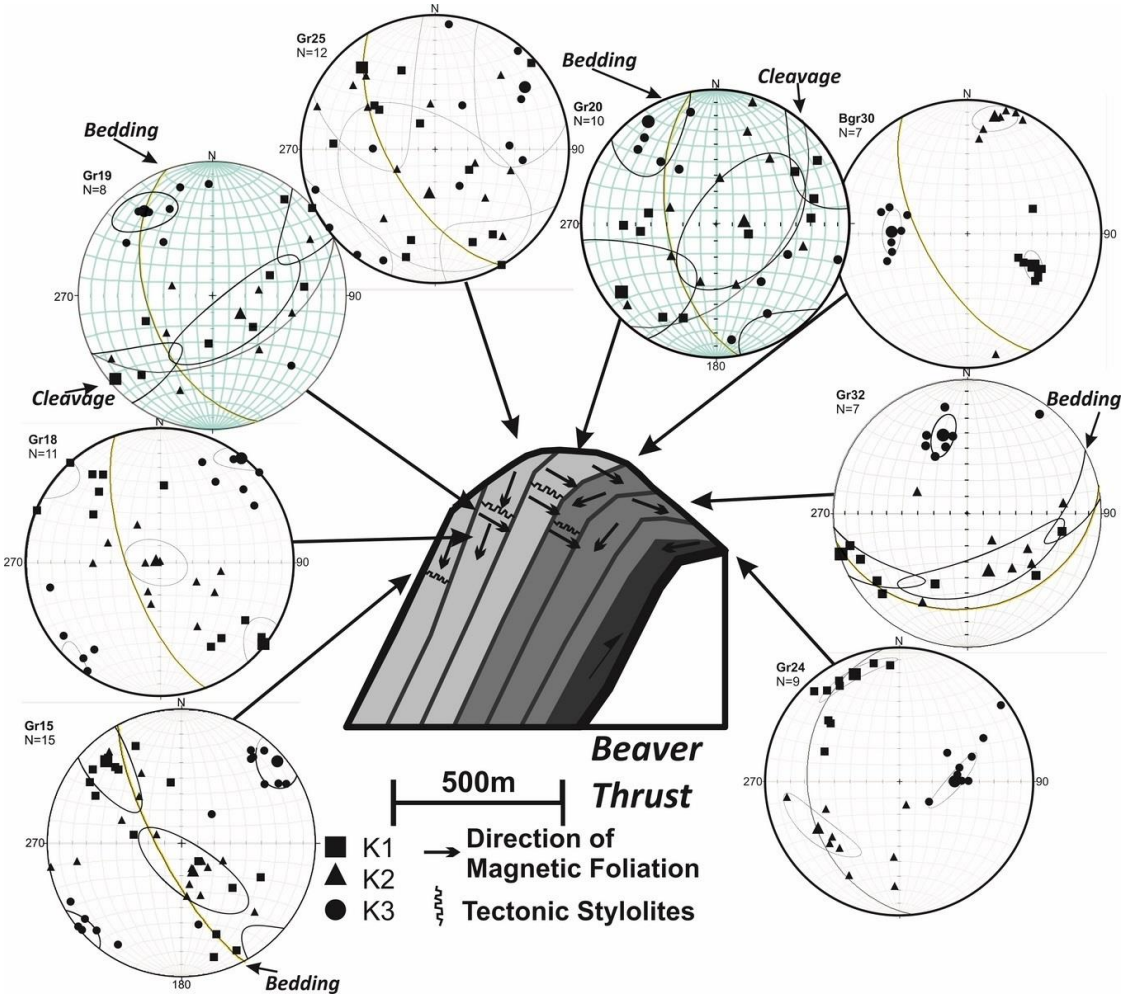

Figure 4. 35 Stereographic projections of principal susceptibility axes for block samples across the Beaver thrust sheet. Also shown is the inclination of magnetic foliation relative to bedding and tectonic stylolites.

4.6. Discussion

The AMS fabrics exhibit a range of fabric types that are commonly seen in fold and thrust belts (Bakhtari et al., 1998; Pares and Parés, 2004; Weil and Yonkee, 2009). These fabric types evolve from bedding controlled to tectonic cleavage controlled through an intermediate stage with blended fabrics (Bakhtari et al., 1998; Borradaile et al., 2012). This evolution of fabric type is evident in the Pj-Tj plots, whereby ellipsoid shapes vary from weakly oblate with flattening parallel to bedding, to prolate with stretching parallel to the extension direction with a final stage of oblate with flattening perpendicular to bedding (Parés, 2004).

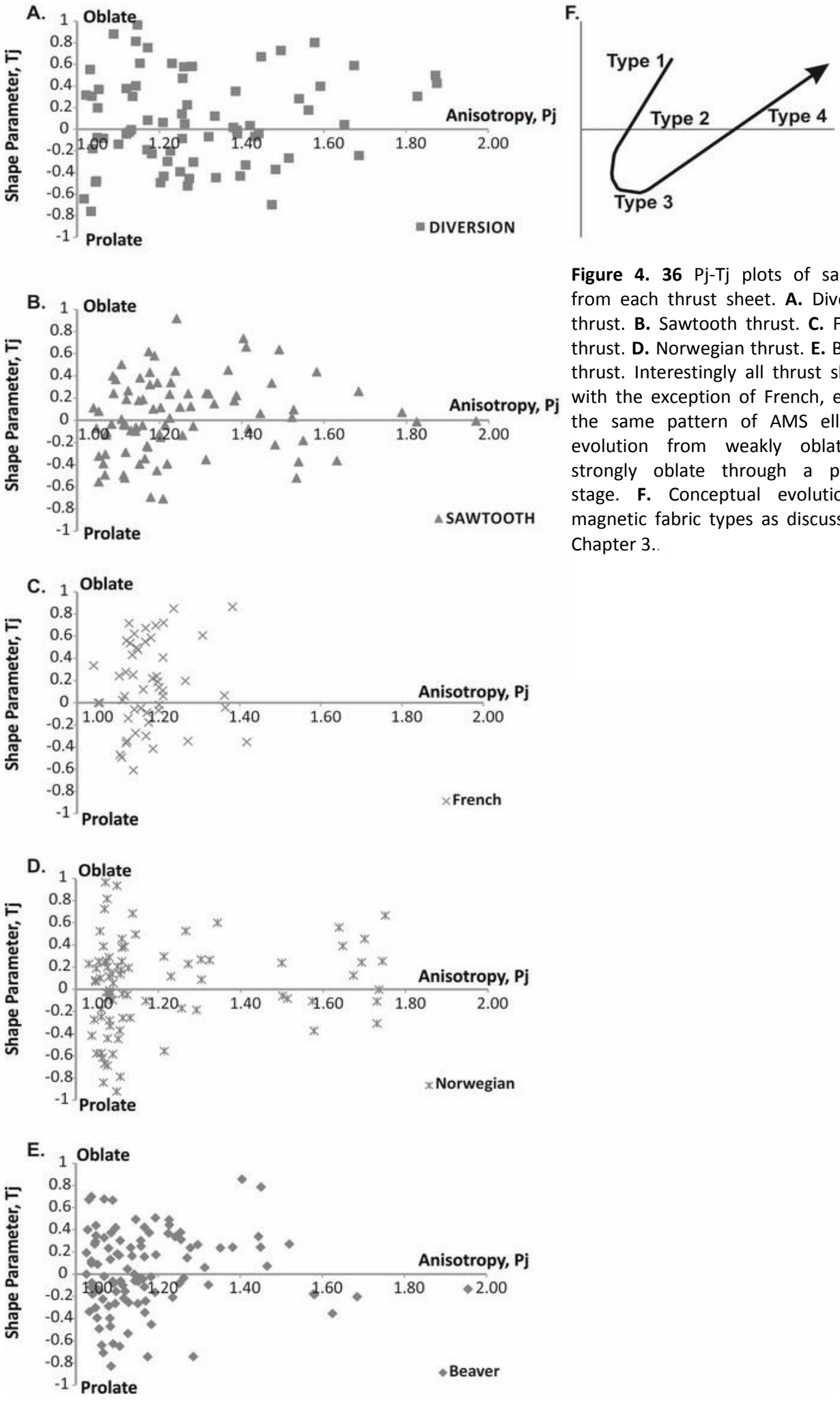

Figure 4. 36 Pj-Tj plots of samples from each thrust sheet. **A.** Diversion thrust. **B.** Sawtooth thrust. **C.** French thrust. **D.** Norwegian thrust. **E.** Beaver thrust. Interestingly all thrust sheets, with the exception of French, exhibit the same pattern of AMS ellipsoid evolution from weakly oblate to strongly oblate through a prolate stage. **F.** Conceptual evolution of magnetic fabric types as discussed in Chapter 3..

Although penetrative tectonic fabrics are poorly developed at an outcrop scale, there is a regular correlation with AMS fabrics and recorded cleavage fabrics at a high angle to bedding, with K1 axes plotting along a cleavage plane or at the cleavage bedding intersection lineation . The poor development of penetrative fabrics in the Madison Limestones may be attributed to the relatively low temperature conditions they experienced. The temperatures of 100˚C-175˚C constrained by illitic mineral assemblages (Gill et al., 2002; Hoffman et al., 1976; O'Brien et al., 2006) are below the temperatures required (200˚C-300˚C) for intracrystalline plastic flow of calcite to become a dominant deformation mechanism (Engelder and Marshak, 1985).

The presence of a tectonic stylolitic fabric consistently at a high angle to bedding suggests that this fabric developed prior to thrusting and rotation of the carbonates. This is further confirmed by the coaxial folding of stylolites with bedding (Ward and Sears, 2007). If any cleavage developed during thrusting it would be expected to develop at a oblique angle to bedding as suggested by Evans and Dunne (Figure 4. 37; 1991) Sanderson (Figure 4.39; 1982). Evans and Dunne (1991) used finite strain variation in the North Mountain thrust sheet of the central Appalachians to help outline its kinematic history. They outlined four typical deformation events associated with thrust sheet evolution (Figure 4. 37):

1. initial Layer Parallel Shortening (LPS);
2. bending and folding at ramp hinge;
3. syn -thrusting related simple shear;
4. and post-emplacement flattening (Evans and Dunne, 1991).

This model shows LPS development preceding or synchronous with the emplacement of an underlying thrust tip (Evans and Dunne, 1991). This is followed by further deformation as the thrust sheet undergoes folding and bending at a ramp hinge, resulting in interlayer slip, non-layer-parallel shortening and strains associated with bending. The third stage is syn-thrusting transport simple shear is parallel to the basal thrust. A final stage of post-emplacement flattening may occur.

Evans and Dunne (1991) also highlighted that the style of penetrative strain recorded in thrust sheets is dependent on whether the right temperature and pressure conditions are present to accommodate grain scale deformation, and that these conditions can vary temporally and spatially within a thrust sheet.

Similar studies in the Wyoming fold and thrust belt suggested that LPS developed in individual thrust sheets prior to thrusting and as a consequence of the overriding thrust slab (Wiltschko and Dorr, 1983). Deformation during thrusting was limited to brittle deformation in the limestones of the hanging wall (Holl and Anastasio, 1992) and plastic deformation in the Cretaceous shale in the footwall, similar to the findings of Wu (1993).

The development of AMS fabrics in sedimentary rocks with a primary bedding fabric undergoing LPS has been well studied (Bakhtari et al., 1998; Borradaile and Jackson, 2010; Pares, 2004; Parés et al., 1999) and can be summarised as follows: Sedimentary fabric characterised by weakly oblate ellipsoids with flattening parallel to bedding have K1 and K2 axes scattered in a girdle representing the magnetic foliation and roughly conforming to bedding and K3 plots as the normal to the magnetic foliation/bedding. As LPS initiates the tectonic fabric is weaker than the primary sedimentary fabric and the AMS ellipsoid can be weakly oblate and

conformable with bedding, but tends towards a triaxial geometry with K1 axes clustering in the direction of extension and defining a magnetic lineation. With increased shortening, the magnetic ellipsoid becomes prolate with K1 axes increasing in definition and K2 axes roughly equal to K3 axes. The final stage involves a magnetic foliation perpendicular to bedding with K1 axes and K2 axes forming a great circle girdle parallel to cleavage. K1 axes, the magnetic lineation, may still be clustered at the intersection of bedding and cleavage, or scattered in the plane of cleavage. This range of ellipsoid geometries is also observed in the Madison limestones for both the paramagnetic and diamagnetic samples, once K1 axes and K3 axes are swapped for the diamagnetic samples (Figure 4.26) It is interesting to note, that despite this variation in magnetic fabric types, there does not appear to be a regular distribution of bedding controlled versus cleavage controlled fabric types within the thrusts sheets.

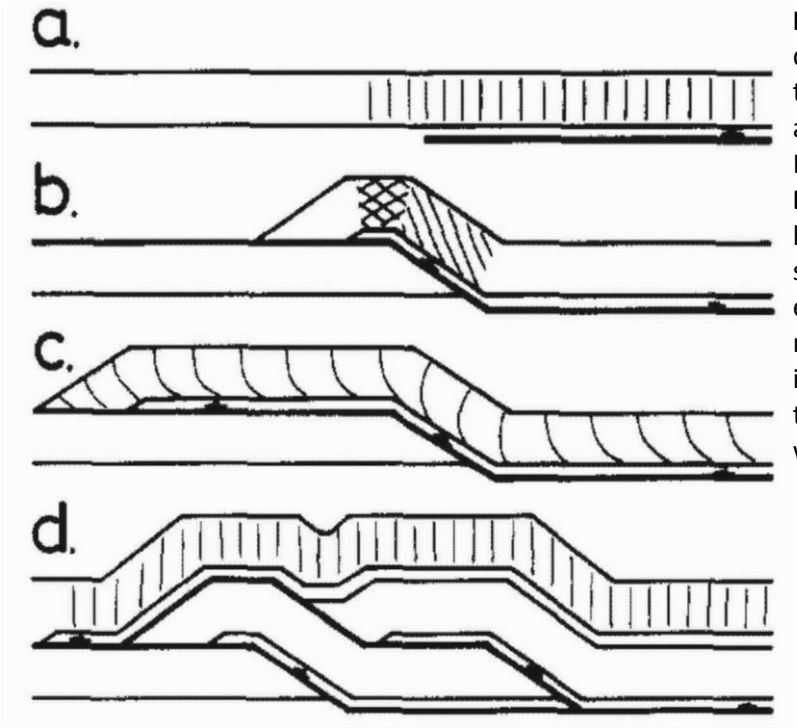

Figure 4. 37 Evolution of deformation events during thrust sheet evolution (Evans and Dunne, 1991). **A.** Initial Layer Parallel Shortening (LPS). **B.** Bending and folding at ramp hinge. **C.** Syn-thrusting related simple shear. **D.** Post-emplacement flattening. The maximum extension direction is shown by short lines, while the crosshatching shows areas with overprinted strains.

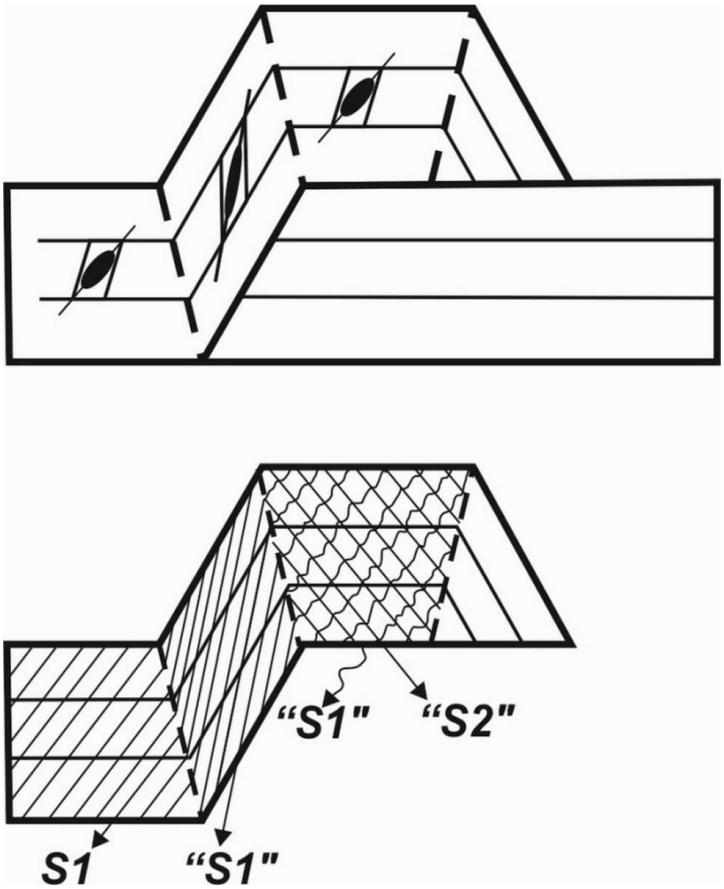

Figure 4. 38 Strain development during thrusting (redrawn from Sanderson 1982). Top figure illustrates hypothetical strain ellipsoids during thrusting. Cross-hatching in lower figure shows areas of overprinted strains.

Both the models of Sanderson (1982) and Evans and Dunne (1991) suggest strain developing within a thrust sheet during thrusting. The AMS results presented and discussed above do not identify any penetrative deformation that could be linked to syn-thrusting strain. Furthermore the only penetrative tectonic fabric identified was consistently perpendicular to bedding and appeared to have a domainal nature. Therefore a schematic model for strain evolution in the Sawtooth Range is proposed in Figure 4.39. The first stage of deformation involves thrust fault initiation, facilitated by brittle deformation in the hangingwall fault boundary as described by Holl and Anastasio (1991). As this fault develops LPS is occurs in the relatively undeformed footwall, which responds by developing an incipient cleavage. Further movement of the thrust fault along the footwall ramp promotes

fracturing in structurally competent units such as the Allan Mountain Limestone and Castle Reef Dolomite. With further faulting the BDZ widens and cleavage development continues in the footwall. When deformation transfers further into the foreland a new thrust fault develops in the footwall and cleavage development ceases as compression is accommodated by a new phase of thrusting.

4.7. Conclusions

The carbonate dominated thrust sheets in the Sawtooth Range were emplaced in a largely passive manner. This rotation was facilitated by brittle deformation at the base of the thrust sheets (Holl and Anastasio, 1992) as well as plastic deformation in the Cretaceous strata of the footwalls. The emplacement of these sheets effectively rotated an early or pre-thrusting LPS fabric. Furthermore no penetrative fabric developed in the carbonates by deformation associated with thrusting has been detected by the AMS analyses. Despite weak/absent penetrative deformation the use of AMS has allowed interpretations to be made of finite strain distributions and as a result thrust sheet deformation can be modelled.

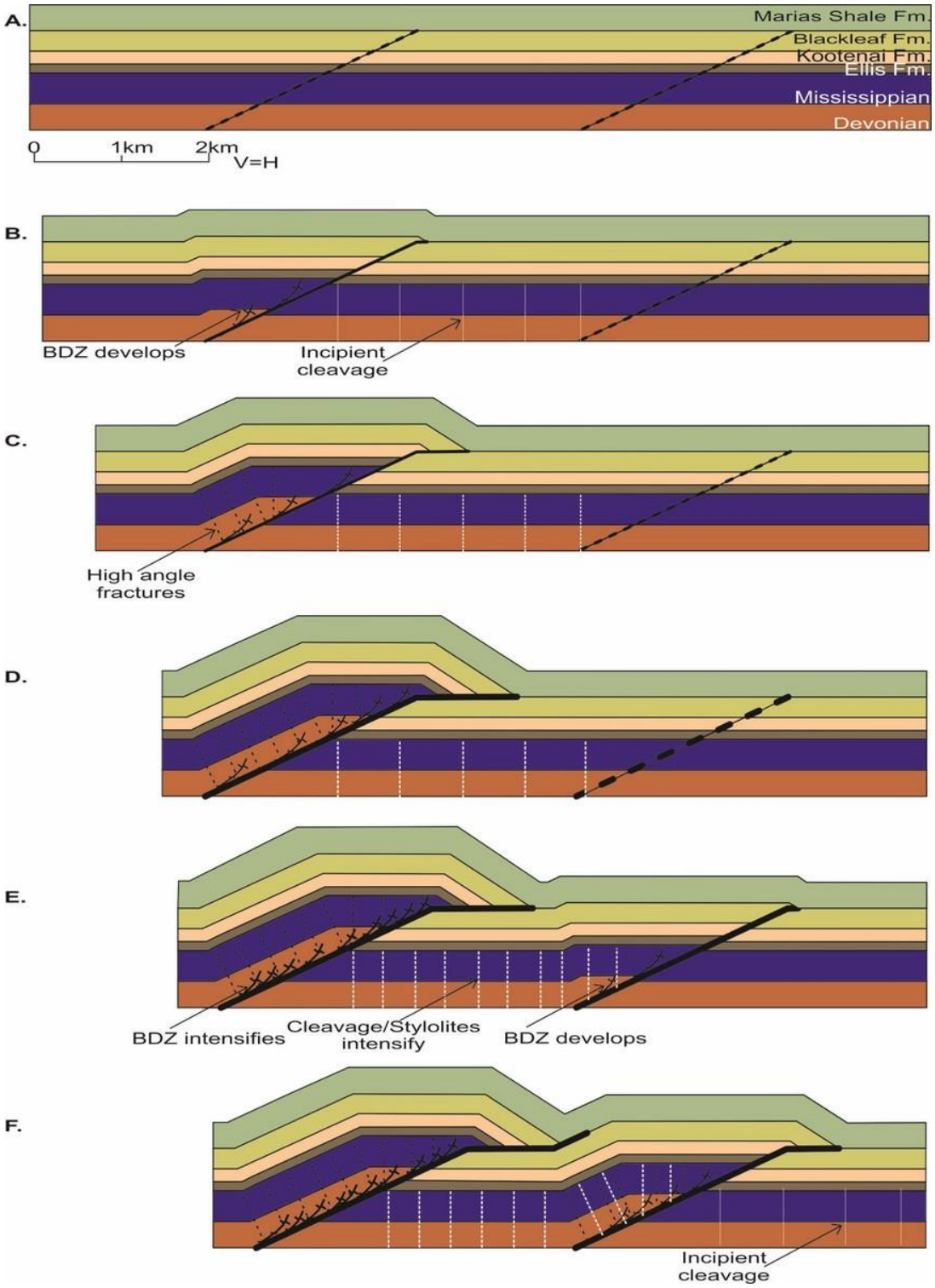

Figure 4. 39 Schematic model of strain evolution in the Sawtooth Range. **A.** Pre-deformation stage. **B.** Minor thrust fault develops, movement is accomodated by brittle deformation along fault surface, footwall undergoes LPS and incipient cleavage develops as a result. **C.** Displacement along fault increases, brittle deformation zone (BDZ) widens and high angle fractures develop in competen strata as they are transported along the footwall ramp. **D.** Continued development of BDZ and high angle fractures. **E.** New thrust fault develops in footwall. Cleavage and tectonic stylolites reach maximum development prior to rotation of strata due to thrusting **F.** BDZ and high angle fractures develop in new thrust sheet.

Chapter 5:

AMS Studies and Clast Based Finite Strain Analysis in Sandstones from the Sevier Thrust Belt, Wyoming.

5. Introduction

The Cordilleran Mountain Belt of North America is one of the world's classic foreland fold and thrust belts. The Sevier Belt represents the thin skinned front of this orogeny, consisting of thrust faults and folds that shortened and transported sequences of Devonian to Cretaceous strata eastward. There is a general increase in deformation westwards which provides an ideal geological setting to explore the potential link between Anisotropy of Magnetic Susceptibility (AMS) and results from clast based strain analyses of sandstones. Studies attempting to define the relationship between AMS and finite strain have been in vogue since the link between layer parallel shortening and AMS was first established. The understanding of this relationship, despite proven strong correlations between the AMS tensors and tectonic directions, is complicated by competing sub-fabrics, as well as the various magnetic properties of the minerals contributing to the AMS fabric.

Rather than trying to estimate finite strain directly from the AMS ellipsoid, AMS is being used to accurately and quickly qualify the petrofabric and determine the origin of that fabric (i.e. whether it is purely sedimentary, composite bedding/tectonic or dominantly tectonic etc.). These AMS results have been compared to a suite of semi-automated strain analysis techniques.

5.1.1. Geological Setting

The Wyoming Salient is a major feature of the Sevier Fold and Thrust Belt and part of the North American Cordillera Complex (Figure 5. 1; Armstrong and Oriel, 1965; DeCelles, 2004; Weil and Yonkee, 2009; Yonkee and Weil, 2010). This Cordillera

complex was formed by subduction of the oceanic Farallon and Kula plates beneath the North American continental plate from the Jurassic to Paleogene (Bird, 1988; DeCelles, 2004; Dickinson and Snyder, 1978; Hildebrand, 2009). The Sevier fold and thrust belt represents the foreland of the Cordilleran orogenic belt (DeCelles and Coogan, 2006). It is best characterised by thin skinned deformation, consisting of thrust faults and related folds (Figure 5. 2; Mitra and Yonkee, 1985; Mitra, 1994) and can be divided into a series of salients that are typically bound by basement cored uplifts (Lawton et al., 1994). The Wyoming section forms a broad salient, bound to the north and south by the basement-cored Gros Ventre and Uinta uplifts of the Laramide foreland (Weil, Yonkee, & Sussman, 2009), is convex to the east, and associated with several major thrust faults (Mitra and Yonkee, 1985).

This Wyoming Salient is divided into two broad systems, a western zone of thrusts that transported Neoproterozoic to Paleozoic strata and an eastern region of thinner cratonic Paleozoic strata. This eastern thrust system is dominated by thin skinned fold thrust structures that were active from the late Cretaceous to early Tertiary and transported Paleozoic and Mesozoic sediments eastward. The foreland of this thrust system interacted with the synchronous basement uplifts attributed to Laramide deformation (Mitra, 1994). The main thrusts in the eastern system are the Crawford, Absaroka, and Hogsback-Darby-Prospect Thrusts (Figure 5. 2). These were emplaced in a piggyback sequence from west to east, respectively, and are thought to share a basal decollement in Cambrian shale (Mitra and Yonkee, 1985). The timing of thrust emplacements is well constrained by synorogenic deposits (Figure 5. 4; Liu et al., 2005) ; the Willard, Paris and Meade thrusts of the western

system were active during the Early Cretaceous, whilst the Crawford and Absaroka thrusts were active during the Middle and Late Cretaceous, respectively, and the Hogsback-Darby-Prospect sequence was emplaced during the Paleocene and Eocene (Wiltschko and Dorr, 1983).

This study is largely concerned with the thin skinned deformation of the eastern thrust system (Mitra and Yonkee, 1985). Spaced cleavage is developed in some lithologies and is thought to have formed during early Layer Parallel Shortening (LPS). Early LPS initiated during footwall deformation as the Willard Meade Thrust slabs were emplaced (Mitra, 1994).

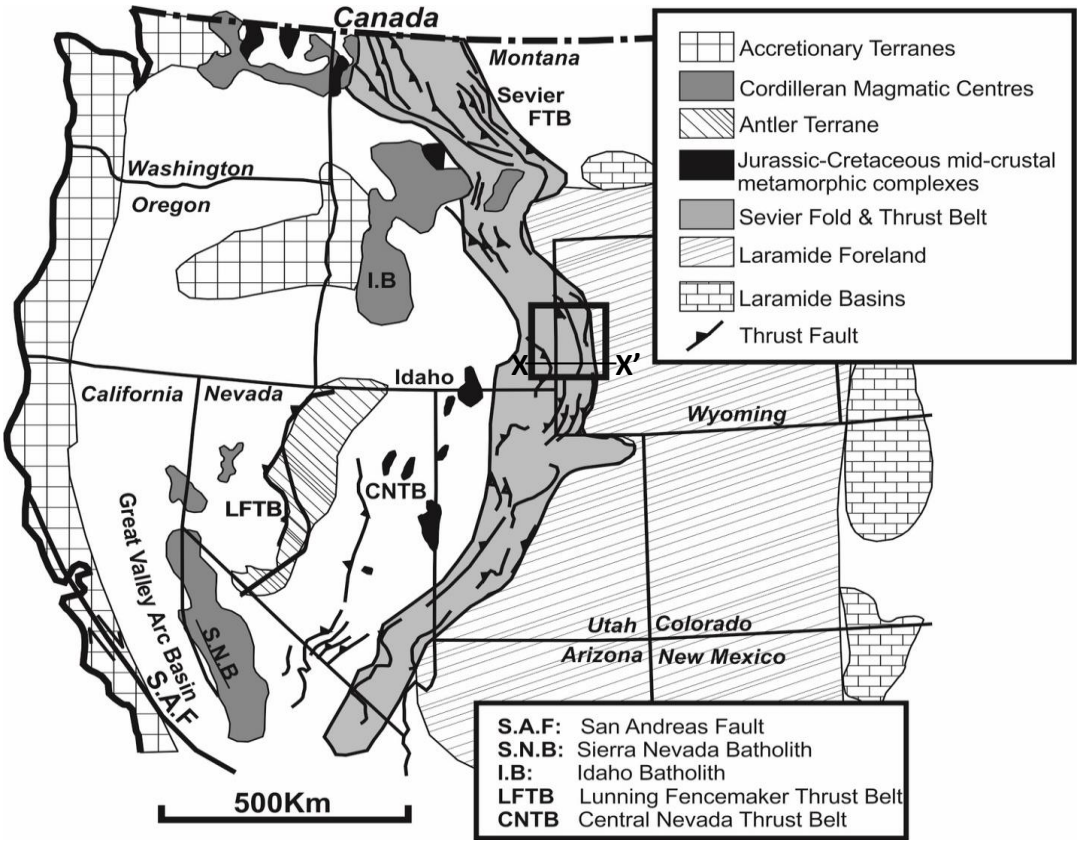

Figure 5. 1 Regional tectonic map of the North American Cordillera redrawn from DeCelles & Coogan (2006). The Sevier Fold and Thrust Belt is highlighted in grey and the field area is marked by the rectangle. Location of cross section in figure 5.2 indicated by X-X'.

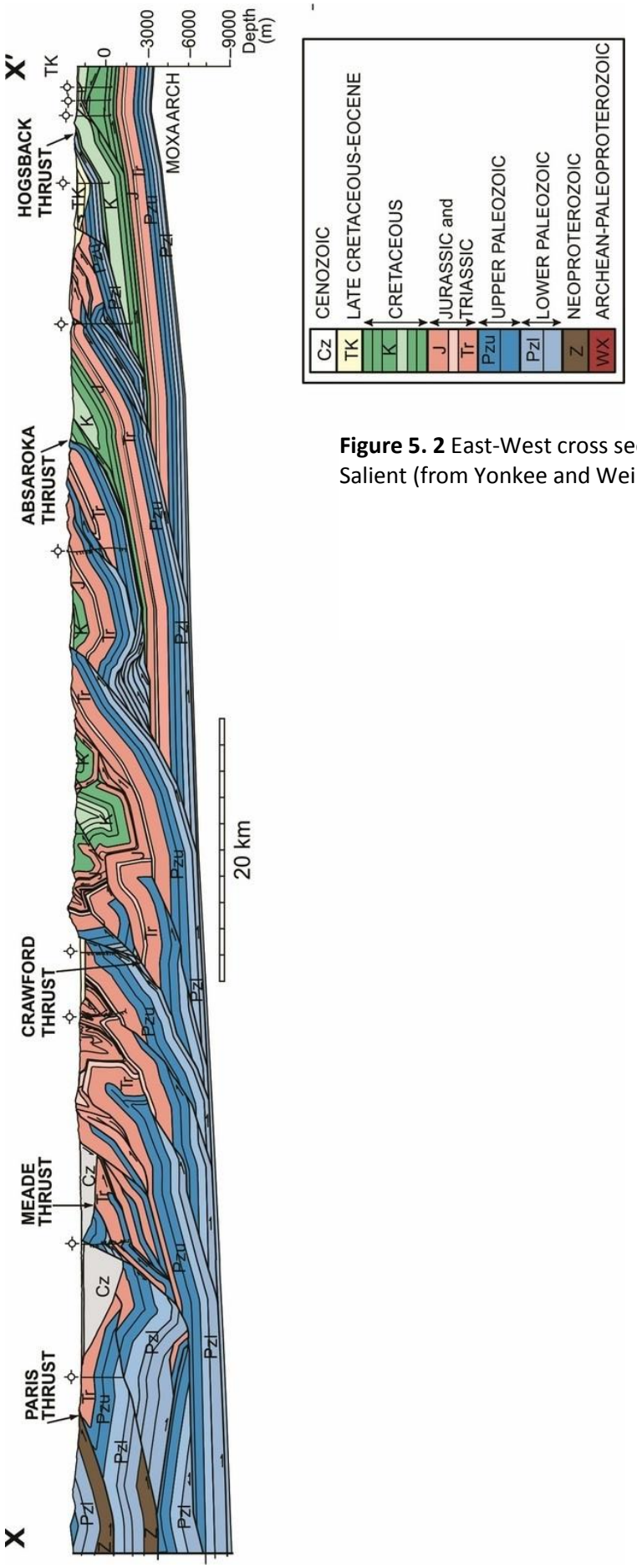

Figure 5. 2 East-West cross section of the Wyoming Salient (from Yonkee and Weil, 2010).

5.1.2. LPS and Petrofabric Development in Thrust Sheets

Fold and thrust belts typically develop through sequential stacking of thrust sheets from the hinterland to the foreland of the orogenic belt (Bally et al., 1970; Boyer and Elliott, 1982; Dahlstrom, 1977, 1969; Mitra, 1994; Price, 1981). Generally thrust sheets are displaced along inclined faults that ascend through the stratigraphy and merge at depth along a basal shear zone or decollement (Boyer and Elliott, 1982). The Wyoming Thrust Belt displays a listric fault geometry with the structures cutting up section towards the east (the direction of transport) and dipping to the west (Mitra and Yonkee, 1985), with the exposed sections of the thrusts displaying ramp-flat geometries (Figure 5. 2; Mitra, 1994, Yonkee and Weil, 2010). The ramps typically occur in more competent intervals, such as thick-bedded carbonate and sandstone, and flats occur in incompetent intervals, such as shale and evaporites (Mitra, 1994). The major thrusts developed sequentially from west to east towards the foreland from the late Jurassic to early Eocene (Wiltschko & Dorr, 1983). The Paris-Willard sheet was emplaced first, and was followed successively by the Meade, Crawford, Absaroka, Darby and Prospect Thrusts (Figure 5. 3 and Figure 5.4; Wiltschko & Dorr, 1983; Mitra & Yonkee, 1985; Liu et al., 2005). The movement on these thrusts was recorded by the deposition of synorogenic conglomerates that provides timing of thrust fault movement and cleavage development (Wiltschko and Dorr, 1983). LPS developed at high angles to bedding in individual thrust sheets, as internal shortening of an individual thrust sheet started after the preceding thrust sheet was emplaced, and prior to movement of the shortening thrust sheet (Wiltschko & Dorr, 1983; Mitra & Yonkee, 1985; Mitra, 1994).

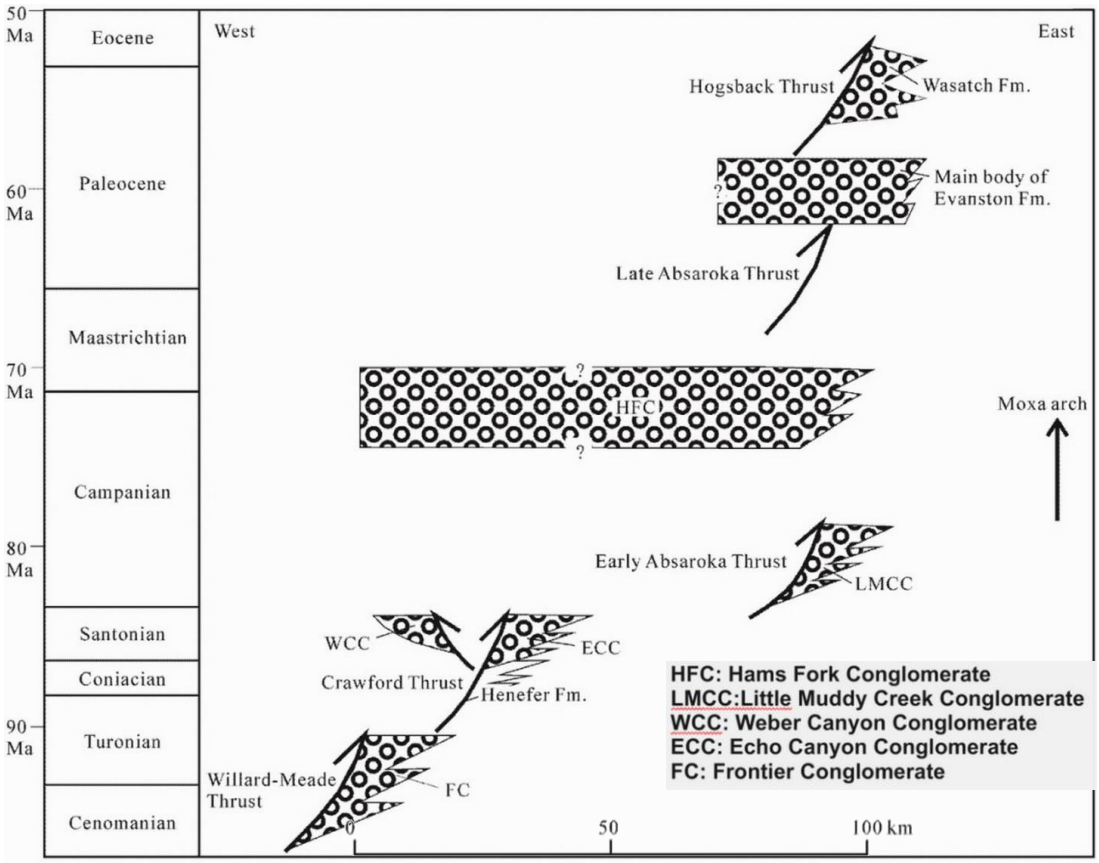

Figure 5. 4 Time-space history of thrust faulting and distribution of synorogenic sediments in the Sevier Thrust Belt (Modified from Liu et al., 2005).

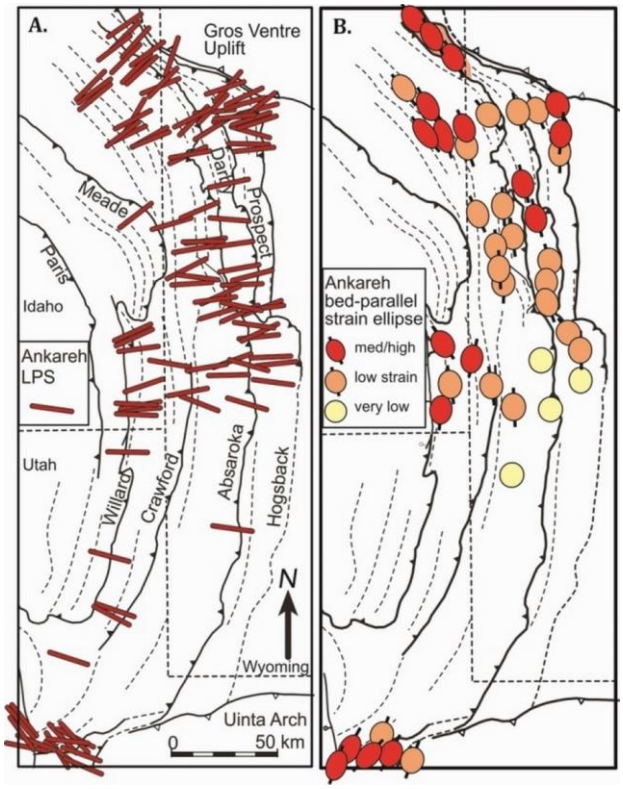

Figure 5. 3 Regional patterns of LPS and strain in the Triassic Ankareh Formation (Modified from Yonkee and Weil, 2010). **A.** LPS directions estimated from cleavage, high-angle fracture sets, and minor faults. **C.** Orientation and magnitude of bed-parallel strain ellipses estimated from shapes of reduction spots. Low strains are recorded in the centre of the salient, with strain increasing westward and towards the salient tips.

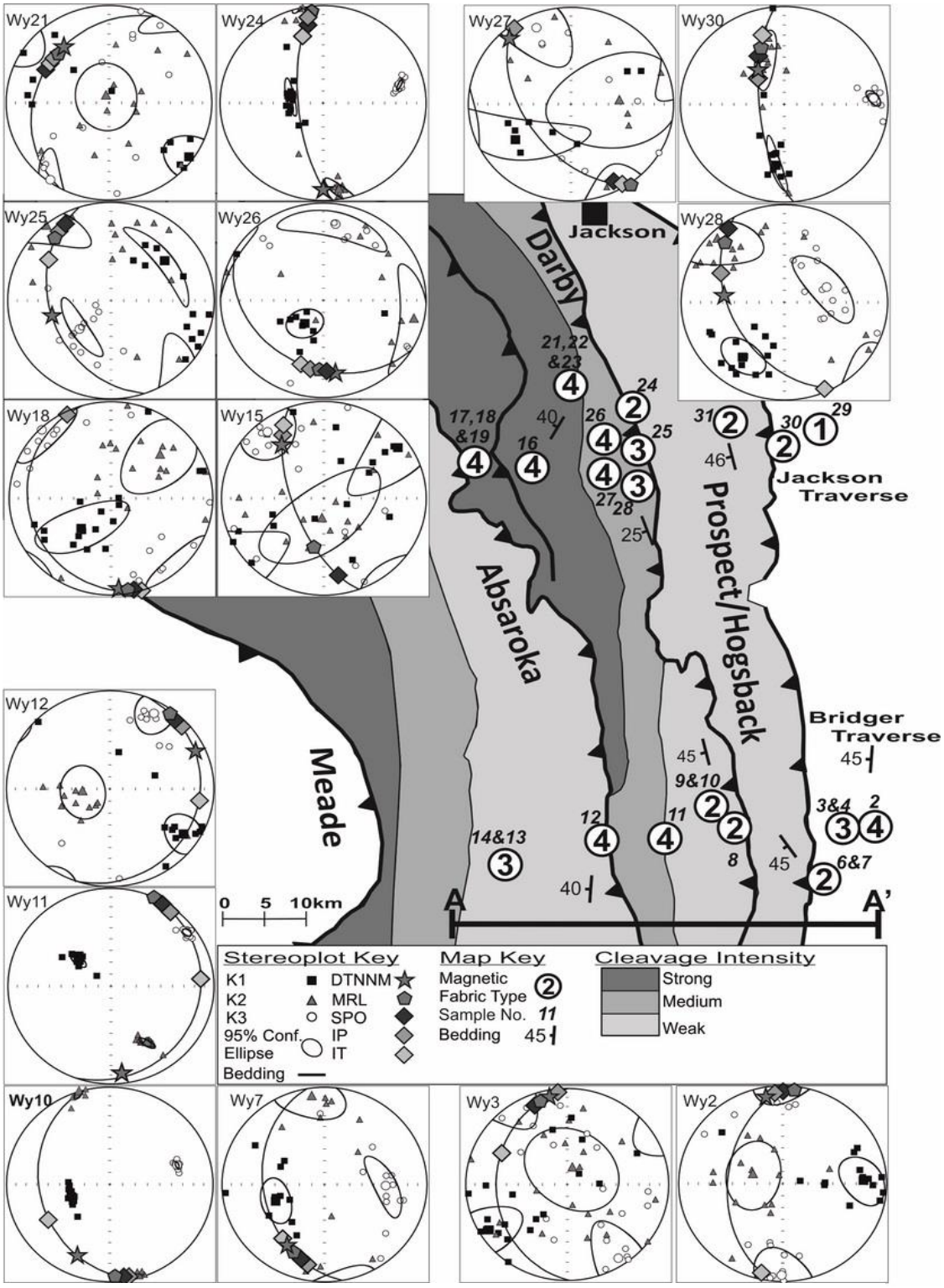

Figure 5. 5 Cleavage intensity map modified from Mitra and Yonkee (1985). Cleavage intensity was determined from field measurements and illite vein width. Increasing cleavage intensities are marked by darker shades of grey. There is a significant increase in cleavage with proximity to the over-riding thrust sheet, with the more westerly thrust sheets displaying greater amounts of deformation. Sample locations are identified in italics with magnetic fabric types indicated in circles. Only stereoplots for samples with both AMS and strain analysis data are shown. Location of cross section in Figure 5.6 is indicated by A-A'.

Regional patterns of LPS have been well documented by Yonkee and Weil (Figure 5. 3; 2010), with low strains recorded in the centre of the salient, with estimated strain increasing westward and towards the salient tips. Deformation temperatures within each thrust sheet was previously determined using illite crystallinity and shows that while there is no continuous temperature gradient across the thrust belt, conditions rarely exceeded 200°C (Mitra & Yonkee, 1985). Additionally, deformation pressures were interpreted to be <5kBars (Yonkee, 1990). In the case of the Wyoming Salient, the compressional deformation has been accommodated by a spaced cleavage with occasional tectonic stylolites, slaty cleavage and pencil cleavage formation, largely induced by pressure solution, due to the depressed thermal gradient associated with the emplacement of an overriding thrust sheet (Mitra & Yonkee, 1985). Cleavage has been described as spaced partings perpendicular to bedding and is orthogonal to the compression direction as evidenced by reduction spot data (Yonkee & Weil, 2010). Cleavage is more developed in the western thrusts systems (Figure 5. 5), due to the higher degree of deformation (Figure 5.6), with estimates for the degree of LPS across the Wyoming salient varying from <5% to 30% (Yonkee & Weil, 2009).

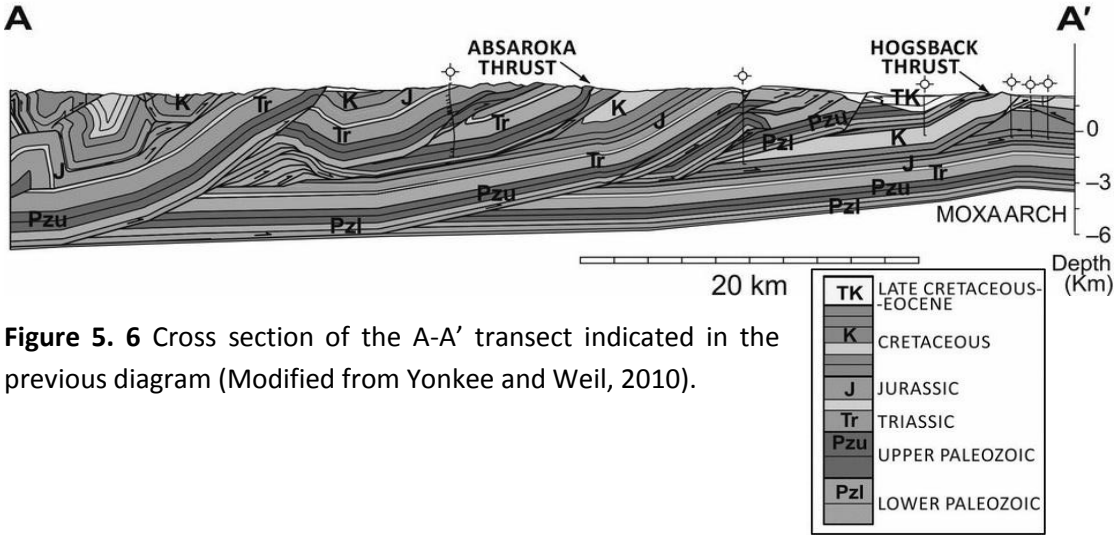

Figure 5. 6 Cross section of the A-A' transect indicated in the previous diagram (Modified from Yonkee and Weil, 2010).

5.1.2.1. Ankareh Formation

The Triassic Ankareh Formation (Figure 5. 7) was chosen for this study due to its suitable mineralogy for AMS studies, it consists of bedded sandstones and calcareous mudstones. The sandstone units vary from quartz arenites to arkose sandstones that are often hematite stained pervasively throughout the matrix (Brandley and Rigby, 1988; Kummel, 1954; Weil and Yonkee, 2009). These rocks are interpreted as continental to near-shore supratidal, meandering stream, and floodplain deposits (Brandley & Rigby, 1988). Bedding structures are typically well defined (Figure 5. 8), with detrital micas moderately aligned along bedding planes in most samples. The majority of samples are texturally mature, in that they are relatively well sorted, have little or no matrix and are composed of sub-rounded to rounded equant grains (Figure 5. 8). Quartz grains are the dominant mineral phase that varies from silt to sand sized consisting of 70-95% of the grains with varying amounts of matrix. Quartz grains are typically interlocking with sutured grain boundary contacts, interpreted as pressure solution contact formed during diagenesis and/or early deformation. Occasionally, sub grain rotation is observed and is more frequent in samples with a higher strain index (Hirth and Tullis, 1992; Passchier and Trouw, 2005). Quartz is also present as the primary matrix material and occurs as mineral overgrowths. Overgrowths when present are usually accompanied by hematite rims between the overgrowth material and the host mineral. Detrital grains of mainly plagioclase with occasional orthoclase feldspars varying from 5–15%. The feldspars invariably feature alteration to a fine grained material, presumably sericite, suggesting widespread hydrothermal alteration. Detrital biotite and muscovite are present in minor amounts (less than 10%) in the

finer grained samples. Calcite occurs as cement in the finer grained samples, and is also rarely present as detrital calcite lithic grains. The presence of hematite rims enclosed in quartz overgrowths suggests that it formed prior to or during diagenesis.

In thin section, cleavage is best seen in the finer grained samples, and is typically present as interleaving, discontinuous and anastomosing seams. The seams are usually less than 0.5mm with spacing of approximately 5mm. The cleavage is often associated with high concentrations of fine grained clays and iron oxides material. These materials are typical of spaced cleavage (Engelder and Marshak, 1985), with seams of residual minerals, encompassing less deformed microlithons, after the dissolution of quartz and calcite. Where this residual material is coarse enough to determine the orientation, the long axis of the crystals is parallel to the long axis of the seams.

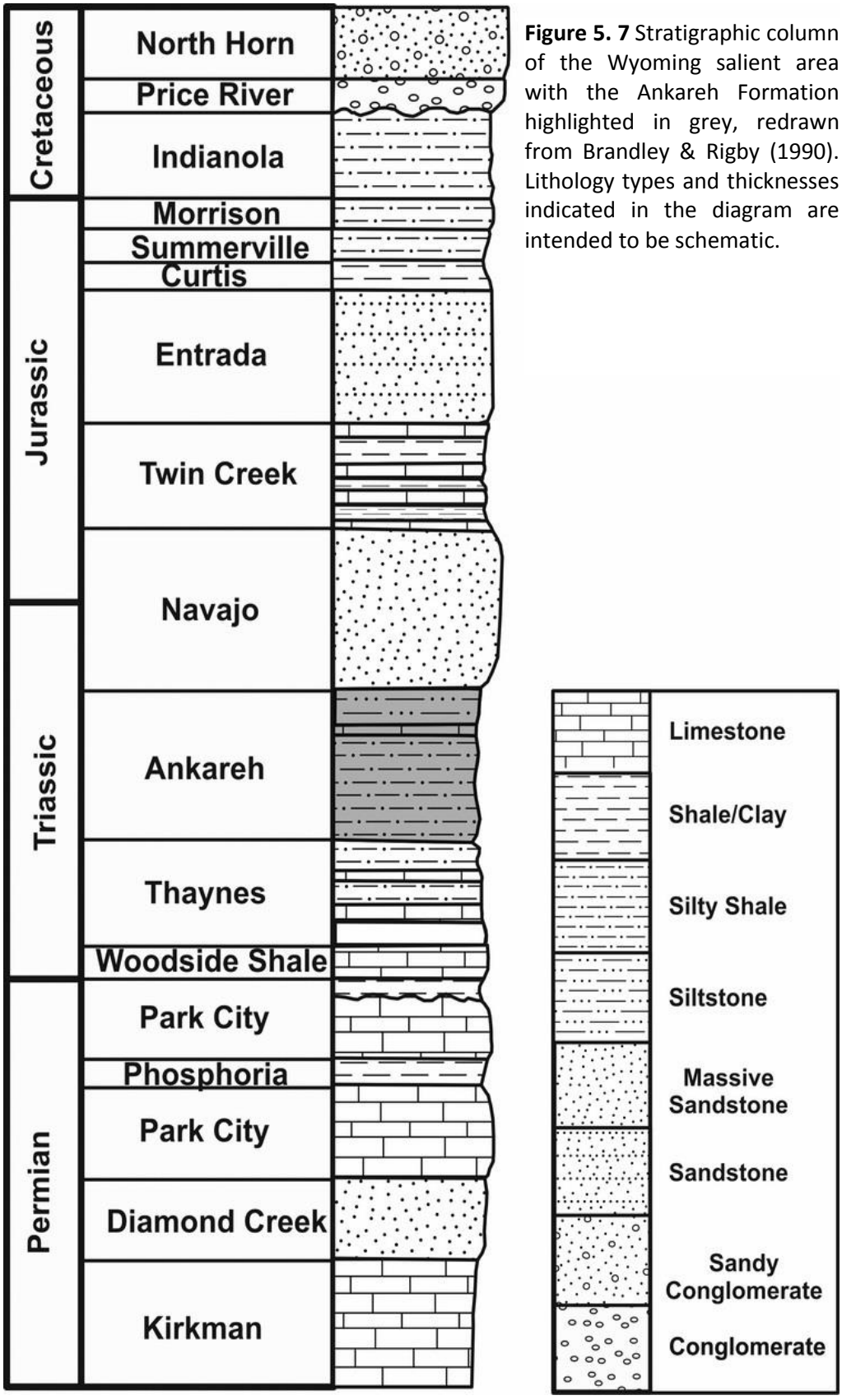

Figure 5. 7 Stratigraphic column of the Wyoming salient area with the Ankareh Formation highlighted in grey, redrawn from Brandley & Rigby (1990). Lithology types and thicknesses indicated in the diagram are intended to be schematic.

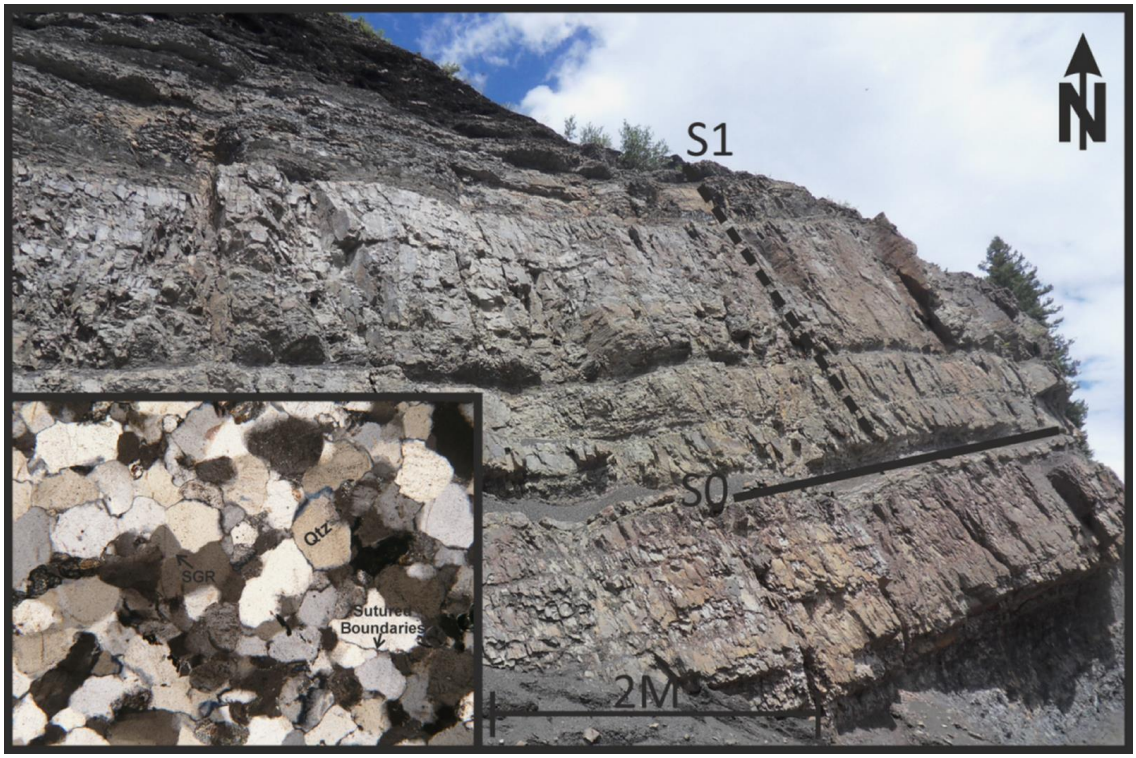

Figure 5. 8 Cleavage/bedding relationships in the Jackson transect. Inset shows microphotograph of Ankareh Formation. Quartz clasts have hematite rims and quartz overgrowths. Clasts are typically interlocking with sutured boundaries, suggesting deformation by pressure solution.

5.2. AMS and Strain Analysis

Oriented block samples for AMS and strain analysis were collected along two parallel transects, Bridger and Jackson, across the Wyoming Salient running from east to west and perpendicular to the regional tectonic grain. Only outcrops with well-defined structural relationships, bedding, cleavage, etc. were sampled. Additionally lithologies with complex sedimentary fabrics, such as syn-sedimentary deformation, burrowing, and cross bedding were avoided, as these might add further complexities to the relationship between bedding and tectonic fabrics. Strain estimates were made from samples with clear relationships between observed structures and AMS properties.

5.2.1. Application of AMS

On average 8-14 core samples were drilled from each block sample. Out of the 35 block samples collected, 27 samples survived drilling and provided enough sub specimens to be statistically viable. Each core sample was cut into 22mm x 25mm right-cylinder specimens with a minimum of five specimens obtained from each sample. This yielded 349 individual specimens for analysis. AMS analyses were carried out using the MFK1-A Kappabridge (AGICO, Czech Republic) at the New Mexico Highlands University Paleomagnetic-Rock Magnetic Laboratory.

5.2.2. Strain Analysis

Strain analysis was carried out on oriented bedding parallel thin sections prepared from AMS cores (Figure 5.9). Out of the 20 samples selected for strain analysis, 15 were suitable for analysis. The MRL (Mulchrone et al., 2003) and DTNNM (Mulchrone, 2002) methods were applied using the semi-automated software and methodologies described in Mulchrone et al. (2013). These methods determine 2D finite strain by determining properties of populations of sedimentary clasts and comparing these data to assumed pre-strain conditions. Bedding plane strain is considered a good proxy for layer-parallel tectonic shortening as compaction tends to act perpendicular to bedding. Furthermore, bedding parallel sections are less likely to be affected by variations in primary fabrics (Paterson and Yu, 1994). Strain analysis required grain boundary maps of a least 150 grains, as recommended by Meere and Mulchrone (2003), and were manually traced from oriented microphotographs. These images were then analysed by the software presented in Mulchrone et al. (2013), which calculated all of the required parameters.

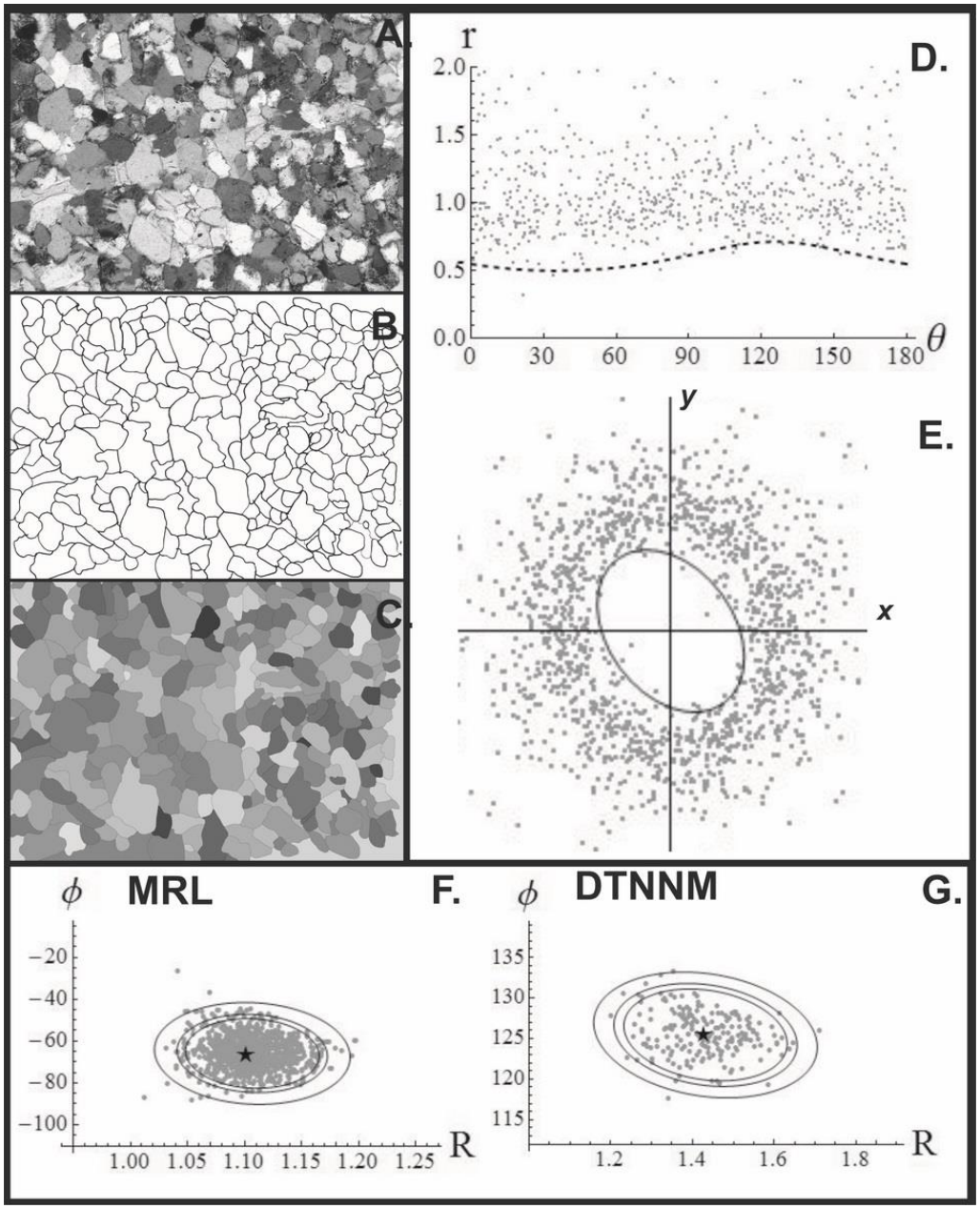

Figure 5. 9 Strain analysis workflow modified from (Mulchrone et al, 2013). **A.** Raw image of Wy26a. **B.** Input image. **C.** Processed image. **D.** Polar plot showing variations in ellipse length ratios versus orientation. **E.** Cartesian plot of the data from **D**. **F.** Bootstrap data for Mean Radial Length Method. The value of the actual estimate is shown by the star, the grey dots represent 1000 estimates. Ellipses shown are the 90, 95 and 99% confidence ellipses. **G.** Bootstrap data for Delaunay Triangulation Nearest Neighbour Method. The value of the actual estimate is shown by the star, the grey dots represent 200 estimates.

5.3. AMS Results

Bulk susceptibility for site samples varies from 0.0025 x 10^{-3} to 1.2 x 10^{-3}, these values suggest that the AMS fabrics are dominated by paramagnetic phyllosilicates

and haematite although the high bulk susceptibility values (< 1.0 x 10^{-3}) detected in some samples suggest trace amounts of titanomagnetite. The presence of titanomagnetite does not appear to have had a major effect on the AMS ellipsoid geometries. The bulk susceptibilities of the specimens have a largely bimodal distribution (Figure 5. 10A). With the majority of specimens (78%) yielding a bulk susceptibilities less than 0.5 x 10^{-3}, 17% is >0.5 x 10^{-3} and <1.2 x 10^{-3}, and 3.4% is >10 x 10^{-3}. The specimens with >10 x 10^{-3} are all from one sample, Wy11. The high bulk susceptibility is indicative of at least 0.1 % magnetite or >1% haemo-ilmenite or >10% haematite (Tarling and Hrouda, 1993). The population of bulk susceptibilities between >0.5 x 10^{-3} and <1.2 x 10^{-3} are indicative of susceptibilities influenced by haematite. The population of specimens with bulk susceptibilities <0.5 x 10^{-3} is largely controlled by paramagnetic minerals, with some contributions from ferromagnetic minerals, probably haematite. Within this subpopulation 74% (or 58% of the total) is <0.3 x 10^{-3} indicating little or no influence from ferromagnetic minerals. The susceptibility plots versus bulk susceptibility are reported in µSI units (1 x 10^{-6}) (Figure 5. 10B), the plot of corrected degree of anisotropy (Pj) vs bulk susceptibility indicates that the degree of anisotropy is not controlled by samples with higher bulk susceptibilities. Figure 5. 10C&D plots the degree of anisotropy (Pj) versus shape parameter (Tj) for individual specimens and for mean samples. The shape parameter, Tj, varies from -0.837 to 0.914, showing a range of ellipsoid shapes from prolate to oblate, but the majority of samples range from weakly oblate to triaxial, with an average of 0.088. The degree of anisotropy, Pj, varies from 1.006 to 1.794 but is typically moderate to low with an average of 1.07 indicating 7% anisotropy. Figure 5. 11 is a plot of the same data in Figure 5. 10C&D,

but plotted in a Borradaile-Jackson Polar plot. This plot is similar to the Tj-Pj plot in that it displays the same information, with the advantage that samples with weaker anisotropies (Pj) plot closer to the origin regardless of shape. It is clear from this plot that the majority of samples weakly oblate geometries, but some prolate and strongly oblate geometries are present. AMS ellipsoid geometries generally evolve in the manner described in Section 3.1, whereby AMS fabrics are dominated by bedding in the east representing Type 1 and gradually change to tectonic dominated AMS ellipsoids in the west, representing Type 4 geometries.

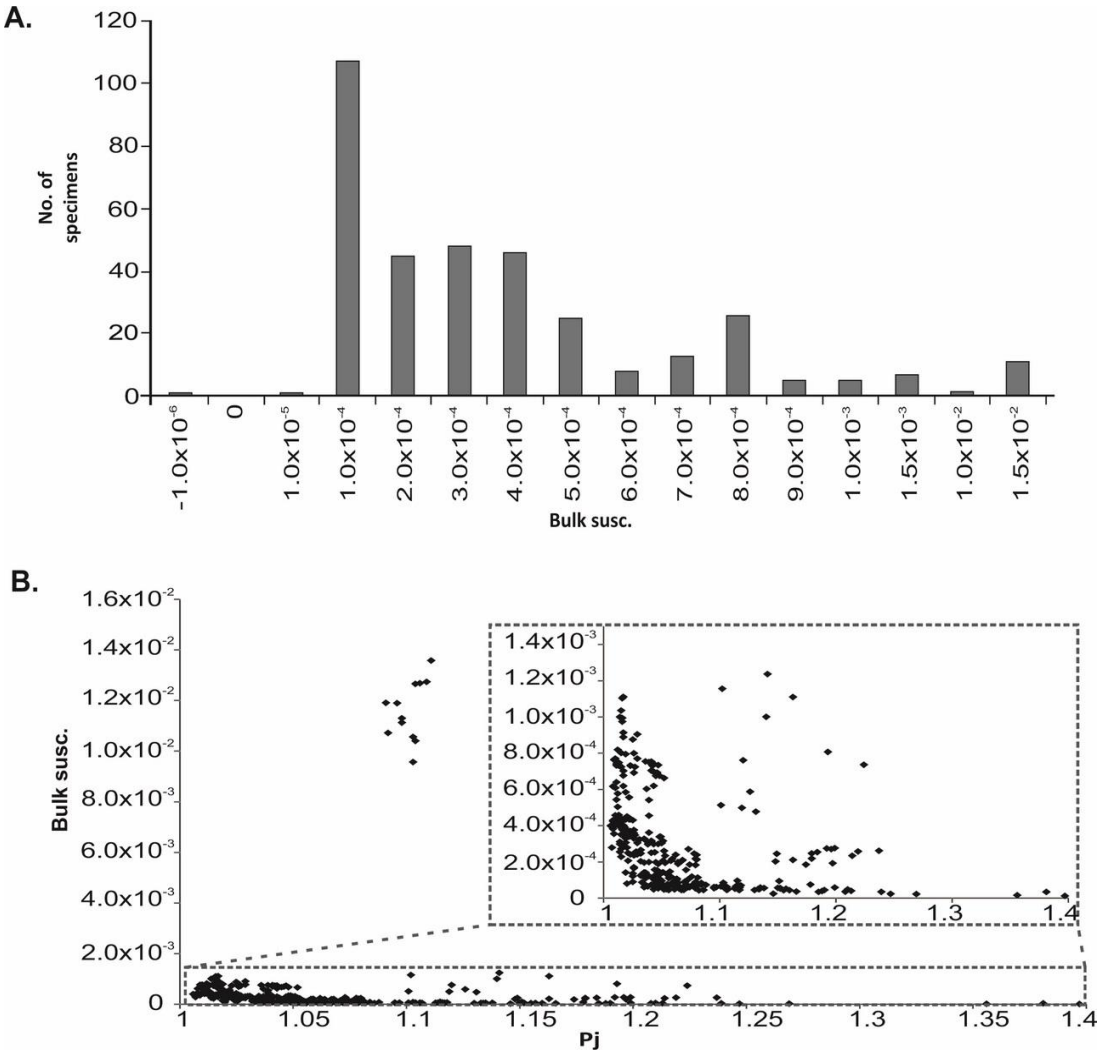

Figure 5. 10 Plots of AMS data. **A.** Histogram of susceptibility values for individual specimens. **B.** Degree of anisotropy versus bulk susceptibility for individual specimens and inset shows a smaller range of bulk susceptibilities. The cluster of specimens with a high bulk susceptibility are all from the same sample Wy11 and possibly represent higher amounts of hematite.

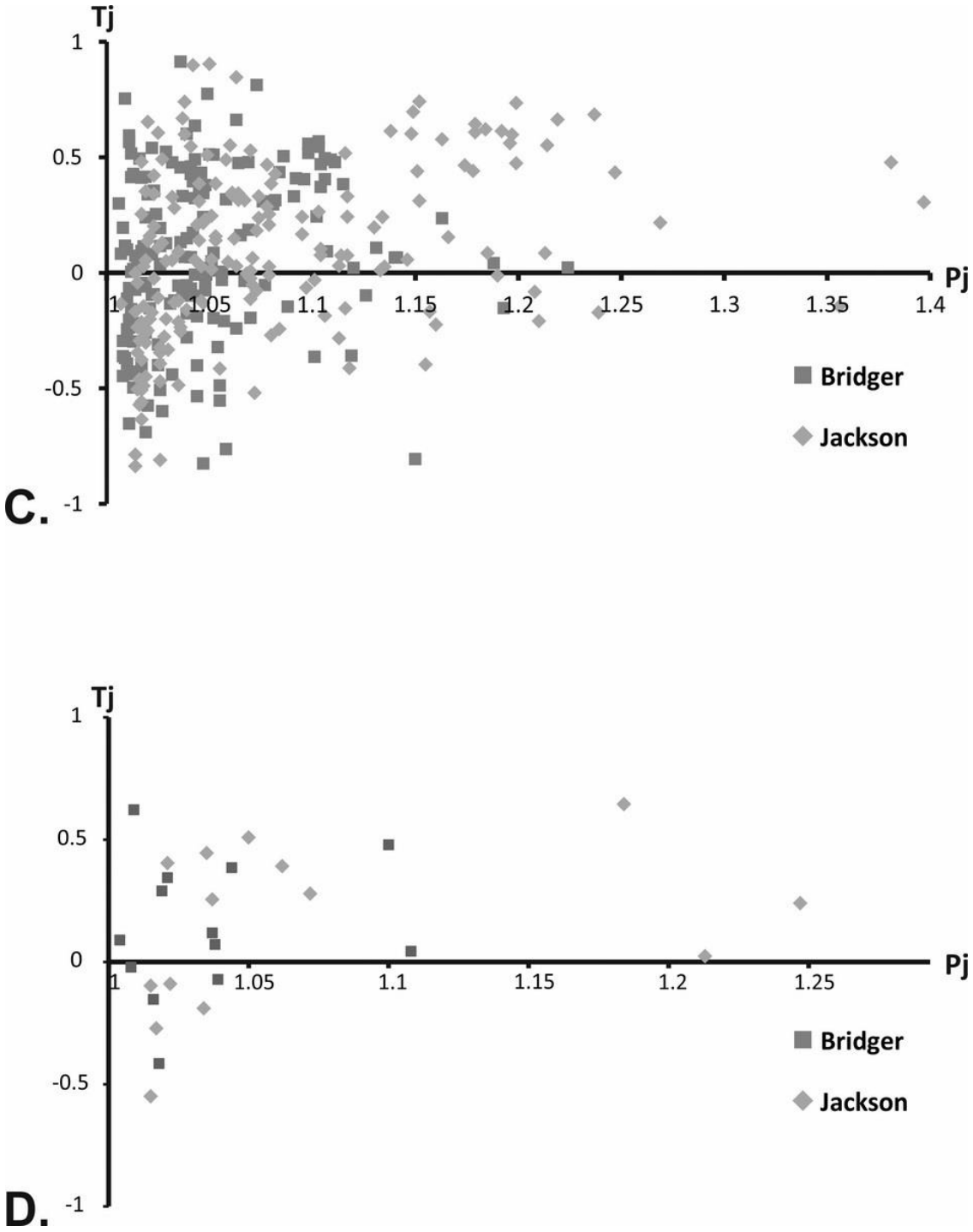

Figure 5. 10 Cont. **C.** Degree of anisotropy (Pj) versus shape parameter (Tj) for individual specimens. **D.** Degree of anisotropy (Pj) versus shape parameter (Tj) for mean samples.

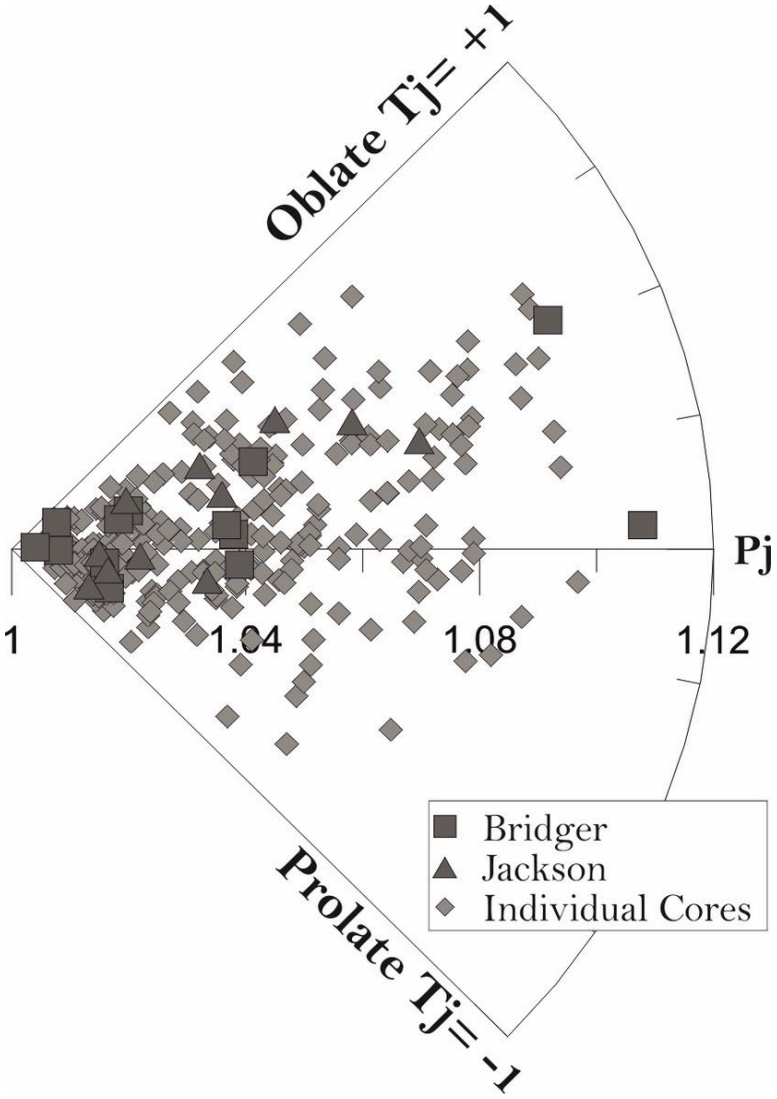

Figure 5. 11 Borradaile-Jackson Polar plot of all individual specimens as well as mean samples. This plot is similar to Tj-Pj plot in that it displays the same information, with the advantage that samples with weaker anisotropies (Pj) plotting closer to the origin regardless of shape.

In order to identify a regional pattern in the magnetic fabrics a series of plots of all the orientations and declinations of all of the principal susceptibility axes are presented below (Figure 5. 12-Figure 5. 20). Figure 5. 12 illustrates the orientations of the maximum susceptibility axis (K1) for all individual specimens in both a rose diagram and a stereographic projection of the contoured distribution of K1. Although there is some scatter it is clear from these plots that K1 is typically plunging approximately 40° towards the SW. Similarly Figure 5. 13 illustrates the intermediate susceptibility axis (K2) for all individual specimens. The rose diagram

illustrates a clear north/south trend, while the contoured plot illustrates a possible North/South girdle with significant scatter. Figure 5. 14 is a similar diagram but for the minimum susceptibility axis (K3). Interestingly the rose diagram of K3 orientations doesn't seem to highlight any strong preffered orientation, whilst the contoured plot identifies a weak girdle, with a small cluster in its centre, plunging to the shallowly to the east. This distribution could be seen to be roughly perpendicular to K2.

To put the distribution of the principal susceptibility axes into more of a structural context, they have been plotted on a stereonet with the bedding planes they were collected from, also shown in orange are typical cleavage planes observed in the field (Figure 5. 15). Despite considerable scatter in this plot it is clear that K1 is largely associated with bedding, but also defines a cluster plunging to the South-West. This southwest cluster aligns closely with the intersection of cleavage and bedding. K2 is typically trending North-South and appears to be aligned with cleavage. K3 is largely scattered, but has a small cluster plotting as the pole to bedding. Figure 5. 16 plots the same data as Figure 5. 15 but has been corrected for bedding tilt. Interestingly this correction results in a horizontal/shallow plunging K1 distribution, but a highly scattered K2 and K3 distribution. A largely horizontal K1 distribution would be typical of a sedimentary fabric. Figures Figure 5. 17 to Figure 5. 20 show the same data as Figure 5. 15, but only showing K1 and K2 (Figure 5. 17 and Figure 5. 18), or K3 (Figure 5. 19 Figure 5. 20) to make their distribution patterns clearer.

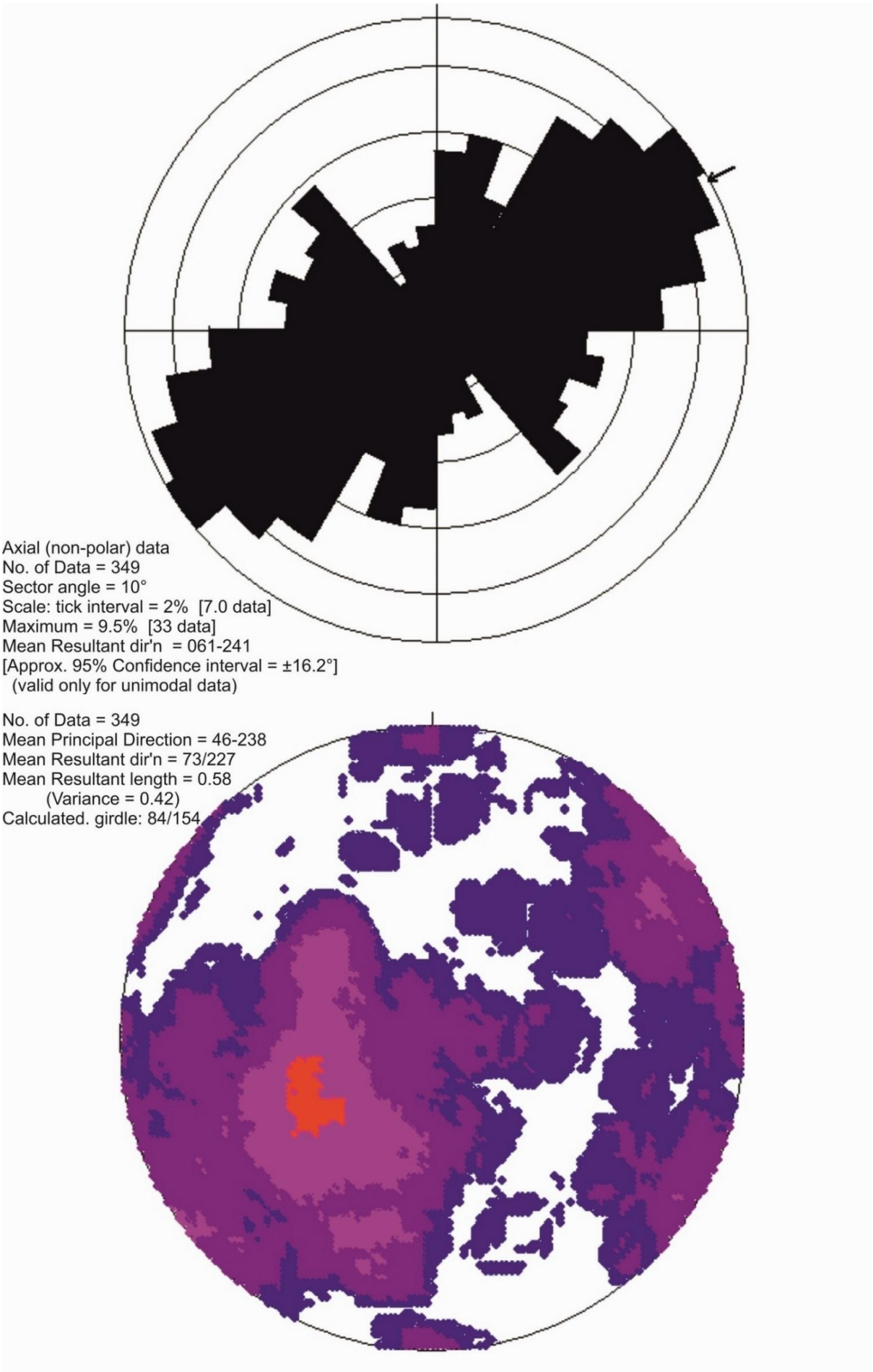

Figure 5. 12 Top: Rose diagram of the K1 orientations for all specimens. **Bottom:** Contoured plot of K1 plunge and trend.

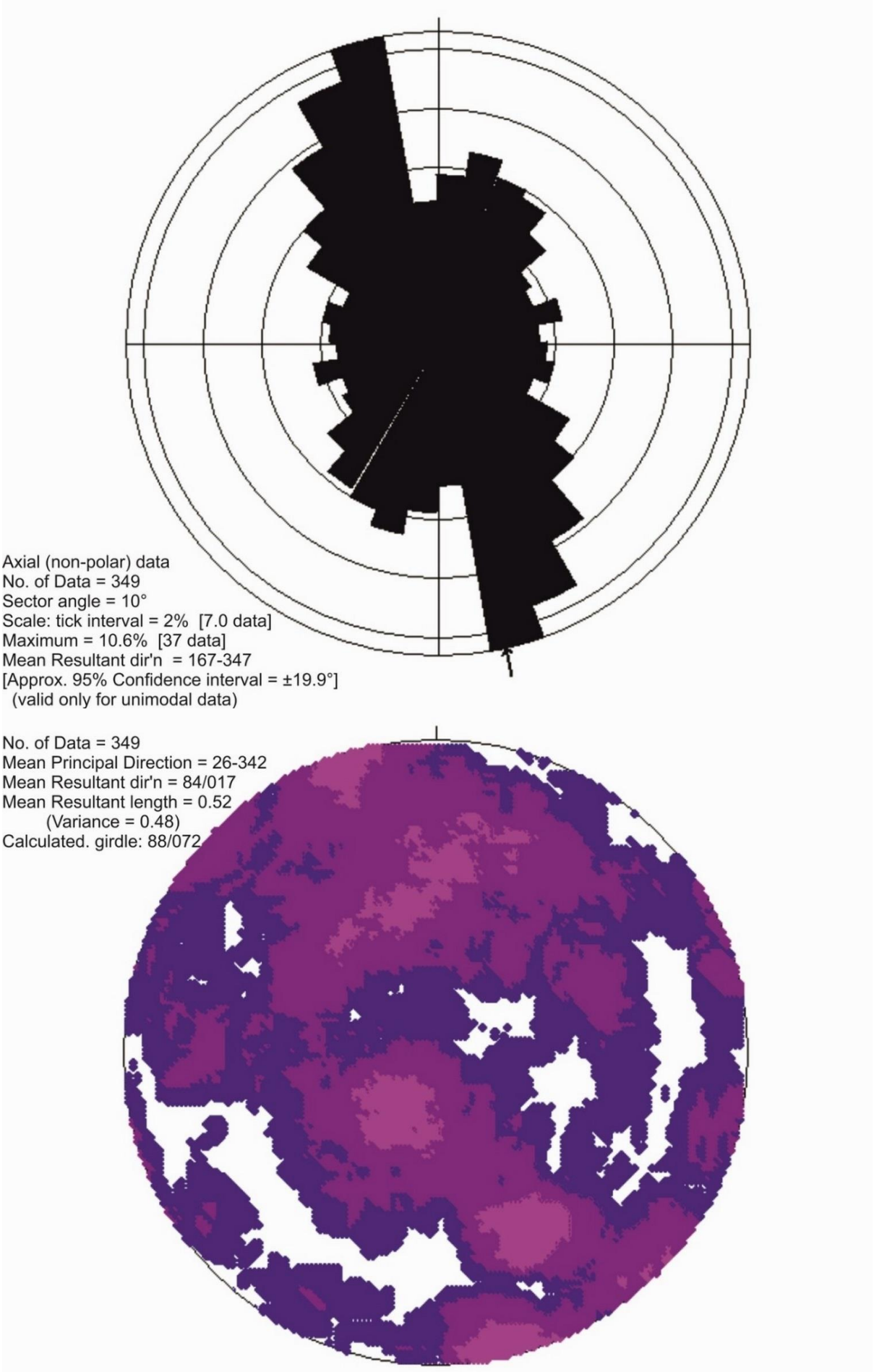

Figure 5. 13 Top: Rose diagram of the K2 orientations for all specimens. **Bottom:** Contoured plot of K2 plunge and trend.

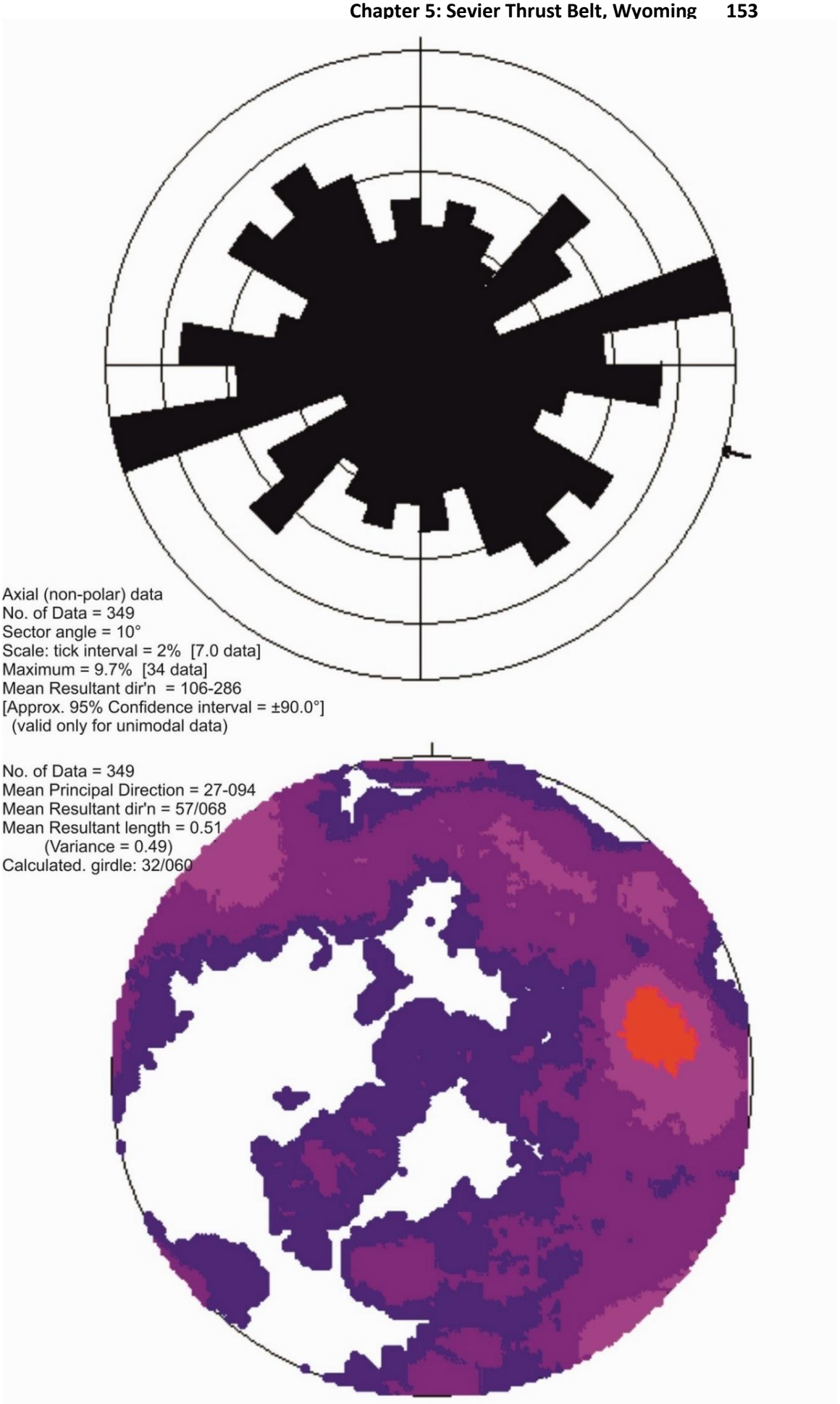

Figure 5. 14 Top: Rose diagram of the K3 orientations for all specimens. **Bottom:** Contoured plot of K3 plunge and trend.

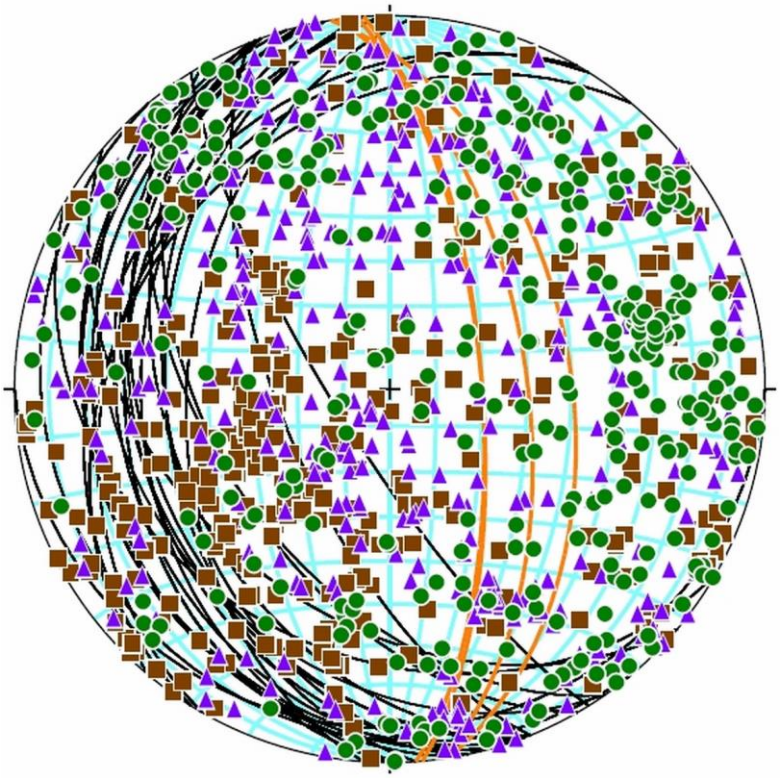

Figure 5. 15 Stereographic projections of principal susceptibility axes for all specimens (K1: red squares; K2: blue triangles; K3: green circles). Individual bedding planes are indicated and primarily dip shallowly westward. Typical cleavage planes are indicated in orange.

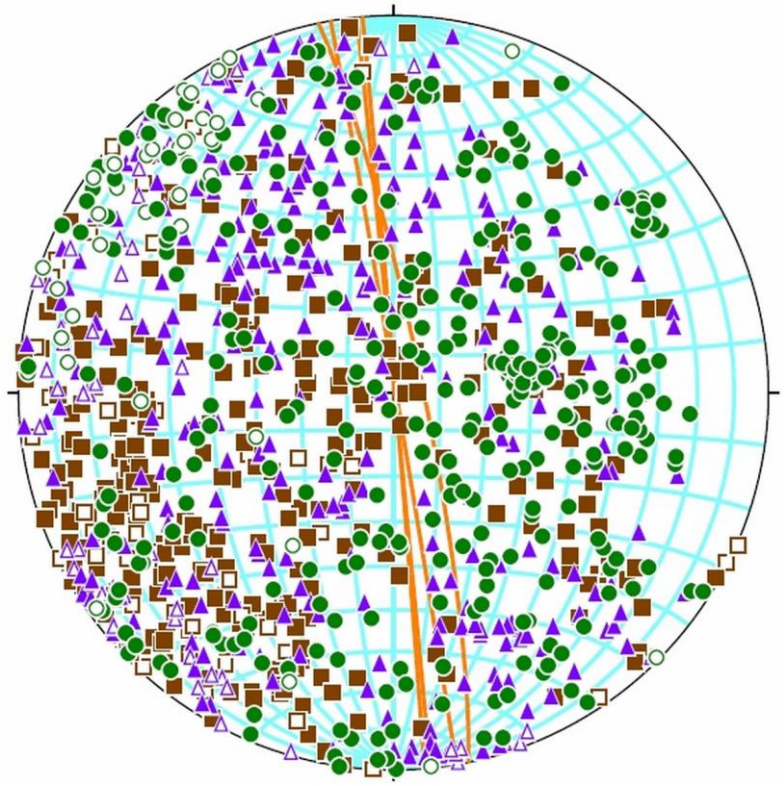

Figure 5. 16 Stereographic projections of principal susceptibility axes for all specimens with correction for bedding. Bedding is now horizontal. Typical cleavage planes are indicated in orange. Hollow symbols represent points on upper hemisphere.

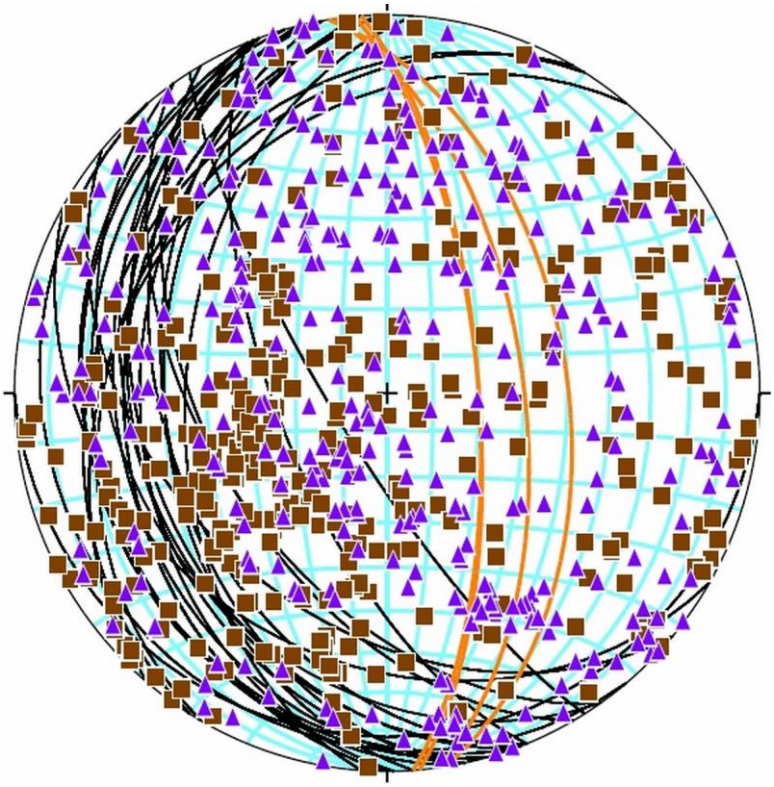

Figure 5. 17 Stereographic projections of maximum and intermediate susceptibility axes (K1 & K2) for all specimens. Individual bedding planes are plotted in black and primarily dip shallowly westward. Typical cleavage planes are plotted in orange.

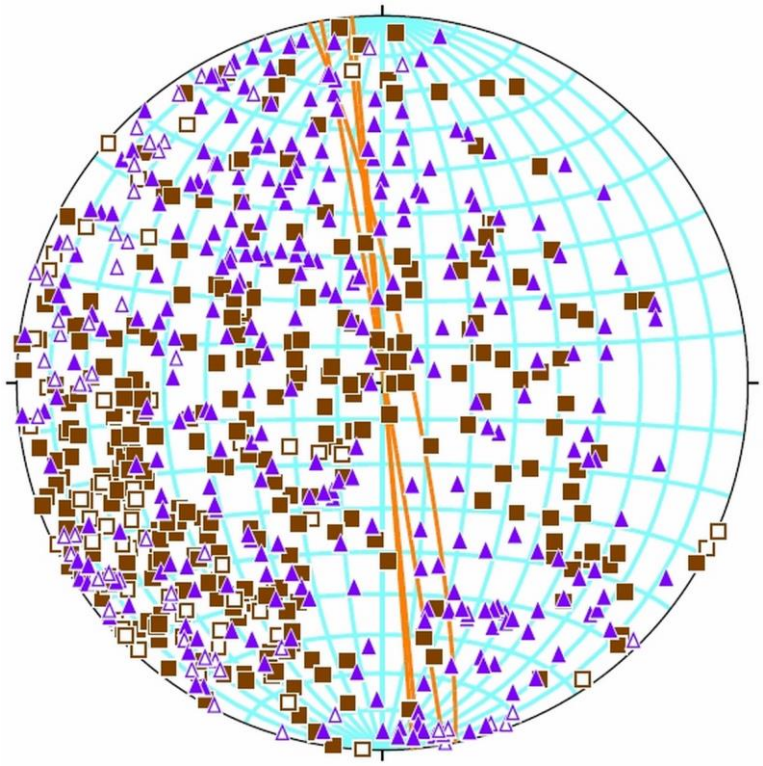

Figure 5. 18 Stereographic projections of maximum and intermediate susceptibility axes for all specimens with correction for bedding. Bedding is now horizontal. Typical cleavage planes are indicated in orange.

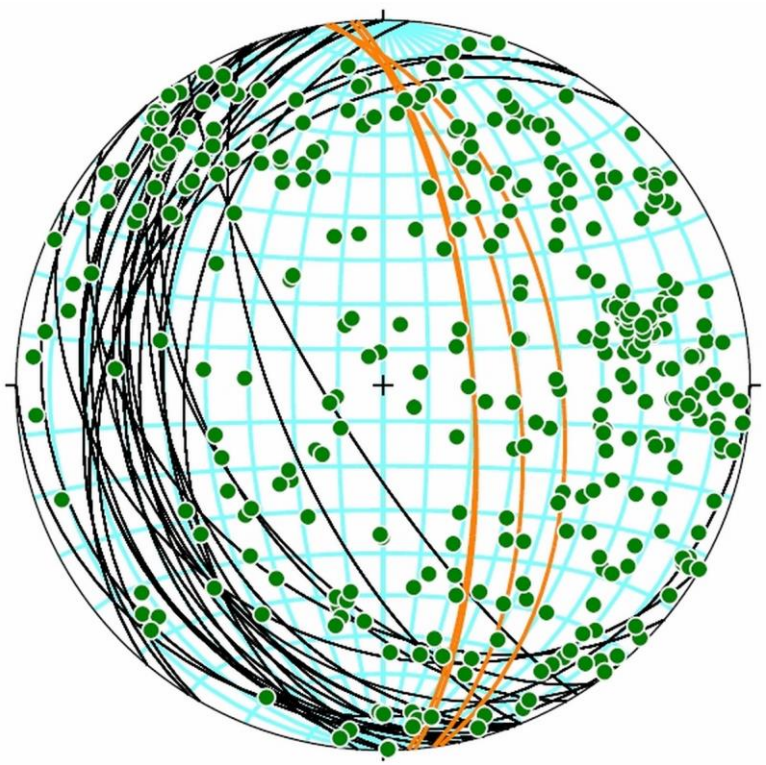

Figure 5. 19 Stereographic projections of the minimum susceptibility axes (K3) for all specimens. Individual bedding planes are plotted in black and primarily dip shallowly westward. Typical cleavage planes are plotted in orange.

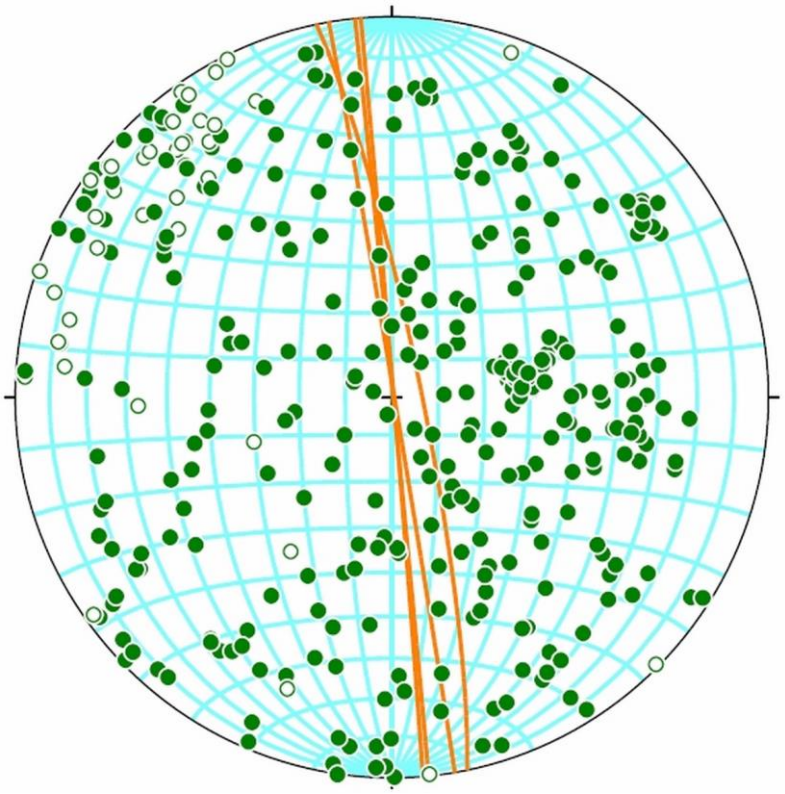

Figure 5. 20 Stereographic projections of minimum susceptibility axes (K3) for all specimens with correction for bedding. Bedding is now horizontal. Typical cleavage planes are indicated in orange.

The large degree of scatter in the regional stereographic plots can be attributed to the range of magnetic fabric types measured in the Wyoming Salient, illustrated in Figure 5.5, but also in Figures 5.21-24. In the Figures 5.21-5.24 each sample is represented by a stereographic projection of the principal axes of the magnetic ellipsoid for each sub-specimen, as well as a plot of bulk susceptibility vs Pj, a Pj-Tj plot and a L/F diagram (for further discussion on the significance of these plots see Chapter 3). These plots were used to determine magnetic fabric types presented in Figure 5.5.

Wy29 and Wy30 (Figure 5.21) have very similar bedding controlled fabrics (K1 and K2 lie on the bedding plane), although Wy29 is tending more towards triaxial rather than oblate and as a result has a larger degree of scatter. Wy26 (Figure 5.21) is also characterised by K1 lying on the bedding plane is more triaxial than Wy29. Wy25 (Figure 5.21) features a magnetic foliation (girdle of K1 and K2) 90° to bedding, possibly representing a tectonic fabric. Wy24 (Figure 5.21) has a very simmilar bedding controlled fabric as Wy30. Wy28 (Figure 5.21) is similar to Wy26 but has a much stronger clustering of K1 and represents a type 3 magnetic fabric. Wy27 (Figure 5.22) has particularly large confidence ellipses and any interpretation should not be regarded. Wy21 (Figure 5.22) clearly has a high degree of scatter but there is a relatively strong foliation 90 degrees to bedding. Wy23 (Figure 5.22) is similar to Wy29 in that the magnetic foliation closely follows the bedding plane but is tending more towards a triaxial/prolate geometry. Wy16 (Figure 5.22) has a very strong magnetic lineation 90° to the bedding plane. Wy18, Wy15 (Figure 5.22) and Wy1 and Wy2 (Figure 5.23) are characterised by a strong magnetic foliation perpendicular to the bedding plane. Wy3 (Figure 5.23) has a large degree of scatter and significantly large confidence ellipses, despite this K1 defines a girdle perpendicular to bedding. Similarly Wy4 (Figure 5.23) has very large confidence ellipses, but in they case they overlap and as a result any interpretation of this sample is rendered meaningless. Wy6 and Wy7 (Figure 5.23) have triaxial geometries with the magnetic foliation lying in the bedding planes. Wy8 and Wy10

(Figure 5.24) have a similar oblate geometry as Wy30 with the magnetic foliation parallel to bedding. Wy11 (Figure 5.24) has a strong magnetic foliation perpendicular to the bedding plane. Wy12 (Figure 5.24) is similar to Wy11 but is tending towards triaxial rather than oblate. Wy13 (Figure 5.24) is tending towards prolate and K1 and K2 are still lying on the bedding plane. Wy14 (Figure 5.24) is characterised by a shallow plunging oblate magnetic foliation that is significantly deviated from the bedding plane, which is probably due to some miscalculation of the drilling angle.

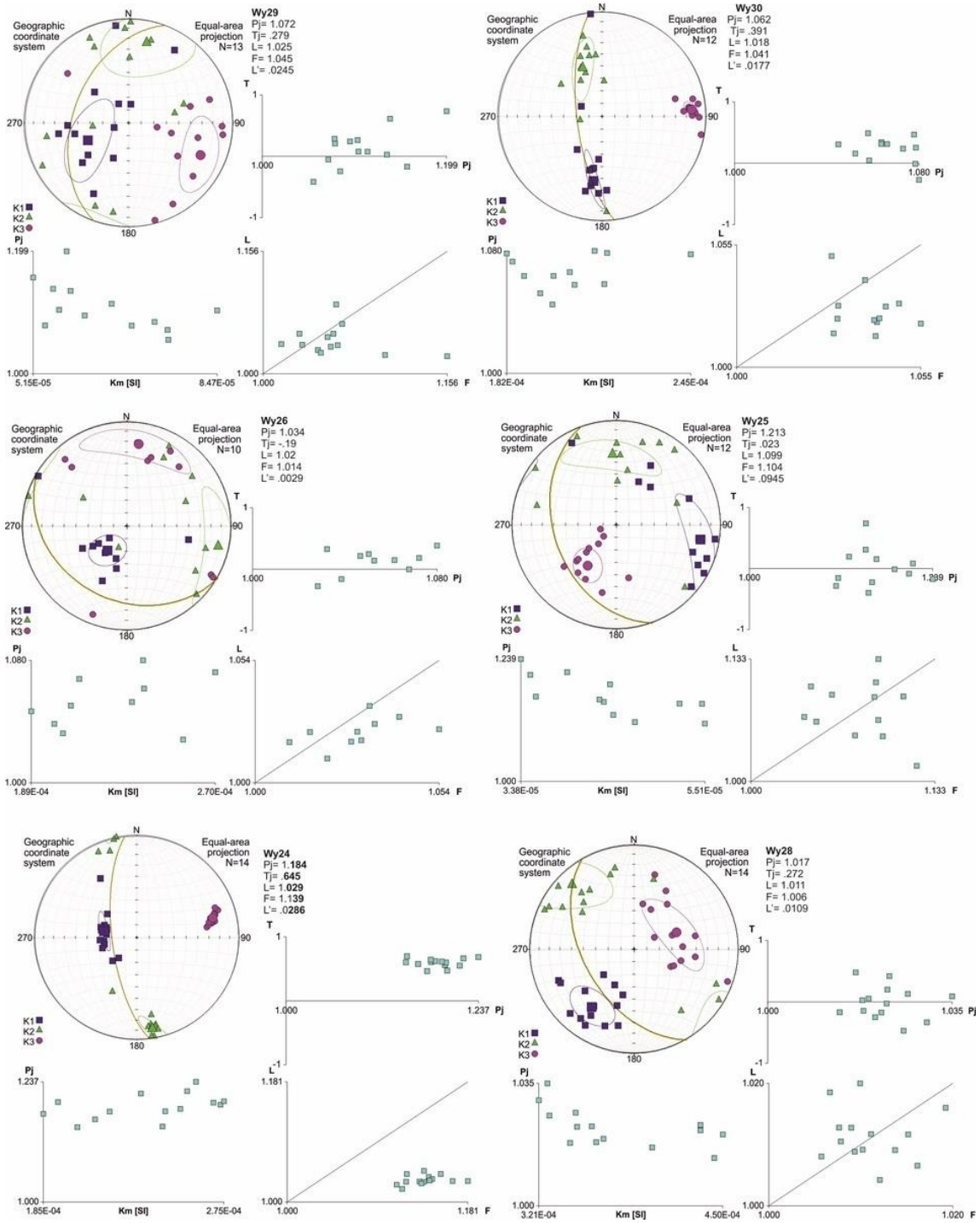

Figure 5. 21 AMS results for individual samples. Shown for each sample is a stereographic projection of the principal susceptibility axes with mean axis orientations represented by the larger symbols. Also included are graphs of characteristic AMS parameters, a Pj-Tj plot, Flinn plot and a plot bulk susceptibility versus Pj (anisotropy) are shown clockwise from upper right to lower left respectively.

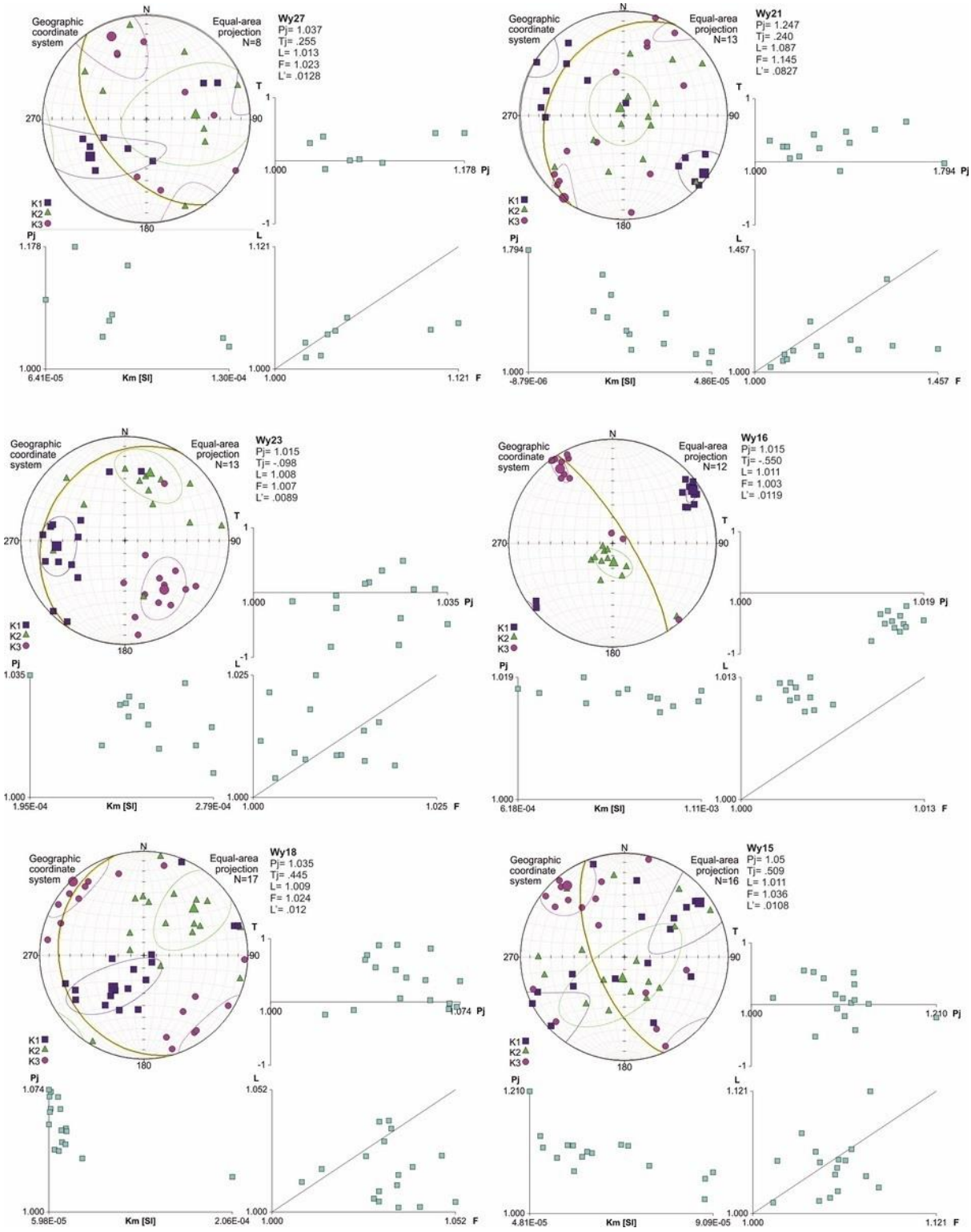

Figure 5. 22 AMS results for individual samples.

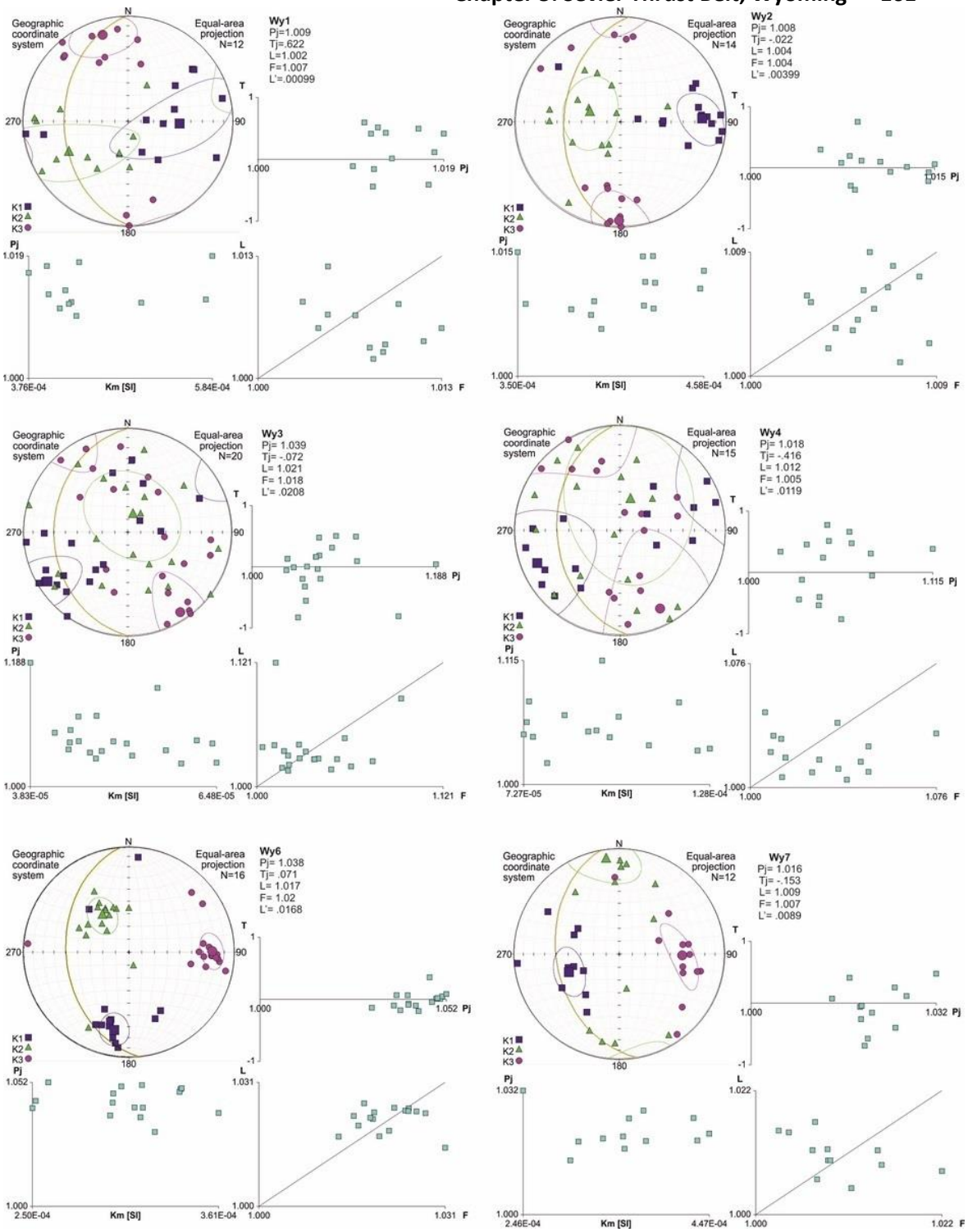

Figure 5. 23 AMS results for individual samples.

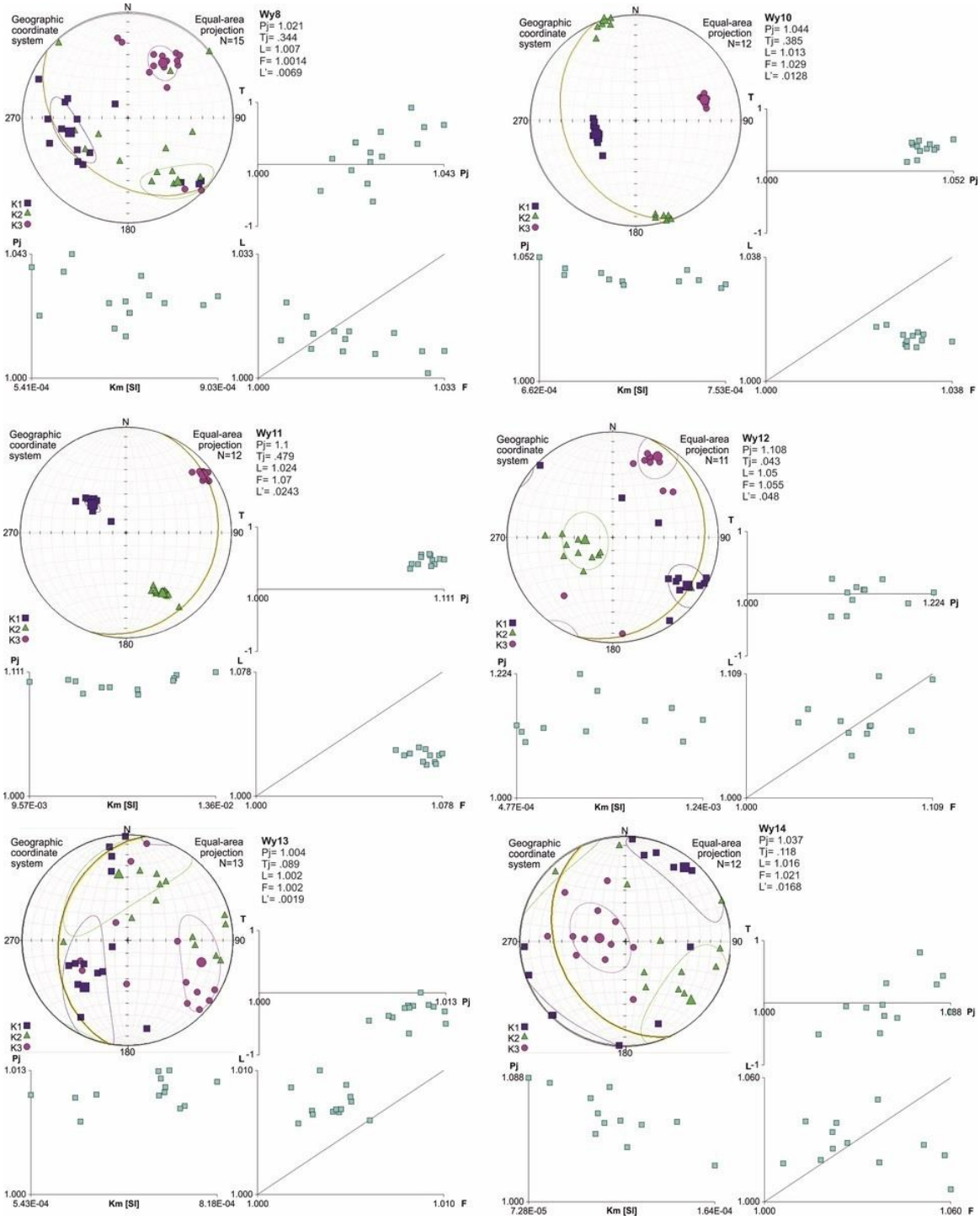

Figure 5. 24 AMS results for individual samples.

5.4. Strain Analysis Results

Axial ratio estimates from the strain analyses show a range of estimates from 1.008 to 1.1969 for MRL and 1.04 to 1.42 for DTNNM (Figure 5. 25). As expected the DTNNM estimates are typically higher than the MRL estimates. Despite both methods showing significant differences in *R* values, the *Φ* orientations usually only vary by 20°; although at times the variations are up to 70° for 5 estimates. There is generally less variation in angle recorded for samples with higher strains.

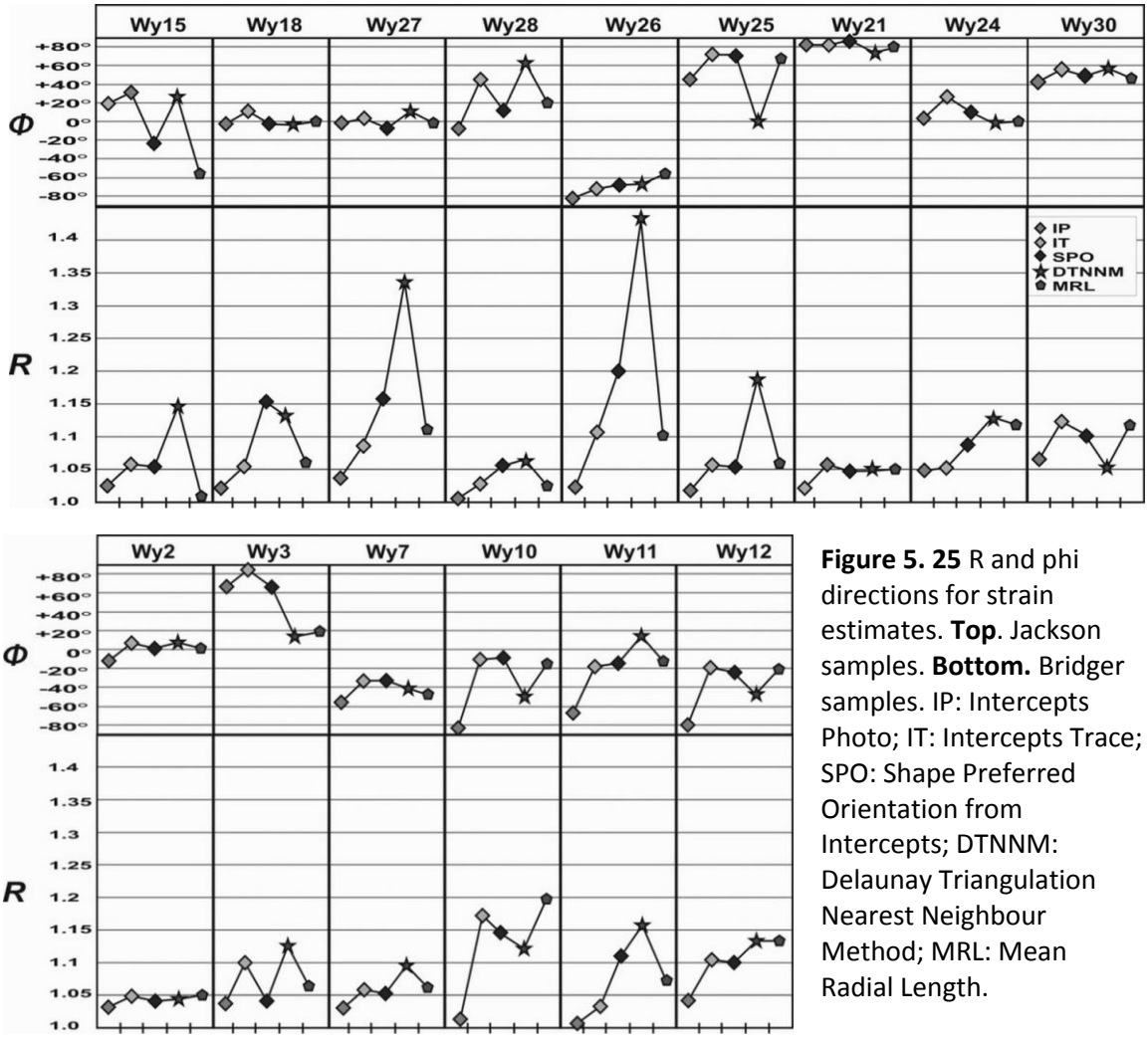

Figure 5. 25 R and phi directions for strain estimates. **Top**. Jackson samples. **Bottom.** Bridger samples. IP: Intercepts Photo; IT: Intercepts Trace; SPO: Shape Preferred Orientation from Intercepts; DTNNM: Delaunay Triangulation Nearest Neighbour Method; MRL: Mean Radial Length.

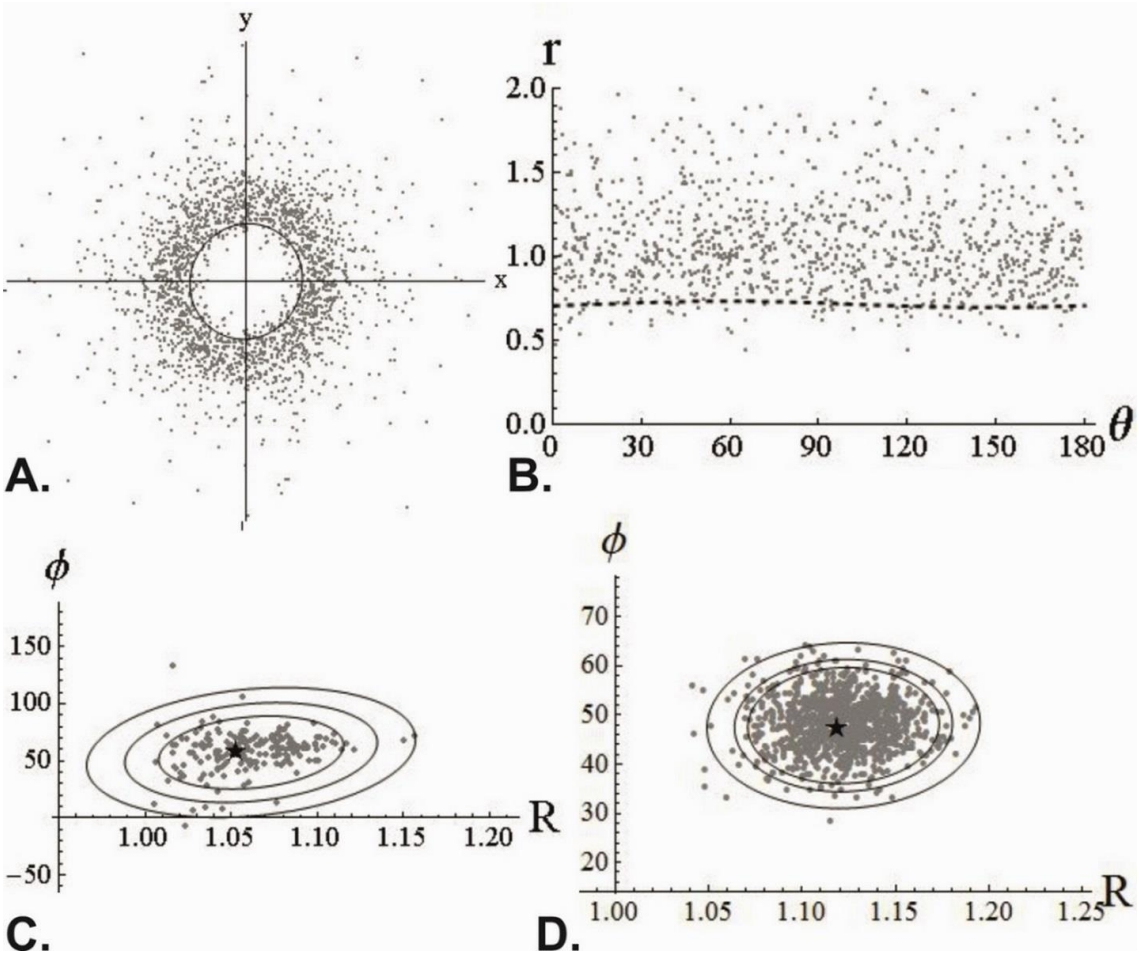

Figure 5. 26 Strain estimates for Wy30 from the DTNNM and MRL analyses. **A.** Fry plot of the nearest neighbour data. **B.** Polar plot of the nearest neighbour data, r (distance from origin) is plotted against orientation. The curve representing the best-fit ellipse is indicated by the dashed line. **C.** R/Φ plot for the DTNNM analysis, the black star represents the estimate and the grey dots represent bootstrap. The bootstrap intervals shown are 90%, 95% and 99%confidence intervals.

Similarly, the Intercepts analyses report low strain estimates. The measurements on the raw images returned the lowest *R* values, ranging from 1.006 to 1.070. The Intercepts of the grain boundary maps ranged from 1.028 to 1.240, while the SPO returned slightly higher values ranging from 1.04 to 1.20. *Φ* values for the intercepts analyses generally only vary by 20° although some samples show variation of up to 50° (Figure 5. 25). These results are comparable to strain data obtained from reduction spots ranging from 1.02-1.24 (Yonkee and Weil, 2010).

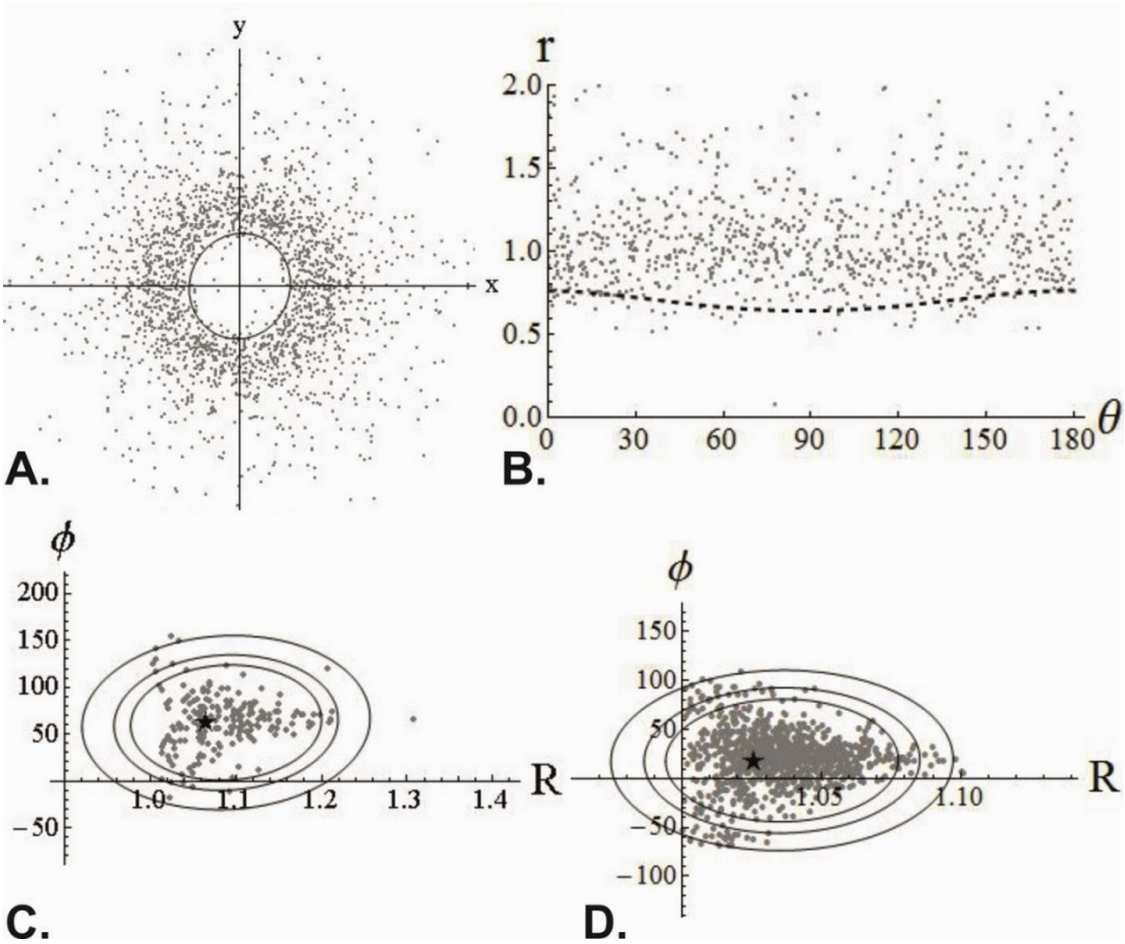

Figure 5. 27 Strain estimates for Wy28 from the DTNNM and MRL analyses.

In order to make it easier to compare the results the strain results have been split into two groups according to which traverse they were collected from, Jackson and Bridger. The strain estimates for the Jackson and Bridger traverses are shown in Figure 5. 26 to Figure 5. 34 and Figure 5. 44 to Figure 5. 49 respectively, while the results from the Intercepts and SPO analyses are shown in Figure 5. 35 to Figure 5. 43 and Figure 5. 50 to Figure 5. 55, a summary of all these results is presented in Figure 5. 25.

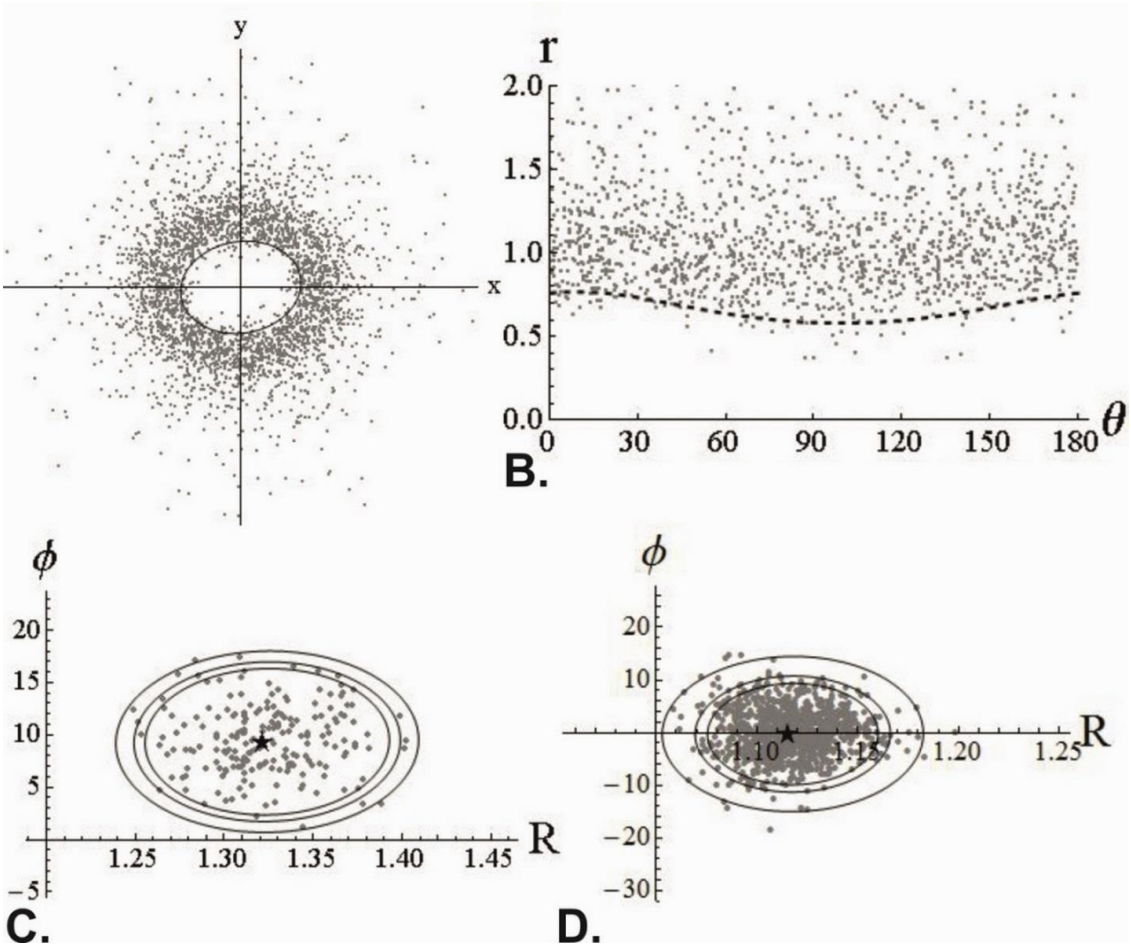

Figure 5. 28 Strain estimates for Wy27 from the DTNNM and MRL analyses.

The DTNNM and MRL results for Wy30 (Figure 5. 26) are clearly low strain estimates represented by the Fry plot (Figure 5. 26A) and polar plot (Figure 5. 26B). The Fry plot shows a largely even distribution of clast centres, additionally it has a very good fit for the best fit ellipse. The polar plot reinforces this low strain result with the best fit curve having a flat line pattern. The graphs of bootstrap data for DTNNM (Figure 5. 26C) and MRL (Figure 5. 26D) show a wide range of Φ orientations which is typical for low strain samples. Similarly the results for Wy28 (Figure 5. 27) are also low strain estimates, represented by a circular Fry plot and near flatline polar plot. Again the confidence intervals for the bootstrap data (Figure 5. 27C&D)show a wide range in Φ orientations.

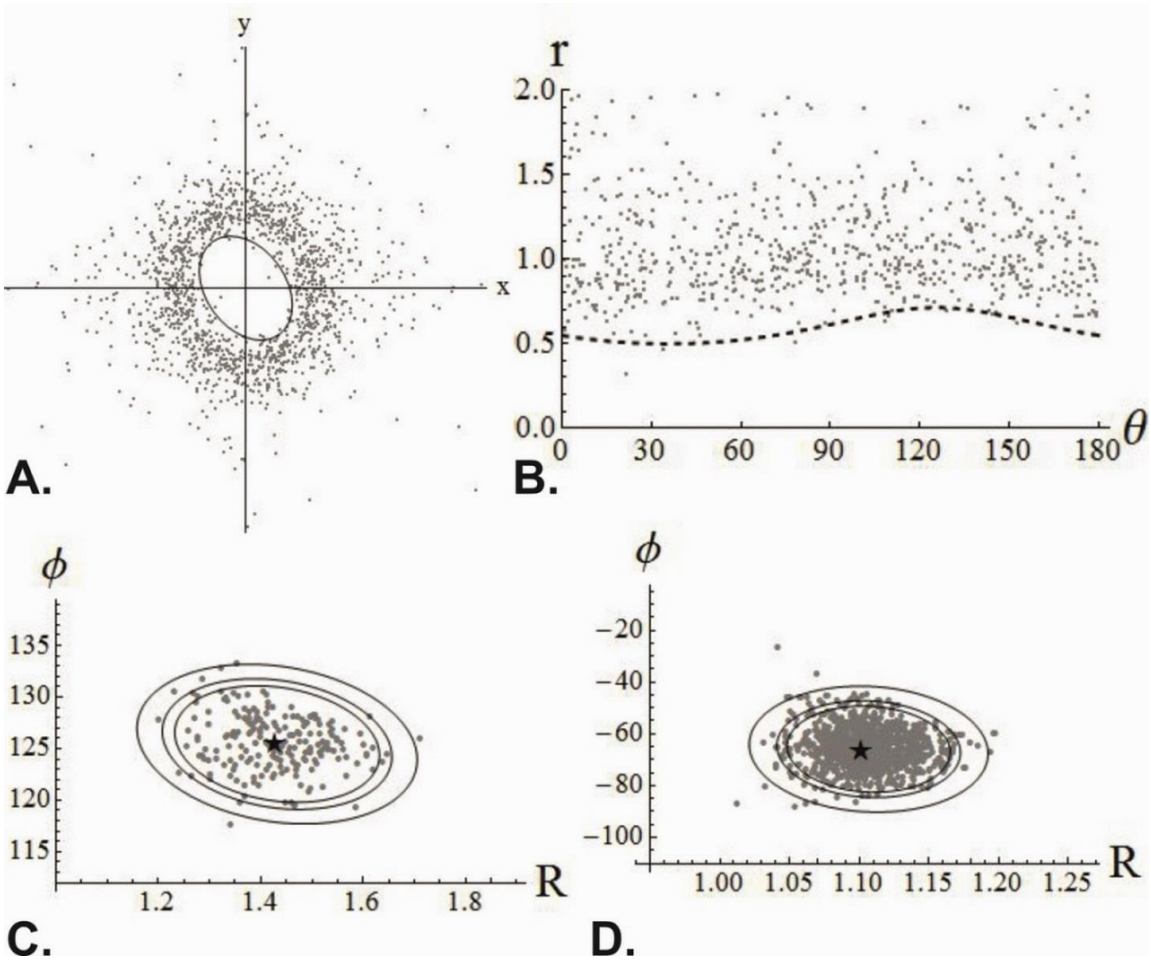

Figure 5. 29 Strain estimates for Wy26 from the DTNNM and MRL analyses.

Wy27 shows a slight increase in strain estimate for both DTNNM and MRL (Figure 5. 28). This can be seen in both the Fry plot (Figure 5. 28A) and the polar plot (Figure 5. 28B). The Fry plot has an elliptical distribution and the polar plot has a slight peak in the best fit curve between 5° and 15°. As is expected for samples with higher strains the confidence ellipses of the bootstrap data become significantly tighter (Figure 5. 28C&D). Additionally DTNNM reports a higher strain estimate than MRL.

Wy26 (Figure 5. 29) has a similar moderate strain estimate as Wy27 and again DTNNM reports a much higher estimate than MRL (Figure 5. 29C&D).

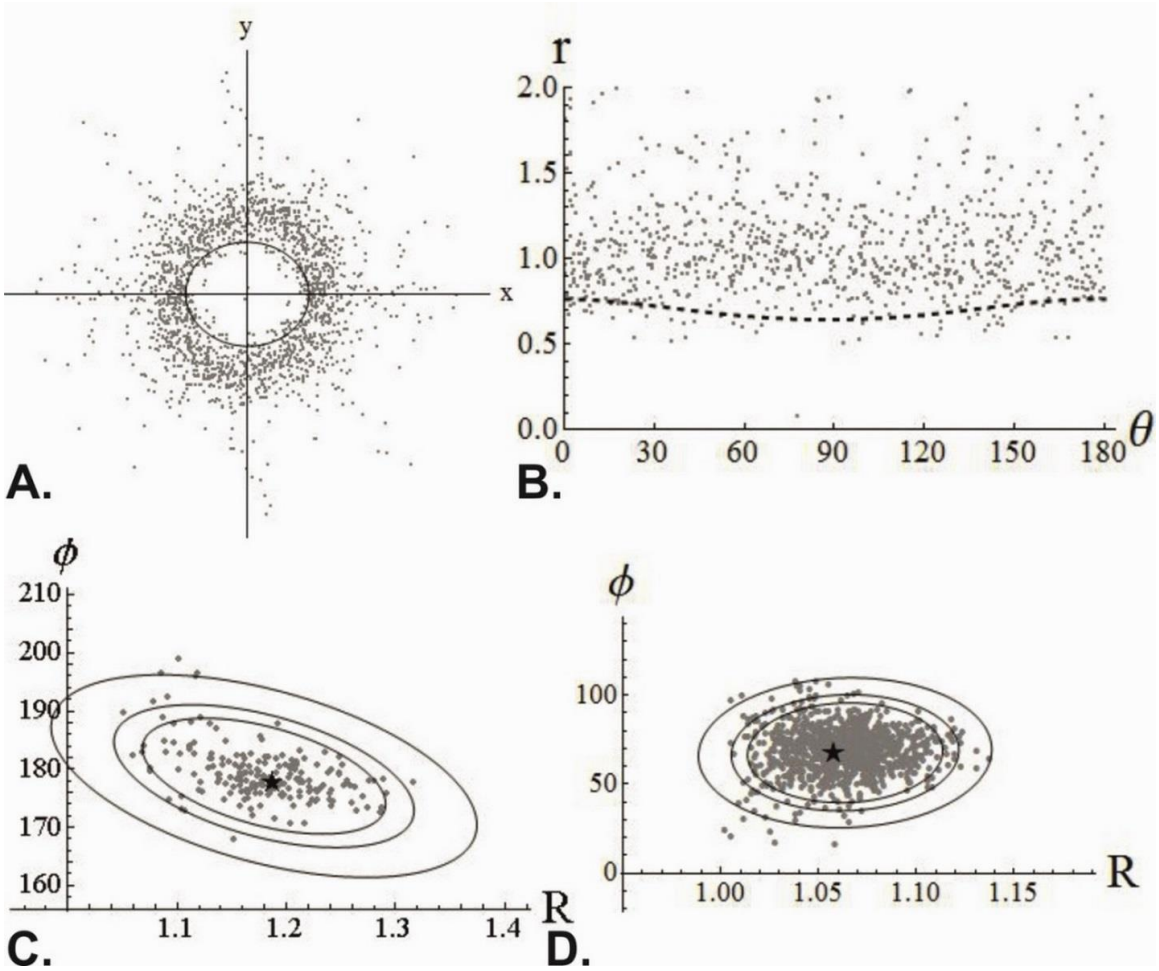

Figure 5. 30 Strain estimates for Wy25 from the DTNNM and MRL analyses.

The DTNNM and MRL results for Wy25 (Figure 5. 30) record lower strain estimates than Wy26 and Wy27, with DTNNM (Figure 5. 30C) recording very different results in both Φ orientation and R compared to MRL (Figure 5. 30D).

Wy24 (Figure 5. 31) has very similar low strain estimates to Wy30 and Wy28, shown by the circular Fry plot (Figure 5. 31A) and the near flatline in the polar plot (Figure 5. 31B). Both the DTNNM and MRL analyses report similar estimates for R, but report very different estimates for Φ orientations (Figure 5. 31C&D) again typical for low strain samples.

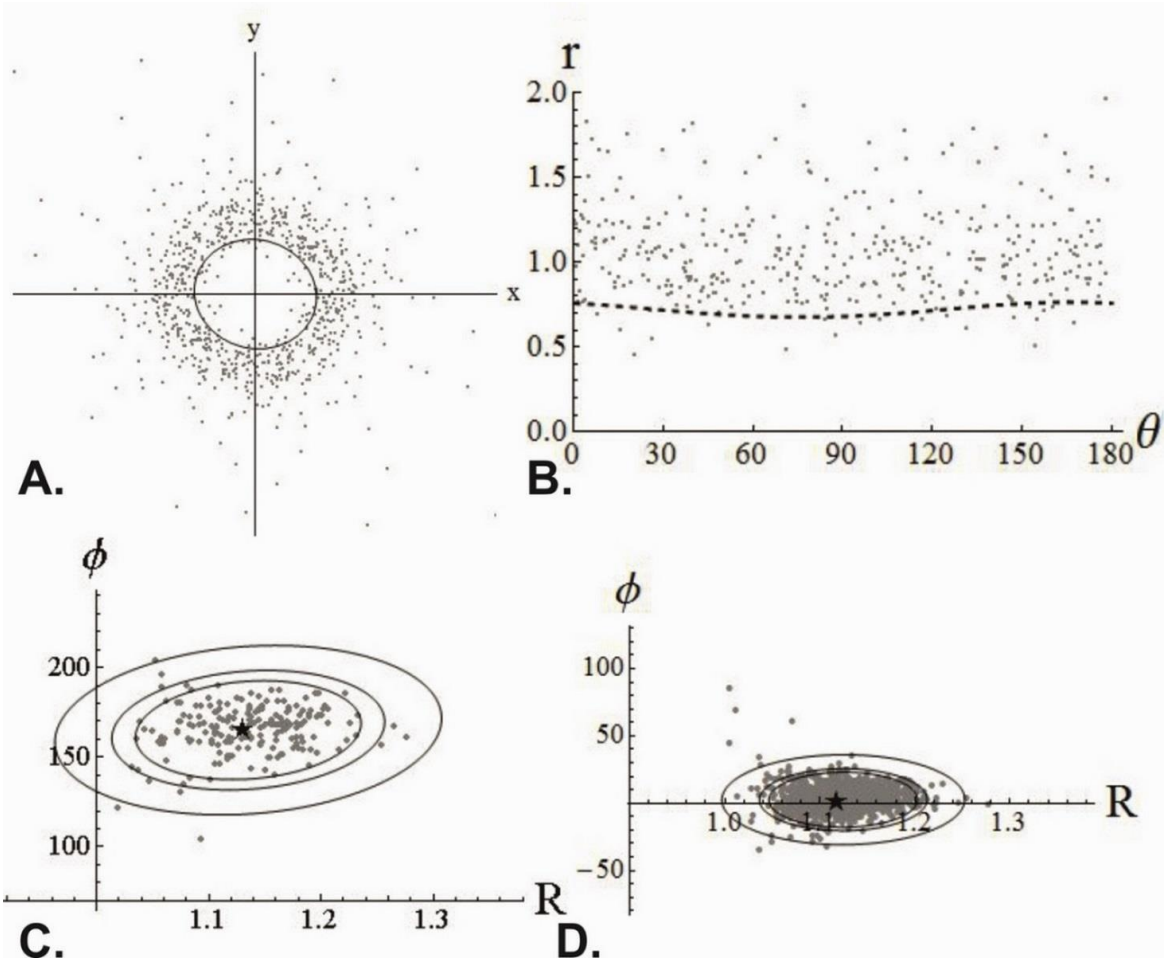

Figure 5. 31 Strain estimates for Wy24 from the DTNNM and MRL analyses.

Wy21 (Figure 5. 32) shows similar results to Wy24 with a circular Fry plot (Figure 5. 32A) and the near flatline in the polar plot (Figure 5. 32B). Interestingly both the DTNNM and MRL analyses report very similar estimates for R and Φ orientations (Figure 5. 32C&D) despite the low strain estimates.

Wy 18 (Figure 5. 33) has a very similar low strain estimate to Wy21 with a near circular Fry plot (Figure 5. 33A) and the flatline in the polar plot (Figure 5. 33B). Again typically for low strain estimates the bootstrap data for the DTNNM and MRL analyses (Figure 5. 33C&D) have very wide confidence intervals.

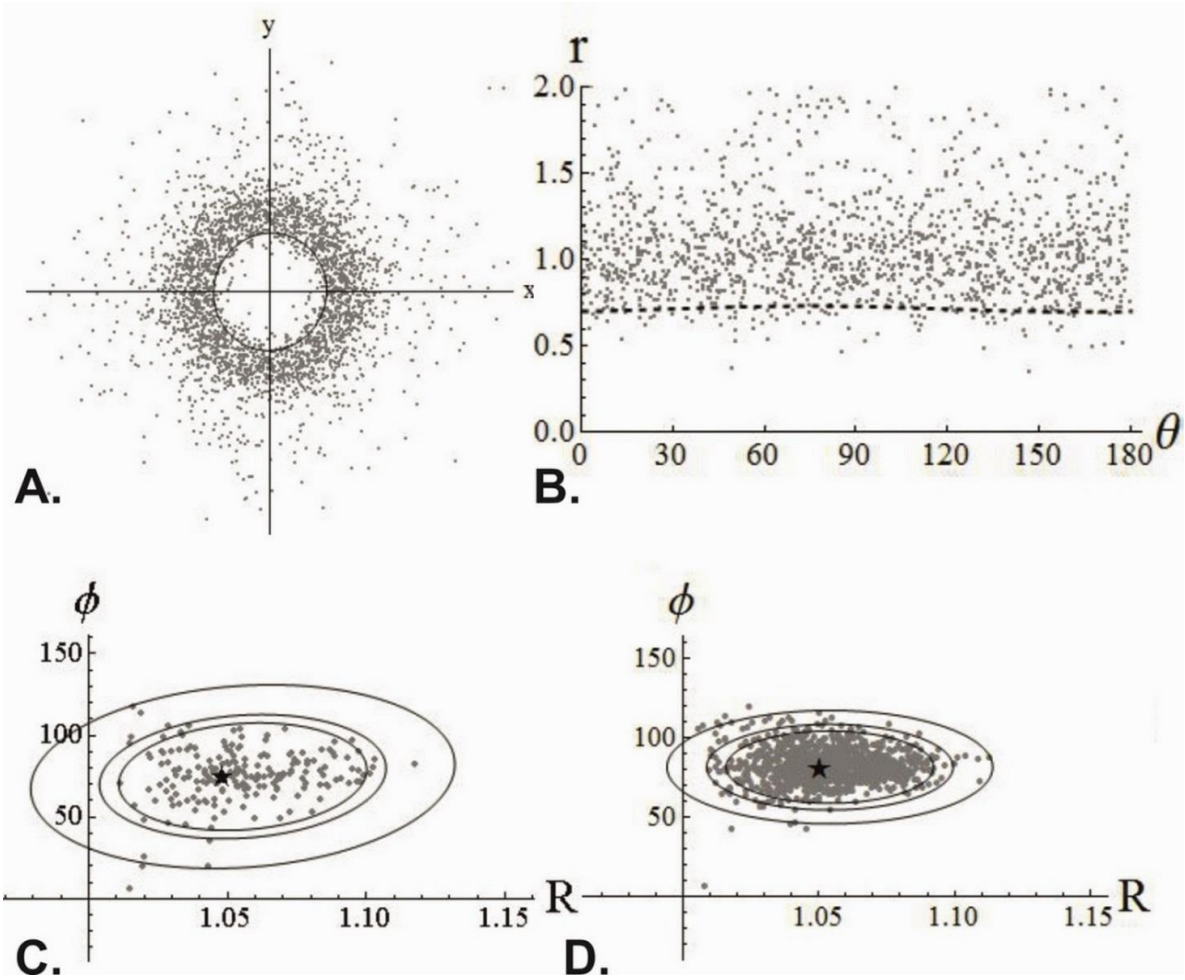

Figure 5. 32 Strain estimates for Wy21 from the DTNNM and MRL analyses.

Wy15 (Figure 5. 34) has a similar low strain estimate as Wy18, but DTNNM analyses report a slightly higher estimate (Figure 5. 34A,B&C) than MRL (Figure 5. 34D). Both of the DTNNM and MRL analyses have very wide confidence intervals of the bootstrap data.

The Intercepts and SPO results for the Jackson traverse are shown in Figure 5. 35 to Figure 5. 40. They typically report very low estimates (below R=1.15) of strain or rock fabric even for samples such as Wy27 and Wy26 where DTNNM analyses report higher strains.

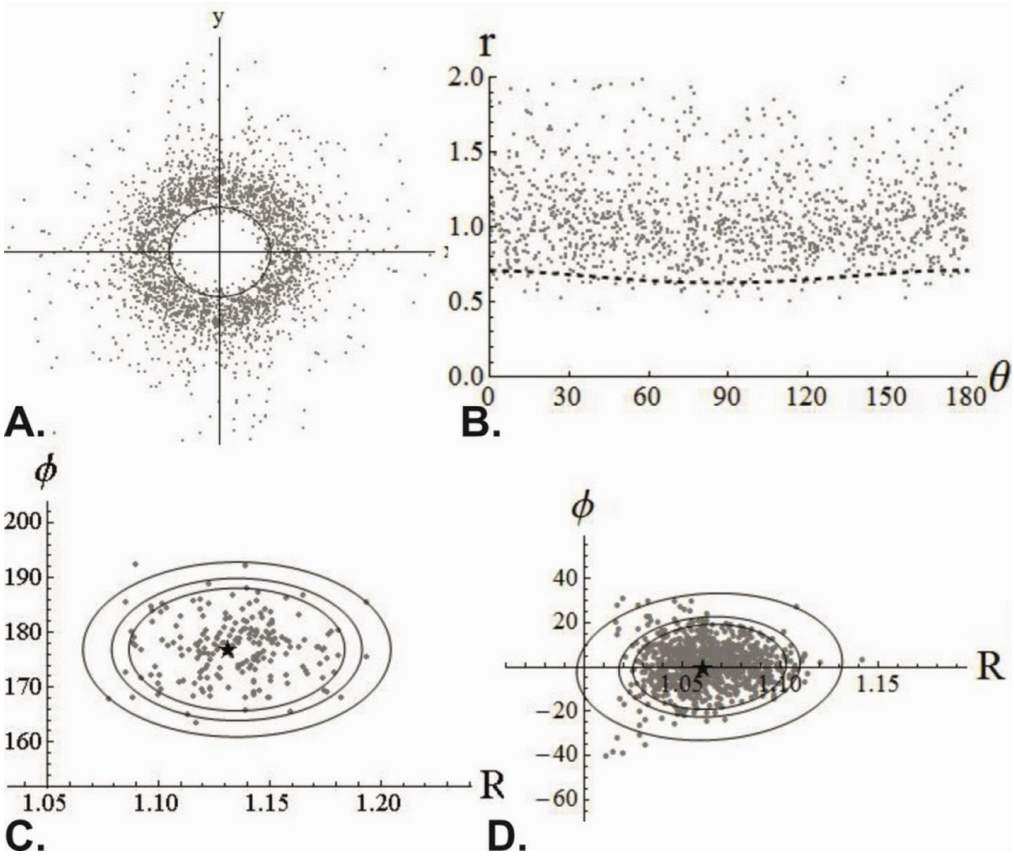

Figure 5. 33 Strain estimates for Wy18 from the DTNNM and MRL analyses.

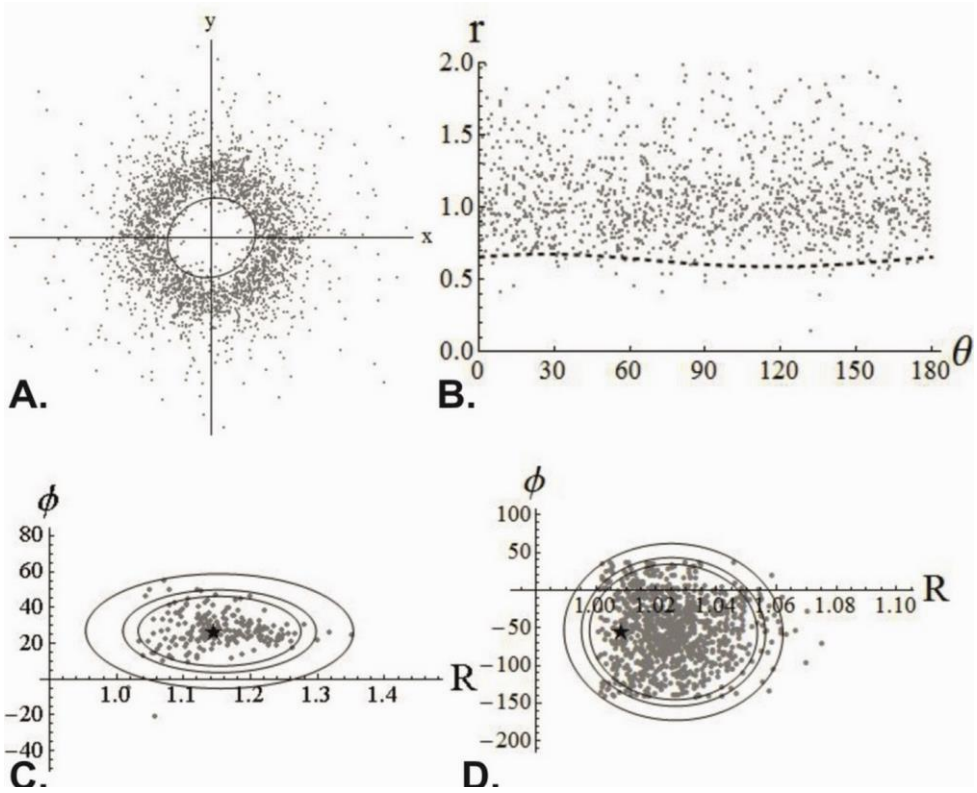

Figure 5. 34 Strain estimates for Wy18 from the DTNNM and MRL analyses.

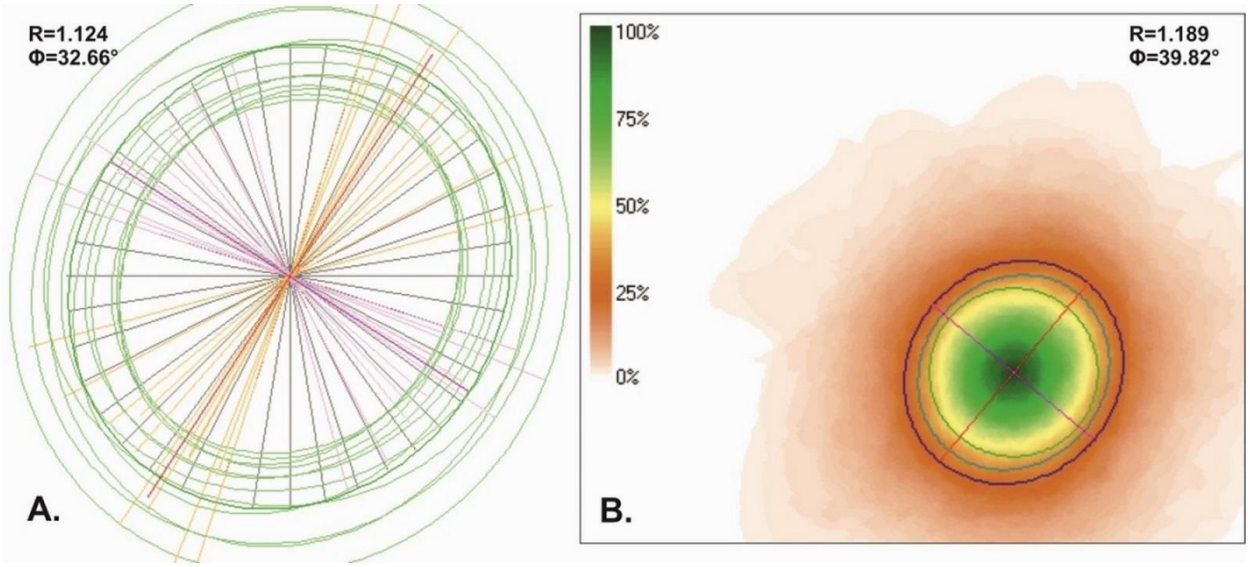

Figure 5. 35 Intercepts and SPO software for Wy30, similar to the strain analyses R and Φ estimates are produced. **A.** Rose of traverses from Intercepts. **B.** Mean shape from SPO.

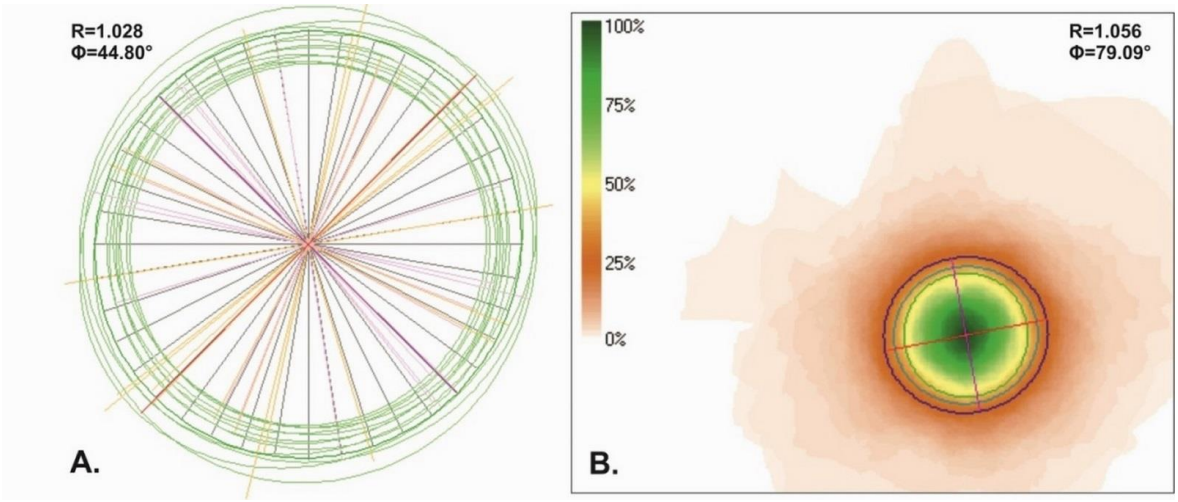

Figure 5. 36 Intercepts and SPO software for Wy28. **A.** Rose of traverses from Intercepts. **B.** Mean shape from SPO.

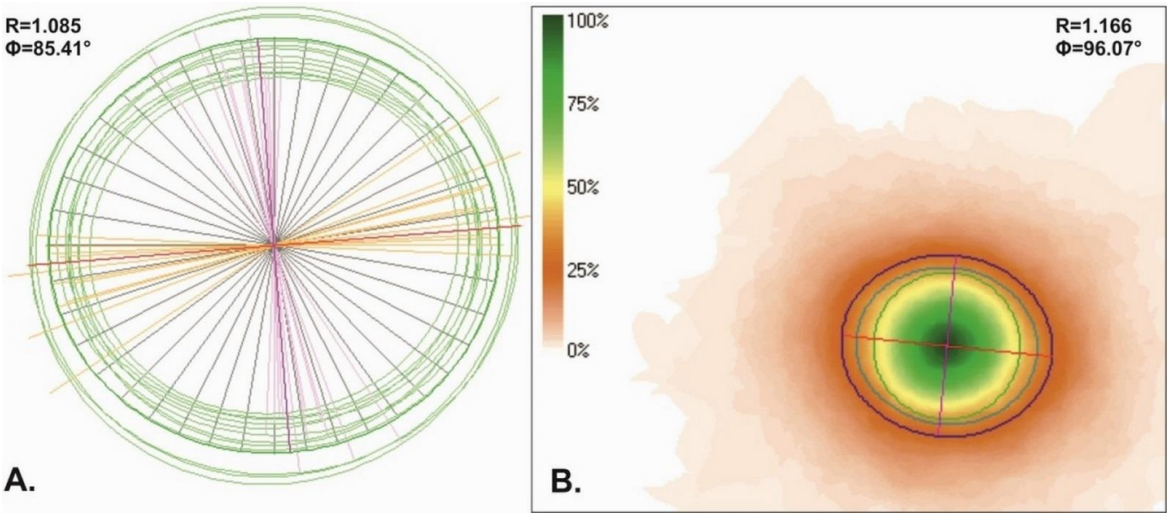

Figure 5. 37 Intercepts and SPO software for Wy27. **A.** Rose of traverses from Intercepts. **B.** Mean shape from SPO.

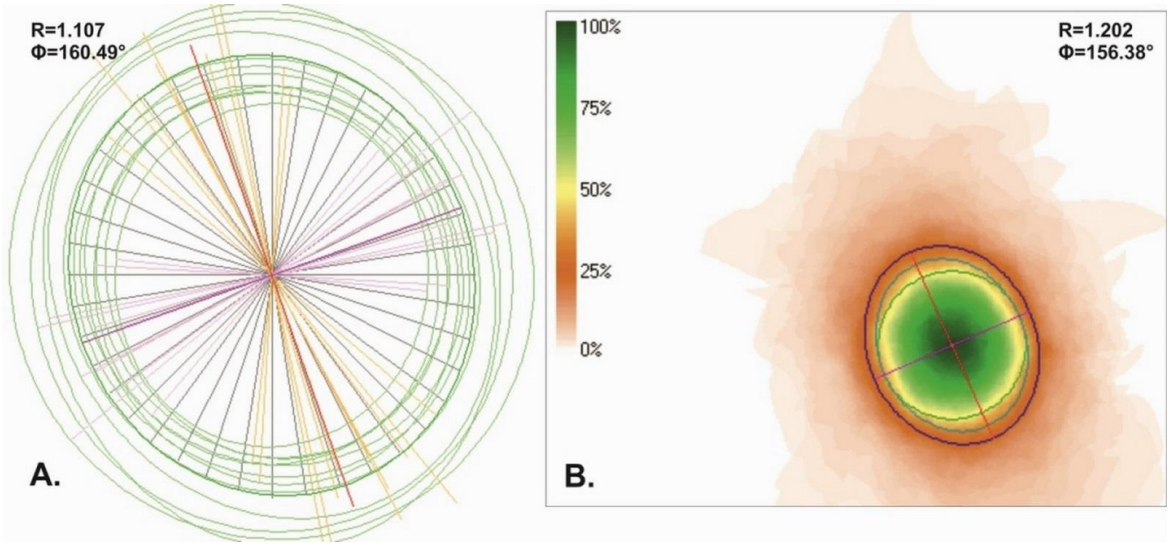

Figure 5. 38 Intercepts and SPO software for Wy26. **A.** Rose of traverses from Intercepts. **B.** Mean shape from SPO.

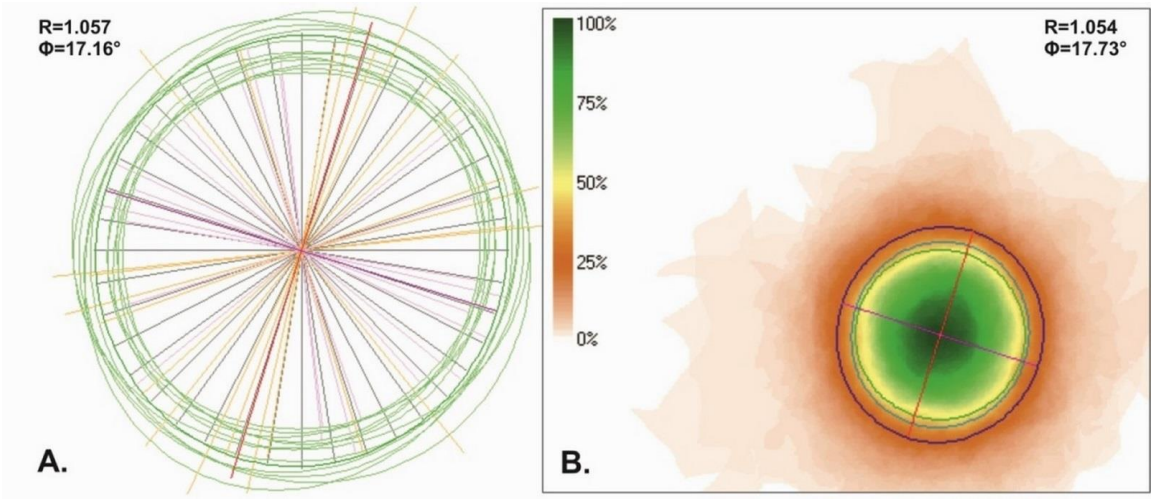

Figure 5. 39 Intercepts and SPO software for Wy25. **A.** Rose of traverses from Intercepts. **B.** Mean shape from SPO.

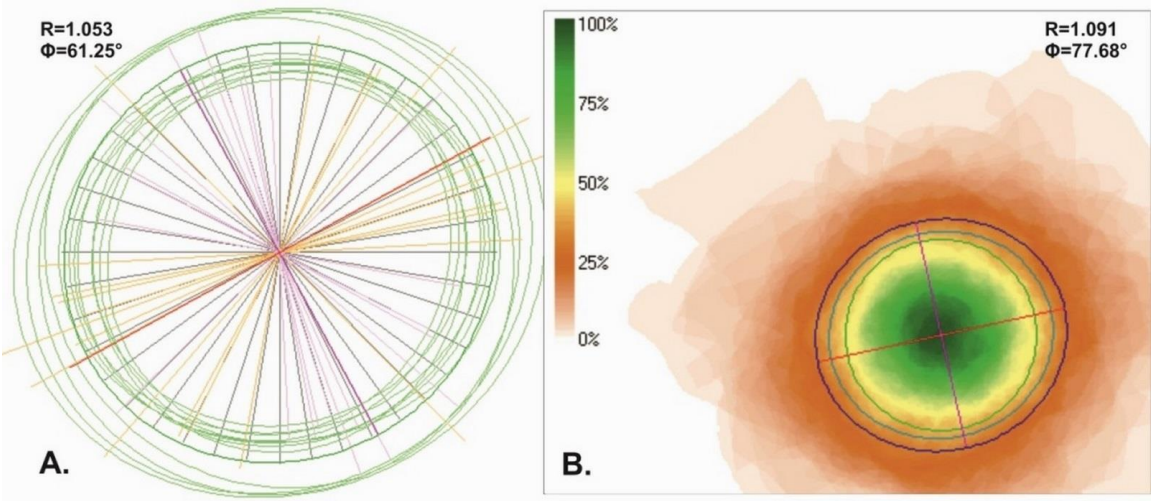

Figure 5. 40 Intercepts and SPO software for Wy24. **A.** Rose of traverses from Intercepts. **B.** Mean shape from SPO.

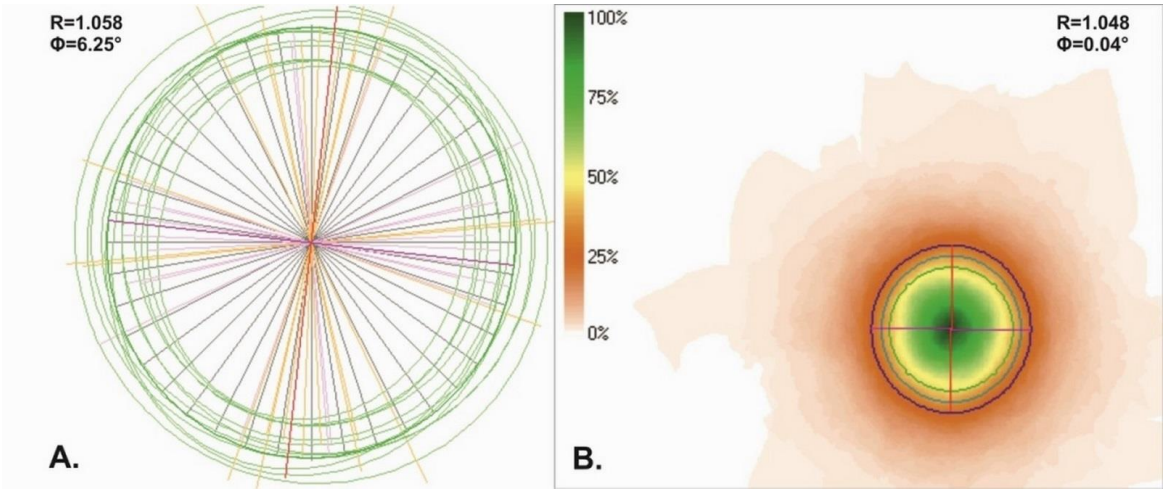

Figure 5. 41 Intercepts and SPO software for Wy21. **A.** Rose of traverses from Intercepts. **B.** Mean shape from SPO.

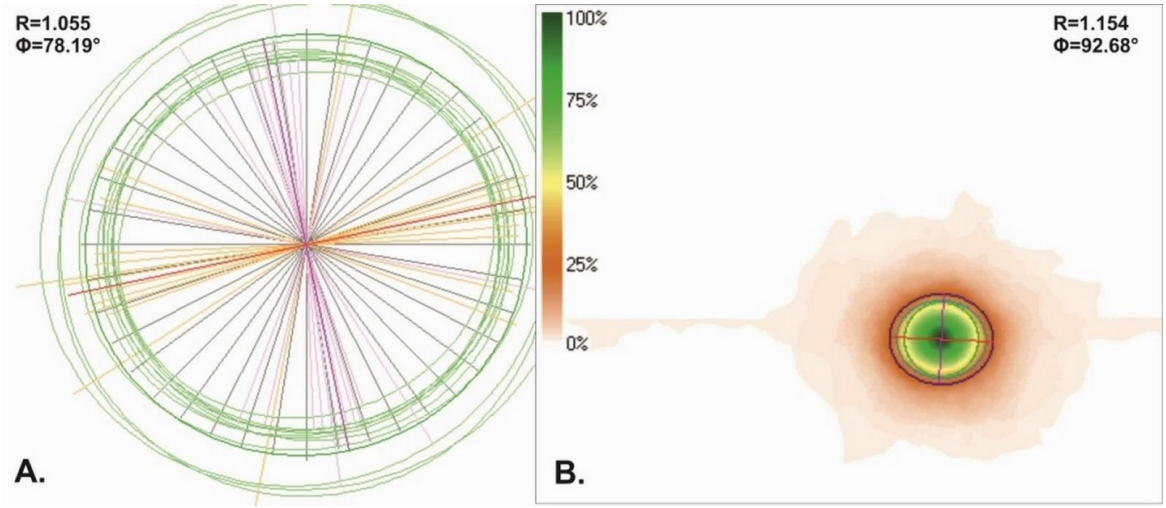

Figure 5. 42 Intercepts and SPO software for Wy18. **A.** Rose of traverses from Intercepts. **B.** Mean shape from SPO.

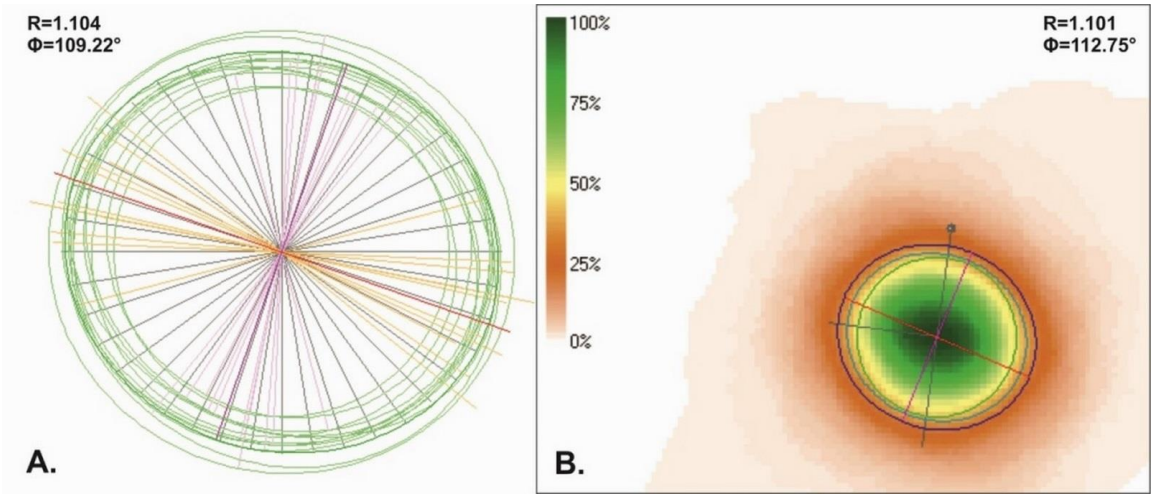

Figure 5. 43 Intercepts and SPO software for Wy15. **A.** Rose of traverses from Intercepts. **B.** Mean shape from SPO.

The strain estimates for the Bridger traverse (Figure 5. 44-Figure 5. 49) are very similar to those of the Jackson traverse, in that they are quite low (R=1.05-1.1), with only one sample,Wy10, with an estimate of R=1.2. The Intercepts results (Figure 5. 50 to Figure 5. 55) are also quite low for the Bridger traverse.

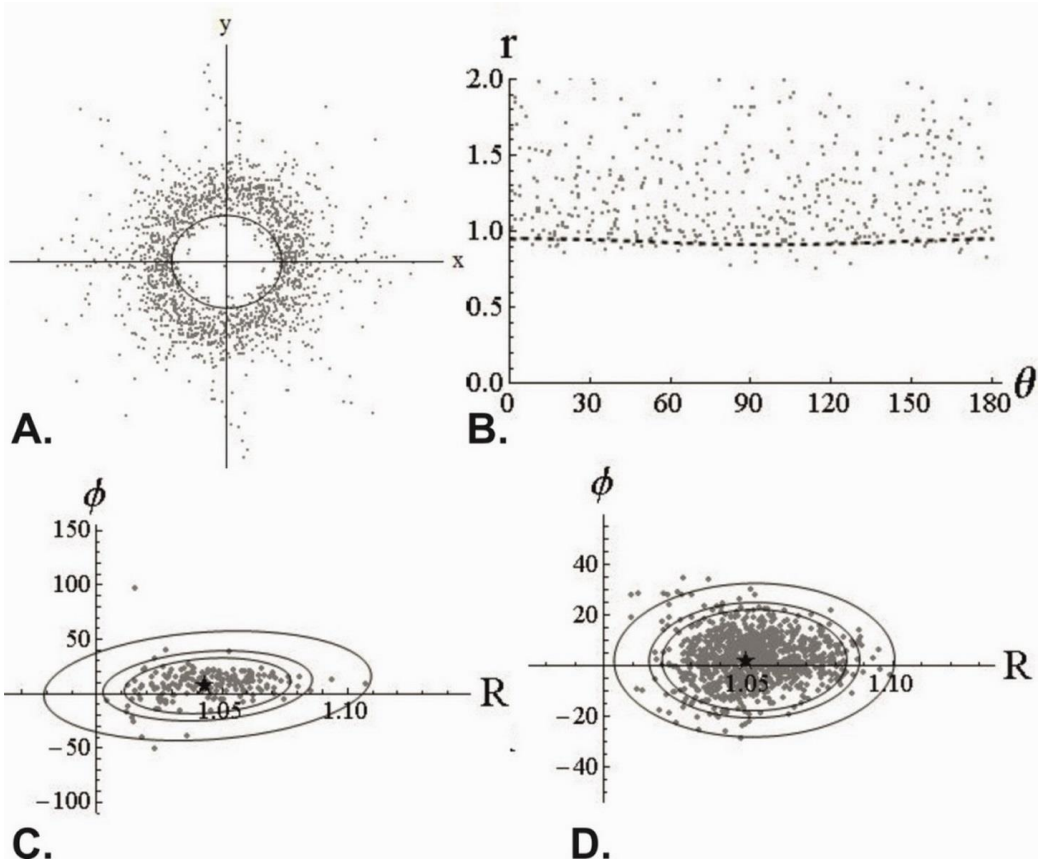

Figure 5. 44 Strain estimates for Wy2 from the DTNNM and MRL analyses.

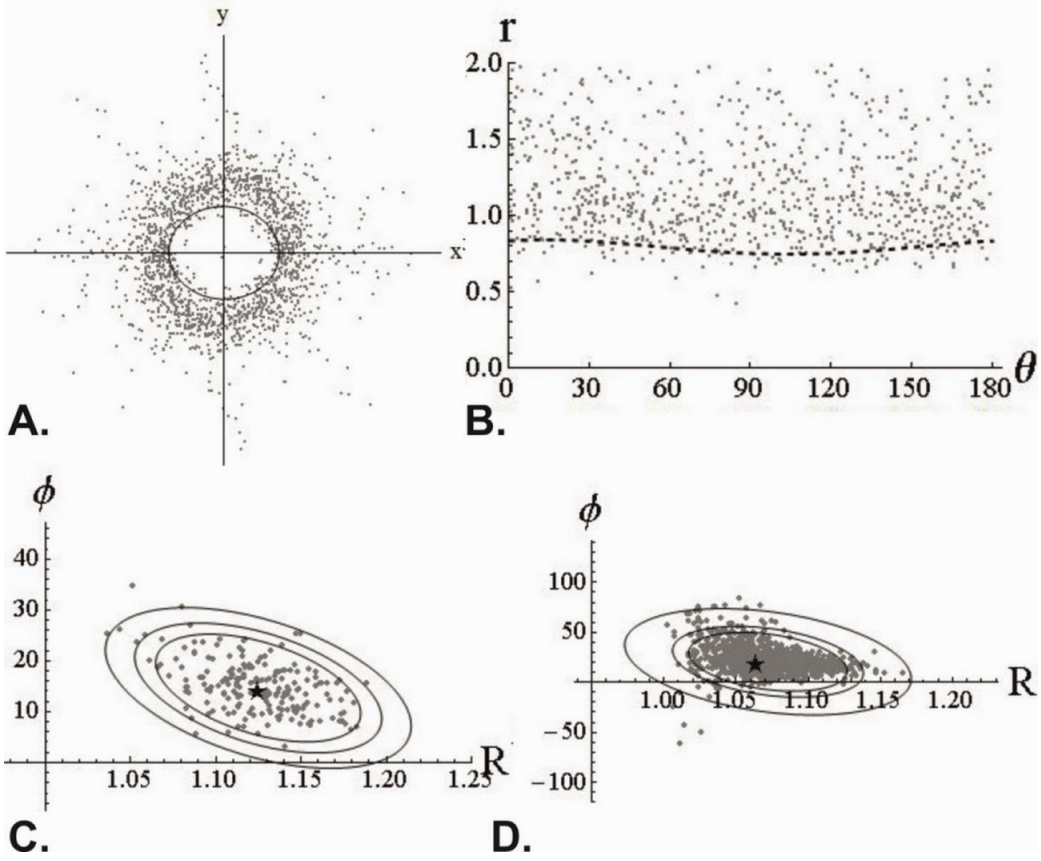

Figure 5. 45 Strain estimates for Wy3 from the DTNNM and MRL analyses.

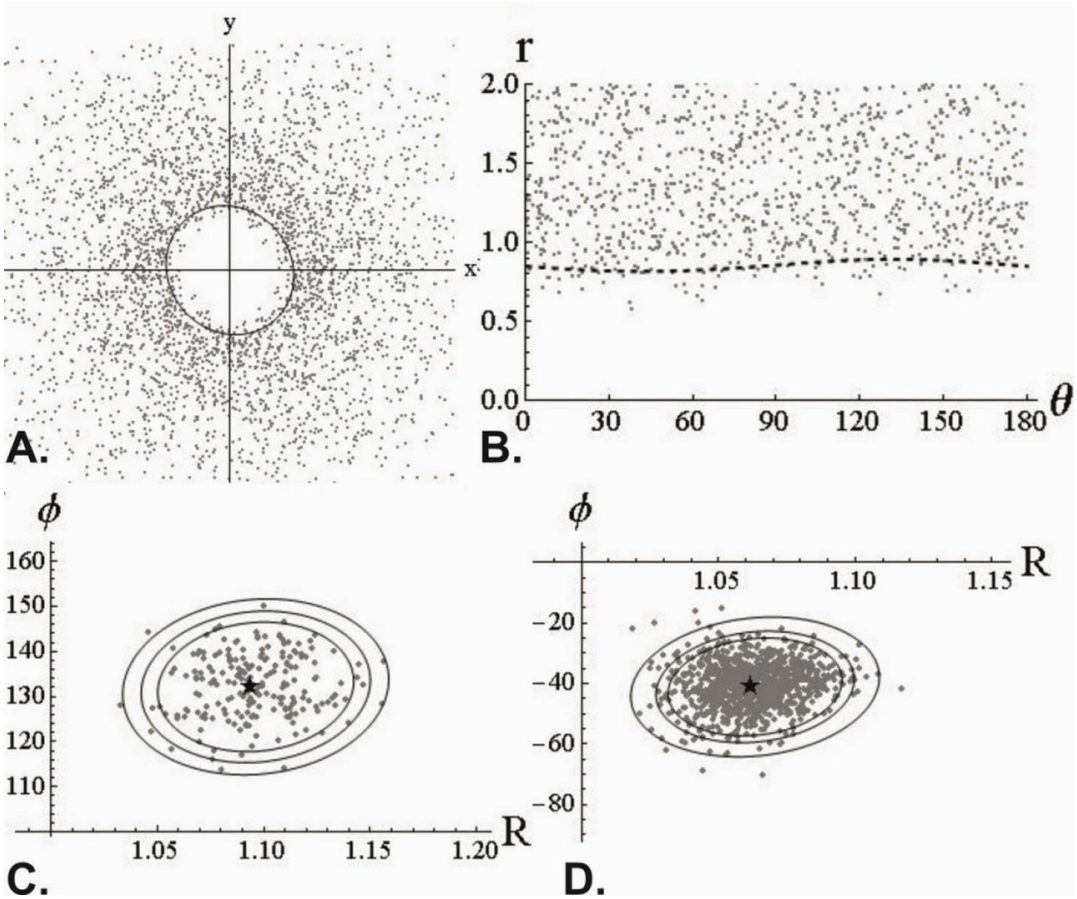

Figure 5. 46 Strain estimates for Wy7 from the DTNNM and MRL analyses.

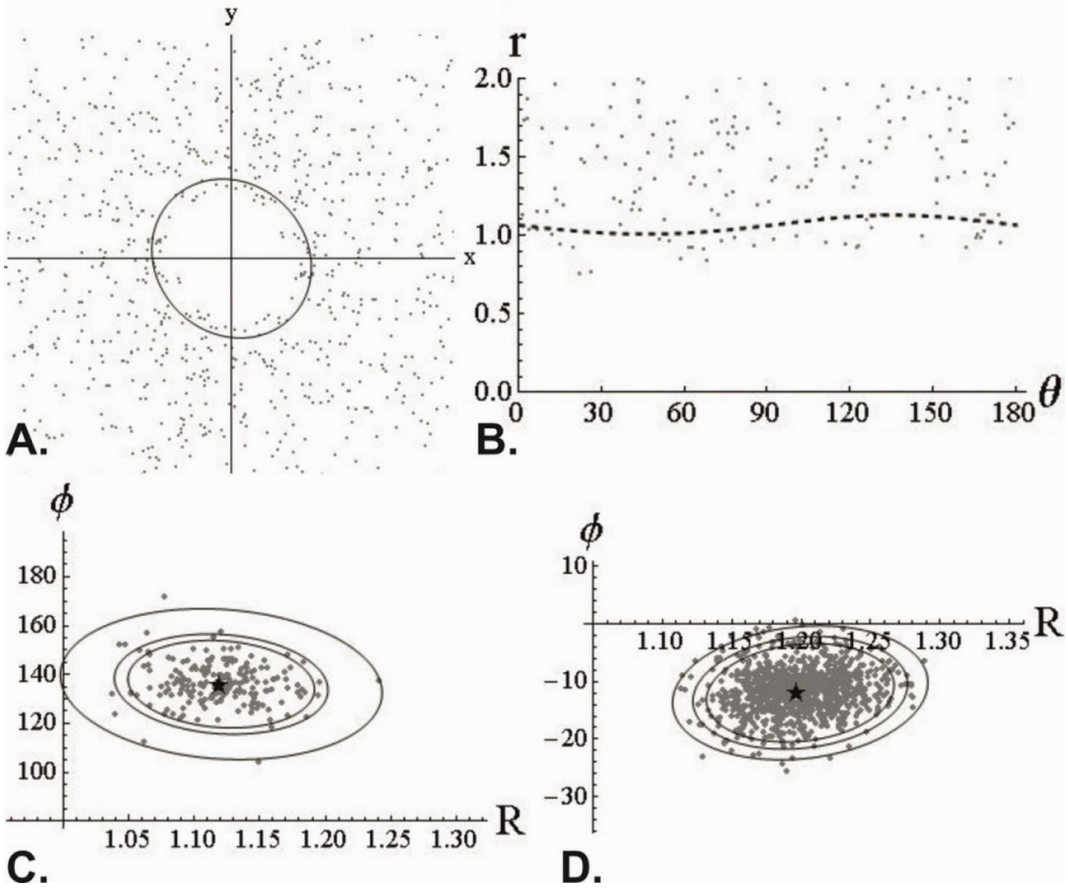

Figure 5. 47 Strain estimates for Wy10 from the DTNNM and MRL analyses.

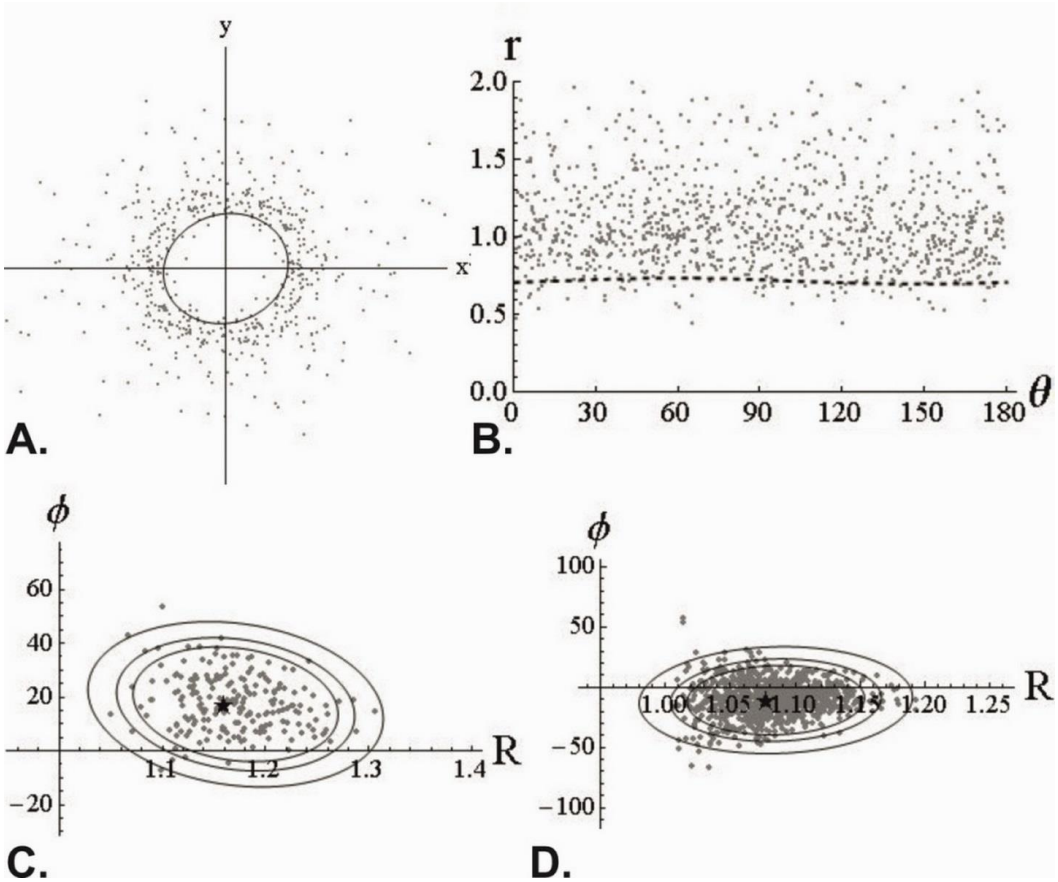

Figure 5. 48 Strain estimates for Wy11 from the DTNNM and MRL analyses.

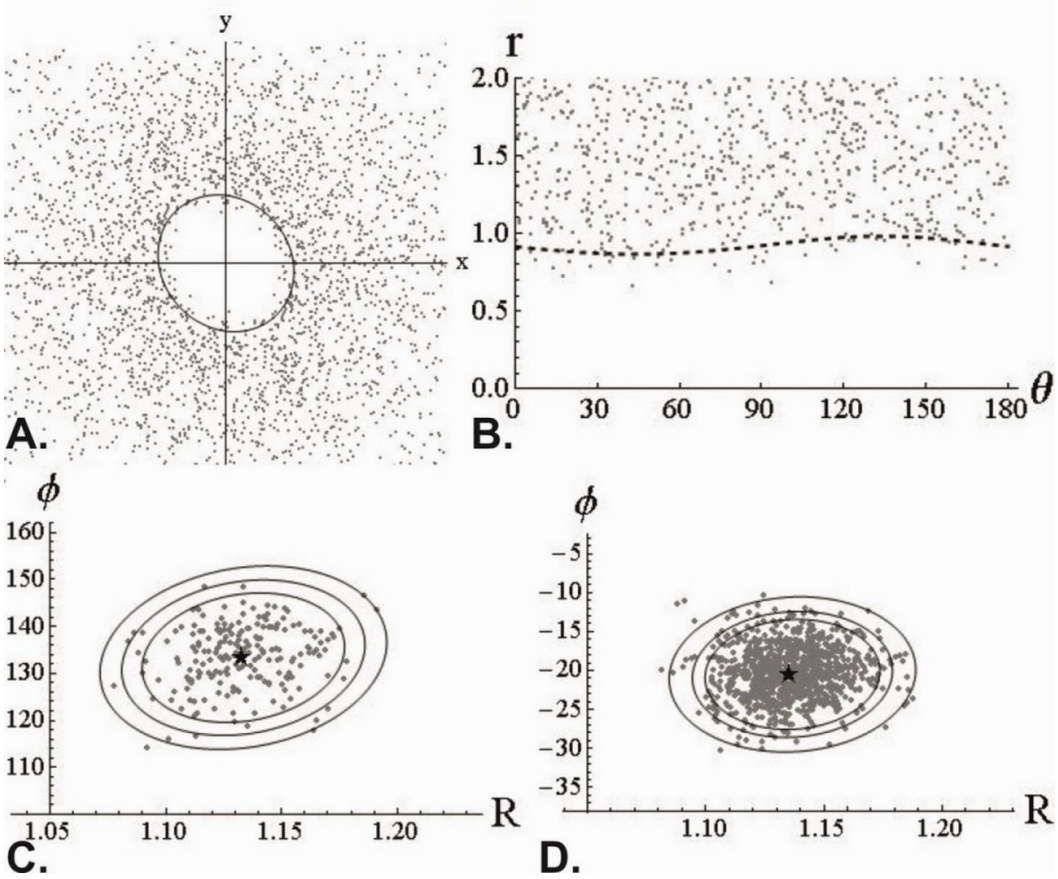

Figure 5. 49 Strain estimates for Wy12 from the DTNNM and MRL analyses.

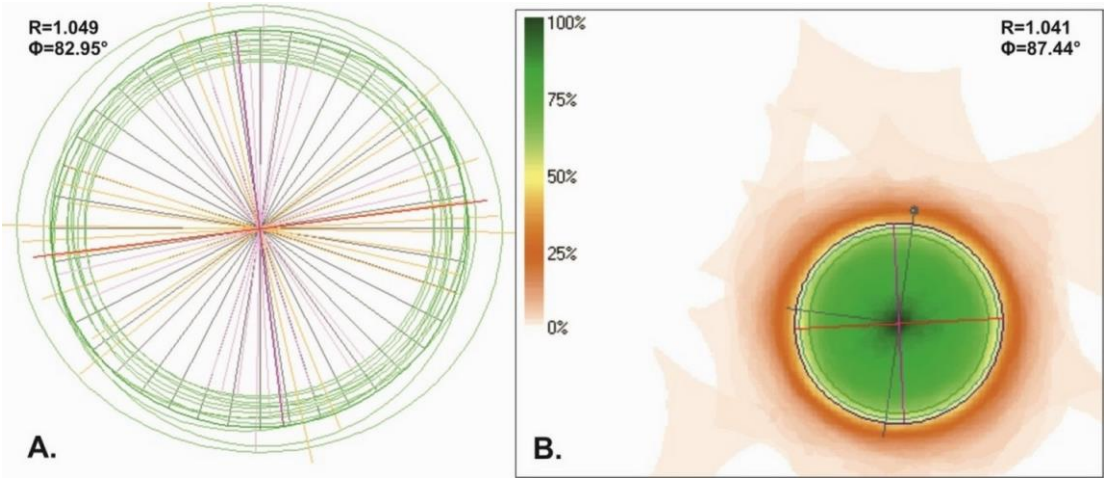

Figure 5. 50 Intercepts and SPO software for Wy2. **A.** Rose of traverses from Intercepts. **B.** Mean shape from SPO.

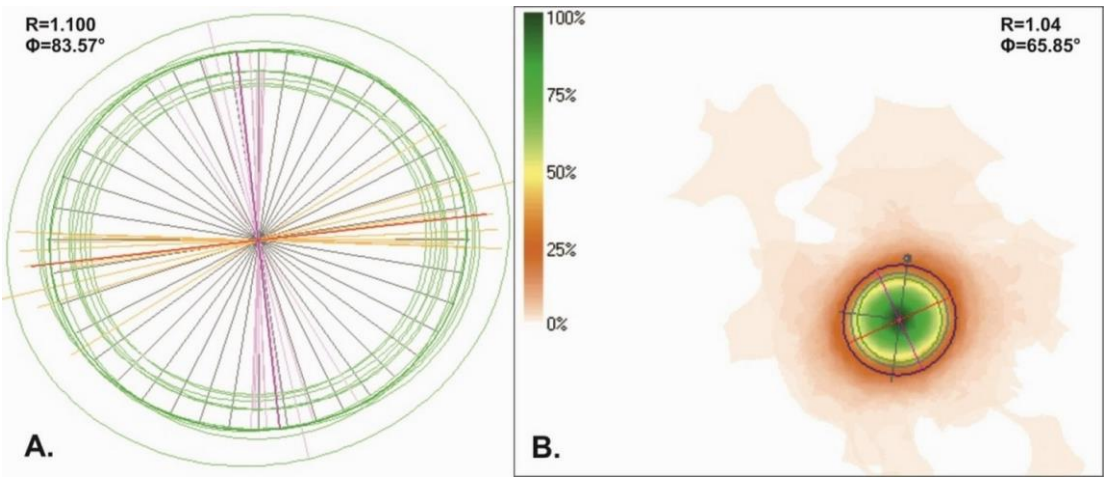

Figure 5. 51 Intercepts and SPO software for Wy3. **A.** Rose of traverses from Intercepts. **B.** Mean shape from SPO.

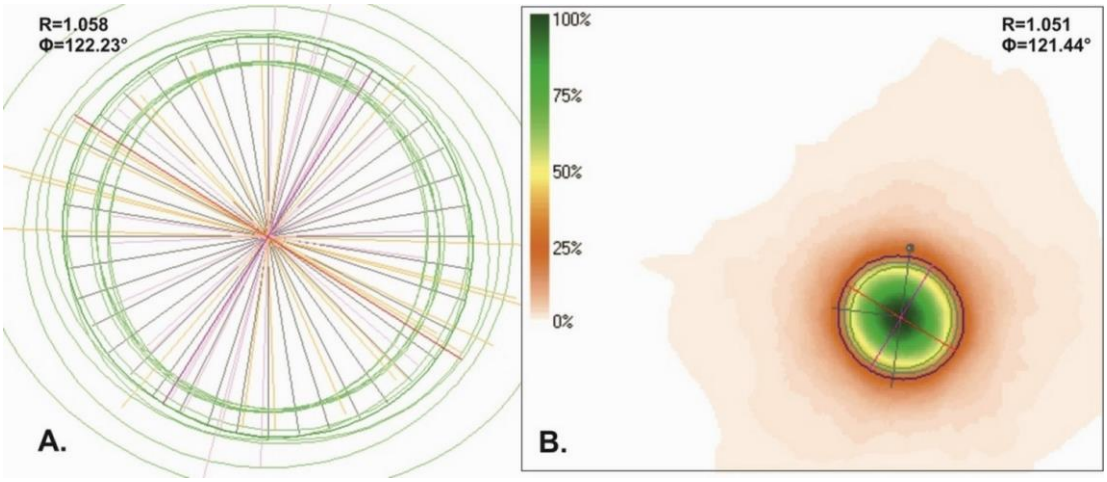

Figure 5. 52 Intercepts and SPO software for Wy7. **A.** Rose of traverses from Intercepts. **B.** Mean shape from SPO.

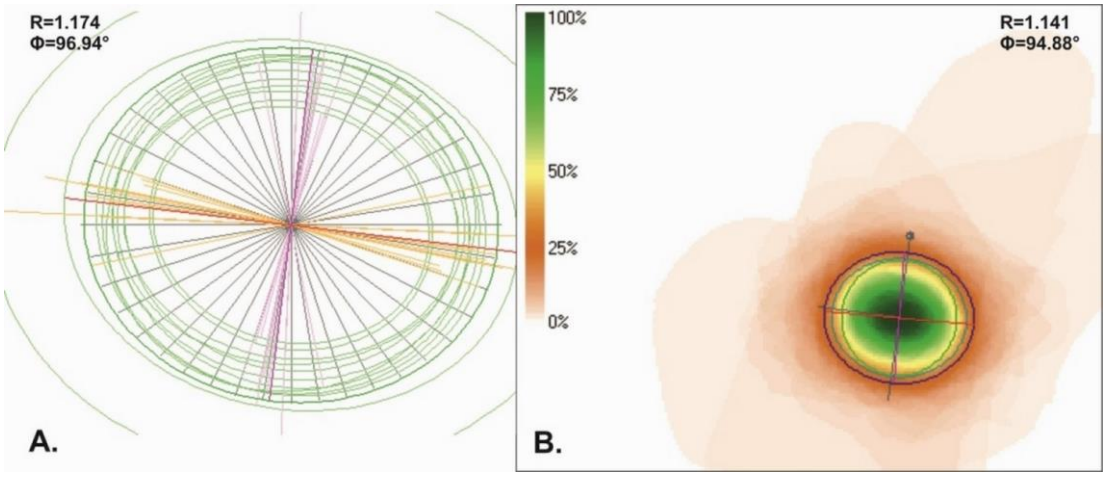

Figure 5. 53 Intercepts and SPO software for Wy10. **A.** Rose of traverses from Intercepts. **B.** Mean shape from SPO.

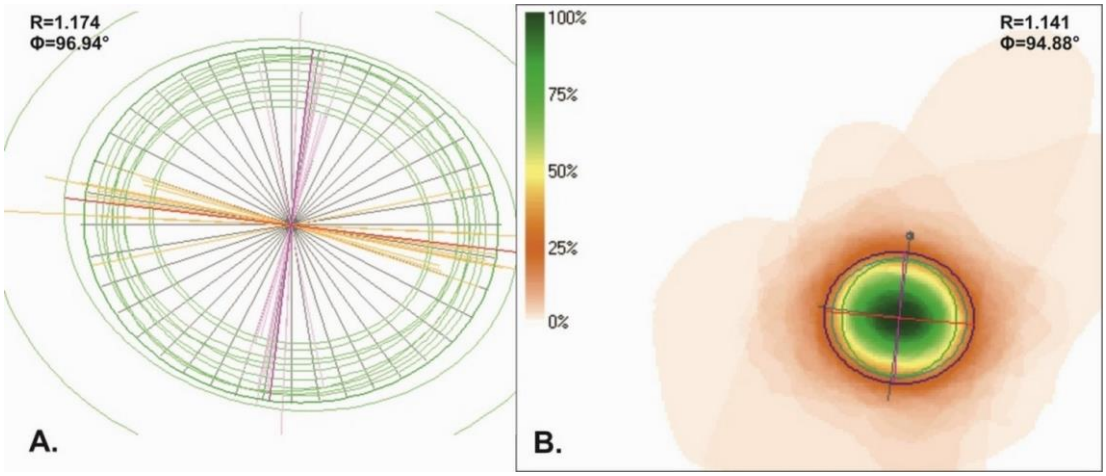

Figure 5. 54 Intercepts and SPO software for Wy11. **A.** Rose of traverses from Intercepts. **B.** Mean shape from SPO.

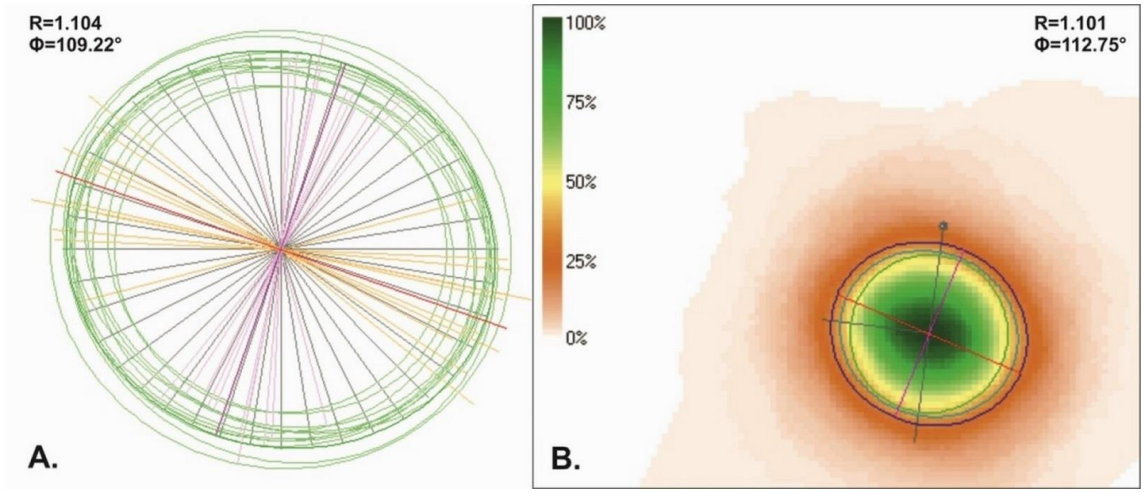

Figure 5. 55 Intercepts and SPO software for Wy12. **A.** Rose of traverses from Intercepts. **B.** Mean shape from SPO.

5.5. Discussion

The majority of samples yield bulk susceptibilities (<5X10^{-4}) suggesting that the magnetic fabrics are controlled by the crystal lattice orientation of paramagnetic and minor ferromagnetic minerals (Tarling and Hrouda, 1993). AMS fabrics that are dominated by phyllosilicates or haematite are generally related to the preferred crystallographic orientation of those minerals (Borradaile and Jackson, 2010). There is no obvious correlation between high anisotropies and bulk susceptibilities, suggesting that the anisotropy is controlled by the bedding and cleavage fabrics rather than the magnetic contribution of constituent minerals, such as magnetite. Therefore, in this case, the AMS fabric reflects the crystalline anisotropy of the phyllosilicate and iron oxide grains. The moderate corrected degree of anisotropy values (Pj), below 1.1 (Figure 5. 10), are typical anisotropy values reported for sedimentary rocks from fold and thrust belts with low grade deformation and a weak spaced cleavage (Weil and Yonkee, 2010, Borradaile and Jackson, 2010). Clay spaced cleavage is typically developed in rocks with anisotropies from 1.0 to 1.1 with slaty cleavage being developed in rocks with higher anisotropies (Pares, 2004).

In a similar study, Weil & Yonkee (2009) used lineation intensity (Ln'):

$$Ln' = Ln\left(\frac{K1 - K2}{Kmean}\right),$$

as a measure of deformation, but samples reported here that fit in the type 4 classification show a strong foliation and a weak lineation despite being at a higher level of deformation. This variation in lineation intensity could also be linked to the magnetic mineralogy with >10% hematite required to produce a prolate fabric, but

only 0.01% titanomagnetite. That said, the magnetic lineation clearly varies with deformation intensity and is largely interpreted as a zone-axis of phyllosilicate and hematite grains parallel to the cleavage bedding intersection lineation.

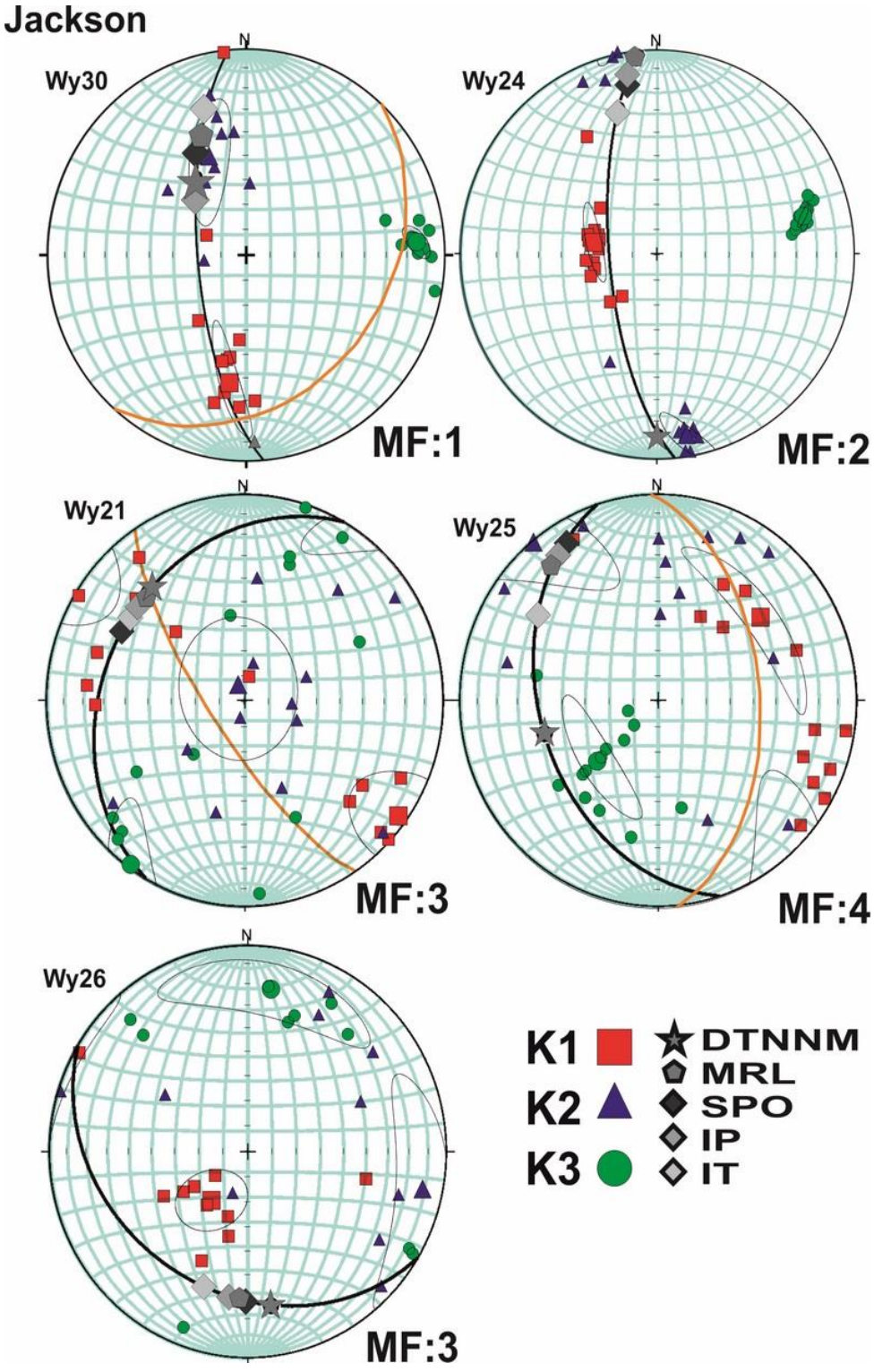

Figure 5. 56 Pitch of strain ellipse long axis orientations vs AMS ellipsoid principal axes for samples from the Jackson transect. The orientation of the estimated bedding parallel strain ellipse from each method is represented by the symbols indicated in the key. Magnetic fabric type is indicated by MF.

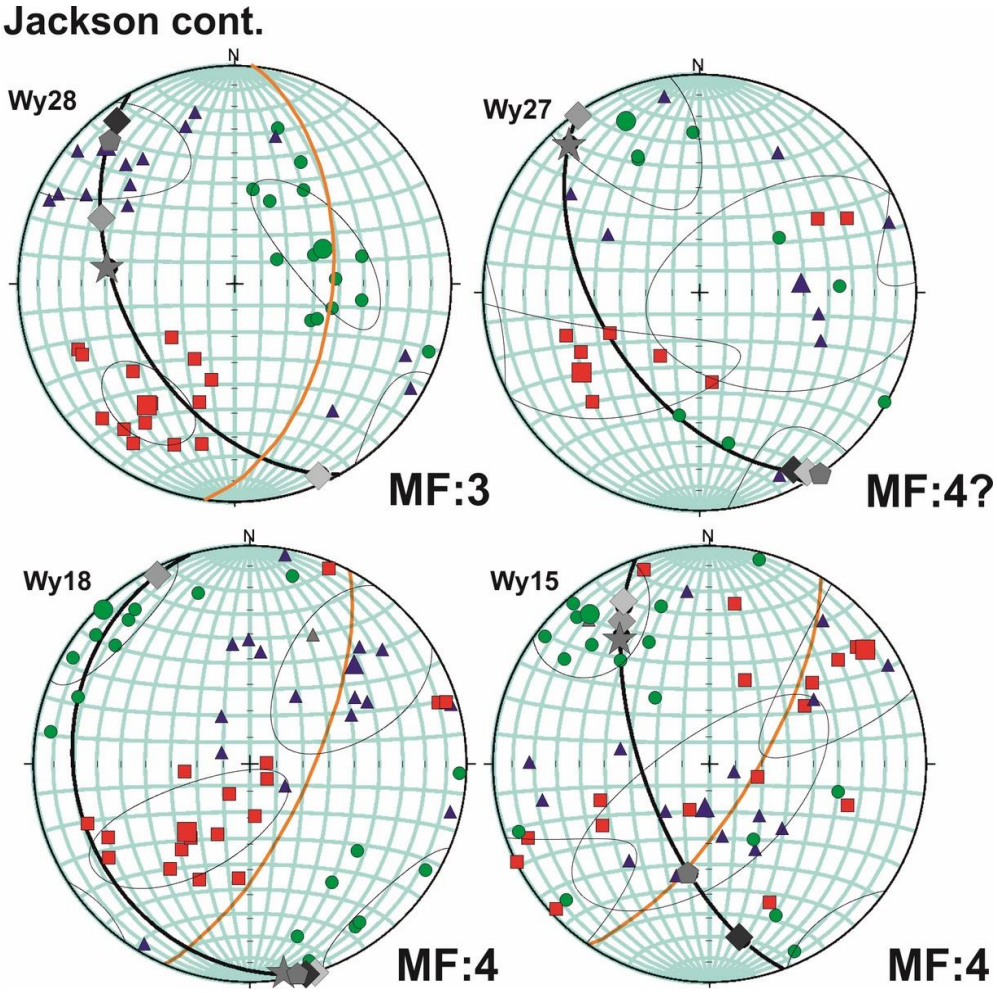
Jackson cont.
Wy28
N
MF:3
Wy27
N
MF:4?
Wy18
N
MF:4
Wy15
N
MF:4

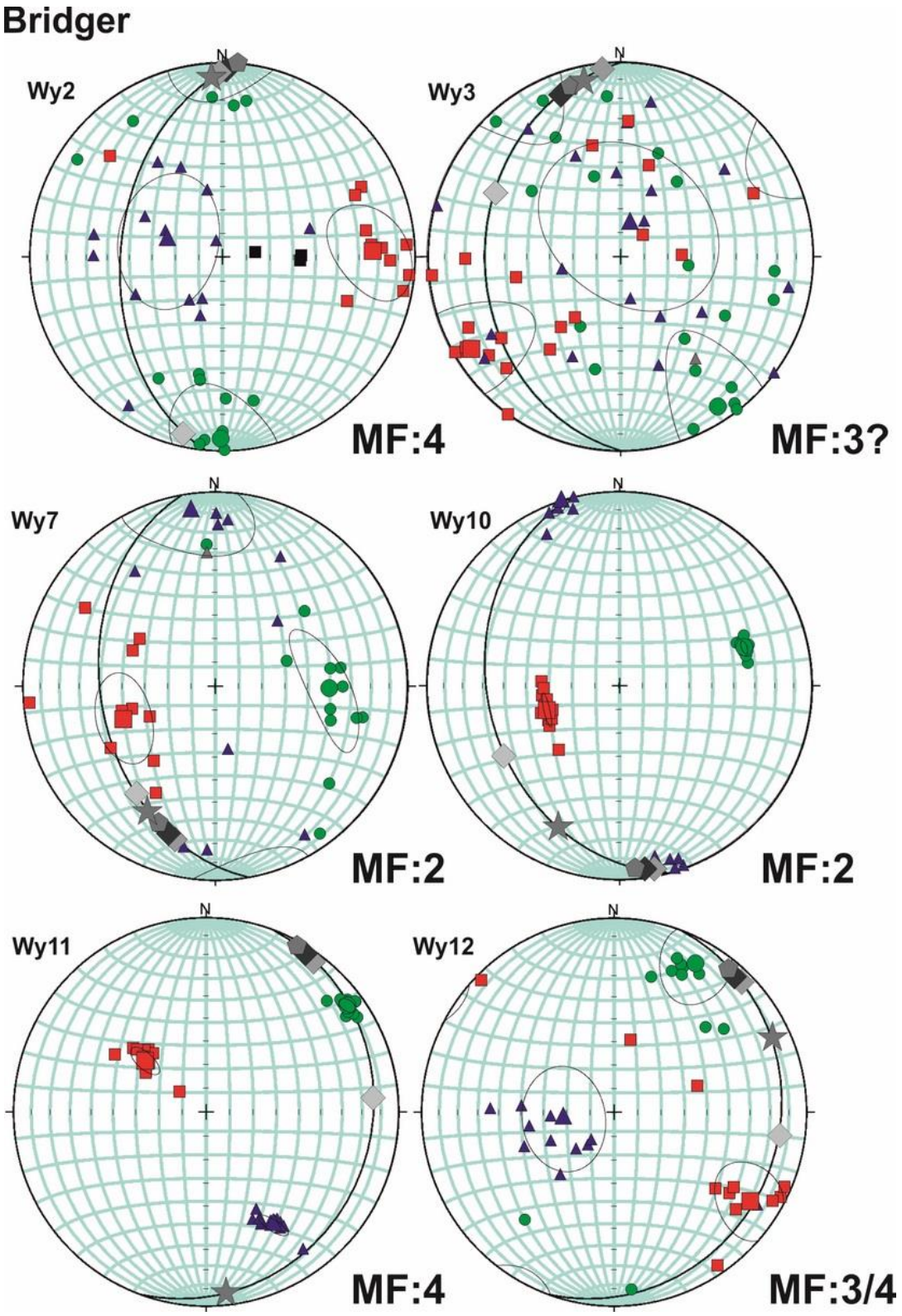

Figure 5. 57 Pitch of estimated strain ellipse long axis orientations vs AMS ellipsoid principal axes for samples from the Bridger transect.

Considering the complexities of correlating AMS results to strain, four magnetic fabric types that relate AMS to bedding and cleavage have been established (Section 3.1). This allows for a simple manner to determine the presence of a tectonic fabric and the relative strength of the fabric compared to bedding: **Type 1** no detectable tectonic fabric and a slightly oblate ellipsoid parallel to bedding; **Type 2** weak tectonic lineation in the plane of bedding and parallel to tectonic trend, magnetic foliation is still dominated by bedding; **Type 3** strong tectonic lineation with no clear magnetic foliation and the magnetic ellipsoid is triaxial; **Type 4** magnetic foliation is at a high angle to bedding and parallel to cleavage while magnetic lineation, if present, is plunging down the cleavage plane or represents the cleavage bedding intersection lineation. Taking these 4 fabric types into account, the samples across both transects show changes in magnetic fabric type from type 1 to type 4 that largely agree with the increase in cleavage intensity (Figure. 3; Mitra, 1994).

Additionally, samples from the Bridger transect have lower strains than the Jackson transect. This is also in agreement with the results from Yonkee and Weil (2010) who concluded that higher strains were localised at the tips of the salient due to interaction with basement cored uplifts. Despite these general regional correlations, there is no clear relationship between degree of anisotropy, Pj, and strain ratio, R, for any of the strain analysis methods (Figure 5.58). Similarly, there is no clear correlation between magnetic lineation intensity, Ln L', and strain ratio, R. This is not surprising considering previous work by Borradaile et al (1981, 1997, 2004, 2010 & 2012) stating that there is rarely a correlation between the magnitudes of the strain ellipse and the AMS ellipsoid. Yet, it is generally

considered that there can be some relationship between the principal axes of these ellipsoids (Borradaile, 2012). To investigate this relationship in the bedding parallel sections, the long axis of the strain ellipse, *Φ,* recorded from DTNNM, MRL and the Intercepts methods were plotted as rakes on the bedding plane surfaces on equal area stereographic projections so that they could be compared to the orientations of the principal axes of the AMS ellipsoid and magnetic lineations and foliations (Figure 5. 56 and Figure 5. 57).

Out of the 15 samples that had interpretable AMS results and usable strain data, 4 samples (Wy30, Wy24, Wy28 & Wy10) had bedding dominant AMS results (Type 1) and the remaining 11 appeared to have some tectonic influence on their petrofabric recorded by AMS. Wy26 and Wy7 display Type 3 AMS results in that there is a strong magnetic lineation at the intersection of bedding and cleavage (Figure 5.56 and 5.57) and both of these samples show a weak correlation between K1 orientations and the estimated long axis of the strain ellipse. The remaining 9 samples display Type 4 geometries with a magnetic foliation (defined by K1 & K2 girdles) perpendicular to bedding and parallel to cleavage. It was expected that the intersection of the magnetic foliation and the bedding plane would closely correlate with the estimated *Φ* of the bedding parallel strain ellipse. This relationship was only clearly evident for two samples (Wy21 & Wy25). This clearly shows that the long axis of the 2D strain ellipse estimated from the bedding plane samples does not always correlate with the trace of the K1 susceptibility axis in the bedding plane (Figure 5. 58). This raises the question of how reliable recorded Phi (*Φ*) orientations are at lower strains.

Both transects have a general increase in strain estimates from west to east, also agreeing with the cleavage distribution (Mitra, 1993) and strain results from Yonkee and Weil (2010).

Differences between AMS and strain calculations can be explained by a number of factors. Strain analysis methods have a number of inherent inaccuracies associated with them, including significant discrepancies in orientations when producing thin sections. Furthermore, the calculations involved in the MRL and DTNNM methods are dependent on certain assumptions concerning passive deformation, primary clast distributions, and shapes being correct. Additionally, as concluded by Paterson and Yu (1994), undeformed sandstones can have significant primary fabrics that can affect small strain ratios (1.5 or less). Therefore, the development of a weak tectonic fabric may not completely overprint the primary fabric resulting in a blended fabric being detected.

Finally, AMS measures the magnetic contribution of all of the minerals present in a sample and, as a result, AMS is dominated by the iron rich minerals such as phyllosilicates. Whereas quartz, despite being a major constituent of most of the samples, has little effect on the AMS results, due to its weak diamagnetic behaviour. On the other hand, strain estimates from DTNNM, MRL and Intercepts are largely based on quartz clasts.

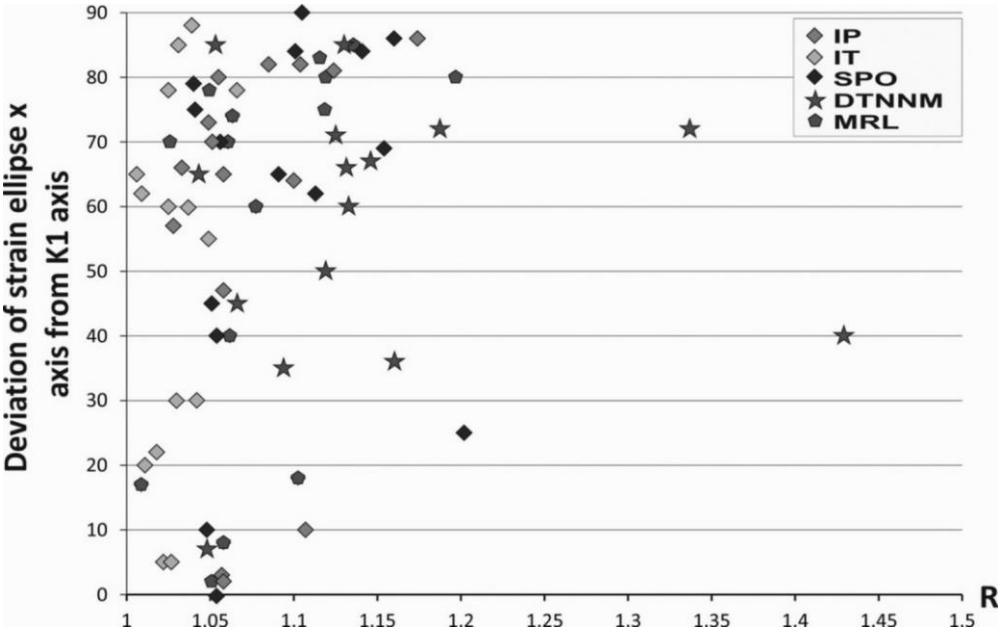

Figure 5. 58 Deviation of estimated strain ellipse x axis from trace of K1 axis in the bedding plane vs axial ratio of estimated strain ellipse (R).

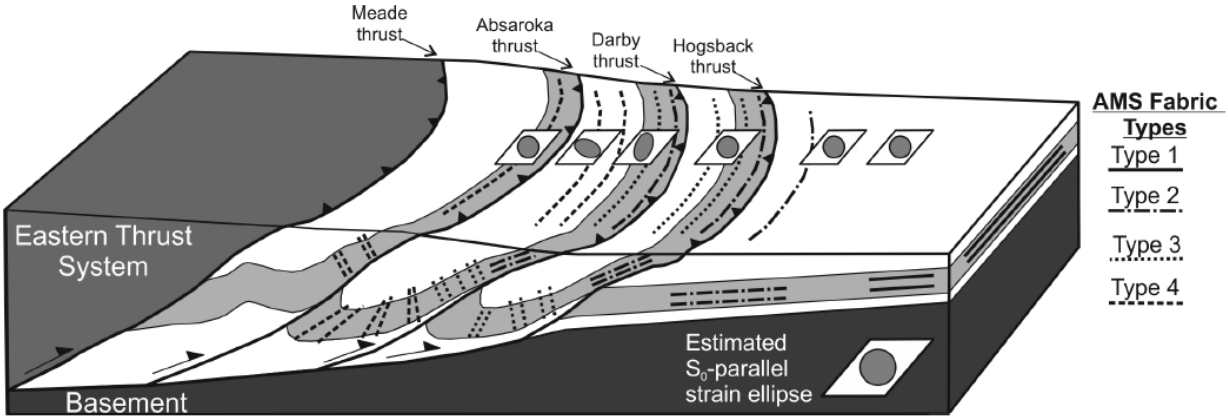

Figure 5. 59 Schematic model of AMS fabric type development during thrust sheet emplacement. Also shown is the estimated bedding parallel strain ellipse from strain analysis techniques, in regimes with poorly developed penetrative deformation these techniques typically report near circular (low-strain) ellipses. As penetrative deformation increases they report more elliptical results, these higher strain results are not always comparable to AMS results or structures observed in the field.

5.6. Conclusions

The AMS fabrics in the sedimentary rocks of the Wyoming Salient are interpreted to be controlled by phyllosilicates and minor amounts of hematite, therefore variation in AMS is not related to mineralogy, but deformation. In these situations, AMS can effectively be used to measure the bulk petrofabric, and as a result shows good correlations with structures observed in the field, such as bedding and cleavage. Despite this there is a poor relationship between the AMS parameters and the estimated strain recorded in bedding parallel sections (Figure 5.59). Stereographic projections of principal axes of the AMS ellipsoid and the long axis of the estimated strain ellipse shows that the long axis does not always correlate with K1 even when K1 lies on the bedding plane. Comparison of strain analysis methods confirms that DTNNM typically produces higher strain estimates than methods such as MRL that are solely dependent on shape and orientation of the clasts. Despite these higher estimates, they are rarely comparable to AMS results or structures observed in the field in low strain regimes such as the Wyoming Salient.

Chapter 6:

The Variscides of Southern Ireland

and the

Deformation of the Munster Basin:

Insights from AMS and Strain Analysis

6. Introduction

This chapter presents a re-evaluation of the development of the Variscan Fold Belt in Southern Ireland and addresses the use of strain analysis techniques and AMS in determining the development and extent of Variscan penetrative tectonic fabrics in the eastern Upper Devonian Munster Basin.

The Variscan Orogeny initiated in the Devonian and culminated during the Late Carboniferous peak and ended in the Permian. It involved the collision of Gondwana and Laurussia, leading to their amalgamation and formation of Pangaea (McCann et al., 2006; Woodcock and Strachan, 2009). The resulting orogenic belt is a broad curvilinear feature that extends across Northern Europe. The traditional front of this orogeny is largely regarded as a narrow zone in Britain and Ireland, where tight folding and thrust dominated tectonics switches to open folding (Cooper et al., 1986, 1984; Gill, 1962; Max and Lefort, 1984; Naylor, 1978a; Sanderson, 1984). This front is poorly defined in outcrop and its exact location is still debated (Cooper et al., 1984; Gardiner, 1978; Gill, 1962; Keeley, 1996; Vermeulen, 2000), as is the role of basement structures during deformation. Whether the orogeny acted in a thick skinned or thin skinned manner is just as debatable (Cooper et al., 1986, 1984; Ford et al., 1991; Max and Lefort, 1984; Sanderson, 1984).

6.1. Regional Tectonics

In order to fully understand the role of the basement and pre-existing structures in the development of the Munster Basin and its subsequent inversion due to the

Variscan Orogeny, earlier orogenic events must be considered. To this end a brief review of the Caledonian and Acadian orogenies is presented below.

The Caledonian Orogeny refers to all Palaeozoic tectonic events associated with the opening and closing of the Iapetus Ocean that occurred on the Margins of Laurentia, Baltica and Avalonia (McCarthy, 2013; McKerrow et al., 2000; Woodcock and Strachan, 2012). The relevant structures for this study are those that formed during the collision of Laurentia and Avalonia which took place between 605-420Ma (McKerrow et al., 2000). This 200Ma period involved a series of orogenic phases, but the most relevant are those of the final closure between 440Ma to 400Ma (Figure 6. 1). This orogeny essentially formed the Laurussian continent or Old Red Sandstone Continent by the end of the Silurian (Woodcock and Strachan, 2012). In Britain and Ireland this major boundary between Laurentia and the micro-continent Avalonia is represented by the Iapetus Suture. Although it is poorly exposed it has been traced across the Scottish-English border through the Solway Firth, north of the Isle of Man and then southwest across Ireland (Figure 6. 1; Woodcock and Strachan, 2012). The trace of the suture in Scotland is evidenced by Ordovician faunal contrasts between the Lake District and the northern belt of the Southern Uplands. Furthermore the Silurian rocks of the Southern Uplands have been interpreted to form part of an accretionary prism that were scraped onto the Laurentian margin as the oceanic crust of the Iapetus ocean was subducted northward beneath Laurentia (Stone et al., 1987; Woodcock and Strachan, 2012). This infers that the Iapetus Suture lies to their south (Woodcock and Strachan, 2012; and references therein). Soper et al. (1992) interpreted deep seismic lines in

the Irish Sea to feature Avalonian crust dipping to the north and underlying Laurentian crust near the Solway Firth. This suture trace continues across Eastern Ireland with the lithologies of the Longford – Down massif being interpreted as a continuation of the Southern Uplands accretionary prism (Woodcock and Strachan, 2012). Also xenoliths of schistose and mylonitic volcanic rocks found in intrusives in the massif are similar to the Borrowdale Volcanic Group of the Lake District, adding further evidence of the thrusting of the Laurentian crust over Avalonia (Woodcock and Strachan, 2012).

Further to the southwest evidence of the suture becomes obscured by Carboniferous Limestones and is thought to follow one of two possible traces. Either along the Silvermines Fault running between the Slieve Aughty and Slieve Bernagh Ordovician and Silurian inliers and the Silurian sequences at Slieve Pheim and Slieve Bloom (Woodcock and Strachan, 2012), or following a more southerly course and possibly merging with the North Kerry Lineament (Woodcock and Strachan, 2012). While determining which trace the Iapetus follows is outside of the scope of this research, regardless of which trace it follows the orientation of the resulting structures is largely ENE-WSW.

The closure of the Iapetus in Ireland was largely associated with sinistral transpressive deformation between the end of the Silurian and Early Devonian up until approximately 410Ma (Dewey and Strachan, 2003; Soper et al., 1992). This deformation became dominantly orogen parallel with significant sinistral strike-slip movement on pre-existing major structures, such as the Great Glen Fault (Dewey and Strachan, 2003). As plate motion between Baltica and Laurentia switched from

sinistral convergence to sinistral divergence, this transpressive regime was replaced by a transtensive regime that maintained sinistral sense of shear at 410Ma (Dewey and Strachan, 2003; Woodcock and Strachan, 2012). This produced a series of transtensional Early Devonian basins. Earliest Devonian deposition in these basins in Ireland is particularly significant as it provides indirect evidence for controlling structures after the closure of the Iapetus. The Dingle Basin is host to the only major outcrops of sedimentary deposits of this age in Ireland (Woodcock and Strachan, 2012). The Dingle Basin initiated during convergence of Avalonia and Laurentia with the North Kerry Lineament (NKL) and Dingle Bay Lineament (DBL), both large scale ENE-WSW striking fault zones, as the main basin bounding and ultimately controlling structures (Richmond and Williams, 2000). The later sedimentary sequences in the Dingle Basin record the onset of transtension followed by Acadian deformation (Meere and Mulchrone, 2006; Richmond and Williams, 2000; Todd, 2000).

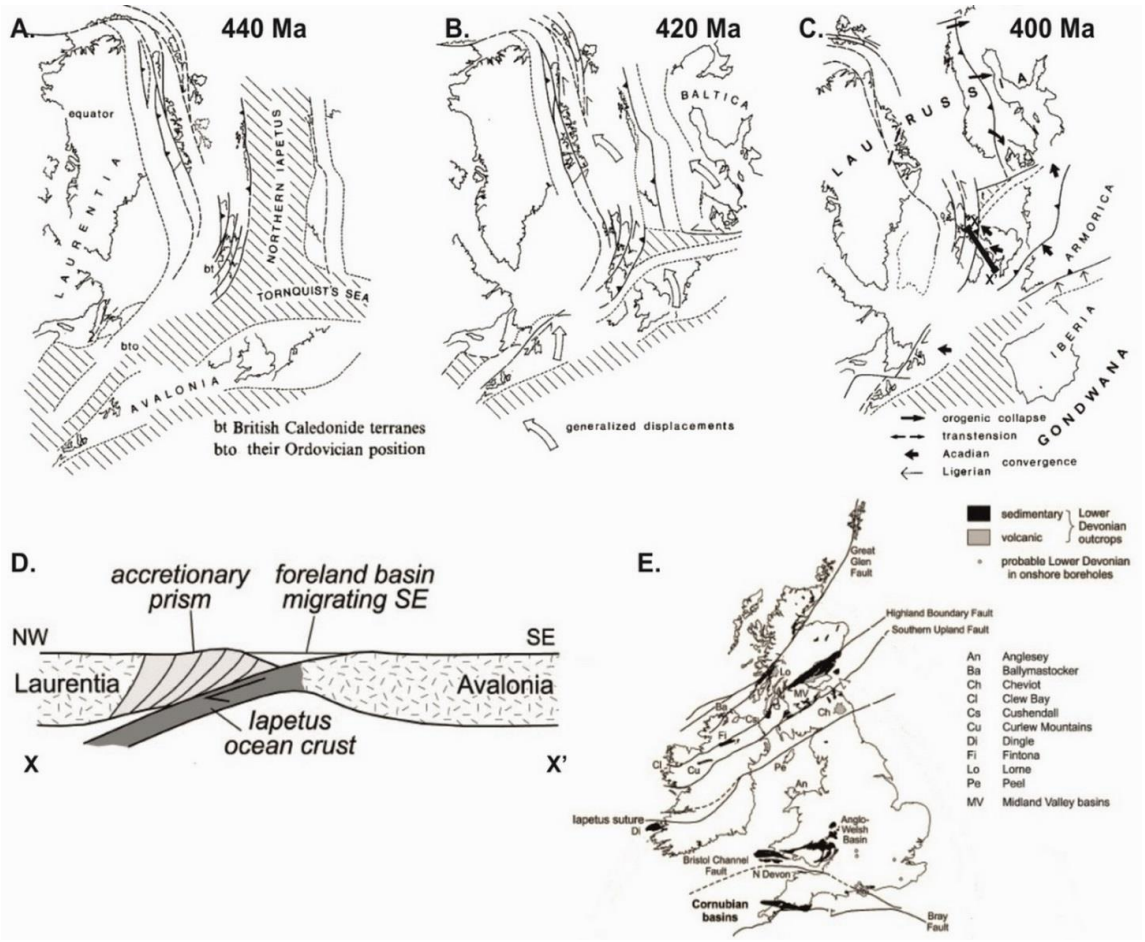

Figure 6. 1 Final closure of the Iapetus Ocean (A,B,C & E after Soper et al., 1992, and D after Woodcock and Strachan, 2012). A. The Iapetus Ocean closes by northward movement of the Avalonian micro-continent towards Laurentia. B. Coeval docking of Avalonia and Baltica with Laurentia. C. Caledonian faults become zones of major sinistral strikeslip movement causing the juxtaposing amalgamation of different British and Irish terranes. D. Cross section of the Iapetus Suture from line indicated in C. E. Major Caledonian structures in Britain and Ireland.

The period of transtension that linked the culmination of the Caledonian and the onset of Acadian compression lasted approximately between 420 and 400Ma (Figure 6. 2; McClay et al., 1986). Acadian deformation in Ireland has been constrained between Mid-Emsian-Mid-Frasnian (402-380) by a significant strain unconformity (Meere and Mulchrone, 2006). This deformation has been interpreted to have been caused by northward subduction of the Rheic Oceanic lithosphere under the southern Avalonian margin (Figure 6. 3 and Figure 6. 4; Woodcock et al., 2007). As a result of this crustal shortening, the deformation was concentrated in Lower Palaeozoic basins on the northwest Avalonian margin

(Woodcock and Strachan, 2012). This was primarily driven by thick-skinned tectonics, as these basins had been considerably thinned and stretched by the previous period of transtension, making them quite weak. The Iapetus Suture itself and the now rigid accretionary prism to its north would have acted as obstacles to northward propagating deformation (Woodcock and Strachan, 2012).

Upon cessation of Acadian compression, orogenic collapse drove a new phase of extension, largely to the south of the Acadian mountain belt possibly concentrated along the Avalonian-Rheic margin. This rifting was focused on pre-existing ENE-WSW Acadian faults and ultimately formed the Munster Basin. Continued extension accommodated deposition of thick clastic sequences supplied from upland areas in the north and northeast. As the basin developed, marine conditions became prevalent in the Late Devonian. This basin was then deformed by the Variscan Orogeny.

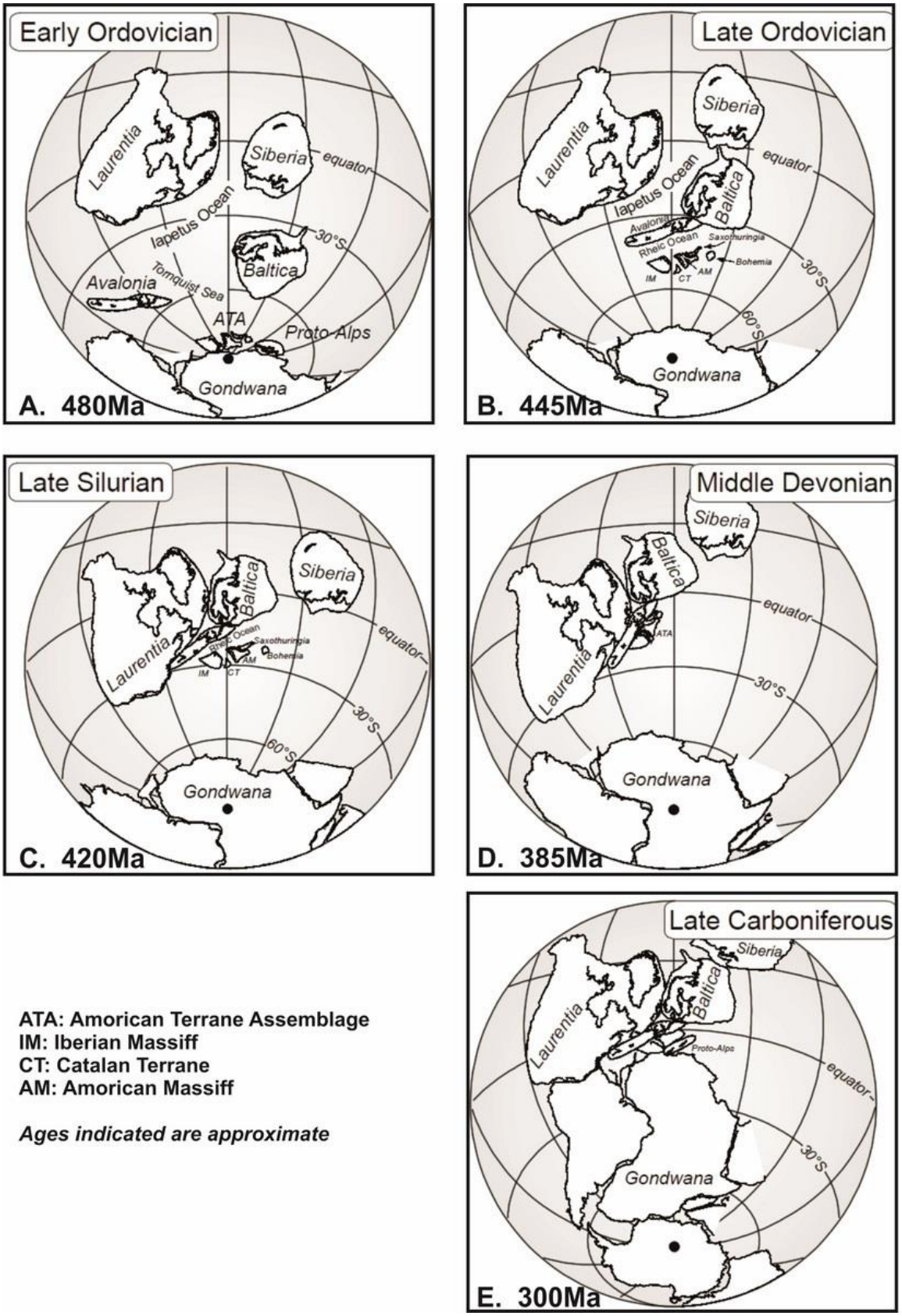

ATA: Amorican Terrane Assemblage
IM: Iberian Massiff
CT: Catalan Terrane
AM: Amorican Massiff

Ages indicated are approximate

Figure 6. 2 Palaeogeographic reconstructions from Early Ordovician to Late Carboniferous (from Schaetz, 2004), detailing the Caledonian Orogeny (A--C), the Acadian Orogeny (D) and the onset of the Variscan Orogeny (E).

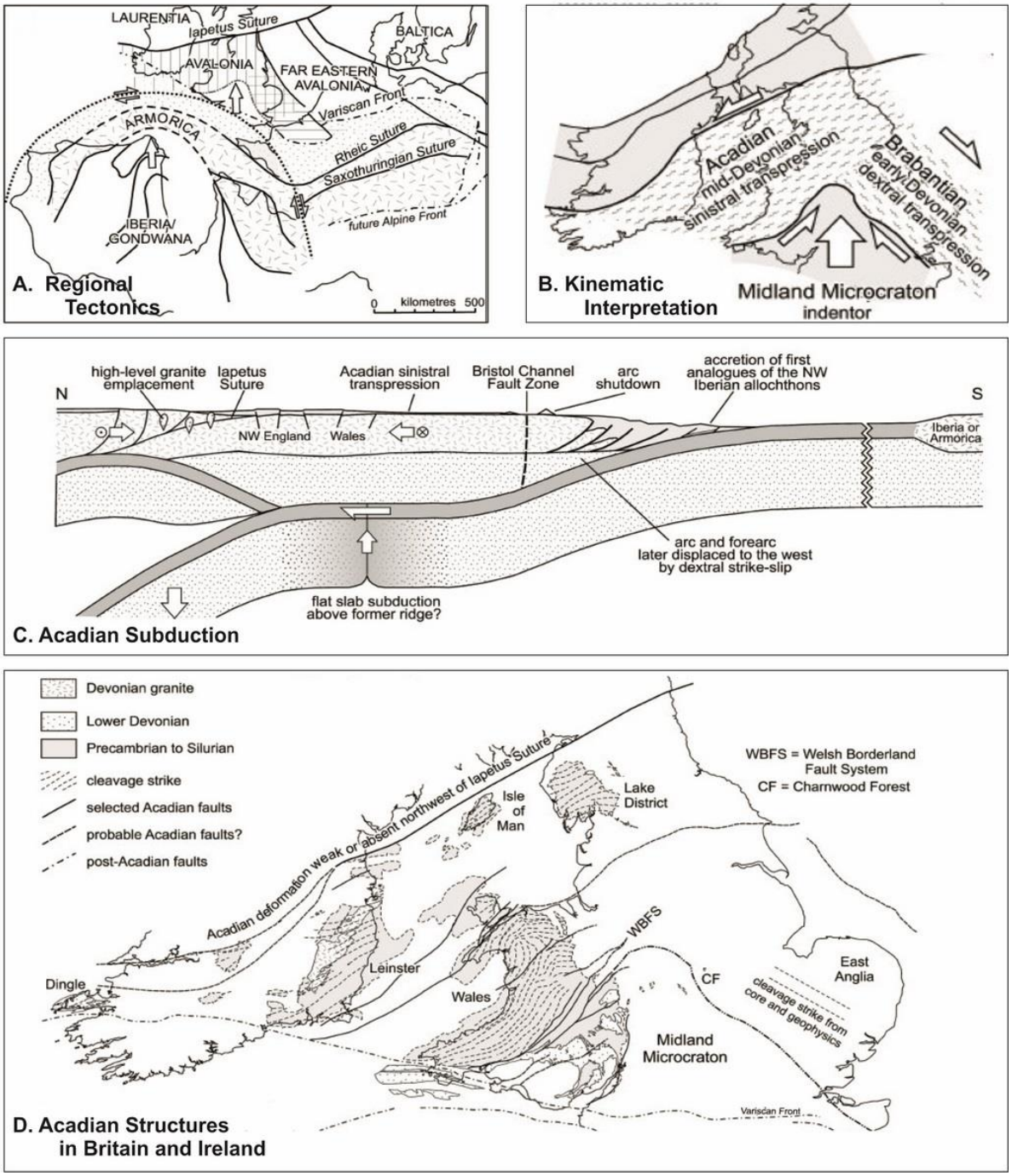

Figure 6. 3 Acadian Structures in Britain and Ireland (From Woodcock and Strachan, 2012). A. Regional tectonics of Acadian deformation. B. Kinematics of Acadian deformation. C. Plate tectonic model of Acadian subduction. D. Location of Acadian deformation in Britain and Ireland.

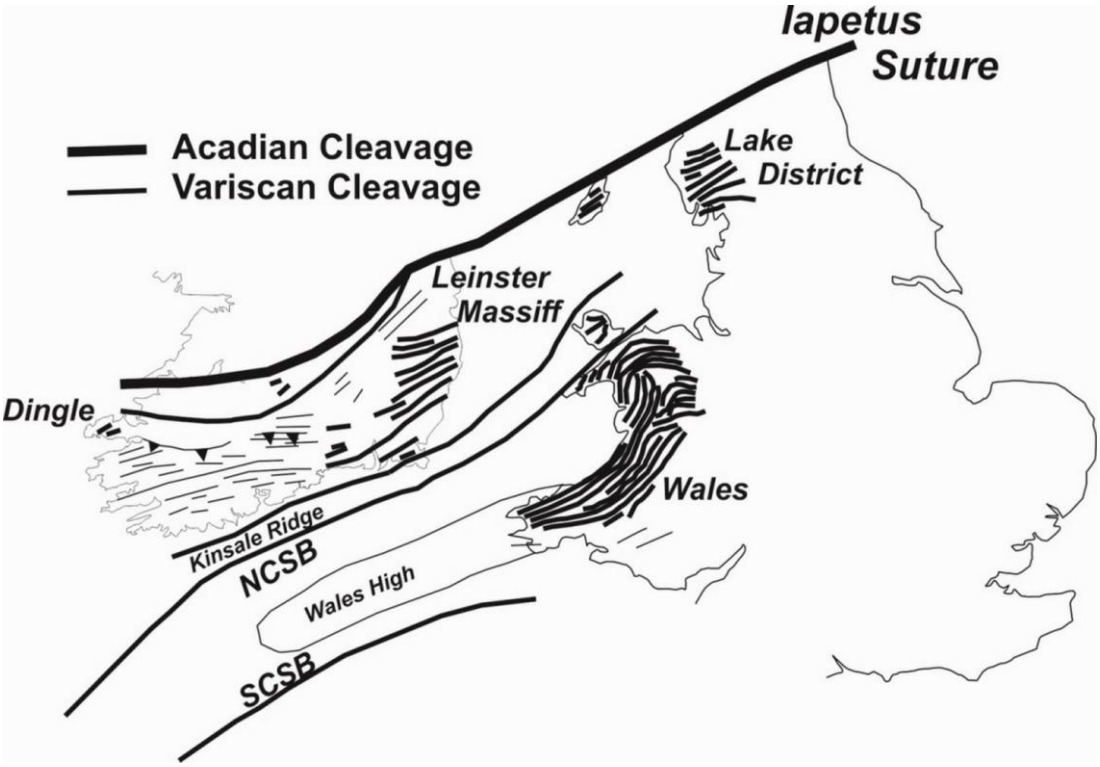

Figure 6. 4 Comparison of Variscan and Acadian cleavage orientations in Britain and Ireland (redrawn from Woodcock and Strachan, 2012). NCSB: North Celtic Sea Basin; SCSB: South Celtic Sea Basin.

The Variscan Orogeny resulted from the Devonian-Early Carboniferous accretion of Gondwana derived terranes/microplates onto the southern margin of Laurussia leading to the development of Pangaea (Timmerman, 2004; Woodcock and Strachan, 2012). The orogeny as a whole is considered to be a classical example of an obduction collision zone, with a prolonged period of deformation ranging over 100Ma (Woodcock & Strachan, 2009). The involved terranes were mainly Neoproterozoic crust with passive margin sequences and accreted Ordovician-Devonian island arcs (Timmerman, 2004). Once the Silurian-Early Devonian Caledonian orogeny concluded and formed Laurussia, its southern margin experienced a phase of rifting in the upper Devonian. This separated Avalonia from the Armorican microplate with a largely E-W trending back arc basin (the Rhenohercynian Ocean) (Timmerman, 2004). The opening of this basin is thought to have initiated by 397 +/-2Ma (Timmerman, 2004). It is generally thought that this

late Carboniferous extension could not have been purely gravity driven and was aided by far field extensional stress (Henk, 1999; Timmerman, 2004). This may have been brought about by dextral translation between Laurussia and Gondwana causing extensional stress (Timmerman, 2004).

Early Carboniferous subduction and closure of the Rhenohercynian Ocean, followed by accretion of a magmatic arc and docking of microcontinents, caused reactivation of older lineaments in the Variscan foreland (Timmerman, 2004). The resulting Variscan Belt is an east-west trending orogenic belt that stretches across most of Europe.

The Variscan orogenic belt is broadly split into a series of zones across Europe, Northern Africa and North America (Figure 6.5; reviews of these zones are presented in Woodcock and Strachan, 2012; Dewey and Burke, 1973). The threefold division of Dewey and Burke (1973) provides a simplistic view of the Variscides across their full extent (Figure 6. 5). Their Zone 1 largely consists of a Lower Carboniferous shelf and Upper Carboniferous coal basins. Zone 2 comprises of a paratectonic zone of Mid-Devonian volcanic activity and northward progressing Upper Mississppian to Lower Pennsylvanian (Namurian) flysch deposits, while Zone 3 is characterised by Precambrian Basement deformed during the Mid-Pennsylvanian (Westphalian) Asturic phase of Variscan deformation, leading to the development of gneissic domes and migmatite belts. Both Zone 3 and southern parts of Zone 2 were intruded by Mid-Upper Pennsylvanian Granites. The boundary between Zone 2 and Zone 3 has been interpreted as a suture zone between Northern and Southern Europe partly evidenced by the Lizard Ophiolite of Cornwall (Laurent, 1972; Dewey and Burke, 1973). This continental collision began during the

Upper Mississippian and had largely ceased by the Upper Pennsylvanian (Dewey and Burke, 1973). The main phase of deformation and crustal thickening was during the Mid-Pennsylvanian (Westphalian) Asturic Phase.

Ireland and the British Isles are largely associated with the northern Rhenohercynian Zone (Figure 6. 6; Woodcock & Strachan, 2012). This zone is composed of Late Paleozoic sedimentary and volcanic sequences, deposited during the extensive thinning of the southern continental margin of Eastern Avalonia, which exhibit multiple phases and styles of deformation, such as oblique thrust traces, lateral ramps, out-of- sequence thrusts and areas of backthrusting (Gill, 1962; Cooper et al., 1984; Woodcock & Strachan, 2012). Additionally the orientation of these structures typically deviates from the classic Variscan E-W trend. This plethora of structures can be accounted for by the rift-fault architecture of the eastern Avalonian continental margin prior to collision; the transpressive nature of the collisional deformation; the multiple phases of Variscan folding and thrusting (Bretonian, Sudetian and Asturian); and the late orogenic extensional collapse (Woodcock & Strachan, 2009).

The orientation of Variscan structures in Irelandtends towards a NE-SW trend and have been attributed to the reactivation of pre-existing Caledonian structures (Gardiner, 1978). Additionally the direction of Variscan compression was directed north-westward, which led to an oblique closure and subsequent inversion of the former extensional basin (Woodcock & Strachan, 2012; Price and Todd, 1984). This would have led to a dextral transpressive regime with orogen parallel shear focused along steeply dipping reactivated Caledonian structures (Sanderson, 1984). These Caledonian structures are either thought to extend to the basement (Sanderson,

1984) or level out to a sole thrust (Cooper et al., 1984). The faulted margins of some basins acted as buttresses to the northward propagating deformation front and would have caused areas of backthrusting (Woodcock & Strachan, 2012). This is perfectly exemplified by the margins of the Munster and South Munster Basins (Figure 6.6C; Meere, 1995).

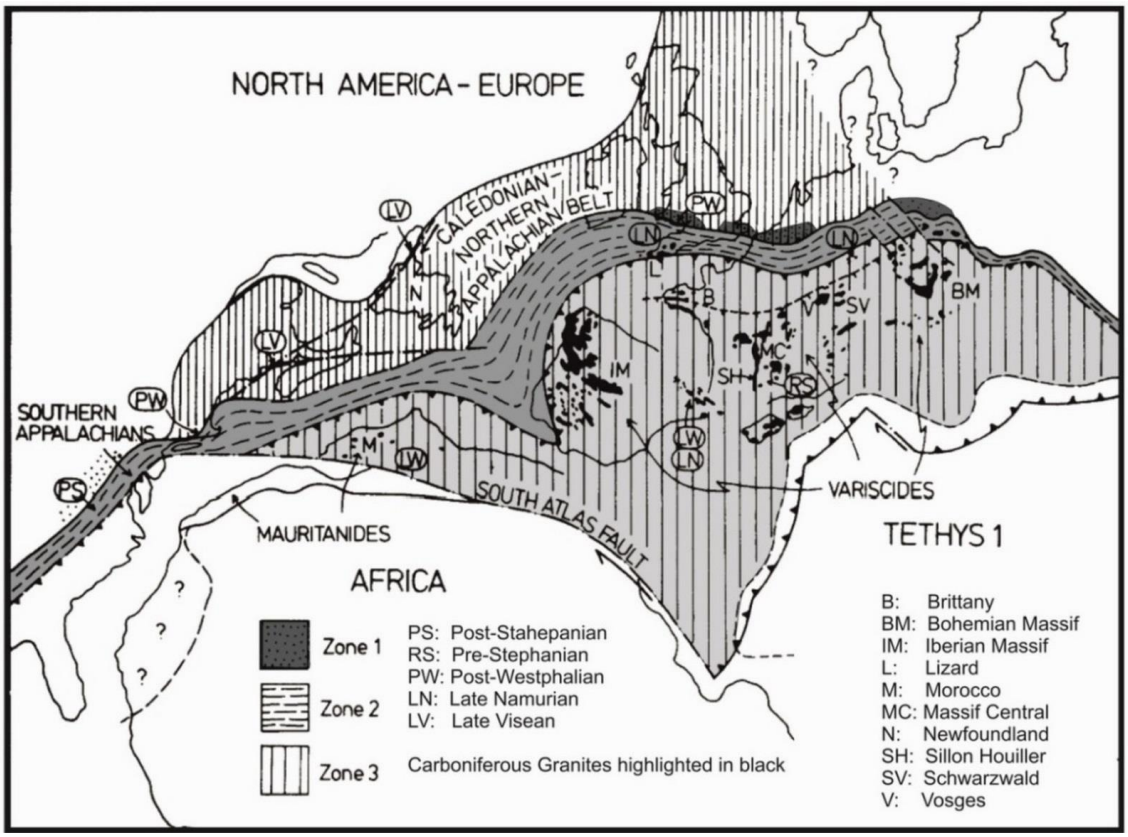

Figure 6. 5 Late Carboniferous paleogeographic reconstruction of the Variscides in Europe and North America. Modified after Dewey and Burke (1973).

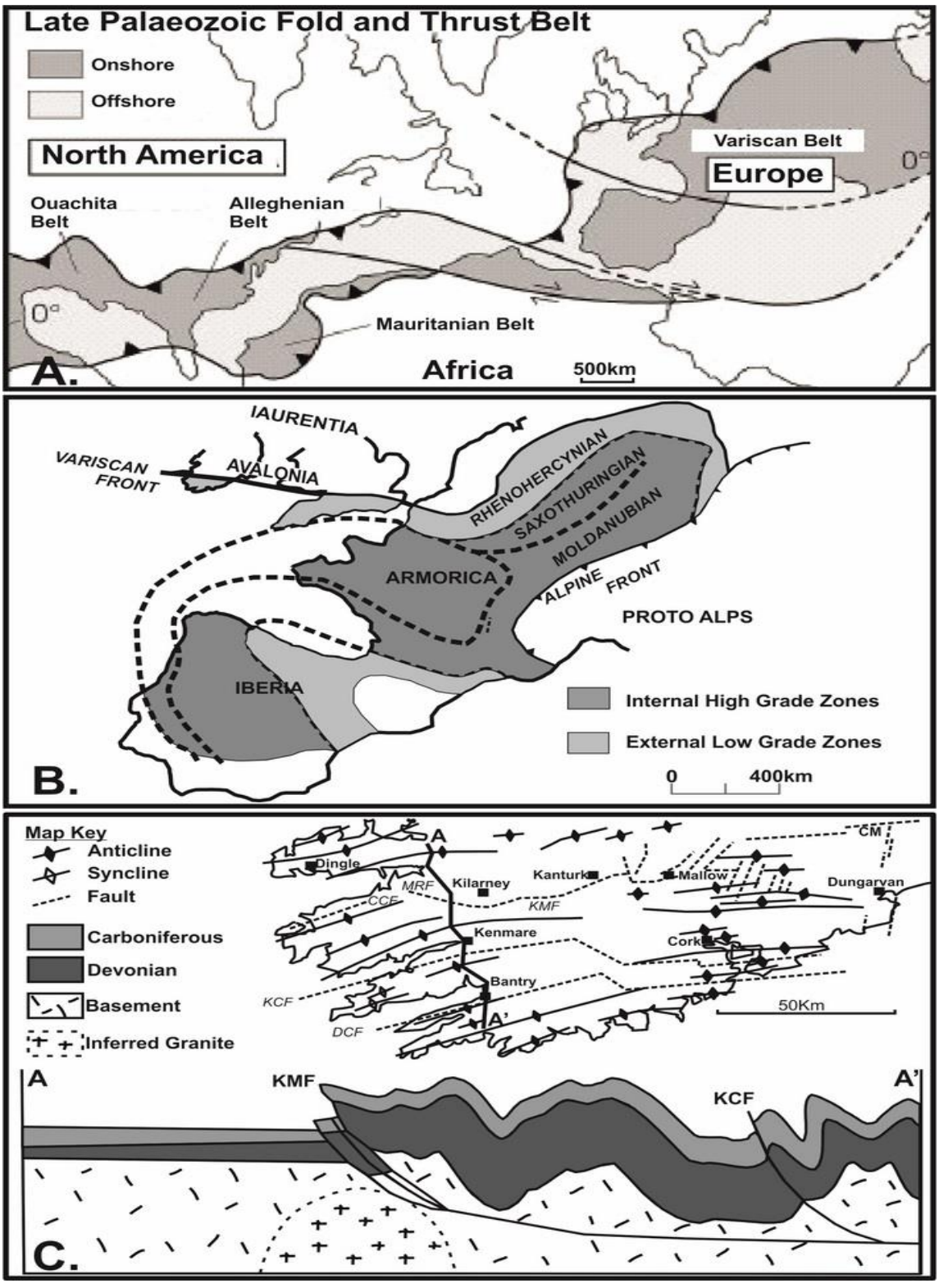

Figure 6. 6 A. Overview of the Variscan Orogenic Belt, modified from Dewey and Burke (1973) . **B.** Structural zones and cratons in the European Variscides, redrawn from Woodcock and Strachan (2012)**. C.** Basic structural map and structural interpretation of the Munster Basin, modified from Meere (1995). CCF: Coomnacronia Fault; MRF: Muckross Fault; KMF: Killarney-Mallow Fault; Kenmare-Cork Fault; DCF: Dunmanus- Castletown Fault; CM: Comeragh Moutains

6.2. The futile search for the Variscan Front

In relatively simple fold and thrust belts it is customary to define an orogenic front. This is typically represented by the last major thrust surface, although there may be minor thrusting or folding between this front and the foreland bulge; this is exhibited in the Rocky Mountains of the North American Cordillera. The definition of a front that represents the limit of an orogenic belt is essentially a cartographic convenience (Shackleton, 1984). Despite this point of view there has been a great deal of research dedicated to defining the 'Variscan Front', which has been described as a distinct structural line in Britain and Ireland (Coward, 1990; Naylor, 1978a). Unfortunately this line is not well-defined across its entirety and not only is its exact location widely disputed, but also the structural styles that define it.

The 'Variscan Front' is shown as a diffuse transition from a more pervasive style of deformation associated with thrusting, within the belt, that dies out to one of markedly heterogeneous deformation in the foreland (Sanderson, 1984; Williams and Chapman, 1986). This diffuse transition area in Ireland is a narrow area where thrusting in thick Upper Palaeozoics in the south gives way to simple folding in thin Upper Palaeozoics to the north (Max and Lefort, 1984).

It is not surprising that with these structural variations along strike on the 'Variscan Front' that attempts have also been to define the front by gravity and magnetic data than by any single geological criterion (Ford et al., 1992; Max and Lefort, 1984; Vermeulen, 2000). Unfortunately despite these attempts no satisfactory front or series of criteria to determine a front have as yet emerged. This may be partly explained by the varying role of the basement structures during Variscan deformation across the orogen. The front in Ireland has been attributed to a variety

of structures, the main contenders including the Dingle Bay Galtee Mountain Fault (DBGF), the South Ireland Lineament (SIL) and the Dingle-Dungarvan Line (DDL) (Figure 6. 7; Cooper and Collins, 1984; Gardiner and MacCarthy, 1981; Gill, 1962; Williams, 1989).

The DBGF is the northern most of these three possible margins extending from Dingle Bay to the north side of the Galtee Mountains (Williams et al. 1989). The SIL is a Caledonian structure that has an E-W trend under ORS Upper Palaeozoic cover and may be related to the shear zone that defines the East Carlow Deformation Zone (ECDZ)(Gardiner and MacCarthy, 1981; Gardiner, 1978; McArdle et al., 1987). The DDL is largely considered as the main location of the Variscan 'Front' (Gill, 1962; Cooper et al., 1984; Price & Todd, 1988). In the west the DDL is defined by the Killarney Mallow Fault Zone (KMFZ), a distinct frontal thrust (Cooper & Collins, 1984, 1986; Meere, 1995a) and coincides with the cleavage front. The KMFZ was one of the major basin controlling faults that was subsequently exploited by Variscan compression (Meere, 1995a). Seismic studies by Landes et al, (2000 & 2003) have shown that pervasive Variscan deformation has been mainly confined to the hangingwall of the KMFZ. They argue that this suggests a thin-skinned style of deformation, but it could lend support to the obstacle tectonics style of deformation suggested by Meere (1995a).

North of the cleavage front, deformation of the Late Palaeozoic cover sequence was not as intense, characterised by the development of open cylindrical folds and the absence of a regionally developed tectonic fabric. The sharp transition in tectonic style at the western end of the orogen is considered by Meere (1992, 1995a) to be a consequence of an obstacle effect of a granitic horst basement block to the north.

This block impeded the development of a significant tectonic fabric north of the front, allowing only the late stage development of the large wavelength open folds without significant cleavage development. Whereas in the east the DDL has been defined as the southern limb of the Dungarvan Syncline, a tight 80 km long near-horizontally plunging syncline, where a number of strike faults are seen in the Upper Palaeozoic strata (Max & Lefort, 1984). The location of this syncline marks a gradual transition from more intense folding and thrusting in the south to more upright, open folding and basement influence to the north of this line. The continuity and horizontal extent of this syncline is unique in southern Ireland since, to the south, very tight triclinic folds are often the rule while to the north fold plunges in Upper Palaeozoic rocks are controlled by the position of major faults and broad domes cored by Lower Palaeozoic rocks (Max & Lefort, 1984).

South of the DDL, observed deformation includes initial LPS and cleavage development, followed by buckling, thrusting and the reactivation of basin controlling faults (Cooper et al. 1984; Price & Todd 1988; Clayton 1989; Meere 1995a,b). Cooper et al. (1984) recognised a transition zone to the north of the DDL that encapsulated elements of both deformation styles where folding is open and upright but a penetrative tectonic fabric persists. Murphy (1990) identified a thrust sequence north of the Knockmealdown Mountains that coincided with the earlier 'cleavage front' of Cooper et al. (1984) and suggested that this may represent the inverted northern margin of the Munster Basin. Additionally there have been attempts to correlate the Variscan Front in Ireland with that in SE Britain (Max & Lefort, 1984; Shackleton, 1984), with Max and Lefort (1984) arguing that the only

feasible lineation of the three discussed above that could be traced across the Celtic Sea is the DDL.

Gardiner (1978) argued that the traditional Variscan Front in Ireland was a localised feature, due to the nature of the Avalonian Basement, and that the actual front lay somewhere to the south. This line of thought was elaborated further by Gardiner and Sheridan (1981), whereby the traditional Variscan Front in Ireland (the DDL) was interpreted to reflect pre-existing structural controls in a localised basin. These pre-existing structures are a result of the interaction of Acadian and Caledonian structures. Gardiner and Sheridan (1981) further argued that no direct correlation could be made between the structures in Southern Ireland and those in Wales. This argument stems from the distinct Caledonian structural trend in the Irish Sea and North Celtic Sea (Figure 6. 8).

Despite the problems and futility of defining such a boundary, it still holds regional significance as any such boundary would mark the northern limit of the Rheno-Hercynian zone of the Variscides (Read & Watson 1975). Before any interpretation of the Variscan deformation can be made in southern Ireland, serious consideration must be given to the Munster Basin, its geometry, margins and fill, as well as the underlying structures that ultimately controlled these factors and its subsequent inversion. Unfortunately little or no direct evidence of basin-basement structures has been observed at outcrop, therefore the majority of observations need to be inferred from the basin fill structures.

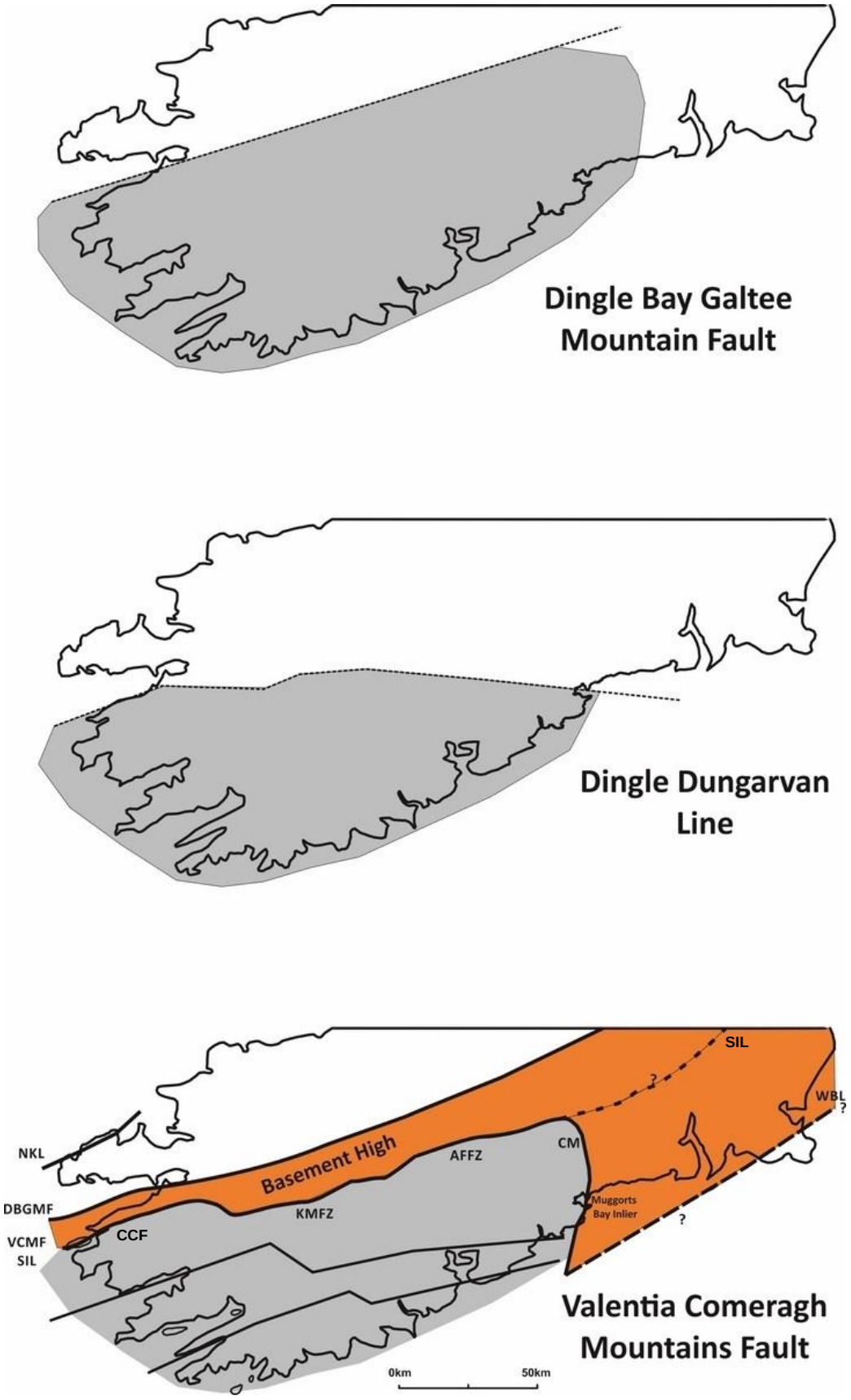

Figure 6. 7 Proposed locations for the Variscan "Front". The location of the Munster Basin indicated in grey. NKL: North Kerry Lineament; DBGMF: Dingle Bay Galtee Mountain Fault; VCMF: Valentia Comeragh Mountain Fault; SIL: Southern Ireland Lineament; KMFZ: Kerry Mallow Fault Zone; AFFZ: Ardfinnan Fault Zone; CM: Comeragh Mountains; WBL: Wexford Bay Lineament. The VCMF is comprised of the Coomnacronia Fault (CCF) in the west, the KMFZ, the AFFZ and the Comeragh Mountain Fault in the east.

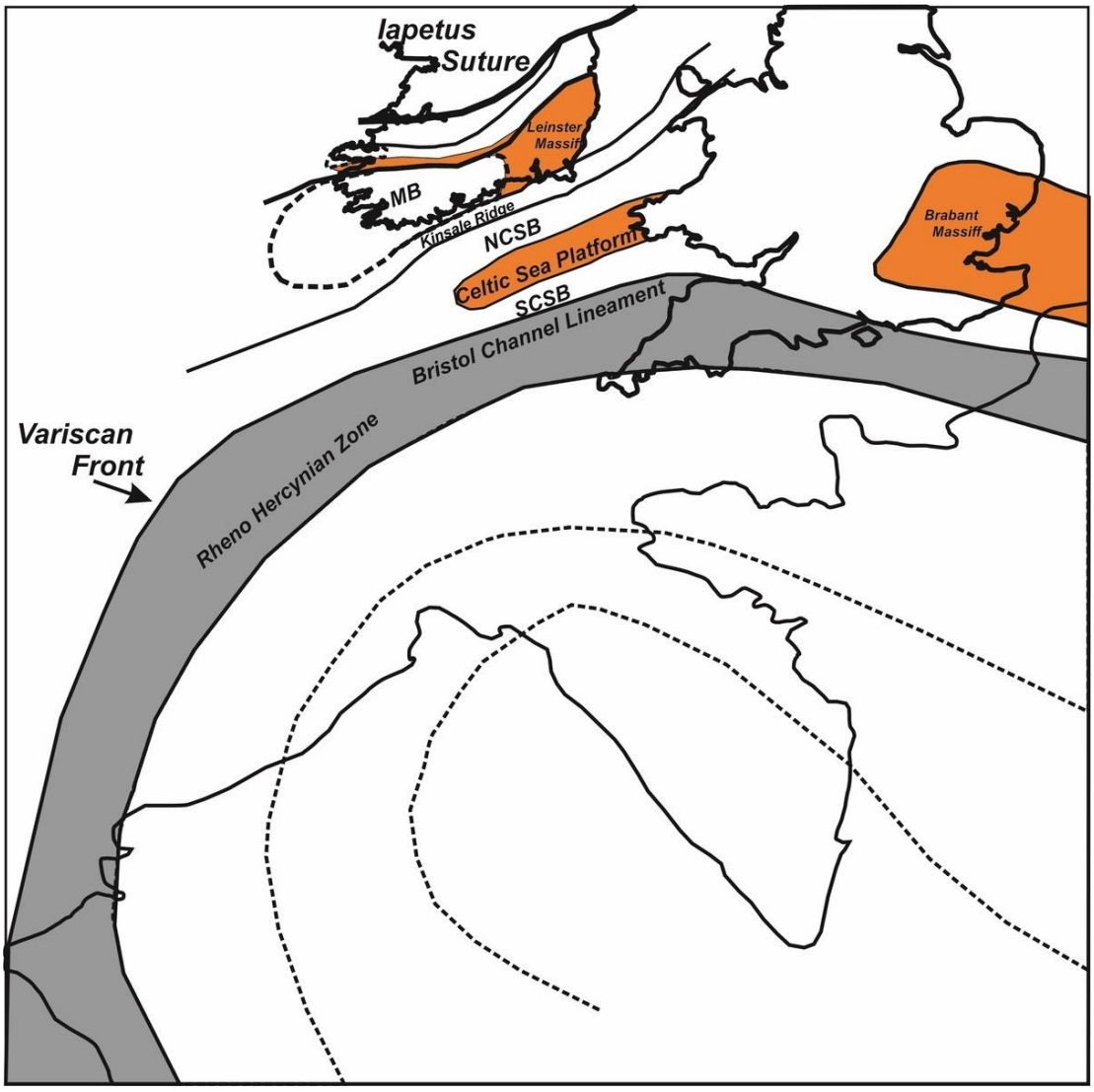

Figure 6. 8 Variscan structures in Western Europe and the alternative front of Gardiner and Sheridan (1981). NCSB: North Celtic Sea Basin; SCSB: South Celtic Sea Basin.

6.3. The Munster Basin

6.3.1. Introduction

The late Devonian and Carboniferous Munster Basin of Southern Ireland (Figure 6. 9), has been traditionally viewed as an extensional half-graben, that became progressively inverted as the Variscan deformation front propagated northward (Naylor, 1978a). This basin formed in the backdrop of post Caledonian and Acadian deformation that was followed by Mid-Upper Devonian extension (Coward, 1990). This extension came about by heterogeneous stretching of the lithosphere

(Coward, 1986; Price and Todd, 1988). The reactivation of earlier Caledonian and Acadian structures was driven by this extension, so that this Devonian basin is bound by faults with similar strikes and dips to Caledonian in an extensional template (Price & Todd, 1988; Coward, 1990). After Caledonian and Acadian deformation had ceased, erosion and orogenic collapse occurred resulting in active extension that persisted throughout the Upper Devonian (Powell, 1989). This resulted in a series of normal faults orientated along the North East- South West trend of previous Caledonian and Acadian shortening, with the main extension direction being to the south (Gardiner and MacCarthy, 1981; Gardiner and Sheridan, 1981; Gardiner, 1978; Price and Todd, 1988; Sanderson, 1984). This extension was dominated by movements on southerly downthrowing faults that formed an a syn-rift, sedimentary basin bound by NE-SW trending faults (Williams & Ford, 1990).

The style of subsequent Variscan deformation was largely affected by the position and reactivation of these pre-existing faults as well as the geometry of the basement floor. During the Early Carboniferous, extension was transferred to previously unextended areas northwards to form the Shannon Trough and southwards to form the South Munster Basin (Price, 1988; Price & Todd, 1988). Despite this dominant N-S extension the Munster Basin did not develop as a simple pull-apart basin, which would have resulted in main depocentre being parallel to the basin axis. Price and Todd (1988) argued that the main depocentre migrated in a perpendicular orientation to the main basin axis. Similarly it has been argued that the Munster Basin exhibits features of both a simple pull-apart basin and a strike-slip basin (Gardiner and MacCarthy, 1981; Gardiner and Sheridan, 1981; MacCarthy,

1990).It has been argued that it developed as a rift basin with sinistral strike-slip components accommodated by reactivation of NE-oriented Caledonian faults under N-S extensional stress (Sanderson, 1984; Price & Todd, 1988).

6.3.2. Basement Structures & Basin Geometry

It is well established in the literature that the geometry of the Munster Basin is controlled by the reactivation of long-lived basement structures of Caledonian or pre-Caledonian age hosted in Avalonian crust (Todd 1989; Williams et al. 1989; Ford et al., 1991, 1992). Despite this, the location and significance of these structures and their representative margins is still debatable. The northern margin is by far the most studied, in part due to its supposed link with the Variscan Front, whereas the southern and eastern margins have only received fleeting attention.

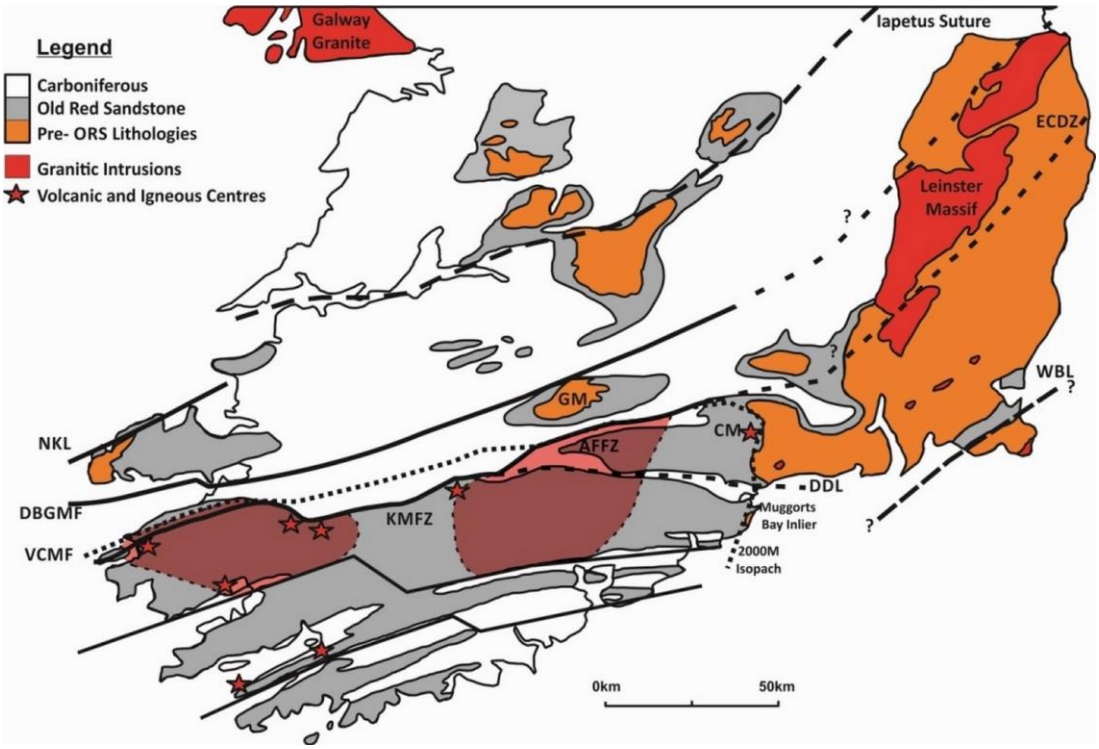

Figure 6. 9 Major structures in Southern Ireland. The location of suspected buried granites in the basement of the Munster Basin are indicated by transparent red shading. NKL: North Kerry Lineament; DBGMF: Dingle Bay Galtee Mountain Fault: VCMF: Valentia Comeragh Mountain Fault; KMFZ: Kilarney Mallow Fault Zone; AFFZ: Ardfinnan Fault Zone; DDL: Dingle Dungarvan Line; ECDZ: East Carlow Deformation Zone; WBL: Wexford Basin Lineament; GM: Galtee Mountains; CM: Comeragh Mountains.

6.3.2.1. Northern margin of the Munster Basin

The northern margin of the Munster Basin, is defined by rapid southward thickening of Upper Devonian sediments and a change in sedimentary facies along an NE-SW trending line from south of Dingle Bay following a line somewhere between the Galtee and Comeragh Mountains (Sanderson, 1984). This northern margin largely coincides with changes in the structural style of the Variscides (Cooper et al., 1984). In the northwest the northern margin is defined by the Dingle Bay Lineament (Price & Todd, 1984). This has been interpreted as a Caledonian structure that was reactivated as a late Devonian southerly dipping normal fault (Todd, 1988). The associated faults of this lineament were reactivated as NE-SW thrust faults during Variscan compression (Todd, 1988). From the eastern end of Dingle Bay the boundary fault zone becomes a NW-SE aligned dextral oblique slip fault (Muckross Fault; Price & Todd, 1988). This margin can be traced eastwards towards the Leinster Massif (Price & Todd, 1988; Graham, 1983). Whether it can be traced along the KMFZ (Price & Todd, 1988) or further north along the DBGF Zone (Williams et al., 1989) is debatable. The Muckross Fault has been interpreted as a transfer zone linking the Dingle Bay Lineament and KMFZ (Price & Todd, 1988).

The Killarney-Mallow Fault generally trends E-W and is a simpler thrust fault with a reverse displacement of 5-7 km (Cooper et al., 1984). The Killarney-Mallow Fault is seen to be the main controlling fault at the northern margin of the Munster Basin (Meere, 1995a; Williams, 1989). Buried granite in its footwall may have contributed to the to its uplift (Meere, 1995a). Many of these structures can be identified in the Bouguer gravity anomaly map of Readman et al. (Figure 6.10; 1997).

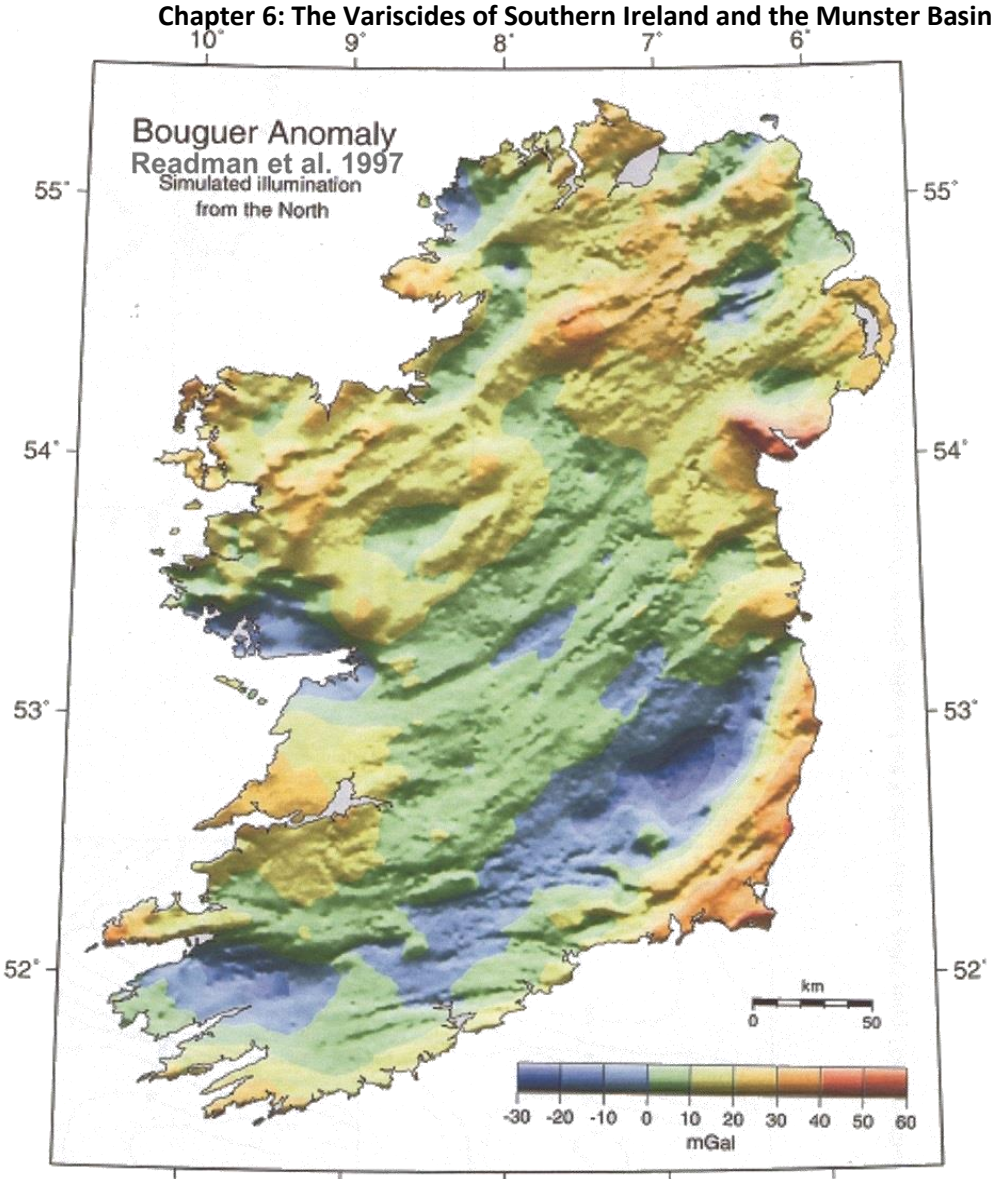

Figure 6. 10 Bouguer gravity anomaly map from Readman et al. (1997). The most striking feature of this map is the correlation of low gravity with granitic massifs. Interestingly the low gravity anomaly associated Leinster Massif appears to continue under the sediments of the Munster Basin.

The confining structures at the eastern end of the basin are much less constrained and the KMFZ cannot clearly be traced eastward (Cooper et al. 1986; Ford 1987). The main faults in this area have been identified as the North Galtee Mountain Fault and major faults north of the Comeragh and Knockmealdown mountains (Gardiner and Sheridan, 1981; Murphy, 1990).

Penney (1980) suggested that the 1500m basin fill isopach (Figure6.11) should be used as an approximation for the location of the marginal fault systems. This would lead to the margin extending from the DBL, north of the Galtee Mountains,

following the Galtee Mountain Fault. Similarly MacCarthy (1990) chose the 1000m isopach to represent the basin margin. Meere (unpublished) favoured the 2000m isopach contour, which traces a similar line and coincides with the Coomnacronia Fault (CCF)(Figure 6.7). The CCF strikes in an ENE-WSW orientation with southerly dip and can be traced in excess of 35km (Vermeulen et al, 2000). Furthermore the 2000m isopach closely follows the KMFZ, runs south of the Galtee mountains, following the Ardfinnan thrust faults and Northern Knockmealdown-Comeragh Mountain Faults. Regardless of which isopach is followed they abruptly turn south at the northeast corner of the Comeragh Mountains. This turning point coincides with a series of N-S faults in the Crotty's Rock area of the Comeraghs, which could be considered to be the eastern margin of the Munster Basin. The eastern margin is controlled by a high in the Avalonian basement (Gardiner, 1978). The Lower Palaeozoic Leinster Massif acted as a stable marginal block to the east which is confirmed by a condensed ORS sequence in this area.

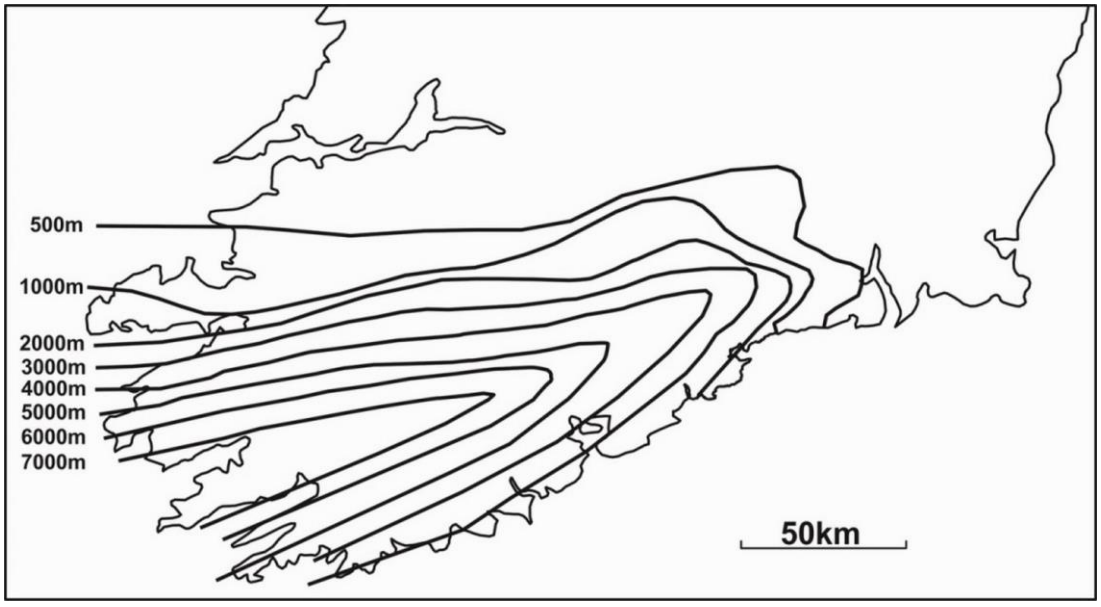

Figure 6. 11 Sediment thickness isopachs for the Munster Basin and surrounding areas (redrawn from MacCarthy 1990).

6.3.2.2. Southern Margin

The Southern margin of the Munster Basin is not exposed onshore and hence is poorly constrained, but it is thought to be close to the modern southern coastline (Naylor, 1983). Southward thinning from the main basin depocentre of Beara and Iveragh Peninsulas suggests that this margin was a relatively positive structure during deposition of the basin fill (Gardiner and MacCarthy, 1981; MacCarthy, 1990). This is further supported by sediment supply from the south (Gardiner and MacCarthy, 1981). Furthermore the basement high has been inferred as a structural boundary separating the Southern Irish Domain and Southern Welsh Domain (Gardiner and Sheridan, 1981).

6.3.2.3. Eastern Margin

The eastern margin of the Munster Basin has been defined by the conglomerate sequences in the Comeragh Mountains (Penney, 1980; Williams, 2000). Due to the considerable amount of conglomerate material, these deposits have been interpreted as a fault controlled alluvial fan (Penney, 1980; Williams, 2000). Additionally the basement floor rises significantly towards the this margin (Gardiner, 1978; Penney, 1980).

6.3.2.4. South Munster Basin

The Carboniferous South Munster Basin is also controlled by a northern fault margin, the Cork-Kenmare Fault (KCF; Figure 6.6C). A distinctive change in the subsidence patterns in the Munster Basin occurred during the latest Devonian and early Carboniferous, coincident with a marine transgression (MacCarthy, 1990).

During the late Devonian the zone of fastest subsidence shifted south as extensional strain shifted to other previously unextended areas. This may have been due to the locking-up of the Devonian faults on rotation. It may also have been due to the extension of thicker crust with pre-existing lines of weakness defined by Caledonian faults in preference to areas hardened by Devonian extensional strain. This shift in extension was accompanied by increased sediment accumulation, forming the South Munster Basin (Price & Todd, 1988; MacCarthy, 1990). The development of this basin closely coincides with a marine transgression during the Fammenian (MacCarthy, 1990). The main faults responsible for this extension were identified by Williams et al. (1989) as the Cork-KenmareFault which they modelled this as an E-W trending fault. MacCarthy (1990) suggested that the Cork-Kenmare Fault and Dunmanus-Castletown Fault had significant transfer faults similar in orientation to the more northerly Muckross Fault (Figure 6.6C). Vermeulen et al. (2000) showed that that the Cork-Kenmare Fault has a ENE-WSW trend rather than the earlier E-W trend suggested by Williams et al. (1989). They also suggested that it merges into the KMFZ at depth and possibly represents a footwall shortcut (Vermeulen et al., 2000).

6.3.2.5. The Role of Basement Structures in Basin Development

From the discussion on the bounding faults of the Munster Basin it is clear that the existing basement structures had a significant role during its development. To understand the geometry of the Munster Basin or the controls that acted upon it during deformation it is necessary to establish the nature of the structures that controlled its formation. As previously discussed the geometry of the Munster Basin was controlled by the reactivation of long-lived basement structures of Caledonian or pre-Caledonian age hosted in Avalonian crust (Gardiner, 1978; Todd, 1989; Williams et al., 1989; Ford et al., 1991, 1992). Badham (1982) suggested the probability of major strike-slip movement in the basement associated with the recognized thrusts and reverse faults. Max & Lefort (1984) further highlighted the stepped or disrupted nature of the basement at depth evidenced by linear edge affects and disruptions of both gravity and magnetic patterns. These observations imply complex basement structures.

The Late Caledonian closure of the Iapetus by sinistral oblique convergence between Laurentia and Avalonia had completed by the Late Silurian (Dewey & Strachan, 2003; Soper & Woodcock, 2003). This was followed by sinistral transtension and formation of a series of small pull-apart basins (Meere & Mulchrone, 2006). This transtensive basin development ceased by the Early-Mid-Devonian with the onset of Acadian compression. Acadian compression, which peaked in the Late Emsian, has been attributed to either the northward convergence of Armorica with eastern Avalonia or the subduction of the Rheic Ocean under Avalonia (Soper & Woodcock, 2003; Meere & Mulchrone, 2006). The northern Avalonian margin experienced dominantly sinistral transcurrent

movements during this event. Acadian transpression was followed by prolonged crustal extension that led to the development of the Munster and South Munster Basins (Meere & Mulchrone, 2006). This extension was driven by far field stresses related to the dextral transtensional rifting of the northern Avalonian margin from the Mid-Devonian to the Late Carboniferous (Soper et al. 1992; Vaughan & Johnston 1992; Holdsworth 1994; Johnston & Philips 1995; D'Lemos et al. 1997). This led to a transtensional regime for the development of the Munster Basin with dominantly N-S extension in the eastern basin margin and a minor component of dextral strike slip displacement along its western section (Sanderson, 1984). The Late Carboniferous saw the onset of Variscan compression, which reactivated normal faults formed during previous periods of extension and inverted the Munster and South Munster Basins (Cooper et al., 1984).

6.3.2.6. Basement Floor-Fill Interface

Extensional basins are typically associated with low angle detachments (Cheadle et al., 1987; Seranne & Seguret, 1987; Enfield & Coward, 1987). It has been argued that the significant extension in the Munster Basin, evidenced by the thickness of the Devonian and Carboniferous sediments ($\beta > 2$ Sanderson, 1984), suggests a similar detachment is present at its base. If any such decollement is/was present, in order for it to satisfy the half-graben geometry, it must have dipped to the south, with a steep northward ramp at the northern margin (i.e. the DDL, DBGF or SIL discussed above)(Price & Todd, 1988). This detachment would have been within the basement structures of the Munster Basin, and linked to steeper faults which controlled Late Devonian sedimentation (Todd, 1988; Williams et al. 1989; Price & Todd, 1988). Ford et al. (1991) concluded through geophysical modelling that any

basal detachment must lie within the pre-Upper Devonian basement at mid-upper crustal levels (approx. 5-9km). The level of this detachment also rises towards the east (Ford et al., 1991).

If this reactivated extensional framework model is correct then it becomes obvious that the basin floor and bounding structures have an inherent control on deformation. The ramp/flat geometry of the surface at the base of the detachment would have had a major influence on the deformation developing above the detachment. The position of the ramps would determine the location of both the extensional and contractional strains. Price & Todd (1988) argued that the coupled pop-ups and triangle zones which are common within the Southern Variscides (Cooper et al., 1984) may be due to the inversion of local half-grabens rather than a consequence of deformation above a northward-propagating sole.

In addition to the basin floor having ramp flat geometry, it was proposed (Gardiner, 1978) and later confirmed by geophysical surveying (Ford et al., 1991; Vermeulen, 2000) that there was a gradual decrease in depth to basin floor from west to east. Ford et al. (1991) combined gravity and seismic data to build two comprehensive cross section models across the Variscides. These models, while interpretative, shed some light on depth of deformation and the lithologies involved. One of the most significant conclusions from this was that the basement had to have been involved in Variscan deformation and that any detachment present has to lie within the basement at mid-upper crustal levels (Ford et al., 1991). The models of Ford et al. (1991) have important implications for the eastern part of the Munster Basin. They clearly show that the basin fill has reduced drastically in volume compared to the west, with ORS typically having a thickness of 2.5 km in agreement with earlier

sedimentary interpretations (Trayner 1985; Murphy 1988), indicating that the basement floor rises towards the east.

The gravity field anomalies are characterised by a buried extension of the Leinster Granite but also by the interface between the basement lithology and the ORS (Ford et al., 1991). These anomalies have been interpreted to show significant rises in basement level. This interpretation if correct requires that the earlier cross section models are re-evaluated, especially the thin skinned models that suggested that the basement rocks were not involved in deformation. Additionally these models cast some doubt that the principal Variscan detachment surface lies at the ORS-basement interface.

The presence of a granitic body in the Avalonian basement might have inhibited subsidence during the Upper Palaeozoic extensional phases due to its buoyant mass (Ford et al., 1991). This might account for the significant variation in depth of the detachment from west to east, as the Variscan decollement might have exploited its upper surface. Additionally this could explain the change in structural styles between the east and west parts of the basin. The Variscan detachment could have exploited the top surface of the inferred granite laccolith. Exploitation of the upper surface of a granite body may have led to a reduction in the deformation of the extensional framework of the basement, hence accounting for the more open style of folding and reduced thrust faults in the north east region of the Munster Basin.

The basement rises significantly towards the northern end of the Knockmealdown Mountains (Ford et al., 1991). This structural rise was previously modelled as a small thrust wedge that controlled the cleavage 'front' (Cooper et al., 1986). In a similar study Vermeulen et al. (2000) confirmed the role of some significant

structures in southern Ireland, particularly the role of the KMFZ and the DBGF. They concluded that the DBGF was a north dipping ENE-WSW fault and its main role was as the southern fault margin to the Dingle Basin. Similarly they concluded that the ENE-WSW KMFZ was the south dipping northern margin of the Munster Basin. These two structures were modelled as the boundaries of a basement ridge or horst, that separated the Dingle and Munster basins. It was further proposed that this ridge was the remnant of a Caledonian shear zone. This shear zone is a likely conduit for the ascent of mafic mantle melts and possibly influenced the siting of buried Caledonian granites. Furthermore if the buried granites in Killarney and at the cornerstone of the Comeraghs are lateral extensions of the Leinster Granite, it would imply that they would have to share the same siting structure that allowed the ascent and emplacement of the Leinster Granite.

An interesting finding of the Varnet study was that the floor of the Munster Basin south of the CKL is not particularly topographically varied (Vermeulen et al., 2000). Vermeulen et al. (2000) suggested that this indicates that underlying basement material might have escaped major deformation. Therefore it can be inferred that the large scale Variscan folds are not cored by folded Avalonian basement and that the basin fill must have detached from the basement and deformed independently (Vermeulen et al., 2000). This further confirms that two styles of deformation would have occurred: thin skinned deformation by folding and thrusting of the basin fill and reactivation of existing basement structures. If the CKL is a footwall shortcut as argued by Vermeulen et al. (2000), it is possible that as this became reactivated it became more involved in deformation north of the SMB.

These observations seem to be consistent with the thick-skinned model, it seems unlikely for Caledonian structures to be reactivated without becoming involved in the deformation. Following this model, structural variation along strike can probably be explained by variation in basement structures.

6.3.2.7. Basin Fill

The Munster Basin accumulated more than 7km of non-marine sediments during the Late to Middle Devonian (Late Givetian to Famennian)(MacCarthy, 1990). These Old Red Sandstones of the Munster Basin are dominantly fluviatile and aeolian in their nature (Penney, 1980; Graham 1983; Todd et al. 1988), and although fluviatile sedimentation is prone to extreme lateral variation, it is now well-established that syndepositional faulting and associated folding influenced facies, stratigraphic and dispersal patterns as the basin developed (Naylor et al. 1988; Price 1988; Todd 1988; Williams et al. 1988). The most significant of these faults have been argued to be reactivated Caledonian structures (Todd, 1988). Although a rift structure has been established for the Munster Basin sediment, transport was mainly from the north (MacCarthy, 1990). This is suggestive of material being shed from an Acadian high (itself centred on reactivated Caledonian structures) to the north. Large south facing fault scarps, accommodate the simplest sedimentological interpretations (MacCarthy, 1990; Penney, 1980), with fault-induced variation in sedimentary facies of the basin fill is described by multiple authors (Todd, 1988; Williams et al., 1988; MacCarthy, 1990). Generally coarser alluvial facies are concentrated around fault-bounded margins of the basin (Price and Todd, 1988) and the alignment of facies belts within the basin is typically parallel with the tectonic strike (Graham 1983). In the east alluvial fan deposits have been identified in the Comeraghs and

Knockmealdowns (Penney, 1980; Murphy, 1990). Subsidence along this southerly facing fault scarp was greatest in the western Iveragh and Beara regions of the basin, and accommodated sediment packages in excess of 6km (Naylor and Jones 1967). This succession is seen to thin rapidly northward across the Dingle Bay lineament. In contrast, the basin fill thickens gradually towards the southern depocentre and thins south of it (Gardiner and MacCarthy, 1981; Gardiner and Sheridan, 1981; MacCarthy, 1990; Price and Todd, 1988). Additionally fill thickness varies from east to west, with the east area having a thinner fill than the west (Ford et al., 1991; Gardiner, 1978; Price and Todd, 1988). This has been ascribed to development of localised half-grabens that led to a complex facies arrangement (Price and Todd, 1988). As discussed above Gardiner (1978) suggested that this was due to a decreasing depth to the basement towards the east. Ford et al. (1991) later confirmed this using geophysical modelling. Penny (1980) described considerable thinning of ORS formations between the Comeraghs and Slievenamon and postulated that this was due to the location of the northern margin of the Munster Basin.

A distinctive change in the subsidence patterns in the Munster Basin occurred during the latest Devonian and Early Carboniferous, coincident with a marine transgression. The zone of fastest subsidence shifted south, with an accompanied increased sediment accumulation, forming the South Munster Basin (Price & Todd, 1988).

6.3.2.8. Role of Igneous and Volcanic Sequences

Further interpretations on basin structure and evolution can be based on evidence from igneous activity in and out of the Munster Basin.

The Leinster Granite emplaced into a shear zone (East Carlow) that was actively sinistrally transtensional due to NW-SE extension (Cooper and Bruck, 1983; O'Mahony, 2000; Grogan, 2004) by 405 +/- 2Ma (O'Connor et al., 1989). This granite has been traced under the Munster Basin fill (Ford et al., 1991; Masson and Jacob, 1998) and has a marked strike swing from NE-SW to a more E-W orientation as it approaches the Munster Basin. Interestingly this largely mirrors the trace of the Iapetus Suture.

Igneous activity within the Munster Basin ranges from Mid-Devonian tholeiitic volcanism (384.5Ma), Late Devonian and Dinantian alkaline basaltic intrusions, to Upper Carboniferous, possibly Permian, alkaline sills (Pracht, 2000). The magmatism associated with the Coomnacronia Fault (CCF) and Valentia Harbour area has been interpreted to be contemporaneous with major basin fault activity during a period of crustal stretching (Pracht, 2000). This activity is considered to be largely synchronous with the Lough Guitane Igneous Complex (384.9Ma; Pracht, 2000) which is also associated with extensional fault activity. These faults would have acted as magma conduits facilitating ascent and controlling emplacement sites (Graham et al., 1995; Pracht, 2000). Similarly magmatism on the Beara Peninsula is focused along ENE-WSW orientated faults. The upper mantle xenoliths found in lamprophyres on Blackball head imply that these faults must be linked to deep-seated basement structures (Pracht, 2000).

In the Comeragh Mountains of the East Munster Basin igneous activity is Upper Devonian in age and largely confined to the Crotty's Rock area (Penney, 1978). Mugearite lava flows are interbedded with conglomerates north of Coumshingaun, striking in a similar orientation to the main east boundary fault of the Comeraghs (NNE-SSW; Penney, 1978). The evolution and southward progression of magmatic centres in the western part of the Munster Basin has been linked with basin development and progressive crustal thinning of the underlying basement (Pracht, 2000).

6.4. Variscan Deformation

The general structure of the southern Irish Variscides is dominated by axially extensive major folds with steeply dipping axial planes (Cooper et al., 1984; Gill, 1962; Naylor, 1978a). The axial traces of these folds have an arcuate trend from NE-SW in the south-west to E-W in the east (Gardiner and Sheridan, 1981). Additionally the folds have a systematic variation in their direction of vergence, with southward vergence in the southern part of the basin, to northward vergence closer to the northern margins (Cooper et al., 1984). Dextral strike-slip faulting along NE-SW to E-W trends suggests a component of E-W simple shear within the zone during the deformation (Sanderson 1984). Price and Todd (1988) argued that the lack of significant lateral offset across major faults, illustrated that this dextral shearing was subordinate to the N-S compression. South of the DBL, a major segment of Gills (1962) Variscan thrust front, structures formed by Variscan deformation are dominantly upright folds, faults and thrusts that typically have ENE-WSW to E-W trends (Figure 6. 12; Gill, 1962; Cooper et al., 1984; Cooper et al., 1986). In this area cleavage is typically well developed and dominantly axially planar to fold axes

(Cooper et al., 1984). North of the thrust front deformation decreases rapidly, with thrusts becoming less frequent and penetrative deformation decreasing from 40% to 12

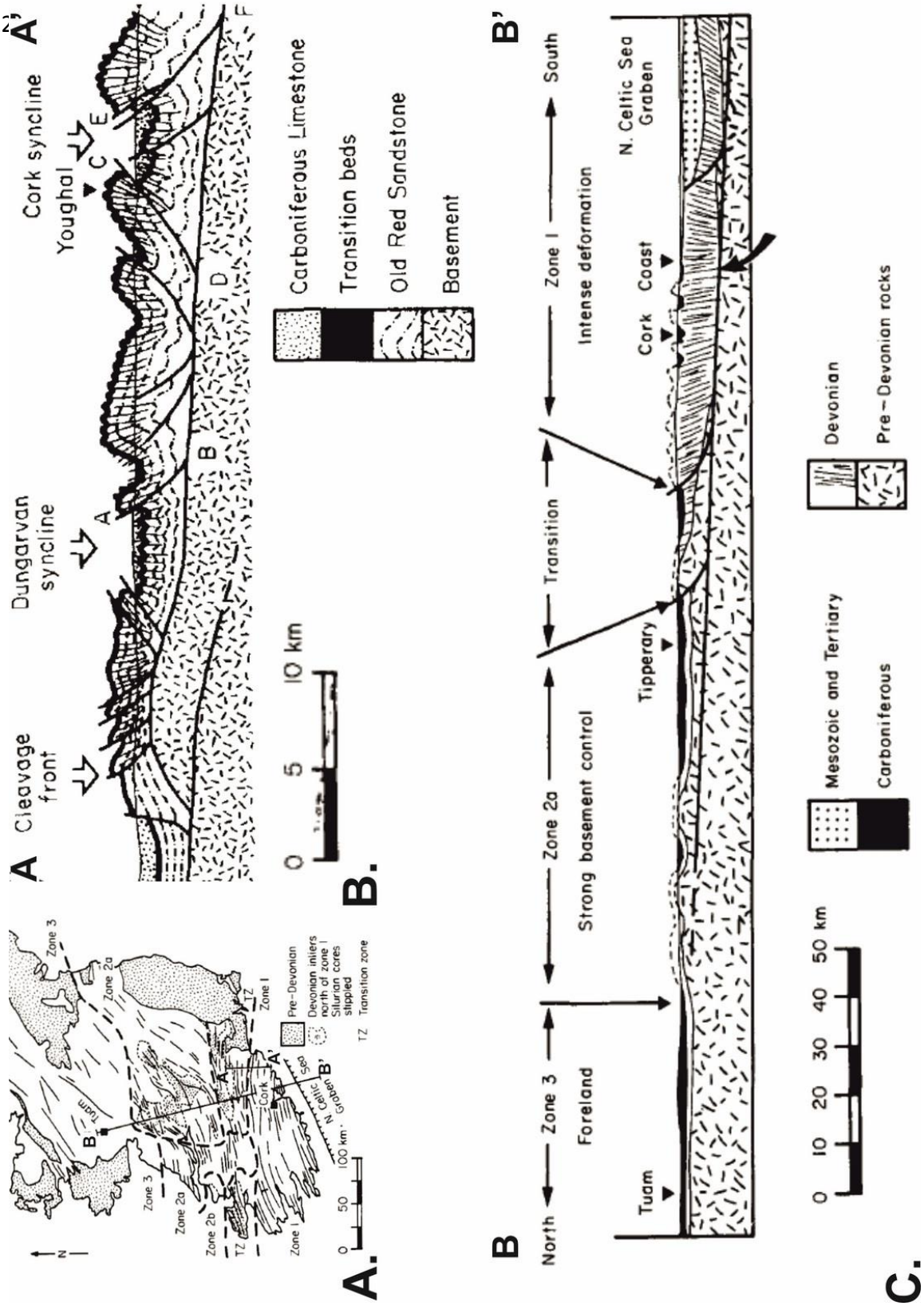

Figure 6. 12 Thin Skinned deformation model of Cooper et al. (1986).

6.4.1. Variscan Structural Zonation

The varying structures observed across the Variscides in Ireland were first organised in to three structural divisions by Gill (1962). Zone 1 was described as a Caledonian platform north of Galway Bay with gentle folding in Carboniferous lithologies. Zone 2 was composed of mainly steeper folds, some minor thrusting and occasional basement influence south of this Caledonian platform and north of the Thrust Front of Zone 3 defined by the DDL. Zone 3 was described as an area of intensely folded, strongly cleaved Palaeozoic sediments with a Variscan trend. Cooper et al. (Figure 6. 13; 1986) rearranged this zonation and incorporated transition zones and sub-zones. Cooper et al.'s (1986) Zone 1 was described as the strongly folded and cleaved Zone 3 of Gill (1962), and included a transition zone whereby there was a gradual decrease in deformation between Zone 1 and Zone 2. The DDL or thrust front was maintained as the northern margin of this zone, while the cleavage front was identified within the transition zone. Zone 2 similar to Gill's original division shows increasing involvement with basement structures and minor folding, while Zone 3 exhibits more dominant involvement of Caledonian structures and rare folding (Cooper et al., 1986).

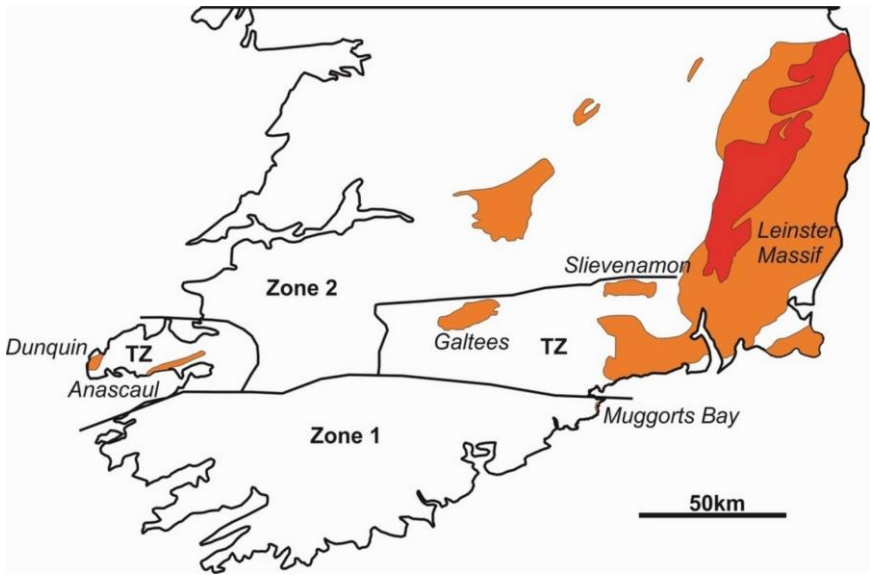

Figure 6. 13 Variscan structural zones modified from Cooper et al. (1984). TZ: Transition Zone. Palaeozoic inliers and Leinster Massif indicated in orange shades.

6.4.2. Thin-Skinned vs Thick-Skinned

It is now well established that this Variscan shortening was accommodated by reactivation of the pre-existing high-angle extensional fault system (Meere, 1995a; Powell, 1989; Price and Todd, 1988). This indicates that Variscan deformation was influenced and potentially controlled by pre-existing Caledonian and Early Devonian extensional structures. The contractional deformation of the Variscan orogeny then overprinted this extensional regime (Price and Todd, 1988). Whether this deformation represents the thin skinned model of Cooper et al. (1984 & 1986) and Ford (1985, 1987) or the thick skinned transpression model of Sanderson (1984) and Max and Lefort (1984) has not been fully resolved. These two models are the most well known and will be discussed here with the alternative models of Price and Todd (1988) and Gardiner and Sheridan (1981). Although the terms Thick-Skinned and Thin-Skinned can be interpreted in different ways, the essential difference is the depth that the near surface structures are considered to extend (Sanderson, 1984).

6.4.2.1. Thin-Skinned Orogenic Models

The idea of a Variscan Thrust Front in southern Ireland was first suggested by Gill (1962) and later supported by Cooper et al. (1984, 1986).This thrust front was argued to be the DDL (discussed above). Naylor and Sevastupolo (1979) first suggested that deformation intensity decreased gradually across the DDL. Cooper et al. (1984, 1986) interpreted the Irish Variscides to be a thin-skinned model of linked faults, formed by deformation involving a northward-propagating sole-thrust over a largely passive basement. Cooper et al. (1986) suggested that this sole-thrust died out somewhere south of Tuam. This sole-thrust would have originated to the

south of Ireland, passing beneath the Celtic Sea (BIRPS & ECORS 1986) presumably back in the hinterland of the Varsican orogen in Europe (Shackleton, 1984).

The thin skinned model has been supported and further developed by numerous authors (Cooper and Trayner, 1986; Ford, 1987). It is quite simple in that it suggests a deforming sediment pile being carried on a northward propagating thrust slab, that exploited structural weaknesses in the basement such as granite - host rock horizons (Cooper et al., 1986). Although the result of extensive field work, this model is not without problems. The cross sections of Cooper et al. (1984, 1986) show no variation in stratigraphic thickness in the ORS from north to south. If the considerable thinning of the ORS sequences from south to north were taken into account, this would require significant rises in the basement to accommodate their model. Additionally the concept of a single sole thrust also seems unlikely considering the extent of reactivated normal faults involved in the deformation. Furthermore thin skinned deformation refers to shortening that only involves the sedimentary cover, the presence of reactivated Caledonian and Acadian structures preclude this thin skinned model.

6.4.2.2. Thick-Skinned Orogenic Models

In contrast to the northward propagating thrust model of Cooper et al. (1986), Max and Lefort (1984) argued for Variscan deformation focused along a dextral shear zone accommodated by reactivated Caledonian structures. Sanderson (1984) proposed a thick-skinned transpressive model for Variscan deformation with components of both N-S compression and dextral shearing. This model essentially featured active basement blocks with their boundaries propagating upwards into the major thrusts within the cover sequences (Figure 6. 14). This thick-skinned

model would lead to crustal thickening within the basin, as well as strain discontinuities and zones of complex strain at its margins (Sanderson, 1984).

Transpressive deformation requires oblique or strike-slip boundary conditions, supporting the dextral strike-slip plate tectonic Variscan model (Badham & Halls, 1975; Badham, 1982). Palaeomagnetic reconstructions of the oblique collision between the European and African plates suggest that dextral shear was a major component of Variscan deformation (Smith, Briden & Drewry, 1973; Scotese et al., 1979). In light of the sinistral strike-slip models for development of the Munster Basin discussed above, it is unlikely that these structures would not reactivate during basin inversion in the opposite sense as they did during basin opening. This coupled with the reactivated Caledonian structures makes it more likely that Variscan deformation in Southern Ireland had a significant basement involvement.

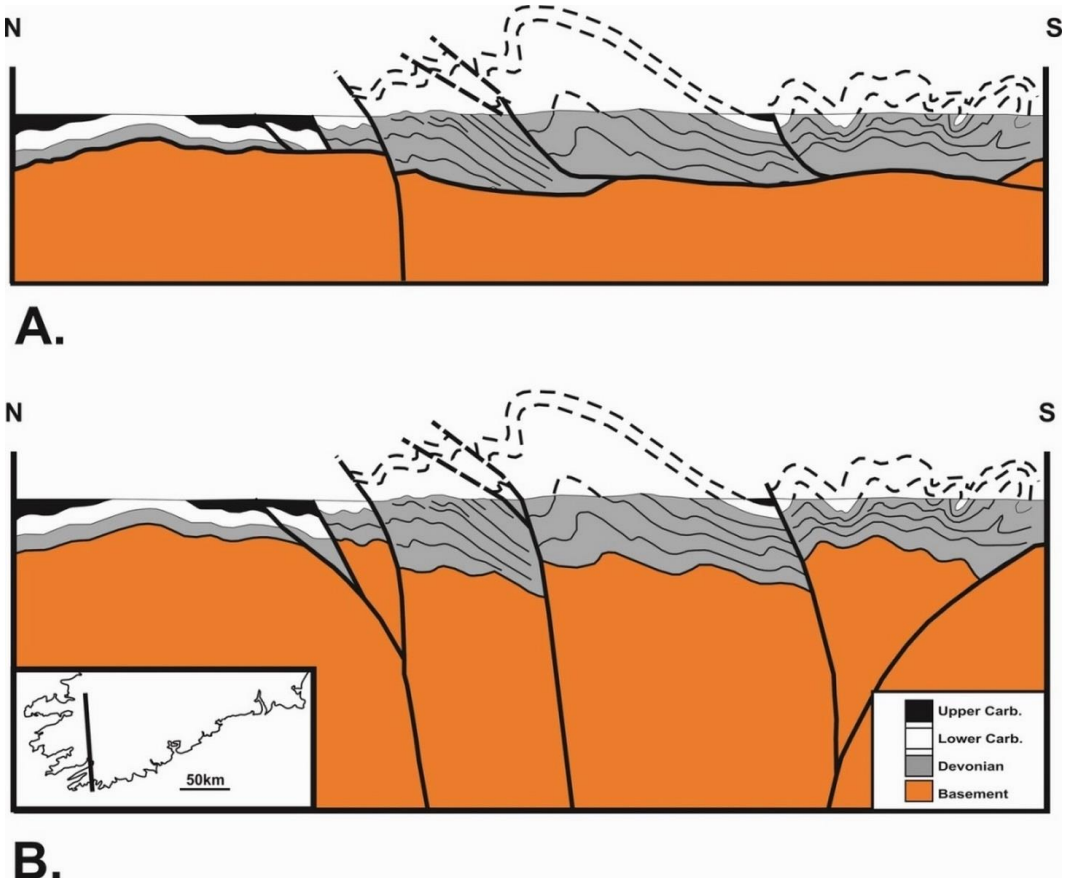

Figure 6. 14 Thin skinned vs thick skinned models, redrawn from Sanderson (1984). **A.** Thin skinned model of Cooper et al. (1984). **B.** Thick skinned model of Sanderson (1984).

6.4.3. Inversion of an Extensional Framework

Neither the thin-skinned or thick-skinned model of Variscan deformation discussed above completely incorporated the original extensional framework or pre-existing basin structures. Despite this both Cooper et al. (1984, 1986) and Sanderson (1984) acknowledge that the major normal faults, which influenced sedimentation during the Late Palaeozoic, were reactivated at the end of the Carboniferous during the Variscan deformation as thrusts. Price and Todd (1988) highlighted the role the extensional structures had on influencing deformation. In their model Variscan shortening developed initially by the contraction of the extensional structures that formed during the late Palaeozoic (Price & Todd, 1988). Their model can be summarised as follows:

1) The development of the Munster Basin initiated in the Late Devonian by extension concentrated on pre-existing ENE-WSW Caledonian faults such as the DBL.

2) The DBL accommodated rapid extension, such that crustal extension was greater than sub-crustal lithospheric extension; leading to a cold rift extension.

3) North and south of the Munster basin some uplift occurred as a result of sub-crustal extension exceeding crustal stretching.

4) Extensional normal faults became locked by the Dinantian and extension shifted north (Shannon Trough) and south (South Munster Basin) of the main Munster basin.

5) End-Carboniferous inversion of the Munster Basin with reactivation of extensional faults as thrusts, e.g. DBL.

Variscan deformation in southern Ireland was as a result centred on the inversion of this original extensional template (Price & Todd, 1988). Hence the geometry of the basin structure exerted a fundamental influence on location, intensity and style of contractional deformation (Price & Todd, 1988). The extensional framework was itself to some extent derived by reactivation of Caledonian structures. Any faults that were suitably oriented with respect to the developing compressional stress field were reactivated (Corfield et al., 1991). This correlation between extensional structures and contractional thrusts is interpreted to indicate that the extensional structural framework of the basin, including a basal low-angle detachment and an array of superjacent normal faults, was reused during transpressive inversion of the basin to produce the fold-thrust belt (Price and Todd, 1988). The basin fill was then deformed above these reactivated basement structures, by layer parallel shortening, buckling and thrusting as described in Cooper et al. (1984, 1986). This essentially suggests that the sedimentary fill of this basin became delaminated from the basement structures, hence accommodating thin-skinned deformation in the cover sequences and thick-skinned reactivation of pre-Variscan structures. Additionally Price and Todd (1988) argue that the basal detachment was a localized inherited feature and had no discrete link to the main European orogen, nor to any of the other basins in Ireland. This supports the earlier argument of Gardiner (1978) that the Variscan Front in Ireland was a localised feature controlled by the pre-existing structural regime.

The reactivated extensional basin model involves elements of both simple and pure shear, with pure shear from north south compression being most dominant. This transpressive element and deformation was concentrated between the extensional

structures with the transpression boundaries coinciding with the original basin margins fits well with the required kinematics for Sanderson's (1984) thick skinned transpressive model, but probably on a thinner scale. This also satisfies Max and Lefort's (1984) dextral shear model to a minor extent.

6.4.4. Basin Inversion Mechanics

Basin inversion, as mentioned above, involves reactivation of pre-existing structures, with reactivation defined as the accommodation of geologically separable displacement events along pre-existing structures (Holdsworth et al., 1997). As a result of this reactivation, the uplift of the basin fill is largely dependent on the re-use of the basin bounding faults (Corfield et al., 1996). Lowell (1995) concluded that transpressive stresses are the most effective cause of inversion, when steep pre-existing faults are reactivated a strike-slip component prevents these faults from locking up due to direct compression. Inversion structures dominated by younger low-angle thrusts rather than reactivated normal faults, imply a dominant element of pure shear compression (Lowell, 1995). Basin inversion and reactivation of an extensional framework typically involves decoupling of the basin fill from the basin floor, as indicated for the Munster Basin by Vermeulen (1998). Decoupling of the fill from the basin floor allows the fill to shorten and deform against buttresses such as the normal fault footwalls Figure 6. 15; Butler, 1989; Meere, 1995a). Furthermore basin inversion with fill-floor detachment accommodates compression of the basin basement back to a similar pre-extensional setting without need for major deformation of that lithology (Figure 6. 15; Cooper et al., 1989).

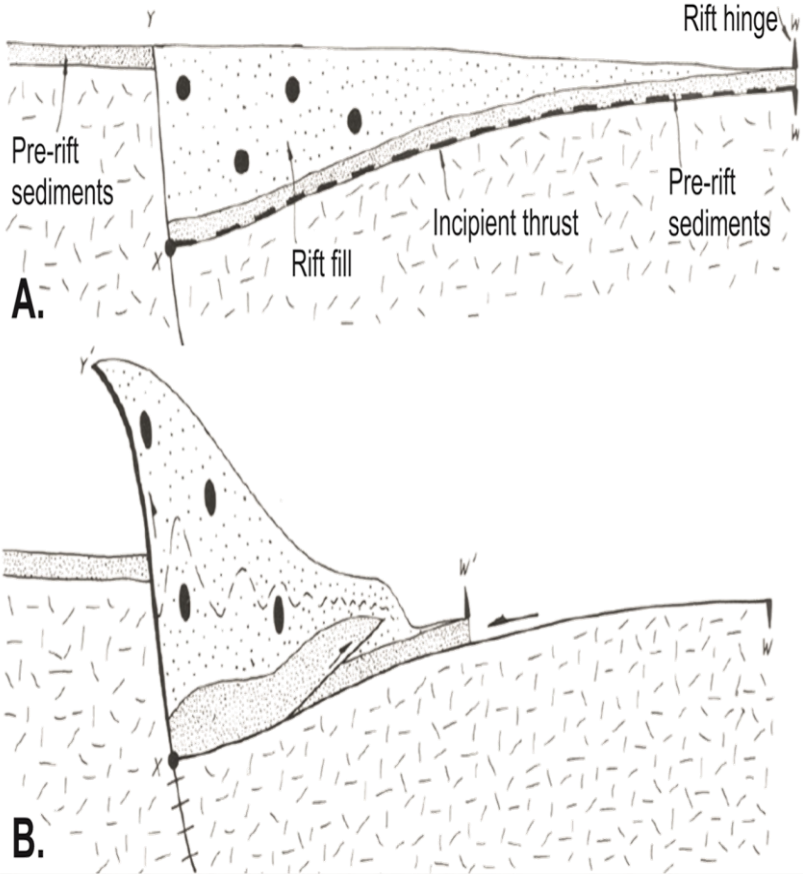

Figure 6. 16 Buttressing structures in a reactivation setting (from Butler, 1989). **A.** Pre-deformation rift structures. **B.** Post-deformation structures, with decollement shown between the basement and cover material. In this model the zone of highest deformation is shown nearest to the buttressing surface, additionally there is no reactivation of the original normal fault.

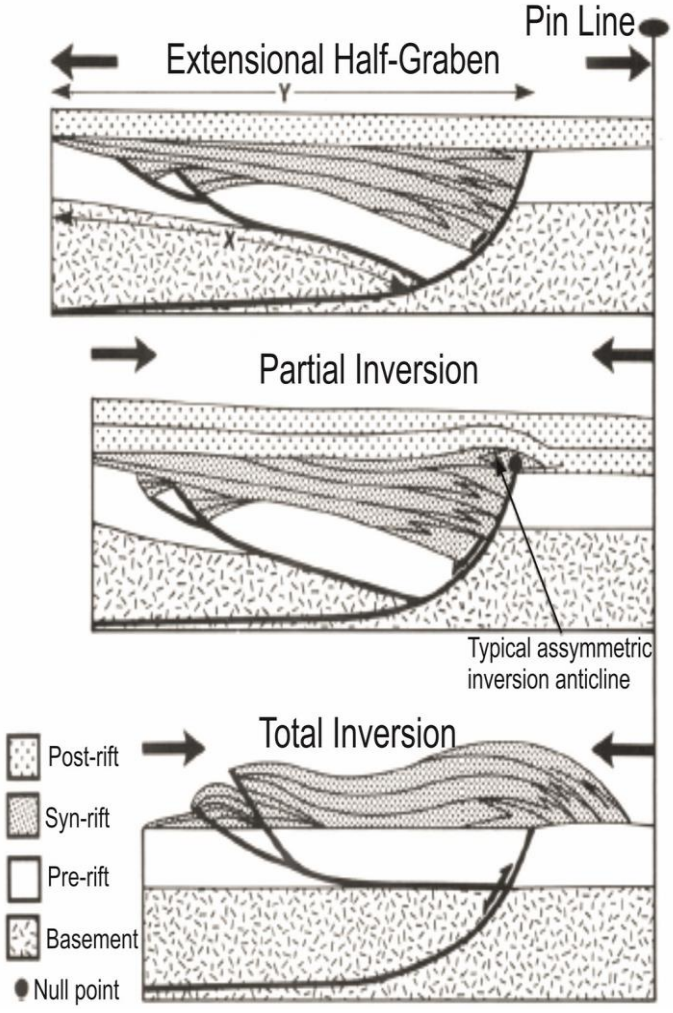

Figure 6. 15 Stages of basin inversion from Cooper et al. (1989).

6.4.5. Deep Seismic Surveys

A series of seismic surveys have been carried out across the Munster Basin, to the west and to the south of the basin. Of particular importance are the Varnet lines (Landes et al., 2000; Vermeulen et al., 1998, 2000). The Varnet lines run approximately north-south from the Shannon estuary to the south coast (Figure 6. 17). Both lines cross cut the general structural trend of the Variscan and Caledonian structures in Southern Ireland (Vermeulen, 1998). Two distinct crustal boundaries have been defined on the Varnet lines at 11-14km and 22km depth (Vermeulen et al., 1998). The upper boundary separates brittle structures in the upper crust from middle crust, additionally these brittle structures merge into a decollement surface at this boundary (Vermeulen et al., 1998). The lower boundary represents the brittle –ductile transition and most major structures stop at this boundary. The KMFZ is identified as a south facing structure and marks the syn-rift boundary of the basin. Vermeulen et al. (1998) inferred that the basement horst of KMFZ and DBGML is controlled by a continuation of the buoyant Leinster Granite Massif. Interestingly the floor of the Munster Basin is interpreted as an undeformed, relatively flat surface from the Varnet lines (Vermeulen et al., 1998).

In addition to the Varnet lines the WIRE lines were used by Klemperer et al. (1991) to establish the presence of Caledonian structures at depth. Their tectonic interpretation of the WIRE lines highlights the steep nature of the Variscan reverse faults (Figure 6. 18).

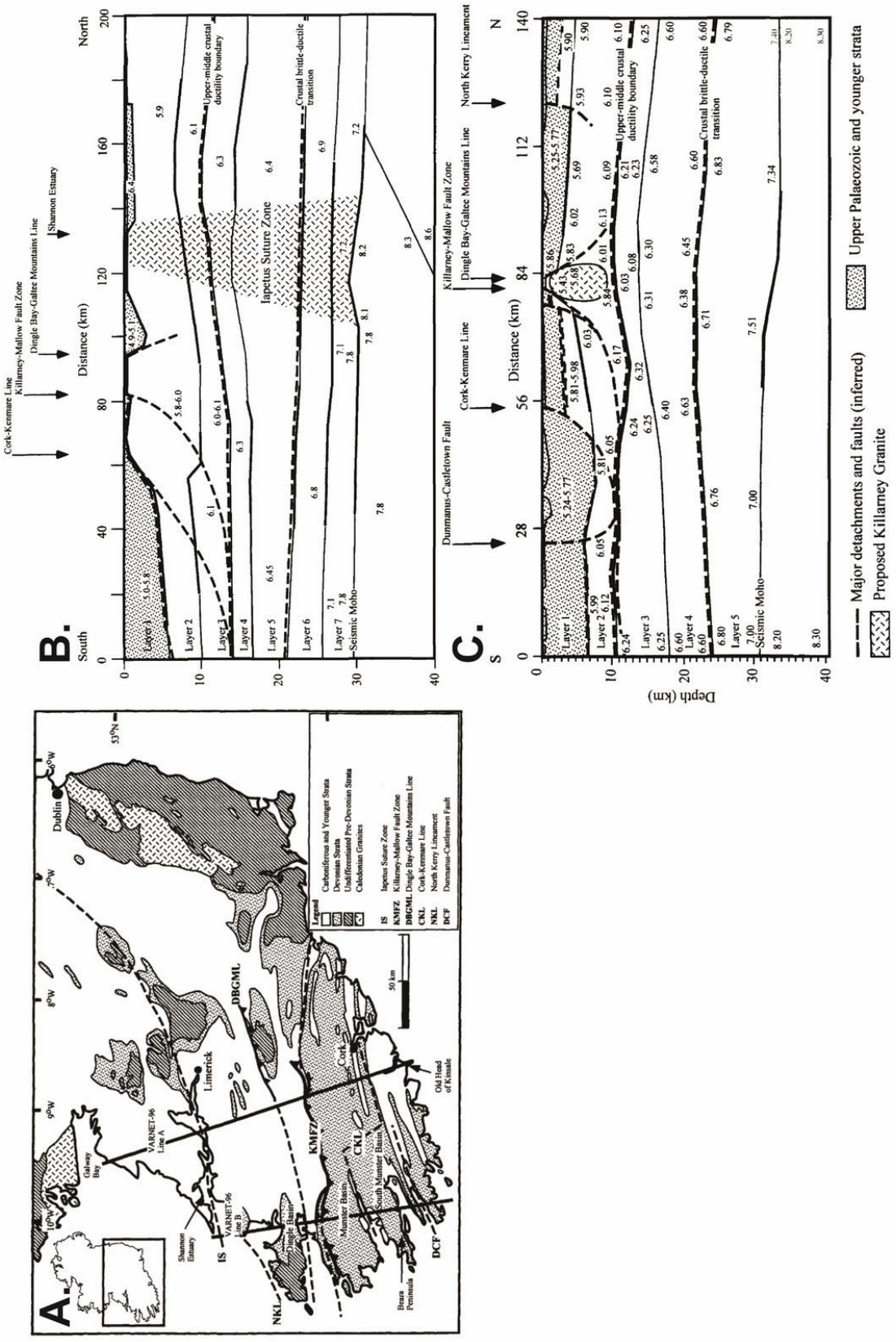

Figure 6. 17 Varnet profiles from Vermeulen et al. (1998). **A.** Map of the Varnet lines. **B.** Varnet line A. **C.** Varnet line B.

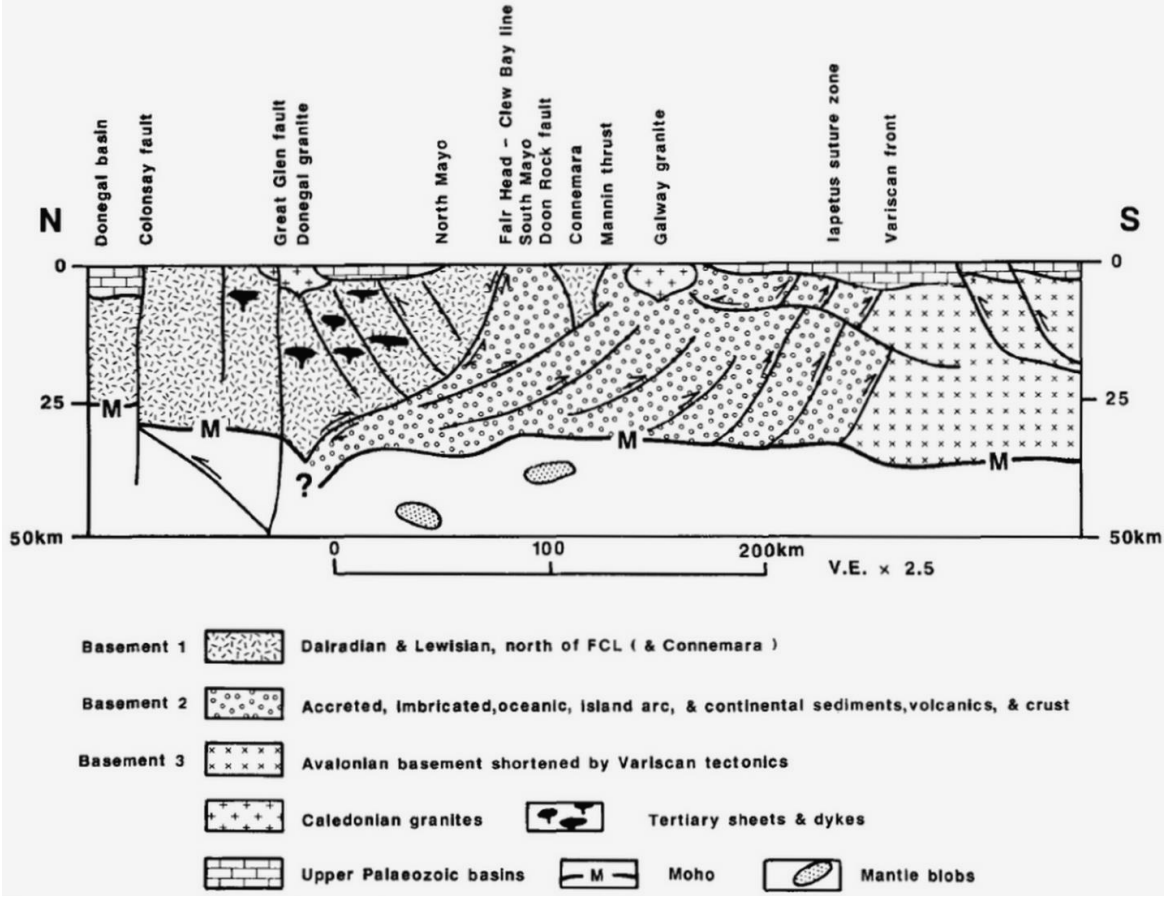

Figure 6. 18 Tectonic interpretation from the West of Ireland based on WIRE profiles (from Klemperer et al., 1991).

6.4.6. Strike Swing Component

It is clear from any geological map of the Munster Basin that the Irish Variscides feature a significant strike swing element. Similarly the South Munster Basin, is controlled by a northern fault margin (the CKFS), that exhibits a regional strike swing consisting of ENE-WSW elements in the west and more E-W elements in the east (Price and Todd, 1988). Occasionally at the eastern margin there are some cases of E-W axial trace trend tending towards a more WNW-ESE trend (Murphy, 1990). This is probably caused by lateral fold/strain retardation along the eastern margin of the Munster Basin.

This regional strike bend in both the Munster Basin and South Munster Basin is more than likely inherited from the Avalonian basement structures (Price and Todd,

1988; Ford et al., 1992). It is also evident that this structural grain is markedly influenced by the geometry of the northern basin margin with sharp lateral truncations of fold axial traces where they come in contact with basin-ward promontories along this margin (Meere, 1995a). Variscan compression was largely orthogonal to the northern basement ridge of Vermeulen et al (2000), and resultingly layer parallel shortening and cleavage development were constrained by this regional strain barrier, similar to the model of Meere (1995a).

Few of the earlier models for basin inversion have entirely accounted for the strike swing of the bounding structures (Cooper et al. 1984, Sanderson 1984, Price & Todd 1988, Meere 1995). Murphy (1990) attributed the arcuate trend of the Irish Variscides to a central surge zone within the orogen. The dominance of sinistral shear on Variscan cross faults required for this model is yet to be found (Meere 1992). Bresser & Walter (1999) suggested that the 10-15 degree clockwise offset of major Variscan faults to regional folds could be due to the strike slip component and to the transpressive tectonic setting during fold development.

6.4.7. Previous Strain Studies

Through strain studies and balanced sections across the western region of the Munster Basin, Meere (1995a) concluded that the basement had a significant role in Variscan deformation as well as producing a significantly thicker orogenic model, compared to the earlier models (Cooper et al., 1984 & 1986; Ford, 1985 & 1987). Similarly Ford et al. (1991) interpreted gravity data to suggest that pre-Upper Devonian basement had to be involved during the Variscan deformation. It has been shown that the KMFZ separates two distinct structural regimes, a high strain

zone to the south (approx. 40% bulk shortening) and a low strain zone (approx. 12% bulk shortening) to the north (Meere, 1995a). This finite strain pattern is observed across the orogen and has been interpreted to be the result of the combined effect of a fault bound, possibly granitic, basement obstacle in the Killarney area and an increased Upper Devonian sedimentary pile thickness at the western end of the Munster Basin (Meere, 1995a). During Variscan compression cleavage development was essentially a coaxial event that was locally orthogonal to the northern basement block, defined by the strike of the northern margin of the Munster Basin. As a result LPS and cleavage development were constrained by this regional strain barrier. Therefore a possible litmus test for the location of a confining basin margin that experienced deformation largely perpendicular to this margin will be the distribution of penetrative strain. The northern margin regardless of its location has largely been agreed to be a half graben structure of Caledonide/Acadian basement. This rigid structure would act as a significant buttress to strain, hence increasing strain at the fill/margin contact, as well as creating a marked decrease in strain beyond this margin. This model of obstacle style tectonics has been discussed by Meere (1995a). It is argued here that the cleavage front or high to low strain transition should be used to define the front.

The gradual transition zones of Variscan deformation of Cooper et al. (1984 and 1986) could imply areas where these obstacles are less well defined. Despite defining the northern limb of the Dungarvan syncline (eastern counterpart of the DDL) as the “Variscan Front” (Figure 6.7; Gill 1962; Cooper et al. 1984 and 1986; Murphy, 1990), the cleavage front was established at the northern tip of the Knockmealdown and Comeragh mountains (Cooper et al., 1984 and 1986; Trayner,

1985). The DDL marked a gradual transition from intense folding and thrusting in the south to more upright, open folding and basement influence to the north of this line (Cooper et al., 1986). While it is hard to argue with this northward decrease in deformation, including penetrative deformation from Ardmore to Dungarvan, there is a marked increase in penetrative deformation and fault activity in the northern region of the Comeragh Mountains, followed by a marked decrease in all styles of deformation directly north of the Comeraghs. Furthermore Wardlaw (1961 and 1962) described moderately high grade deformation of limestones associated with high angle reverse faulting in the Ardfinnan syncline, along strike from the northern end of the Comeraghs. Similarly Murphy (1990) discussed a 'thrust sequence' north of the Knockmealdown Mountains, which he suggested to be the inverted northern margin of the Munster Basin, again along strike from the northern end of the Comeraghs. If the cleavage front is taken as the principal criterion for defining of the Variscan front, then it would coincide conveniently with the northern margin of the Munster Basin.

6.5. Revised Model

Considering the models and geophysical studies discussed above, a revised model for the northern margin of the Munster Basin and the Variscan Front is required. As earlier proposed by Gardiner (1978) these two structures are inherently linked, therefore any proposed model needs to satisfy sedimentological distributions as well as the strain distribution. With this in mind the Valentia Comeragh Mountain Fault (VCMF)(Meere *pers comm*) satisfies both of these criteria reasonably well. The VCMF is proposed to follow the ENE-WSW Coomnacronia Fault (CCF) in the western

end of the basin where, it merges with the Muckross Fault, a transfer fault between the CCF and the KMFZ, before following the Killarney Mallow Fault Zone to the Ardfinnan Fault Zone (AFFZ) (Figure 6.7 and 6.9). At this point it is difficult to exactly determine the orientation or location of its continuation. The presence of a well-defined cleavage in the Comeragh Mountains suggests that the VCFS continues on a ENE-WSW trend, staying north of the Comeragh Mountains and possibly merging with a Caledonian structure in the East Carlow Deformation Zone.

This proposed line for the VCFS closely follows the 2000m isopach of MacCarthy (1990) with the exception of a marked offset along the KMFZ, possibly due to the higher level of deformation seen at this structure. Additionally it coincides with the northern edge of conglomerate lithologies at the northern end of the Knockmealdown and Comeragh Mountains that have both been interpreted as alluvial fans, with paleoflow directions to the south (Capewell, 1957; Penney, 1980; Murphy, 1990). Furthermore there is a relatively thin sedimentary cover sequence north of the VCMF and a distinct thickening of this cover sequence to the south of this structure. This line of evidence alone suggests that the VCMF had a significant role in the development of the Munster Basin and was possibly the main controlling fault at the northern margin.

As described above the VCMF is thought to merge eastward with the ECDZ, but the continuation of that of that horst is debatable. In a study of magnetic data across the ECDZ, McArdle et al. (1987) argued that the ECDZ extended westwards following a line of significant thrusting at Ardfinnan and Mitchelstown (WardLaw, 1961) and that it merged with the South Irish Lineament (SIL) of Gardiner and McCarthy (1981). The SIL was described to largely follow the DBL and KMFZ

towards the Mitchelstown area where it develops a sharp bend and largely parallels the Iapetus Suture, running north of the Leinster Massif (Gardiner and MacCarthy, 1981). This SIL could be the same structure as VCMF and represent the southern boundary of the Caledonian shear zone ridge of Vermeulen et al. (2000). Furthermore if the buried granites in Killarney and at the cornerstone of the Comeraghs are lateral extensions of the Leinster Granite, it would imply that they would have to share the same siting structure that allowed the ascent and emplacement of the Leinster Granite.

If the VCMF merges with the ECDZ, an eastern boundary for the Munster Basin needs to be defined. If, as discussed above the 2000m isopach is chosen to define the basin margin, then this would coincide with the eastern extent of conglomerates in the Comeragh Mountains as well as a series of NNE-SSW faults in the Crottys Rock area (Figure 6.20) that define a basin-ward thickening of basin fill to the west. A basement high of the ECDZ is probably present at the eastern margin. Gravity data suggests that the Leinster granite may extend as far south as Portlaw (Murphy, 1974). Penney (1980) described beryl in quartz veins on Croaghaun Hill (directly east of the Crottys Rock Fault) that may be caused by late stage hydrothermal activity associated with a buried granite. Both suggest the presence of a raised basement in that area. Additionally to the south of the Crottys Rock area and along strike of the faults exposed there, the Muggorts Bay Inlier is exposed, possibly representing a basement high, immediately east of the basin margin. Further to the south along strike lies the Ballyquin Shear Zone, an area of intense deformation and distinct dextral shearing. This shear zone could represent an area of complex strain discussed in Sanderson's thick-skinned model (1984).

The gradual decrease in depth to basement floor towards the north east of the basin could account for the marked differences in deformation style. The most intense folding and thrusting is delineated by the Dingle Dungarvan Line. North of this structure detachment of the sedimentary cover from the basement is not as intense, hence the more open style of folding. LPS continues further north of this structure and is effectively terminated at the VCFS.

6.6. Eastern Munster Basin

In order to attempt resolution of the series of unanswered problems above AMS and strain analyses have been carried out in the Comeragh Mountain and Ardmore areas of the eastern Munster Basin. The lithologies of the eastern Munster Basin are characterised by coarse conglomeratic alluvial fan sediments deposited in the Devonian that give way to Carboniferous fluvio-tidal sediments (Figure 6. 19 and Figure 6. 20).

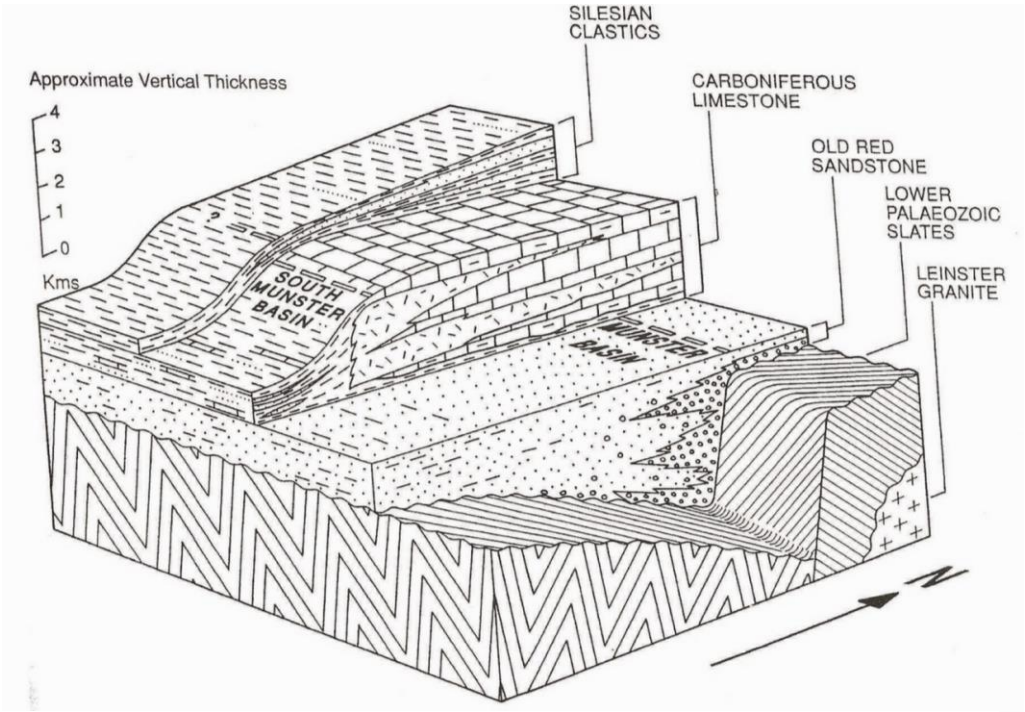

Figure 6. 19 Schematic for sedimentation patterns in the Munster Basin (from Keeley, 1996).

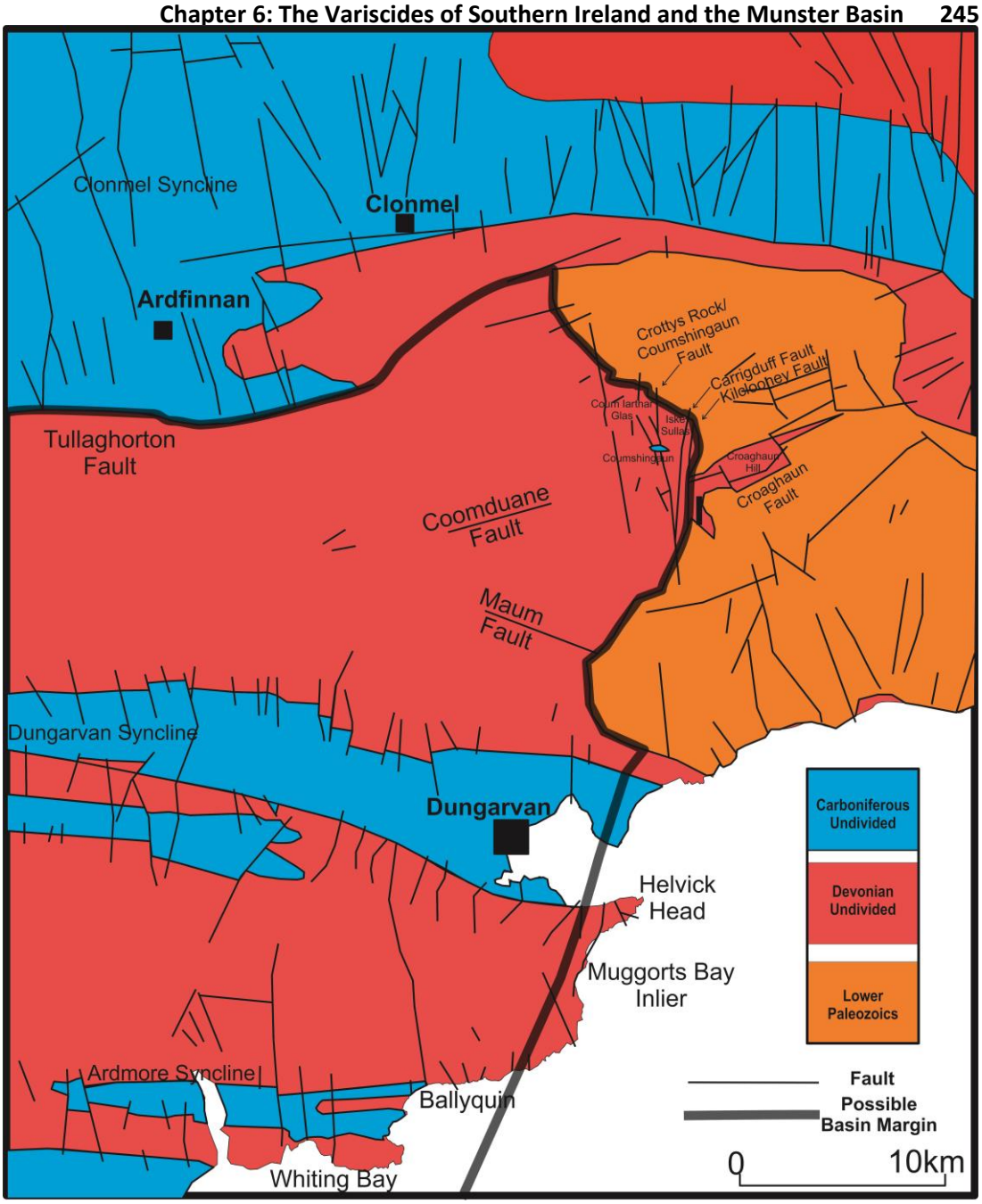

Figure 6. 20 Main lithologies and structures of the eastern Munster Basin. Major structures are reproduced from Sleeman and McConnell (1995) while faults from the Comeragh Mountain area are reproduced from Capewell (1957) and Penney (1980).

6.6.1. Lithologies of the East Munster Basin

6.6.1.1. Old Red Sandstone Successions

The Devonian Old Red Sandstone of East Munster is divided into four successions (Figure 6. 21): the Galtee Mountain Succession, the Slievenamon-Portlaw Succession, the Comeragh Mountain Succession and the East Cork Succession (Sleeman and McConnell, 1995). The Galtee Mountain Succession is interpreted to

be a proximal alluvial fan sequence derived from the north (Sleeman and McConnell, 1995). This succession lies outside of the study area and will not be discussed in detail. The Slievenamon-Portlaw Succession is exposed north of the Comeragh Mountain range on the flanks of Slievenamon and the Portlaw area and it has been interpreted as an extra-basinal sequence. The Comeragh Mountain Succession has been interpreted to be an alluvial fan sequence, with basal conglomerate clasts derived from a Lower Palaeozoic source to the east. The East Cork Succession represents central basin deposits and is characterised by finer grained lithologies (Sleeman and McConnell, 1995).

6.6.1.2. The Slievenamon-Portlaw Succession

The Slievenamon-Portlaw Succession is limited to the north and east of the Comeragh Mountain range. This extra-basinal sequence has three main formations: the Coumshingaun Formation, the Carrigmaclea Formation and the Kiltorcan Formation. The Coumshingaun Formation in this succession is only present as a very thin bed of conglomerates overlying the Lower Palaeozoic (Penney, 1980; Sleeman and McConnell, 1995). The Carrigmaclea Formation is composed of quartz conglomerates and coarse to pebbly sandstones (Sleeman and McConnell, 1995). This formation was deposited in a braided stream environment (Sleeman and McConnell, 1995). Similar to the Coumshingaun Formation in this area it is quite thin and poorly exposed (Sleeman and McConnell, 1995). The Kiltorcan Formation is characterised by a thick sequence (525m) of white to yellow sandstones Slievenamon-Portlaw Succession (Penney, 1978; Murphy, 1985; Sleeman and McConnell, 1995).

6.6.1.3. The Comeragh Mountain Succession

The Comeragh Mountain Succession is the thickest sequence of Old Red Sandstone in the East Munster Basin and is largely dominated by conglomerate formations. The main lithologies in the area are the Coumshingaun Conglomerate Formation, the Comeragh Conglomerate Sandstone Formation, the Nier Group and the Kiltorcan Formation (Capewell, 1957; Penney, 1980). The deposition of these sequences was largely fault controlled, furthermore their deposition was a on a steep eastward rising Lower Palaeozoic surface (Capewell, 1957; Penney, 1980).

The 850m basal conglomerates of the Coumshingaun Group were deposited as an alluvial fan that displays an upward coarsening trend, representing a response to uplift in the source area to the east (Penney, 1980; Sleeman and McConnell, 1995). The overlying sequences were deposited as a fan-margin sequences of braided stream sediments, terminal alluvial fan systems and their associated floodplain sediments (Sleeman and McConnell, 1995). The unconformable contact between the Coumshingaun Formation and the underlying Palaeozoic typically features a breccia of Lower Palaeozoic slate fragments in the base of the Coumshingaun Formation (Penney, 1980). The Lower Palaeozoic volcanic, intrusive and sedimentary clasts of the Lower Coumshingaun Formation suggest that the source of this material was immediately to the east (Capewell, 1956). Two mica- granite and tourmaline bearing clasts in the upper parts of the formation suggest gradual increase in provenance range (Capewell, 1957). They have been inferred to have been deposited in a piedmont setting to the west of a Palaeozoic basement high in the east. The contact between them is either unconformable as mentioned above,

or faulted As a result the exact relationship between the ORS sequences and the Palaeozoic basement is not always clear.

The sequence rapidly thins out towards the north, west and south of the main N-S fault between Coumshingaun and Croaghaun (Capewell, 1956; Penney, 1980). Penney (1980) interpreted the northward thinning to mark the location of the northern margin of the Munster Basin, between Glenpatrick and Slevenamon. The southward thinning of the Coumshingaun and Treanearla Formations becomes well marked south of the Maum Fault towards the cliff section at Ballyvoyle (Penney, 1980), possibly alluding to the significance of this fault, whilst the compact sequence exposed at Ballyvoyle is thought to represent an area of extreme thinning as an out of basin sequence. Westward thinning of the conglomerate units is more gradual and accompanied by the overlap of the Nier and Kiltorcan Formations.

Overlying the Coumshingaun Formation is the Comeragh Conglomerate-Sandstone Group, which is divided into the Coumaraglin Formation, the Treanearla Formation, the Sheskin Formation and the Kilnafrehan Formation (Sleeman and McConnell, 1995). The Coumaraglin Formation only outcrops in the Coumaraglin area and is characterised by coarse-medium grained green sandstones, with a significant percentage of feldspar clasts (Sleeman and McConnell, 1995). The Treanearla Formation conformably lies on the Coumshingaun Formation and is composed of thick-bedded conglomerates and matrix supported conglomerates (Penney, 1980; Sleeman and McConnell, 1995). The Sheskin Formation overlies the Treanearla Formation and is comprised of interbedded conglomerates, sandstones and siltstones that largely fine upwards (MacCarthy et al., 1978; Sleeman and

McConnell, 1995). The overlying Kilnafrehan Formation is composed of red conglomerates and sandstones (Sleeman and McConnell, 1995).

In the Croaghaun area of the Comeragh Mountains a conglomeratic formation, similar to the Comeragh Group, the Croaghaun Formation is exposed (Capewell, 1957; Penney, 1980). The relationship of this formation to surrounding formations is debatable. Penney (1980) argued that the formation was a lateral equivalent of the Comeragh Group, while Capewell (1957) argued that the Croaghaun Formation was older than the Comeragh Group. Similarly Gardiner (1983) suggested that the Croaghaun Formation could represent an earlier Devonian basin that had been inverted. The main difference between this formation and the surrounding Comeragh Group is that it is dominantly green and is folded around a north-south axial trend rather than the usual east west Variscan trend (Penney, 1980).

The Comeragh Group is succeeded by the overlying Nier Group and Kiltorcan Formation. The Nier Group is dominantly composed of purple silty sandstones and is divided into the Ballytrasna and Knockmealdown Formations (Capewell, 1957).

The Ballytrasna Formation is typically present as a red sandstone but contains large amounts of quartz pebbles (Sleeman and McConnell, 1995). Similarly the Knockmealdown Formation is dominantly red sandstone with conglomerates at the base (Sleeman and McConnell, 1995).

In the Comeraghs the Kiltorcan Formation is characterised by a large amount of feldspathic material, interpreted by Penney (1980) to coincide with the unroofing of the Leinster Granite. The Kiltorcan has a largely consistent thickness across the area, which Sleeman and McConnell (1995) inferred to suggest that there was little or no fault influence active during its deposition. The Kiltorcan is largely comprised

of cross-stratified sandstone units with upward fining sequences deposited in high sinuosity single channel river systems (Murphy, 1985).

6.6.1.4. The East Cork Succession

The East Cork Succession occurs south of the Dungarvan Syncline. It is divided into the Gortanamill Formation, the Ballytrasna Formation and the Gyleen Formation. The Gortanamill Formation is composed of green fine sand and siltstones deposited in a fluvial distributary system (Sleeman and McConnell, 1995). In the East Cork Succession the Ballytrasna Formation is dominantly composed of red sandstones and much finer than in the Comeragh Succession (Sleeman and McConnell, 1995). The Gyleen Formation is dominantly mudstones with occasional sandstones and is characterised by fining upward sequences (MacCarthy, 1978). Additionally it has been interpreted to be equivalent to the Kiltorcan Formation in the north (Sleeman and McConnell, 1995).

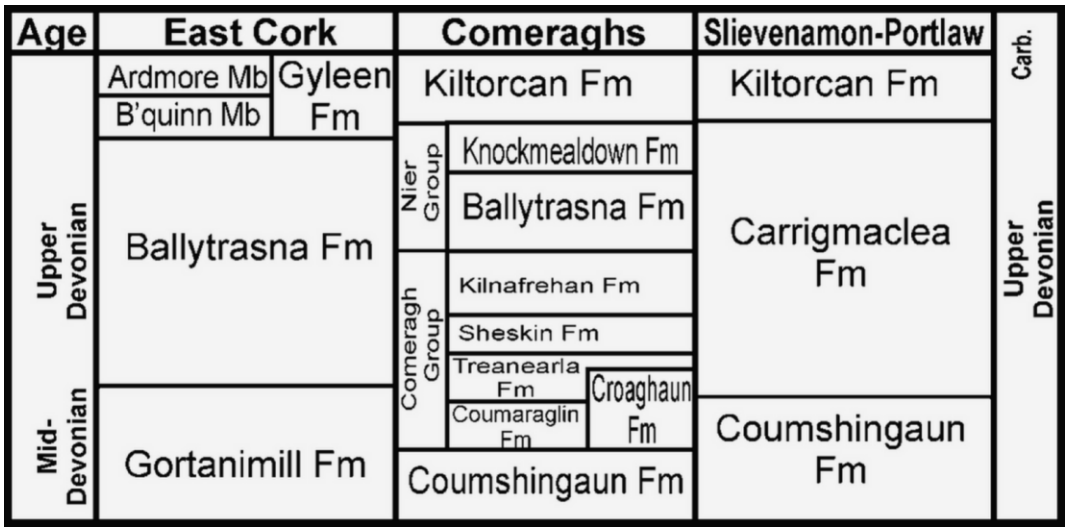

Figure 6. 21 Old Red Sandstone successions of the East Cork and Waterford area, redrawn from Sleeman and McConnell (1995).

6.6.2. Lower Carboniferous

In the North Munster Shelf the Lower Carboniferous exhibits widespread lateral variation (Figure 6. 22; Sleeman and McConnell, 1995), but the only unit relevant to this study is the Crows Point Formation.

6.6.2.1. Crows Point Formation

The Crows Point Formation is a thick-bedded, coarse and pebbly sandstone that lies near the base of the Carboniferous, overlying the Castle Slate Member. It only outcrops between Youghal and Helvick Head. In the Ardmore area the formation is characterised by thin quartz pebble conglomerate layers (Sleeman and McConnell, 1995). The pebble clasts are typically between 1 and 3cm. This unit has largely been interpreted to have been deposited in an estuarine fluvio-tidal environment (MacCarthy, 1979; Murphy, 1985). Additionally the sediment source for the Crows Point is in the east from Lower Palaeozoic material, but it also features considerable reworking of material (Murphy, 1985).

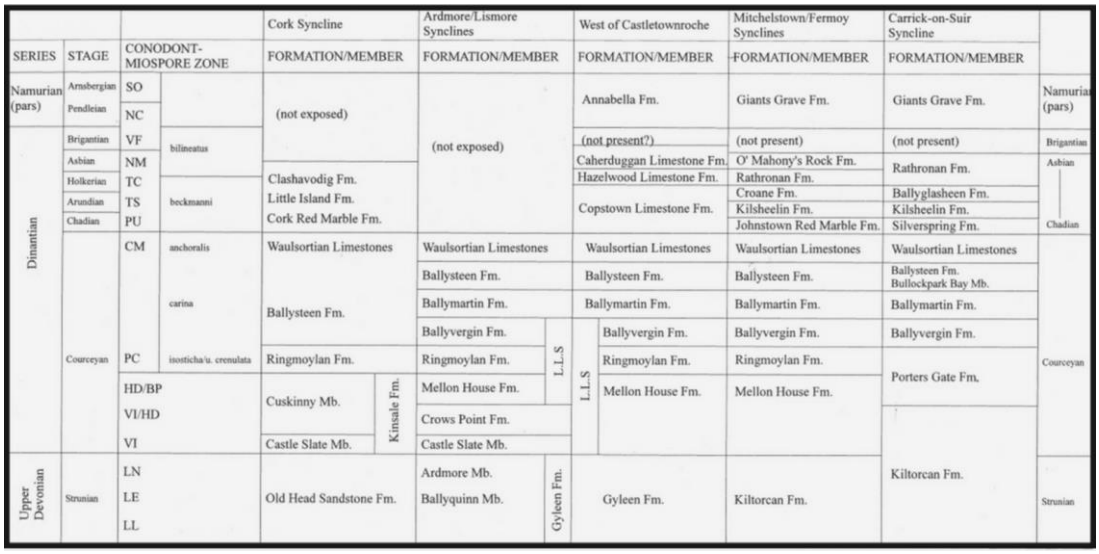

Figure 6. 22 Carboniferous divisions in East Cork and Waterford according to Sleeman and McConnell (1995).

6.6.3. Structures in the eastern Munster Basin Area

The eastern Munster Basin is characterised by large scale open folding and high angle faults, unfortunately due to poor exposure exact relationships have not been defined.

6.6.3.1. Regional Fold Patterns

Regional folding in the area has a relatively simple pattern with three major fold anticlines striking east-west present in the area: the Watergrasshill, Knockmealdown and Galtee Mountain Anticlines (Sleeman and McConnell, 1995).

The Galtee Anticline is a large open structure, whereas increasingly tighter and steeper minor folds are present towards the south, such as the westward plunging Knockmealdown and Watergrasshill Anticlines. A similar decrease in fold amplitude is seen from west to east, evidenced in the Knockmealdown Anticline where folds become increasingly more open in the Comeragh Mountains than in the Knockmealdown Mountains.

6.6.3.2. Fault Populations

The main faults in the area can be divided into three groups: a N-S group, a WNW-ESE group and an ENE-WSW group (Capewell, 1957). The N-S trending group is the most prevalent across the area. These faults are best exemplified by the Coumshingaun Fault and the Kilclooney/Carrigduff Fault (Figure 6.20). The Coumshingaun Fault is a sub-vertical fault that extends from Crottys Rock to Fauscoum. It has a minimum westward downthrow of 120m and merges with the Carrigduff Fault south of the Mahon River (Capewell, 1957). It is possible that the majority of these N-S faults are splays of the main bounding fault of the eastern

margin of the Munster Basin, the Carrigduff Fault. It is argued here that this fault continues as far south as Ballyvoyle if not as far as Helvick Head.

The WNW-ESE group are best exposed in the south of the Comeraghs (Capewell, 1957), namely the Maum Fault and a series of smaller faults in Coumknockmahon, as well as some other small faults in the Coum Iarthar Glas. These faults closely parallel the faults and fold axes seen in the Dungarvan Syncline.

The ENE-WSW group become more dominant towards the north of the Comeraghs (Capewell, 1957). These faults are steep to sub-vertical and parallel the inferred trace for the northern margin of the Munster Basin, as well as the dominant structural trend of the Lower Palaeozoic basement (Mc Ardle et al., 1981).

6.6.3.3. Cleavage

Penetrative deformation in the Munster Basin is largely restricted to a single pervasive cleavage that is typically perpendicular to bedding and parallel to fold axial planes (Bresser and Walter, 1999; Capewell, 1956; Cooper and Collins, 1984a; Cooper et al., 1986; Naylor, 1978b; Naylor et al., 1981). Meere et al. (2013) reported cleavage from the South Munster Basin that dipped steeply parallel to the axial plane in mudstones and a less steep cleavage that converges towards the axial plane in coarser sandstones. This pattern of cleavage development was interpreted as the result of significant layer-parallel shortening prior to the onset of regional folding. Similarly cleavage morphology (Engelder and Marshak, 1985; Powell, 1979) varies depending on lithology, with a continuous penetrative cleavage in fine grained lithologies and a spaced disjunctive cleavage in coarser lithologies (Bresser and Walter, 1999; Naylor et al., 1981). Cleavage has generally been described as a pressure solution cleavage (Bresser and Walter, 1999; Cooper and Collins, 1984a;

Cooper et al., 1986; Meere et al., 2013; Naylor et al., 1981; Nenna and Aydin, 2011; Sanderson, 1984), with minor authigenic mica growth focused in the cleavage planes (Bresser and Walter, 1999). The microlithons between the phylosillicate rich cleavage domains are typically quartz rich (Murphy, 1985).

Cleavage development has usually been described as an early (pre-folding) event (Coe and Selwood, 1963; Cooper et al., 1986, 1984; Ford, 1987), but there has been some debate as to whether cleavage development continued syn-folding (Trayner & Cooper, 1984; Price 1986; Meere, 1992) or whether there were multiple cleavage forming events and polyphase deformation in the South Munster Basin (Gill, 1962; Selwood, 1963). Polyphase deformation was interpreted from cleaved diorite sills that cross cut folds (Coe and Selwood, 1963; Coe, 1966), although these have been interpreted as syntectonic intrusions emplaced during one continuous deformation regime, due to the lack of two distinct cleavages in the field (Sanderson, 1984). Similarly Capewell (1975) described only one compressional episode and only one cleavage. Murphy (1985) reported particularly low angles between bedding and cleavage in fine grained lithologies on fold limbs in the Dungarvan and Lismore area, and attributed this to continuous cleavage formation throughout LPS and folding. This orientation of cleavage with respect to bedding is not observed in the coarser units, suggesting that this intense reorganisation of cleavage in the finer grained lithologies is probably largely due to flexural slip folding, but does not rule out syn-folding cleavage development. Cleavage development synchronous with folding has been proposed by some authors (Price, 1986; Meere, 1992; Meere et al., 2013). LPS and the resulting cleavage formation have been interpreted from extensive field work to form prior to or at the early stages of folding, with cleavage

typically at high angles to bedding (Figure 6. 24; Cooper et al., 1986). Trayner and Cooper, (1984) argued that the presence of sheared cleavage is suggestive of cleavage development during initial stages of folding. Cleavage parallel shearing has been described by Bresser and Walter (1999) and attributed to a late stage dextral strike slip component.

The deformation sequence in the South Munster Basin has been split into three phases by Meere et al. (Figure 4.24; 2013):

Phase one is represented by an early phase of LPS and development of a slaty cleavage orthogonal to bedding in mudstones and a more disjunctive spaced cleavage in sandstones.

LPS continues in Phase two, with initial cleavage domains becoming concentrated at regularly spaced intervals into wider disjunctive dissolution zones in sandstones.

Phase three includes the onset of folding and rotation of the stratigraphy. As folding develops, the cleavage domains in the sandstones are preferentially exploited by high-angle reverse shear.

Sanderson (1984) described sutured boundaries between quartz clasts, with occasional fibrous quartz/chlorite/mica pressure fringes, and attributed this deformation to pressure solution controlled diffusion creep. Beach and King (1978) discussed the extensive marginal solution of quartz clasts in cleavage domains and considerable recrystallisation of a fine clay matrix to white mica in cleavage domains in the Caha Mt. Formation. Similarly Sanderson (1984) described sutured boundaries between quartz clasts, with occasional fibrous quartz/chlorite/mica pressure fringes, and attributed this deformation to pressure solution controlled

diffusion creep. Beach and King (1978) inferred that the reactions involved in the pressure solution involved transformation of chlorite and a fine clay matrix to white mica. The transformation of chlorite consumes silica, reducing quartz in the cleavage domain, while the fine clay to mica reaction releases silica, this released silica typically is removed from the cleavage domain by diffusive transfer, resulting in an overall loss of silica from the cleavage domains (Beach and King, 1978). It is important to note that both reactions cause a 15-35% decrease of volume of the minerals (Beach and King, 1978).

Field evidence suggests cleavage intensity generally decreases northwards towards the Dingle Dungarvan Line (Murphy, 1990. Furthermore cleavage intensity observed in the Crows Point Formation appears to decrease on an eastward trend from Whiting Bay towards Ballyquin. This eastward decrease may suggest a basin boundary control on cleavage development, with the Ballyquin exposures thought to sit at the basin margin or just external to the basin. Their position on the basin margin may be further supported by the extensive shearing deformation that cross-cuts and deforms the Variscan cleavage. This localised late stage shearing could support Sanderson's (1984) transpression model with complex deformation at the basin margins. These minor shear zones appear to be conjugate (Figure 6.25 and Figure 6.26) and are characterised by ductile realignment of clasts that were originally aligned in an east-west cleavage (Figure 6.25 and Figure 6.26). The conjugate pairs imply continued north-south compression. Within the shear zones quartz pebbles are stretched and flattened, whereas in the cleavage planes pebbles maintain their rounded near spherical shape. This ductile deformation of Variscan cleavage might be indicative of late stage deformation, possibly associated with

fault movement. The conjugate shear planes are themselves overprinted by apparently conjugate, brittle-ductile curved tension gashes. Similar curved tension gashes are also present in the Whiting Bay exposures.

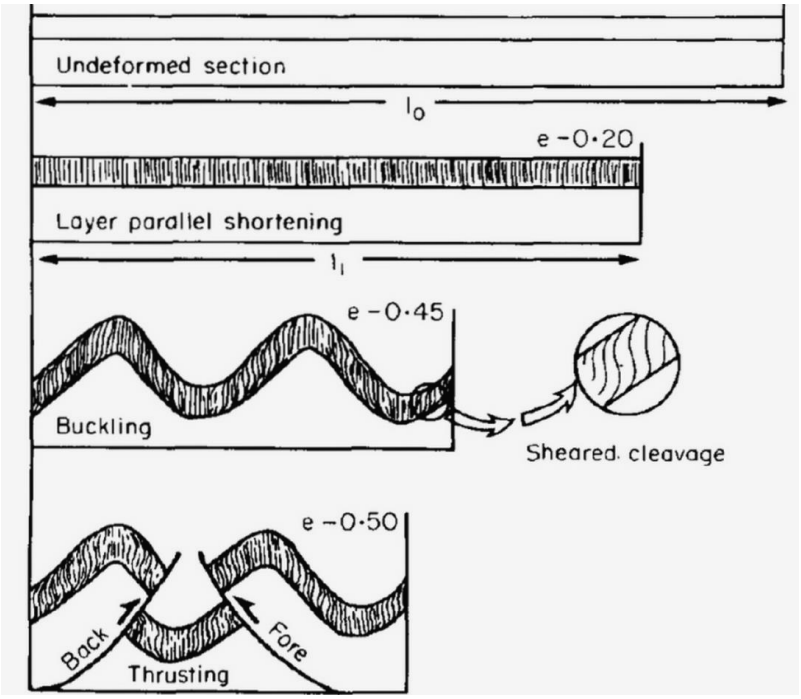

Figure 6. 24 Deformation sequence of the Irish Variscides from Cooper et al. (1986).

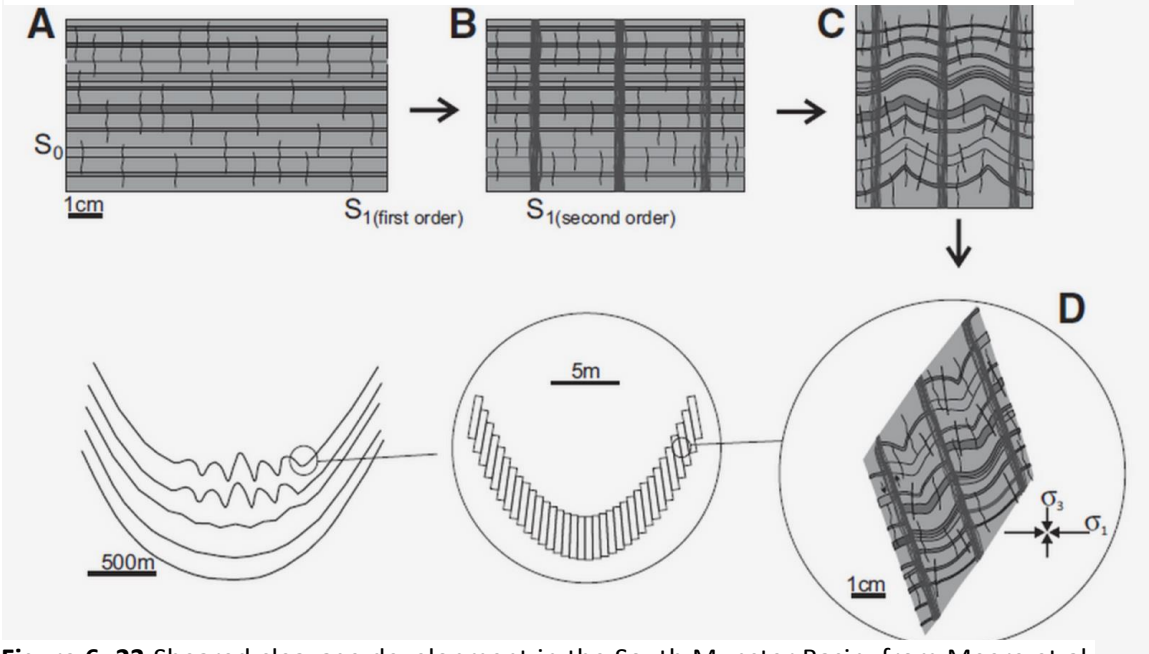

Figure 6. 23 Sheared cleavage development in the South Munster Basin, from Meere et al. (2013). A Initial cleavage development. B. Development of cleavage domains. C. Buckling and compressional faulting of cleavage domains. D. Regional and outcrop scale folding, leading to reverse simple shear along cleavage planes.

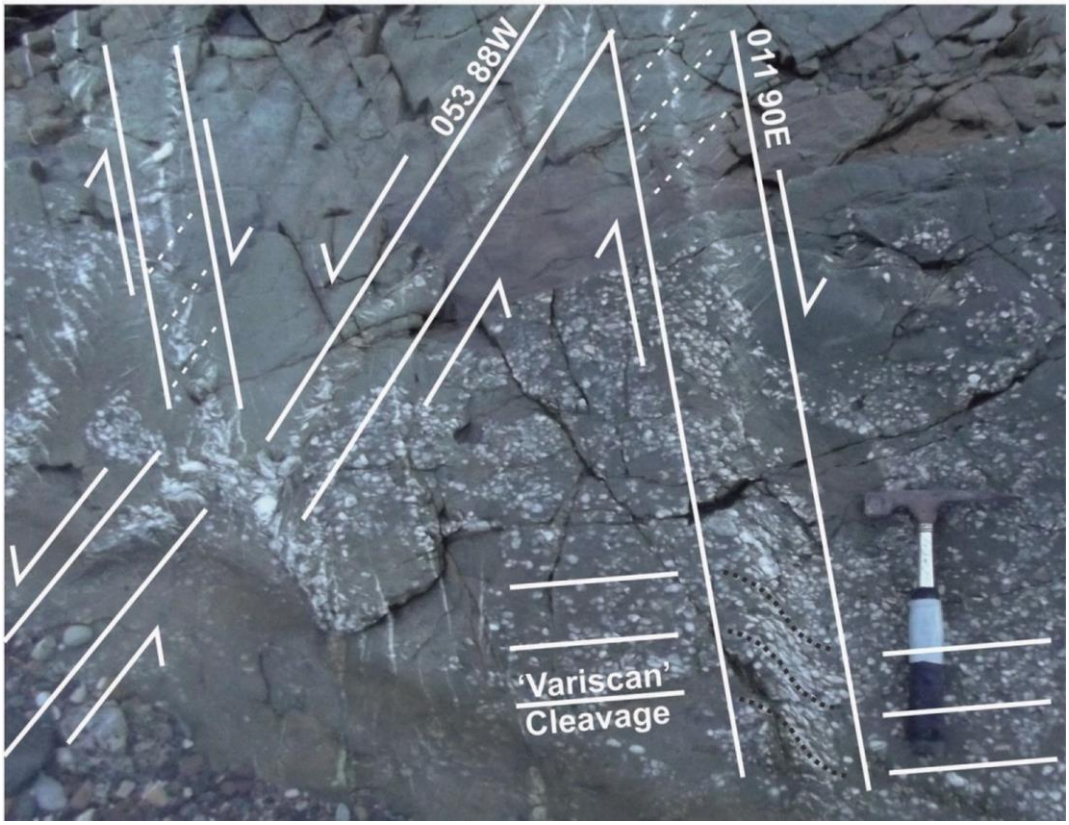

Figure 6. 25 Overview of shearing at Ballyquin. N51 58.324 W7 42.147.

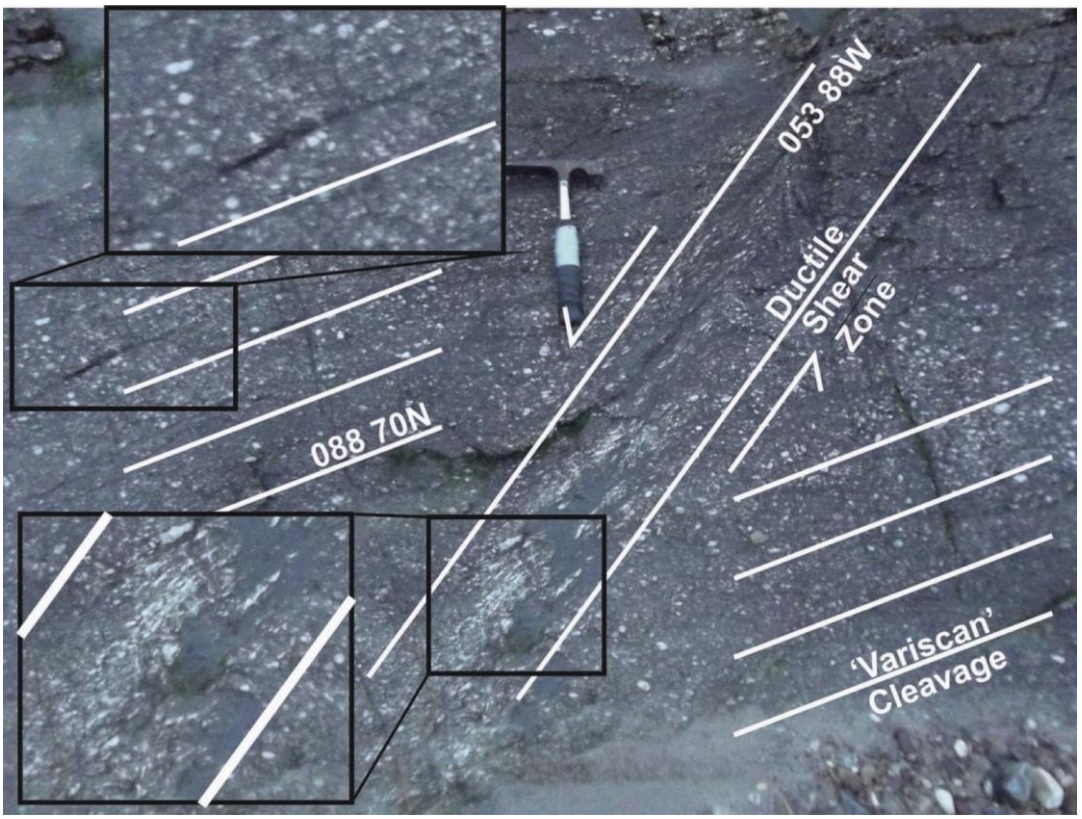

Figure 6. 26 Sinistral shear zone at Ballyquin, with clear deformation and reorientation of 'Variscan Cleavage'. N51 58.324 W7 42.147.

North of the Dungarvan syncline cleavage is generally less intense than to the south, but there is an cleavage intensity increases from the Coumfea area of the Comeragh Mountains towards the Clonmel Syncline (Figure 6.20). Furthermore the style of cleavage is quite different from the tightly spaced and occasionally sheared cleavage of the southern Munster Basin to a more spaced disjunctive cleavage and a realignment of clasts in coarse sands and conglomerate units. This cleavage does not appear to be present north of the Comeragh Mountains.

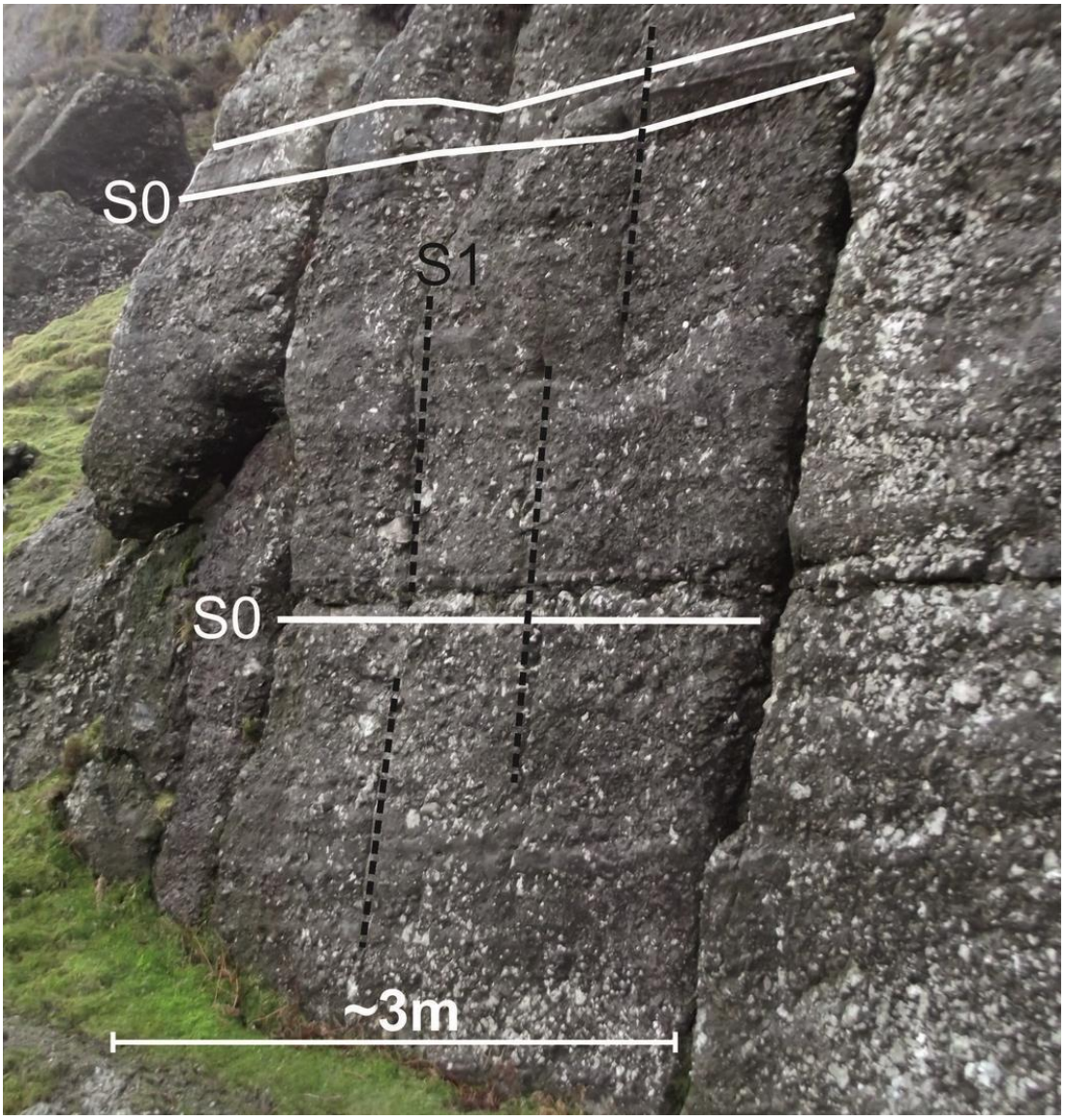

Figure 6. 27 Cleavage bedding relationships in Coum Mahon. N52 13.579 W7 32.664.

Figure 6. 28 Bedding/cleavage relationships in Coumshingaun. N52 14.915 W7 30.960.

Figure 6. 29 Bedding in the Slievenamon area, despite tectonic folding of beds there is no trace of a penetrative tectonic fabric. N52 20.477 W7 27.601.

A similar distribution of deformation is observed on a microstructural scale, with the most intense deformation textures observed in the Whiting Bay area and no observed microstructural deformation in the Slievenamon area.

Quartz clasts in the Whiting Bay area exhibit a range of microstuctures from grain boundary bulging to dominantly sub-grain rotation with minor occurrences of grain boundary migration (Figure 6. 30). In the conglomerates of the Comeragh Mountains despite relatively strong realignment of grains, quartz clasts display minor grain boundary bulging and the lithic clasts appear largely undeformed with the exception of pressure solution seams that are largely parallel to cleavage (Figure 6. 31 and Figure 6. 32). North of the Comeraghs the ORS units of the Slievenamon area exhibit no microstructural evidence of tectonic deformation (Figure 6. 33).

Figure 6. 30 Microstructures observed in the Crows Point Formation from Whiting Bay. Grain boundary bulging (BLG) and sub grain rotation (SGR) appear to be the dominant deformation mechanisms. Image is approximately 2mm across.

Figure 6. 31 Microstructures observed in a sandy unit from Coumshingaun. A weak pressure solution cleavage is observed, which appears to deform the matrix and lithic clasts equally. Image is approximately 2mm across.

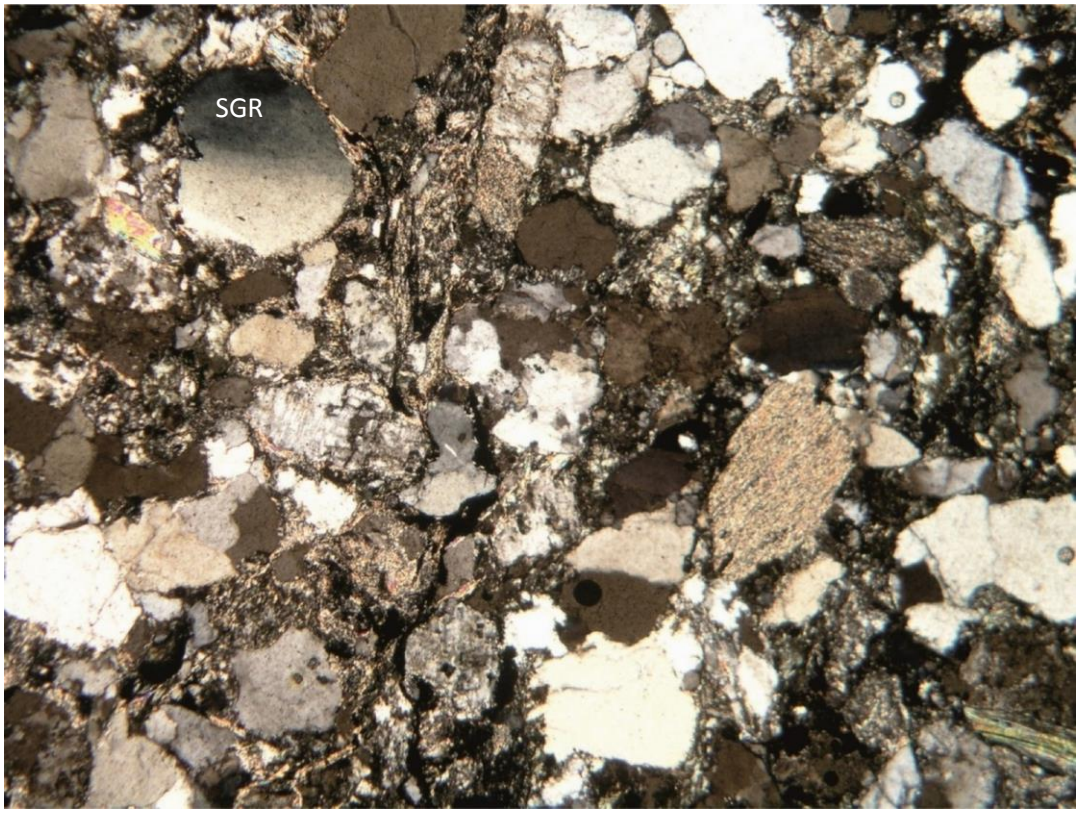

Figure 6. 32 Microstructures observed in the Comeragh Conglomerate in the Knocknafrinn area in the northern Comeraghs. Quartz grains have been deformed by minor amounts of sub-grain rotation and grain boundary bulging. Image is approximately 2mm across.

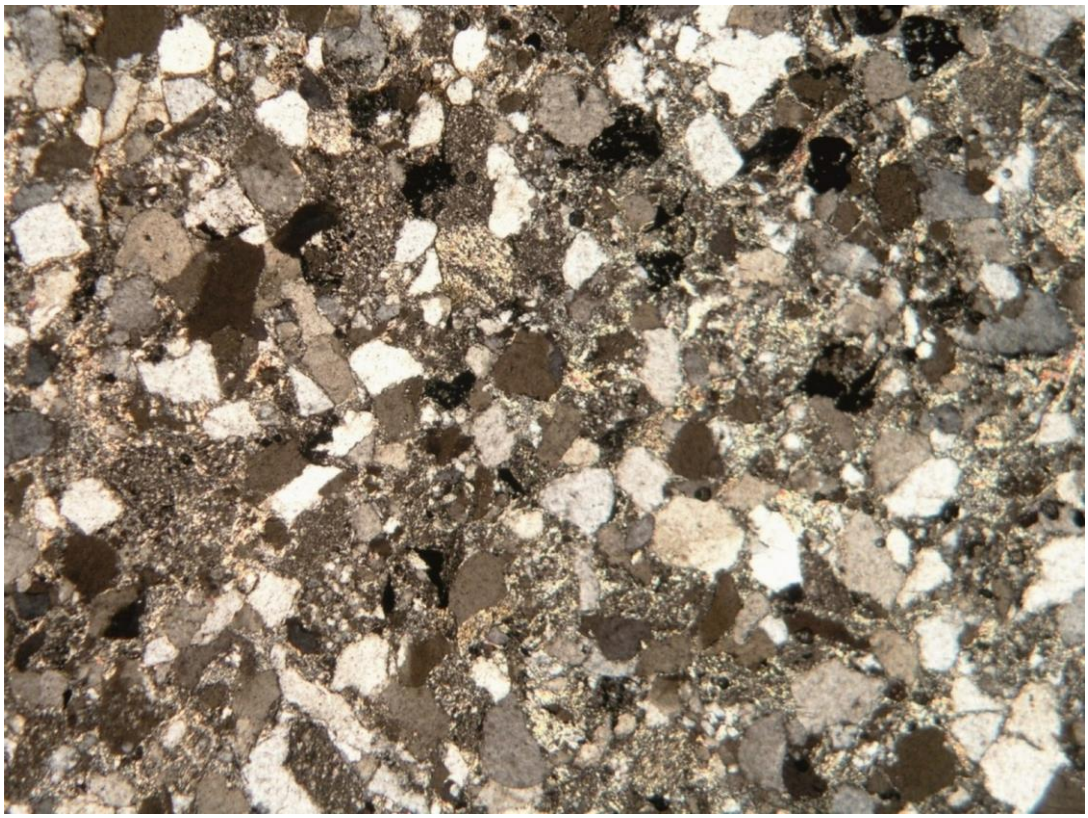

Figure 6. 33 Microstructures observed in the Slievenamon area . No deformation of grains or a preferred fabric is visible . Image is approximately 2mm across.

6.7. AMS and Strain Analysis

Oriented block samples for AMS and strain analysis were collected from sites along the eastern margin of the Munster Basin, as well as sites that were out of the basin. This sampling distribution allows investigation into the strain distribution across basinal, marginal and extra-basinal lithologies. The samples for this study were taken from the Comeragh Mountain Succession, the Slievenamon-Portlaw Succession and the East Cork Succession as well as the Crows Point Formation of the Lower Carboniferous. Only outcrops with well-defined structural relationships bedding, cleavage, etc. were sampled. Additionally lithologies with complex sedimentary fabrics, such as syn-sedimentary deformation, burrowing, cross bedding etc. were avoided, as these might add further complexities to the relationship between bedding and tectonic fabrics. Strain and AMS data and was obtained from 26 and 19 sites respectively

Strain analysis was carried out using the DTNNM and MRL methodologies described in Chapter 2 on three mutually perpendicular thin sections from each sample. Detailed strain analysis of this kind allowed for the development of 3D strain ellipsoid models using Mathematica.

On average 8-14 core samples, measuring 25.4mm in diameter and 22mm in length, were drilled from each block sample. Out of the 30 block samples collected, 19 samples survived drilling and provided enough sub specimens to be statistically viable. This yielded 230 individual cores for analysis. AMS analyses were carried out using methods described in chapter 3. Additionally high temperature low field magnetic susceptibility measurements were carried out to clarify the magnetic source.

6.7.1. High-Temperature Low Field Magnetic Susceptibility

The high temperature, low-field susceptibility measurements were made using a CS4 furnace attachment for the Agico MFK1-A Kappabridge. The experiment involves taking susceptibility measurements during a stepwise heating/cooling (from 25°C to 700°C) of individual powdered samples. This experiment provides an evaluation of the magnetic carriers in a sample, by interpreting Curie Point data. The Curie Points of ferromagnetic minerals, which are highly sensitive to temperature, represent the point where super-exchange coupling forces breakdown due to heating (Dunlop and Özdemir, 1997). This causes the spontaneous magnetic ordering that characterises ferromagnetic minerals to cease and they then behave super-paramagnetically (this effect ceases once the sample is cooled below the Curie Point). Therefore heating of a ferromagnetic mineral creates an increase in its bulk susceptibility until the Curie Point is reached and then all ferromagnetic behaviour is essentially removed. The temperature at which this occurs is dependent on composition of the mineral. The Curie Points of some pure ferromagnetic minerals include magnetite 580°C (this temperature decreases linearly with increasing Ti content), hematite 675°C, pyrrhotite 310°C, and greigite 330°C (Dunlop and Ozdemir, 1997). Conversely paramagnetic minerals decrease in susceptibility during heating, whereas diamagnetic minerals are not affected by temperature changes. This allows the three magnetic behaviours to be identified by examining the overall morphologies of the heating-cooling curves (Dunlop and Ozdemir, 1997). Not only can these experiments provide information about the particular minerals in a sample, the grainsize of ferromagnetic minerals can be estimated using the shape of the Hopkinson Peak (Dunlop and Ozdemir, 1997). The

Hopkinson Peak can be identified by either a convex bump or a positive slope in anisotropy immediately prior to the Curie Point (Liss et al., 2004). Narrow abrupt peaks represent single domain grains while mixed or multi-domain grains are represented by a smoother peak (Dunlop and Ozdemir, 1997). Heating may lead to new mineral growth during the experiment, which can affect the susceptibility of the sample and is usually identified by non-reversibility of the cooling curve.

The location of samples used for Curie Point experiments are shown in Figure 6. 34, and their heating and cooling profiles are shown in Figures 6.35 & 36. All of the samples presented have irreversible cooling curves indicating phase changes during the experiments. All samples, with the exception of BB11, show a relatively well defined Hopkinson Peak between 528-570°C. This is indicative of the Curie Point of magnetite (Curie points of the most important minerals are listed in Table 6.1), with varying amounts of Ti. With the exception of BB1, the Hopkinson Peaks are represented by abrupt spikes prior to sudden decreases in susceptibility, suggesting the presence of SD magnetite grains. BB12 features a more gradual sloping Hopkinson Peak, suggestive of MD magnetite. Samples BB12, BB13 and BB6 also display a smaller similar peak between 657-670°C, suggestive of the hematite Curie Point. The distinctly different heating curve shown by BB11 is interesting considering the uncertainty regarding the origin of the Croaghaun Formation.

BQB1 and BQB2, taken from the Crows Point Formation at Ballyquin, have the most pronounced Hopkinson Peaks, between 540-580°C, again suggesting the presence of SD magnetite grains, but of a higher percentage than the other samples. Additionally they both have minor increases in susceptibility between 262-303°C. This is representative of a monoclinic pyrrhotite Curie Point (Dunlop and Ozdemir,

2001). Pyrrhotite is not normally found in sedimentary sequences, but could be derived detritus from exhumed metamorphic basement rocks (Horng and Roberts, 2006). The Crows Point Formation represents a distinct change to an eastern source of sediment deposited fluvio-tidal sequence at the base of the Carboniferous. This change in provenance might explain the different heating curves.

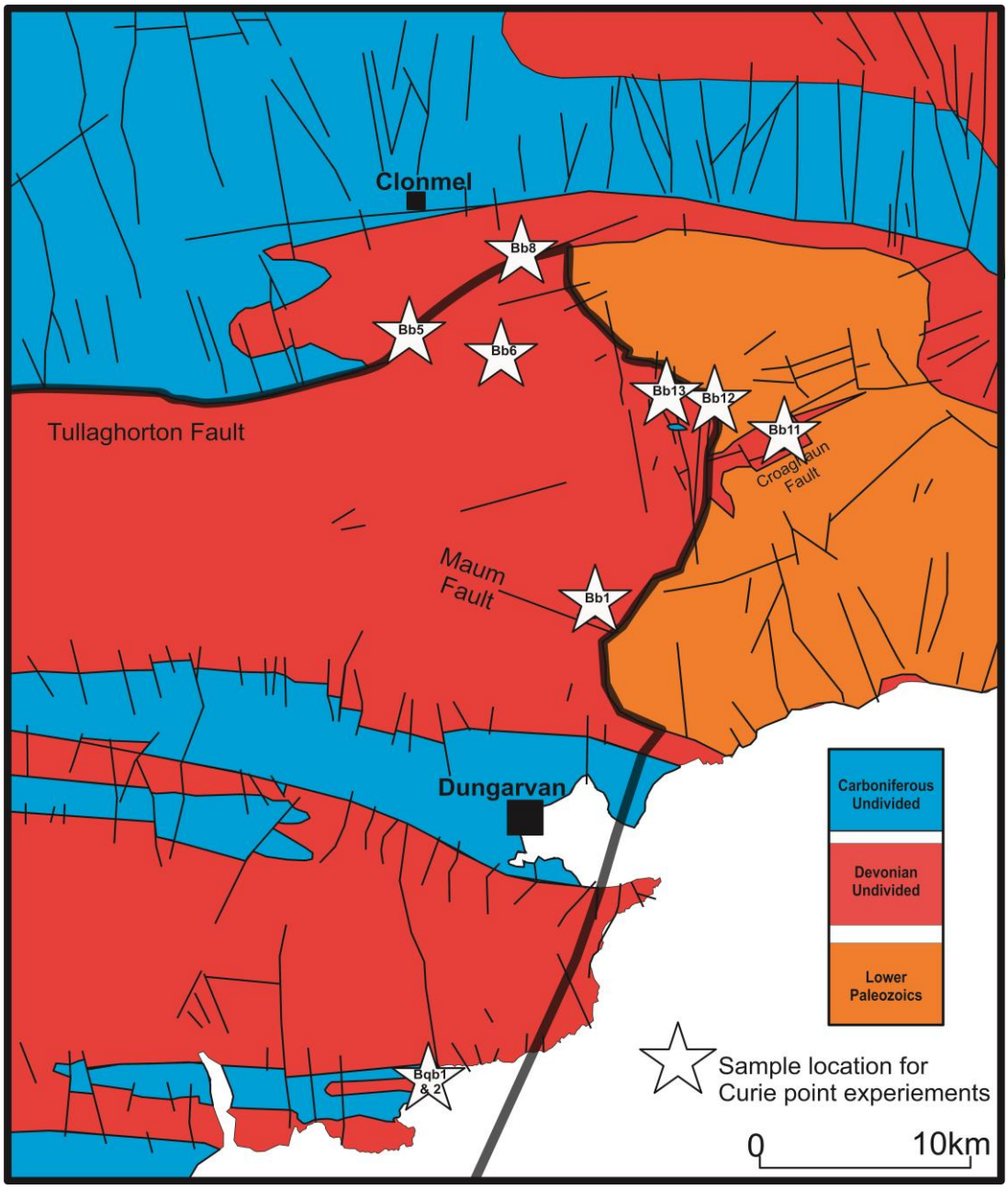

Figure 6. 34 Location of samples used for Curie Point experiments.

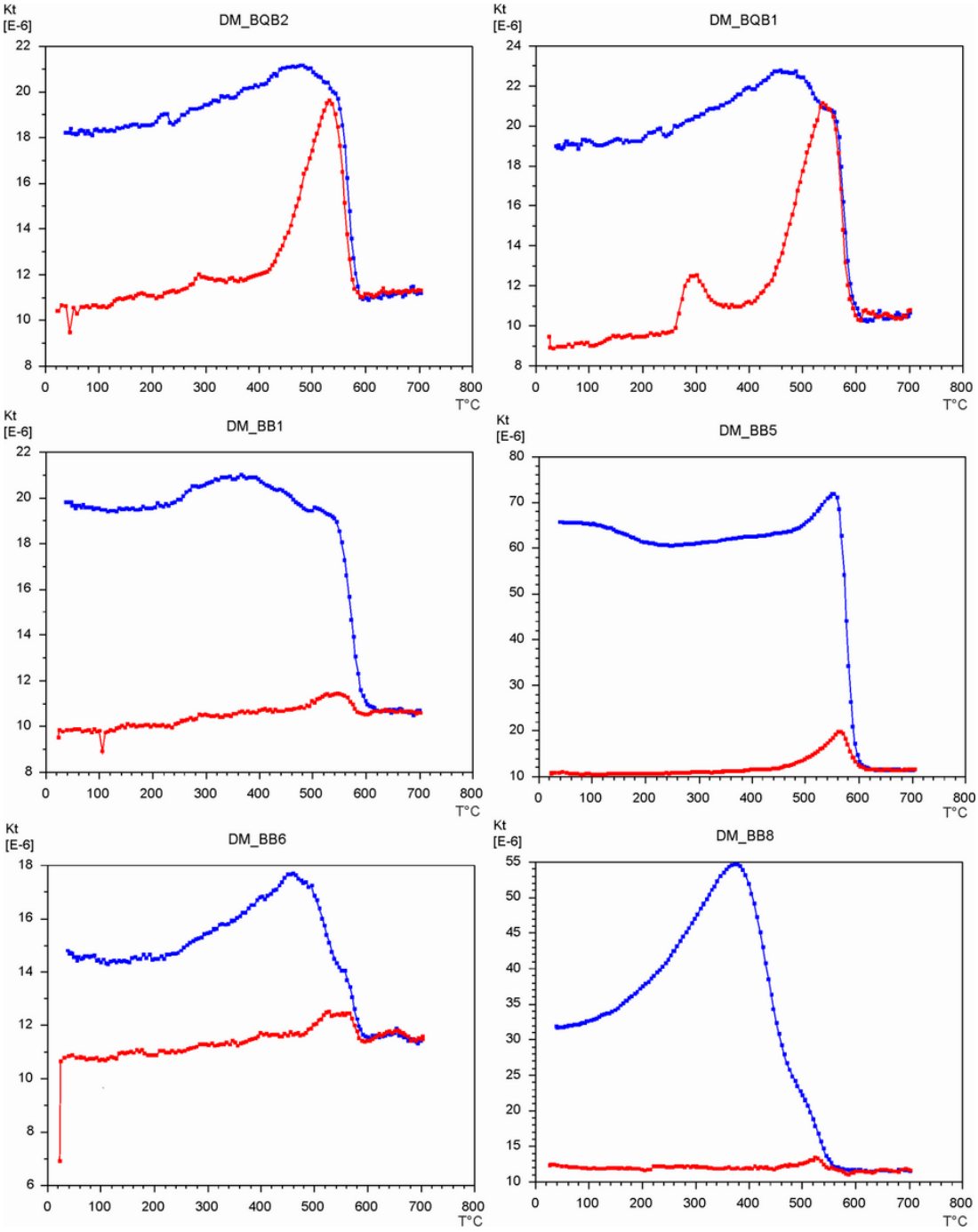

Figure 6. 35 Heating and cooling curves for samples shown in the previous figure. The heating and cooling curves are represented by the red and blue lines respectively.

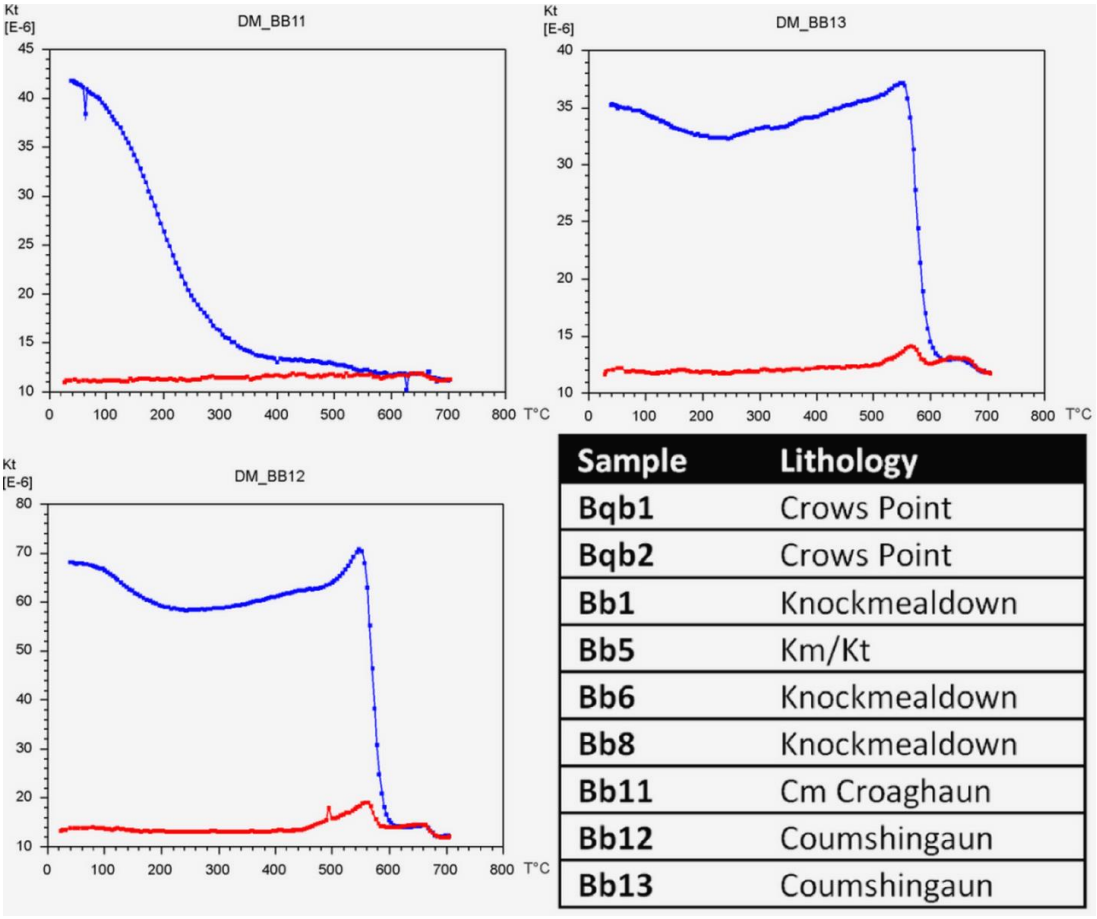

Sample	Lithology
Bqb1	Crows Point
Bqb2	Crows Point
Bb1	Knockmealdown
Bb5	Km/Kt
Bb6	Knockmealdown
Bb8	Knockmealdown
Bb11	Cm Croaghaun
Bb12	Coumshingaun
Bb13	Coumshingaun

Figure 6. 36 Heating and cooling curves and sample list with lithologies.

Mineral	Curie Temperature (°C)
Magnetite	580
Maghemite	590-675
Titano-Magnetite	150
Hematite	675 (Neel temp)
Pyrrhotite	Mono 270 / Hex 325
Greigite	333

Table 6. 1 Table of important magnetic mineral Curie Point temperatures.

6.7.2. AMS Results

Bulk susceptibility for all specimens varies from $2.07X10^{-6}$ to $1.6X10^{-3}$, and an average of $5.11X10^{-4}$. Bulk susceptibility for mean samples varies from $3.25X10^{-5}$ to $8.99X10^{-5}$, with an average of $4.32X10^{-4}$. These values in conjunction with the Curie Point experiments suggest that the AMS fabrics are dominated by paramagnetic phyllosilicates, rather than ferromagnetic minerals, such as haematite. Some of the higher bulk susceptibility values detected in some specimens might suggest minor amounts of haematite. The bulk susceptibilities of the specimens have a largely bimodal distribution, with a very weak susceptibility group ($\leq 4X10^{-4}$) and a relatively higher susceptibility group ($\geq 5X10^{-4}$) (Figure 6. 37 and Figure 6. 38.).

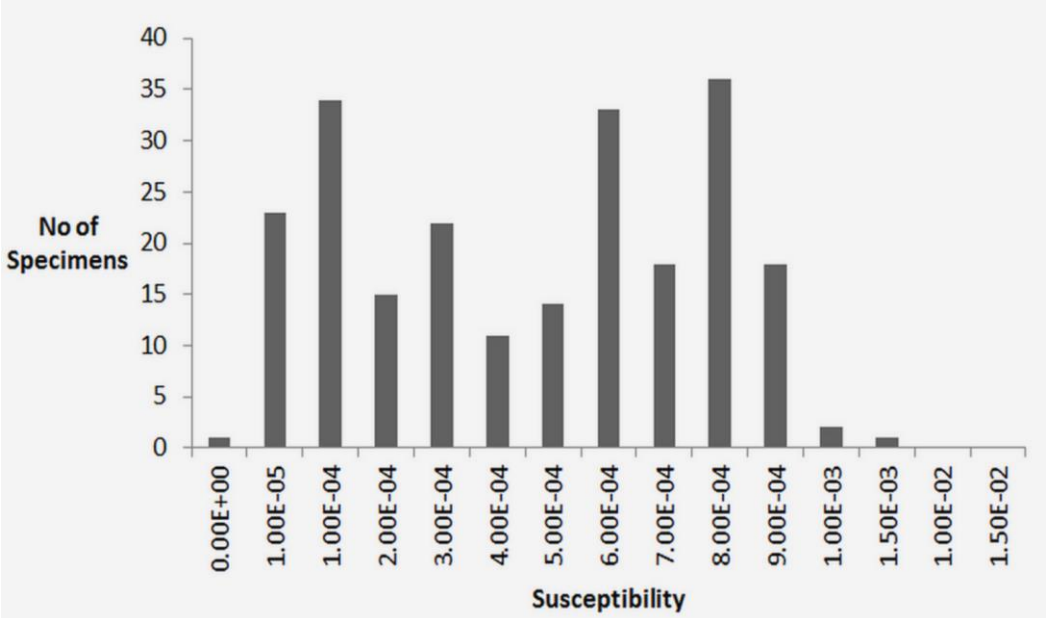

Figure 6. 37 Plot of bulk susceptibility for all individual specimens. Two groups can are visible, a low susceptibility group ($<4X10^{-4}$) and a higher susceptibility group ($>5X10^{-4}$). The magnetic response of the low susceptibility is controlled by paramagnetic minerals, such as phyllosilicates, while the higher susceptibility group may have minor amounts of ferromagnetic minerals such as hematite.

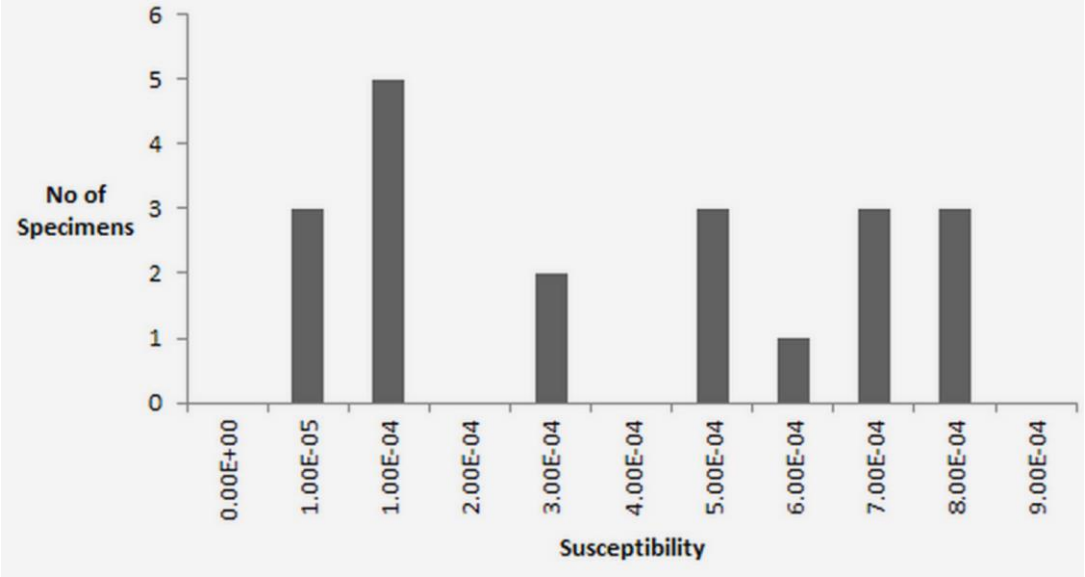

Figure 6. 38 Plot of bulk susceptibility for samples. Both the low susceptibility and high susceptibility groups are visible.

Furthermore it can be seen from the plot of degree of anisotropy (Pj) vs bulk susceptibility (Figure 6. 39 and 6. 40) that the degree of anisotropy is not controlled by samples with higher bulk susceptibilities. This suggests that the magnetic fabric or anisotropy is controlled by the cleavage or bedding rather than a highly magnetic mineral. Similarly there is no clear correlation between the shape parameters of the samples and their bulk susceptibility (Figure 6.41 and 6.42). The shape parameter, Tj, varies from -0.482 to 0.837 (only two samples display a bulk prolate shape), showing a range of ellipsoid shapes from prolate to oblate, but the majority of samples are moderately to strongly oblate, with an average of 0.9802 (Figure 6.43 and 6.44). The degree of anisotropy, Pj, varies from 1.008 to 1.35 and is typically low with an average of 1.04775, but not so low that their results cannot be considered significant.

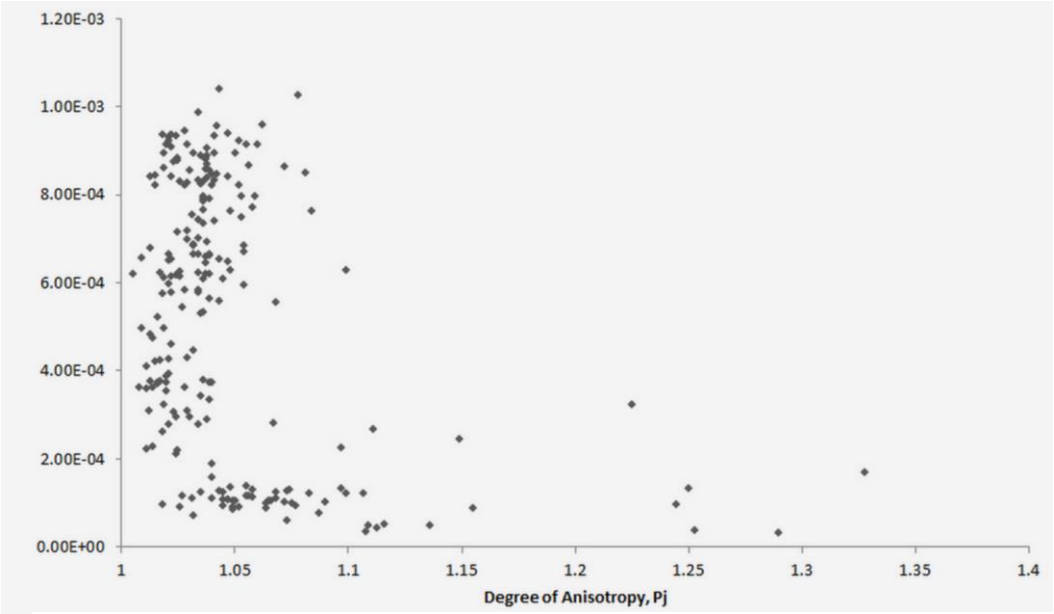

Figure 6. 39 Plot of degree of anisotropy versus susceptibiliy for individual specimens. There is no clear relationship between anisotropy and susceptibility.

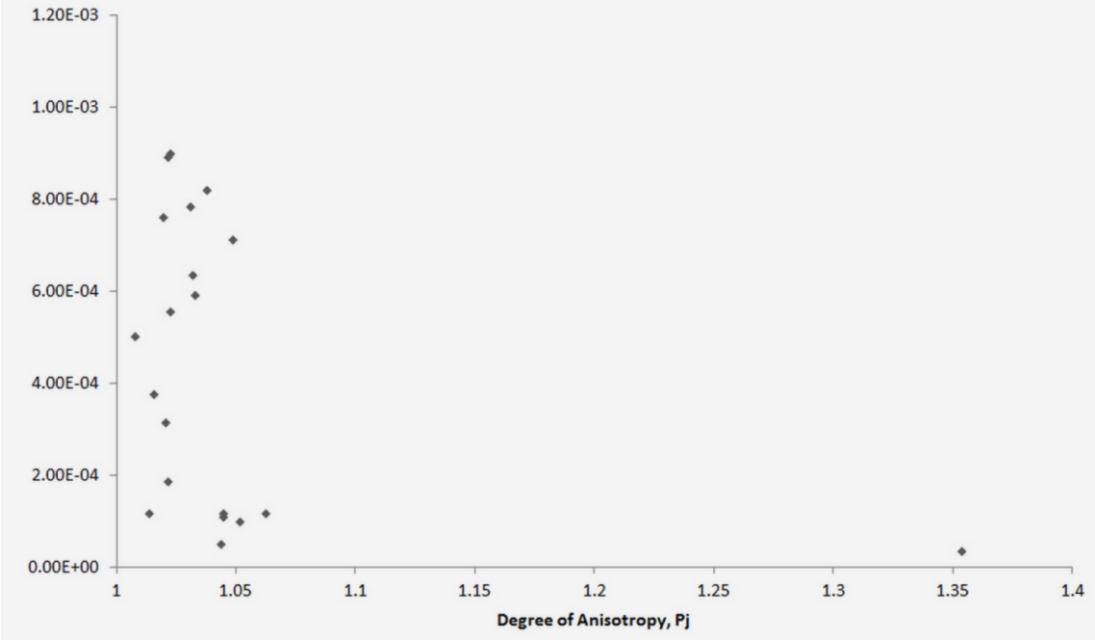

Figure 6. 40 Plot of degree of anisotropy versus susceptibiliy for samples. Again there is no clear relationship between anisotropy and susceptibility.

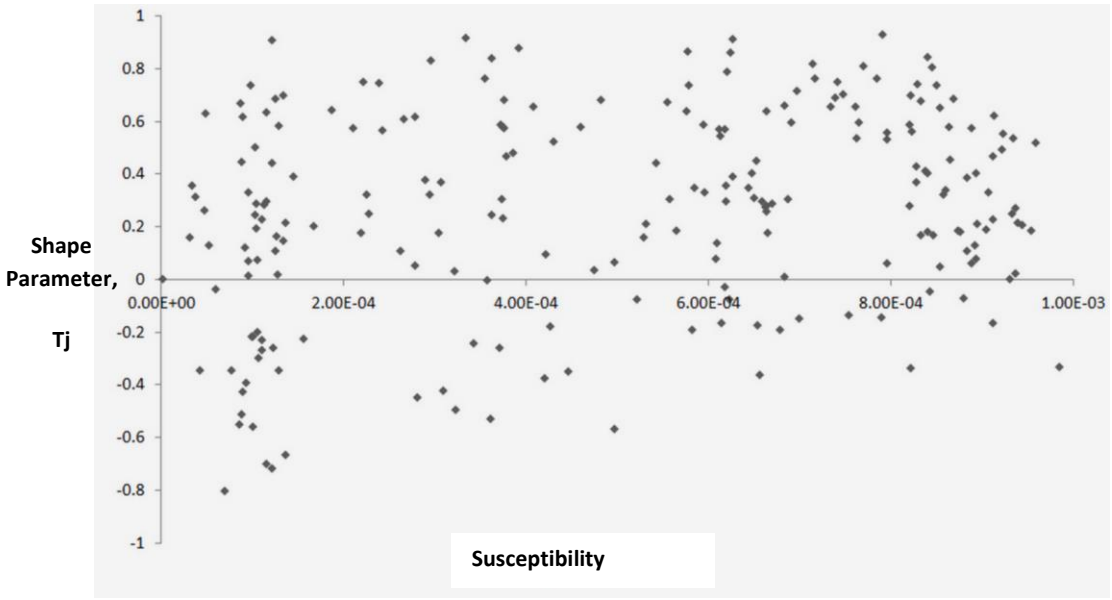

Figure 6. 41 Plot of susceptibility versus shape parameter for individual specimens. Similar to the plots of anisotropy versus susceptibility, there appears to be no clear correlation between magnetic ellipsoid shape and susceptibility.

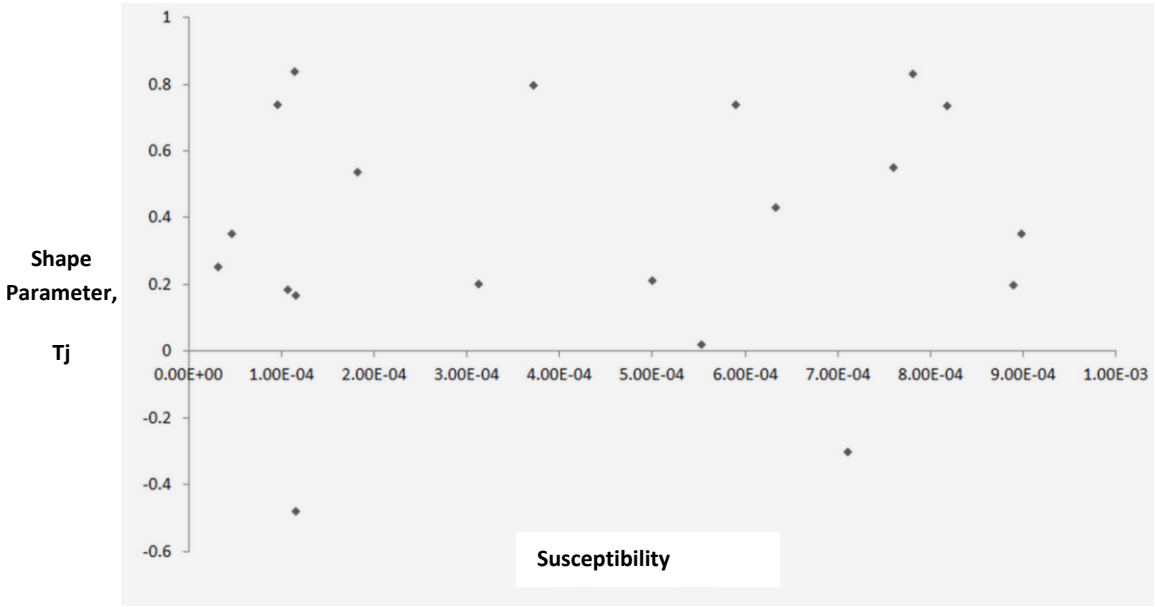

Figure 6. 42 Plot of susceptibility versus shape parameter for samples. Similar to Again there appears to be no clear correlation between magnetic ellipsoid shape and susceptibility.

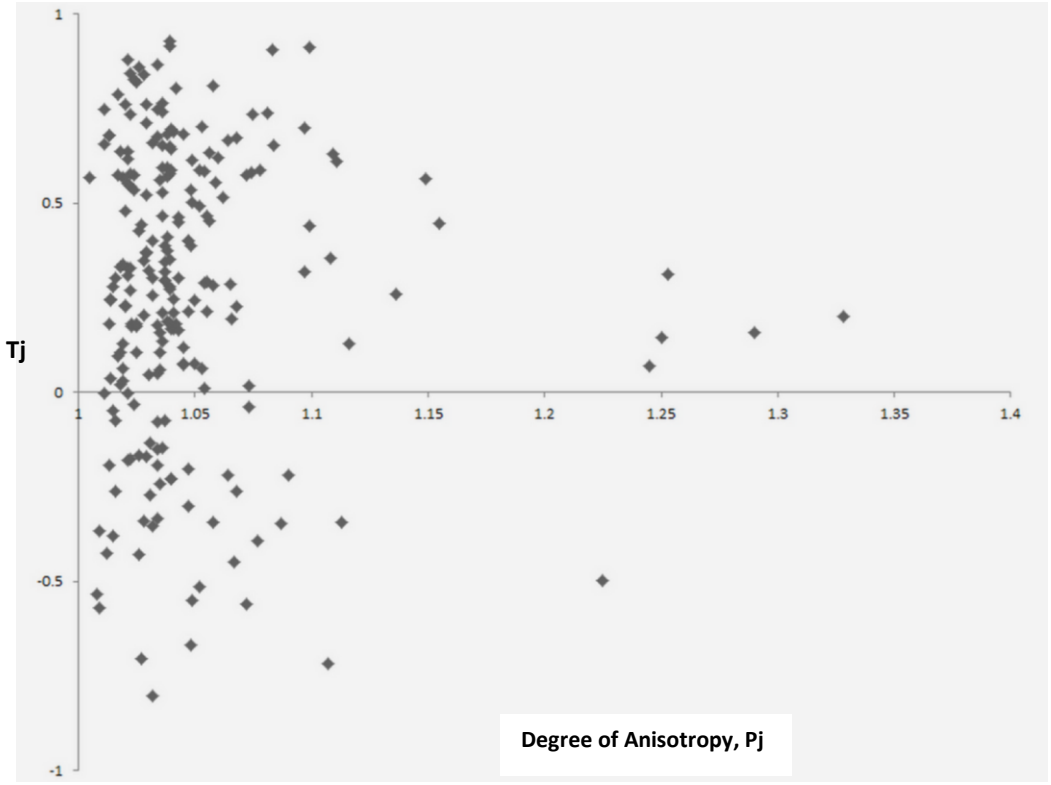

Figure 6.43 Plot of anisotropy versus shape parameter for individual specimens. The majority of specimens have a weakly oblate shape (i.e. they have a Pj value of <1.05 and a positive Tj value) this is typically suggestive of magnetic fabrics that are dominantly controlled by bedding. There are some weakly prolate specimens (negative Tj values), suggestive of a weak tectonic fabric. Even less samples have well defined oblate shapes, suggestive of a stronger tectonic fabric.

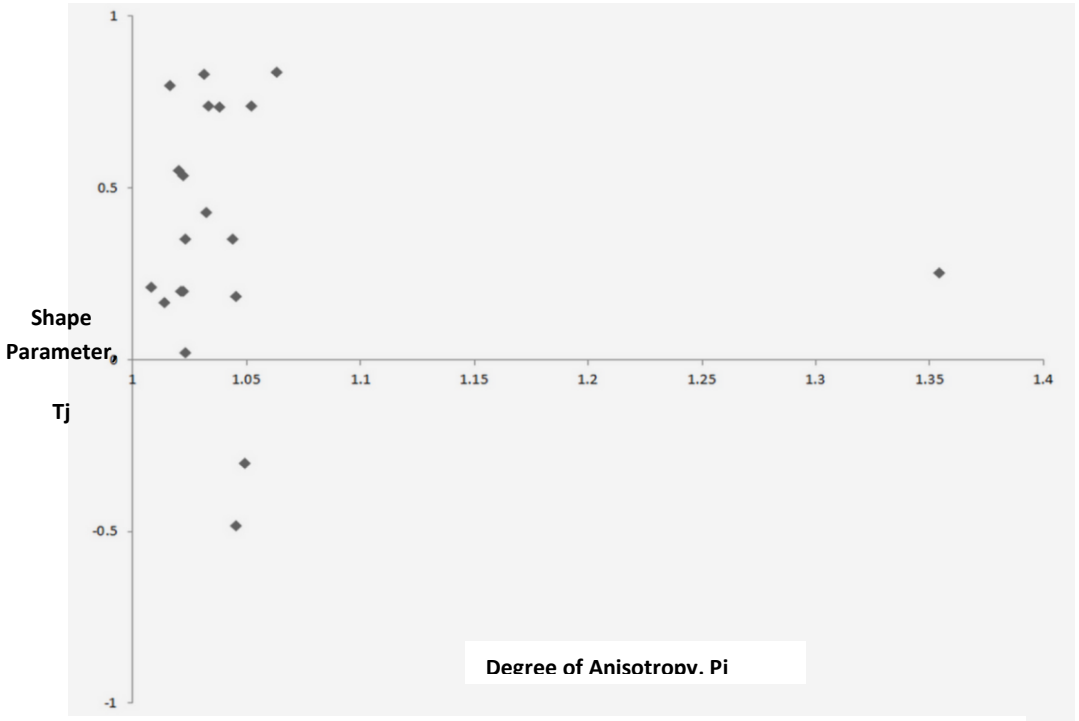

Figure 6. 44 Plot of anisotropy versus shape parameter for mean samples. A similar distribution is seen as in the previous diagram.

6.7.2.1. Orientations of Principal Susceptibility Axes

The orientation of the principal susceptibility axes of all the individual specimens is plotted in Figure 6. 45. At first look this stereonet looks significantly scattered, but it can be seen that K1 is largely clustered around 05=>085, and K2 and K3 are dispersed in a north south girdle. Plotting the orientations of the principal susceptibilities separately (Figure 6. 46 to Figure 6. 48) illustrates a clear regional trend for K1: the axis of maximum susceptibility (the magnetic lineation), is largely horizontal and orientated east-west. The calculated mean plane of K1 is and the principal eigenvector (mean cluster lineation) is 6=>85.9. K2, the intermediate susceptibility axis, has a much larger degree of scatter than either K1 or K3 (Figure 6. 47). The contoured stereonet illustrates this scatter, but also shows a weak horizontal north-south cluster, as well as a weak north-south girdle. This is also seen in the Woodcock plot (Figure 6. 49), whereby K2 sits very close to the girdle/cluster transition. The distribution of the K3 axes largely forms a north-south girdle, additionally there is a considerable vertical cluster of points within this girdle with two weaker horizontal clusters of points.

The locations of individual block samples and their representative stereographic projections of the principal susceptibility axes are shown in Figure 6.50. From this figure the distribution of the principal susceptibility axes becomes more clear. North of the Dungarvan Syncline the magnetic foliation (K1 and K2) correlates well with observed bedding, with the magnetic lineation (K1) occasionally correlating with S1. South of the Dungarvan Syncline the magnetic foliation occasionally correlates with Variscan cleavage (S1). This distribution is further discussed in the following section on magnetic fabric types.

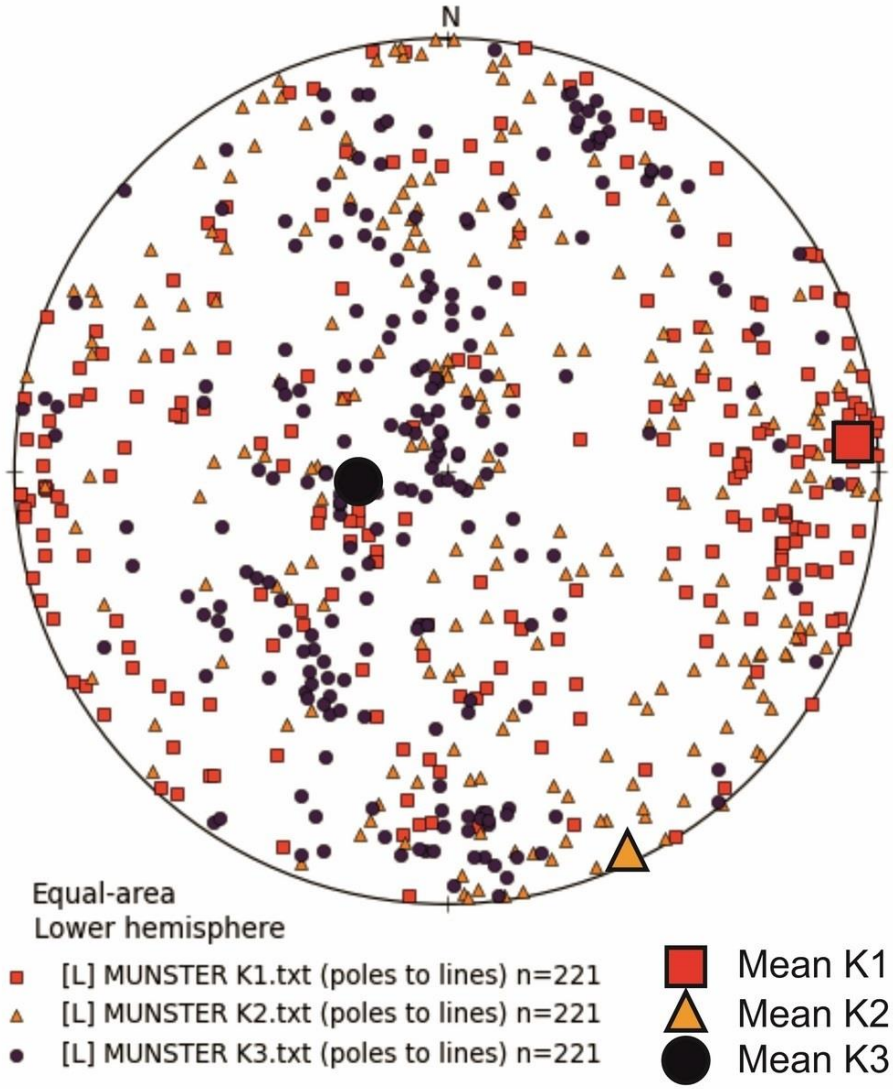

Figure 6. 45 Stereonet of principal susceptibility axes for individual specimens.

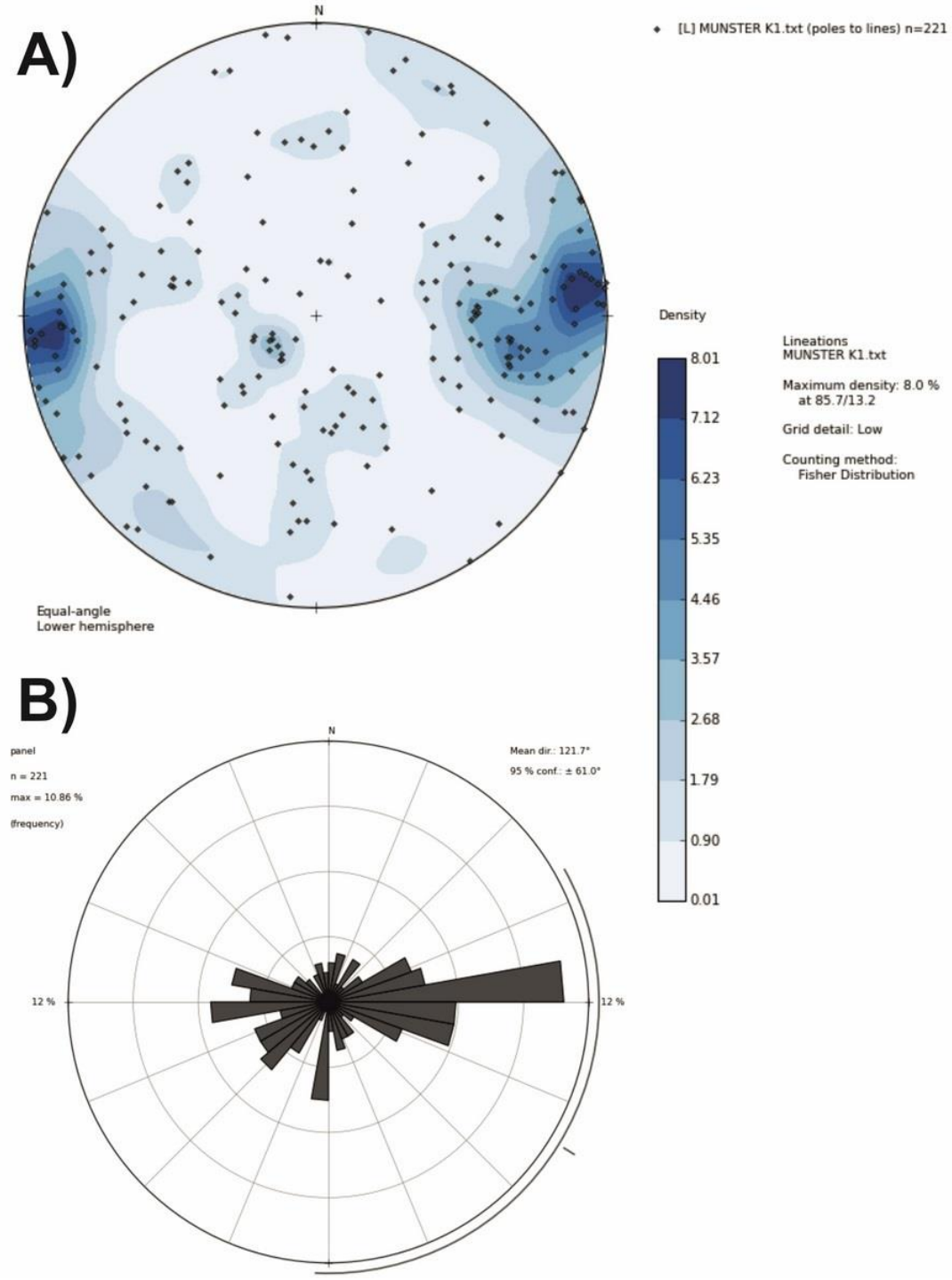

Figure 6. 46 Orientation of K1 for individual specimens. A) Contoured plot for K1 B) Rose diagram of K1 orientations.

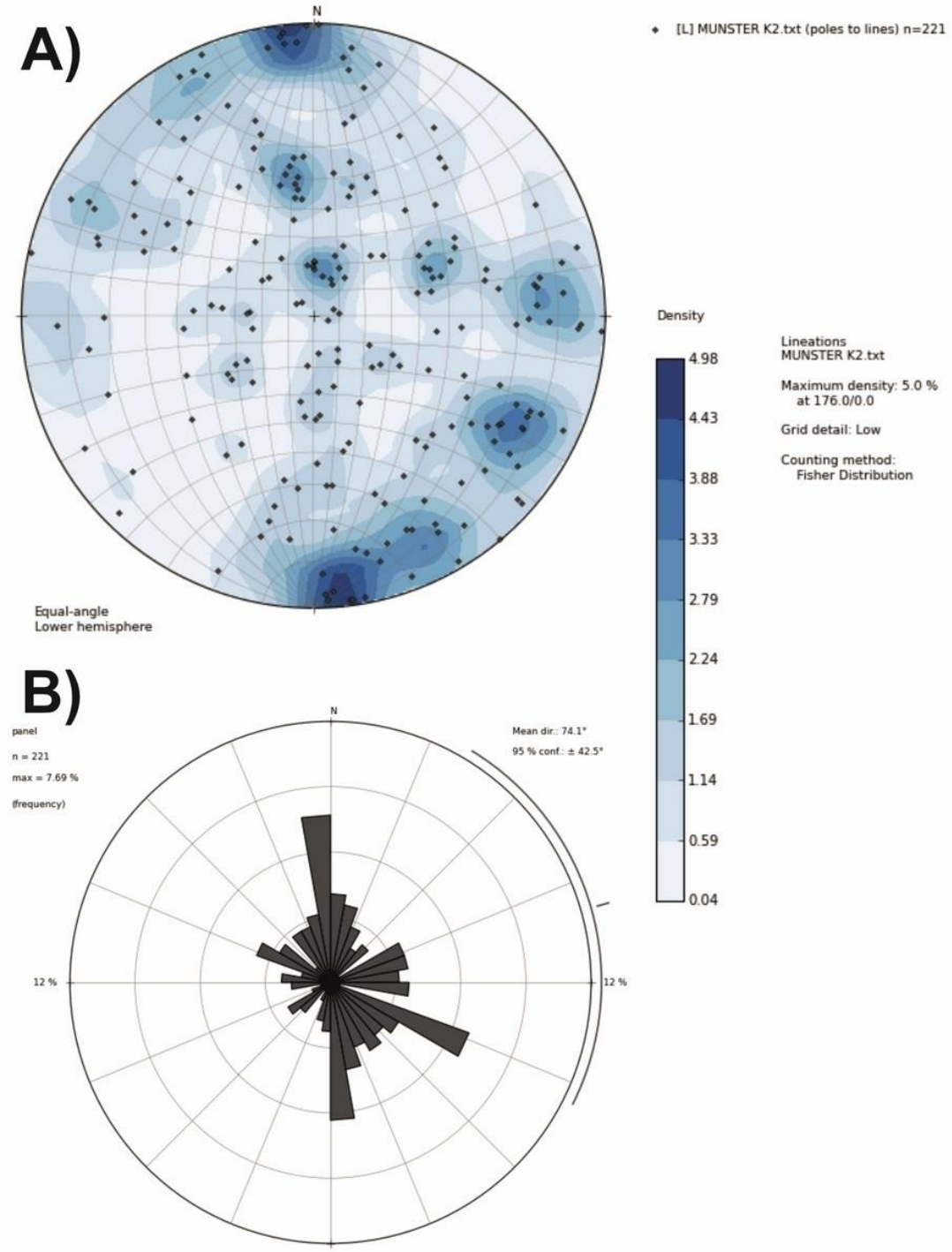

Figure 6. 47 Orientation of K2 for individual specimens. A) Contoured plot for K2 B) Rose diagram of K2 orientations.

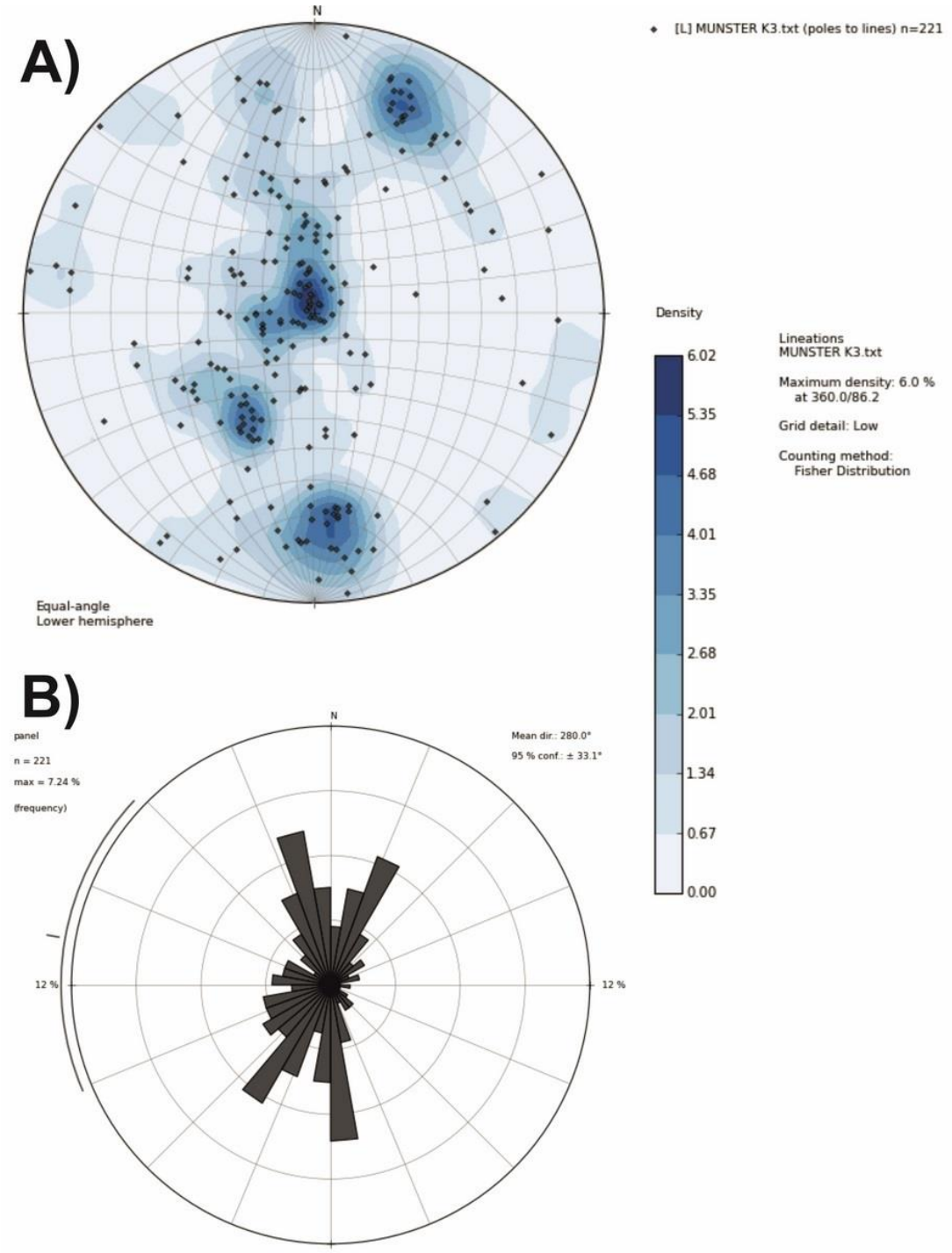

Figure 6. 48 Orientation of K3 for individual specimens. A) Contoured plot for K3 B) Rose diagram of K3 orientations.

A)

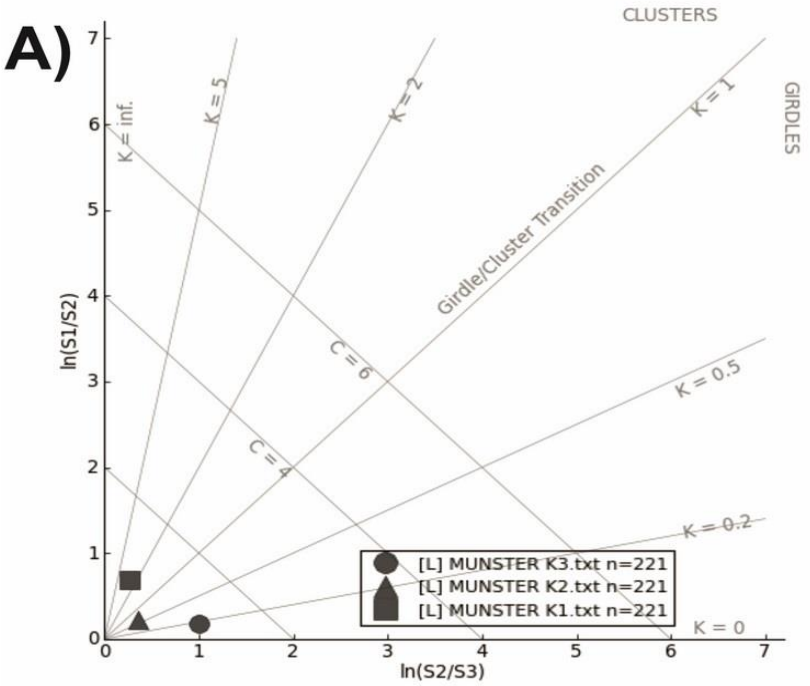

B)

	K1	K2	K3
Expected Distribution	Cluster	Girdle	Girdle
Mean Plane: Dip dir/dip	265.9/83.6	239.4/32.7	281.0/76.6
Radius of confidence at 5%	11.31 degrees	9.86 degrees	7.73 degrees
K Value	K = 1.70	K = 1.92	K = 2.50
Eigenvectors	1: 85.9 / 6.4 2: 182.8 / 46.9 3: 350.1 / 42.4	1: 149.4 / 0.1 2: 59.2 / 57.3 3: 239.4 / 32.7	1: 253.2 / 75.0 2: 9.4 / 6.8 3: 101.0 / 13.4
Shape Parameter: K	2.65	0.65	0.18
Strength Parameter: C	0.94	0.58	1.18
Normalised Eigenvalues	S1: 0.528 S2: 0.266 S3: 0.206	S1: 0.424 S2: 0.338 S3: 0.238	S1: 0.468 S2: 0.389 S3: 0.143

Figure 6. 49 Woodcock diagram for individual specimens

6.7.2.2. Magnetic Fabric Types

The stereographic projections for individual samples are presented in Figure 6.50, from this figure the magnetic fabric types across the area can be determined and are presented in Figure 6. 51. In terms of the ellipsoid geometries they generally evolve in the manner described in section 3.1, whereby AMS fabrics range from bedding controlled (Type 1) to tectonically controlled (Type 4). The samples with the most tectonic influence are in the south, with a marked decrease in tectonic influence northwards regardless of whether the samples are within basin or not. There is a slight increase in tectonic influence parallel to the Tullaghorton fault.

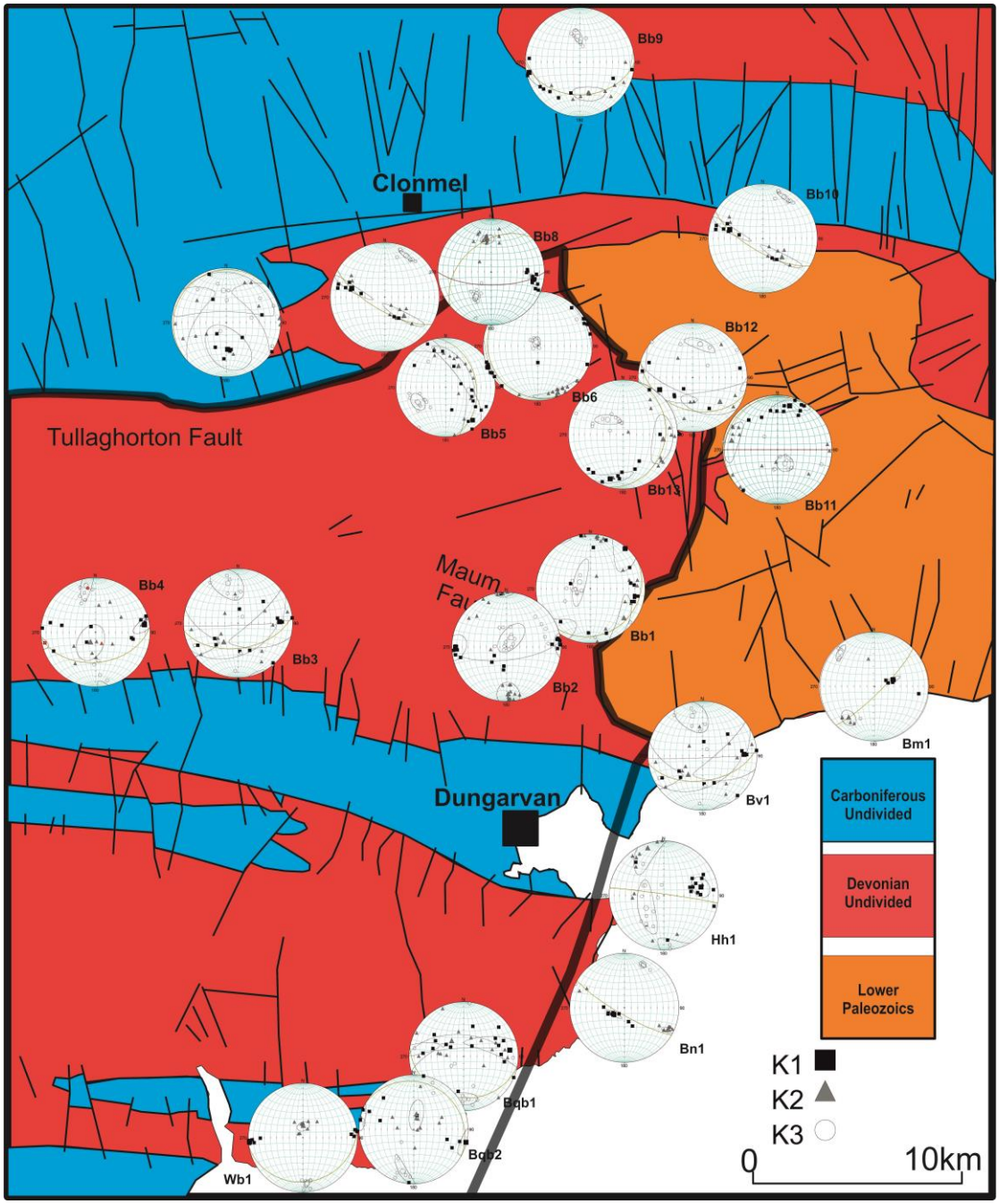

Figure 6. 50 Map showing stereographic projection of principal susceptibility axes for each sample analysed.

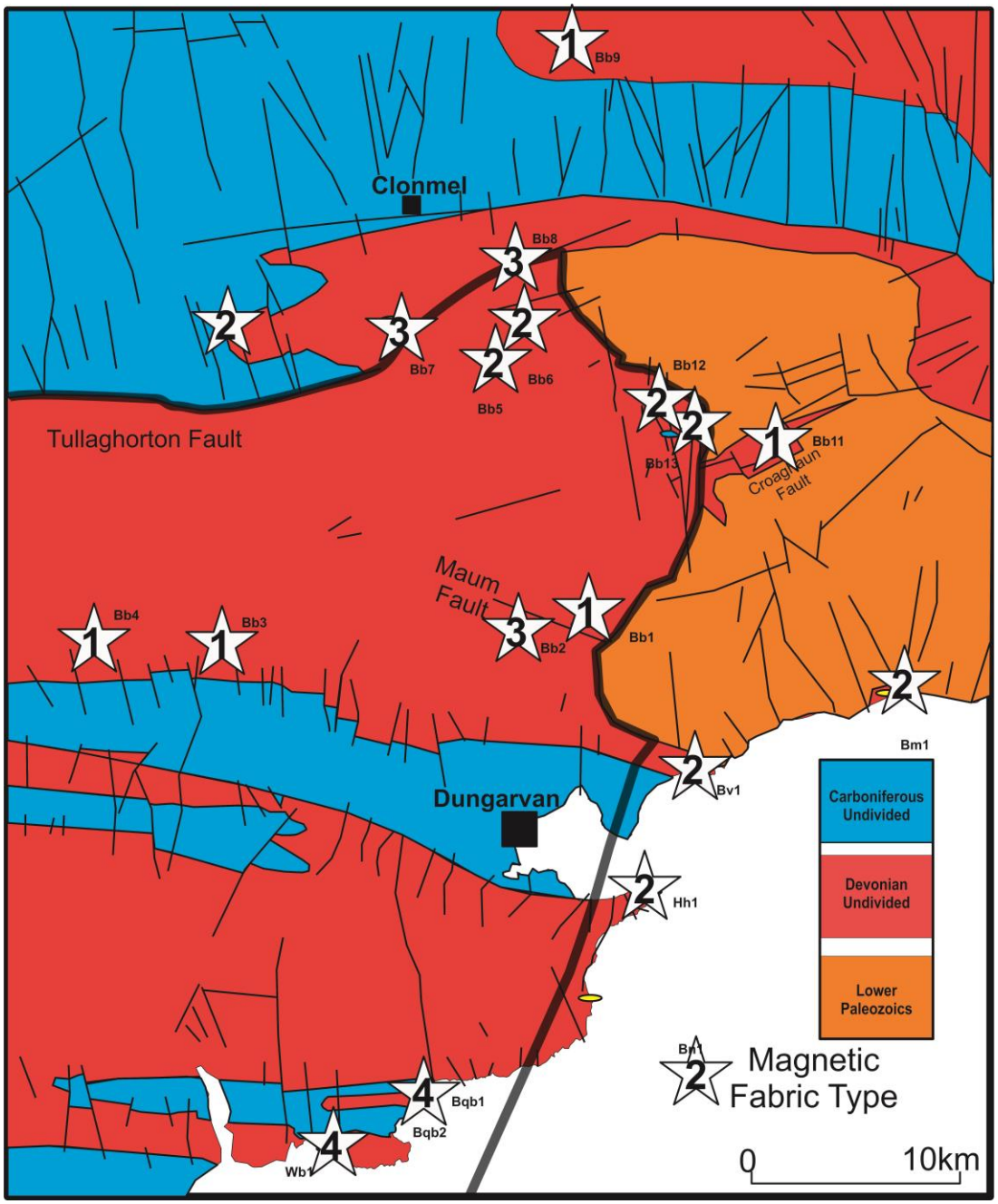

Figure 6. 51 Map of AMS fabric types, previously described in Chapter 3. It is interesting to note that the only purely tectonic fabric types are from south of the DDL, although there is a large concentration of intermediate types near the northern margin of the Comeragh Mountains.

6.7.3. Strain Results

Considering the results from the Wyoming Salient, the DTNNM and MRL methods (Mulchrone et al., 2013) were considered to provide a representative suite of strain analyses. Unlike the Wyoming Salient study three mutually perpendicular sections

were analysed from each sample (Fig. 6.52), this approach was taken due to the complexity of the deformation history of the Munster Basin. This approach also allowed for the modelling of 3D ellipsoids, but this turned out to be rather unproductive considering the low strains reported. The results from the DTNNM and MRL analyses show a wide range of results, varying from 1.03-1.9 and 1.02-1.6 respectively, but the majority of samples yielded low strains estimates.

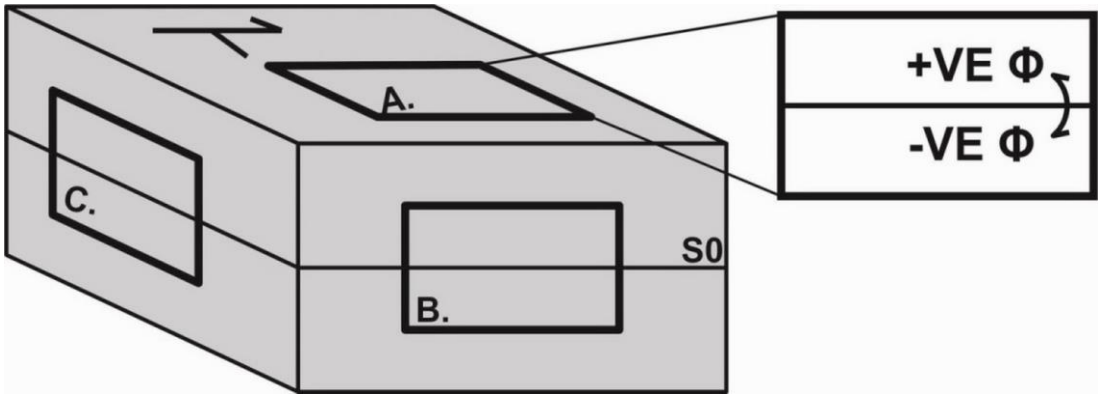

Figure 6. 52 Schematic diagram of thin section orientations. A sections are parallel to the bedding plane. B sections are parallel to the strike of bedding, but perpendicular to the plane of bedding. C sections are perpendicular to both the bedding plane and the strike of the bedding plane. The inset illustrates the relative orientation of negative and positive Φ values, the long axis of the estimated strain ellipse.

6.7.3.1. Bedding Parallel Sections

The estimated strain results from both the DTNNM and MRL analyses for bedding parallel sections (A sections) are shown in Figure 6. 53 and Figure 6. 54. Both maps show the orientation and axial ratio of the estimated strain ellipse. Interestingly there is a distinct strain gradient defined by the DDL for both methods, with higher strains to the south of the Dungarvan syncline. Although there are some higher strains recorded in the northern Comeraghs, but not as strong as would be expected considering the microstructures shown in Figure 6.31 and 6.32. The

distribution largely agrees with the AMS ellipsoids reported in Figure 6. 50, where samples with a dominantly tectonic influence are to the south, while bedding dominated samples are to the north.

The results and confidence intervals for individual samples are shown in Figure 6. 55 to Figure 6. 76. These figures show the Fry plot, a polar plot and R/Φ plots for both the DTNNM and MRL estimates. The Fry and polar plots are used to determine the degree of fit for the DTNNM data (for a detailed discussion see Chapter 2). The R/Φ plots show the actual estimate (small star) from either DTNNM or MRL data and bootstrapped estimates (circles), from which the 90%, 95% and 99% confidence ellipses are calculated.

A summary plot of all the estimated R values from both methods is presented in Figure 6. 77. It is clear from the summary plot (Figure 6.77) that DTNNM produces higher strain estimates than the MRL technique. The higher strain estimates from DTNNM compared to MRL are not suprising, considering that MRL only accounts for grain rotation and/or grain shape change and does not account for matrix deformation. On the other hand DTNNM accounts for movement of grains relative to each other and includes some measure of matrix deformation.

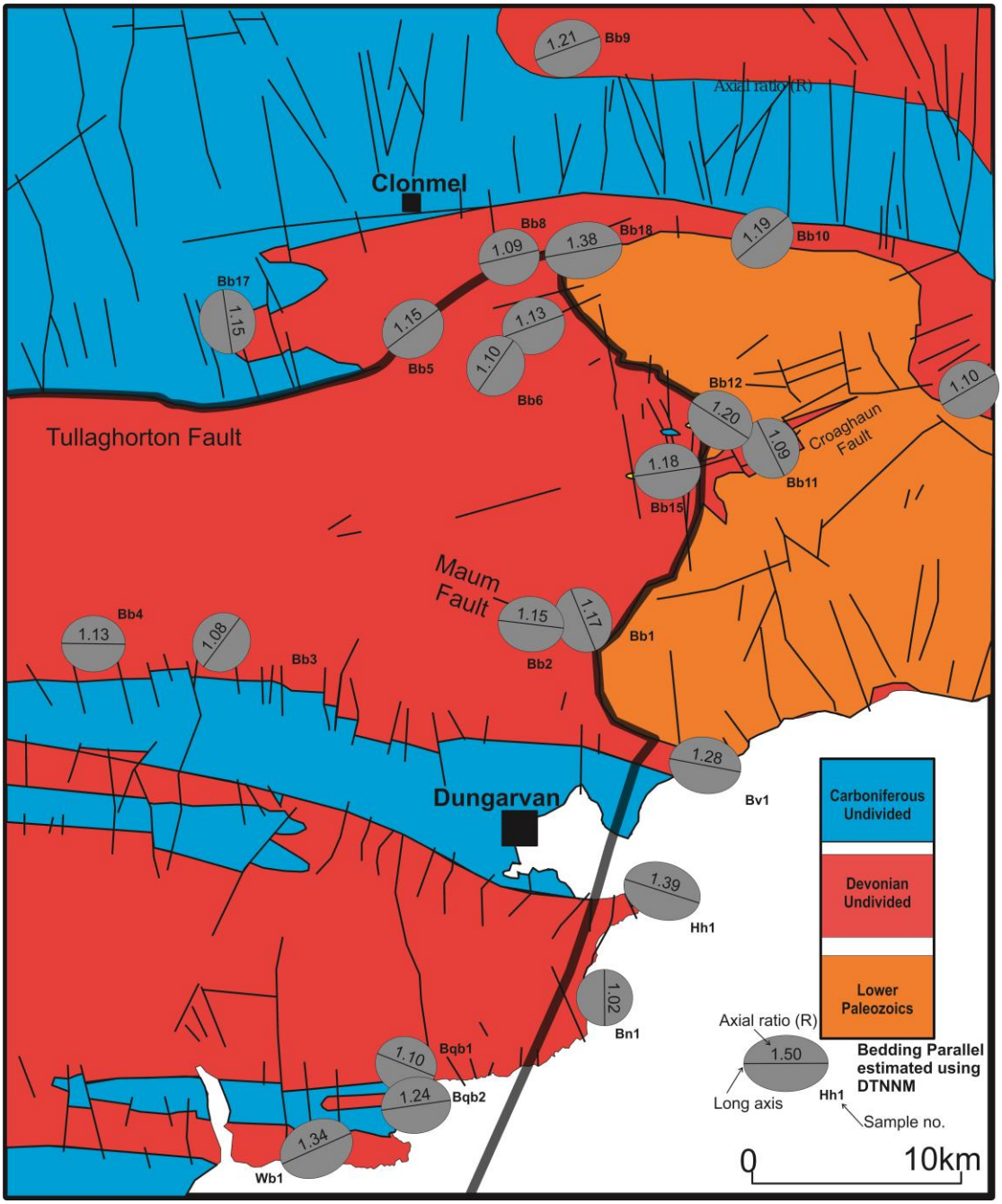

Figure 6. 53 Map of strain ellipses estimated using the DTNNM technique from bedding parallel planes (A sections).

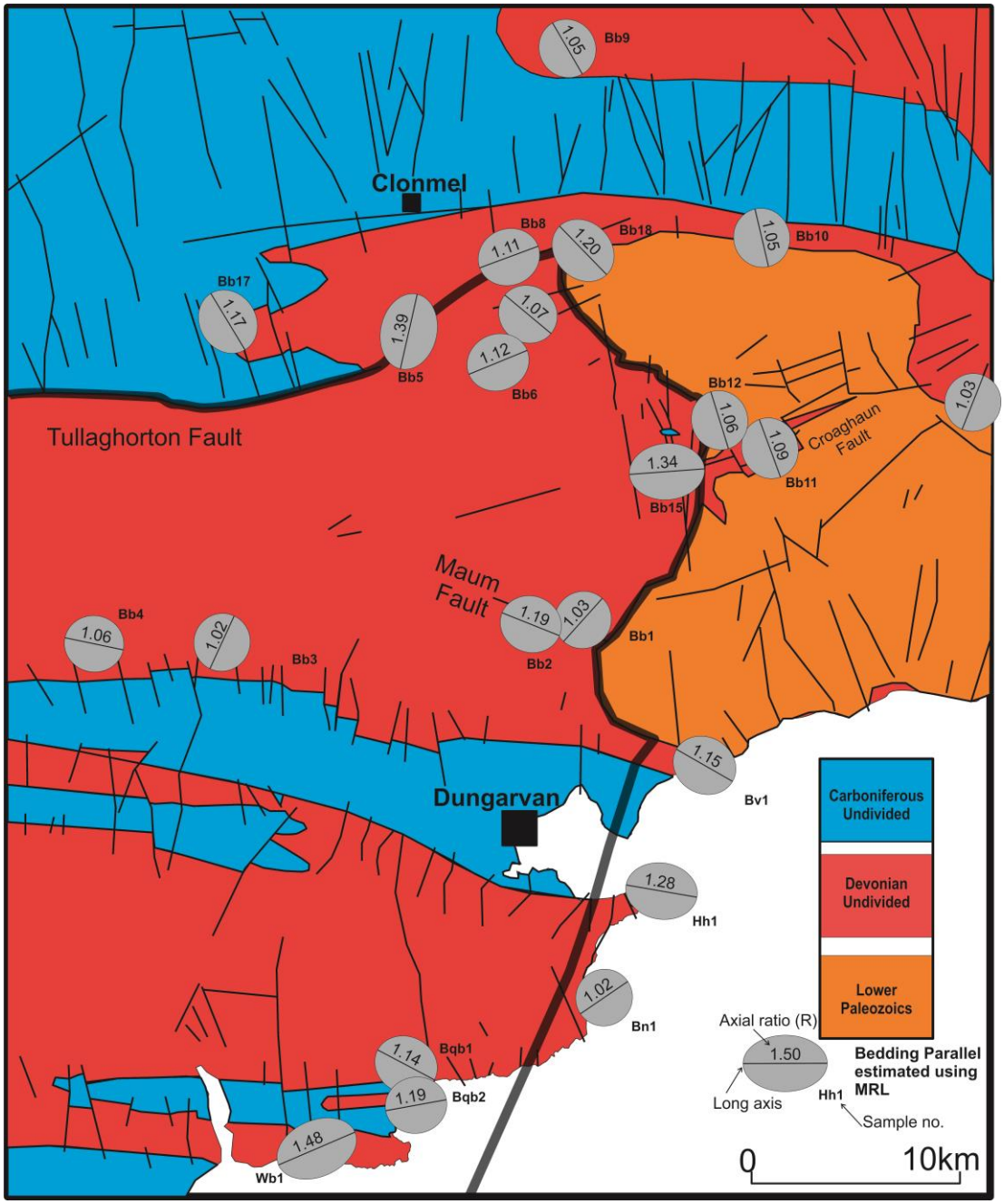

Figure 6. 54 Map of strain ellipses estimated using the MRL technique from bedding parallel planes (A sections).

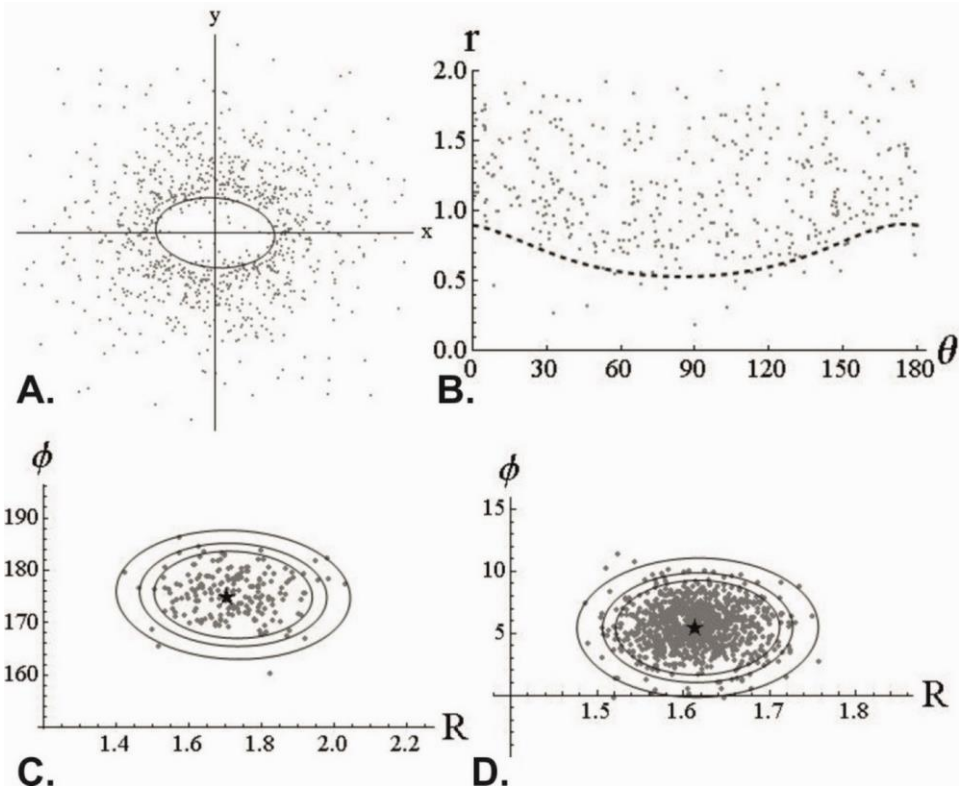

Figure 6. 55 Strain estimates for Wb1A from the DTNNM and MRL analyses. **A.** Fry plot of the nearest neighbour data.**B.** Polar plot of the nearest neighbour data.**C.** DTNNM strain estimate and bootstrap data. **D.** MRL strain estimate and bootstrap data.

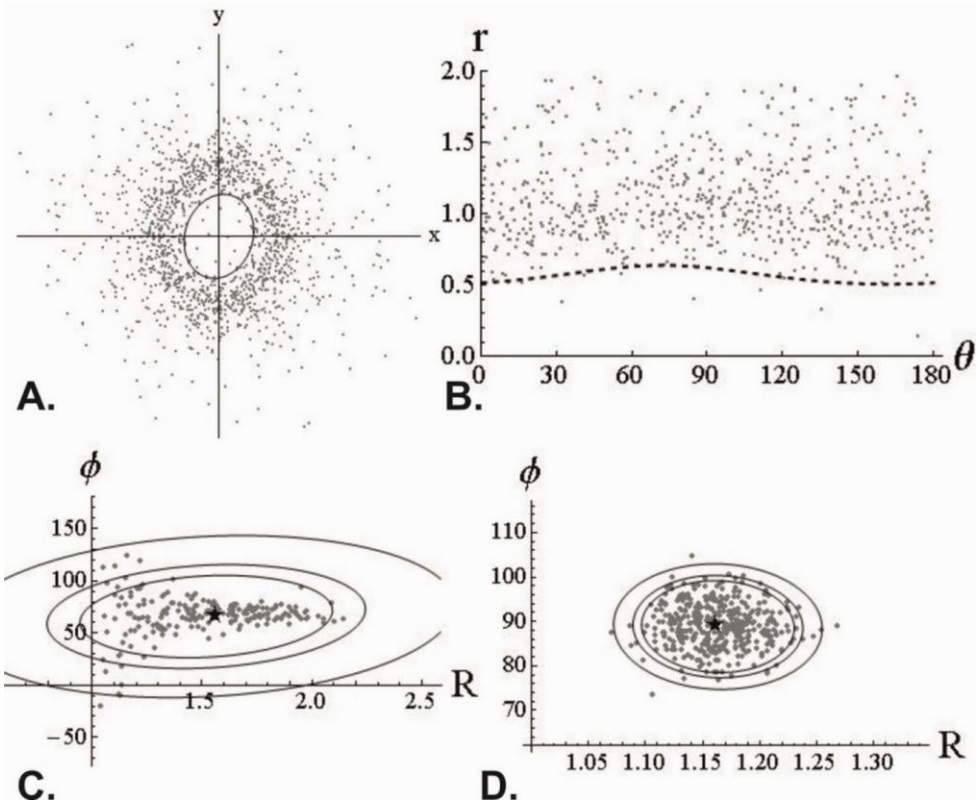

Figure 6. 56 DTNNM and MRL strain estimates for BQ1A.

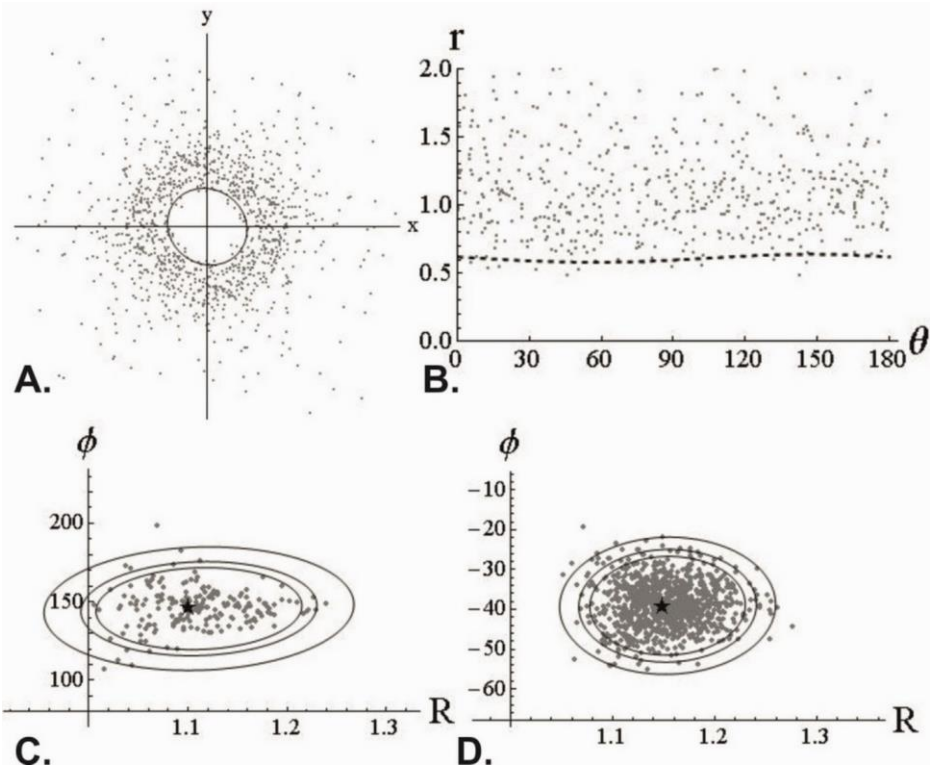

Figure 6. 57 DTNNM and MRL strain estimates for BQ2A.

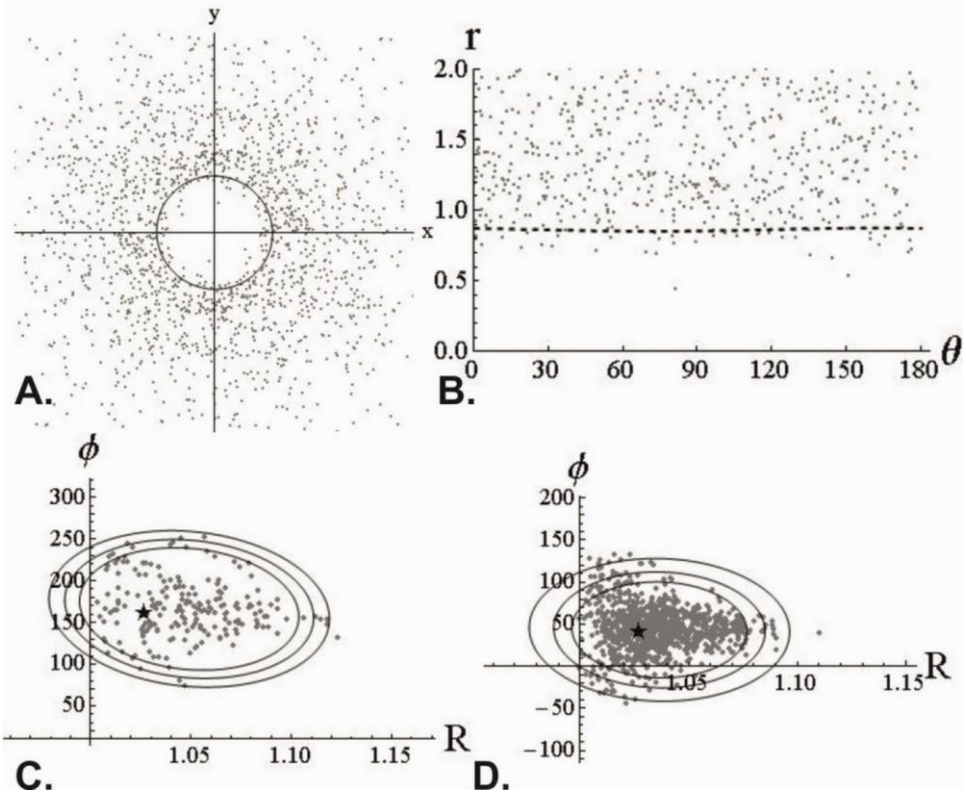

Figure 6. 58 DTNNM and MRL strain estimates for BN1A.

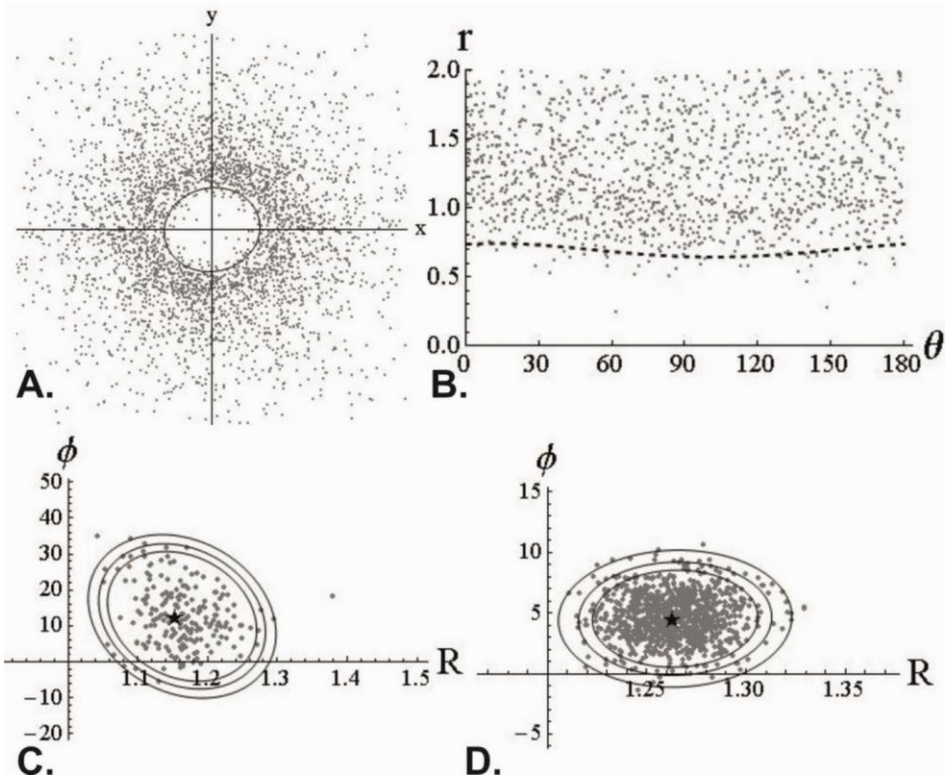

Figure 6. 59 DTNNM and MRL strain estimates for HH1A.

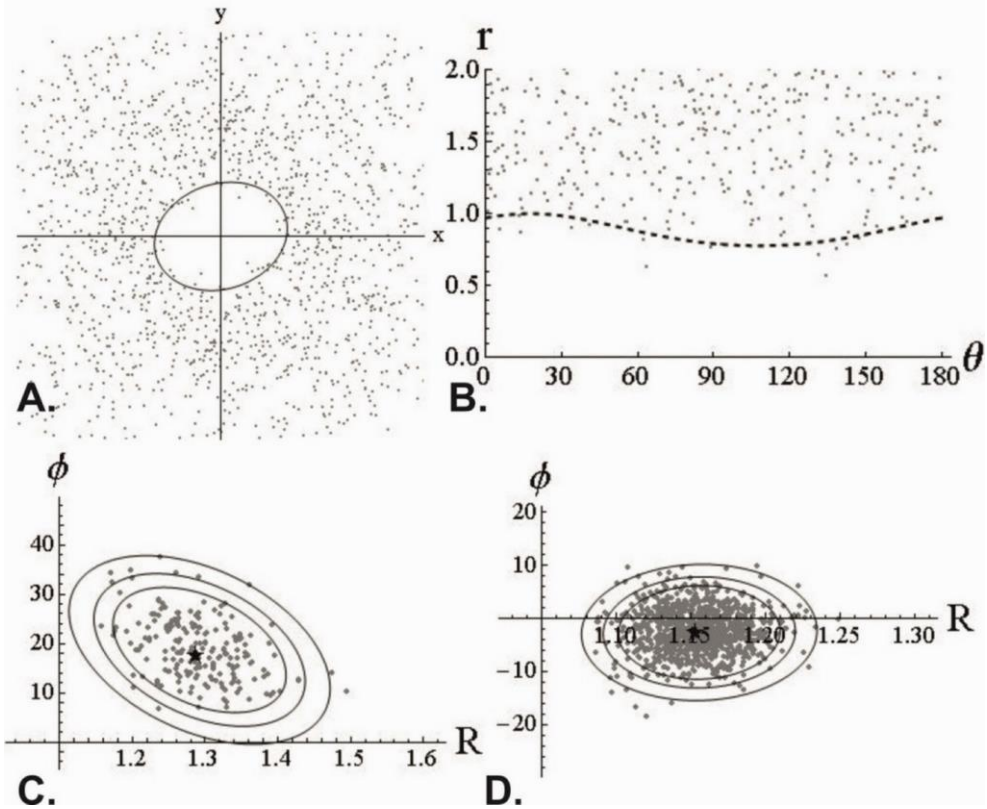

Figure 6. 60 DTNNM and MRL strain estimates for BV1A.

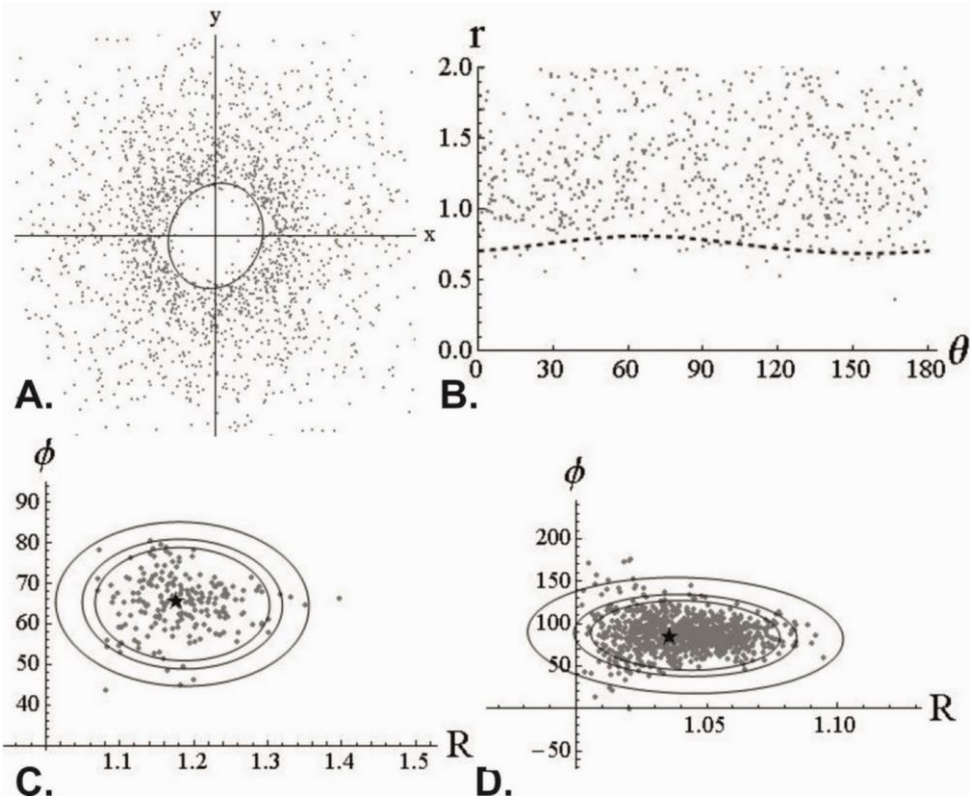

Figure 6. 61 DTNNM and MRL strain estimates for BB1A.

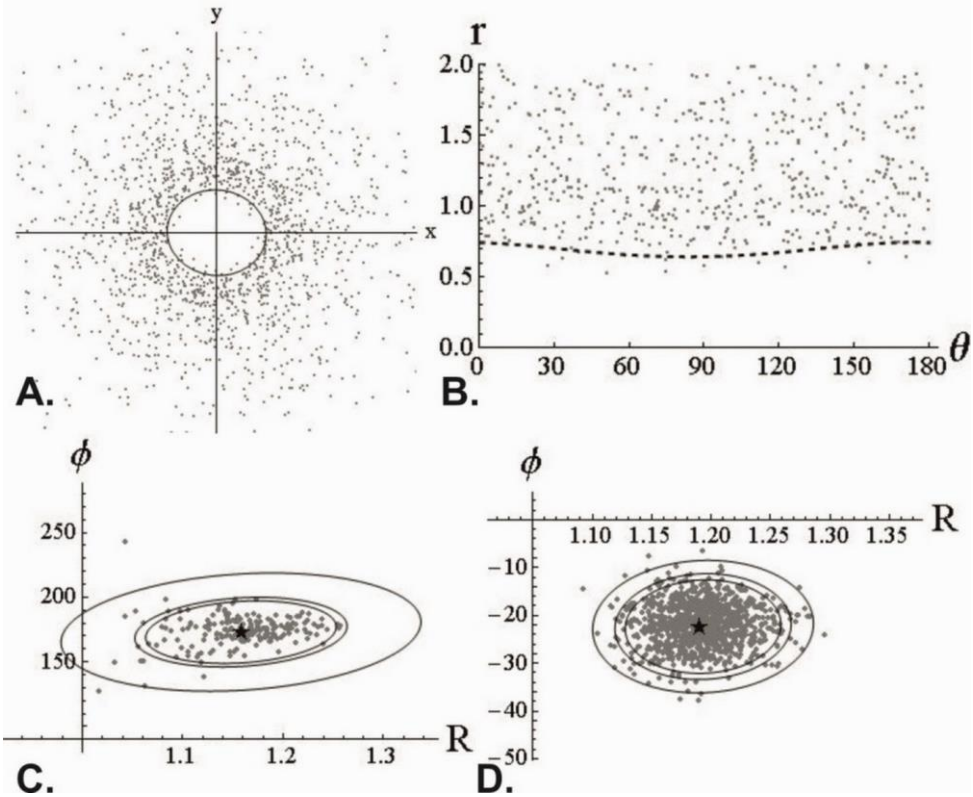

Figure 6. 62 DTNNM and MRL strain estimates for BB2A.

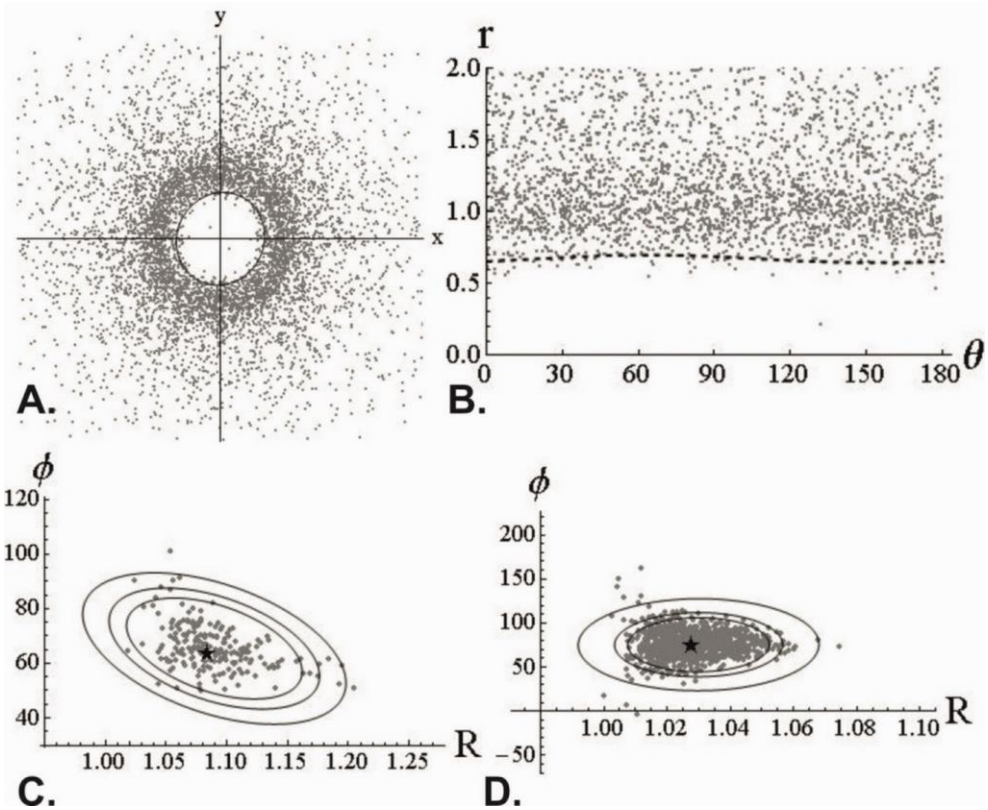

Figure 6. 63 DTNNM and MRL strain estimates for BB3A.

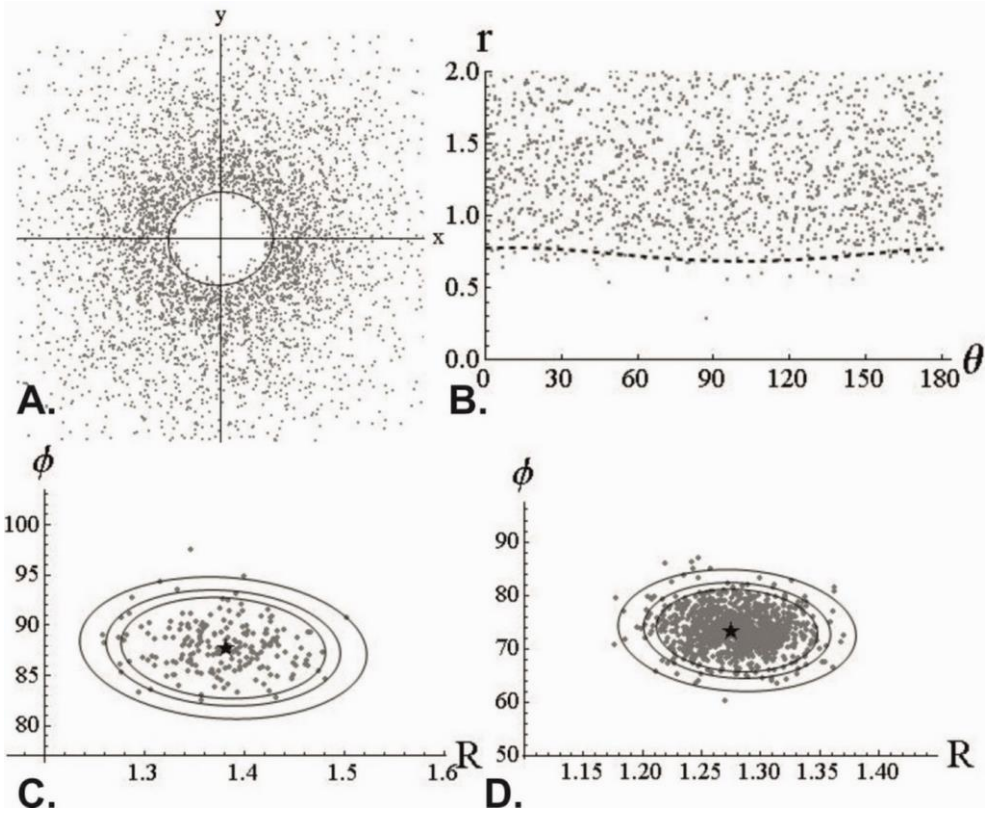

Figure 6. 64 DTNNM and MRL strain estimates for BB4A.

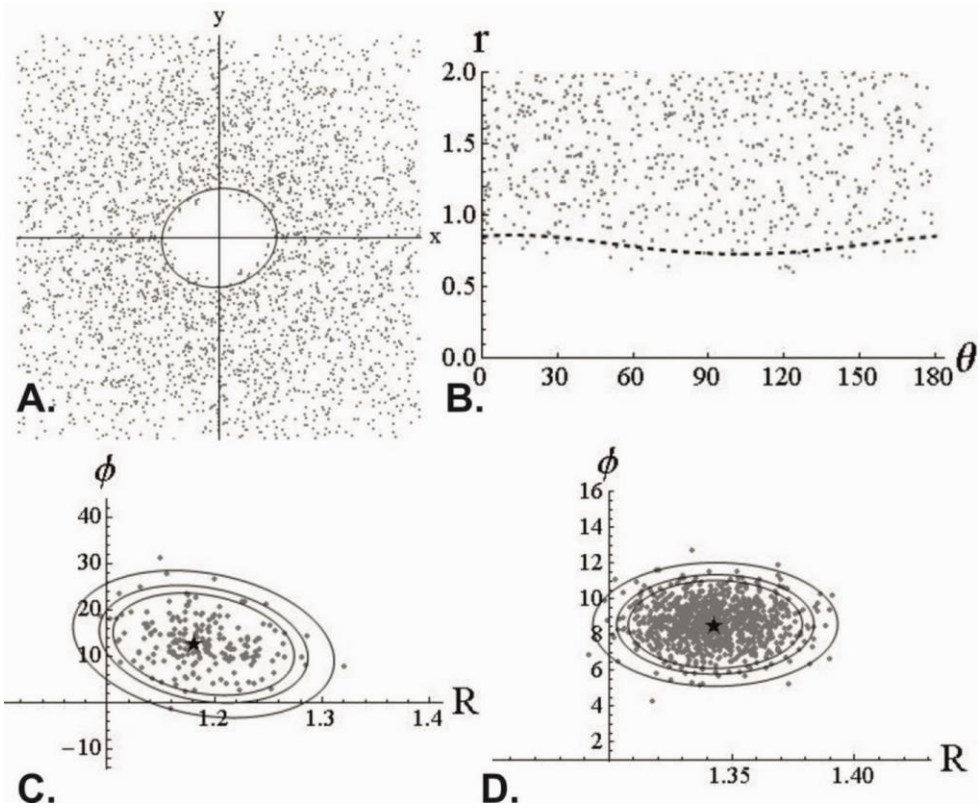

Figure 6. 65 DTNNM and MRL strain estimates for BB15A.

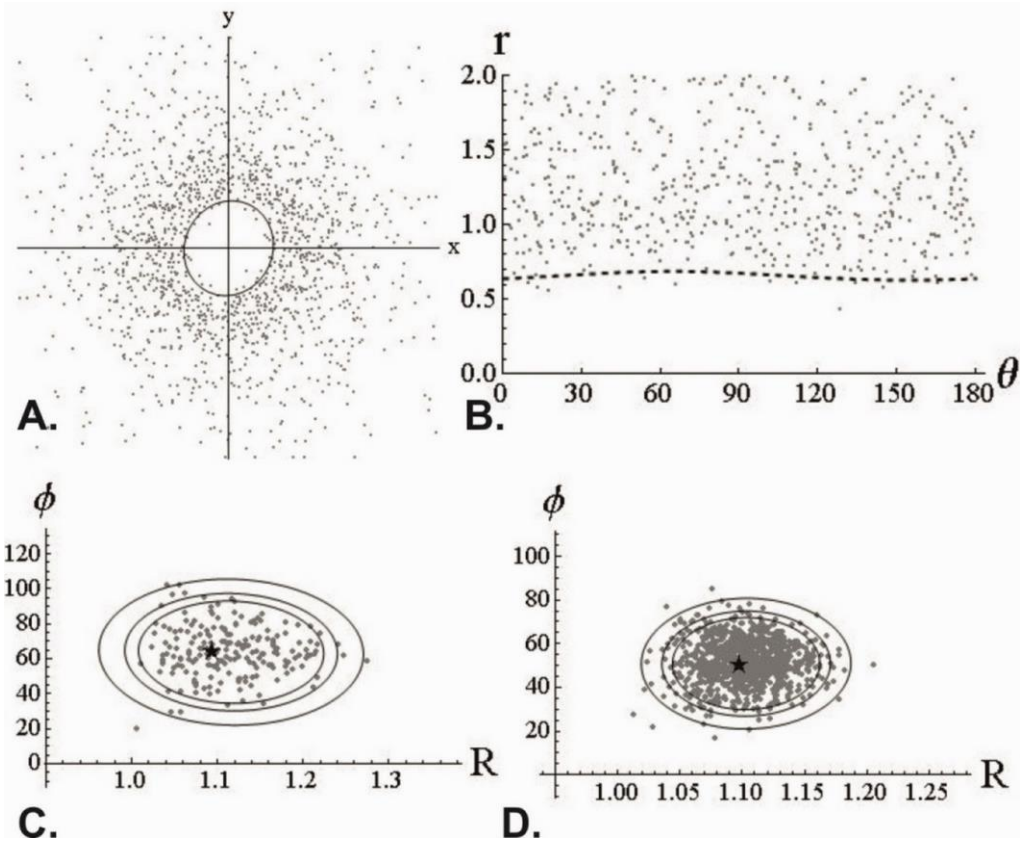

Figure 6. 66 DTNNM and MRL strain estimates for BB11A.

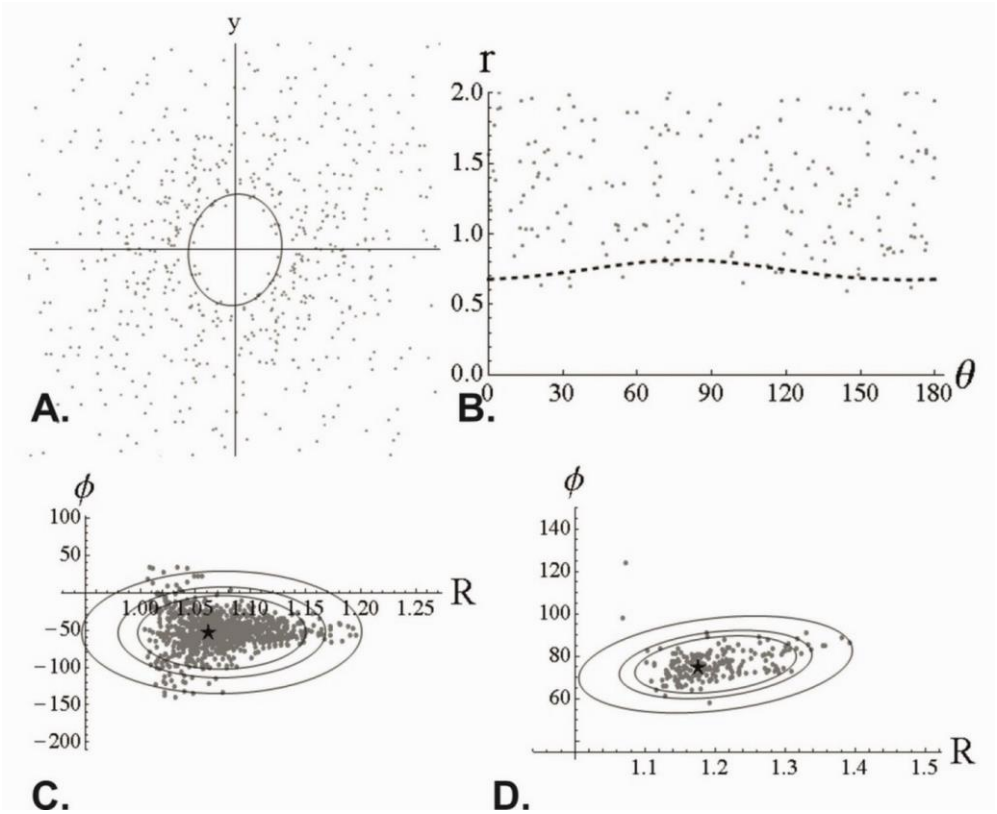

Figure 6. 67 DTNNM and MRL strain estimates for BB12A.

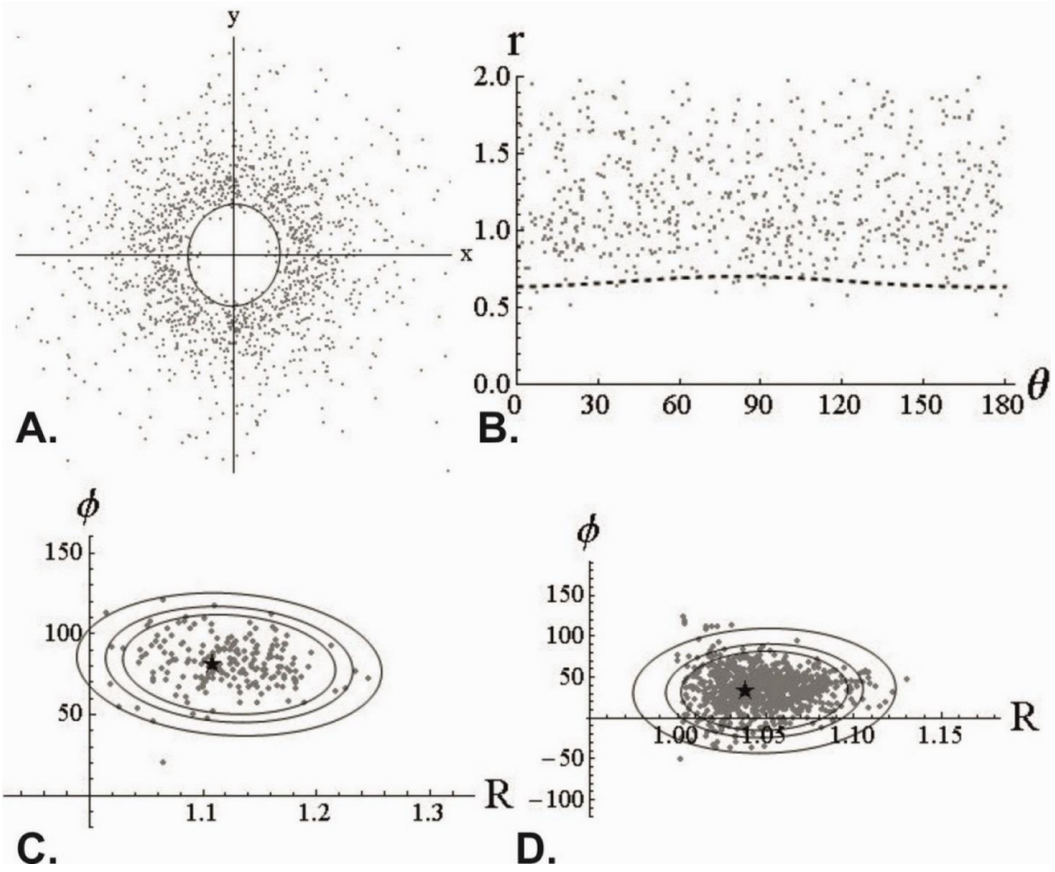

Figure 6. 68 DTNNM and MRL strain estimates for BB14A.

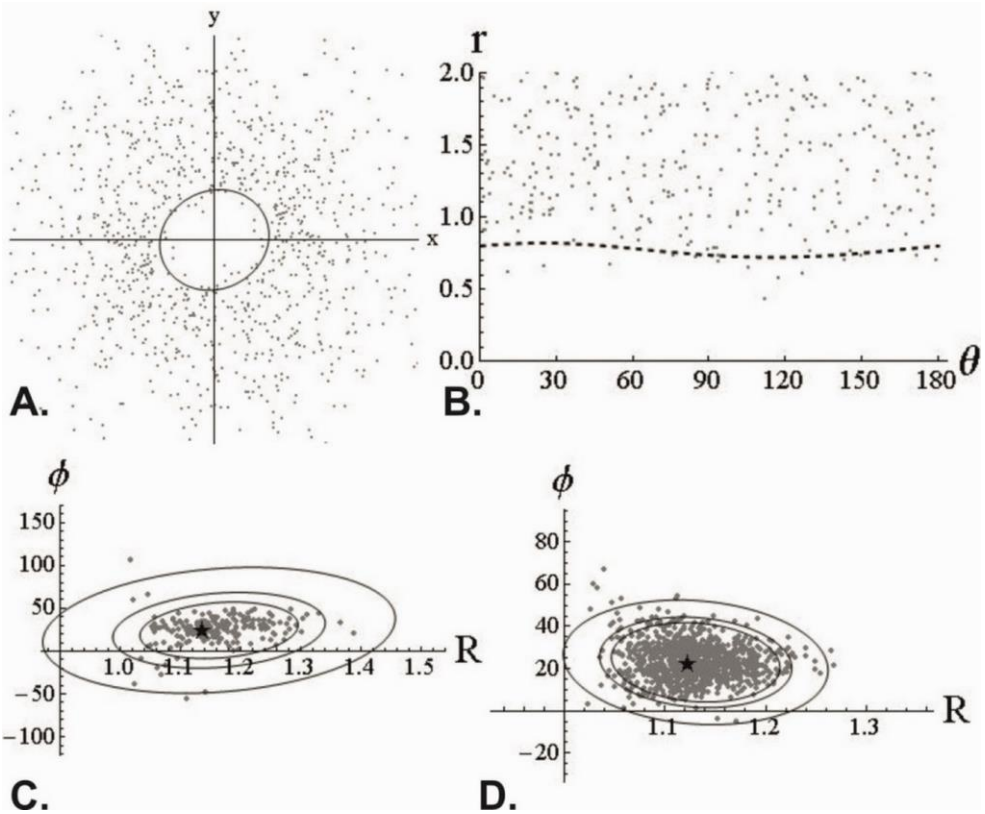

Figure 6. 69 DTNNM and MRL strain estimates for BB6A.

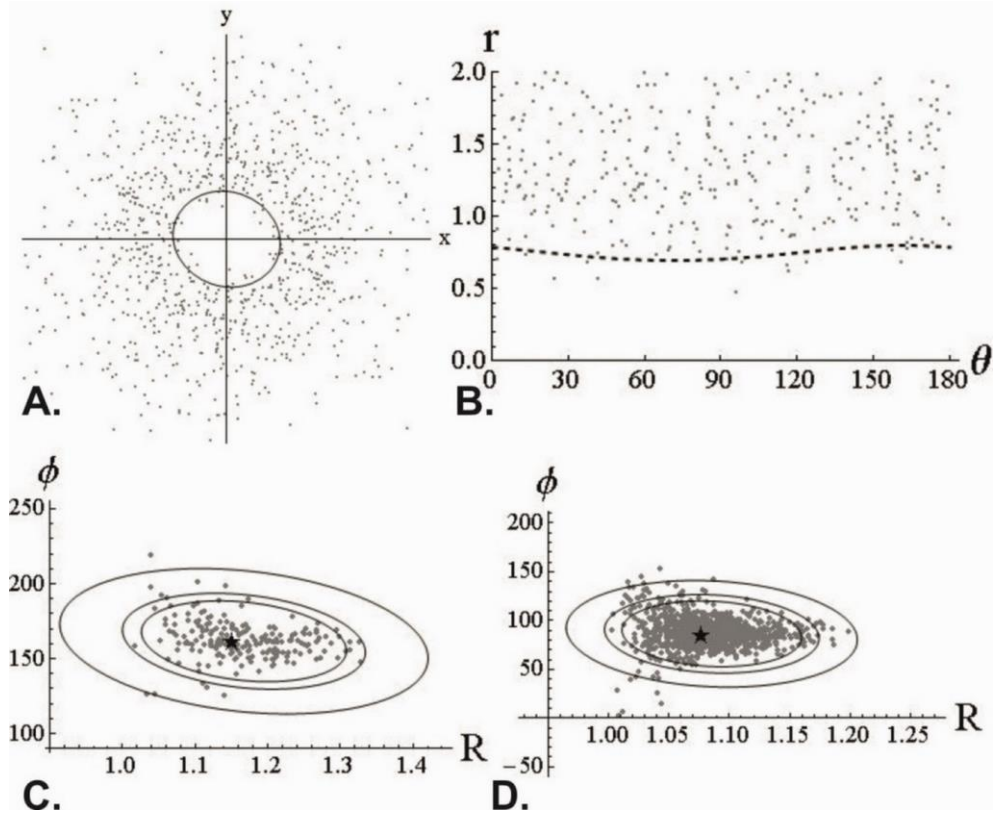

Figure 6. 70 DTNNM and MRL strain estimates for BB7A.

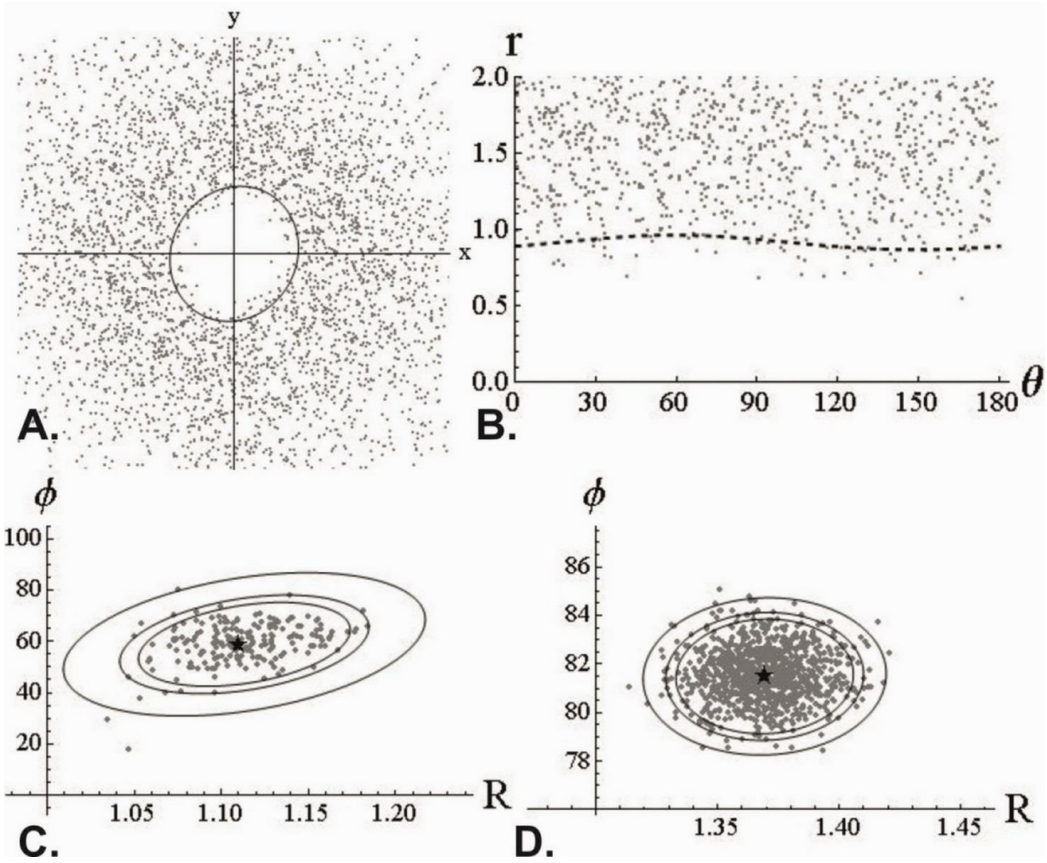

Figure 6. 71 DTNNM and MRL strain estimates for BB5A.

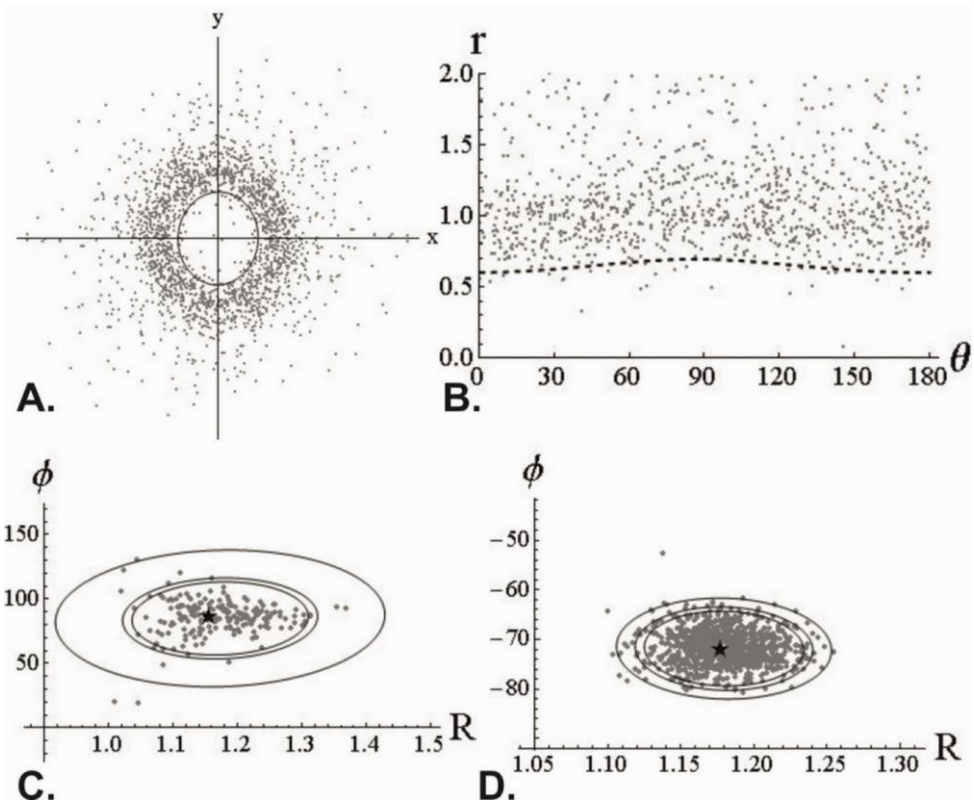

Figure 6. 72 DTNNM and MRL strain estimates for BB17A.

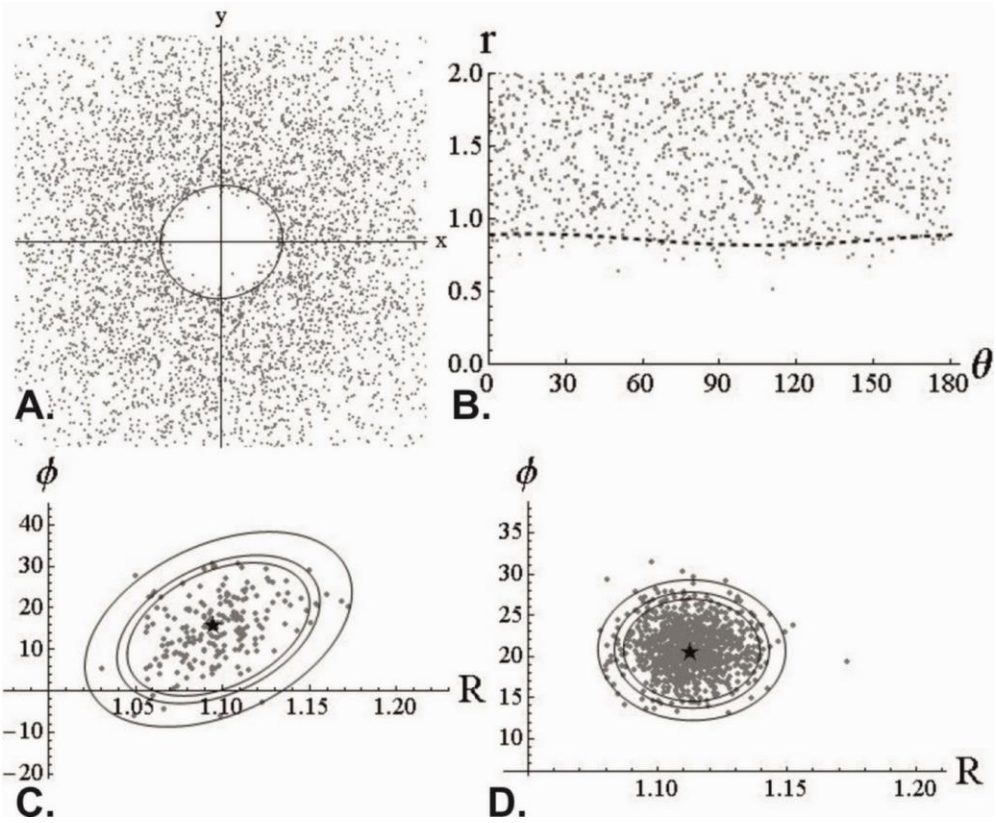

Figure 6. 73 DTNNM and MRL strain estimates for BB8A.

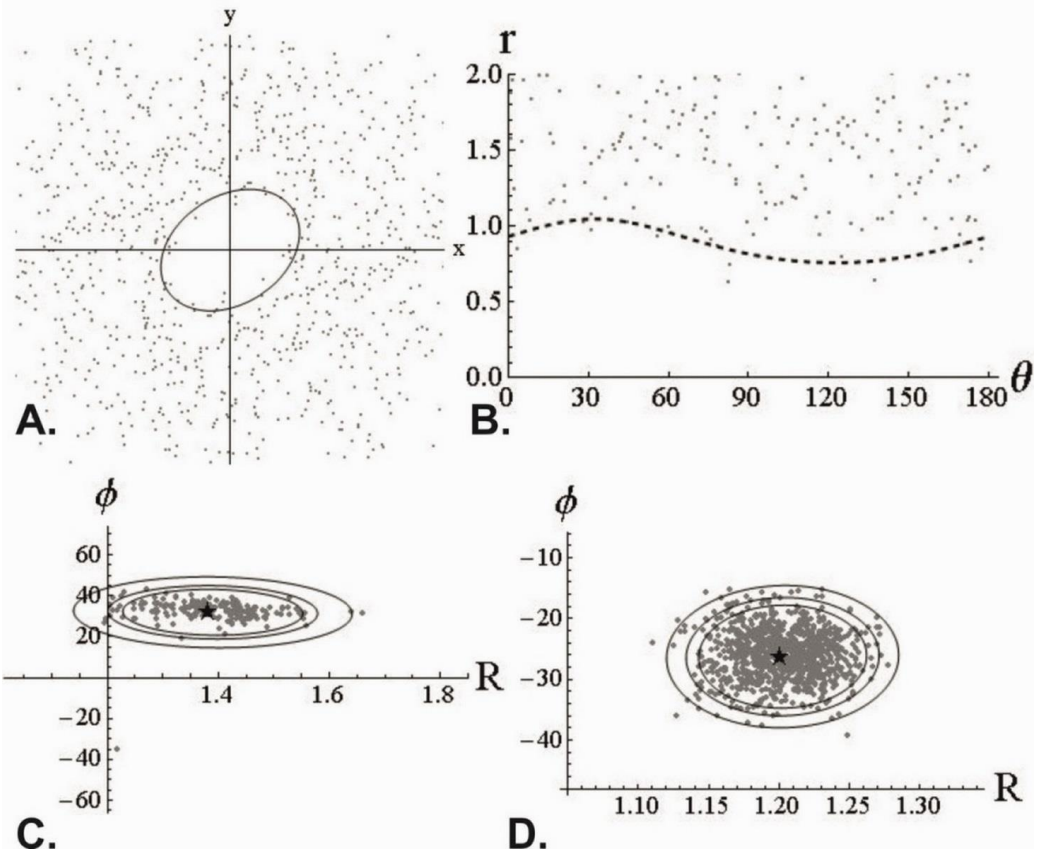

Figure 6. 74 DTNNM and MRL strain estimates for BB18A.

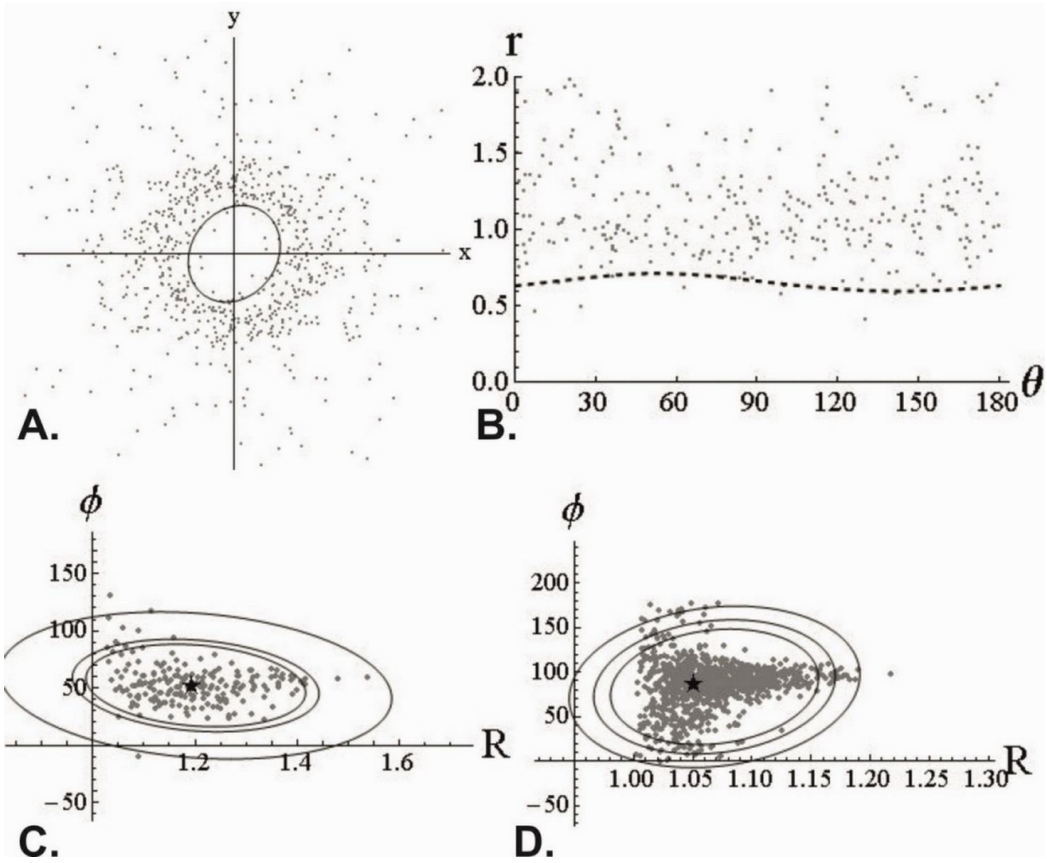

Figure 6. 75 DTNNM and MRL strain estimates for BB10A.

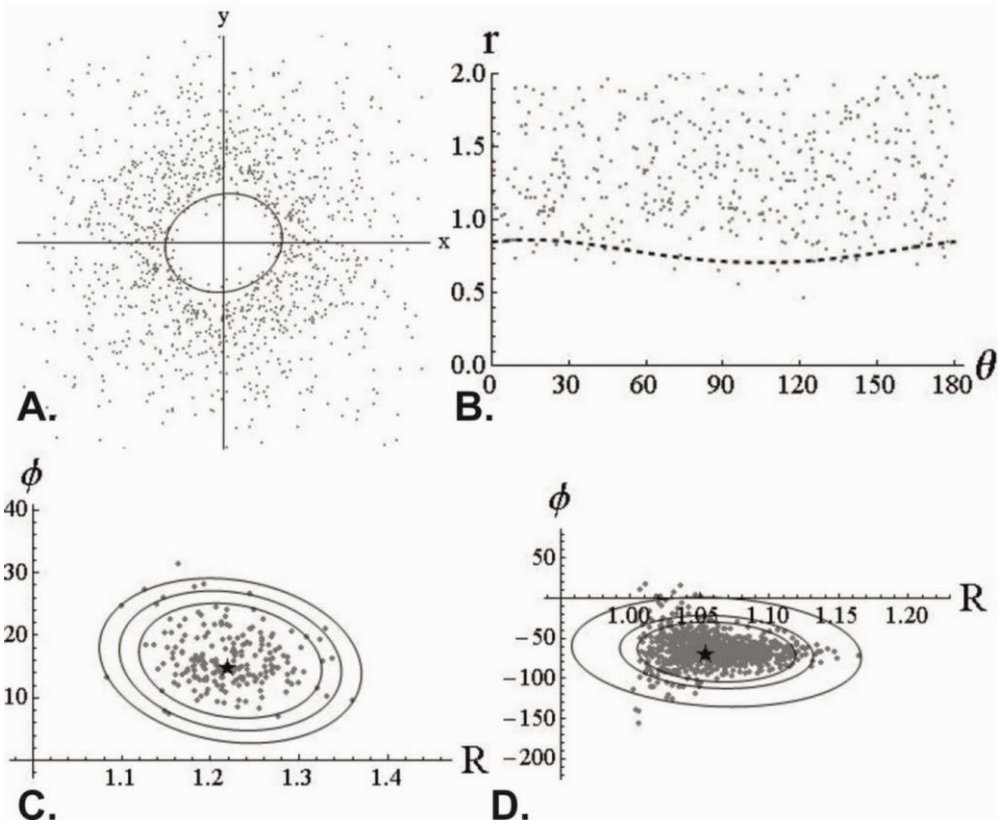

Figure 6. 76 DTNNM and MRL strain estimates for BB9A.

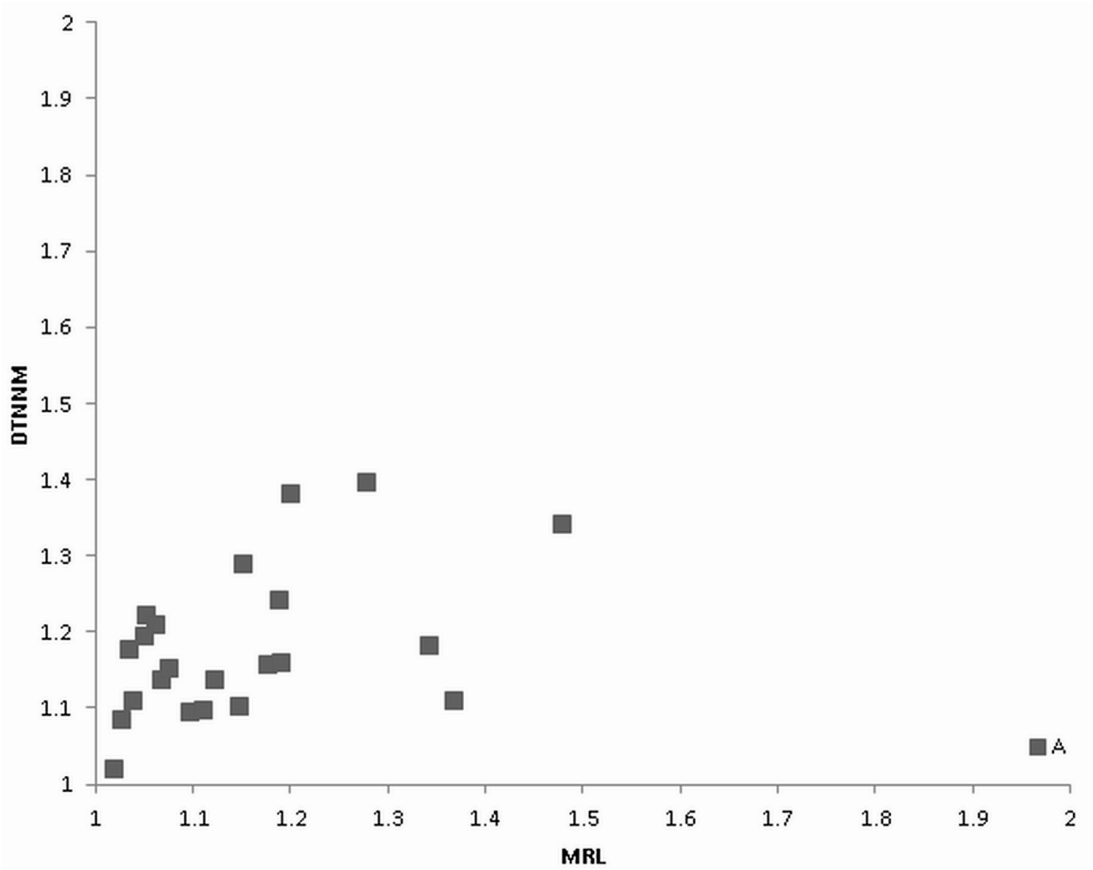

Figure 6. 77 Estimated R values for DTNNM and MRL analyses of the bedding plane parallel (A) sections. DTNNM has produced higher strain estimates than MRL.

6.7.3.2. C SECTIONS

The C sections, which are orthogonal to the bedding plane and strike are largely cut parallel to the orogenic shortening direction and in areas of higher strain they should display a tectonic fabric at a high angle to bedding . Similar to the A sections the strain analyses report largely low strains across the eastern Munster Basin with higher strains to the south of the DDL (Figure 6. 78). The estimated axial ratios and phi orientations from the DTNNM and MRL analyses for individual samples are presented in Figure 6. 79 to Figure 6. 100. Summary plots are presented in Figure 6. 101 and Figure 6. 102. Figure 6. 101 illustrates the estimated R values for both DTNNM and MRL, again DTNNM typically yields higher strain estimates than MRL. Figure 6. 102 is an R/Phi plot of both the MRL and DTNNM analyses. This plot is useful in that a Phi value of 0° is parallel to bedding, and estimated strain ellipses with Phi values approaching 90° or -90° are suggestive of a relatively strong tectonic fabric. Despite low strains this plot shows that approximately half of the samples have estimated strain ellipses with long axes at a high angle (>70°) to bedding.

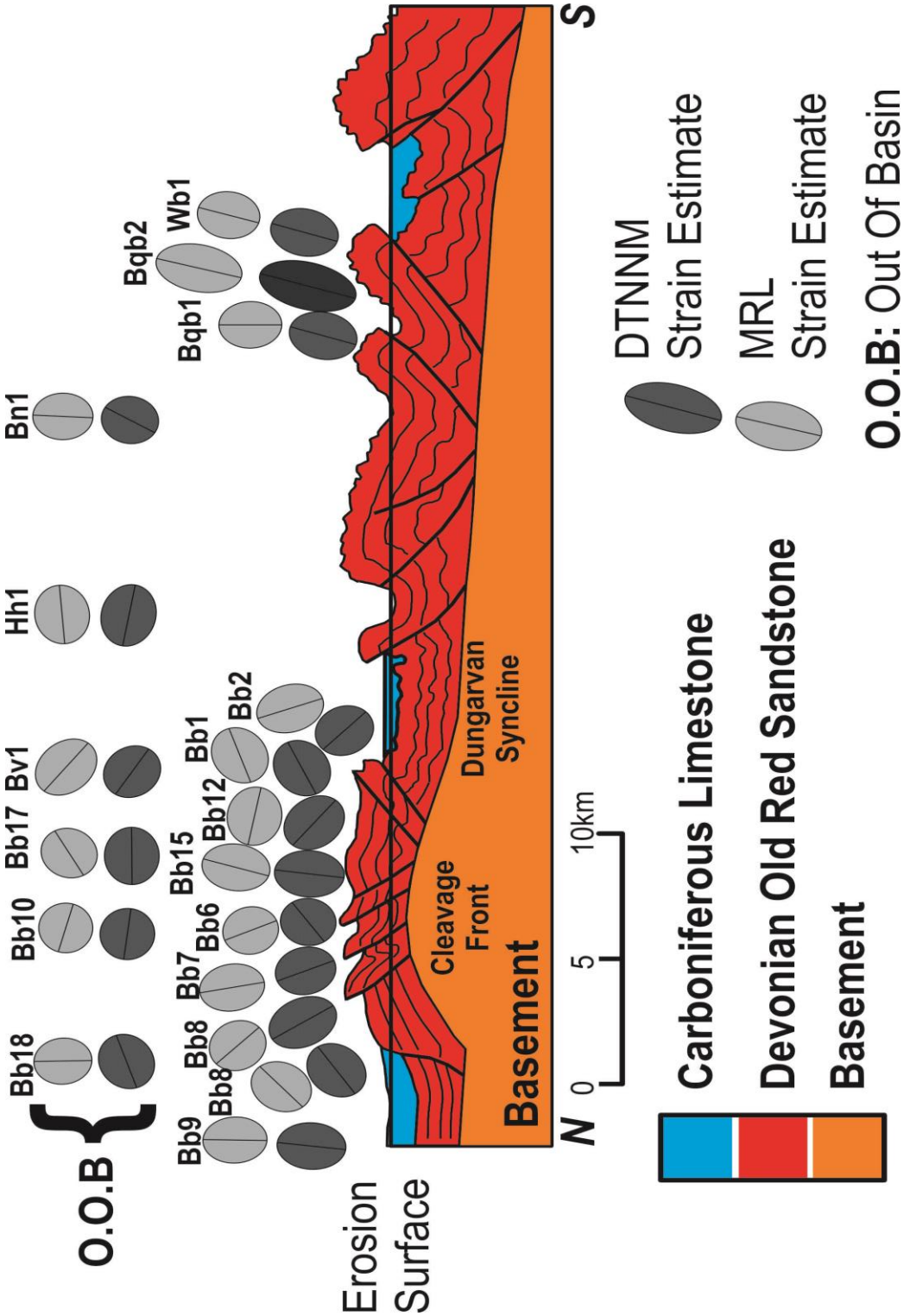

Figure 6. 78 Schematic cross section showing relative location of estimated strain ellipses from C sections.

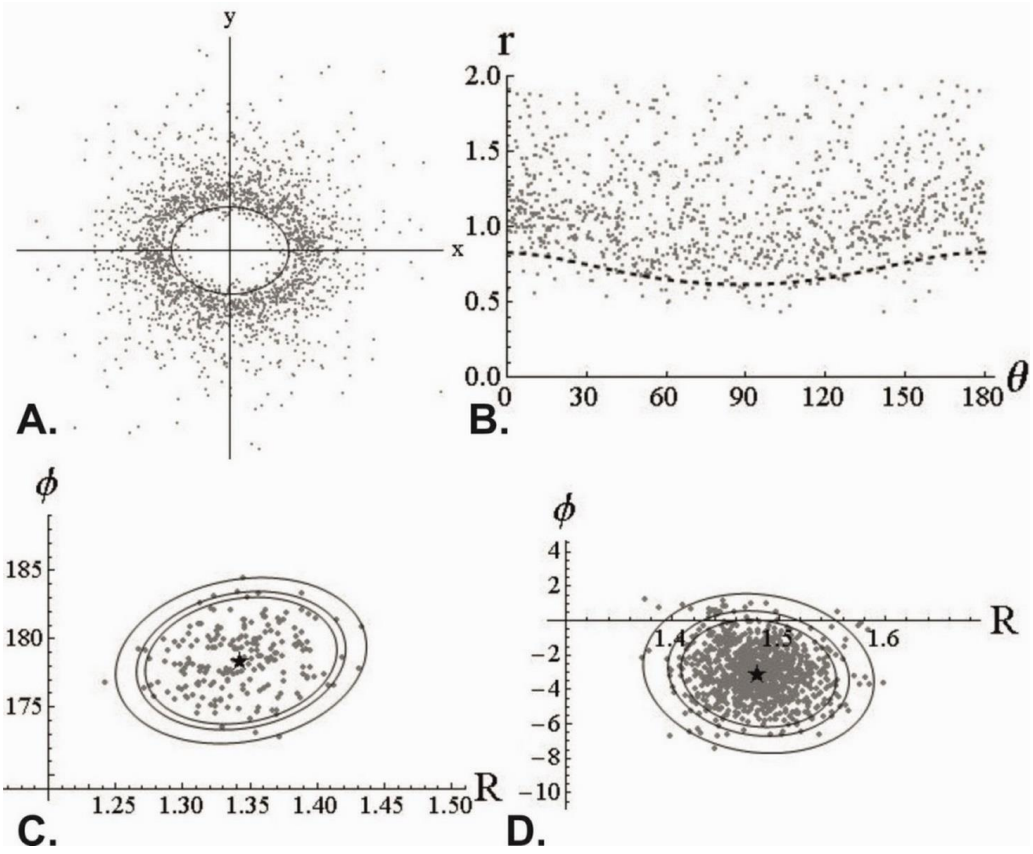

Figure 6. 79 DTNNM and MRL strain estimates for WB1C.

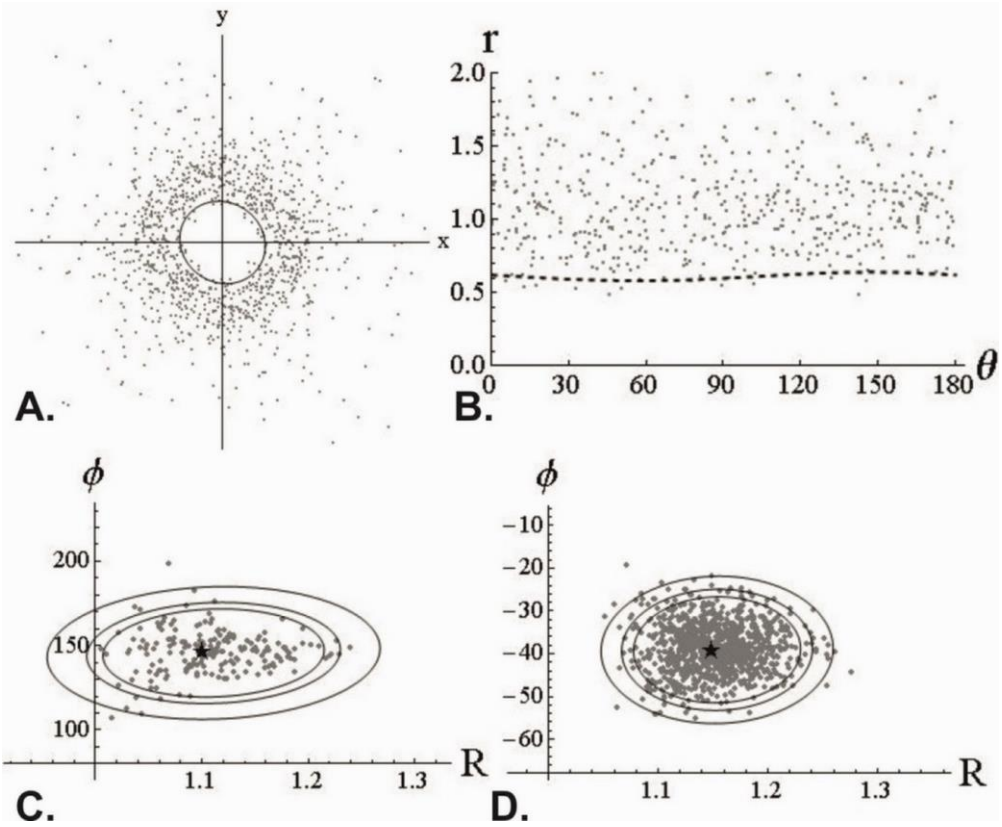

Figure 6. 80 DTNNM and MRL strain estimates for BQ1C.

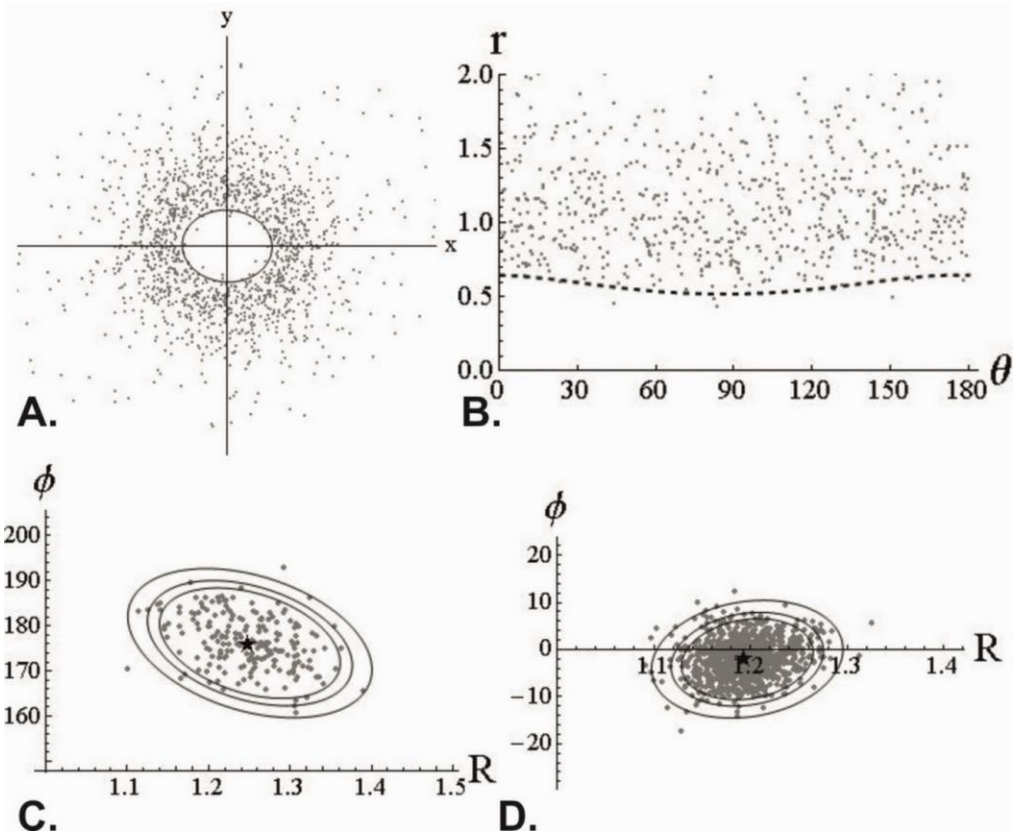

Figure 6. 81 DTNNM and MRL strain estimates for BQ2C.

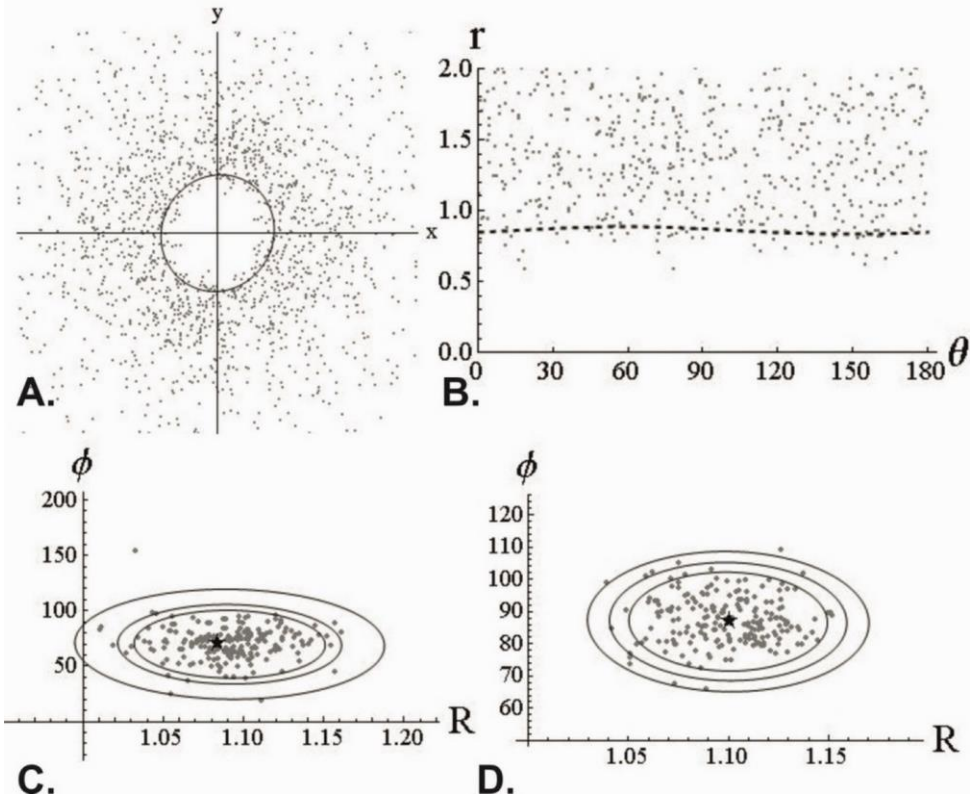

Figure 6. 82 DTNNM and MRL strain estimates for BN1C.

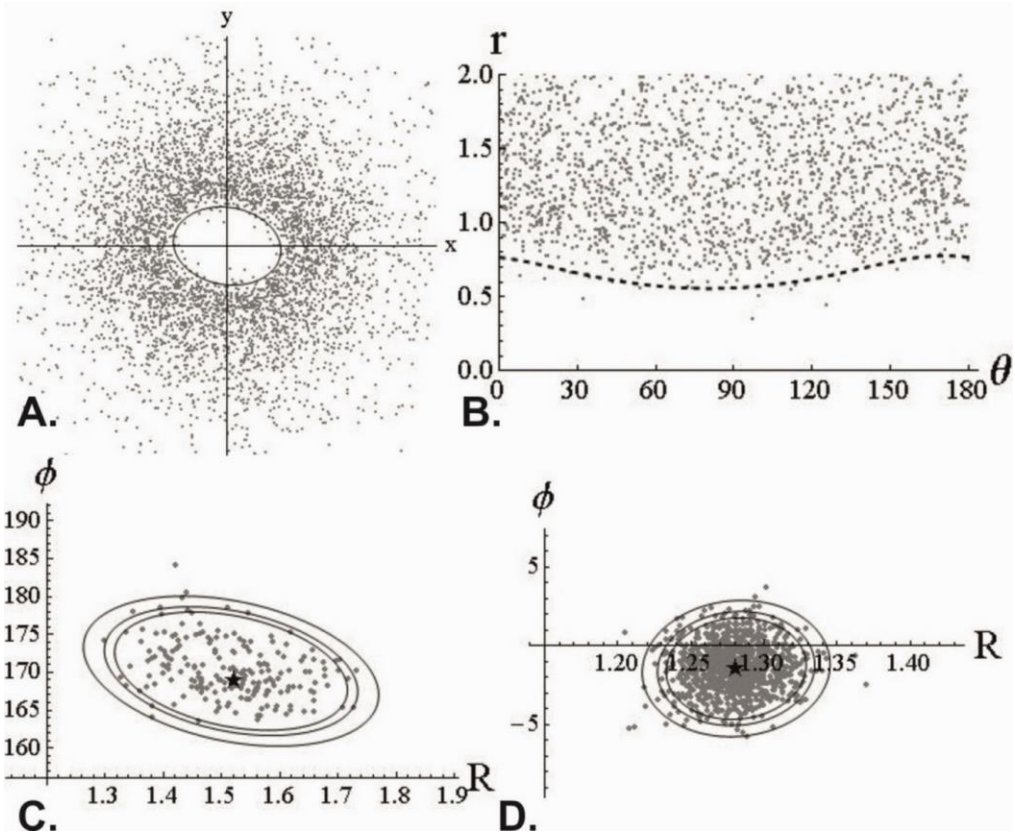

Figure 6. 83 DTNNM and MRL strain estimates for HH1C.

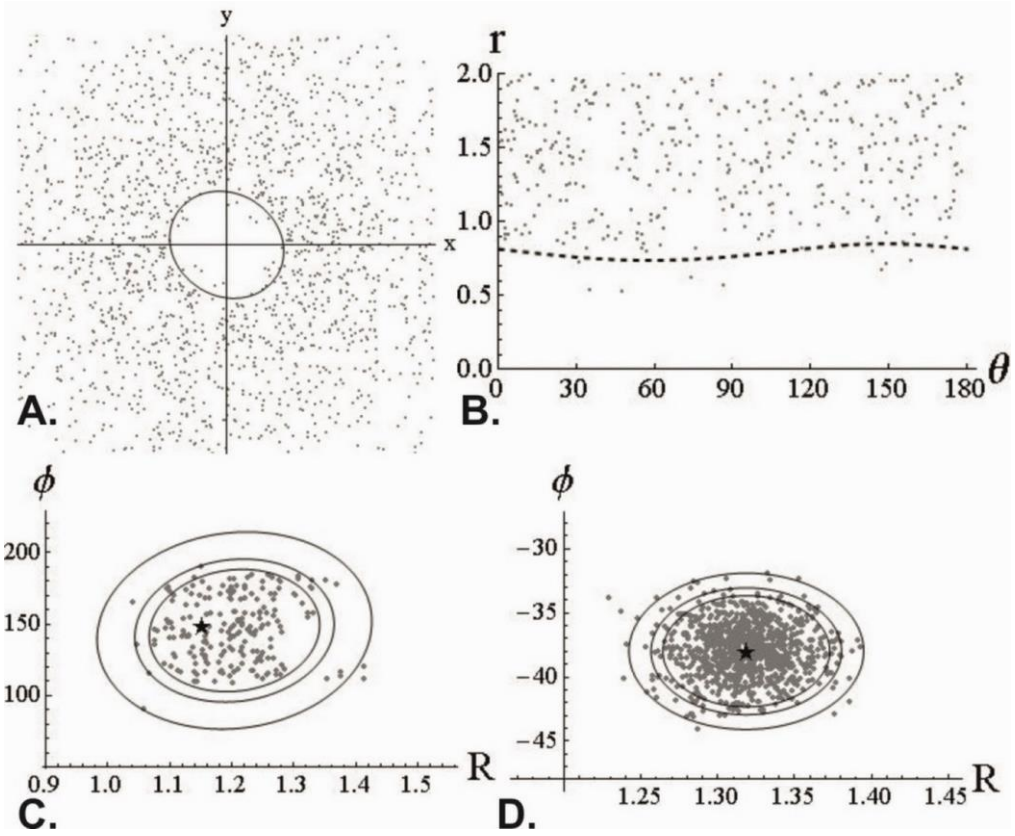

Figure 6. 84 DTNNM and MRL strain estimates for BV1C.

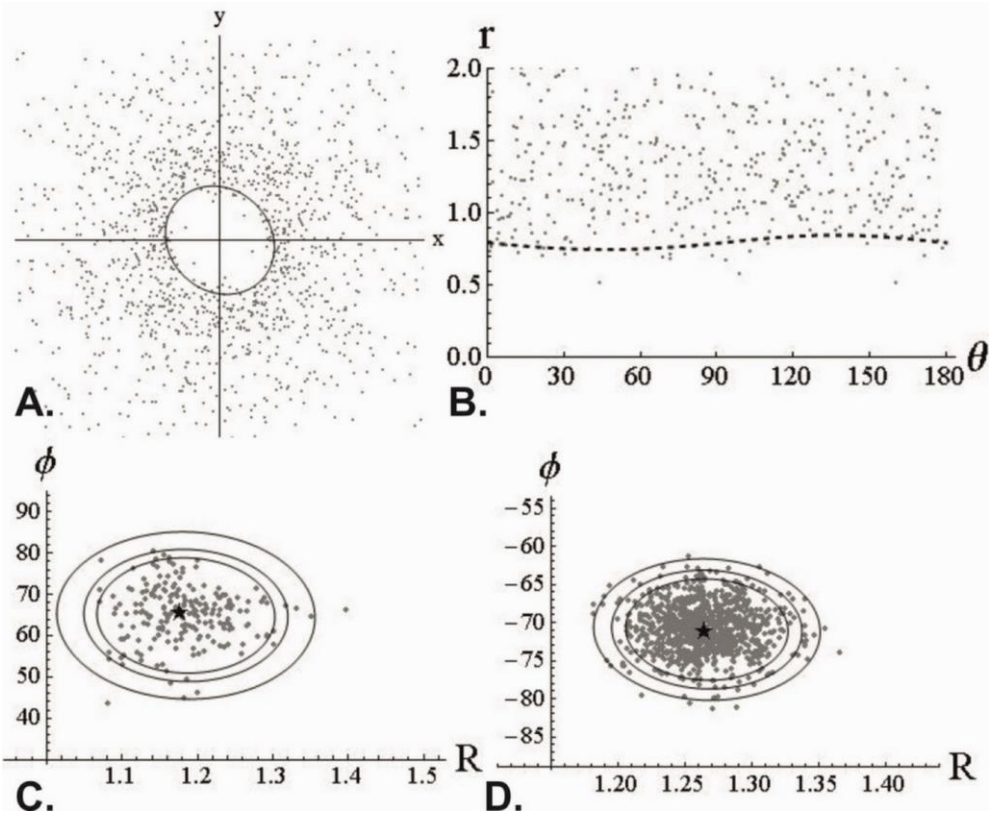

Figure 6. 85 DTNNM and MRL strain estimates for BB1C.

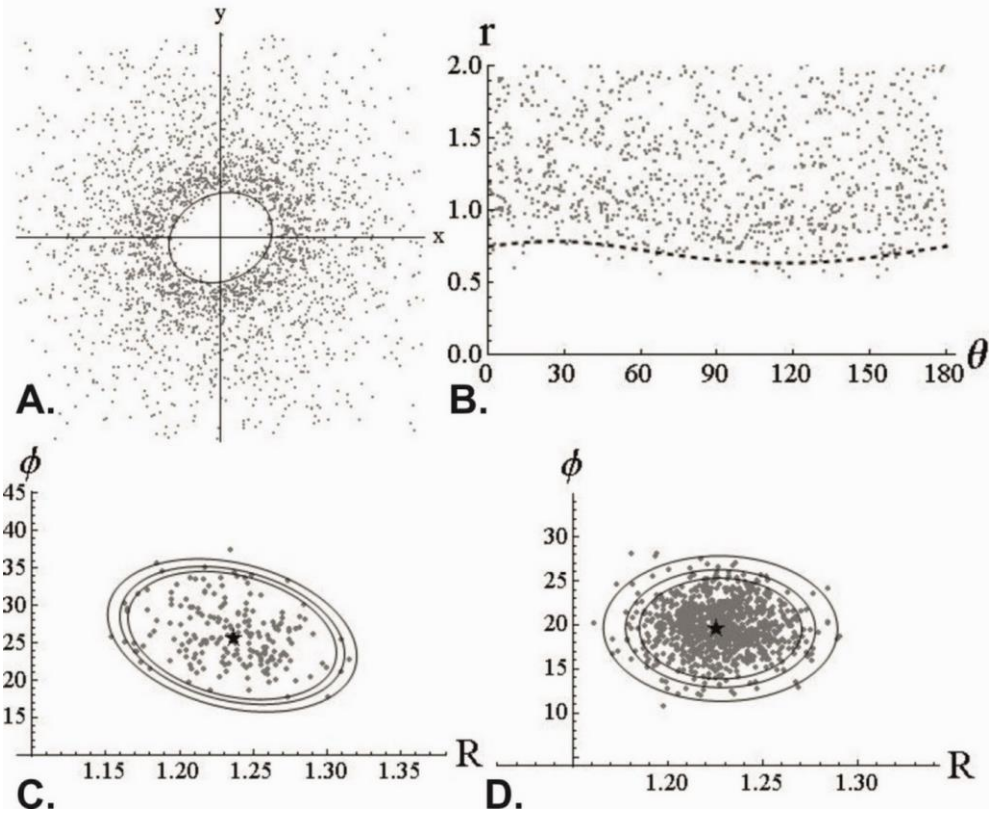

Figure 6. 86 DTNNM and MRL strain estimates for BB2C.

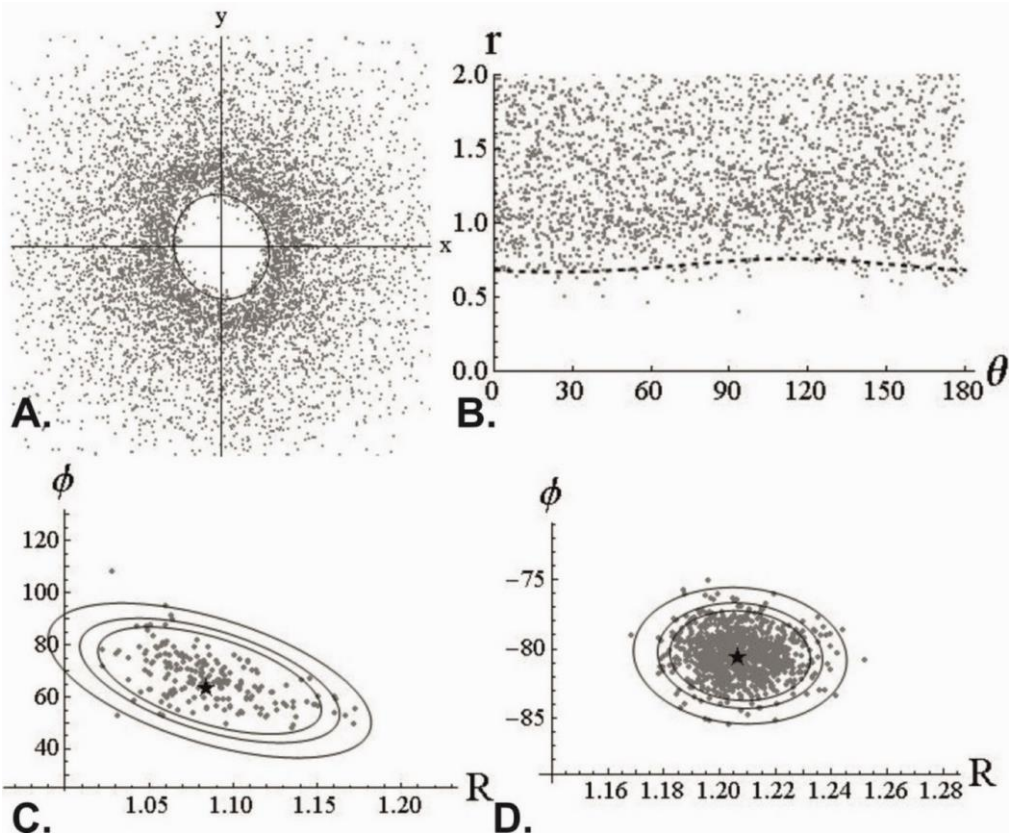

Figure 6. 87 DTNNM and MRL strain estimates for BB3C.

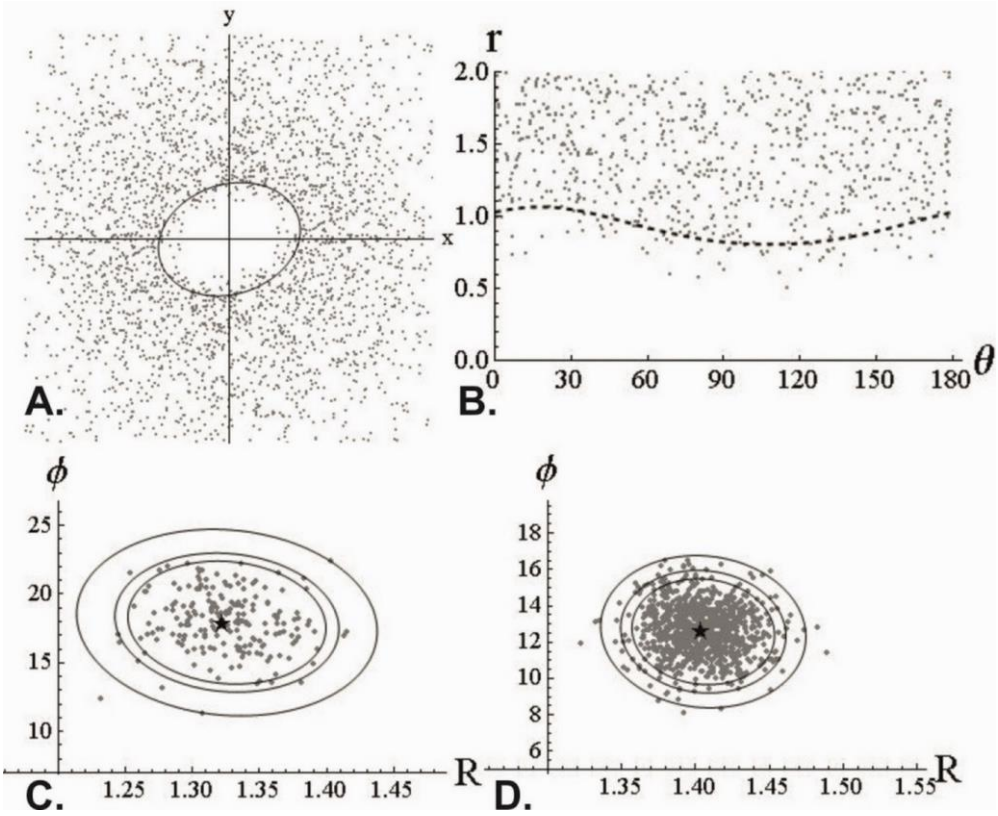

Figure 6. 88 DTNNM and MRL strain estimates for BB4C.

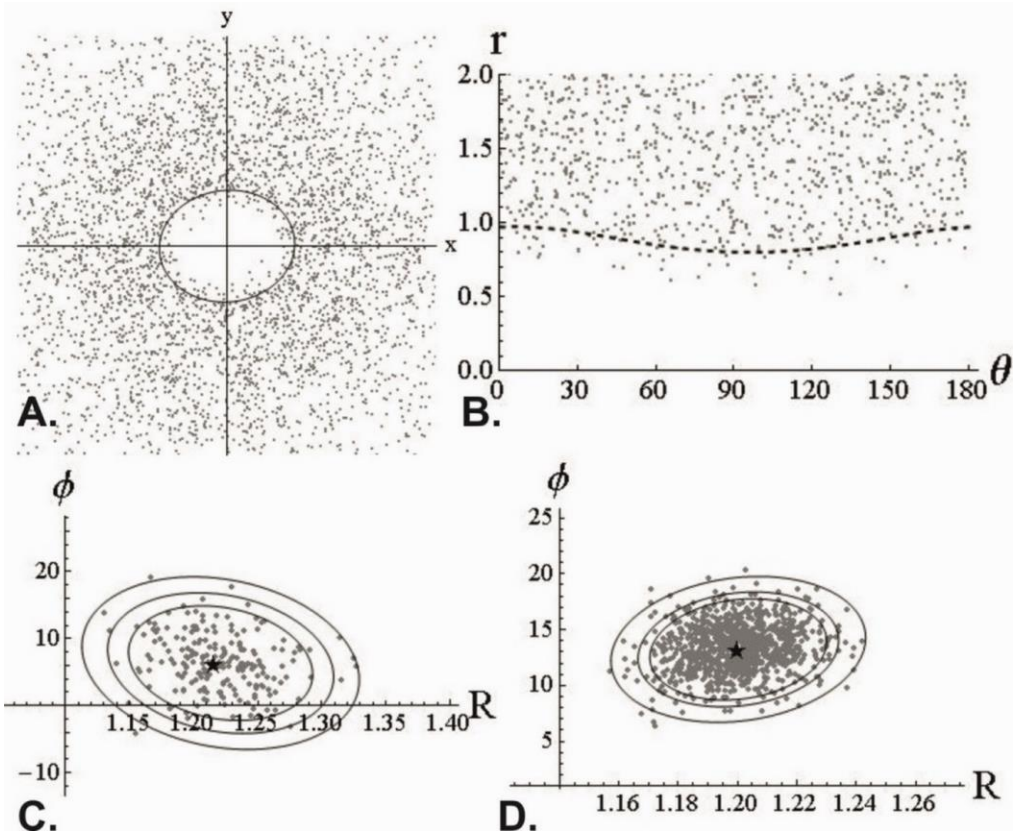

Figure 6. 89 DTNNM and MRL strain estimates for BB15C.

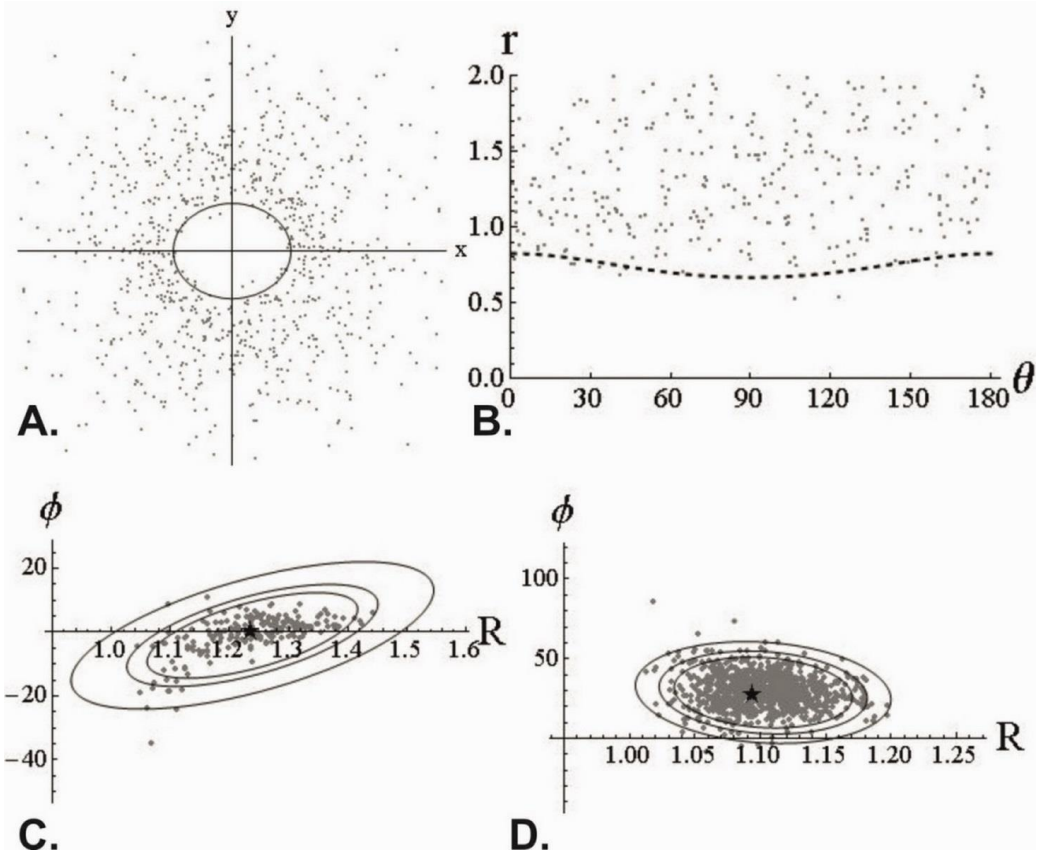

Figure 6. 90 DTNNM and MRL strain estimates for BB11C.

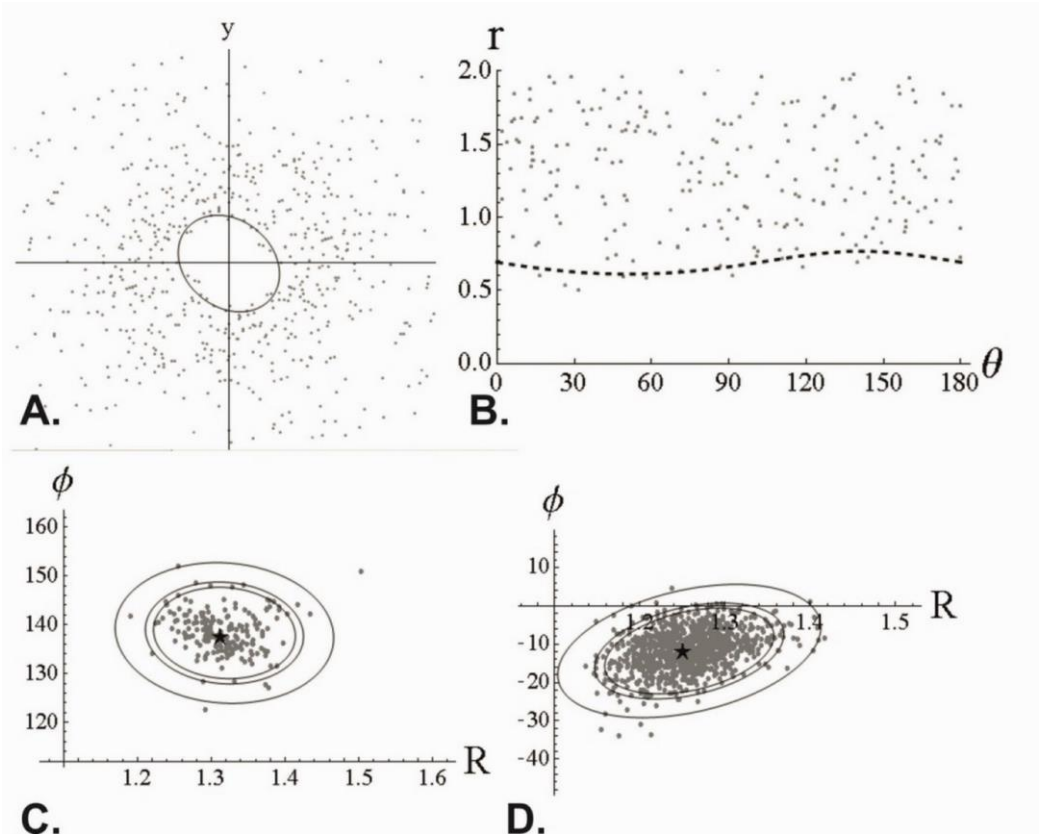

Figure 6. 91 DTNNM and MRL strain estimates for BB12C.

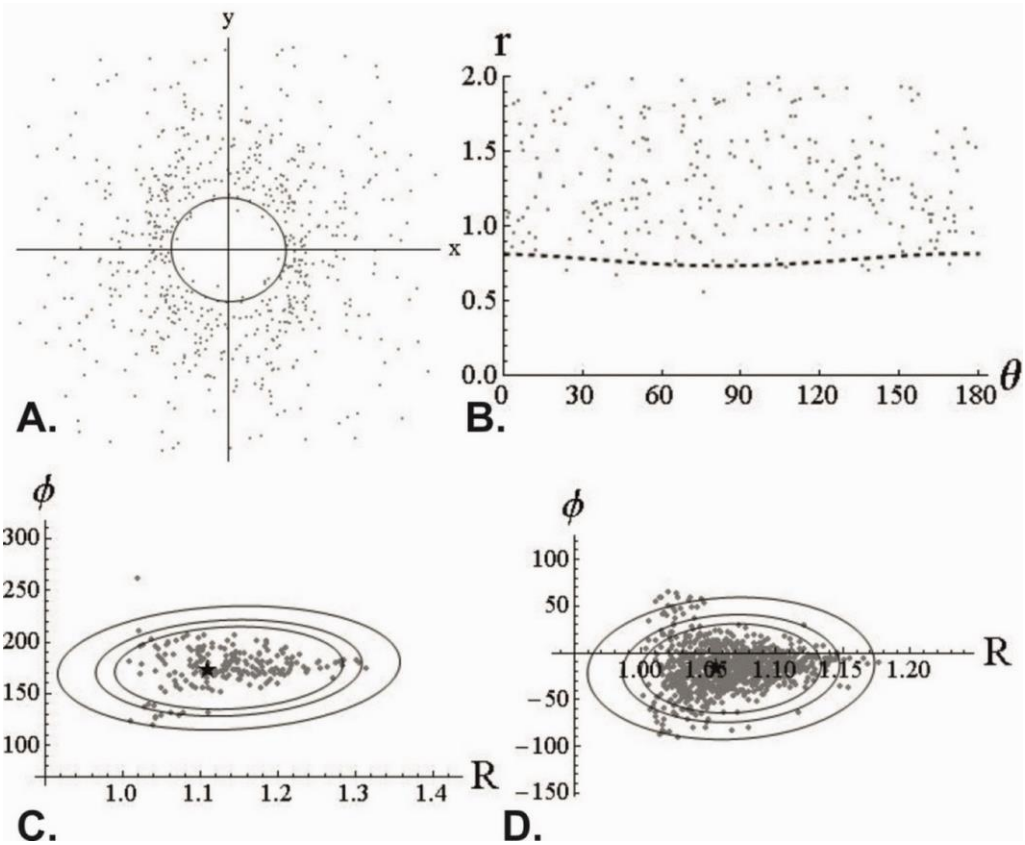

Figure 6. 92 DTNNM and MRL strain estimates for BB14C.

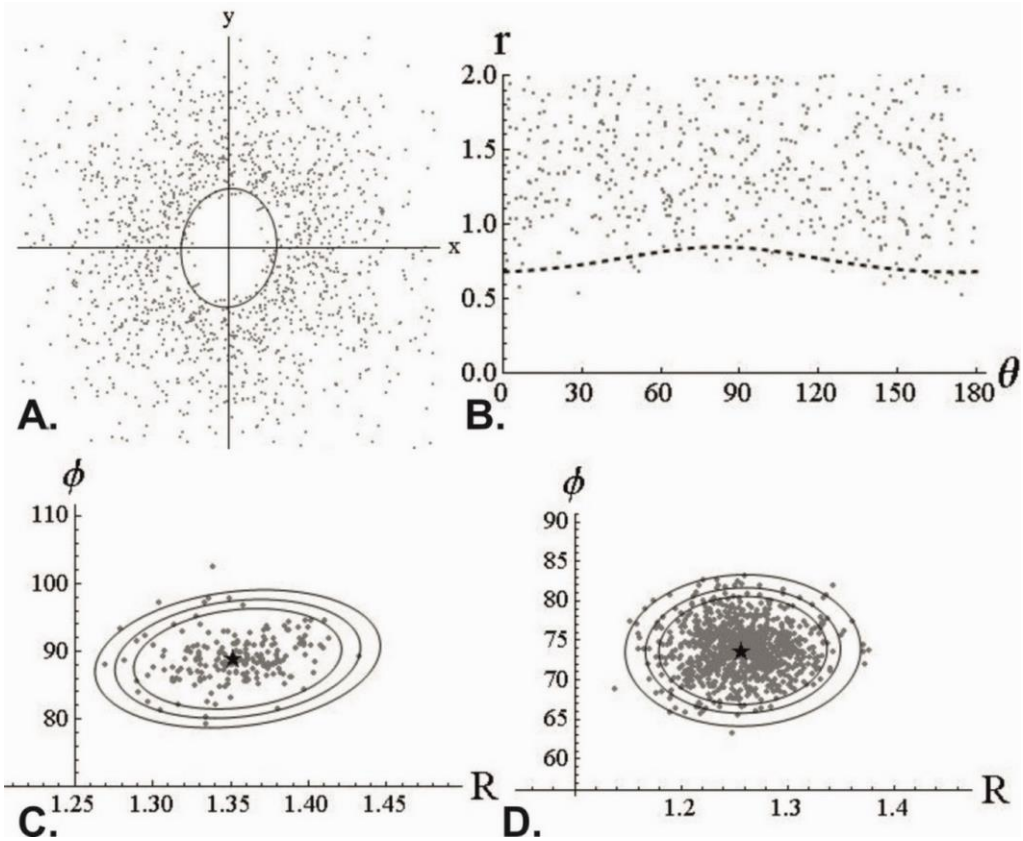

Figure 6. 93 DTNNM and MRL strain estimates for BB6C.

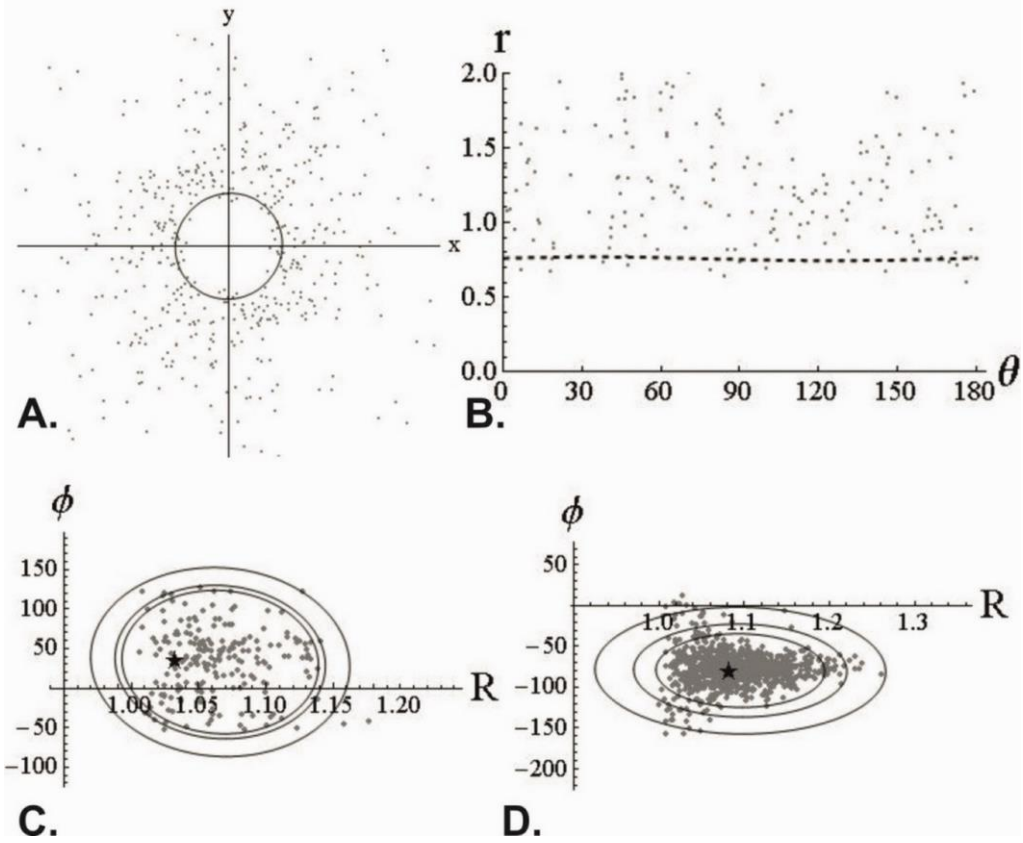

Figure 6. 94 DTNNM and MRL strain estimates for BB7C.

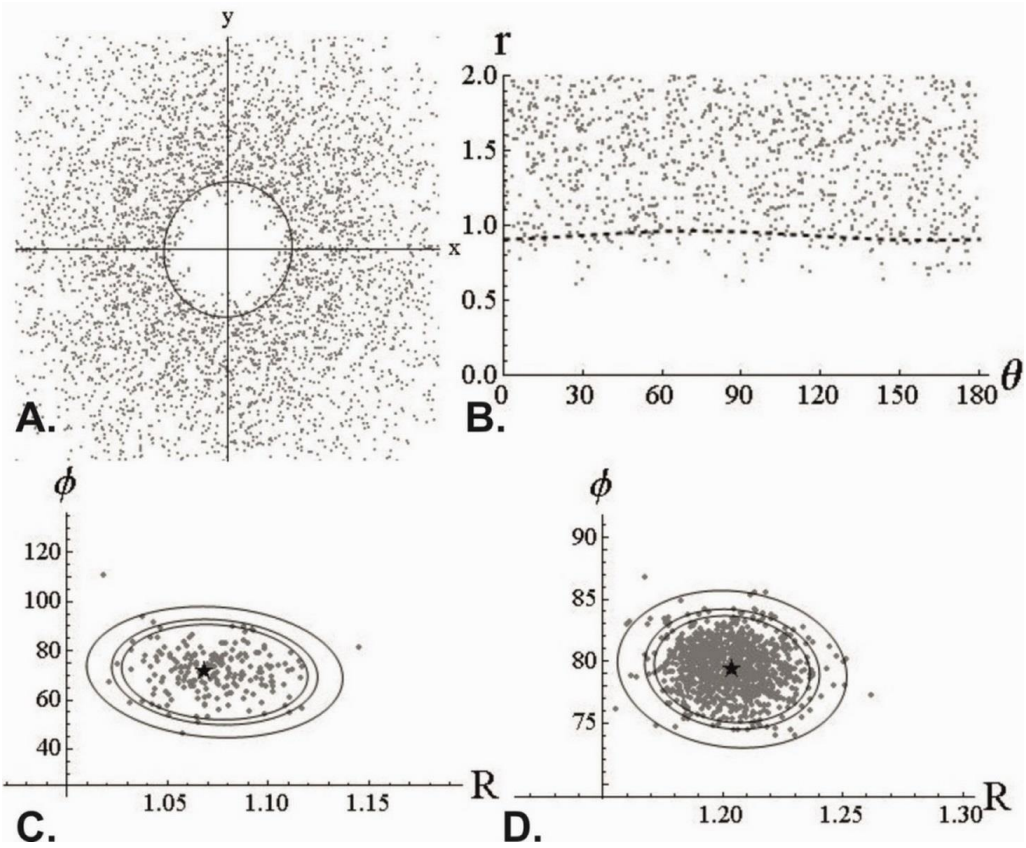

Figure 6. 95 DTNNM and MRL strain estimates for BB5C.

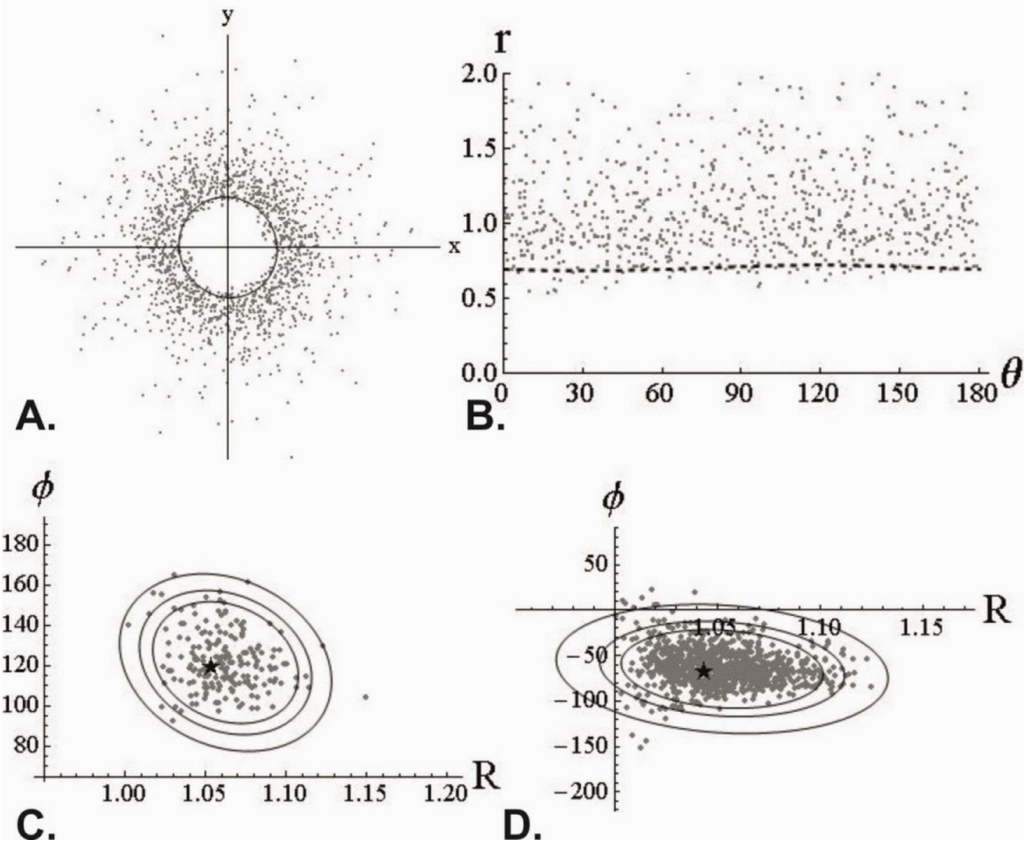

Figure 6. 96 DTNNM and MRL strain estimates for BB17C.

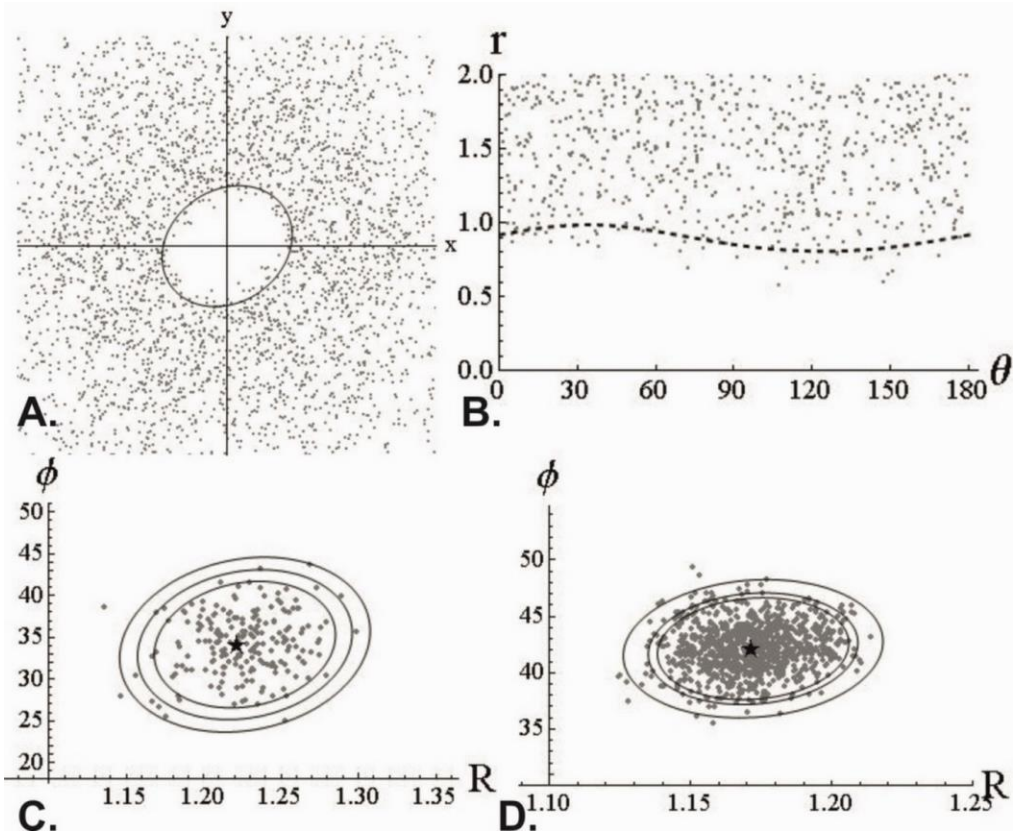

Figure 6. 97 DTNNM and MRL strain estimates for BB8C.

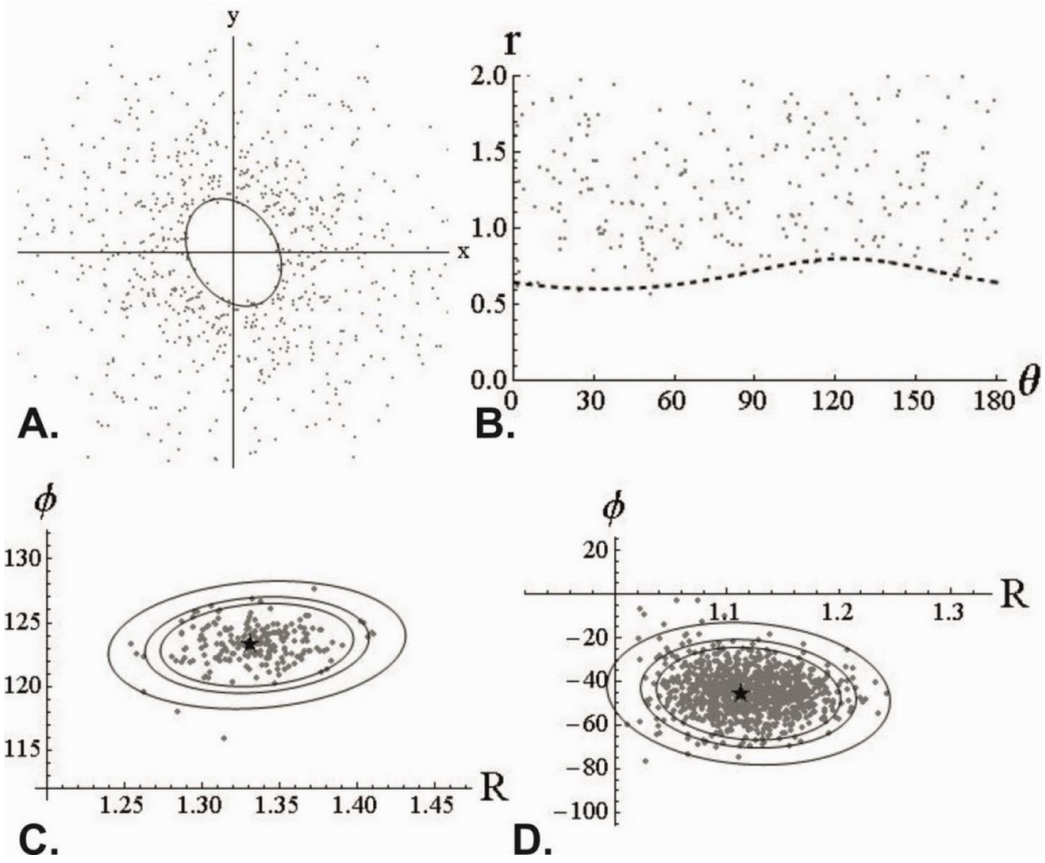

Figure 6. 98 DTNNM and MRL strain estimates for BB18C.

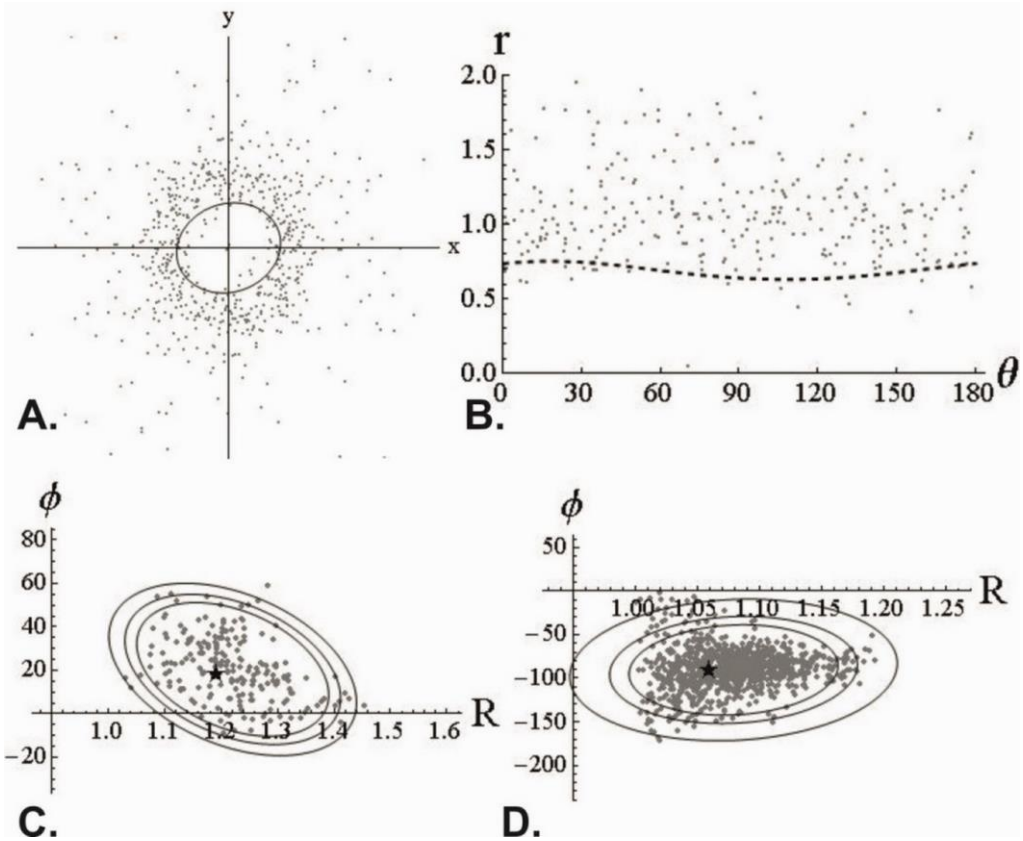

Figure 6. 99 DTNNM and MRL strain estimates for BB10C.

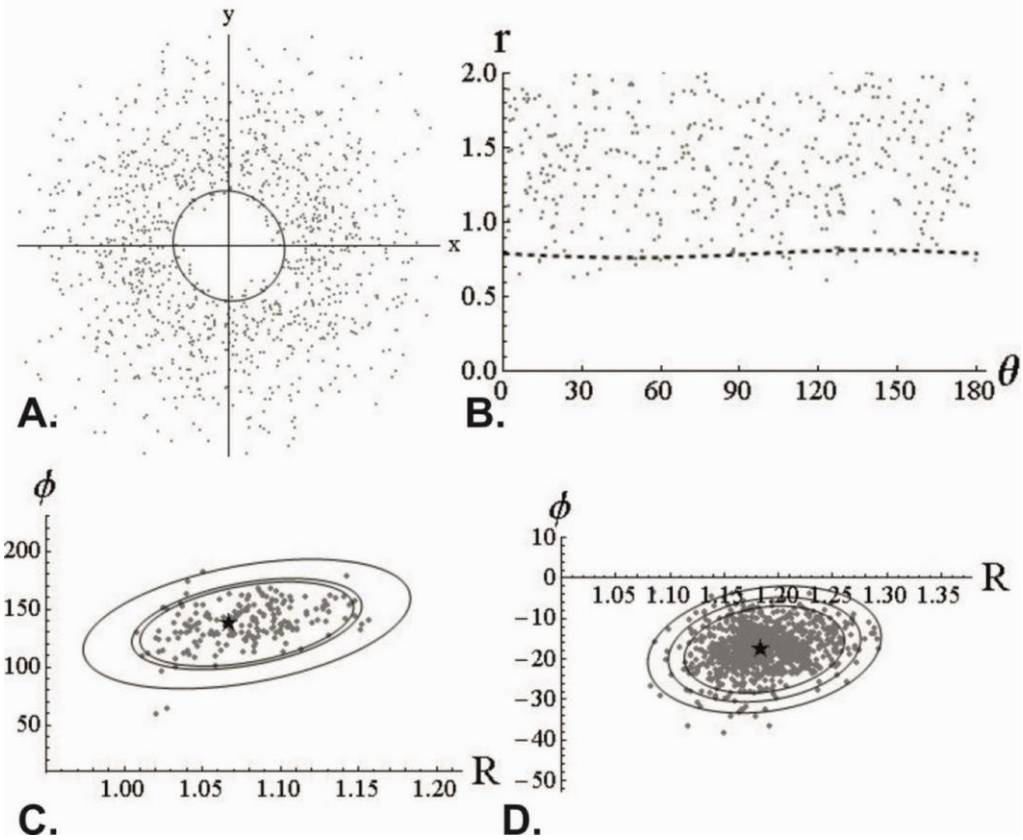

Figure 6. 100 DTNNM and MRL strain estimates for BB9C.

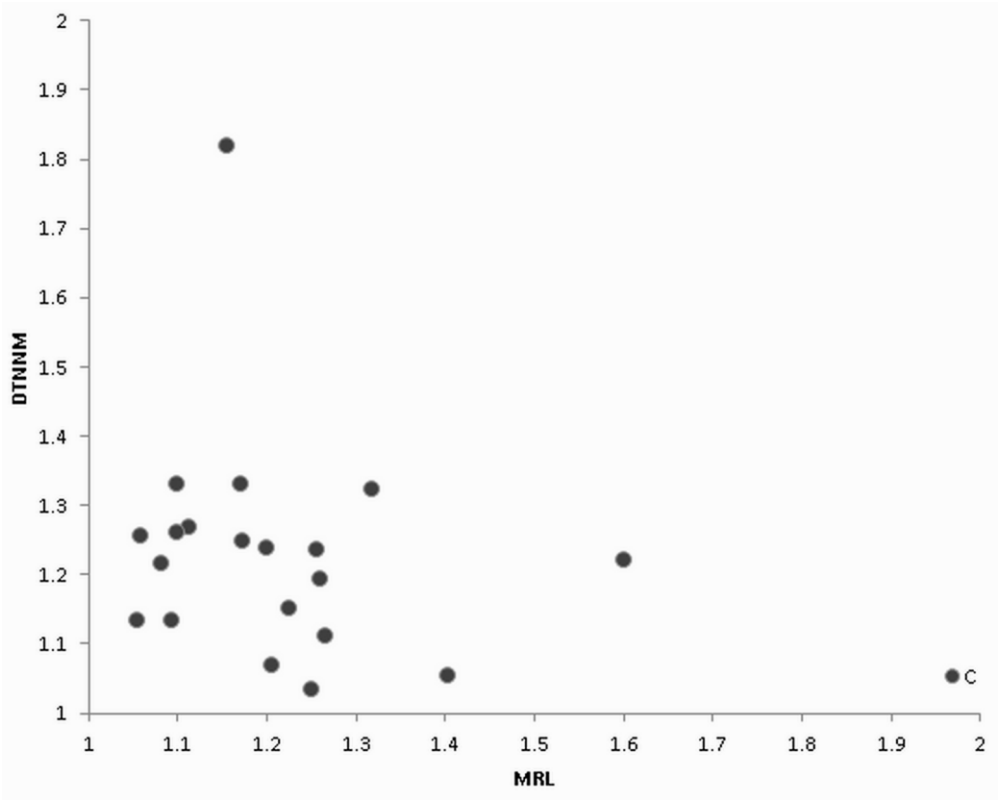

Figure 6. 101 . Estimated R values for DTNNM and MRL analyses of the orogen parallel sections. DTNNM has produced higher strain estimates than MRL.

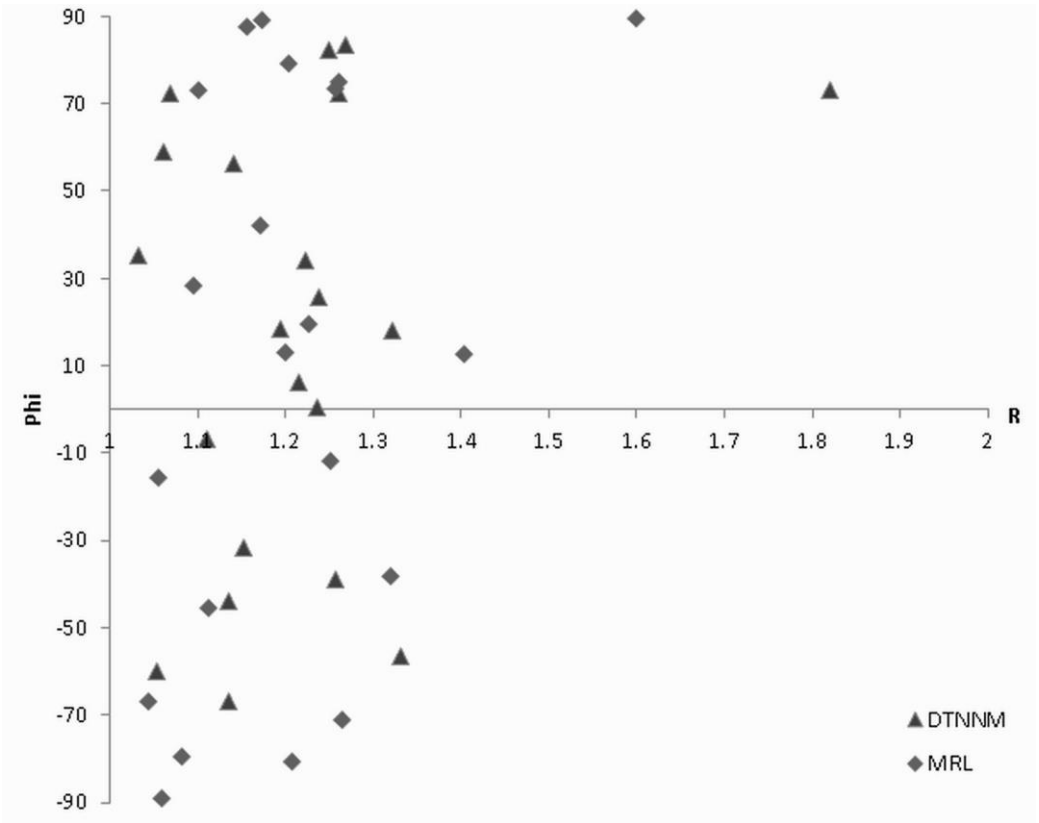

Figure 6. 102 R/Phi for the C sections, in this case Phi orientations represent deviations away from the trace of bedding in the section.

6.7.3.3. Strike Parallel Sections

The estimated axial ratios and phi orientations from both DTNNM and MRL analyses of the strike parallel sections (B sections) are presented in Figure 6. 103 to Figure 6. 119. Summary plots are presented in Figure 6. 120 and Figure 6. 121. Figure 6. 120 illustrates the estimated R values for both DTNNM and MRL. It is clear from this plot that the strain is again typically low, less than 1.3 for most samples, but also that DTNNM yields higher strain estimates than MRL. Figure 6. 121 is an R/Phi plot of both the MRL and DTNNM analyses, as expected for the strike parallel sections the majority of samples show low strain and the Phi orientations are near parallel to bedding. Only 11 results record Phi orientations that are nearly orthogonal to bedding, but again these are typically weak, with only one sample with an R value >1.3. There is one sample (BB12) that has a DTNNM R value of 1.9 but this is bedding parallel and is interpreted to be a bedding fabric rather than a result of tectonic strain. This value raises a serious issue with the validity of these methods, as if bedding fabrics can yield results of R=1.9, then estimating true strain in low strain environments becomes problematic.

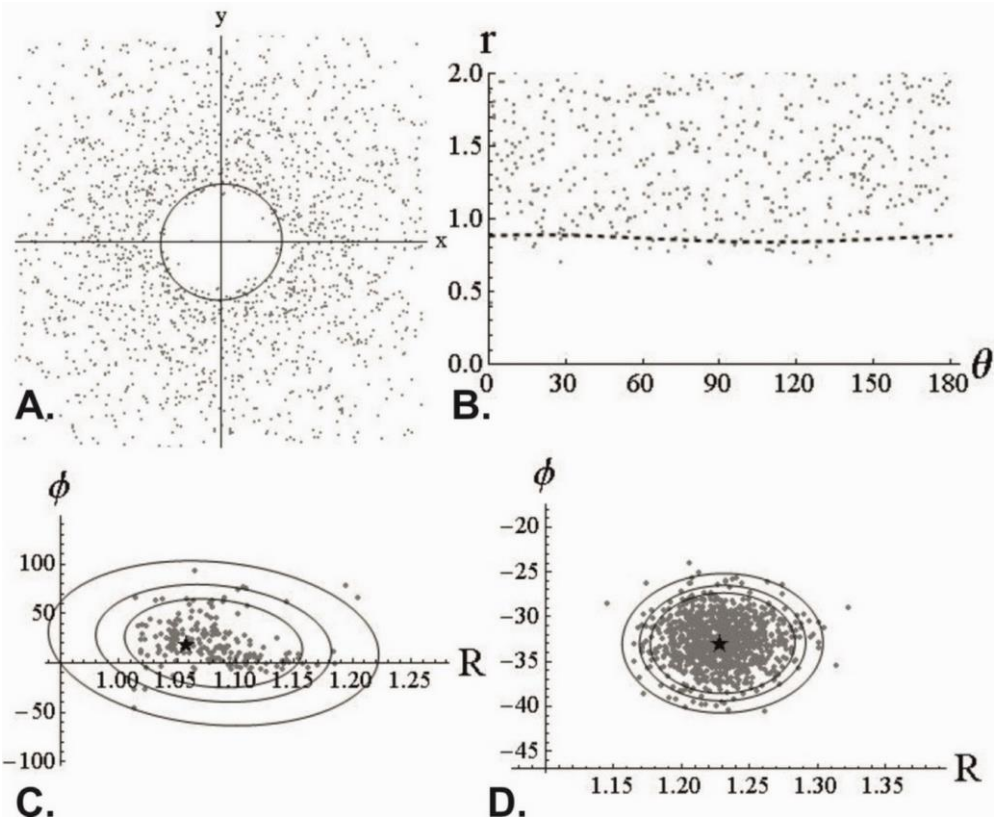

Figure 6. 103 DTNNM and MRL strain estimates for BV1B.

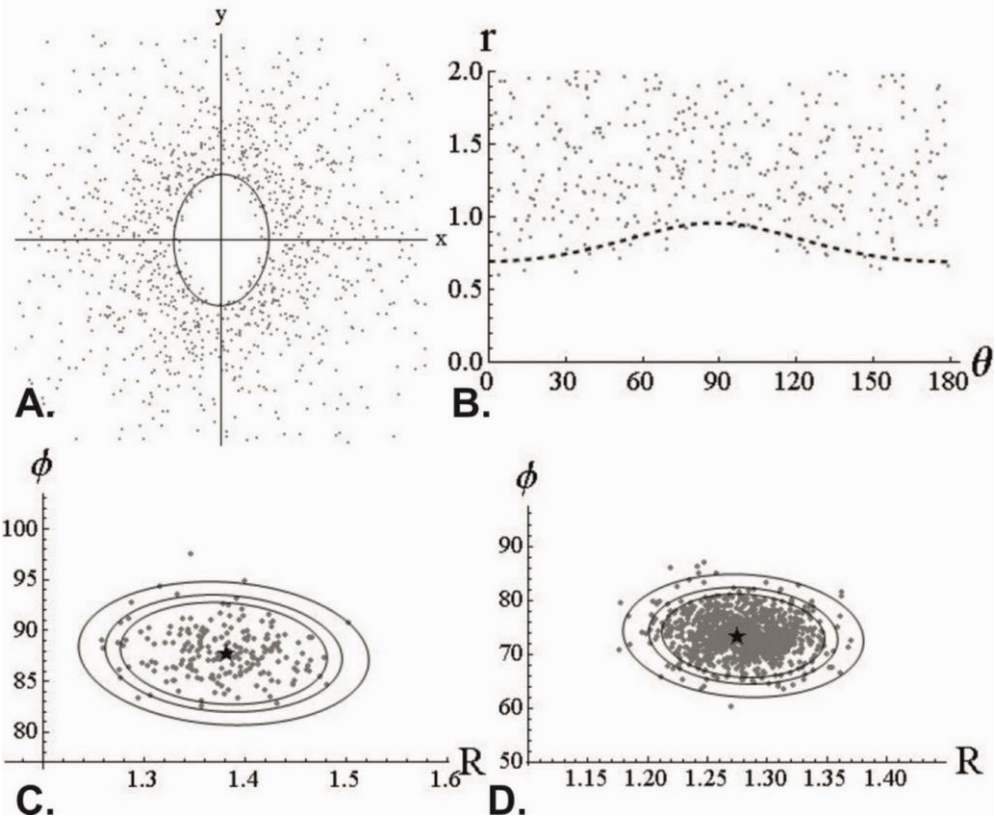

Figure 6. 104 DTNNM and MRL strain estimates for BB1B.

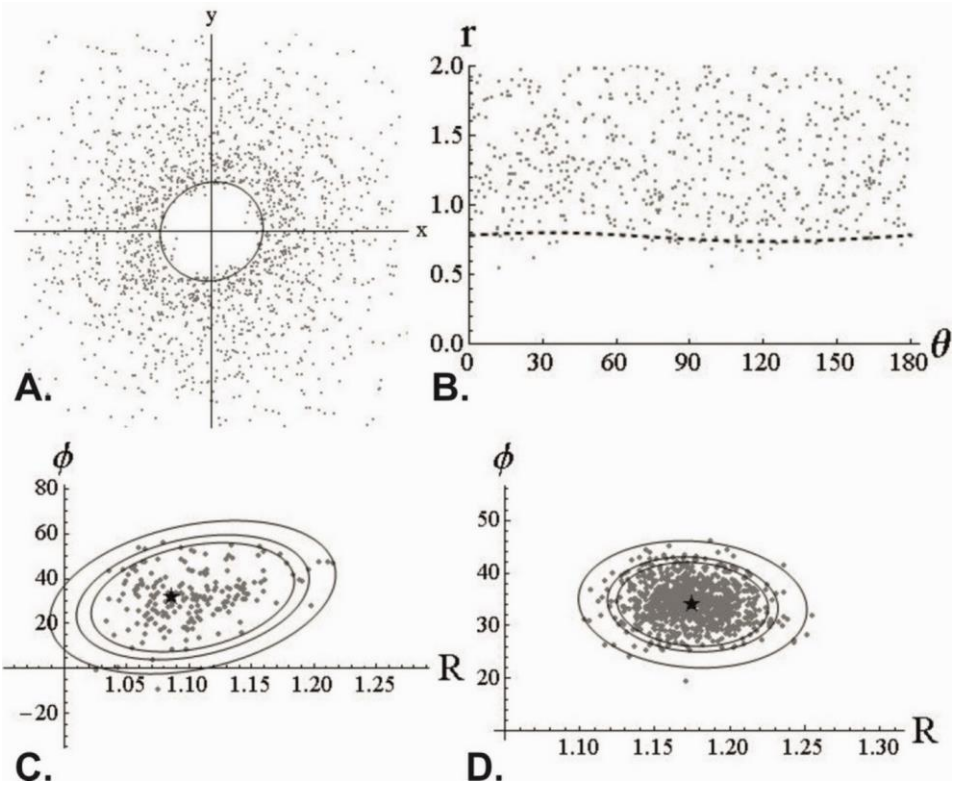

Figure 6. 105 DTNNM and MRL strain estimates for BB2B.

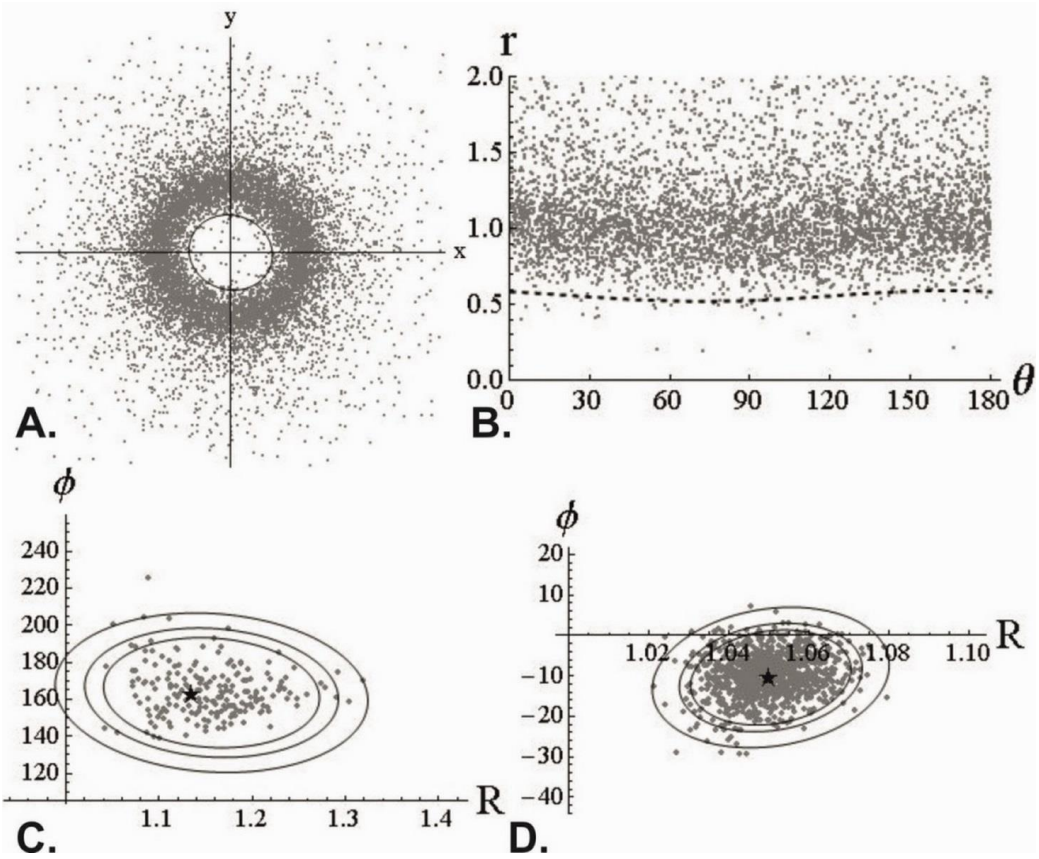

Figure 6. 106 DTNNM and MRL strain estimates for BB3B.

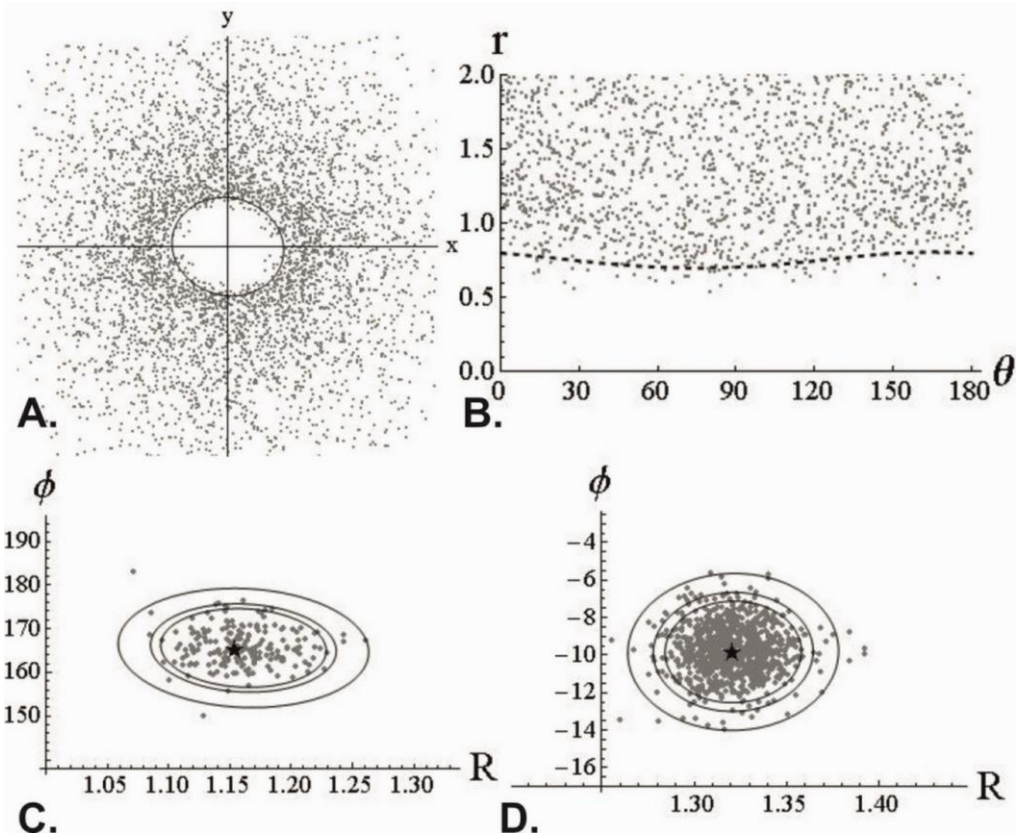

Figure 6. 107 DTNNM and MRL strain estimates for BB4B.

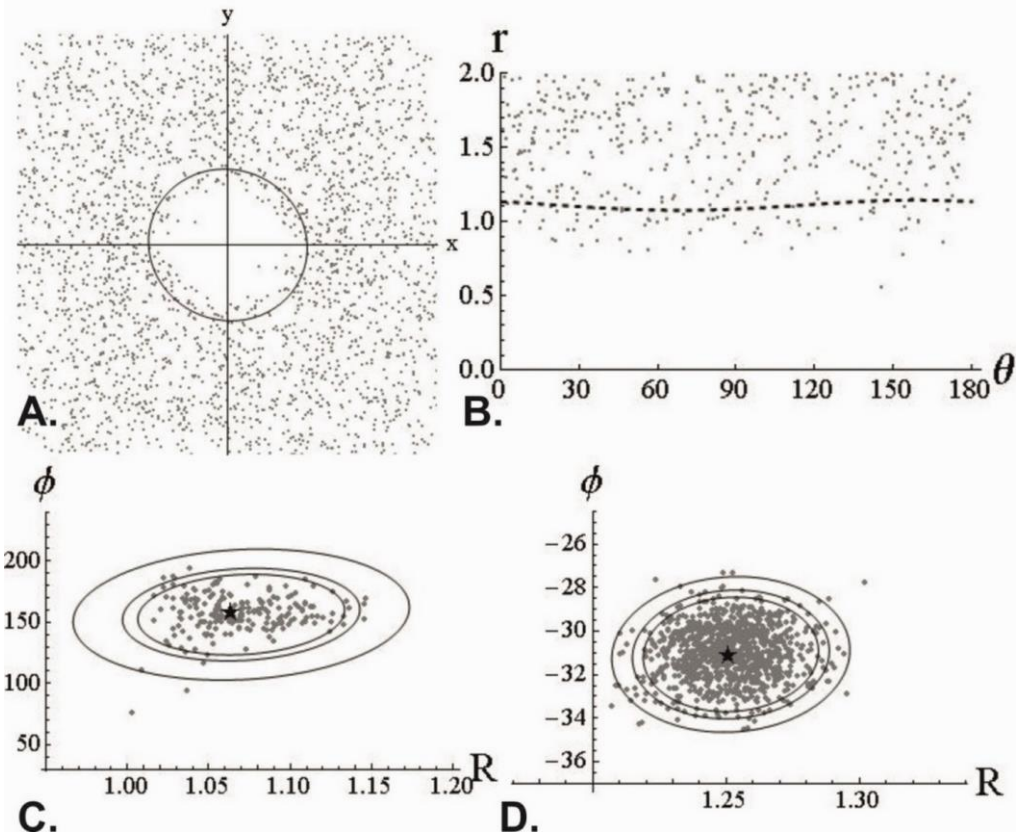

Figure 6. 108 DTNNM and MRL strain estimates for BB15B.

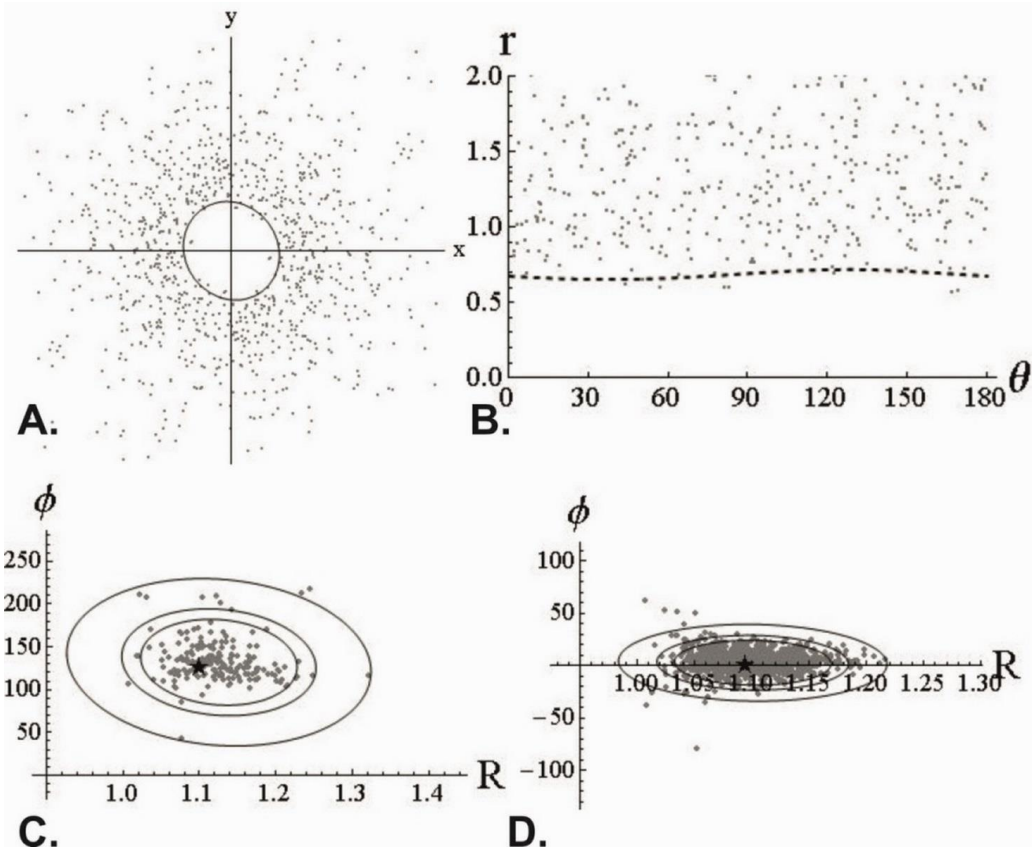

Figure 6. 109 DTNNM and MRL strain estimates for BB11B.

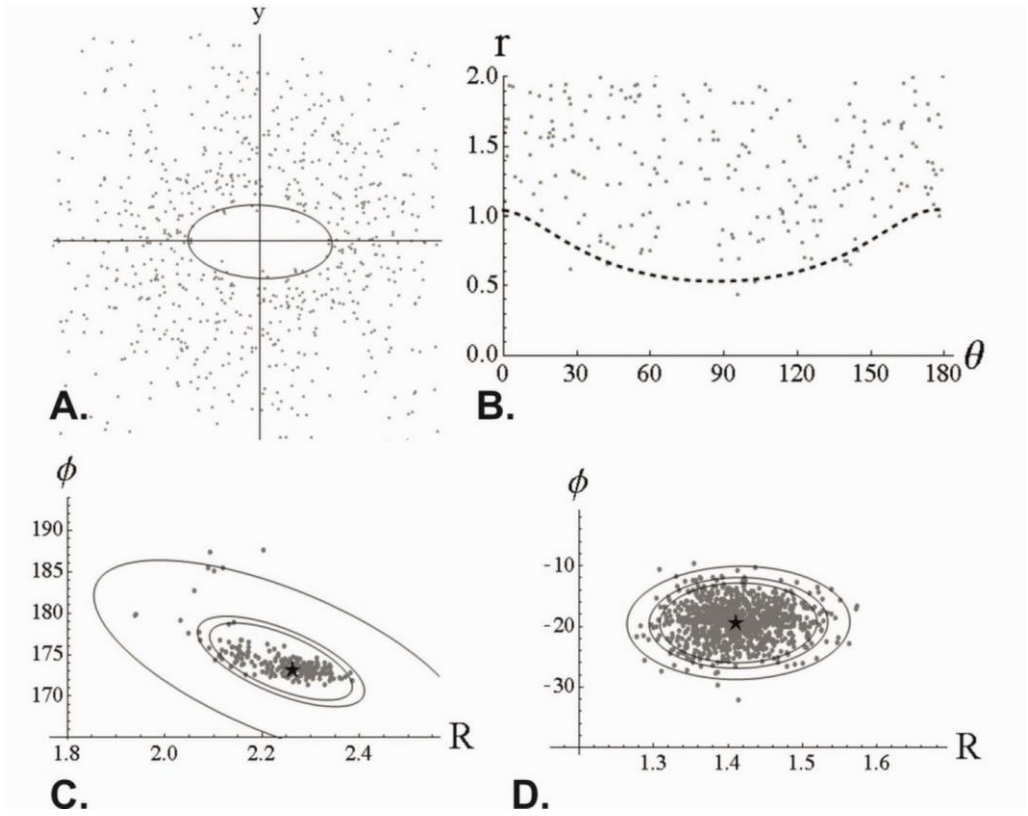

Figure 6. 110 DTNNM and MRL strain estimates for BB12B.

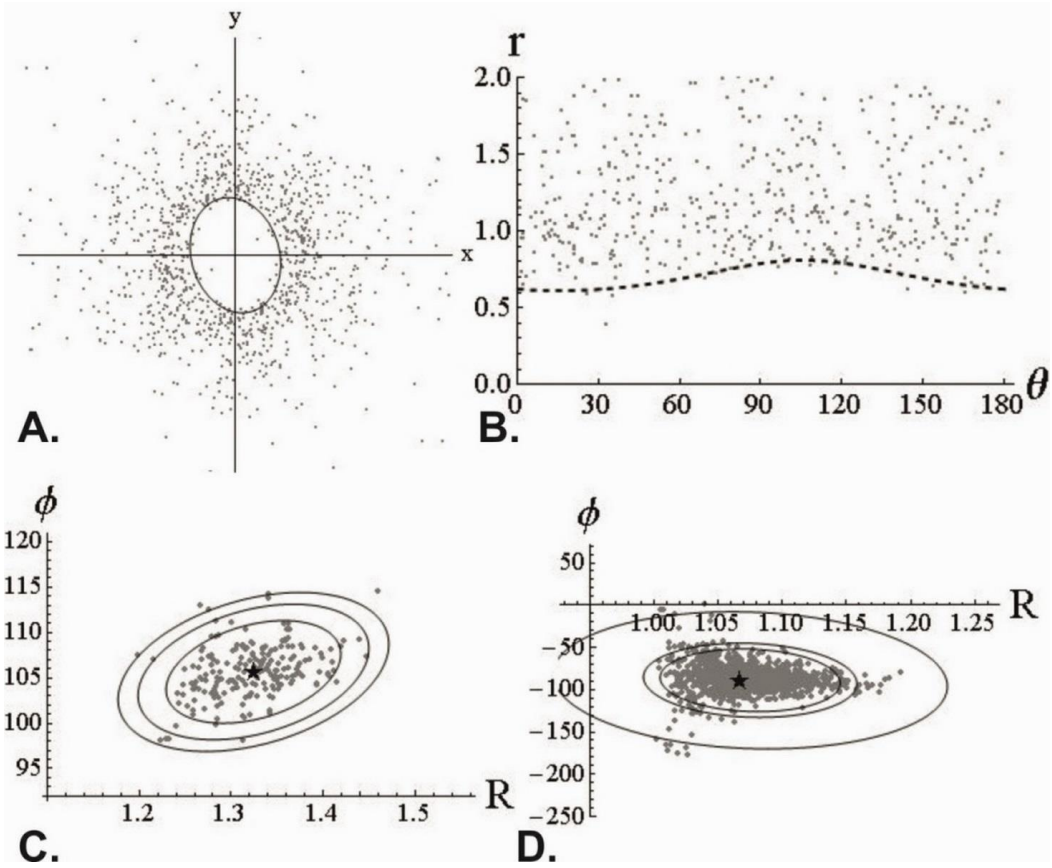

Figure 6. 111 DTNNM and MRL strain estimates for BB14B.

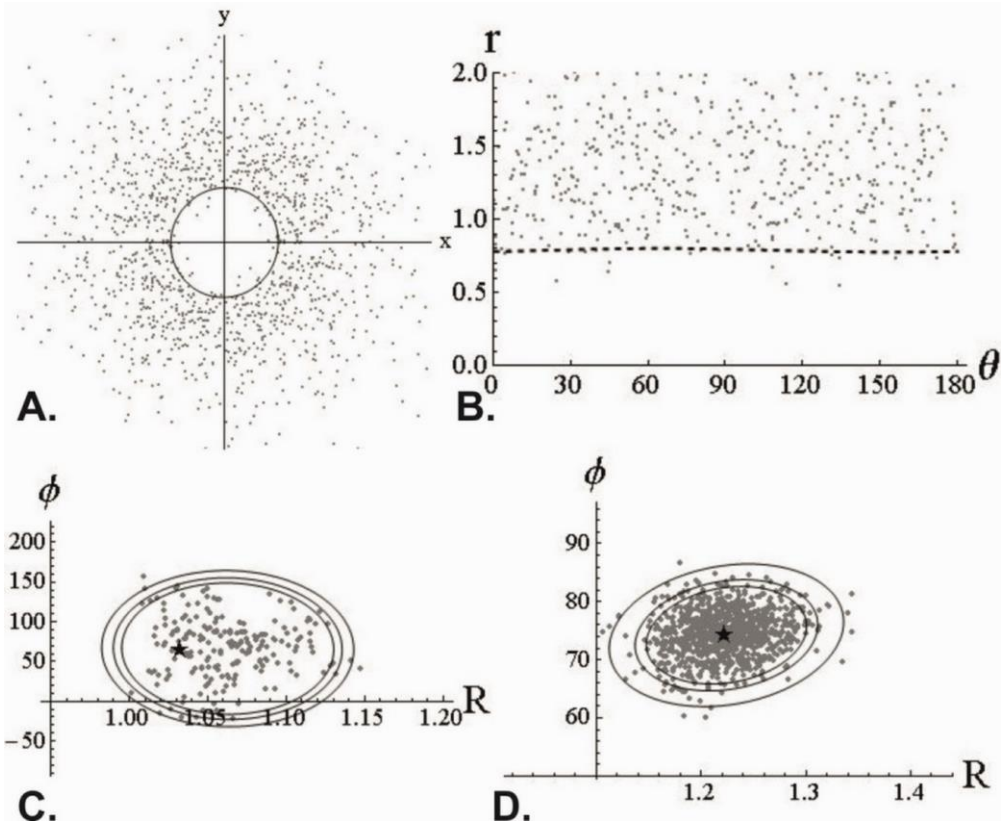

Figure 6. 112 DTNNM and MRL strain estimates for BB6B.

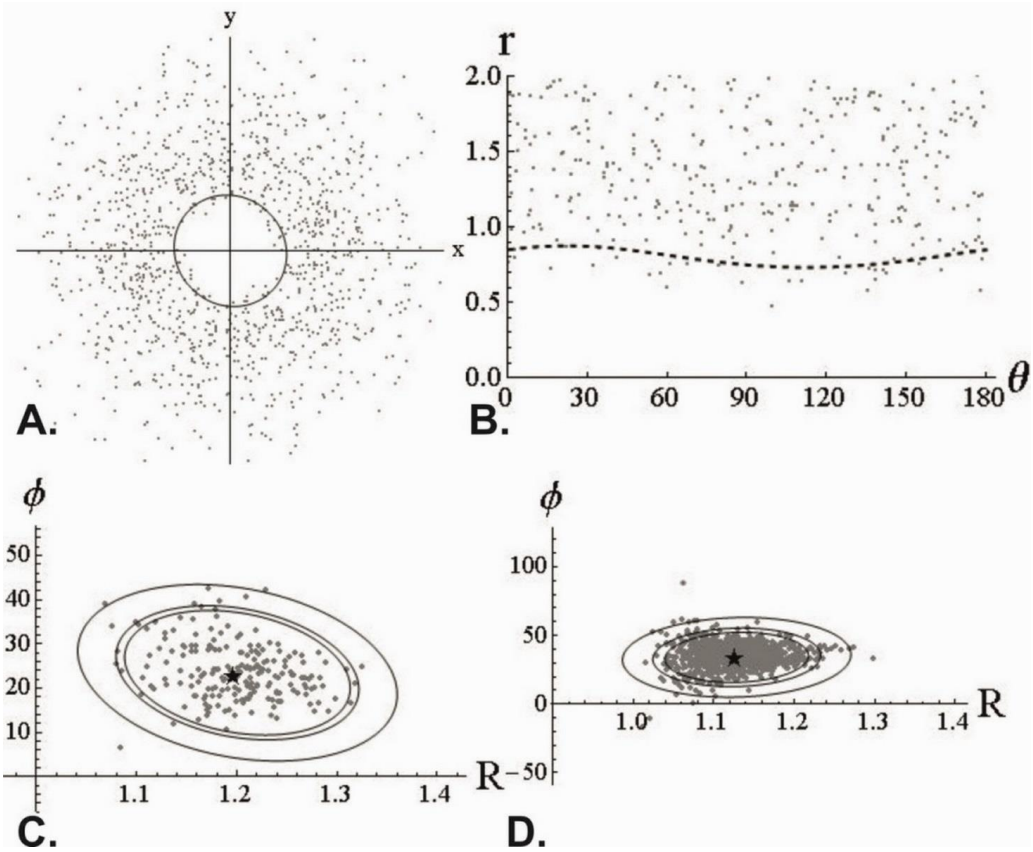

Figure 6. 113 DTNNM and MRL strain estimates for BB7B.

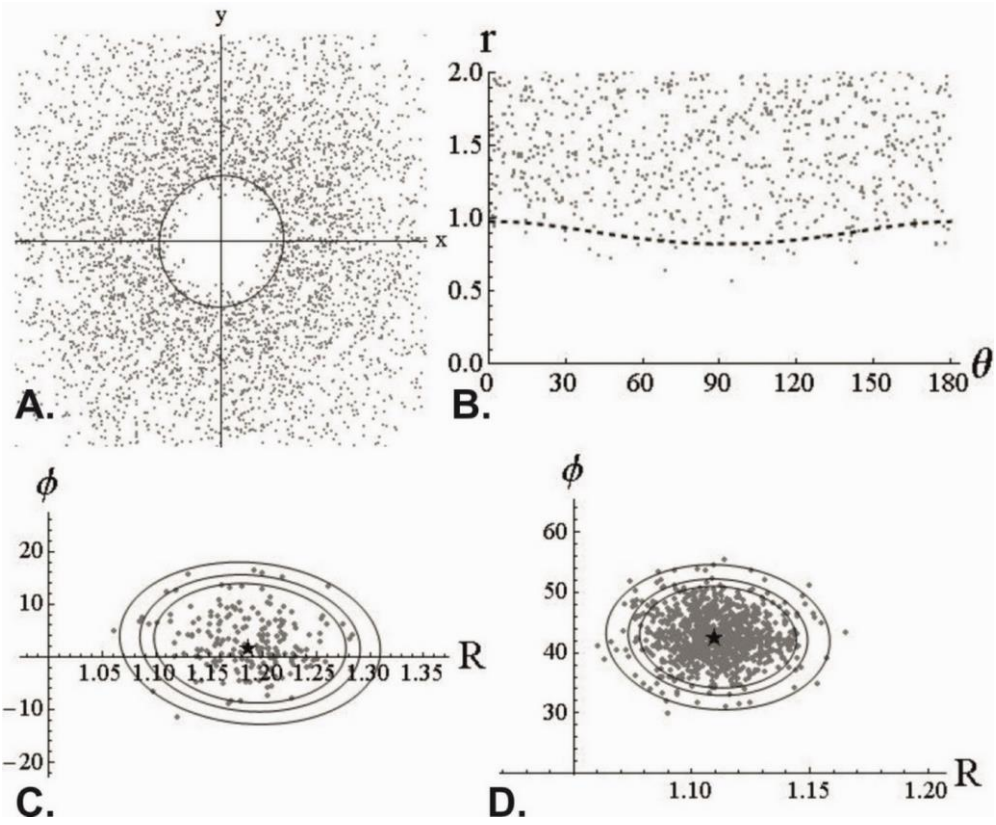

Figure 6. 114 DTNNM and MRL strain estimates for BB5B.

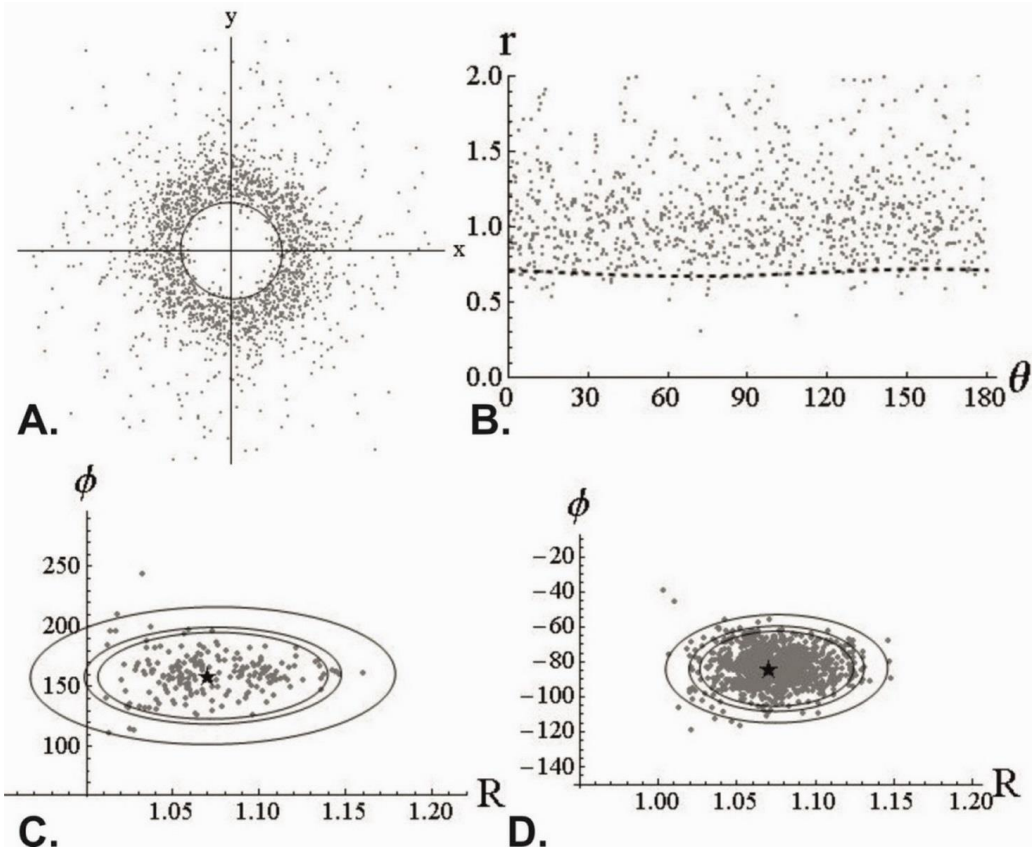

Figure 6. 115 DTNNM and MRL strain estimates for BB17B.

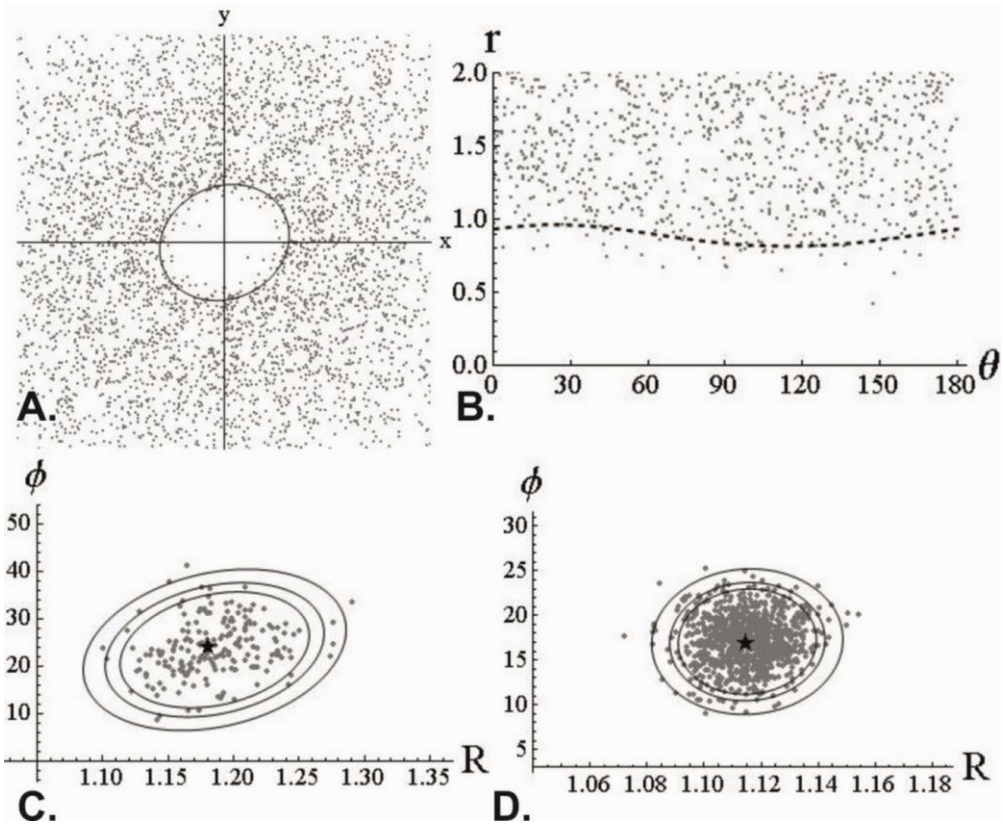

Figure 6. 116 DTNNM and MRL strain estimates for BB8B.

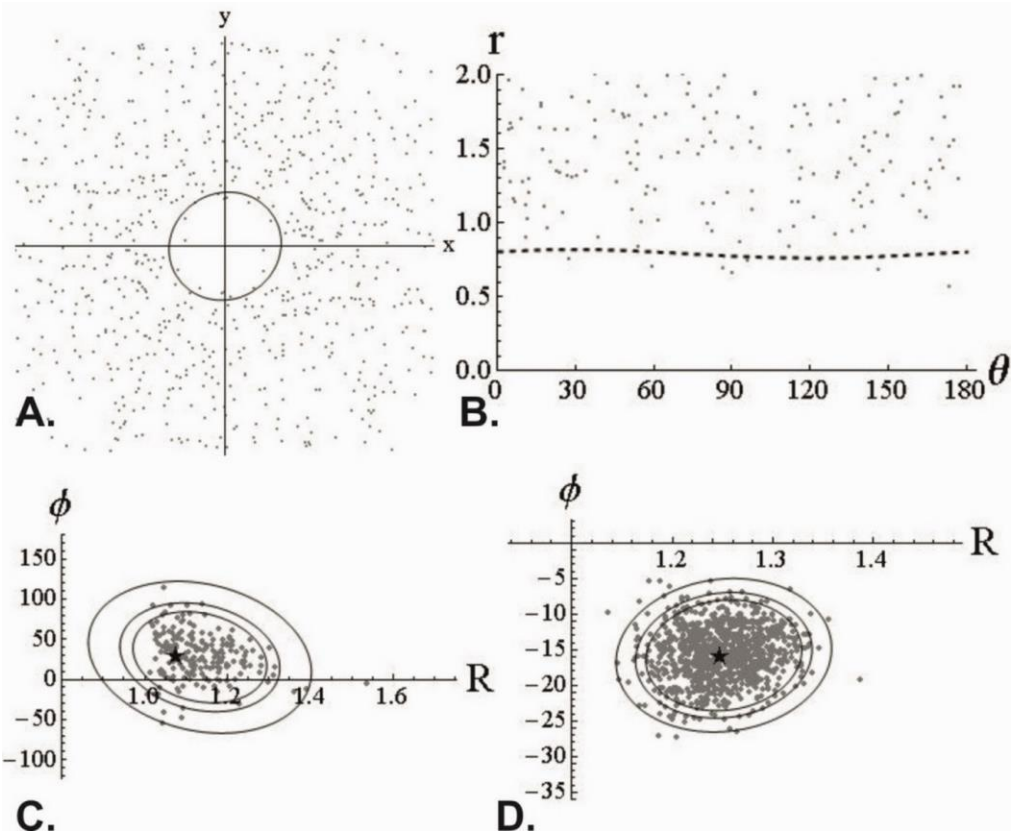

Figure 6. 117 DTNNM and MRL strain estimates for BB18B.

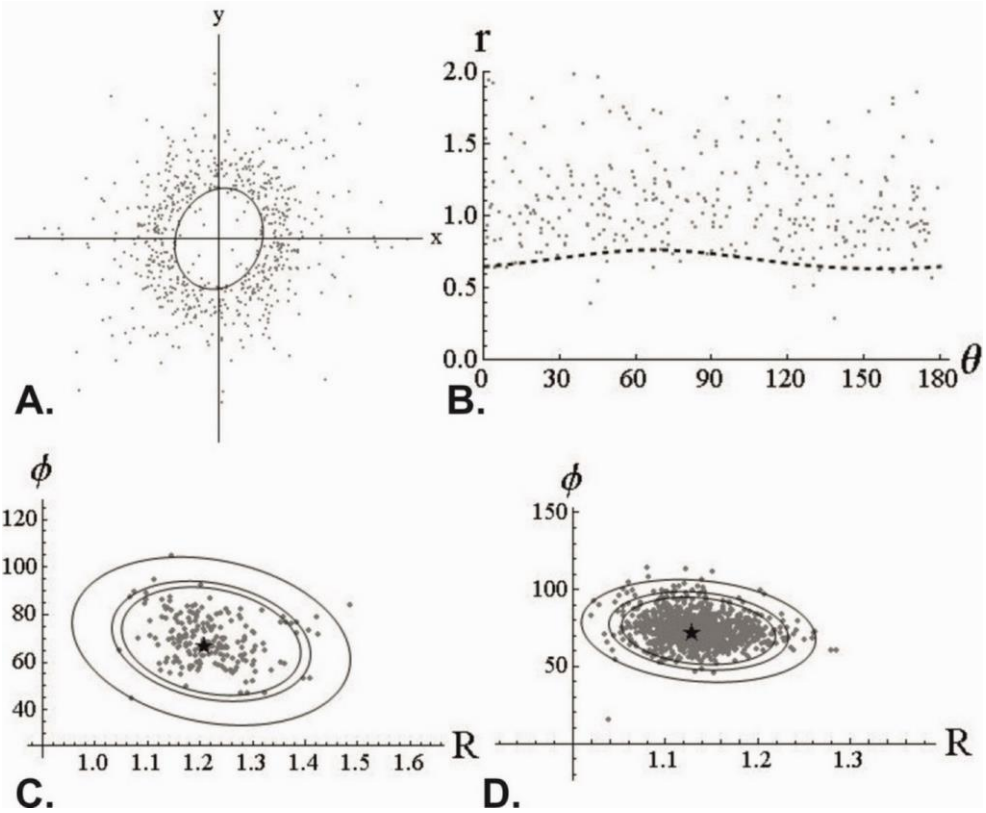

Figure 6. 118 DTNNM and MRL strain estimates for BB10B.

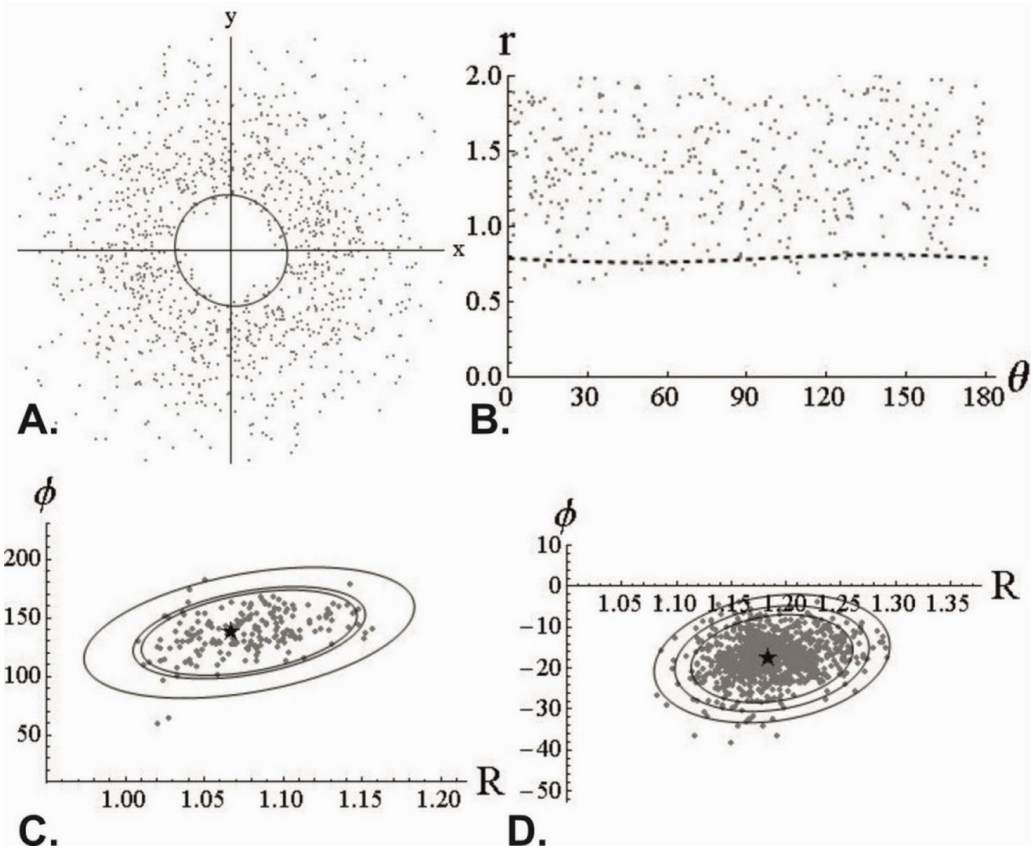

Figure 6. 119 DTNNM and MRL strain estimates for BB9B.

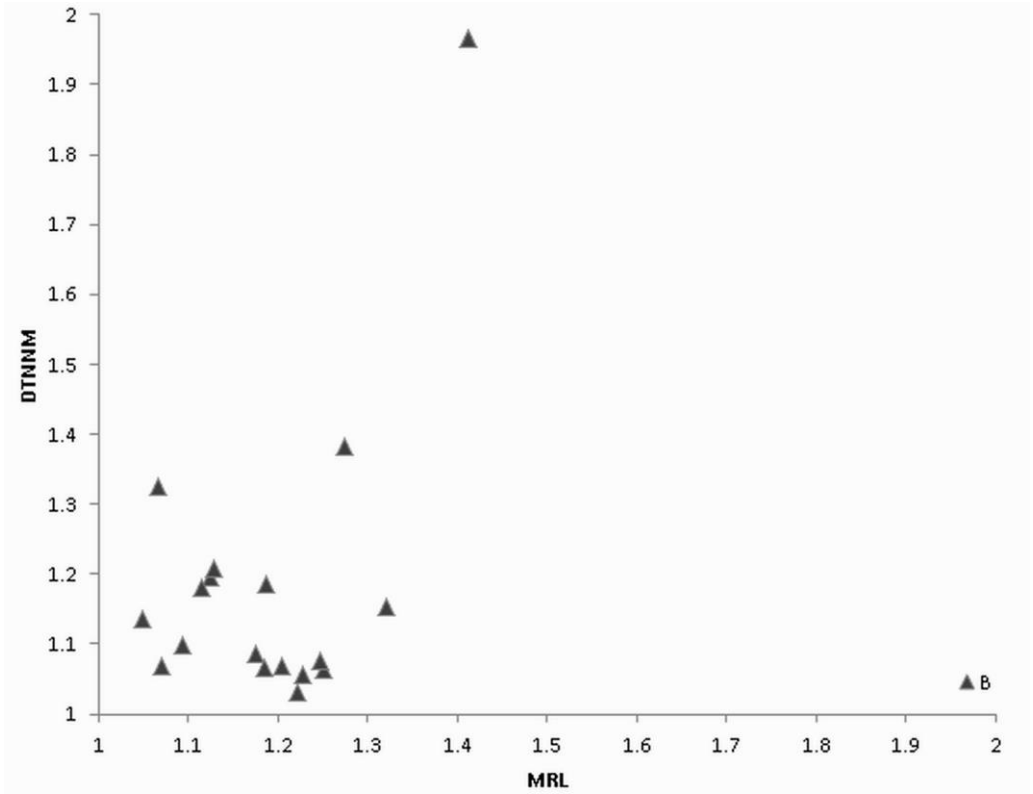

Figure 6. 120 Estimated R values for DTNNM and MRL analyses of the strike parallel sections. DTNNM has produced higher strain estimates than MRL.

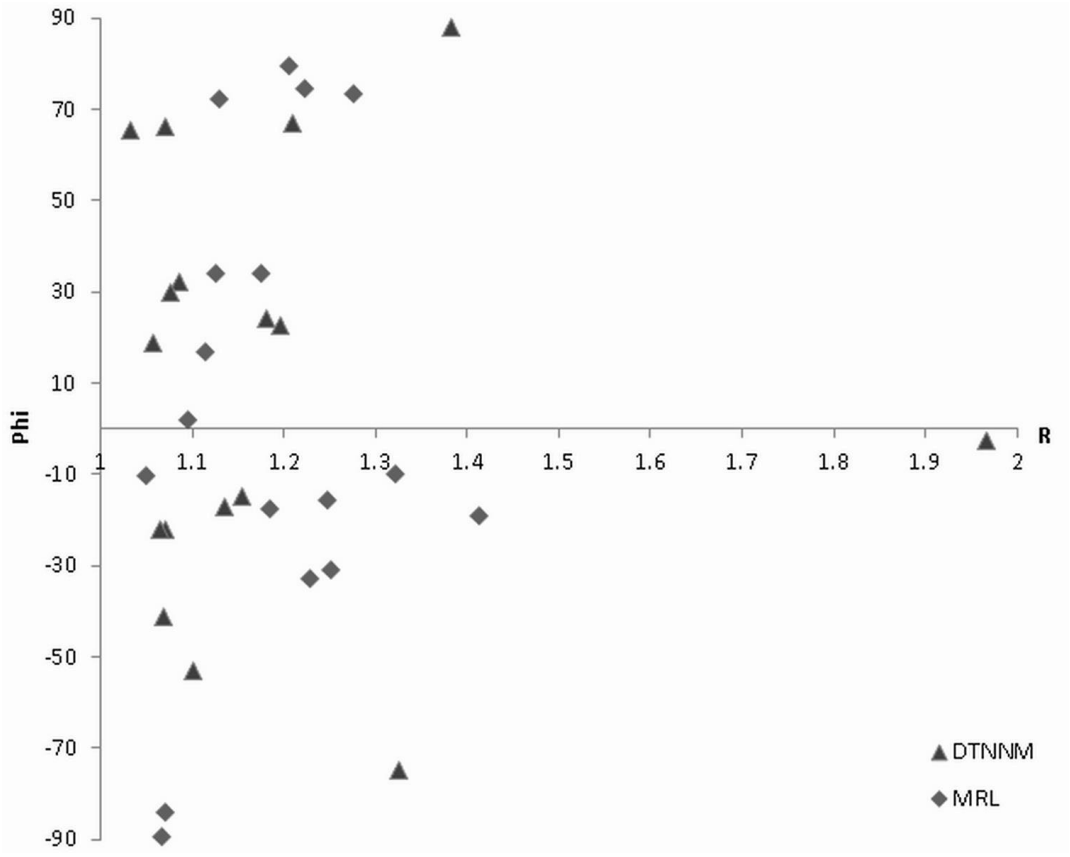

Figure 6. 121 R/Phi for the strike parallel sections, in this case Phi orientations represent deviations away from the trace of bedding in the section.

6.8. Discussion and Conclusion

As previously described the bulk susceptibility for most samples is a $<9X10^{-4}$, these values are consistent with paramagnetic minerals, minor haematite and trace magnetite, confirmed by the Curie Point experiments. Therefore the magnetic fabrics presented above can be regarded to be controlled by the preferred crystallographic orientation of those minerals, and as a result the AMS reflect either bedding or tectonic fabrics, or a combination of the two.

In terms of magnetic fabric types discussed in Chapter 3, unsurprisingly the only purely tectonic fabric types are from south of the DDL, although there is a large concentration of intermediate types near the northern margin of the Comeragh Mountains, which give way to sedimentary fabric types north of the Comeraghs.

This distribution of magnetic fabric types agrees with earlier research that the strongest tectonic fabrics are present south of the DDL (Cooper et al., 1984 and 1986). Interestingly the area of strongest tectonic fabrics according to AMS in the eastern Munster Basin does not coincide with the DDL, but further south with the Cork-Kenmare line (Figure 6.122).

The strain analyses produce a similar distribution of moderately high to low strains from south to north, again with the highest strains reported in the Whiting Bay and Ballyquin areas, both in close proximity to the Cork-Kenmare Line.

Estimated strain results from the Eastern Munster Basin are surprisingly low, compared to the higher strains recorded in the western Munster Basin (Meere, 1995a). This could be due to a number of reasons, particularly the decrease in depth to basement, which may reduce the butressing effect during inversion discussed earlier.

Considering that strain analysis techniques that utilise sedimentary clasts as strain markers have been shown to be ineffective at low strains, it is recommended here that other methods, such as AMS, are used to determine the degree of deformation across the basin.

Despite this there is a clear strain gradient from south to north, whereby strain decreases rapidly towards the north. Similarly there is another possible strain gradient across the northern margin of the Comeragh Mountains, with little no real indication of strain north of the Comeraghs. This is confirmed by both AMS and microstructural analysis.

Strain analysis of the Irish Variscides, raises more problems with the strain analysis techniques, beyond the inherent inaccuracies such as passive strain and clast distribution. The estimated strain in the B sections is comparable to that of those measured in the A and C sections. This is interesting as the B sections should be expected to display considerably lower strains than the bedding parallel sections or the sections cut perpendicular to the trace of cleavage. In particular the high DTNNM estimate of R=1.9 that is parallel to bedding for the B section from BB12, is a highly significant primary fabric. The presence of a strong primary fabric is confirmed by AMS with the magnetic foliation parallel to bedding. Such a high primary fabric would seriously negate weak strains (<1.5; Paterson and Yu, 1994). The relatively weak tectonic fabrics observed in the Comeragh area may not have completely overprinted the strong primary fabric, leading to the development of blended fabrics and ultimately largely inconclusive strain results.

Both the AMS and strain analyses largely coincide with previous structural studies and the field evidence. The lower strains and significantly more open styles of deformation in the eastern Munster Basin could imply the more dominant role of the basement structures in the area, but without up to date and high quality seismic geophysical surveys, this remains entirely circumspect.

The signifiacnt conclusion of this case study is that the cleavage 'front' of Murphy (1990) can be extended from the Knockmealdowns to the Comeraghs (Figure 6.122), although the style of deformation changes from a tightly spaced thrust faults to more open steeply dipping reverse faults. Additionally the complex shearing deformation observed at Ballyquin is suggestive of the transpression

model of Sanderson (1984) and probably indicates the proximity of an eastern margin controlling fault (Figure 6.122). The Muggorts bay Inlier and the condensed ORS sequence at Ballyvoyle as well as the lack of significant deformation at Helvick Head lend some support to this (Figure 6.122).

While this study lends no new significant evidence to the debate concerning the location of a Variscan 'Front' it is the authors opinion that the significant Caledonian structures that provided a framework for the deformation of the Munster Basin can not be ignored. A significant reactivated Caledonian ridge or shear zone that correlates with the KMFZ and runs between the Galtee Mountains/Slievenamon and the Knockmealdowns/Comeragh Mountains was identified by Vermeulen et al. (2000). This ridge not only acted as a the northern margin of the Munster Basin, but would have acted as the main buttressing structure during basin inversion. Similar smaller faults, such as the Cork-Kenmare Line, acted as minor butressing structures and controlled deposition of the South Munster Basin. Unsuprisingly the areas with the highest deformation recorded in this study closely correlate with both of those structures.

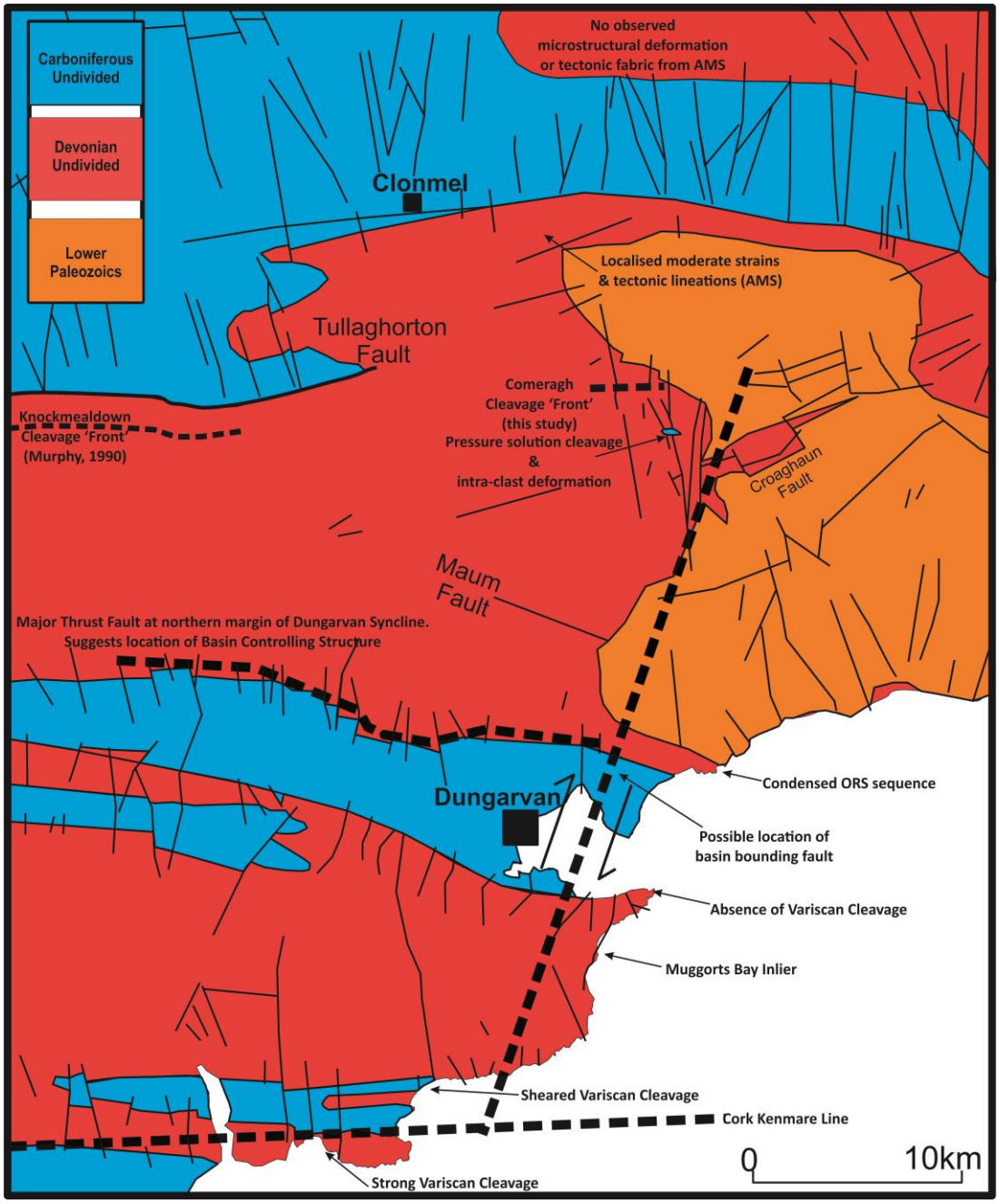

Figure 6.122 Summary of conclusions and potential interpretation of the Eastern Munster Basin.

Chapter 7:

Discussion and Conclusions

7. Discussion and Conclusion

As this thesis was written in a manner so that each chapter has a self contained discussion and brief conclusion, I aim to keep this chapter as concise as possible. Conclusions from the three main study areas are summarised, as are any specific problems and suggestions for potential future work. Additionally the various merits of the automated strain analysis techniques and AMS are briefly discussed.

7.1. Summary of Regional Conclusions

7.1.1. Sawtooth Range, Montana

The carbonate thrust sheets of the Sawtooth Range display an interesting range of deformation styles, from brittle structures associated with the mechanism of thrust sheet emplacement at the base of each sheet to a more penetrative deformation associated with the emplacement of the overriding thrust sheet (discussed in Chapter 4). The Sun River Canyon area was originally targeted as a locality to test the semi-automated strain analysis techniques discussed in Chapter 2 and compare them to AMS analyses, due to excellent exposures of repeated sequences. Unfortunately the majority of lithologies in this area are too fine grained to carry out accurate strain analysis. Despite this setback, the exposures of the Sun River Canyon, provided an excellent setting to study the development of incipient tectonic fabrics in a fold and thrust belt, as well as an opportunity to further establish the ability of AMS to detect these incipient tectonic fabrics.

The samples analysed using AMS can be effectively split into two groups, diamagnetic and paramagnetic. Regardless of their magnetic behaviour both groups

exhibit the full range of magnetic fabric types typically found in fold and thrust belts (Bakhtari et al., 1998; Pares and Parés, 2004; Weil and Yonkee, 2009). AMS ellipsoid shapes varied from weakly oblate with flattening parallel to bedding, to triaxial, then prolate with stretching parallel to the extension direction and finally oblate with flattening perpendicular to bedding. These fabric types and a four-fold classification scheme are discussed in detail in Chapter 3.

Although penetrative tectonic fabrics are poorly developed at an outcrop scale, there is a regular correlation with AMS fabrics and recorded cleavage fabrics at a high angle to bedding, with the magnetic lineation (K1) plotting along cleavage plane or at the cleavage bedding intersection lineation.

Conclusions from the AMS analysis confirmed that penetrative deformation developed as a response to the emplacement of the overriding thrust sheet and no penetrative deformation developed within the thrust sheet being emplaced

7.1.1.1. Problems Encountered

One of the biggest problems encountered in the study of the Sawtooth Range was the highly fractured nature of the Madison Limestones. This severely reduced the number of samples that survived, but also where samples could successfully be collected. Additionally a regular problem encountered in AMS analyses of rocks with a dominant diamagnetic response such as limestones and dolomites is the relatively weak response to the applied field, sometimes these weak responses can be low enough that they are close to the sensitivity limits of the kappabridge . This leads to significantly large confidence intervals and introduces a slight degree of doubt for the exact response of some samples, particularly for samples that have a

complicated magnetic fabric, such as the presence of two competing petro-fabrics, i.e. bedding and cleavage.

This is an inherent problem when working with diamagnetic materials, although Hirt et al. (2012) showed that the degree of anisotropy increases with a decrease in temperature for carbonate and phyllosilicate minerals. A slightly more practical approach is to increase the number of individual specimens analysed per block sample in order to reduce the uncertainty.

7.1.1.2. Future work

Although the above research identifies clear trends in the development of an incipient tectonic fabric in the thrust sheets of the Sawtooth Range using AMS alone, a possible further study would be to analyse a single thrust sheet with a higher sampling density. This would allow for a more complete profile of the subtle changes in magnetic fabrics, and ultimately a better understanding of the development of penetrative deformation in a thrust sheet. Additionally a more complete microstructural analysis, including a study of calcite twinning, would complement this analysis.

Another study of direct relevance to the petroleum industry would be to establish the effects on porosity and permeability that this interplay of brittle and penetrative deformation structures have in foreland thrust belt systems.

7.1.2. Sevier Belt, Wyoming

The eastern thrust system of the Wyoming Salient provided an opportunity to carry out a similar AMS analysis as that carried out in the Limestones of the Sawtooth Range, except in coarser grained clastic sediments, which allowed for strain analysis using the automated techniques discussed in Chapter 2.

Similar to the thrust sheets of the Sawtooth Range the eastern thrust system is dominated by thin skinned fold and thrust structures. Spaced cleavage developed during early Layer Parallel Shortening (LPS), which initiated during footwall deformation as the overlying thrust sheets were emplaced (Mitra, 1994).

The samples analysed from the Ankareh Formation of the Wyoming Salient had relatively weak, but positive susceptibilities ($<0.5X10^{-3}$ SI), these values are typical of samples whose magnetic response is dominated by phyllosilicates and minor amounts of hematite. Therefore AMS can be effectively applied to determine the relative strength and orientation of the petrofabric. The four-fold classification of magnetic fabrics types defined in Chapter 3 correlated well with both the bedding/cleavage relationships observed in the field and the cleavage intensity map of Mitra and Yonkee (1985). Although the moderate values for the corrected degree of anisotropy (Pj), <1.1, are expected for sedimentary units in fold and thrust belts with low grade deformation and a weak spaced cleavage (Pares, 2004; Borradaile and Jackson, 2010), Pj values can not be used independently to determine degree of deformation. Similarly the magnetic lineation intensity (Ln') cannot be used for this purpose. Weil & Yonkee (2009) used Ln' as a measure of deformation, but samples reported here that fit in the Type 4 classification show a strong foliation and a weak lineation despite being at a higher level of deformation.

That said the orientation of the magnetic lineation itself does vary with deformation intensity and regularly correlates with the cleavage bedding intersection lineation, which is in agreement with earlier research (Bakhtari et al., 1998; Pares, 2002; Rochette and Vialon, 1984; Rochette, 1987; Rochette et al., 1992).

It was found that despite evidence of tectonic fabrics from AMS analyses and clear strain markers recorded by Yonkee and Weil (2010), the semi-automated strain analysis techniques are not sensitive enough to accurately determine strain. Only two of the samples analysed yielded strain estimates >1.2 (both from DTNNM analysis), the rest of the samples not only yielded low strain estimates, but the long axis of the estimated strain ellipses deviated significantly from the traces of cleavage and the magnetic foliation in the bedding plane.

Despite the low strain estimates there was a slight gradient with estimated strains increasing towards the west in both transects, again agreeing with the cleavage distribution (Mitra and Yonkee, 1985) and strain results from Yonkee and Weil (2010). Another conclusion from the Wyoming study is that DTNNM yielded higher estimates of strain ratios compared to either the MRL or intercepts suite.

7.1.2.1. Future Work

Further study in the Wyoming Salient could include extending the study area further westward into the Absaroka and Meade thrust sheets. This would provide samples with higher degrees of deformation and allow a comparison of AMS and the strain analysis techniques for higher strains.

7.1.3. Variscides, Southern Ireland

The Variscides of Southern Ireland provided an interesting field area to further compare AMS and strain analysis techniques. The question of a 'Variscan Front' has dominated most of the previous research carried out on the Irish Variscides. While now a largely redundant question, there is an inherent link between the northern margin of the Munster Basin and a deformation front.

Most earlier research has placed the main deformation front at the Dingle Dungarvan Line (DDL)(Gill, 1962; Cooper et al., 1984 and 1986), more recent geophysical work suggests that it could be further north (Readman et., 1997; Vermeulen et al., 2000), and some structural studies have placed it in Clare (Bresser and Walter, 1999) possibly being associated with an eastward extension of the ECDZ and the Caledonian structure that facilitated the ascent and emplacement of the Leinster Granite.

It was hoped that AMS and strain analyses of the eastern Munster Basin might yield some insights into the location of a major deformation front. The AMS analyses yielded average bulk susceptibilities of $.51x10^{-3}$, again largely dominated by phyllosilicates and minor amounts of hematite. The four-fold classification scheme of magnetic fabric types again correlated well with the bedding/cleavage relationships observed in the field, but also confirmed that the most intense tectonic fabrics are present south of the DDL. The vast majority of samples yielded yielded corrected degree of anisotropy (PJ) values less than 1.1, with only one sample from Ballyquin yielding a Pj value of 1.35.

The strain analyses although yielding particularly low strain estimates correlated with most of the higher deformation areas identified by AMS. Both the AMS and

strain analyses show that the most intense deformation is limited to south of the DDL, but also that there is a slight increase in deformation at the northern of the Comeragh Mountains. Although no exact gradient has been determined it largely coincides with the cleavage front of Cooper et al. (1986).

Additionally, similar to the strain estimates of the Wyoming study, DTNNM typically yielded higher estimates of strain ratios compared to MRL for samples from the Munster Basin.

7.1.3.1. Problems

One of the most distinct problems of working in the eastern Munster Basin is the paucity of insightful outcrop inland. There is no exposed contact between the basin fill and its basement structures, which leaves any conclusions made on the structural relationship of these two elements largely open to interpretation.

7.1.3.2. Future Work

There are still many unanswered questions regarding the deformation of the Munster Basin and strain and AMS analyses have yielded few extra insights into this process. With this in mind, there is plenty of scope for more geophysical surveys in the eastern Munster Basin, as well as an updated review of Irish Variscides focusing on the role of the Caledonian structural template.

.

7.2. Use of Anisotropy of Magnetic Susceptibility (AMS) to Detect Strain

As discussed in Chapter 3, many attempts have been made at correlating the AMS ellipsoid with the strain ellipsoid. The pitfalls of this approach include complex mineral assemblages that have very different magnetic contributions, but also fundamentally unlike the strain ellipsoid, which is a hypothetical construct that allows visualisation of shape change due to deformation, the AMS ellipsoid, represents inherent properties of the sample being analysed, and is not always a sphere in the unstrained state.

Considering these complexities, quantifying strain directly from AMS results is not to be recommended. That said AMS is highly effective at identifying fabrics and to take advantage of that a four-fold classification, modified from the three-fold of Bakhtari et al. (1998), has been established. This classification scheme relates AMS to bedding and cleavage and allows for simple determination of the presence and relative strength of a tectonic fabric compared to bedding. These fabric types are:

Type 1 no detectable tectonic fabric and a slightly oblate ellipsoid parallel to bedding;

Type 2 weak magnetic/tectonic lineation in the plane of bedding and parallel to tectonic trend, magnetic foliation is still parallel with bedding;

Type 3 stronger magnetic/tectonic lineation and a triaxial magnetic ellipsoid;

Type 4 magnetic foliation is at a high angle to bedding and parallel to cleavage while the magnetic lineation, if defined, is plunging down the cleavage plane or represents the cleavage bedding intersection lineation.

7.3. The Effectiveness of Semi-Automated DTNNM and MRL Techniques

One of the main conclusions of this thesis is the inaccuracy of the DTNNM and MRL methods in low strain environments. This insensitivity can be explained by a number of inherent inaccuracies associated with these methods. The calculations involved in the MRL and DTNNM methods assume that deformation is essentially passive and that original pre-strain clast distributions, shapes and orientations yield strain estimates near 1.0. The problem of non-passive deformation (when clasts and matrix deform at different rates due to differing rheological properties) has been previously discussed by Meere et al. (2008), this typically leads to deformation being concentrated in the matrix, while clasts may be relatively undeformed. This is a fundamental flaw in clast based techniques.

There has been little research done on the nature of these primary fabrics, one of the key papers addressing this, Paterson and Yu (1994), concluded that undeformed sandstones have significant primary fabrics that can mask the effect of low strain ratios (<1.4). Considering that few samples analysed in this study yielded a strain ellipse ratio greater than 1.5, it is not entirely possible to determine just how effective these methods actually are. However it has become clear that DTNNM provides a higher estimate of strain ratios then MRL (Figure 7.1).

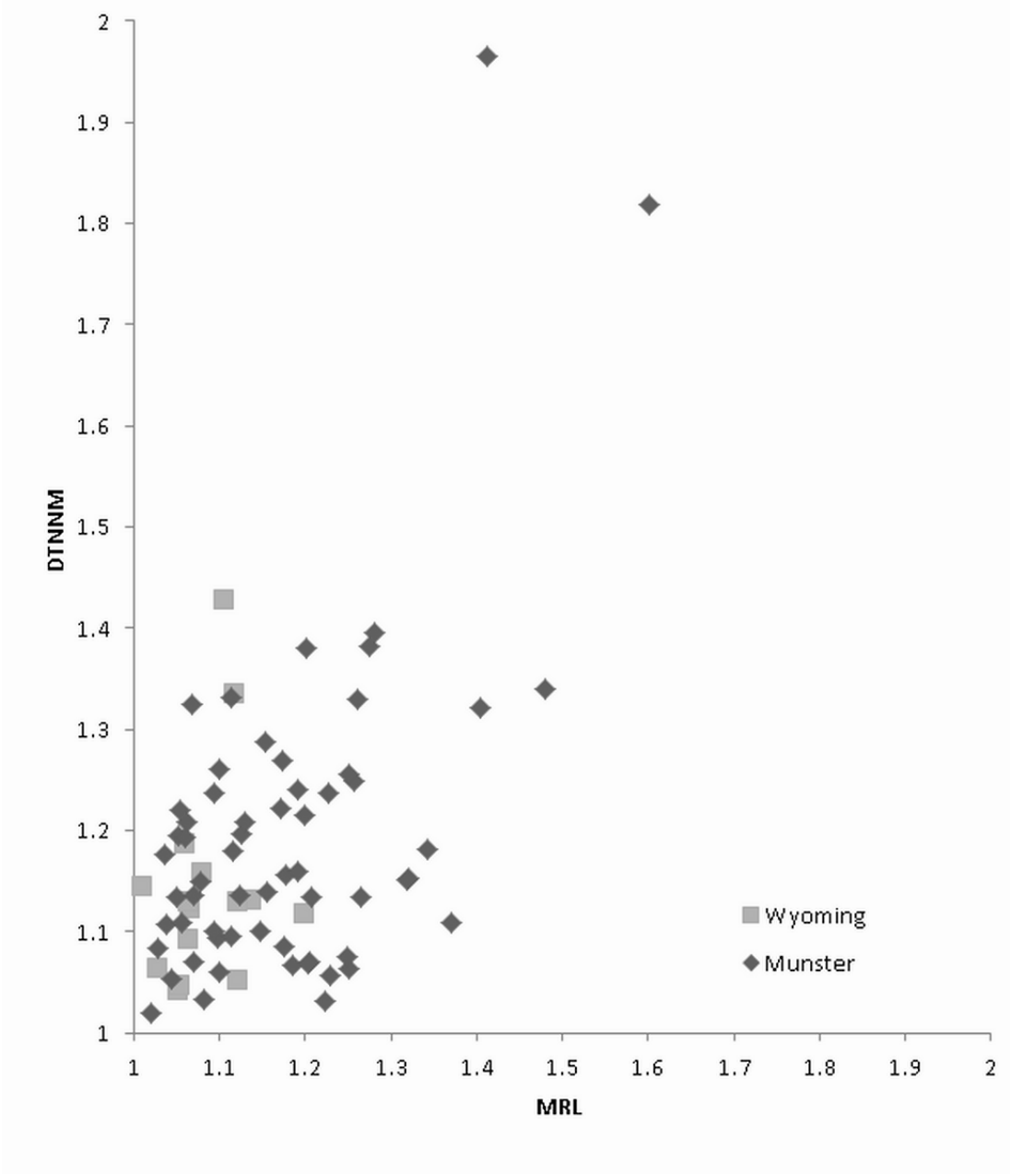

Figure 7. 1 Comparison of estimated strain ratios for MRL and DTNNM methods from both Munster and Wyoming.

7.4. Strain analysis vs AMS

In this study there is a clear discrepancy between the strain analysis results and the AMS analyses. This is in part due to the high sensitivity of AMS and the inaccuracies in the strain analysis methods when measuring, but also because of what the two separate techniques measure. AMS measures the magnetic contribution of all of

the minerals present in a sample and, as a result in most sandstones AMS is dominated by iron rich phyllosilicate minerals. While this provides a very valuable tool for evaluating petrofabrics, it must be noted that quartz, a major constituent of most clastic sedimentary rocks, has little effect on the AMS results, due to its weak diamagnetic behaviour. Conversely strain estimates from the DTNNM and MRL methods are largely based on quartz clasts.

AMS despite being highly effective, is much more labour intensive (block collection and specimen preparation) than strain analysis techniques and requires access to a kappabridge. The strain analysis techniques, despite the accuracy of these methods at low strains being under question in this thesis, are capable of quantifying deformation at moderate to high strains, and they are not as labour intensive as AMS (although considerable patience is required) and only require access to oriented thin sections and a computer with an installation of Mathematica.

7.5. Further Work

An interesting avenue of potential future work would be to analyse a wide range of non-deformed sedimentary lithologies in order to build a complete database of primary fabrics and their elliptical properties for different rock types. This might allow for a minimum strain threshold to be established, after which point strain estimates can be expected to be reliable.

Additionally applying strain analysis techniques to artificially deformed sediments might also yield more insights on the evolution of primary fabrics during deformation.

7.6. Conclusions

Estimating finite strain is a fundamental part of quantifying deformation patterns and processes. The general approach, in the absence of independent strain markers, i.e. reduction spots, is to estimate finite strain from either object-to-object separations (DTNNM) or the random orientation (MRL) of populations of deformed objects, such as sedimentary clasts. Unfortunately, these methods are regularly applied in low strain environments such as the forelands of fold and thrust belts.

This thesis suggests that in such low strain environments, where estimates of the axial strain ratio are less than 1.4, the traditional clast-based strain analysis techniques (DTNNM and MRL) are not capable of accurately identifying or quantifying deformation. This is in part due to the assumptions these methods are based on, but also the presence of preferred orientation of clasts due to bedding.

However, the Anisotropy of Magnetic Susceptibility (AMS) analyses are more than capable of detecting the presence of incipient tectonic fabrics, but also their orientation and relative strengths. An important suggestion for all studies using these traditional strain analysis techniques would therefore be, where possible, to fully analyse primary pre-strain preffered orientations in the lithologies being studied.

References

Ailleres, L., Champenois, M., Macaudiere, J., Bertrand, J., 1995. Use of image analysis in the measurement of finite strain by the normalized Fry method: Geological implications for the'Zone Houillere' (Brianconnais zone, French Alps). Mineral. Mag. 59, 179–187.

Allmendinger, R., 1992. Fold and thrust tectonics of the western United States exclusive of the accreted terranes. Cordilleran orogen Conterminous US Boulder, Color. Geol. Soc. Am. Geol. North Am. 3, 583–607.

Amrouch, K., Robion, P., Callot, J.-P., Lacombe, O., Daniel, J.-M., Bellahsen, N., Faure, J.-L., 2010. Constraints on deformation mechanisms during folding provided by rock physical properties: a case study at Sheep Mountain anticline (Wyoming, USA). Geophys. J. Int. 182, 1105–1123.

Armstrong, F., Oriel, S., 1965. Tectonic development of Idaho-Wyoming thrust belt. Am. Assoc. Pet. Geol. Bull. 49, 1847–1866.

Aubourg, C., Rochette, P., Vialon, P., 1991. Subtle stretching lineation revealed by magnetic fabric of Callovian-Oxfordian black shales (French Alps). Tectonophysics 185, 211–223.

Averbuch, O., Lamotte, D.F. de, Kissel, C., 1992. Magnetic fabric as a structural indicator of the deformation path within a fold-thrust structure: a test case from the Corbières (NE Pyrenees, France). J. Struct. Geol. 14, 461–474.

Bakhtari, H.R., Frizon de Lamotte, D., Aubourg, C., Hassanzadeh, J., 1998. Magnetic fabrics of Tertiary sandstones from the Arc of Fars (Eastern Zagros, Iran). Tectonophysics 284, 299–316.

Balch, A., 1987. A Seismic-stratigraphic investigation of the Madison and associated aquifers: application to ground-water exploration, Powder River Basin, Montana-. US Geol. Surv. Prof. Pap.

Bally, A., Gordy, P., Stewart, G., Keating, L., 1966. Structure, seismic data, and orogenic evolution of southern Canadian Rocky Mountains. Bull. Can. Pet. Geol. 14, 337–381.

Bird, P., 1984. Laramide crustal thickening event in the Rocky Mountain foreland and Great Plains. Tectonics 3, 741–758.

Bird, P., 1988. Formation of the Rocky Mountains, western United States- A continuum computer model. Science 239.4847 , 1501–1507.

Borradaile, G., 1976. A strain study of a granite–granite gneiss transition and accompanying schistosity formation in the Betic orogenic zone, SE. Spain. J. Geol. Soc. London. 132, 417–428.

Borradaile, G., 1988. Magnetic susceptibility, petrofabrics and strain. Tectonophysics 156, 1–20.

Borradaile, G., 1991. Correlation of strain with anisotropy of magnetic susceptibility (AMS). Pure Appl. Geophys. 135, 15–29.

Borradaile, G., Almqvist, B., Geneviciene, I., 2012. Anisotropy of magnetic susceptibility (AMS) and diamagnetic fabrics in the Durness Limestone, NW Scotland. J. Struct. Geol. 34, 54–60.

Borradaile, G.J., 1987. Analysis of strained sedimentary fabrics: review and tests. Can. J. Earth Sci. 24, 442–455.

Borradaile, G.J., Henry, B., 1997. Tectonic applications of magnetic susceptibility and its anisotropy. Earth-Science Rev. 42, 49–93.

Borradaile, G.J., Jackson, M., 2004. Anisotropy of magnetic susceptibility (AMS): magnetic petrofabrics of deformed rocks. Geol. Soc. London, Spec. Publ. 238, 299–360.

Borradaile, G.J., Jackson, M., 2010. Structural geology, petrofabrics and magnetic fabrics (AMS, AARM, AIRM). J. Struct. Geol. 32, 1519–1551.

Borradaile, G.J., Shortreed, C., 2011. Magnetic fabrics in L–S tectonites: How many specimens? J. Struct. Geol. 33, 481–486.

Borradaile, G.J., Tarling, D.H., 1981. The influence of deformation mechanisms on magnetic fabrics in weakly deformed rocks. Tectonophysics 77, 151–168.

Bouchez, J.L., 1997. Granite is never isotropic: an introduction to AMS studies of granitic rocks. Bouchez, J.L., Hutton, D.H.W., Stephens, W.E., (eds.), Grantie From Segreg. Melt to Emplace. Fabr. Kluwer Acad. Publ. Dordr. 95–112.

Boyer, S., Elliott, D., 1982. Thrust systems. Am. Assoc. Pet. Geol. Bull. 66, 1196–1230.

Brandley, R.T., Rigby, J.K., 1988. Depositional history and paleogeography of the early to late Triassic Ankareh Formation, Spanish Fork Canyon, Utah. Brigham Young Univ. Geol. Stud. 36, 135–152.

Bresser, G., Walter, R., 1999. A new structural model for the SW Irish Variscides: the Variscan front of the NW European Rhenohercynian. Tectonophysics 309, 197–209.

Burchfiel, B., Cowan, D., Davis, G., 1992. Tectonic overview of the Cordilleran orogen in the western United States. Geol. North Am. 3, 407–479.

Burmeister, K.C., Harrison, M.J., Marshak, S., Ferré, E.C., Bannister, R. a., Kodama, K.P., 2009. Comparison of Fry strain ellipse and AMS ellipsoid trends to tectonic fabric trends in very low-strain sandstone of the Appalachian fold–thrust belt. J. Struct. Geol. 31, 1028–1038.

Bustin, R., 1983. Heating during thrust faulting in the rocky mountains: friction or fiction? Tectonophysics 95, 309–328.

Butler, R.W.H., 1989. The influence of pre-existing basin structure on thrust system evolution in the Western Alps. Geol. Soc. London, Spec. Publ. 44, 105–122.

Capewell, J., 1956. The stratigraphy, structure and sedimentation of the Old Red Sandstone of the Comeragh Mountains and adjacent areas, County Waterford, Ireland. Q. J. Geol. Soc. 112, 393–412.

Cloos, E., 1947. Oölite deformation in the South Mountain fold, Maryland. Geol. Soc. Am. Bull. 58, 843–918.

Colpron, M., Nelson, J., Murphy, D., 2007. Northern Cordilleran terranes and their interactions through time. GSA TODAY 17, 4.

Cooper, M. a., Collins, D., Ford, M., Murphy, F.X., Trayner, P.M., 1984. Structural style, shortening estimates and the thrust front of the Irish Variscides. Geol. Soc. London, Spec. Publ. 14 , 167–175.

Cooper, M. a., Williams, G.D., de Graciansky, P.C., Murphy, R.W., Needham, T., de Paor, D., Stoneley, R., Todd, S.P., Turner, J.P., Ziegler, P. a., 1989. Inversion tectonics -- a discussion. Geol. Soc. London, Spec. Publ. 44, 335–347.

Cooper, M., Collins, D., Ford, M., Murphy, F.., Trayner, P.., O'Sullivan, M., 1986. Structural evolution of the Irish Variscides. Journal of the Geological Society 143, 53–61.

Cooper, M., Trayner, P., 1986. Thrust-surface geometry: implications for thrust-belt evolution and section-balancing techniques. J. Struct. Geol. 8, 305–312.

Corfield, S., Gawthorpe, R., Gage, M., Fraser, A., Besly, B., 1996. Inversion tectonics of the Variscan foreland of the British Isles. J. Geol. Soc. London. 153, 17–32.

Coward, M., 1986. Heterogeneous stretching, simple shear and basin development. Earth Planet. Sci. Lett. 80, 325–336.

Coward, M.P., 1990. The Precambrian, Caledonian and Variscan framework to NW Europe. Geol. Soc. London, Spec. Publ. 55, 1–34.

Dahlstrom, C., 1970. Structural geology in the eastern margin of the Canadian Rocky Mountains. Bull. Can. Pet. Geol. 18, 332–406.

Dahlstrom, C.D. a., 1969. Balanced cross sections. Can. J. Earth Sci. 6, 743–757.

Darwin, C., 1846. Geology of the Voyage of the Beagle, Under the Command of Capt. Fitzroy, RN During the Years 1832 to 1836.

Davidson, S.S.G., Anastasio, D.D.J., Bebout, G.E.G., Holl, J.E., Hedlund, C. a., 1998. Volume loss and metasomatism during cleavage formation in carbonate rocks. J. Struct. Geol. 20, 707–726.

Davis, G., Reynolds, S., 1996. Structural geology of rocks and regions,, New York. John Wiley and Sons.

Debacker, T.N., Robion, P., Sintubin, M., 2004. The anisotropy of magnetic susceptibility (AMS) in low-grade, cleaved pelitic rocks: influence of cleavage/bedding angle and type and relative orientation of magnetic carriers. Geol. Soc. London, Spec. Publ. 238, 77–107.

DeCelles, P.G., 2004. Late Jurassic to Eocene evolution of the Cordilleran thrust belt and foreland basin system, western U.S.A. Am. J. Sci. 304, 105–168.

DeCelles, P.G., Coogan, J.C., 2006. Regional structure and kinematic history of the Sevier fold-and-thrust belt, central Utah. Geol. Soc. Am. Bull. 118, 841–864.

Dennis, J., 1967. International tectonic dictionary: English terminology.

DeSitter, L., 1964. Structural Geology. Mc Graw-Hill.

Dewey, J.F., Burke, K.C.A., 1973. Tibetan, Variscan and Precambrian basement reactivation: products of continental collision. J. Geol. 81, 683–692.

Dewey, J.F., Strachan, R.A., 2003. Changing Silurian–Devonian relative plate motion in the Caledonides: sinistral transpression to sinistral transtension. J. Geol. Soc. London. 160, 219–229.

Dickinson, W., Snyder, W., 1978. Plate tectonics of the Laramide orogeny. Geol. Soc. Am. Mem. 151, 355–366.

Dickinson, W.R., 2004. Evolution of the North American Cordillera. Annu. Rev. Earth Planet. Sci. 32, 13–45.

Dunlop, D.J., Ozdemir, O., 1997. Rock Magnetism: Fundamentals and Frontiers. Cambridge Univ. Press.

Dunnet, D., 1969. A technique of finite strain analysis using elliptical particles. Tectonophysics 7, 117–136.

Dunnet, D., Siddans, A., 1971. Non-random sedimentary fabrics and their modification by strain. Tectonophysics 12, 307–325.

Efron, B., 1979. Bootstrap methods: another look at the jackknife. Ann. Stat. 7, 1–26.

Efron, B., Gong, G., 1983. A leisurely look at the bootstrap, the jackknife, and cross-validation. Am. Stat. 37, 36–48.

Einstein, A., 1923. On the Electrodynamics of moving Bodies. Princ. Relativ. (english Transl. Einsteins' 1905 Zur Elektrodynamik bewegter Körper), Methuen Company, Ltd. London 1–24.

Elliott, D., 1970. Determination of Finite Strain and Initial Shape from Deformed Elliptical Objects. Geol. Soc. Am. Bull. 81, 2221–2236.

Engelder, T., Marshak, S., 1985. Disjunctive cleavage formed at shallow depths in sedimentary rocks. J. Struct. Geol. 7, 327–343.

Erslev, E., 1988. Normalized center-to-center strain analysis of packed aggregates. J. Struct. Geol. 10, 201–209.

Erslev, E., Ge, H., 1990. Least-squares center-to-center and mean object ellipse fabric analysis. J. Struct. Geol. 12, 1047–1059.

Etheridge, M., Vernon, R., 1981. A deformed polymictic conglomerate—the influence of grain size and composition on the mechanism and rate of deformation. Tectonophysics 79, 237–254.

Evans, M., Dunne, W., 1991. Strain factorization and partitioning in the North Mountain thrust sheet, central Appalachians, USA. J. Struct. Geol. 13, 21–35.

Evans, M.., Lewchuk, M.., Elmore, R.., 2003. Strain partitioning of deformation mechanisms in limestones: examining the relationship of strain and anisotropy of magnetic susceptibility (AMS). J. Struct. Geol. 25, 1525–1549.

Ferrill, D. a., Morris, A.P., Evans, M. a., Burkhard, M., Groshong, R.H., Onasch, C.M., 2004. Calcite twin morphology: a low-temperature deformation geothermometer. J. Struct. Geol. 26, 1521–1529.

Flinn, D., 1956. On the deformation of the Funzie conglomerate, Fetlar, Shetland. J. Geol. 480–505.

Flinn, D., 1962a. On folding during three-dimensional progressive deformation. Q. J. Geol. Soc. 118.

Flinn, D., 1962b. On folding during three dimensional progressive deformation. Q. J. Geol. Soc. London 118, 385–428.

Flinn, D., 1965. On the Symmetry Principle and the Deformation Ellipsoid. Geol. Mag. 102, 36–45.

Ford, M., 1987. Practical application of the sequential balancing technique: an example from the Irish Variscides. J. Geol. Soc. London. 144, 885–891.

Ford, M., 1987. Practical application of the sequential balancing technique: an example from the Irish Variscides. J. Geol. Soc. London.

Ford, M., Brown, C., Readman, P., 1991. Analysis and tectonic interpretation of gravity data over the Variscides of southwest Ireland. J. Geol. Soc. London. 148, 137–148.

Ford, M., Klemperer, S.L., Ryan, P.D., 1992. Deep structure of southern Ireland: a new geological synthesis using BIRPS deep reflection profiling. J. Geol. Soc. London. 149, 915–922.

Fry, N., 1979. Random point distributions and strain measurement in rocks. Tectonophysics 60, 89–105.

Fuentes, F., DeCelles, P., Constenius, K., 2012. Regional structure and kinematic history of the Cordilleran fold-thrust belt in northwestern Montana, USA. Geosphere 8, 1104–1128.

Fuentes, F., DeCelles, P., Gehrels, G., 2009. Jurassic onset of foreland basin deposition in northwestern Montana, USA: Implications for along-strike synchroneity of Cordilleran orogenic activity. Geology 37, 379–382.

Fuller, M.D., 1963. Magnetic Anisotropy and Paleomagnetism. J. Geophys. Res. 68, 293–309.

Gardiner, P., 1978. Is the Hercynian Front in Ireland a local feature? Natureture 271, 538–539.

Gardiner, P., MacCarthy, I., 1981. The Late Paleozoic evolution of southern Ireland in the context of tectonic basins and their transatlantic significance, in: CSPG Special Publications: Geology of the North Atlantic Borderlands- Memoir 7. pp. 683–725.

Gardiner, P., Sheridan, D., 1981. Tectonic framework of the Celtic Sea and adjacent areas with special reference to the location of the Variscan Front. J. Struct. Geol. 3, 317–331.

Gay, N., 1968a. Pure shear and simple shear deformation of inhomogeneous viscous fluids. 1. Theory. Tectonophysics 5, 211–234.

Gay, N., 1968b. Pure shear and simple shear deformation of inhomogeneous viscous fluids. 2. The determination of the total finite strain in a rock from objects such as deformed pebbles. Tectonophysics 5, 295–302.

Gill, J.. J., Elmore, R.R.., Engel, M.. M., 2002. Chemical remagnetization and clay diagenesis: testing the hypothesis in the Cretaceous sedimentary rocks of northwestern Montana. Phys. Chem. Earth, Parts A/B/C 27, 1131–1139.

Gill, W., 1962. The Variscan fold belt in Ireland, in: Coe, K. (Ed.), Some Aspects of the Variscan Fold Belt. Manchester University Press, pp. 49–64.

Graham, J.. ., Russell, K.. ., Stillman, C.J., 1995. Late Devonian Magmatism in West Kerry and Its Relationship to the Development of the Munster Basin. Irish J. Earth Sci. 7–23.

Graham, J.W., 1954. Magnetic susceptibility anisotropy, an unexploited petrofabric element. Geol. Soc. Am. Bull. 65, 1257–1258.

Harker, A., 1885. III.—The Cause of Slaty Cleavage: Compression v. Shearing. Geol. Mag. (Decade III) 2, 15–17.

Harrison, J., 1972. Precambrian Belt basin of northwestern United States: Its geometry, sedimentation, and copper occurrences. Geol. Soc. Am. Bull. 83, 1215–1240.

Haughton, S., 1856. LII. On slaty cleavage, and the distortion of fossils. London, Edinburgh, Dublin Philos. Mag. J. Sci. 12, 409–421.

Heilbronner, R., 2000. Automatic grain boundary detection and grain size analysis using polarization micrographs or orientation images. J. Struct. Geol. 22, 969–981.

Hildebrand, R., 2009. Did westward subduction cause Cretaceous-Tertiary orogeny in the North American Cordillera? Geol. Soc. Am. 457.

Hirt, A.M., Almqvist, B.S.G., 2012. Unraveling magnetic fabrics. Int. J. Earth Sci. 101, 613–624.

Hirt, A.M., Lowrie, W., Clendenen, W.S., Kligfield, R., 1988. The correlation of magnetic anisotropy with strain in the Chelmsford Formation of the Sudbury Basin, Ontario. Tectonophysics 145, 177–189.

Hirth, G., Tullis, J., 1992. Dislocation creep regimes in quartz aggregates. J. Struct. Geol. 14, 145–159.

Hobbs, A.B.E., Talbot, J.L., 1966. The Analysis of Strain in Deformed Rocks. J. Geol. 74, 500–513.

Hobbs, B., Means, W., Williams, P., 1976. An outline of structural geology. Vol. 570. New York: Wiley, 1976.

Hoffman, J., Hower, J., Aronson, J., 1976. Radiometric dating of time of thrusting in the disturbed belt of Montana. Geology 4, 16–20.

Holdsworth, R.E., Butler, C. a., Roberts, a. M., 1997. The recognition of reactivation during continental deformation. J. Geol. Soc. London. 154, 73–78.

Holl, J., Anastasio, D., 1992. Deformation of a foreland carbonate thrust system, Sawtooth Range, Montana. *Geological Society of America Bulletin* 104.8 (1992): 944-953.

Holl, J., Anastasio, D., 1995. Cleavage development within a foreland fold and thrust belt, southern Pyrenees, Spain. J. Struct. Geol. 17, 357–369.

Holst, T., 1982. The role of initial fabric on strain determination from deformed ellipsoidal objects. Tectonophysics 82, 329–350.

Housen, B. a., Richter, C., van der Pluijm, B. a., 1993. Composite magnetic anisotropy fabrics: experiments, numerical models and implications for the quantification of rock fabrics. Tectonophysics 220, 1–12.

Housen, B., Pluijm, B. van der, 1991. Slaty cleavage development and magnetic anisotropy fabrics. J. Geophys. Res. 96, 9937–9946.

Hunt, C.P., Moskowitz, B.P., Bannerjee, S., 1995. Magnetic properties of rocks and minerals. Ahrens, T.J. (ed.). Rock Phys. Phase Relations A Handb. Phys. Constants. Am. Geophys. Union 3, 189–204.

Imaz, A.G., Pocoví, A., Lago, M., Parés, J.M., 2000. Effect of lithostatic pressure and tectonic deformation on the magnetic fabric (anisotropy of magnetic susceptibility) in low-grade metamorphic rocks. J. Geophys. Res. 105, 21305.

Ising, G., 1942. On the magentic properties of varved clay. Ark. Mat. Astron. och Fys. 29A, 1–37.

Jelinek, V., 1981. Characterization of the magnetic fabric of rocks. Tectonophysics 79, T63–T67.

Jelinek, V., 1984. On a mixed quadratic invariant of the magnetic-susceptibility tensor. Z. Geophys 56, 58–60.

Jelínek, V., 1978. Statistical processing of anisotropy of magnetic susceptibility measured on groups of specimens. Stud. Geophys. Geod. 22, 50–62.

Jones, E., Childers, R., 2001. Contemporary College Physics, McGraw-Hill. McGraw-Hill, Incorporated.

Keeley, M., 1996. The Irish Variscides: problems, perspectives and some solutions. Terra Nov. 8, 259–269.

Kissel, C., Barrier, E., Laj, C., Lee, T., 1986. Magnetic fabric in “undeformed” marine clays from compressional zones. Tectonics 5, 769–781.

Kligfield, R., Carmignani, L., Owens, W., 1981. Strain analysis of a Northern Apennine shear zone using deformed marble breccias. J. Struct. Geol. 3, 421–436.

Kligfield, R., Lowrie, W., Hirt, A., Siddans, A., 1983. Effect of progressive deformation on remanent magnetization of Permian redbeds from the Alpes Maritimes (France). Tectonophysics 98, 59–85.

Kummel, B., 1954. Triassic stratigraphy of southeastern Idaho and adjacent areas. US Gov. Print. Off.

Landes, M., Prodehl, C., Hauser, F., Jacob, A., Vermeulen, N.J., 2000. VARNET-96: influence of the Variscan and Caledonian orogenies on crustal structure in SW Ireland. Geophys. J. Int. 140, 660–676.

Launeau, P., Archanjo, C.J., Picard, D., Arbaret, L., Robin, P.-Y., 2010. Two- and three-dimensional shape fabric analysis by the intercept method in grey levels. Tectonophysics 492, 230–239.

Launeau, P., Cruden, A.R., 1998. Magmatic fabric acquisition mechanisms in a syenite: Results of a combined anisotropy of magnetic susceptibility and image analysis study. J. Geophys. Res. 103, 5067–5089.

Launeau, P., Robin, P.Y.F., 1996. Fabric analysis using the intercept method. Tectonophysics 267, 91–119.

Launeau, P., Robin, P.-Y.F.P., 2005. Determination of fabric and strain ellipsoids from measured sectional ellipses—implementation and applications. J. Struct. Geol. 27, 2223–2233.

Lawton, T., Boyer, S., Schmitt, J., 1994. Influence of inherited taper on structural variability and conglomerate distribution, Cordilleran fold and thrust belt, western United States. Geology 22, 339–342.

Lisle, R., 1977a. Estimation of the tectonic strain ratio from the mean shape of deformed elliptical objects. Geol. en Mijnb. 56, 140–144.

Lisle, R., 1977b. Clastic grain shape and orientation in relation to cleavage from the Aberystwyth Grits, Wales. Tectonophysics 39, 381–395.

Lisle, R., 1985. Geological Strain Analysis: A Manual for the RF/Φ Method. Pergamon Press.

Lisle, R., Savage, J., 1983. Factors influencing rock competence: Data from a Swedish deformed conglomerate. GFF 104, 219–224.

Liu, S., Nummedal, D., Yin, P., Luo, H., 2005. Linkage of Sevier thrusting episodes and Late Cretaceous foreland basin megasequences across southern Wyoming (USA). Basin Res. 17, 487–506.

Lowell, J., 1995. Mechanics of basin inversion from worldwide examples. Geol. Soc. London, Spec. Publ. 88, 39–57.

Lüneburg, C.M., Lampert, S.A., Lebit, H.D., Hirt, A.M., Casey, M., Lowrie, W., 1999. Magnetic anisotropy, rock fabrics and finite strain in deformed sediments of SW Sardinia (Italy). Tectonophysics 307, 51–74.

MacCarthy, I., 1990. Alluvial sedimentation patterns in the Munster Basin, Ireland. Sedimentology 37, 685–712.

Mamtani, M. a., Vishnu, C.S., 2011. Does AMS data from micaceous quartzite provide information about shape of the strain ellipsoid? Int. J. Earth Sci. 101, 693–703.

Mandal, N., Samanta, S., Bhattacharyya, G., Chakraborty, C., 2003. Deformation of ductile inclusions in a multiple inclusion system in pure shear. J. Struct. Geol. 25, 1359–1370.

Marshak, S., Engelder, T., 1985. Development of cleavage in limestones of a fold-thrust belt in eastern New York. J. Struct. Geol. 7, 345–359.

Masson, F., Jacob, A., 1998. A wide-angle seismic traverse through the Variscan of southwest Ireland. Geophys. J. Int. 134, 689–705.

Masuda, T., Koike, T., Yuko, T., Morikawa, T., 1991. Discontinuous grain growth of quartz in metacherts: the influence of mica on a microstructural transition. J. Metamorph. Geol. 9, 389–402.

Matthews, P., Bond, R., Berg, J. Van Den, 1974. An algebraic method of strain analysis using elliptical markers. Tectonophysics 24, 31–67.

Max, M.D., Lefort, J.P., 1984. Does the Variscan front in Ireland follow a dextral shear zone? Geol. Soc. London, Spec. Publ. 14, 177–183.

McArdle, P., Gardiner, P., Feely, N., Colthurst, J., 1987. A possible eastern extension of the East Carlow Deformation Zone: A preliminary note. Geol. Surv. Irel. Bull.

McCann, T., Pascal, C., Timmerman, M.J., Krzywiec, P., López-Gómez, J., Wetzel, L., Krawczyk, C.M., Rieke, H., Lamarche, J., 2006. Post-Variscan (end carboniferous-Early Permian) basin evolution in western and central Europe. Geol. Soc. London Memoirs 32, 355–388.

McCarthy, W., 2013. An Evaluation of Orogenic Kinematic Evolution Utilizing Crystalline and Magnetic Anisotropy in Granitoids. Unpublished PhD Thesis. University College Cork.

McClay, K.R., Norton, M.G., Coney, P., Davis, G., 1986. Collapse of the Caledonide orogen and the Old Red Sandstone. Nature 343, 147–149.

McKerrow, W.S., MaC Niocaill, C., Dewey, J.F., 2000. The Caledonian Orogeny redefined. J. Geol. Soc. London. 157, 1149–1154.

McNaught, M., 1994. Modifying the normalized Fry method for aggregates of non-elliptical grains. J. Struct. Geol. 16, 493–503.

McNaught, M., 2002. Estimating uncertainty in normalized Fry plots using a bootstrap approach. J. Struct. Geol. 24, 311–322.

Means, W., 1976. Stress and strain: basic concepts of continuum mechanics for geologists.

Meere, P. a., Mulchrone, K.F., Timmerman, M., 2013. Shear folding in low-grade metasedimentary rocks: Reverse shear along cleavage at a high angle to the maximum compressive stress. Geology 41, 879–882.

Meere, P., Mulchrone, K.K.F., Sears, J.W., Bradway, M.D., 2008. The effect of non-passive clast behaviour in the estimation of finite strain in sedimentary rocks. J. Struct. Geol. 30, 1264–1271.

Meere, P.A., Mulchrone, K.K.F., 2003. The effect of sample size on geological strain estimation from passively deformed clastic sedimentary rocks. J. Struct. Geol. 25, 1587–1595.

Meere, P.A., Mulchrone, K.K.F., 2006. Timing of deformation within Old Red Sandstone lithologies from the Dingle Peninsula, SW Ireland. J. Geol. Soc. London. 163, 461–469.

Meere, P.A.P., 1995. The structural evolution of the western Irish Variscides: an example of obstacle tectonics? Tectonophysics 246, 97–112.

Miall, A., 1990. Principles of sedimentary basin analysis. New York: Springer-Verlag.

Miall, A., 2009. Initiation of the Western Interior foreland basin. Geology 37, 383–384.

Mitra, G., 1994. Strain variation in thrust sheets across the Sevier fold-and-thrust belt (Idaho-Utah-Wyoming): Implications for section restoration and wedge taper evolution. J. Struct. Geol. 16, 585–602.

Mitra, G., 1994. Strain variation in thrust sheets across the Sevier fold-and-thrust belt (Idaho-Utah-Wyoming): Implications for section restoration and wedge taper evolution. J. Struct. Geol. 16, 585–602.

Mitra, G., Yonkee, W.A., 1985. Relationship of spaced cleavage to folds and thrusts in the Idaho-Utah-Wyoming thrust belt. J. Struct. Geol. 7, 361–373.

Mitra, G., Yonkee, W.A., Adolph Yonkee, W., 1985. Relationship of spaced cleavage to folds and thrusts in the Idaho-Utah-Wyoming thrust belt. J. Struct. Geol. 7, 361–373.

Mitra, S., 1986. Duplex structures and imbricate thrust systems: geometry, structural position, and hydrocarbon potential. Am. Assoc. Pet. Geol., Bull.;(United States).

Monger, J., Price, R., Tempelman-Kluit, D., 1982. Tectonic accretion and the origin of the two major metamorphic and plutonic welts in the Canadian Cordillera. Geology 10, 70–75.

Mookerjee, M., Nickleach, S., 2011. Three-dimensional strain analysis using Mathematica. J. Struct. Geol. 33, 1467–1476.

Moskowitz, B., 1991. Hitchhiker's guide to magnetism. Environmental Magnetic Workshop. Unpublished Review. Institute of Rock Magnetism. Michigan.

Mudge, M., 1970. Origin of the disturbed belt in northwestern Montana. Geol. Soc. Am. Bull. 81, 377–392.

Mudge, M., 1972. Pre-Quaternary rocks in the Sun River Canyon area, northwestern Montana.

Mudge, M., 1982. A resume of the structural geology of the Northern Disturbed Belt, northwestern Montana.

Mudge, M., Earhart, R., 1983. Bedrock geologic map of part of the northern disturbed belt, Lewis and Clark, Teton, Pondera, Glacier, Flathead, Cascade, and Powell counties, Montana. USGS.

Mudge, M., Sando, W., Dutro, JT, J., 1962. Mississippian rocks of Sun River Canyon area, Sawtooth Range, Montana. Assoc. Pet. Geol. Bull.

Mukul, M., 1998. A spatial statistics approach to the quantification of finite strain variation in penetratively deformed thrust sheets: an example from the Sheeprock Thrust Sheet, Sevier. J. Struct. Geol. 20, 371–384.

Mulchrone, K., Meere, P., 2001. A Windows program for the analysis of tectonic strain using deformed elliptical markers. Comput. Geosci. 27, 1251–1255.

Mulchrone, K., Meere, P., Choudhury, K., 2005. SAPE: a program for semi-automatic parameter extraction for strain analysis. J. Struct. Geol. 27, 2084–2098.

Mulchrone, K.F., 2002. Application of Delaunay triangulation to the nearest neighbour method of strain analysis 25, 689–702.

Mulchrone, K.F., 2005. DTNNM: A windows program for strain analysis using the Delaunay triangulation nearest neighbour method. Comput. Geosci. 31, 978–988.

Mulchrone, K.F., O'Sullivan, F., Meere, P.A., 2003. Finite strain estimation using the mean radial length of elliptical objects with bootstrap confidence intervals. J. Struct. Geol. 25, 1587–1595.

Murphy, F., 1990. The Irish Variscides: a fold belt developed within a major surge zone. J. Geol. Soc. London. 147, 451–460.

Nagata, T., 1961. Rock Magnetism. Maruz. Tokyo.

Naylor, D., 1978a. A Structural Section across the Variscan Fold Belt , Southwest Ireland. J. Earth Sci. 1, 63–70.

Naylor, D., 1978b. A structural section across the Variscan fold belt, southwest Ireland. J. Earth Sci. 1, 63–70.

Naylor, D., Sevastopulo, G., Sleeman, A., Reilly, T., 1981. The Variscan fold belt in Ireland. Variscan Orogen Eur. 60, 49–66.

Nenna, F., Aydin, A., 2011. The formation and growth of pressure solution seams in clastic rocks: A field and analytical study. J. Struct. Geol. 33, 633–643.

Nevin, C., 1949. Structural geology. New York.

O'Brien, V.J., Elmore, R.D., Engel, M.H., Evans, M.A., 2006. Origin of orogenic remagnetizations in Mississippian carbonates, Sawtooth Range, Montana. J. Geophys. Res. Earth 112, 297–301.

O'Driscoll, B., Stevenson, C.T.E., Troll, V.R., 2008. Mineral Laminations in Layered Gabbro. J. Petrol. 49, 1221.

O'Driscoll, B., Stevenson, C.T.E., Troll, V.R., O'Driscoll, B., 2008. Mineral Lamination Development in Layered Gabbros of the British Palaeogene Igneous Province: A Combined Anisotropy of Magnetic Susceptibility, Quantitative Textural and Mineral Chemistry Study. J. Petrol. 49, 1187–1221.

Oliva-Urcia, B., Rahl, J.M., Schleicher, A.M., Parés, J.M., 2010. Correlation between the anisotropy of the magnetic susceptibility, strain and X-ray Texture Goniometry in phyllites from Crete, Greece. Tectonophysics 486, 120–131.

Owens, W.H., 1984. The calculation of a best-fit ellipsoid from elliptical sections on arbitrarily orientated planes. J. Struct. Geol. 6, 571–578.

Panozzo, R., 1984. Two-dimensional strain from the orientation of lines in a plane. J. Struct. Geol. 6, 215–221.

Pares, J.M., 2002. Evaluating magnetic lineations (AMS) in deformed rocks. Tectonophysics 350, 283–298.

Pares, J.M., 2004. How deformed are weakly deformed mudrocks? Insights from magnetic anisotropy. Geol. Soc. London, Spec. Publ. 238, 191–203.

Parés, J.M., 2004. How deformed are weakly deformed mudrocks? Insights from magnetic anisotropy. Geol. Soc. London, Spec. Publ. 238, 191–203.

Pares, J.M., Parés, J.M., 2004. How deformed are weakly deformed mudrocks? Insights from magnetic anisotropy. Geol. Soc. London, Spec. Publ. 238, 191–203.

Parés, J.M., van der Pluijm, B.A., 2002. Evaluating magnetic lineations (AMS) in deformed rocks. Tectonophysics 350, 283–298.

Parés, J.M., van der Pluijm, B.A., 2002. Phyllosilicate fabric characterization by Low-Temperature Anisotropy of Magnetic Susceptibility (LT-AMS). Geophys. Res. Lett. 29, 2215.

Parés, J.M., van der Pluijm, B.A., Dinarès-Turell, J., 1999a. Evolution of magnetic fabrics during incipient deformation of mudrocks (Pyrenees, northern Spain). Tectonophysics 307, 1–14.

Parés, J.M., van der Pluijm, B.A., Dinarès-Turell, J., 1999. Evolution of magnetic fabrics during incipient deformation of mudrocks (Pyrenees, northern Spain). Tectonophysics 307, 1–14.

Parés, J.M., van der Pluijm, B.A., Dinarès-Turell, J., Pare, J.M., Pluijm, B.A. Van Der, Dinare, J., Parrs, J.M., Dinarbs-turell, J., 1999b. Evolution of magnetic fabrics during incipient deformation of mudrocks (Pyrenees, northern Spain). Tectonophysics 307, 1–14.

Park, R., 1997. Foundation of structural geology. Routledge

Passchier, C.W., Trouw, R.A.J., 2005. Microtectonics. Springer Berlin Heidelb. New York.

Pastor-Galán, D., Gutiérrez-Alonso, G., Meere, P.A., Mulchrone, K.F., 2009. Factors affecting finite strain estimation in low-grade, low-strain clastic rocks. J. Struct. Geol. 31, 1586–1596.

Paterson, S., Yu, H., 1994. Primary fabric ellipsoids in sandstones: implications for depositional processes and strain analysis. J. Struct. Geol. 16, 505–517.

Peach, C., Lisle, R., 1979. A Fortran IV program for the analysis of tectonic strain using deformed elliptical markers. Comput. Geosci. 5, 325–334.

Penney, S., 1980. A new look at the Old Red Sandstone succession of the Comeragh Mountains, County Waterford. J. Earth Sci. 3, 155–178.

Penney, S.R., 1978. Devonian Lavas from the Comeragh Mountains, County Waterford. J. Earth Sci. 1, 71 – 76.

Petronis, M.S., O'Driscoll, B., Stevenson, C.T.E., Reavy, R.J., 2012. Controls on emplacement of the Caledonian Ross of Mull Granite, NW Scotland: Anisotropy of magnetic susceptibility and magmatic and regional structures. Geol. Soc. Am. Bull. 124, 906–927.

Powell, C., 1979. A morphological classification of rock cleavage. Tectonophysics 58, 21–34.

Powell, C.M., 1989. Structural controls on Palaeozoic basin evolution and inversion in southwest Wales. J. Geol. Soc. London. 146, 439–446.

Pracht, M., 2000. Controls on magmatism in the Munster Basin, SW Ireland. Geol. Soc. London, Spec. Publ. 180, 303–317.

Price, C. a., Todd, S.P., 1988. A model for the development of the Irish Variscides. J. Geol. Soc. London. 145, 935–939.

Price, C., Todd, S., 1988. A model for the development of the Irish Variscides. J. Geol. Soc. London. 145, 935–399.

Price, R. a., 1981. The Cordilleran foreland thrust and fold belt in the southern Canadian Rocky Mountains. Geol. Soc. London, Spec. Publ. 9, 427–448.

Price, R.A., Sears, J.W., 2000. 5 . A preliminary palinspastic map of the Mesoproterozoic BElt-Purcell Supergroup, Canada and USA: Implications for the tectonic setting and structural evolution of the Purcell Anticlinorium and the Sullivan Deposit. Mineral Deposits Division, Special Publication 1 (2000): 61-81.

Ramsay, J., 1969. The measurement of strain and displacement in orogenic belts. Geol. Soc. London, Spec. Publ. 3, 43–79.

Ramsay, J.G., 1967. Folding and fracturing of rocks. International Series in the Earth and Planetary Sciences. McGraw-Hill, Incorporated.

Ramsay, J.G., Huber, M.I., 1983. The Techniques of Modern Structural Geology. Volume I: Strain Analysis. Academic Press, London.

Readman, P.W., O'Reilly, B.M., Murphy, T., O'Reilly, B.M., 1997. Gravity gradients and upper-crustal tectonic fabrics, Ireland. J. Geol. Soc. London. 154, 817–828.

Richmond, L.K., Williams, B.P.J., 2000. A new terrane in the Old Red Sandstone of the Dingle Peninsula, SW Ireland. Geol. Soc. London, Spec. Publ. 180, 147–183.

Robin, P., 1977. Determination of geologic strain using randomly oriented strain markers of any shape. Tectonophysics 42, T7–T16.

Robin, P.-Y.F., 2002. Determination of fabric and strain ellipsoids from measured sectional ellipses — theory. J. Struct. Geol. 24, 531–544.

Rochette, P., 1987. Magnetic susceptibility of the rock matrix related to magnetic fabric studies. J. Struct. Geol. 9, 1015–1020.

Rochette, P., 1987. Magnetic susceptibility of the rock matrix related to magnetic fabric studies. J. Struct. Geol. 9, 1015–1020.

Rochette, P., Jackson, M.J., Aubourg, C., 1992. Rock magnetism and the interpretation of anisotropy of magnetic susceptibility. Rev. Geophys. 30, 209–226.

Rochette, P., Vialon, P., 1984. Development of planar and linear fabrics in Dauphinois shales and slates (French Alps) studied by magnetic anisotropy and its mineralogical control. J. Struct. Geol. 6, 33–38.

Saint-Bezar, B., Hebert, R.L., Aubourg, C., Robion, P., Swennen, R., Frizon de Lamotte, D., 2002. Magnetic fabric and petrographic investigation of hematite-bearing sandstones within ramp-related folds: examples from the South Atlas Front (Morocco). J. Struct. Geol. 24, 1507–1520.

Saleeby, J., Busby, C., Oldow, J., 1992. Early Mesozoic tectonic evolution of the western US Cordillera. Geol. Soc. Am.

Sanderson, D., 1982. Models of strain variation in nappes and thrust sheets: a review. Tectonophysics 88, 201–223.

Sanderson, D.J., 1984. Structural variation across the northern margin of the Variscides in NW Europe. Geol. Soc. London, Spec. Publ. 14, 149–165.

Schmidt, V., Günther, D., Hirt, A., 2006. Magnetic anisotropy of calcite at room-temperature. Tectonophysics 418, 63–73.

Sears, J.W., 2001. Lewis-Eldorado-Hoadley Thrust Slab in the Northern Montana Cordillera , USA : Implications for steady-state orogenic processes 301, 359–373.

Sedgwick, A., 1835. XXV.—Remarks on the Structure of large Mineral Masses, and especially on the Chemical Changes produced in the Aggregation of Stratified Rocks during different Periods after their Deposition. Trans. Geol. Soc. London 3, 461–486.

Seymour, D., Boulter, C., 1979. Tests of computerised strain analysis methods by the analysis of simulated deformation of natural unstrained sedimentary fabrics. Tectonophysics 58, 221–235.

Shackleton, R., 1984. Thin-skinned tectonics, basement control and the Variscan front. Geol. Soc. London, Spec. Publ. 14, 125–129.

Shackleton, R.M., 1984. Thin-skinned tectonics, basement control and the Variscan front. Geol. Soc. London, Spec. Publ. 14, 125–129.

Sharpe, D., 1847. On slaty cleavage. Q. J. Geol. Soc. 3, 74–105.

Shimamoto, T., Ikeda, Y., 1976. A simple algebraic method for strain estimation from deformed ellipsoidal objects. 1. Basic theory. Tectonophysics 36, 315–337.

Sleeman, A., McConnell, B., 1995. Sleeman, A. G., and B. J. McConnell. Geology of East Cork-Waterford: A Geological Description of East Cork, Waterford and Adjoining Parts of Tipperary and Limerick to Accompany the Bedrock Geology 1: 100,000 Scale Map Series, Sheet 22, East Cork-Waterford. Geological Survey of Ireland.

Soper, N., Strachan, R.A., Holdsworth, R.E., Gayer, R.A., Greiling, R.O., 1992. Sinistral transpression and the Silurian closure of Iapetus. J. Geol. Soc. London. 149, 871–880.

Sorby, H., 1849. On the origin of slaty cleavage. Proc. Geol. Polytech. Soc. West Rid. Yorksh. 3, 300–312.

Sorby, H., 1856. XVIII. On the theory of the origin of slaty cleavage. London, Edinburgh, Dublin Philos. Mag. J. Sci. 12, 127–129.

Stevenson, C.T.E., Hutton, D.H.W., Price, A.R., 2008. The Trawenagh Bay Granite and a new model for the emplacement of the Donegal Batholith. Earth Environ. Sci. Trans. R. Soc. Edinburgh 97, 455–477.

Stevenson, C.T.E.E., Owens, W.H., Hutton, D.H.W.W., Hood, D.N., Meighan, I.G., 2007. Laccolithic, as opposed to cauldron subsidence, emplacement of the

Eastern Mourne pluton, N. Ireland: evidence from anisotropy of magnetic susceptibility. J. Geol. Soc. London. 164, 99–110.

Stone, P., Floyd, J.D., Barnes, R.P., Lintern, B.C., 1987. A sequential back-arc and foreland basin thrust duplex model for the Southern Uplands of Scotland. J. Geol. Soc. London. 144, 753–764.

Tarling, D.H., Hrouda, F., 1993. The Magnetic Anisotropy of Rocks. Chapman Hall.

Timmerman, M.J., 2004. Timing, geodynamic setting and character of Permo-Carboniferous magmatism in the foreland of the Variscan Orogen, NW Europe. Geol. Soc. London, Spec. Publ. 223, 41–74.

Todd, S.P., 2000. Taking the roof off a suture zone: basin setting and provenance of conglomerates in the ORS Dingle Basin of SW Ireland. Geol. Soc. London, Spec. Publ. 180, 185–222.

Treagus, S.H., Treagus, J.E., 2002. Studies of strain and rheology of conglomerates. J. Struct. Geol. 24, 1541–1567.

Tripathy, N.R., Srivastava, H.B., Mamtani, M. a., 2009. Evaluation of a regional strain gradient in mylonitic quartzites from the footwall of the Main Central Thrust Zone (Garhwal Himalaya, India): Inferences from finite strain and AMS analyses. J. Asian Earth Sci. 34, 26–37.

Van der Pluijm, B. a., Vrolijk, P.J., Pevear, D.R., Hall, C.M., Solum, J., 2006. Fault dating in the Canadian Rocky Mountains: Evidence for late Cretaceous and early Eocene orogenic pulses. Geology. 34, 837.

Vermeulen, N., 2000. Wide-angle seismic control on the development of the Munster Basin, SW Ireland. Geol. Soc. … 180, 223–237.

Vermeulen, N., Shannon, P., Landes, M., Masson, F., 1998. Seismic evidence for subhorizontal crustal detachments beneath the Irish Variscides. Irish J. Earth … 17, 1–18.

Vermeulen, N.J., Shannon, P.M., Masson, F., Landes, M., 2000. Wide-angle seismic control on the development of the Munster Basin, SW Ireland. Geol. Soc. London, Spec. Publ. 180, 223–237.

Vernon, R.H., 2004. A practical guide to Rock Microstructure. Cambridge Univ. Press 43–165.

Vitale, S., Mazzoli, S., 2005. Influence of object concentration on finite strain and effective viscosity contrast: insights from naturally deformed packstones. J. Struct. Geol. 27, 2135–2149.

Voight, W., Kinoshita, S., 1907. Bestimmung absoluter Werte von Magnetiserungxzahlen, inbesondere fur Kristalle. Ann. der Phys. Bern 24, 492–514.

Ward, E., Sears, J., 2007. Reinterpretation of fractures at Swift Reservoir, Rocky Mountain thrust front, Montana: Passage of a Jurassic forebulge? Geol. Soc. Am. Spec. Pap. 433, 197–210.

Weil, A. B., Yonkee, a., Sussman, a., 2009. Reconstructing the kinematic evolution of curved mountain belts: A paleomagnetic study of Triassic red beds from the Wyoming salient, Sevier thrust belt, U.S.A. Geol. Soc. Am. Bull. 122, 3–23.

Weil, A.B., Yonkee, a., 2009. Anisotropy of magnetic susceptibility in weakly deformed red beds from the Wyoming salient, Sevier thrust belt: Relations to layer-parallel shortening and orogenic curvature. Lithosphere 1, 235–256.

Westphal, H., Eberli, G., Smith, L., Grammer, G., Kislak, J., 2004. Reservoir characterization of the Mississippian Madison Formation, Wind River basin, Wyoming. Am. Assoc. Pet. Geol. Bull. 88, 405–432.

Wheeler, J., 1986. Strain analysis in rocks with pretectonic fabrics. J. Struct. Geol. 8, 887–896.

Williams, E., Bamford, M.L.F., Cooper, M.A., Edwards, H.E., Ford, M., Grant, G., MacCarthy, I.A.J., McAfee, A., O'Sullivan, M., 1989. Tectonic controls and sedimentary response in the Devonian-Carboniferous Munster and South Munster basins, south-west Ireland. role tectonics Devonian Carbonif. Sediment. Br. Isles 6 123–141.

Williams, E.A., 2000. Flexural cantilever models of extensional subsidence in the Munster Basin (SW Ireland) and Old Red Sandstone fluvial dispersal systems. Geol. Soc. London, Spec. Publ. 180, 239–268.

Williams, E.A., Ford, M., Bay, D., 1990. Discussion of a model for the development of the Irish Variscides Journal , Vol 145 , pp . 935-939

Williams, G., Chapman, T., 1986. The Bristol-Mendip foreland thrust belt. J. Geol. Soc. London. 143, 63–73.

Wiltschko, D., Dorr, J., 1983. Timing of deformation in overthrust belt and foreland of Idaho, Wyoming, and Utah. Am. Assoc. Pet. Geol. Bull. 67, 1304–1322.

Wojtal, S., Mitra, G., 1986. Strain hardening and strain softening in fault zones from foreland thrusts. Geol. Soc. Am. Bull. 97, 674–687.

Wood, D., 1973. Patterns and magnitudes of natural strain in rocks. Philos. Trans. R. Soc. London. Ser. A, Math. Phys. Sci. 274, 373–382.

Wood, D., 1974. Current views of the development of slaty cleavage. Annu. Rev. Earth Planet. Sci. 2, 369.

Wood, D.S.D., Oertel, G., Singh, J., Bennett, H.F., 1976. Strain and Anisotropy in Rocks. Philos. Trans. R. Soc. A Math. Phys. Eng. Sci. 283, 27–42.

Woodcock, N.H., Strachan, R.A., 2012. Geological History of Britain and Ireland. Blackwell Publ.

Woodcock, N.N.H., Soper, N.J., Strachan, R. a., 2007. A Rheic cause for the Acadian deformation in Europe. J. Geol. Soc. London. 164, 1023–1036.

Wu, S., 1993. Fractal strain distribution and its implications for cross-section balancing. J. Struct. Geol. 15, 1497–1507.

Yonkee, a., Weil, a. B., 2010. Reconstructing the kinematic evolution of curved mountain belts: Internal strain patterns in the Wyoming salient, Sevier thrust belt, U.S.A. Geol. Soc. Am. Bull. 122, 24–49.

Yu, H., Zheng, Y., 1984. A statistical analysis applied to the R f/ ϕ method. Tectonophysics 110, 151–155.

Appendix 1: Mathematica code for Image analysis, semi-automatic parameter extraction and strain analysis; Article and link to Mathematica code

The strain analysis software used in this study was written for the Mathematica platform, due to its ability to handle the different tasks required for accurate strain anlysis. It is available from https://github.com/daithimaccarthaigh and has been publishhed in Computers and Geoscience (Mulchrone et al., 2013). This article is included here for reference.

Computers & Geosciences 61 (2013) 64–70

Contents lists available at ScienceDirect

Computers & Geosciences

journal homepage: www.elsevier.com/locate/cageo

Mathematica code for image analysis, semi-automatic parameter extraction and strain analysis

Kieran F. Mulchrone [a], Dave J. McCarthy [b,*], Patrick A. Meere [b]

[a] Department of Applied Mathematics, University College, Cork, Ireland
[b] School of Biological, Earth and Environmental Sciences, University College, Cork, Ireland

ARTICLE INFO

Article history:
Received 14 June 2013
Received in revised form
30 July 2013
Accepted 1 August 2013
Available online 9 August 2013

Keywords:
Image analysis
Semi-automatic parameter extraction
Strain analysis

ABSTRACT

Geological strain analysis is a common task for structural geologists. This contribution presents software written on top of the Mathematica platform which allows for rapid semi-automatic strain analysis. After an initial step of manual identification of strain markers, the software performs image analysis, parameter extraction and strain analysis using the shape and relative spatial positioning of markers. Bootstrap estimates of sampling errors are calculated and suitable graphical output is generated. Three representative samples of lithologies typically used in strain analysis are analysed to test the software.

1. Introduction

In the absence of high quality strain markers such as reduction spots, the estimation of geological strain using populations of deformed objects is a very important approach for understanding the processes and products of deformation on all scales of the Earth's lithosphere. This general approach to strain analysis by estimating finite strain from randomly oriented populations of deformed objects, the so-called the R_f/ϕ method, was first introduced in the late sixties (Ramsay, 1967). Subsequently, alternative methods based on marker shape and orientation have been developed (Borradaile, 1976; Dunnet and Siddans, 1971; Dunnet, 1969; Elliott, 1970; Lisle, 1985, 1977a, 1977b; Matthews et al., 1974; Mulchrone and Meere, 2001; Mulchrone et al., 2003; Peach and Lisle, 1979; Robin, 1977; Shimamoto and Ikeda, 1976; Yu and Zheng, 1984). A second strain analysis methodology is based on using object to object separation and assumes that the marker objects are anti-clustered and that the relative position of the centres of these objects is directly related to the orientation and magnitude of the finite strain ellipse (Ramsay, 1967). Fry (1979) developed a graphical approach using this centre to centre method that was subsequently further improved as the Normalised Fry Method (Erslev, 1988) and the enhanced Normalised Fry Method (Erslev and Ge, 1990). McNaught (1994) further extended these methods by facilitating the use of non-elliptical markers by determining best-fit ellipses for these irregular shaped objects. Mulchrone (2003) went on to show that the use of Delaunay triangulation, to characterise nearest neighbour separations, was a less subjective and more efficient strain analysis technique.

One of the key limiting steps in the automation of these strain analysis techniques is the recognition and fitting of best fit ellipses to geological strain markers such as sedimentary clasts. A number of methods for automated image analysis have been successfully utilised in the past for geological strain analysis (Ailleres et al., 1995; Erslev and Ge, 1990; Masuda et al., 1991; McNaught, 1994). Panozzo (1984) utilised digitised sets of points representing linear or elliptical objects in her projection method, while Mukul (1998) developed an approach that involved manually tracing quartz grain boundaries and subsequently, using third party image analysis software, identified the centroids and areas of the grains. Heilbronner (2000) developed a 'Lazy Grain Boundary' method that can be used in a fully automatic or semi-automatic mode to identify sedimentary grain boundaries. More recently Mulchrone et al. (2005) developed a parameter extraction program (SAPE) that rapidly extracts the required data by using a simple region-growing algorithm to identify regions of interest. The second moments are subsequently calculated for each region enabling the common strain analysis parameters to be readily computed. This current study will present a new piece of software that links a routine for image analysis, ellipse fitting and parameter extraction with software for the Mean Radial Length (Mulchrone et al., 2003) and the Delaunay Triangulation Nearest Neighbour Method (Mulchrone, 2003) strain analysis techniques. Integration of image analysis, parameter extraction and strain analysis routines will significantly reduce the time and labour intensity of geological strain analysis studies.

* Corresponding author. Tel.: +353 214 204 581.
E-mail address: davemccarthycork@gmail.com (D.J. McCarthy).

0098-3004/$ - see front matter © 2013 Elsevier Ltd. All rights reserved.
http://dx.doi.org/10.1016/j.cageo.2013.08.001

2. Methodology

The primary motivation for producing the software was to provide a single integrated system for semi-automatic image-based strain analysis. The software incorporates methods for data extraction from digital images and strain analysis of the resulting data. The methodology for extraction of object data from suitable images closely follows the approach of Mulchrone et al. (2005). From an algorithmic perspective, the most difficult part of extracting information about a population of objects in a digital image is identification of boundaries or regions occupied by those objects. Several fully automatic methods have been developed (e.g. Heilbronner, 2000), however often the results are not entirely accurate and this strongly depends on the characteristics of the particular image being analysed. Typically structural geologists work with microphotographs of quartz-rich clastic sediments which present particular difficulties for automatic methods due to undulose extinction, deformation bands, diffuse boundaries and colour similarities. On the other hand, object identification is usually a trivial exercise for geologists. Once the regions have been identified, parameters such as the aspect ratio, orientation, second moments and the centroid of the object must be extracted. Humans can also perform this task, but in a subjective manner that may introduce unwarranted biases into the data acquired (Mulchrone and Choudhury, 2004). Additionally, accurate parameter estimation and recording of parameters is time consuming. By contrast, parameter estimation is a trivial task for computers.

The idea driving our approach of data capture is to divide the tasks involved in parameter extraction according to human/computer aptitude. Therefore, the human user is given the task of identifying regions. The raw input for this activity is a digital image, which may be a microphotograph of the thin section or a field photograph of a suitable rock surface containing the marker objects. This is referred to as the **raw image** (see Fig. 1A, D and G; Fig. 1D and G from Ramsay and Huber, 1983). The end result of this activity must be a white digital image with object boundaries identified in black (see Fig. 1B, E and H), which is referred to as the **input image**. There are many possible approaches to producing the input image such as tracing objects in the raw image in graphical software packages such as Freehand or CorelDraw. Alternatively, high quality prints of the raw image are physically traced using an inking pen and tracing paper. Subsequently, the tracing is digitally scanned to produce the input image. Manual tracing was found to be the fastest and the most mentally bearable method. The approach of tracing followed by image analysis was first advocated by Mukul (1998) leading to high quality datasets (Mukul and Mitra, 1998).

Established methods for strain analysis are applied to the extracted data (Mulchrone, 2013; Mulchrone et al., 2003; Mulchrone, 2003). Mean Radial Length (MRL) is part of the R_f/ϕ suite of methods and estimates strain based on the distribution of grain shapes (Mulchrone et al., 2003). On the other hand the mutual spatial arrangement of objects can be used to estimate strain using Fry-type methods (Hanna and Fry, 1979). Here suitable object-object pairs are identified using Delaunay Triangulation Nearest Neighbour Method (DTNNM; Mulchrone, 2003) and the best fit ellipse to the central vacancy in the resulting Fry plots is estimated using the algorithm of Mulchrone (Mulchrone, 2013). In addition to identifying the best fit strain parameters the sampling error associated with each method is calculated using the bootstrap method (McNaught, 2002; Mulchrone et al., 2003).

3. Software description

The Mathematica code presented here consists of a collection of useful methods for image analysis, parameter extraction and strain analysis. The methods are grouped together in a

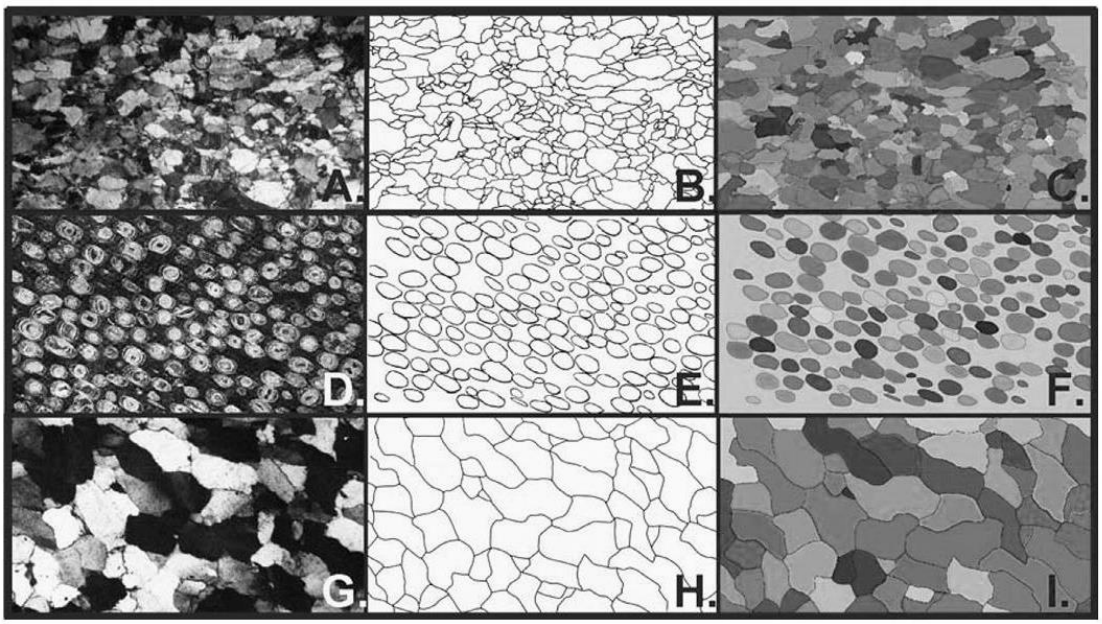

Fig. 1. A. Microphotograph of the arenite, B. Manual trace of grain boundaries. C. Identification of grain boundaries in Mathematica. D. Microphotograph of the oolite example (Ramsay and Huber, 1983), E. Manual trace of ooid boundaries, F. Identification of ooid boundaries in Mathematica, G. Microphotograph of the quartzite example (Ramsay and Huber, 1983), H. Manual trace of quartz boundaries, I. Identification of quartz boundaries in Mathematica.

Table 1
The methods, associated parameters and their description for image and strain analysis.

Method	Parameters	Description
AnalyzeImage	Filename_	The file to be analysed. Optionally include the directory location but typically this is specified using the standard Mathematica SetDirectory command.
RefineImageData	origanalysis_	This is the output from the call to AnalyzeImage
	excludelist_	A list of region labels to be excluded
	fittedellipses_	If set to 1 the fitted ellipses and labels are output, if set to 0 just the coloured identified regions are output in the image.
ExtractData	analysis_	The output from either AnalyzeImage or RefineImageData
AnalysePolarData	data_	First element of the output from ExtractData
	zeta_	The asymmetry coefficient
BootstrapPolar	data_	First element of the output from ExtractData
	zeta_	The asymmetry coefficient
	reps_	The number of bootstrap repetitions to perform
CreateNNPlotPolar	data_	First element of the output from ExtractData
	result_	The result returned from AnalysePolarData
CreateNNPlotCartesian	data_	First element of the output from ExtractData
	result_	The result returned from AnalysePolarData
CreateBootStrapPlot	bootdata_	Output from BootstrapPolar
	type_	If it takes the value 1 (default) it uses elliptical confidence intervals otherwise it generates polygonal confidence intervals.
	ptcolour_	Colour of data points defaulting to black
	starcolour_	Colour of star represent the actual estimate defaulting to black
	contcolour_	Colour of the confidence interval contours defaulting to black.
MRL	data_	Second element of the output from ExtractData
BootStrapMRL	data_	Second element of the output from ExtractData
	reps_	The number of bootstrap repetitions to perform

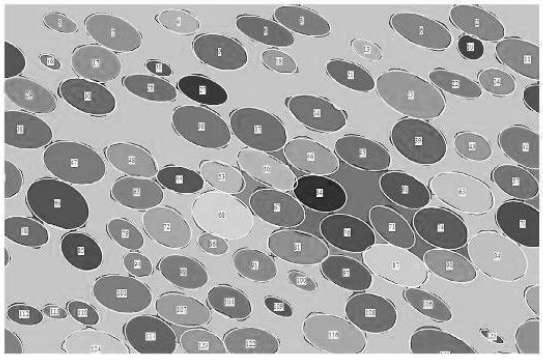

Fig. 2. Example of part of an analysed image with labelled clasts overlain with best fit ellipses.

Mathematica package which can be easily integrated with an existing installation. In this section a brief discussion and description of the data formats, analyses and graphical outputs are provided. A summary of the methods and their arguments is given in Table 1.

3.1. Image analysis

Three methods facilitate analysis of the input images. AnalyzeImage[filename_] takes the name of the input image file to be analysed as an argument and produces an image with the identified regions coloured, their best fit ellipses and a label for later use (see Fig. 2). It also returns a reference which contains the estimated parameters for each identified region (i.e. equivalent disk radius, centroid, long axis, short axis, orientation and label) and a reference to the analysed image. Internally the method takes advantage of Mathematica's in-built image processing abilities which (1) converts the image to a binary format, (2) inverts the binary image and (3) performs a watershed analysis to identify the regions. Each identified region is given a unique label which can be used later on for refinement.

Often the use of AnalyzeImage completes the image analysis step, however, there may be circumstances where regions are erroneously identified. In order to rectify this the user can use the method RefineImageData[origanalysis_, excludelist_, fittedellipses_: 1] to perfect the analysis. The argument origanalysis_ is the output from the call to AnalyzeImage, excludelist_ is a list of regions to be excluded from the analysis (identified by the labels produced by AnalyzeImage) and fittedellipses_ gives the user the option of displaying fitted ellipses or not in the image produced.

Finally ExtractData[analysis_] takes the output from either AnalyzeImage or RefineImageData as an argument and returns the data relevant to both the MRL and DTNNM methods of strain analysis. The output consists of two lists. The first list is the data for DTNNM analysis and is in the form {avradius, x, y} i.e. average object radius and coordinates of the object centroid. The second list is the data for MRL analysis and takes the form {a, b, φ} i.e. long axis, short axis and ellipse orientation.

A typical sequence of commands are

```
(* Load the package. NOTE: this needs to be wherever the
package file is stored. *)
In[1]:=« "C:\\Users\\km\\Dropbox\\Strain Analysis Notebook.m"
(* Set the working directory to be where your image files are
located *)
In[2]:=SetDirectory["C:\\Users\\km\\Dropbox"]
Out[2]="C:\\Users\\km\\Dropbox\\"
(* Analyse the image *)
res1=AnalyzeImage["test.bmp"];
(* Optionally refine the analysis to remove certain regions *)
res2=RefineImageData[res1, {2, 3, 4, 5, 6, 48, 41}, 1]; (See
Fig. 2)
(* Finally grab the data: note mres is used as input to strain
analysis methods *)
mres=ExtractData[res2];
```

3.2. Strain analysis

The software procedures for strain analysis are concerned with (1) analysing the relative spatial positioning of strain markers using DTNNM (Mulchrone, 2003) and the automatic identification

of the associated strain (Mulchrone, 2013), (2) analysis the shapes of markers using the method of MRL (Mulchrone et al., 2003), (3) providing bootstrap sampling error estimates for both analyses and (4) providing suitable graphical output. In addition, there are several utility methods called inside other methods and are not designed for direct usage.

Spatial data may be analysed using a Polar or Cartesian coordinate system, however the polar approach tends to outperform the Cartesian formulation (Mulchrone, 2013) and is thus implemented here. The method AnalyseDataPolar[data_, zeta_] takes as input the first element of the data returned from ExtractData[] above and the second argument is zeta corresponding to asymmetry coefficient (Mulchrone, 2013). The asymmetry coefficient controls how data are weighted when fitting an ellipse to the data. Typically, the larger the value of zeta, the higher the weighting that is applied to a fewer number of centrally located points (which may cause the sampling error to increase). The output generated is a list of data containing the long axis, the short axis and orientation of the best fit ellipse to the central vacancy. The long and short axes are returned because they are required to generate graphical output later. Internally the method calls a utility method GetNearestNormalPointsDT[] which calculates the Delaunay triangulation and subtracts the points on the convex hull which generates the raw data required for the method of Mulchrone (2013). The method BootStrapPolar[data_, zeta_, reps_] is used to estimate the sampling error associated with an analysis. The arguments have the same meaning as for AnalysePolar except that reps_ determines how many bootstrap repetitions are applied. Usually a value of between 200 and 400 is more than sufficient. The spatial analysis is computationally intensive and bootstrap analyses may be time consuming. The output from BootStrapPolar consists of the original result (same as that from AnalysePolar) plus an additional list of individual bootstrap results.

The bootstrap is a general computational technique invented by Efron (1979) to construct approximate sampling distributions for complex statistical estimates. The basic principal of the bootstrap is multiple samples of a given dataset can be generated by repeatedly resampling the original dataset with replacement. Multiple parameter estimates are calculated by analysis of the multiple samples. The distribution of the parameter estimates found closely approximates the true sampling distribution of the parameters. Typically for a univariate dataset the percentiles for the dataset of parameter estimates allow estimation of suitable confidence intervals. In higher dimensions (in 2D strain analysis that data are bivariate), elliptical regions centred on the mean are found which enclose a specified percentage of the data using the built-in EllipsoidQuantile function of Mathematica.

There are three methods for generated graphical output for the DTNNM strain analysis. The first method (CreateNNPlotPolar [data_, result_]) displays the data in polar form in a plot of r (distance from origin) versus orientation and superimposes the curve representing the best-fit ellipse (see Fig. 3). CreateNNPlotCartesian[data_, result_] creates a more familiar Fry style plot (Fry, 1979) in Cartesian coordinates (see Fig. 4A, D and G). Finally CreateBootStrapPlot[bootdata_, type_, ptcolour_, starcolour_, contcolour_] creates a plot of the bootstrap data along with confidence intervals at the 90%, 95% and 99% levels for the location of the true value as well as the location of the estimate from AnalyseDataPolar (see Fig. 3). This method can also be used to create a bootstrap plot for datasets generated from MRL.

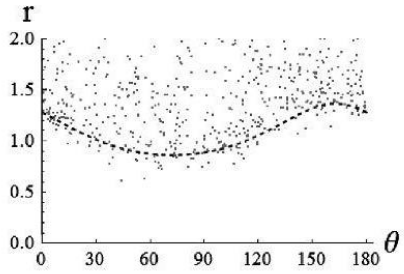

Fig. 3. Example of a polar plot for the oolite example. r (distance from origin) is plotted against orientation and superimposes the curve representing the best-fit ellipse.

MRL is relatively simple in implementation compared with DTNNM. There are two methods available. The first method MRL [data_] takes as input the second element of the data returned from ExtractData[] above and outputs the axial ratio and orientation of the calculated strain ellipse. The second method BootStrapMRL[data_, reps_] takes as first argument the second element of the data returned from ExtractData[] and as second argument the number of bootstrap repetitions to perform. Note that MRL is much faster than DTNNM and so taking 1000 repetitions is very feasible. The output comprises the original result (i.e. from MRL) plus an additional list of individual bootstrap results.

A typical sequence of commands is as follows:

```
(* note mres is the return value from ExtractData[] *)
(* Do a DTNNM analysis *)
nnres=AnalyseDataPolar[mres[[1]], 10000]
(* Create a graphical representation *)
CreateNNPlotPolar[mres[[1]], nnres]
(* Create a Fry-type plot of the result *)
CreateNNPlotCartesian[mres[[1]], nnres]
(* Perform a bootstrap analysis *)
(* Quiet prevents unnecessary feedback, note this takes some
time to \complete! *)
bsres=Quiet[BootStrapPolar[mres[[1]], 10000, 200]];
(* Create a graphic of the bootstrap data *)
(* Plot the bootstrap results with confidence intervals at 90, 95
and 99% level *)
CreateBootStrapPlot[bsres]
(* Do strain analysis using Mean Radial Length (MRL)
Mulchrone et al. (2003) *)
(* Single Analysis returns axial ratio and orientation *)
MRL[mres[[2]]]
bsMRL=BootStrapMRL[mres[[2]], 1000];
(* Plot Bootstrap results *)
CreateBootStrapPlot[bsMRL]
```

4. Example applications

In this section three samples are analysed using the software system presented above. These samples have been selected to represent the typical lithologies that are used in geological strain analysis.

4.1. Sample locations and background geology

The first sample used in this study is a medium grained quartz arenite from the Lower Carboniferous Crows Point Formation (MacCarthy et al., 1978; MacCarthy, 1974; Murphy, 1985) taken from a shear zone on the north limb of the Ardmore Syncline in County Waterford, Ireland. In thin section (see Fig. 1A) the sample displays a strong fabric, dominated by elongate flattened quartz grains, which are typically parallel to pressure solution cleavage planes. The analysed thin section is composed of 80% quartz grains that are typically 1mm elongate, rounded to sub-angular and monocrystalline.

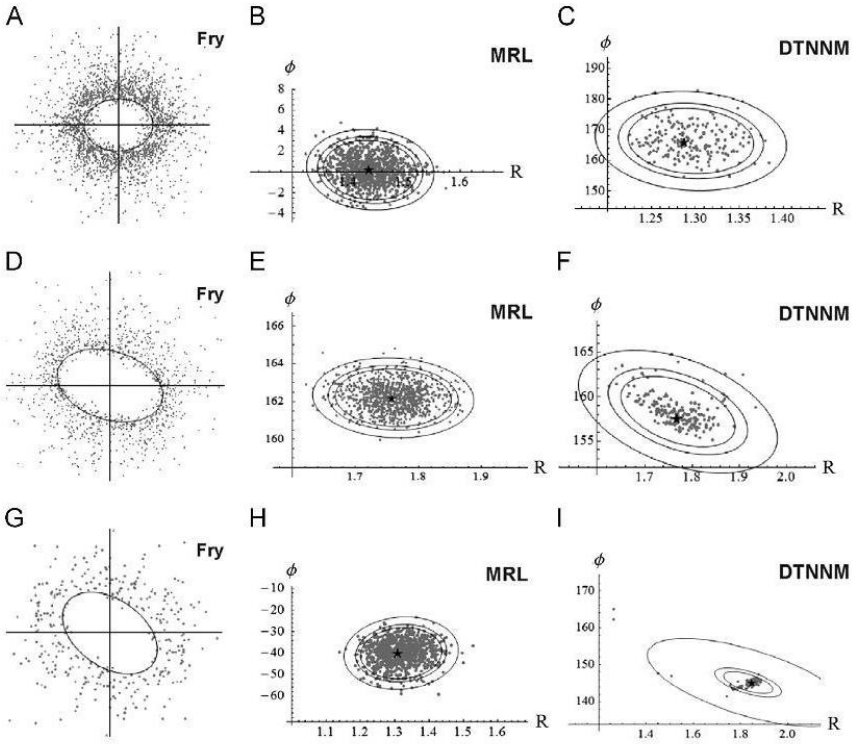

Fig. 4. A. Fry plot of data from the arenite. B. Bootstrap data of MRL data from the arenite, bootstrap intervals show 90%, 95% and 99% confidence intervals. C. Bootstrap data of DTNNM data from the arenite. D. Fry plot of data from the oolite (Ramsay and Huber, 1983). E. Bootstrap data of MRL data from ooid boundaries, F. Bootstrap data of DTNNM data from ooid boundaries. G. Fry plot of data from the Quartzite (Ramsay and Huber, 1983). H. Bootstrap data of MRL data from quartz boundaries, I. Bootstrap data of DTNNM data from quartz boundaries.

The other two examples analysed here (see Fig. 1D and G) are photomicrographs of an oolite (Page 112, Fig 7.7. from Ramsay and Huber, 1983) and a quartzite (Page 118, Fig 7.16. from Ramsay and Huber, 1983). These images were used because they are familiar to the majority of structural geologists and their strain estimates are firmly established. Additionally they represent two very different lithologies compared to the sandstone described above.

4.2. Image preparation

Grain boundary maps are manually traced from microphotographs of thin sections taken in cross polarised light. Typically sandstones are analysed and in these cases only quartzofeldspathic grain boundaries are identified and traced. Essentially the goal is to ensure that objects of similar size and rheology are analysed. Hence creating reliable comparisons and ensuring that minerals such as biotite, with exceptionally elongate crystal shapes and differing rheological properties do not affect the analysis.

When tracing grain boundaries there are a few factors that need to be taken into consideration. Firstly each grain boundary needs to be a closed loop, otherwise they will not be detected by the image analysis routine. Secondly, grain boundaries need to be traced with an ink pen of a significant thickness (0.5 mm), so that when they are scanned at low resolution the grain boundaries maintain their integrity, i.e. no spurious gaps appear. The reasoning behind low resolution scanning of the traced boundaries is twofold; smaller sized images are easier for Mathematica to handle resulting in faster analysis, while at higher scanning resolutions we have found that more spurious objects are identified. Experience has shown that the ideal file size and image format is a bitmap of approximately 500 kb, this roughly equates to an A4 page of manually traced grain boundaries, scanned at 200–300 dpi, resulting in an image of 2340 × 1700 pixels. The last thing to consider is the number of objects used in the analysis. It has been established that approximately 150 grains is sufficient (Meere and Mulchrone, 2003). Sample sets with significantly fewer objects than this can result in large errors in the strain estimates, whereas larger data sets do not improve the quality of the estimates and can dramatically increase the computing time required.

For the majority of sandstones it is relatively easy to include only quartzofeldspathic grain boundaries and for the samples used in this study very little post processing was required. Unfortunately with interlocking or closely spaced grains it can be particularly difficult to exclude unwanted mineral boundaries or voids between grains Problematic objects can be excluded from the analysis using RefineImageData[]. We have found that selective editing of the manual image prior to analysis is the most efficient method for reducing any errors created. For examples that are not completely interlocking it is usually possible to keep grains separate and distinct.

Besides the manual selection of objects to be analysed the only other significant user input in the analysis process is the determination of a zeta value (see Section 3.2 and Mulchrone, 2013). The

function of zeta is to decide to what extent data inliers are weighted. The effects of this function are seen in the Fry or Cartesian plot produced in the first stage of the analysis (i.e. Fig. 4A). A higher zeta value applies a higher weighting to points near the inner void of the data (Mulchrone, 2013), it has been found in this study that zeta values between 100 and 4000 should be sufficient to accommodate a best fit of the data. The inclusion of this function allows the user to ensure that a best fit is achieved by preferential weighting of data points. This function can also be used as a measure of the quality of the data, with poor quality data the best fit is poorly correlated, regardless of the zeta value.

4.3. Results

The analysis of the arenite yielded $R=1.3$ and $R=1.4$ for DTNNM and MRL respectively. The resulting Fry plot exhibits a significant population of central inliers which leads to a sizeable sampling error. In this case a low value for Zeta was selected so that less weight was given to the centrally located data when fitting the ellipse (Fig. 4A). The confidence intervals for the DTNNM and MRL methods do not significantly overlap (Fig. 4B and C), which is indicative of the sensitivity of the two methods to different types of strain.

The analysis of the oolite yielded $R=1.68$ and $R=1.76$ for DTNNM and MRL respectively. These values are very close to the estimates of Ramsay and Huber (1983), $R=1.7$ and $R=1.79$ by the Fry method and centre to centre techniques respectively. The Fry plot of the centre to centre data gives a relatively well defined best fit ellipse as there are very few centrally located points to negatively affect the best fit ellipse (Fig. 4D). The confidence ellipses for the bootstrapped data for MRL and DTNNM overlap suggesting that both methods are identifying the same strain behaviour (Fig. 4E and F).

Analysis of the quartzite yielded results of $R=1.78$ and $R=1.31$ for DTNNM and MRL respectively. The value estimated by Ramsay and Huber (1983) by the Fry method was $R=1.7$. The Fry plot of the centre to centre data clearly identifies the best fit ellipse (Fig. 4G). However there are extreme values on the bootstrap plot for DTNNM. This can be readily explained by the small number of data points in the central region and this in turn is related to the small number of clasts used ($N=81$). In this sample the confidence intervals for the DTNNM and MRL analyses do not overlap (Fig. 4H and I). Once again this suggests the different techniques are sensitive to different strain behaviours.

4.4. Discussion

The automatic misidentification of regions as clasts may create errors in the strain estimates produced by the above methods may be a concern. It could be argued that the inclusion of extra mineral species or voids may only represent a small portion of the total data and therefore would only lead to small errors in the estimates. It is our contention that even with data sets in excess of 150 objects, as recommended by Meere and Mulchrone (2003), the inaccuracies produced by these extra grains may be significant. To investigate this we have analysed the oolite sample with this in mind. This resulted in an image with 204 correctly identified ooids and 19 misidentified regions using the image analysis techniques above. This data set yielded strain estimates of $R=1.36$ and $R=1.63$ for DTNNM and MRL respectively, both significantly lower than the values reported earlier ($R=1.68$ and $R=1.74$) using a data set without misidentified objects. DTNNM is most affected by this issue, probably because these misidentified regions introduce spuriously close object-object separations. We propose two methods to counter for this effect, (1) a second trace is manually produced, that carefully ensures no interstitial areas are created, or (2) unwanted objects are removed using the RefineImageData[] method. We strongly endorse the second approach because it does not involve artificially modifying the input image.

4.5. Conclusion

Geological strain analysis forms an integral component of any detailed regional tectonic study. Historically a fundamental limitation on the breadth of this approach has been the labour intensive nature of such techniques. In this contribution we present a collection of procedures written on top of the Mathematica platform which allows for rapid semi-automatic strain analysis. The methodology involves an initial step of manual identification of strain markers. After this the procedure is fully automatic. The software performs image analysis to identify regions and extract the relevant parameters for subsequent strain analysis using the DTNNM and MRL methods. It calculates bootstrap estimates of sampling errors and generates suitable graphical output.

The software has been tested using three samples which are representative of typical lithologies used in geological strain analysis. The strain estimates obtained compare well with previously published estimates and the software was found to perform well.

Acknowledgements

We would like to thank an anonymous reviewer and Frederick Vollmer for careful reviews which helped to improve the manuscript. Dave McCarthy acknowledges the support of an IRCSET Embark scholarship.

Appendix A. Supporting information

Supplementary data associated with this article can be found in the online version at http://dx.doi.org/10.1016/j.cageo.2013.08.001.

References

Ailleres, L., Champenois, M., Macaudiere, J., Bertrand, J.., 1995. Use of image analysis in the measurement of finite strain by the normalized Fry method: geological implications for the'Zone Houillere' (Brianconnais zone, French Alps). Mineralogical Magazine 59, 179–187.
Borradaile, G., 1976. A strain study of a granite–granite gneiss transition and accompanying schistosity formation in the Betic orogenic zone, SE, Spain. Journal of the Geological Society 132, 417–428.
Dunnet, D., 1969. A technique of finite strain analysis using elliptical particles. Tectonophysics 7, 117–136.
Dunnet, D., Siddans, A., 1971. Non-random sedimentary fabrics and their modification by strain. Tectonophysics 12, 307–325.
Efron, B., 1979. Bootstrap methods: another look at the jackknife. The Annals of Statistics 7, 1–26.
Elliott, D., 1970. Determination of finite strain and initial shape from deformed elliptical objects. Geological Society of America Bulletin 81, 2221–2236.
Erslev, E., 1988. Normalized center-to-center strain analysis of packed aggregates. Journal of Structural Geology 10, 201–209.
Erslev, E., Ge, H., 1990. Least-squares center-to-center and mean object ellipse fabric analysis. Journal of Structural Geology 12, 1047–1059.
Fry, N., 1979. Random point distributions and strain measurement in rocks. Tectonophysics 60, 89–105.
Hanna, S., Fry, N., 1979. A comparison of methods of strain determination in rocks from southwest Dyfed (Pembrokeshire) and adjacent areas. Journal of Structural Geology 1, 155–162.
Heilbronner, R., 2000. Automatic grain boundary detection and grain size analysis using polarization micrographs or orientation images. Journal of Structural Geology 22, 969–981.
Lisle, R., 1977a. Estimation of the tectonic strain ratio from the mean shape of deformed elliptical objects. Geologie en Mijnbouw 56, 140–144.
Lisle, R., 1977b. Clastic grain shape and orientation in relation to cleavage from the Aberystwyth Grits, Wales. Tectonophysics 39, 381–395.
Lisle, R., 1985. Geological Strain Analysis: A Manual for the R_f/ϕ Method. Pergamon Press.

MacCarthy, I., Gardiner, P., Horne, R., 1978. The lithostratigraphy of the Devonian–Early Carboniferous succession in parts of Counties Cork and Waterford, Ireland. Bulletin of the Geological Survey of Ireland 2, 265–305.
MacCarthy, I.A.J., 1974. The Lithostratigraphy and Sedimentology of the Devonian–Early Carboniferous Succession in Parts of Counties Cork and Waterford (PhD Thesis). National University of Ireland.
Masuda, T., Koike, T., Yuko, T., Morikawa, T., 1991. Discontinuous grain growth of quartz in metacherts: the influence of mica on a microstructural transition. Journal of Metamorphic Geology 9, 389–402.
Matthews, P., Bond, R., Berg, J., Van Den, 1974. An algebraic method of strain analysis using elliptical markers. Tectonophysics 24, 31–67.
McNaught, M., 1994. Modifying the normalized Fry method for aggregates of non-elliptical grains. Journal of Structural Geology 16, 493–503.
McNaught, M., 2002. Estimating uncertainty in normalized Fry plots using a bootstrap approach. Journal of Structural Geology 24, 311–322.
Meere, P.A., Mulchrone, K.F., 2003. The effect of sample size on geological strain estimation from passively deformed clastic sedimentary rocks. Journal of Structural Geology 25, 1587–1595.
Mukul, M., 1998. A spatial statistics approach to the quantification of finite strain variation in penetratively deformed thrust sheets: an example from the Sheeprock Thrust Sheet, Sevier. Journal of Structural Geology20, 371–384.
Mukul, M., Mitra, G., 1998. Finite strain and strain variation analysis in the Sheeprock Thrust Sheet: an internal thrust sheet in the Provo salient of the Sevier Fold-and-Thrust belt, Central Utah. Journal of Structural Geology 20, 385–405.
Mulchrone, K., 2013. Fitting the void: data boundaries, point distributions and strain analysis. Journal of Structural Geology 46, 22–23.
Mulchrone, K., Meere, P., 2001. A Windows program for the analysis of tectonic strain using deformed elliptical markers. Computers & Geosciences 27, 1251–1255.
Mulchrone, K., Meere, P., Choudhury, K., 2005. SAPE: a program for semi-automatic parameter extraction for strain analysis. Journal of Structural Geology 27, 2084–2098.
Mulchrone, K.F., 2003. Application of Delaunay triangulation to the nearest neighbour method of strain analysis. Journal of Structural Geology 25, 689–702.
Mulchrone, K.F., Choudhury, K.R., 2004. Fitting an ellipse to an arbitrary shape: implications for strain analysis. Journal of Structural Geology 26, 143–153.
Mulchrone, K.F., O'Sullivan, F., Meere, P.A., 2003. Finite strain estimation using the mean radial length of elliptical objects with bootstrap confidence intervals. Journal of Structural Geology 25, 1587–1595.
Murphy, F.X., 1985. The Lithostratigraphy and Structural Geology of the Dungarvan Syncline and Adjacent Areas, Co. Waterford, Southern Ireland(PhD Thesis). National University of Ireland.
Panozzo, R., 1984. Two-dimensional strain from the orientation of lines in a plane. Journal of Structural Geology 6, 215–221.
Peach, C., Lisle, R., 1979. A Fortran IV program for the analysis of tectonic strain using deformed elliptical markers. Computers & Geosciences 5, 325–334.
Ramsay, J.G., Huber, M., 1983. The techniques of modern structural geology. Strain Analysis, London: Academic Press.
Ramsay, J.G., 1967. Folding and fracturing of rocks. New York, MacGraw-Hill, 568p.
Robin, P., 1977. Determination of geologic strain using randomly oriented strain markers of any shape. Tectonophysics 42, T7–T16.
Shimamoto, T., Ikeda, Y., 1976. A simple algebraic method for strain estimation from deformed ellipsoidal objects. 1. Basic theory. Tectonophysics 36, 315–337.
Yu, H., Zheng, Y., 1984. A statistical analysis applied to the R_f/ϕ method. Tectonophysics 110, 151–155.

Appendix 2: AMS data for Chapter 4; Sawtooth Range, NW Montana

A2.1. The AMS data for the samples collected in the Sawtooth Range are presented here, with tables for both the individual specimen data and the mean sample data. The individual specimen data are split into two groups, depending on their magnetic response, i.e. diamagnetic or paramagnetic.

Diamagnetic Specimens

Name	S0 Strike	Dip		Field	Freq.	Km	L	F	P	Pj	T	U	K1dec	K1inc	K2dec	K2inc	K3dec	K3inc
Beaver																		
GR25																		
A1	150	25	w	200	F1	-6.0329	1.115	1.101	1.227	1.227	-0.061	0.1	305.9	43.7	134.9	45.9	40.2	4.6
A2	150	25	w	200	F1	-4.0967	1.095	1.305	1.429	1.45	0.49	-0	273.1	25.2	110.8	63.8	6.4	7
B1	150	25	w	200	F1	-5.3821	1.111	1.188	1.32	1.323	0.243	-0	329.9	72	142.6	17.8	233.3	2.1
C1	150	25	w	200	F1	-4.7818	1.131	1.107	1.252	1.252	-0.096	0.2	194.7	30.4	289.3	7.8	32.1	58.4
D1	150	25	w	200	F1	-4.6333	1.146	1.122	1.286	1.286	-0.084	0.1	48.2	4	316.2	26.7	146.2	62.9
D2	150	25	w	200	F1	-4.7776	1.273	1.036	1.319	1.352	-0.744	0.8	305.3	47.9	106.8	40.6	204.8	9.3
E1	150	25	w	200	F1	-5.0943	1.137	1.232	1.401	1.405	0.236	-0	337	36.4	215.9	35.1	97.2	34.3
E2	150	25	w	200	F1	-5.1846	1.03	1.463	1.506	1.579	0.856	-1	195	17.7	301.1	41.1	87.3	43.6
F1	150	25	w	200	F1	-5.2349	1.251	1.169	1.463	1.466	-0.179	0.3	121.1	65.6	307.3	24.3	216.3	2.3
G1	150	25	w	200	F1	-4.9545	1.114	1.133	1.263	1.263	0.072	-0	157.9	26	354.3	63.1	251.1	6.6
H1	150	25	w	200	F1	-4.0654	1.212	1.197	1.451	1.451	-0.035	0.1	150.1	0.2	240.5	63.5	60	26.5
B2	150	25	w	200	F1	-4.4884	1.019	1.166	1.188	1.208	0.785	-1	145.8	24	42.3	27.7	270.4	51.8
bgr16																		
A1	153	55	w	200	F1	-15.56	1.008	1.202	1.212	1.242	0.915	-1	43.8	8.6	304.1	47.8	141.3	40.9
A2	153	55	w	200	F1	-20.296	1.06	1.124	1.191	1.195	0.337	-0	276.5	64.8	56.2	19.8	151.8	15.1
A3	153	55	w	200	F1	-14.841	1.142	1.208	1.38	1.382	0.175	-0	337.1	30.3	173	58.7	71.2	7.1
B1	153	55	w	200	F1	-16.021	1.108	1.183	1.311	1.314	0.242	-0	60.3	9.5	162	50.4	322.7	37.9
B2	153	55	w	200	F1	-19.272	1.189	1.215	1.445	1.445	0.06	0	19.2	62.8	272.1	8.6	177.9	25.6
B3	153	55	w	200	F1	-22.796	1.069	1.144	1.223	1.228	0.338	-0	56.4	2.7	324.1	40.7	149.6	49.2
C2	153	55	w	200	F1	-17.949	1.059	1.162	1.23	1.239	0.444	-0	38.2	10.3	147.6	61.2	303	26.5
GR18																		
A3	160	70	w	200	F1	-3.2178	1.116	1.067	1.19	1.193	-0.257	0.3	305.7	39	120	50.8	213.5	2.8
B1	160	70	w	200	F1	-0.8387	1.325	1.224	1.621	1.625	-0.165	0.3	124.2	23.7	328.1	64.3	218.3	9.2
B2	160	70	w	200	F1	-2.2666	1.11	1.051	1.166	1.17	-0.355	0.4	327.1	23.4	119.8	64.1	232.4	10.6
B4	160	70	w	200	F1	-3.8947	1.076	1.045	1.125	1.126	-0.243	0.3	318	0.4	142.1	89.6	48	0
C2	160	70	w	200	F1	-1.8801	1.132	1.146	1.297	1.297	0.046	0	322.6	18.7	191.2	62.9	59.2	18.9
C3	160	70	w	200	F1	-3.3798	1.275	1.521	1.94	1.955	0.266	-0	292.8	0.8	200.6	69.9	23.1	20.1
C4	160	70	w	200	F1	-12.19	1.015	1.011	1.026	1.026	-0.135	0.1	148.8	27	289	56.5	49.1	18.3
E1	160	70	w	200	F1	-1.4155	1.147	1.202	1.379	1.381	0.146	-0	319.3	31.4	99.8	51.7	216.7	19.6

Name	S0 Strike	Dip		Field	Freq.	Km	L	F	P	Pj	T	U	K1dec	K1inc	K2dec	K2inc	K3dec	K3inc
GR19																		
A1	160	70	w	200	F1	-7.8248	1.074	1.035	1.112	1.114	-0.356	0.4	249.1	46	103	38.7	358.3	17.5
A2	160	70	w	200	F1	-7.7596	1.097	1.079	1.184	1.184	-0.1	0.1	70.3	52.2	198.4	25.6	301.8	25.8
B1	160	70	w	200	F1	-9.5885	1.063	1.023	1.087	1.09	-0.454	0.5	84.3	31.6	229.9	53.3	343.6	16.7
B2	160	70	w	200	F1	-7.3802	1.085	1.075	1.166	1.167	-0.064	0.1	221.6	22	84.2	61.3	319	17.6
C1	160	70	w	200	F1	-5.9028	1.093	1.13	1.235	1.236	0.157	-0	36.8	10.9	282.5	65	131.3	22.2
C2	160	70	w	200	F1	-7.9305	1.093	1.06	1.158	1.159	-0.209	0.2	127.2	58.6	237.4	11.9	334	28.6
D1	160	70	w	200	F1	-7.6626	1.059	1.101	1.165	1.167	0.251	-0	184.1	60.8	60.6	17.1	323.1	22.9
F1	160	70	w	200	F1	-6.9987	1.058	1.148	1.214	1.221	0.423	-0	48.7	0.7	139.4	45	318	45
GR20																		
A1	160	70	w	200	F1	-16.479	1.007	1.029	1.036	1.038	0.625	-1	279.6	47.8	16.9	6.6	112.8	41.4
A2	160	70	w	200	F1	-9.2496	1.037	1.045	1.084	1.084	0.097	-0	264.6	43	40	37.4	150	24.1
B1	160	70	w	200	F1	-14.852	1.039	1.014	1.053	1.055	-0.472	0.5	86.3	29.6	233.4	56	347.3	15.3
B2	160	70	w	200	F1	-10.084	1.079	1.059	1.143	1.144	-0.139	0.2	106.6	69.3	227.1	10.9	320.5	17.4
C1	160	70	w	200	F1	-7.5307	1.045	1.04	1.086	1.086	-0.061	0.1	57.8	11.5	161.7	49.8	318.7	37.9
C2	160	70	w	200	F1	-9.6848	1.075	1.007	1.083	1.092	-0.83	0.8	75.4	25.3	288.6	60.5	172.2	14.1
D1	160	70	w	200	F1	-9.2073	1.063	1.053	1.12	1.12	-0.084	0.1	209.7	21.2	105.1	33	326.4	49.1
D2	160	70	w	200	F1	-9.7693	1.054	1.039	1.096	1.096	-0.155	0.2	199.1	26.9	5	62.4	106.2	5.8
E1	160	70	w	200	F1	-9.3759	1.043	1.025	1.069	1.069	-0.266	0.3	56.3	29.8	194.7	52.5	313.9	20.5
D3	160	70	w	200	F1	-9.344	1.036	1.034	1.071	1.071	-0.021	0	269.3	31.7	19.1	28.6	141.7	44.6
GR21																		
A1	162	68	w	200	F1	-10.275	1.043	1.056	1.101	1.101	0.133	-0	287.5	38.6	68.3	44.1	179.8	20.8
A2	162	68	w	200	F1	-8.2236	1.063	1.093	1.162	1.163	0.182	-0	64.8	18.4	255.8	71.3	155.9	3.3
B2	162	68	w	200	F1	-10.561	1.078	1.071	1.154	1.154	-0.044	0.1	297.6	26.6	35.4	15.2	152	58.8
B3	162	68	w	200	F1	-10.437	1.059	1.055	1.117	1.117	-0.034	0.1	16.7	69.7	222	18.5	129.3	8.1
C1	162	68	w	200	F1	-9.2982	1.113	1.071	1.193	1.194	-0.218	0.3	275.7	45	13.5	7.8	111.1	44
C2	162	68	w	200	F1	-8.9313	1.034	1.107	1.144	1.151	0.507	-0	39.4	37.6	297	15.5	188.9	48.2
D1	162	68	w	200	F1	-9.8626	1.082	1.047	1.133	1.134	-0.265	0.3	93.4	9.8	348.1	56.8	189.5	31.4
D3	162	68	w	200	F1	-8.2	1.065	1.108	1.181	1.183	0.239	-0	300.7	26.6	189.9	35.4	58.5	43
E1	162	68	w	200	F1	-9.4878	1.043	1.041	1.086	1.086	-0.025	0	318.5	49.5	124.8	39.7	220.5	6.8
E2	162	68	w	200	F1	-9.5391	1.032	1.07	1.104	1.107	0.372	-0	257.6	27.8	31.2	52.6	154.7	22.9
F1	162	68	w	200	F1	-8.9046	1.061	1.013	1.075	1.08	-0.651	0.7	50.6	7.4	308.7	57.9	145.1	31

Name	S0 Strike	Dip		Field	Freq.	Km	L	F	P	Pj	T	U	K1dec	K1inc	K2dec	K2inc	K3dec	K3inc
F2	162	68	w	200	F1	-9.1823	1.068	1.037	1.107	1.108	-0.289	0.3	278	19.7	32.2	48.9	173.8	34.3
F3	162	68	w	200	F1	-7.6618	1.03	1.057	1.089	1.091	0.303	-0	40.4	39.3	288.1	24.9	174.8	40.5
G2	162	68	w	200	F1	-10.53	1.048	1.011	1.06	1.063	-0.628	0.6	33.3	11.8	283.8	58.1	130	29.2
G3	162	68	w	200	F1	-10.197	1.063	1.014	1.078	1.083	-0.641	0.7	238.2	43.2	354.8	25.5	105.1	36
GR30																		
E1	152	76	w	200	F1	-6.015	1.039	1.055	1.096	1.097	0.17	-0	124.7	38.3	7.3	30.2	251.2	37
F1	152	76	w	200	F1	-4.3342	1.03	1.074	1.106	1.109	0.419	-0	115.2	38.5	16.1	11.3	272.7	49.2
G1	152	76	w	200	F1	-7.9688	1.035	1.031	1.067	1.067	-0.063	0.1	69	46.5	166.8	7.4	263.6	42.6
GR23																		
A2	151	63	w	200	F1	-4.271	1.062	1.089	1.157	1.158	0.172	-0	339.7	14.1	248.5	4.7	140.4	75.1
A3	151	63	w	200	F1	-5.1909	1.048	1.092	1.144	1.146	0.303	-0	337.4	10.8	72.4	24.7	225.6	62.7
B2	151	63	w	200	F1	-6.479	1.04	1.123	1.168	1.175	0.493	-0	32.6	35.4	131.5	12.2	237.5	51.9
B3	151	63	w	200	F1	-7.0558	1.1	1.014	1.116	1.127	-0.745	0.8	321.3	36.9	224.4	9.1	122.7	51.6
C2	151	63	w	200	F1	-5.9831	1.129	1.037	1.171	1.179	-0.536	0.6	248.5	40.6	355.4	18.8	104.2	43.5
C3	151	63	w	200	F1	-5.3147	1.024	1.053	1.078	1.08	0.373	-0	180.7	0.1	271	75.3	90.7	14.7
D1	151	63	w	200	F1	-5.5204	1.052	1.084	1.14	1.142	0.234	-0	321.6	15.4	55.5	13.8	185.4	69
GR32																		
A1	78	30	s	200	F1	-10.142	1.07	1.063	1.137	1.137	-0.052	0.1	226.2	13.9	121.5	45.7	328.6	41
A2	78	30	s	200	F1	-3.7388	1.108	1.153	1.278	1.279	0.163	-0	101	28.4	206	25.6	330.8	50.1
E1	78	30	s	200	F1	-6.8098	1.08	1.132	1.222	1.225	0.238	-0	246.4	14.6	141.4	44.9	349.7	41.4
E2	78	30	s	200	F1	-13.997	1.017	1.038	1.056	1.057	0.367	-0	232.8	17.2	128.9	37.8	342.3	47.1
B1	78	30	s	200	F1	-8.0575	1.118	1.038	1.16	1.167	-0.493	0.5	254.3	10.5	138.8	66.7	348.3	20.5
C1	78	30	s	200	F1	-8.1971	1.029	1.023	1.053	1.053	-0.114	0.1	132	31	291.6	57.3	36.4	9.3
D1	78	30	s	200	F1	-10.047	1.039	1.047	1.088	1.088	0.088	-0	204	41.6	85.1	28.5	332.6	35.1
GR24																		
A1	174	32	w	200	F1	-1.9532	1.368	1.088	1.488	1.52	-0.575	0.6	329.3	13.5	229.7	34.8	77.1	51.9
A2	174	32	w	200	F1	-2.188	1.207	1.387	1.674	1.685	0.271	-0	347.8	10.7	248.4	40.9	89.6	47.1
A3	174	32	w	200	F1	-2.0238	1.315	1.199	1.576	1.581	-0.204	0.3	328.2	17.2	227.7	30.6	83.3	54
B2	174	32	w	200	F1	-4.2142	1.143	1.097	1.254	1.255	-0.185	0.2	316.7	8.4	221.2	33	59.2	55.7
C1	174	32	w	200	F1	-6.1278	1.044	1.1	1.148	1.152	0.377	-0	321.6	14.5	164.2	74.4	53.1	5.7

Name	S0 Strike	Dip		Field	Freq.	Km	L	F	P	Pj	T	U	K1dec	K1inc	K2dec	K2inc	K3dec	K3inc
C2	174	32	w	200	F1	-6.0642	1.086	1.075	1.168	1.168	-0.067	0.1	310.3	33.4	184	41.9	62.7	30
D1	174	32	w	200	F1	-4.1624	1.162	1.076	1.25	1.256	-0.346	0.4	310.8	30.9	207.7	20.7	89.4	51.4
D2	174	32	w	200	F1	-0.8835	1.542	2.278	3.513	3.584	0.311	-0	355.6	14.1	261.3	16.5	124.2	68
B1	174	32	w	200	F1	-4.8539	1.134	1.032	1.17	1.181	-0.601	0.6	291.9	39.8	182.4	21.8	71.2	42.3
Norwegian																		
BGR21																		
A2	160	42	W	200	F1	-3.141	2.575	2.182	5.62	5.635	-0.096	0.5	54.1	33.5	236.1	56.5	144.7	0.9
A4	160	42	W	200	F1	-7.4059	1.617	2.424	3.919	3.998	0.297	0	238.7	27.8	113.7	47.4	346	29.4
A5	160	42	W	200	F1	-5.2975	1.099	3.033	3.332	3.815	0.843	-1	219	17	112	43.8	324.6	41.3
A6	160	42	W	200	F1	-4.8537	1.764	2.341	4.13	4.169	0.2	0.1	110.3	47.8	229.9	24.1	336.2	32.2
B1	160	42	W	200	F1	-2.795	2.72	5.333	14.503	14.92	0.252	0.4	95.6	57.6	349.2	10.2	253.1	30.4
B2	160	42	W	200	F1	-3.5246	2.163	2.355	5.095	5.099	0.052	0.3	11.4	0.5	103.2	73.6	281.3	16.4
B3	160	42	W	200	F1	-10.275	1.319	1.317	1.736	1.736	-0.003	0.1	265.1	48.2	66.7	40.3	164.7	9.2
B4	160	42	W	200	F1	-7.6211	1.749	1.847	3.23	3.231	0.046	0.2	41.4	29.6	211.6	60.1	309	4.3
B6	160	42	W	200	F1	-4.2855	2.984	1.208	3.605	3.993	-0.705	0.8	242.3	17.9	147	16	17.7	65.6
C1	160	42	W	200	F1	-8.719	1.151	1.453	1.671	1.701	0.454	-0	323.5	72.7	198.3	10.2	105.7	13.8
C2	160	42	W	200	F1	-4.9187	1.934	2.879	5.569	5.655	0.232	0.2	30	37.2	232.8	50.6	128.7	11.3
C3	160	42	W	200	F1	-8.9355	1.355	1.276	1.729	1.731	-0.11	0.2	18.2	58.5	215	30.3	120.6	7.5
C4	160	42	W	200	F1	-8.8588	1.733	1.117	1.935	2.028	-0.665	0.8	61.9	46.9	235.4	42.9	328.4	3.2
C5	160	42	W	200	F1	-13.176	1.24	1.211	1.501	1.502	-0.06	0.2	256	24.2	125.5	55.4	357.1	23.2
GR35																		
A1	170	69	W	200	F1	-6.4698	1.033	1.102	1.139	1.145	0.494	-0	175.2	29.1	317	54.7	74.7	18.2
A2	170	69	W	200	F1	-7.9459	1.054	1.01	1.065	1.07	-0.671	0.7	71.8	45.1	173.3	11.2	273.8	42.8
C2	170	69	W	200	F1	-3.8078	1.165	1.282	1.494	1.5	0.238	-0	117	22.1	10.7	34.6	232.9	47
D1	170	69	W	200	F1	-3.7831	1.097	1.158	1.271	1.273	0.228	-0	60.6	36.9	157.3	8.8	258.6	51.7
F2	170	69	W	200	F1	-3.4454	1.143	1.099	1.255	1.257	-0.172	0.2	103.6	64.6	332.8	17.2	237.1	18.1
F3	170	69	W	200	F1	-5.1107	1.096	1.123	1.231	1.231	0.116	-0	40.4	69.1	306.3	1.6	215.7	20.8
G1	170	69	W	200	F1	-1.5992	1.252	1.335	1.672	1.674	0.125	0	112.6	41.4	280.9	48	17.4	5.9
G2	170	69	W	200	F1	-4.2217	1.156	1.042	1.204	1.215	-0.557	0.6	286.2	52.1	89.2	36.7	185.4	8.3
B2	170	69	W	200	F1	-3.6585	1.083	1.003	1.087	1.099	-0.922	0.9	240.9	22.4	348.6	36.4	126.5	45.2
B1	170	69	W	200	F1	-2.8137	1.11	1.442	1.6	1.639	0.557	-0	88.4	29.8	326.9	42.4	200.3	33.1

Name	S0 Strike	Dip		Field	Freq.	Km	L	F	P	Pj	T	U	K1dec	K1inc	K2dec	K2inc	K3dec	K3inc
E1	170	69	W	200	F1	-5.0229	1.07	1.132	1.21	1.214	0.295	-0	92.8	67.4	353.4	3.9	261.8	22.2
E2	170	69	W	200	F1	-6.5562	1.057	1.053	1.113	1.113	-0.041	0.1	101.5	54.4	252	31.9	351	14.1
F1	170	69	W	200	F1	-2.8545	1.129	1.155	1.305	1.305	0.087	-0	84.5	72.2	334.8	6.2	243	16.6
GR39																		
A1	170	61	W	200	F1	-3.5117	1.108	1.192	1.32	1.325	0.263	-0	351.4	33.6	147.4	54	253.6	11.5
B2	170	61	W	200	F1	-1.6753	1.228	1.412	1.734	1.744	0.253	-0	183.8	46	9	43.8	276.5	2.6
B1	170	61	W	200	F1	-1.0802	1.524	1.816	2.767	2.781	0.172	0.1	167.5	44.1	335.1	45.3	71.4	6.2
A2	170	61	W	200	F1	-1.9145	1.092	1.546	1.687	1.751	0.665	-1	236.1	25.8	334.9	17.7	95.6	57.9
C1	170	61	W	200	F1	-1.3295	1.218	1.383	1.685	1.694	0.243	-0	181.2	26.7	293.7	37.2	65.2	41.1
C3	170	61	W	200	F1	-1.1622	1.834	1.313	2.408	2.459	-0.38	0.6	169.7	9.4	263	18.9	54.5	68.8
D2	170	61	W	200	F1	-1.7706	1.16	1.403	1.628	1.648	0.39	-0	157.7	12.8	327.1	77	67.2	2.3
F1	170	61	W	200	F1	-0.2824	2.639	4.435	11.703	11.92	0.211	0.4	310.5	30.7	149.4	57.8	45.6	8.5
E1	170	61	W	200	F1	-11.585	1.02	1.045	1.065	1.067	0.387	-0	329.1	21.6	207.2	53.1	71.4	28.3
E2	170	61	W	200	F1	-1.8679	1.424	1.205	1.717	1.731	-0.309	0.4	236.6	28.6	346.1	31.5	113.8	44.8
GR36																		
G2	164	49	w	200	F1	-4.4974	1.055	1.188	1.254	1.267	0.525	-0	182.9	51.7	310.8	25.9	54.6	26.1
GR5																		
A1	118	42	w	200	F1	-2.8111	1.128	1.767	1.993	2.089	0.652	-1	267	37.3	117	48.7	9	15.2
B1	118	42	w	200	F1	-5.1369	1.164	1.11	1.291	1.293	-0.186	0.2	150	55.3	250.8	7.4	345.7	33.7
C2	118	42	w	200	F1	-4.7523	1.359	1.149	1.562	1.578	-0.376	0.5	247.8	37.8	127.9	32.7	11	35.3
A2	118	42	w	200	F1	-3.6284	1.101	1.181	1.3	1.304	0.268	-0	248.3	45.4	130.4	24.8	22	34.3
GR37																		
A1	180	58	w	200	F1	-5.8169	1.049	1.074	1.127	1.128	0.192	-0	149	27.9	277.4	49.5	43.5	26.7
A2	180	58	w	200	F1	-6.7004	1.064	1.057	1.124	1.125	-0.051	0.1	334.9	14.2	232.2	41.1	79.7	45.4
B1	180	58	w	200	F1	-9.2139	1.087	1.01	1.098	1.108	-0.789	0.8	339	49.8	183.2	37.6	83.7	12.1
B2	180	58	w	200	F1	-7.365	1.046	1.012	1.059	1.062	-0.577	0.6	287.9	50.6	172.4	19.5	69.2	32.7
B3	180	58	w	200	F1	-6.5444	1.053	1.027	1.081	1.083	-0.329	0.3	155.5	28.9	308.7	58.2	58.8	12
C1	180	58	w	200	F1	-8.0451	1.043	1.04	1.085	1.085	-0.029	0.1	145.8	3.7	248.3	73.5	54.8	16
C2	180	58	w	200	F1	-7.8888	1.071	1.032	1.104	1.107	-0.372	0.4	333.9	6.4	124.8	82.7	243.5	3.5
D2	180	58	w	200	F1	-5.4113	1.049	1.011	1.061	1.065	-0.616	0.6	336.7	20.1	189.6	66.5	71.1	11.7
D3	180	58	w	200	F1	-7.2651	1.03	1.045	1.076	1.077	0.2	-0	344.2	29.3	153.8	60.3	251.7	4.5
E1	180	58	w	200	F1	-5.4548	1.04	1.034	1.076	1.076	-0.078	0.1	173	55.7	326.3	31.4	64	12.5

Name	S0 Strike	Dip		Field	Freq.	Km	L	F	P	Pj	T	U	K1dec	K1inc	K2dec	K2inc	K3dec	K3inc
French																		
C2	160	30	w	200	F1	-5.8099	1.103	1.089	1.2	1.201	-0.069	0.1	35.7	88.6	147.4	0.5	237.4	1.3
GR13																		
A1	10	30	w	200	F1	-23.366	1.026	1.025	1.052	1.052	-0.002	0	149.5	20	304.8	68.1	56.4	8.4
B2	10	30	w	200	F1	-9.2932	1.125	1.05	1.181	1.187	-0.415	0.4	144.6	16.3	241.9	23.6	23.2	60.7
C1	10	30	w	200	F1	-6.439	1.088	1.049	1.142	1.144	-0.274	0.3	341.5	62.2	138.4	25.9	233	9.5
B1	10	30	w	200	F1	-8.8603	1.024	1.13	1.157	1.169	0.672	-1	324.2	13.1	209.5	61	60.5	25.4
A2	10	30	w	200	F1	-7.0939	1.098	1.094	1.202	1.202	-0.02	0.1	196.1	22.2	291.9	14	51.8	63.4
D1	10	30	w	200	F1	-7.9779	1.074	1.026	1.102	1.106	-0.47	0.5	153.7	45	3.2	41	259.5	15.2
D2	10	30	w	200	F1	-9.1079	1.079	1.038	1.12	1.123	-0.346	0.4	43.3	71.6	153.7	6.6	245.7	17.1
E1	10	30	w	200	F1	-8.8692	1.013	1.027	1.04	1.041	0.334	-0	164.1	21.7	58.6	33.8	280.4	48.1
UC2	10	30	w	200	F1	-9.3868	1.053	1.06	1.117	1.117	0.058	-0	358.6	34.6	119.3	36.5	240.1	34.7
HOME																		
BGR16																		
A1	162	55	w	200	F1	-15.56	1.008	1.202	1.212	1.242	0.915	-1	43.8	8.6	304.1	47.8	141.3	40.9
A2	162	55	w	200	F1	-20.296	1.06	1.124	1.191	1.195	0.337	-0	276.5	64.8	56.2	19.8	151.8	15.1
A3	162	55	w	200	F1	-14.841	1.142	1.208	1.38	1.382	0.175	-0	337.1	30.3	173	58.7	71.2	7.1
B1	162	55	w	200	F1	-16.021	1.108	1.183	1.311	1.314	0.242	-0	60.3	9.5	162	50.4	322.7	37.9
B2	162	55	w	200	F1	-19.272	1.189	1.215	1.445	1.445	0.06	0	19.2	62.8	272.1	8.6	177.9	25.6
B3	162	55	w	200	F1	-22.796	1.069	1.144	1.223	1.228	0.338	-0	56.4	2.7	324.1	40.7	149.6	49.2
C2	162	55	w	200	F1	-17.949	1.059	1.162	1.23	1.239	0.444	-0	38.2	10.3	147.6	61.2	303	26.5
BGR10																		
A1	149	40	w	200	F1	-30.173	1.162	1.026	1.192	1.209	-0.71	0.7	9.1	64.6	186.9	25.3	277.3	0.9
A2	149	40	w	200	F1	-32.761	1.079	1.098	1.184	1.185	0.101	-0	106.6	53	240.4	27.6	343	22.6
A3	149	40	w	200	F1	-32.646	1.047	1.069	1.12	1.12	0.188	-0	24.9	20.6	159	61.6	287.6	18.6
A4	149	40	w	200	F1	-31.132	1.102	1.061	1.17	1.172	-0.241	0.3	211.2	25.4	3.6	61.8	115.7	11.4
A5	149	40	w	200	F1	-33.487	1.084	1.026	1.111	1.116	-0.522	0.5	37	32.7	241.8	54.8	134.6	11.8
B1	149	40	w	200	F1	-34.023	1.025	1.058	1.084	1.087	0.398	-0	213.3	3.8	305.5	30.8	116.9	58.9
B2	149	40	w	200	F1	-30.117	1.106	1.05	1.161	1.165	-0.348	0.4	108.2	58.5	203.9	3.5	296	31.3
C1	149	40	w	200	F1	-30.68	1.056	1.111	1.174	1.177	0.32	-0	25.2	30.6	289.4	9.7	183.7	57.6
C2	149	40	w	200	F1	-31.449	1.069	1.057	1.13	1.131	-0.094	0.1	27.6	26.9	193.5	62.4	294.7	5.8

Name	S0 Strike	Dip		Field	Freq.	Km	L	F	P	Pj	T	U	K1dec	K1inc	K2dec	K2inc	K3dec	K3inc
C3	149	40	w	200	F1	-32.797	1.028	1.062	1.092	1.094	0.366	-0	207.6	8.4	316.1	65	114	23.4
D1	149	40	w	200	F1	-29.528	1.101	1.043	1.148	1.152	-0.396	0.4	52.6	3.5	145.9	43.1	319	46.7
D2	149	40	w	200	F1	-33.649	1.06	1.055	1.118	1.118	-0.045	0.1	20.4	10.6	160.4	76.3	288.8	8.6
D3	149	40	w	200	F1	-34.01	1.101	1.062	1.169	1.17	-0.231	0.3	74.8	5.4	169	37.4	337.9	52.1
D4	149	40	w	200	F1	-31.743	1.046	1.12	1.171	1.177	0.43	-0	93.6	48.2	192.2	7.6	288.8	40.8
BGR11																		
A1	151	32	w	200	F1	-33.492	1.112	1.081	1.202	1.203	-0.156	0.2	53.3	57.2	189.8	25	289.4	19.7
A2	151	32	w	200	F1	-36.301	1.103	1.133	1.25	1.25	0.117	-0	210.6	11.4	114.1	29.5	319.3	57.9
A3	151	32	w	200	F1	-26.944	1.085	1.108	1.203	1.203	0.113	-0	45.2	19.1	139.8	13.1	262.3	66.6
A4	151	32	w	200	F1	-35.92	1.076	1.061	1.142	1.142	-0.101	0.1	107.6	43.8	205.8	8.4	304.3	45
A5	151	32	w	200	F1	-33.015	1.08	1.073	1.159	1.159	-0.047	0.1	72.2	27.4	250.8	62.6	341.9	0.6
B1	151	32	w	200	F1	-34.827	1.062	1.092	1.159	1.16	0.188	-0	194.1	27.4	308.8	38.8	79.3	38.9
B2	151	32	w	200	F1	-32.844	1.044	1.101	1.15	1.153	0.381	-0	20.1	6.4	120.6	58.5	286.3	30.7
C1	151	32	w	200	F1	-31.507	1.105	1.109	1.225	1.225	0.018	0	71.2	21.1	169.3	20	298.8	60.2
C2	151	32	w	200	F1	-38.044	1.043	1.076	1.122	1.124	0.265	-0	27.8	0.2	297.2	73.7	117.8	16.3
E1	151	32	w	200	F1	-32.422	1.199	1.09	1.306	1.313	-0.357	0.4	33.7	16.6	291.8	34.5	145	50.6
E2	151	32	w	200	F1	-32.552	1.035	1.138	1.178	1.188	0.58	-1	52.9	11.9	170.7	65.7	318.3	20.9
F1	151	32	w	200	F1	-30.849	1.059	1.085	1.149	1.15	0.177	-0	55.6	28.1	230	61.8	324.3	2.4
F2	151	32	w	200	F1	-37.548	1.044	1.023	1.067	1.069	-0.308	0.3	73.2	38.1	202.6	39	318.3	28.2
BGR12																		
A2	169	30	w	200	F1	-22.715	1.094	1.158	1.267	1.27	0.239	-0	260	11.7	12.1	61.1	164.2	26
A3	169	30	w	200	F1	-28.29	1.138	1.103	1.255	1.256	-0.137	0.2	53.2	21.7	288	55.4	154.1	25.6
A4	169	30	w	200	F1	-26.101	1.113	1.146	1.275	1.276	0.123	-0	87.2	9.3	319	75.1	179.1	11.5
A5	169	30	w	200	F1	-27.603	1.108	1.083	1.199	1.2	-0.126	0.2	94.8	26.7	205	34.4	336	43.8
B2	169	30	w	200	F1	-19.722	1.336	1.141	1.523	1.538	-0.375	0.5	103.6	13	206.5	44.1	1.2	43
B3	169	30	w	200	F1	-26.87	1.13	1.179	1.332	1.333	0.148	-0	51.2	60.1	214.4	28.9	308.4	7.2
B4	169	30	w	200	F1	-27.789	1.111	1.186	1.317	1.32	0.237	-0	98.6	1	191.3	70.2	8.3	19.7
B5	169	30	w	200	F1	-22.415	1.08	1.132	1.222	1.225	0.233	-0	214	20.7	71.4	64.6	309.4	14.1
C2	169	30	w	200	F1	-17.385	1.294	1.194	1.545	1.549	-0.184	0.3	43.4	79.3	282.9	5.5	192	9.1
BGR13																		
B	178	50	w	200	F1	-3.261	1.375	2.194	3.016	3.115	0.423	-0	130.6	72.3	6.3	10.2	273.7	14.3

Name	S0 Strike	Dip		Field	Freq.	Km	L	F	P	Pj	T	U	K1dec	K1inc	K2dec	K2inc	K3dec	K3inc
GR6																		
A3	8	32	w	200	F1	-0.8817	1.906	5.06	9.644	10.33	0.431	0.1	334	44.6	134.9	43.7	234.3	9.7
B3	8	32	w	200	F1	-1.2759	1.407	1.399	1.969	1.969	-0.008	0.2	153.6	51.7	340.5	38.1	247.9	3.3
D2	8	32	w	200	F1	-1.3129	1.21	1.383	1.674	1.684	0.259	-0	123.5	9.7	16.1	60.3	218.7	27.8
E2	8	32	w	200	F1	-1.9694	1.386	1.164	1.614	1.631	-0.365	0.5	147.5	28	315.4	61.5	54.8	5.1
E3	8	32	w	200	F1	-1.4851	1.365	1.103	1.505	1.533	-0.522	0.6	152.4	15.8	313.2	73.3	60.9	5.2
G2	8	32	w	200	F1	-2.3812	1.14	1.125	1.282	1.282	-0.055	0.1	333.5	12.3	98.2	69	239.7	16.7
H1	8	32	w	200	F1	-1.1846	1.227	1.24	1.522	1.522	0.025	0.1	336.7	9.7	96.5	71	243.9	16.2
H2	8	32	w	200	F1	-0.3971	2.633	1.431	3.768	3.945	-0.46	0.7	315.6	35.7	160	51.7	54.4	12
GR8																		
A1	140	40	w	200	F1	-6.6637	1.039	1.031	1.072	1.072	-0.11	0.1	289.5	32.7	130.2	55.5	25.8	9.7
B1	140	40	w	200	F1	-6.7471	1.049	1.016	1.066	1.068	-0.493	0.5	113.7	5.2	240.3	81.3	23.1	6.9
C1	140	40	w	200	F1	-6.0908	1.08	1.026	1.109	1.113	-0.496	0.5	286.8	41.4	97.8	48.3	192.8	4.5
D1	140	40	w	200	F1	-6.933	1.033	1.054	1.088	1.089	0.241	-0	185.5	40.2	73.3	24.1	321.1	40.2
F1	140	40	w	200	F1	-6.7721	1.133	1.048	1.187	1.194	-0.455	0.5	138.4	39.1	276.7	42.6	28.9	22.3
G1	140	40	w	200	F1	-6.8483	1.074	1.04	1.116	1.118	-0.29	0.3	277.6	41.3	146.5	36.8	34.2	26.9
DIVERSION																		
BGR8																		
A1	161	31	w	200	F1	-20.146	1.181	1.177	1.389	1.389	-0.01	0.1	76.3	47.6	218.4	35.8	323.4	19.6
A2	161	31	w	200	F1	-24.101	1.039	1.171	1.216	1.231	0.609	-1	230.6	34	113.5	34	352.1	37.7
A3	161	31	w	200	F1	-16.294	1.2	1.299	1.559	1.563	0.177	-0	44.1	15.1	229.8	74.8	134.5	1.5
B2	161	31	w	200	F1	-30.776	1.164	1.068	1.244	1.251	-0.393	0.4	222.3	55.5	29.7	33.9	123.7	5.9
B3	161	31	w	200	F1	-26.969	1.142	1.046	1.195	1.203	-0.495	0.5	186.6	62.2	42	23.3	305.7	14.4
C1	161	31	w	200	F1	-19.171	1.109	1.241	1.377	1.386	0.352	-0	72.3	14.3	323.9	51.1	172.7	35.2
C2	161	31	w	200	F1	-25.915	1.185	1.066	1.263	1.273	-0.456	0.5	233.4	28.3	113.6	42.7	344.8	34.2
C3	161	31	w	200	F1	-21.655	1.262	1.096	1.383	1.397	-0.433	0.5	98.6	1.2	6.1	63.9	189.2	26
D1	161	31	w	200	F1	-18.277	1.05	1.203	1.264	1.28	0.581	-1	48.3	10.1	181.6	75.5	316.5	10.4
D2	161	31	w	200	F1	-25.423	1.117	1.13	1.262	1.262	0.05	0	213.1	8.3	113.6	48.7	310.1	40.1
D3	161	31	w	200	F1	-18.536	1.189	1.056	1.256	1.269	-0.524	0.6	215.4	32.7	306.1	1.2	37.9	57.2
E1	161	31	w	200	F1	-22.974	1.174	1.089	1.278	1.283	-0.304	0.4	260.4	55.6	25.1	21.3	125.9	25.7
E2	161	31	w	200	F1	-21.746	1.172	1.178	1.38	1.38	0.016	0.1	150.3	12.5	251.3	40.6	46.6	46.7
E3	161	31	w	200	F1	-16.248	1.052	1.378	1.45	1.496	0.728	-1	188	16.8	322.8	66.8	93.2	15.5

Name	S0 Strike	Dip		Field	Freq.	Km	L	F	P	Pj	T	U	K1dec	K1inc	K2dec	K2inc	K3dec	K3inc
BGR7																		
A1	159	28	w	200	F1	-30.516	1.005	1.074	1.079	1.089	0.881	-1	215.3	8	315	50.1	118.8	38.8
A2	159	28	w	200	F1	-33.682	1.034	1.029	1.064	1.064	-0.085	0.1	239	22.3	145.6	8.2	36.7	66.1
A3	159	28	w	200	F1	-28.65	1.061	1.056	1.12	1.12	-0.044	0.1	208.4	11.2	111.9	29.8	316.7	57.7
B1	159	28	w	200	F1	-27.86	1.098	1.066	1.17	1.171	-0.19	0.2	256.5	3.5	150.5	77.4	347.2	12.1
B2	159	28	w	200	F1	-27.18	1.002	1.125	1.127	1.147	0.965	-1	206.2	20.2	109.8	16.7	343.2	63.3
C1	159	28	w	200	F1	-21.827	1.102	1.138	1.254	1.255	0.141	-0	256.2	55.4	56.9	33	152.8	9
C2	159	28	w	200	F1	-29.922	1.018	1.136	1.157	1.172	0.754	-1	9.8	39.7	100.4	0.8	191.4	50.3
D2	159	28	w	200	F1	-33.667	1.012	1.023	1.035	1.036	0.305	-0	235.7	64.5	335.8	4.8	68	25
D1	159	28	w	200	F1	-28.232	1.075	1.09	1.171	1.172	0.084	-0	52.2	59.4	271	24.7	173	16.8
D3	159	28	w	200	F1	-30.804	1.13	1.085	1.226	1.227	-0.202	0.3	251	9.8	344.6	20	136.3	67.5
D4	159	28	w	200	F1	-22.664	1.048	1.189	1.246	1.26	0.577	-1	225.1	11.7	329.1	49.6	125.8	38
GR3																		
A1	168	29	w	200	F1	-0.91	1.505	1.372	2.064	2.068	-0.128	0.3	325.5	9.8	215.6	63.1	60	24.8
C1	168	29	w	200	F1	-1.1702	1.271	1.299	1.65	1.65	0.043	0.1	8.2	17.5	115	42.6	261.6	42.3
G1	168	29	w	200	F1	-4.6984	1.107	1.066	1.181	1.182	-0.226	0.3	206.7	26.9	305.6	17	64.3	57.4
BGR4																		
A1	179	22	w	200	F1	-6.0512	1.23	1.473	1.812	1.828	0.304	-0	232.3	19.6	134.3	21.4	1	60.3
A2	179	22	w	200	F1	-34.861	1.027	1.114	1.144	1.153	0.61	-1	59	2.1	207.5	87.6	328.9	1.3
A3	179	22	w	200	F1	-29.905	1.04	1.095	1.139	1.143	0.401	-0	106.7	61.3	260.5	26.2	356	11
A4	179	22	w	200	F1	-15.742	1.093	1.106	1.209	1.209	0.062	-0	71.5	21.3	213.6	63.7	335.6	14.7
B1	179	22	w	200	F1	-7.5772	1.292	1.907	2.464	2.533	0.431	-0	174.3	59.8	287	12.6	23.5	26.9
B2	179	22	w	200	F1	-28.293	1.06	1.176	1.247	1.257	0.471	-0	234.1	2.5	119.3	84	324.3	5.5
B3	179	22	w	200	F1	-19.543	1.131	1.109	1.255	1.256	-0.086	0.1	273.7	60.4	76.5	28.5	170.5	7.4
B4	179	22	w	200	F1	-29.958	1.136	1.071	1.217	1.22	-0.299	0.3	126.1	13.3	226.4	37	19.7	49.9
C1	179	22	w	200	F1	-7.1051	1.379	1.216	1.677	1.686	-0.243	0.4	61.3	17.7	175.3	51.8	319.5	32.6
C2	179	22	w	200	F1	-16.501	1.211	1.183	1.433	1.433	-0.067	0.2	355	35.7	91.8	9.3	194.2	52.8
C3	179	22	w	200	F1	-18.758	1.143	1.054	1.204	1.211	-0.435	0.5	296.7	43.9	32.3	5.8	128.3	45.5
C4	179	22	w	200	F1	-7.0488	1.263	6.414	8.098	9.899	0.777	-1	6.1	77.4	215	11.1	123.8	5.9

Paramagnetic Specimens

Name	S0 Strike	Dip		Km	L	F	P	Pj	T	U	K1dec	K1inc	K2dec	K2inc	K3dec	K3inc
Beaver																
Gr15																
A1	152	76	w	27.0235	1.029	1.027	1.057	1.057	-0.043	-0.057	159	27.8	289.6	51	54.8	25
A2	152	76	w	25.09421	1.023	1.017	1.04	1.041	-0.149	-0.158	319.2	17.4	133.5	72.5	228.7	1.6
A3	152	76	w	19.94429	1.027	1.019	1.046	1.046	-0.181	-0.191	350	52.3	258.8	0.9	168.1	37.7
B1	152	76	w	27.28132	1.014	1.024	1.039	1.039	0.271	0.262	298.8	27.8	160.3	54.8	39.7	19.8
B2	152	76	w	25.58964	1.026	1.022	1.048	1.048	-0.078	-0.089	318.9	25.9	114.8	61.9	224	9.9
C1	152	76	w	25.05021	1.017	1.031	1.048	1.049	0.294	0.283	303.6	19.3	169.3	63.4	40	17.6
C2	152	76	w	25.20156	1.01	1.026	1.037	1.038	0.438	0.43	334.8	21.2	134.3	67.5	242	7.2
D1	152	76	w	24.83472	1.005	1.03	1.035	1.038	0.699	0.694	152.8	10.7	285.5	74.4	60.7	11.2
D2	152	76	w	25.77155	1.029	1.037	1.067	1.067	0.119	0.103	319.4	28.8	174.2	56.2	58.6	16.1
E1	152	76	w	35.38729	1.026	1.004	1.031	1.033	-0.71	-0.714	164.1	12.4	259.2	21.9	46.8	64.5
E2	152	76	w	24.21304	1.032	1.016	1.048	1.049	-0.339	-0.349	137.1	74.7	321.2	15.2	230.9	1
F1	152	76	w	26.85324	1.008	1.017	1.026	1.026	0.347	0.342	131.3	47.8	329.7	40.7	231.7	9.2
F2	152	76	w	26.98228	1.012	1.017	1.029	1.029	0.192	0.185	113.5	35.6	316.9	52	211.9	11.5
G1	152	76	w	25.5937	1.014	1.033	1.047	1.048	0.4	0.391	279.5	60.5	133.9	25	36.9	14.6
YG2	152	76	w	24.98294	1.032	1.017	1.049	1.05	-0.303	-0.314	309.7	15.3	159.2	72.5	42	8.2
GR17																
A1	151	87	w	34.58023	1.01	1.039	1.049	1.052	0.583	0.575	137.2	45.7	45.4	1.8	313.7	44.2
B1	151	87	w	23.78009	1.029	1.013	1.042	1.043	-0.395	-0.403	132.3	18.7	226.1	11.1	345.2	68
B2	151	87	w	22.67202	1.021	1.016	1.037	1.038	-0.116	-0.125	125.6	34.4	234.3	25.1	352.3	45.1
C1	151	87	w	25.87175	1.038	1.03	1.069	1.069	-0.119	-0.136	153.2	7.7	59.2	27	257.8	61.7
C2	151	87	w	25.23347	1.005	1.025	1.029	1.032	0.676	0.672	335.1	29.7	113.8	52.8	233	20.3
C3	151	87	w	15.19946	1.013	1.07	1.084	1.09	0.671	0.66	109.3	23.9	2.6	32.9	228	47.4
E1	151	87	w	22.11077	1.01	1.053	1.064	1.069	0.666	0.658	174.6	51.5	83.4	1	352.6	38.4
F1	151	87	w	26.62074	1.027	1.054	1.082	1.084	0.328	0.311	154	38.4	36.5	30.2	280.6	36.9
G1	151	87	w	22.56576	1.034	1.044	1.079	1.079	0.132	0.113	113.9	23.8	216.4	26.1	347.6	53.3
GR18																
A1	160	70	w	5.340343	1.086	1.037	1.126	1.129	-0.392	-0.417	140.9	27.7	267.7	48.8	34.8	27.9
D2	160	70	w	3.303989	1.065	1.184	1.261	1.271	0.457	0.41	3.3	42.2	150.2	42.7	256.9	17.3

Name	S0 Strike	Dip		Km	L	F	P	Pj	T	U	K1dec	K1inc	K2dec	K2inc	K3dec	K3inc
GR30																
B1	152	76	w	22.69306	1.053	1.027	1.082	1.083	-0.311	-0.329	115	55.4	17.6	5	284.2	34.2
C1	152	76	w	21.93323	1.044	1.019	1.064	1.066	-0.398	-0.411	119.2	39.4	8.9	23	256.5	41.9
C2	152	76	w	11.21284	1.058	1.036	1.097	1.098	-0.226	-0.248	121.7	37.8	26.2	7	287.5	51.3
Norwegian																
GR38																
A1	155	45	W	9.773486	1.033	1.074	1.109	1.112	0.376	0.354	274.3	53	161	16.6	60.3	32
A2	155	45	W	1.574236	1.285	1.224	1.573	1.574	-0.107	-0.217	299.7	16.5	202.8	22.1	63.3	61.9
C2	155	45	W	8.588888	1.071	1.026	1.099	1.103	-0.449	-0.467	308	25	190.5	44.8	56.9	34.7
D2	155	45	W	3.38708	1.091	1.073	1.17	1.17	-0.105	-0.144	332.4	21.9	68.5	14.7	189.7	63.1
F2	155	45	W	2.804508	1.057	1.25	1.322	1.344	0.6	0.554	188.9	36.9	339.2	49.2	87.3	15
G2	155	45	W	8.100996	1.003	1.084	1.087	1.1	0.934	0.931	300.7	56.5	158.9	27.5	59.4	17.6
F1	155	45	W	11.24317	1.035	1.044	1.081	1.081	0.114	0.095	325.9	23.1	197.9	55.3	67.1	24.4
D1	155	45	W	11.0589	1.048	1.039	1.09	1.09	-0.098	-0.12	305.5	25.1	182.5	49.3	51	29.7
GR34																
A1	172	68	W	14.82494	1.044	1.063	1.11	1.11	0.173	0.148	191.5	43.5	333.8	39.8	81.4	19.9
A2	172	68	W	17.48373	1.067	1.017	1.085	1.09	-0.585	-0.598	193.6	34.3	347.6	52.9	94.8	12.6
B1	172	68	W	24.81837	1.027	1.033	1.06	1.06	0.099	0.084	199.3	45.1	351.6	41.5	94.6	14.2
B2	172	68	W	23.8173	1.028	1.078	1.108	1.112	0.455	0.435	196.7	41.4	6.5	48.1	102.2	5
B3	172	68	W	28.6166	1.08	1.047	1.13	1.132	-0.256	-0.284	201.5	33.4	357.7	54.3	103.9	11.3
C1	172	68	W	20.90604	1.045	1.06	1.108	1.108	0.136	0.11	192.1	65.2	3.1	24.5	94.7	3.4
C2	172	68	W	13.87076	1.043	1.041	1.086	1.086	-0.033	-0.053	201.8	43.1	33.5	46.3	297.4	5.9
D1	172	68	W	21.15257	1.019	1.106	1.128	1.138	0.683	0.667	205.5	44.4	354.5	41.2	99.1	16.1
E1	172	68	W	14.9415	1.006	1.062	1.068	1.076	0.815	0.809	200.5	28.3	6.4	61	107.3	6
D2	172	68	W	33.65097	1.039	1.059	1.1	1.101	0.204	0.181	208.1	55.1	7.8	33.2	104.1	9.6
BGR20																
A1	152	54	W	138.7782	1.038	1.023	1.061	1.062	-0.247	-0.261	283.4	68.5	56.7	15.1	150.8	14.9
A2	152	54	W	139.3174	1.02	1.029	1.049	1.05	0.188	0.176	256.6	60.2	46.7	26.4	143.2	12.8
B1	152	54	W	153.6234	1.042	1.038	1.082	1.082	-0.051	-0.071	251.4	72.9	81.7	16.8	350.8	2.9
C1	152	54	W	155.5052	1.026	1.045	1.073	1.074	0.257	0.24	235.6	18.4	96.7	66.2	330.6	14.6
C2	152	54	W	138.9965	1.009	1.055	1.064	1.07	0.724	0.717	230	12	112.7	65.2	324.8	21.4
C3	152	54	W	135.0794	1.012	1.019	1.032	1.032	0.228	0.22	232.3	29.5	77.5	58	328.8	11.3

Name	S0 Strike	Dip		Km	L	F	P	Pj	T	U	K1dec	K1inc	K2dec	K2inc	K3dec	K3inc
D1	152	54	W	105.6978	1.013	1.043	1.056	1.059	0.524	0.514	225.4	19.3	85.7	65.3	320.7	14.8
D2	152	54	W	138.0435	1.027	1.011	1.038	1.039	-0.418	-0.425	53.6	49.1	231.4	40.9	322.3	1.1
D3	152	54	W	140.1888	1.028	1.051	1.08	1.081	0.287	0.269	262.9	39.9	61.7	48.1	163.8	10.7
D4	152	54	W	145.1459	1.037	1.049	1.089	1.089	0.136	0.115	259.6	33.6	72.4	56.2	167.4	3.3
E1	152	54	W	157.7654	1.026	1.042	1.069	1.07	0.238	0.222	244.1	47.1	94	38.9	351.2	15.3
E2	152	54	W	138.6977	1.02	1.034	1.055	1.056	0.25	0.237	264.5	30.9	35.7	47.7	157.7	25.8
E3	152	54	W	150.856	1.022	1.026	1.048	1.048	0.081	0.069	312.7	68.1	71.7	11.1	165.5	18.7
GR36																
A1	164	49	w	18.23635	1.034	1.078	1.115	1.118	0.383	0.36	200.7	40.9	24.3	49	292.3	1.8
A2	164	49	w	17.44709	1.022	1.025	1.048	1.048	0.067	0.055	147	43.4	262.3	24.3	12	36.8
B1	164	49	w	20.1076	1.036	1.025	1.061	1.062	-0.18	-0.195	167.4	41.6	57.3	21.2	307.6	40.9
B2	164	49	w	15.29526	1.053	1.02	1.075	1.077	-0.444	-0.459	148.7	54.9	245.7	4.9	339.2	34.6
C1	164	49	w	19.20676	1.041	1.04	1.082	1.082	-0.011	-0.031	198.6	52.9	324.5	23.9	67.3	26.5
C2	164	49	w	12.70712	1.06	1.011	1.071	1.077	-0.689	-0.698	167.7	51.2	54	17.9	311.8	33.1
D1	164	49	w	17.42018	1.051	1.028	1.081	1.082	-0.281	-0.299	199.9	40.6	320.3	30.6	74.1	34.3
D2	164	49	w	22.33035	1.037	1.035	1.074	1.074	-0.029	-0.047	193.6	41.6	15	48.4	284.2	0.7
E1	164	49	w	17.61538	1.055	1.005	1.06	1.067	-0.841	-0.845	181.5	55.9	71.7	13	333.8	31
E2	164	49	w	12.39766	1.042	1.047	1.091	1.091	0.055	0.033	192.2	73	6.5	16.9	97	1.6
F1	164	49	w	21.22089	1.037	1.01	1.047	1.05	-0.579	-0.587	182.8	41.7	53.5	35.5	301.2	28.1
F2	164	49	w	18.14834	1.028	1.016	1.044	1.045	-0.274	-0.284	190	32.6	8	57.4	99.5	0.9
G1	164	49	w	21.63376	1.001	1.061	1.062	1.072	0.964	0.963	107.6	20.9	220.2	45.2	0.6	37.4
H1	164	49	w	17.02455	1.04	1.068	1.111	1.112	0.252	0.227	173	55.9	54.3	18	314.4	27.8
H2	164	49	w	11.87922	1.069	1.04	1.112	1.114	-0.259	-0.284	168.7	57.4	22.4	28	284.1	15.3
GR5																
1B2	118	42	w	2.50127	1.409	1.788	2.519	2.545	0.258	0.038	248.8	18.3	343.6	14.4	109.7	66.4
C1	118	42	w	6.885662	1.252	1.209	1.514	1.514	-0.085	-0.187	94.8	2.4	190.2	65.3	3.7	24.6
French																
GR33																
A1	160	30	w	6.461302	1.09	1.075	1.172	1.172	-0.09	-0.129	249.8	27.5	143.5	28.3	16	48.5
A2	160	30	w	5.94225	1.069	1.088	1.163	1.163	0.118	0.081	157	37.8	319.2	50.8	60.1	8.7
B1	160	30	w	8.318814	1.082	1.11	1.201	1.202	0.137	0.092	327.3	50.3	133.9	38.9	229.3	6.6
C1	160	30	w	6.979366	1.076	1.113	1.198	1.199	0.189	0.146	255.4	48.8	136.8	22.8	31.4	32.2

Name	S0 Strike	Dip		Km	L	F	P	Pj	T	U	K1dec	K1inc	K2dec	K2inc	K3dec	K3inc
D2	160	30	w	6.123326	1.104	1.024	1.13	1.139	-0.61	-0.629	277.5	20.5	100.6	69.5	7.9	1
E1	160	30	w	8.487027	1.079	1.036	1.118	1.121	-0.364	-0.388	215.2	17.2	111	38.4	324.3	46.5
E2	160	30	w	0.9720907	1.536	1.814	2.788	2.8	0.162	-0.089	51.1	84.6	178.6	3.3	268.9	4.3
GR11																
A1	40	35	w	5.000754	1.02	1.311	1.336	1.383	0.865	0.846	111.4	19	202.6	3.5	302.5	70.6
B1	40	35	w	7.209562	1.095	1.107	1.212	1.212	0.059	0.011	99.3	37.8	8	1.7	275.8	52.1
B2	40	35	w	8.064007	1.1	1.068	1.175	1.176	-0.179	-0.218	51.1	18.2	152.7	31.5	295.7	52.5
C1	40	35	w	6.945601	1.025	1.166	1.195	1.213	0.72	0.698	22.8	4	117.7	50.6	289.6	39.1
C2	40	35	w	7.463999	1.068	1.109	1.184	1.186	0.22	0.179	61.3	26.6	154.5	6.3	256.7	62.5
D1	40	35	w	7.277497	1.051	1.226	1.289	1.309	0.606	0.565	29	10	122.6	19.8	273.7	67.7
D2	40	35	w	7.797783	1.099	1.151	1.265	1.267	0.197	0.14	82.2	17.1	172.7	1.6	267.8	72.8
E1	40	35	w	6.251484	1.08	1.072	1.157	1.157	-0.051	-0.087	57.3	15.9	159.3	36.1	307.8	49.5
E2	40	35	w	6.887421	1.106	1.056	1.168	1.17	-0.3	-0.335	63	22	169.3	34.8	307.3	46.9
F2	40	35	w	9.606407	1.038	1.062	1.103	1.104	0.24	0.217	49.2	15.4	152.2	39.3	302.3	46.6
G1	40	35	w	9.026531	1.041	1.074	1.118	1.12	0.275	0.249	38.2	16	133.9	19.3	271.2	64.5
G2	40	35	w	7.335275	1.07	1.052	1.126	1.126	-0.142	-0.171	53.8	25.3	165.6	38.2	299.3	41.2
A1	40	35	w	6.192307	1.089	1.112	1.211	1.211	0.108	0.06	49.2	9.8	142.8	20.1	294.7	67.5
GR12																
A2	10	30	w	11.86828	1.028	1.095	1.125	1.131	0.537	0.516	133.8	29.3	23.8	31.3	257.2	44.5
B1	10	30	w	16.18107	1.036	1.092	1.131	1.136	0.43	0.405	133.3	40.8	17.9	26.4	265.3	37.8
B2	10	30	w	8.960353	1.034	1.104	1.141	1.147	0.495	0.47	145.4	27.7	30	39.2	259.9	38.3
B3	10	30	w	6.609751	1.033	1.134	1.171	1.182	0.586	0.559	137.2	37.8	19.8	30.7	263.1	37.1
C1	10	30	w	13.51572	1.034	1.121	1.16	1.168	0.548	0.522	133.1	47.4	11	26	264	31
C2	10	30	w	12.55015	1.036	1.105	1.145	1.15	0.476	0.45	137.6	35	21.1	32.5	261	38.2
D1	10	30	w	14.58508	1.024	1.106	1.133	1.141	0.621	0.601	139.2	38.1	20.5	31.5	264	36.1
E1	10	30	w	14.75427	1.024	1.089	1.116	1.122	0.559	0.54	141.8	32.3	26.8	33.8	263.2	39.5
D2	10	30	w	14.31589	1.016	1.1	1.118	1.128	0.715	0.701	112	49.1	2.7	16	260.5	36.4
A1	10	30	w	10.44953	1.025	1.15	1.179	1.194	0.695	0.673	345.2	3.9	81.3	57.4	252.8	32.3
A3	10	30	w	14.4149	1.049	1.083	1.136	1.138	0.25	0.22	135.3	34	21	31.4	259.9	40.1

Name	S0 Strike	Dip		Km	L	F	P	Pj	T	U	K1dec	K1inc	K2dec	K2inc	K3dec	K3inc
GR10																
A1	171	31	w	4.380018	1.078	1.026	1.105	1.11	-0.493	-0.512	187.4	24.4	299.2	39.3	74.3	40.8
A2	171	31	w	14.62971	1.028	1.028	1.056	1.056	-0.002	-0.015	182.1	30.6	274.1	3.4	9.8	59.2
A3	171	31	w	6.229147	1.053	1.056	1.112	1.112	0.023	-0.004	162.1	17.1	264.3	34.6	50.3	50.3
A4	171	31	w	6.288426	1.07	1.116	1.194	1.196	0.237	0.194	184.4	9.4	296.1	66	90.6	21.9
B1	171	31	w	3.465597	1.156	1.179	1.363	1.363	0.065	-0.012	349.3	7.3	253.3	39.3	88	49.8
B2	171	31	w	3.395889	1.057	1.141	1.206	1.212	0.406	0.366	208.9	44.1	114.6	4.4	20.2	45.6
B3	171	31	w	3.475459	1.261	1.117	1.407	1.418	-0.355	-0.428	229	28.4	339.8	33.3	108.2	43.5
B4	171	31	w	6.250693	1.173	1.08	1.267	1.273	-0.348	-0.399	211.8	21.3	321.2	40.4	101.3	42
C1	171	31	w	7.316744	1.015	1.194	1.211	1.238	0.848	0.834	343.5	19.7	251.3	6	145.2	69.4
C3	171	31	w	8.899445	1.072	1.064	1.141	1.141	-0.062	-0.095	225.8	56.3	105.8	18.4	6	27.1
C3	171	31	w	1.327449	1.605	1.313	2.108	2.127	-0.269	-0.435	305.3	8	210.8	29.3	49	59.4
C5	171	31	w	5.762592	1.176	1.16	1.365	1.365	-0.044	-0.121	163.1	27.8	269.7	28.6	37.1	48.1
HOME																
BGR14																
A3	172	52	w	4.090075	1.308	2.204	2.882	3.006	0.493	0.28	83.6	34.3	289.7	52.8	182.4	12.7
A5	172	52	w	6.762605	1.169	1.689	1.975	2.04	0.54	0.413	6.4	26.5	269.2	14.1	154.1	59.4
A7	172	52	w	7.348316	2.076	1.152	2.392	2.55	-0.675	-0.781	71.7	14	330.9	36.9	178.8	49.7
A8	172	52	w	5.667671	1.403	3.019	4.237	4.527	0.531	0.247	22.6	34.2	217.4	54.9	117.4	7
B1	172	52	w	16.08849	1.134	1.376	1.56	1.582	0.436	0.344	284.1	6.6	185.5	52.6	19	36.6
B2	172	52	w	3.689874	1.597	3.549	5.667	6.019	0.461	0.092	113.6	16.3	220.6	45	9.2	40.5
B4	172	52	w	5.721454	1.818	1.556	2.829	2.84	-0.149	-0.392	24.6	23.6	221.4	65.5	117.4	6.3
C1	172	52	w	4.34382	1.419	3.203	4.545	4.881	0.538	0.243	279.1	10.4	19.9	45.5	179.3	42.6
C2	172	52	w	9.371246	1.211	1.26	1.525	1.526	0.094	-0.011	127.7	68.4	289	20.6	21.4	6.3
C3	172	52	w	8.486076	1.357	1.345	1.825	1.825	-0.015	-0.164	223.9	32.7	340.5	34.9	103.7	38
C5	172	52	w	3.107073	1.713	3.074	5.265	5.447	0.352	-0.027	157.3	56.6	283.6	21.3	23.8	24.4
BGR15																
A1	171	56	w	79.0371	1.039	1.03	1.07	1.071	-0.134	-0.151	115.1	39.6	280.5	49.5	19.1	7.2
A2	171	56	w	95.30098	1.052	1.053	1.108	1.108	0.008	-0.018	262.9	13.7	171.3	6.4	56.8	74.8
B1	171	56	w	104.4512	1.018	1.022	1.04	1.04	0.111	0.101	176.7	2.9	84	43.1	269.8	46.8
B2	171	56	w	104.4298	1.043	1.019	1.063	1.064	-0.392	-0.405	0.6	57.2	238.3	19	138.8	25.6
C1	171	56	w	79.03203	1.057	1.053	1.113	1.113	-0.04	-0.066	280.1	27.4	23.5	24.1	148.5	52.1

Name	S0 Strike	Dip		Km	L	F	P	Pj	T	U	K1dec	K1inc	K2dec	K2inc	K3dec	K3inc
C2	171	56	w	91.30161	1.024	1.028	1.053	1.053	0.08	0.067	49.3	52.7	178.9	25.9	281.9	24.8
D1	171	56	w	104.9517	1.042	1.039	1.084	1.084	-0.036	-0.056	238.2	34.9	142.8	7.6	42.3	54
D2	171	56	w	112.0396	1.039	1.011	1.051	1.053	-0.556	-0.565	23.3	6	285.8	51.3	118	38.1
E1	171	56	w	76.12588	1.034	1.017	1.052	1.053	-0.325	-0.337	202.2	20.3	101.4	26.9	324.4	55.2
E2	171	56	w	96.72013	1.025	1.021	1.047	1.047	-0.073	-0.085	177.6	52.8	271.6	3	3.8	37.1
BGR12																
A1	169	30	w	11.9864	1.206	1.174	1.416	1.416	-0.079	-0.165	78.8	4.8	324.7	78.3	169.7	10.6
C1	169	30	w	8.876576	1.815	1.248	2.266	2.33	-0.457	-0.607	283.7	2.2	35.9	84.3	193.5	5.3
BGR13																
A1	178	50	w	25.89808	1.144	1.06	1.213	1.219	-0.395	-0.436	236.9	16.2	351.8	55.5	137.4	29.5
A2	178	50	w	14.28853	1.071	1.359	1.455	1.491	0.635	0.577	82.9	5.4	198.4	77.6	351.9	11.1
A3	178	50	w	5.705043	1.278	1.835	2.345	2.405	0.425	0.242	73.5	6.6	170.4	46.1	337.3	43.2
D1	178	50	w	14.66045	1.269	1.164	1.476	1.481	-0.222	-0.313	246.3	16.2	337.1	2.8	76.7	73.6
B2	178	50	w	15.19048	1.135	1.219	1.383	1.387	0.222	0.144	51.5	29.9	178.2	46.1	303	28.8
C1	178	50	w	20.24947	1.138	1.024	1.165	1.179	-0.694	-0.714	42	1.2	310.3	55	132.8	34.9
C2	178	50	w	12.70054	1.056	1.306	1.38	1.411	0.66	0.613	237.1	79.7	62	10.3	331.9	0.9
GR6																
A1	8	32	w	2.516063	1.135	1.288	1.463	1.473	0.333	0.247	140.6	12	15.4	69.8	234.1	16
B2	8	32	w	4.734115	1.042	1.312	1.367	1.404	0.737	0.7	280.2	65.6	151	16	55.6	17.9
C1	8	32	w	1.456332	1.31	1.365	1.788	1.789	0.07	-0.074	305.8	5.2	207.4	57.9	39.1	31.5
C2	8	32	w	3.186002	1.106	1.097	1.214	1.214	-0.044	-0.092	336.6	59.7	154.8	30.3	245.3	0.8
D1	8	32	w	5.815245	1.073	1.064	1.143	1.143	-0.064	-0.097	131	35.8	336.5	51.4	230.3	12.5
E1	8	32	w	6.584081	1.025	1.077	1.104	1.108	0.502	0.484	312.8	44.1	160.6	42.4	57.1	14.3
F2	8	32	w	2.344192	1.087	1.246	1.353	1.367	0.451	0.39	311.4	33.1	146.9	55.9	46.1	7.2
G1	8	32	w	9.020181	1.029	1.13	1.163	1.174	0.617	0.593	283.4	49.6	172.4	17	69.9	35.4
DIVERSION																
BGR6																
A1	162	22	w	147.5921	1.007	1.014	1.022	1.022	0.316	0.312	187.1	13.4	49.1	72.3	279.9	11.4
A2	162	22	w	121.4576	1.007	1.024	1.031	1.032	0.552	0.546	187	59.4	89.1	4.6	356.4	30.2
B1	162	22	w	133.9968	1.032	1.011	1.043	1.045	-0.489	-0.498	200.5	22.2	359.9	66.5	107.5	7.5
B2	162	22	w	190.1721	1.013	1.003	1.016	1.017	-0.644	-0.646	332.1	38	153.3	52	62.5	0.6
C1	162	22	w	117.2303	1.02	1.03	1.05	1.05	0.198	0.186	10.8	49	164.5	38	265.1	13.2

Name	S0 Strike	Dip		Km	L	F	P	Pj	T	U	K1dec	K1inc	K2dec	K2inc	K3dec	K3inc
C2	162	22	w	116.2104	1.033	1.012	1.045	1.047	-0.479	-0.488	316.7	18.8	55.1	23.1	191.4	59.5
D1	162	22	w	126.2072	1.022	1.015	1.037	1.038	-0.181	-0.19	50.9	29.3	273.5	52.7	153.3	21
D2	162	22	w	113.1599	1.016	1.035	1.052	1.053	0.369	0.358	206.7	20.8	308.1	27.4	84.7	54.4
E1	162	22	w	145.5507	1.027	1.004	1.031	1.034	-0.76	-0.763	251	34.4	123.1	41.9	3.3	29
E2	162	22	w	104.0016	1.026	1.022	1.049	1.049	-0.077	-0.089	288.7	79.5	34.4	2.9	124.9	10.1
GR3																
A2	168	29	w	1.558602	1.163	1.571	1.827	1.872	0.499	0.381	177.9	19.7	51.7	58.8	276.7	23.1
B1	168	29	w	2.875044	1.135	1.175	1.334	1.335	0.121	0.05	198.6	10.4	106.7	10	333.7	75.4
D1	168	29	w	0.7251576	1.129	3.287	3.711	4.26	0.815	0.687	167.6	50.9	42.7	24.9	298.5	28
F1	168	29	w	4.034755	1.226	1.081	1.325	1.338	-0.449	-0.504	152.8	49.7	304.2	36.6	45.2	14.4
BGR5																
A1	156	25	w	5.006504	2.095	1.401	2.935	3.009	-0.374	-0.586	356	44.5	138.5	38.9	245.3	19.7
A2	156	25	w	4.805749	1.296	4.045	5.242	5.944	0.687	0.436	252.8	33.4	4.9	29.7	126.1	42.2
A3	156	25	w	7.011117	1.218	1.779	2.167	2.233	0.489	0.334	252.4	44.2	37.1	40	143.4	18.5
B1	156	25	w	11.43037	1.106	1.473	1.629	1.674	0.589	0.505	254.1	61.9	32.6	21.8	129.6	16.9
B2	156	25	w	5.058525	1.73	3.478	6.016	6.292	0.389	-0.012	224.1	8.4	333.8	66.4	130.7	21.9
B3	156	25	w	9.127095	1.192	1.545	1.842	1.875	0.425	0.296	227.8	71.2	7	14.4	100	11.8
B4	156	25	w	8.256574	1.233	1.728	2.13	2.184	0.447	0.289	231.2	38.3	350.4	31.7	106.6	35.6
B5	156	25	w	12.3021	1.297	1.162	1.508	1.515	-0.267	-0.361	194.3	19	293.6	24.9	71.1	57.8
B6	156	25	w	15.95728	1.357	1.056	1.433	1.474	-0.698	-0.742	348.8	60.5	257.3	0.8	166.9	29.5
B7	156	25	w	15.36478	1.146	1.373	1.574	1.592	0.398	0.3	160.8	40	264.6	15.8	11.5	45.7
C1	156	25	w	15.08843	1.185	1.199	1.421	1.421	0.034	-0.054	211.5	25.7	82.3	52.7	314.5	25
C2	156	25	w	4.498767	1.418	3.449	4.889	5.302	0.56	0.259	143	85.3	301.2	4.4	31.3	1.7
C3	156	25	w	12.23775	1.059	1.334	1.412	1.448	0.671	0.621	166.7	48.9	270	11.4	9.4	38.9
C4	156	25	w	8.580649	1.044	1.925	2.009	2.185	0.878	0.833	142.8	18.1	272.1	62.7	46.1	19.7
C5	156	25	w	5.185506	1.196	2.485	2.971	3.215	0.672	0.507	116.4	66.5	21.6	2.1	290.7	23.4
BGR3																
A1	162	21	w	31.54969	1.035	1.079	1.117	1.12	0.377	0.354	11.8	1.7	256.9	86	101.9	3.7
A2	162	21	w	47.81911	1.056	1.042	1.101	1.101	-0.139	-0.163	241.3	11.4	20.5	75	149.3	9.5
B1	162	21	w	10.67964	1.303	1.129	1.47	1.483	-0.372	-0.452	140.3	38.9	345.4	48.3	240.8	12.7
B2	162	21	w	15.31583	1.16	1.138	1.32	1.32	-0.069	-0.137	236.7	27.5	122.3	38.4	351.9	39.3
B3	162	21	w	38.55405	1.044	1.085	1.133	1.135	0.304	0.275	50.2	31.3	228.8	58.7	319.8	0.6

Name	S0 Strike	Dip		Km	L	F	P	Pj	T	U	K1dec	K1inc	K2dec	K2inc	K3dec	K3inc
C1	162	21	w	11.83594	1.165	1.314	1.532	1.54	0.282	0.183	99.1	6.2	193.4	35.3	0.5	54
C2	162	21	w	10.05968	1.042	1.452	1.513	1.578	0.802	0.763	79.6	31.1	291.1	54.7	178.9	15
C3	162	21	w	32.05849	1.096	1.155	1.266	1.268	0.225	0.169	245.9	20.9	20.8	61.6	148.7	18.4
D1	162	21	w	33.73383	1.063	1.06	1.127	1.127	-0.027	-0.057	63.6	1.2	328.7	76.5	153.9	13.4
D2	162	21	w	31.1262	1.064	1.064	1.132	1.132	-0.005	-0.036	94.6	21	267.6	68.8	3.7	2.3
D3	162	21	w	54.27773	1.011	1.116	1.128	1.143	0.814	0.803	64	45.6	277.2	39.3	172.4	17.2
BGR2																
A1	178	22	w	13.32522	1.252	1.119	1.401	1.41	-0.332	-0.405	279.1	19.5	132.7	67	13.3	11.8
B1	178	22	w	5.06206	1.372	3.528	4.841	5.305	0.599	0.317	117.4	31.1	233.7	36.3	359	38.2
B2	178	22	w	8.997904	1.187	1.171	1.39	1.39	-0.043	-0.124	26	24.3	147.8	49.5	280.7	30.2
D3	178	22	w	12.37768	1.21	1.192	1.442	1.442	-0.04	-0.13	166.8	24.6	67.1	20.1	302.4	57.3
E1	178	22	w	3.160316	1.514	2.664	4.032	4.187	0.406	0.098	270.7	28.1	166.9	24.1	42.8	51.4
E2	178	22	w	5.245758	1.881	1.25	2.351	2.427	-0.478	-0.63	22.2	58.3	167.8	27	265.8	15.3
E3	178	22	w	5.079308	1.302	1.919	2.498	2.566	0.424	0.227	175.4	39.5	337.9	49.2	78.1	8.8

Block Samples

Anisotropy of Magnetic Susceptibility Data from Rocky Mountain Front																					
SITE		**N**	**K1**	**K2**	**K3**	**Km**	**K1**	***K1 95%***	**K2**	***K2 95%***	**K3**	***K3 95%***	**L**	**F**	**P**	**Pj**	**T**	**U**
							Dec/Inc	***Error***	**Dec/Inc**	***Error***	**Dec/Inc**	***Error***						
Field Block Samples																		
BGR2	Home	12	1.006	0.833	0.514	0.784	253.1/35	*70.1/19.4*	112.9/47.7	*70.2/42.3*	358.4/20.7	*43.3/19.5*	1.207	1.620	1.955	1.997	0.438	0.297
BGR3	Home	11	1.046	1.007	0.947	1.000	80.8/5.1	55.5/19.7	190.9/75.6	55.0/50.4	349.5/13.5	51.3/23.6	1.04	1.064	1.105	1.11	0.249	0.225
BGR4	Home	12	-0.93	-0.98	-1.09	-1.000	213.9/76.3	69/29.7	48.5/18.9	69/27.5	329.7/6.1	48.5/18.9	1.11	1.05	1.165	1.17	-0.35	0.387
BGR5	Home	16	1.183	1.007	0.796	0.995	261.4/58.9	48.2/29.4	16.3/14.3	49.2/32.5	113.8/27	35.5/29.1	1.18	1.264	1.485	1.49	0.184	0.087
Gr3	Home	10	0.472	0.309	0.008	0.263	174.6/.1	*58.3/42.1*	84.4/57.7	*61.8/24.6*	264.6/32.3	*52.6/30.1*	2.069	-3.175	-6.568	0.000	0.000	0.296
BGR6	Home	10	1.004	1.003	0.993	1.000	210.8/28.2	79.0/32	344.6/52.3	79/47.4	107.7/22.9	48.1/32.9	1	1.01	1.011	1.01	0.725	0.724
BGR7	Home	11	-0.96	-1.01	-1.03	-1.000	234.1/11.5	32.9/22	348.4/63.8	51.3/28.6	139.1/23.2	50.4/22	1.03	1.048	1.075	1.08	0.299	-0.03
BGR8	Home	14	-0.94	-1.01	-1.06	-1.000	227.1-12.3	48.5/25.1	101.7/69.3	51.9/41.2	320.8/16.3	47.6/28.4	1.05	1.071	1.125	1.13	0.159	-0.13
Gr8	Home	6	-0.976	-0.978	-1.046	-1.000	281.1/35.4	*71.6/5.1*	138.5/48.2	*71.6/13.9*	25.5/19.3	*16.9/6.3*	1.069	1.003	1.072	1.082	-0.919	0.922
Gr6	Home	16	0.162	0.073	-0.235	0.000	324.1/15	*47.7/9.9*	149.7/74.9	*47.8/16.1*	54.5/1.4	*17.9/9.2*	2.232	-0.309	-0.691	0.000	0.000	0.549
BGR13	Diversion	11	1.014	0.622	0.336	0.657	60.8/20.7	30.1/8.4	202.4/64.3	27.3/18.6	325.1/14.6	27.9/16.7	1.55	1.418	2.198	2.2	-0.11	-0.3
BGR12	Diversion	12	-0.49	-0.7	-0.79	-0.659	79.1/14.9	30.4/12	193.4/57.1	61.7/11.7	340.7/28.6	62.3/22	1.12	1.439	1.618	1.65	0.513	-0.42
BGR11	Diversion	13	-0.94	-1.01	-1.04	-1.000	44.1/12.6	28.4/13.7	149.1/49.4	39.4/27.9	304.1/37.9	39.3/13.3	1.03	1.073	1.107	1.11	0.388	-0.37
BGR10	Diversion	14	-0.97	-0.99	-1.04	-1.000	36.6/16.5	43.8/24.3	163/63.4	44.9/25.3	300.3/20.2	32.9/16.2	1.05	1.028	1.08	1.08	-0.3	0.315
BGR16	Diversion	7	-0.94	-1	-1.06	-1.000	40.7/28	56.4/25.4	272.2/49.5	57.1/21.4	146.2/26.7	28.7/24.7	1.06	1.06	1.012	1.12	0.024	0.004
BGR15	Diversion	10	1.009	0.999	0.992	1.000	241.4/18.4	59.1/28.5	332.4/2.9	67.9/58.6	71.1/71.4	67.8/28	1.01	1.007	1.018	1.02	-0.02	-0.18
BGR14	Diversion	14	1.193	0.726	0.536	0.818	247.7/7.2	33.1/21.2	350.3/60	46.1/32.1	153.7/29	46.2/20.6	1.64	1.356	2.227	2.24	-0.24	-0.42
Gr10	French	13	1.104	0.992	0.863	0.986	276.9/24.2	*37.7/8.2*	169.9/33.1	*50.9/37.6*	35.7/46.9	*51/5.4*	1.112	1.150	1.279	1.280	0.134	0.074
Gr11	French	13	1.071	1.016	0.913	1.000	58/19.8	*20.3/8*	155.7/20.5	*20.5/11.9*	239/15	*13.2/6.2*	1.054	1.113	1.173	1.177	0.341	0.306
Gr12	French	11	1.052	1.024	0.924	1.000	138.6/35	*11.1/2.9*	20.7/33.7	*11.3/3.3*	260.5/37	*4.2/3.7*	1.027	1.108	1.138	1.146	0.583	0.561
Gr13	French	9	-0.966	-1.006	-1.028	-1.000	155.2/6.4	*30.9/15.4*	320.5/83.4	*56.6/26.8*	65/1.7	*56.1/16.5*	1.022	1.042	1.064	1.065	0.308	-0.293
Gr33	French	8	0.828	0.740	0.682	0.750	210/83.5	*27.3/14.7*	338.5/4.1	*49/19.2*	68.9/5.1	*50.5/13*	1.120	1.084	1.214	1.215	-0.017	0.211

Anisotropy of Magnetic Susceptibility Data from Rocky Mountain Front																		
SITE		**N**	**K1**	**K2**	**K3**	**Km**	**K1**	***K1 95%***	**K2**	***K2 95%***	**K3**	***K3 95%***	**L**	**F**	**P**	**Pj**	**T**	**U**
							Dec/Inc	***Error***	**Dec/Inc**	***Error***	**Dec/Inc**	***Error***						
Gr37	Norwegian	10	-0.970	-0.990	-1.040	-1.000	156.1/1.7	*37.1/8.3*	252.5/75.3	*36.5/15.1*	65.6/14.6	*15.2/12.4*	1.051	1.020	1.072	1.074	-0.422	0.436
Gr5B	Norwegian	6	-0.133	-0.371	-0.496	-0.333	259.3/26	*15.2/10.2*	145.5/39.6	*39.4/13.6*	12.8/39.3	*39.9/9.3*	1.336	2.790	3.727	3.985	0.560	-0.313
Gr36	Norwegian	16	0.915	0.859	0.851	0.875	183.1/51.1	*10.1/5.9*	32.5/35.1	*59.8/8.4*	291.9/14.6	*59.8/6.5*	1.056	1.009	1.076	1.083	-0.075	0.076
BGR20	Norwegian	13	1.02	1.007	0.973	1.000	248.8/48	34/14.3	65.2/42	33.7/11.7	156.7/1.6	15.8/11	1.01	1.035	1.048	1.05	0.449	0.439
Gr39	Norwegian	12	-0.494	-0.713	-0.957	-0.721	334.4/22.5	*52.1/25.2*	195.1/61.4	*52.3/36.8*	71.6/16.8	*38.4/27*	1.341	1.443	1.936	1.938	0.111	0.052
Gr35	Norwegian	14	-0.768	-0.875	-0.928	-0.857	99.6/39.8	*33.4/15.2*	303.6/47.6	*56/25.4*	200/12.2	*55/17.1*	1.060	1.140	1.210	1.215	0.382	-0.341
BGR19	Norwegian	11	1.035	0.998	0.967	1.000	313.1/19.9	16.7/4.8	202.3/44.5	16.7/5.3	60/38.9	6.3/3.6	1.04	1.031	1.07	1.07	-0.09	-0.11
Gr34	Norwegian	10	1.043	1.004	0.953	1.000	199/43.4	*11.9/4.0*	0.4/45	*11.7/10.3*	100/9.4	*10.4/4.4*	1.038	1.053	1.094	1.094	0.160	0.138
Gr38	Norwegian	8	1.060	1.002	0.938	1.000	316.4/22.5	*26.4/8.7*	204.2/42.5	*26.1/15*	66.1/39.1	*31.2/11.3*	1.058	1.068	1.130	1.130	0.082	0.052
BGR21	Norwegian	17	-0.68	-0.83	-1.13	-0.880	217.8/4.3	59.4/31.4	114/72.4	59.2/50.6	309.1/17	51.1/34	1.36	1.213	1.654	1.66	-0.02	0.347
Gr24	Beaver	9	-0.840	-0.983	-1.177	-1.000	337.5/14.5	*21.9/3.9*	238.9/30.1	*27.1/8.5*	89.9/55.9	*21.8/4.4*	1.198	1.170	1.401	1.402	-0.069	0.152
Gr23	Beaver	8	-0.800	-0.976	-1.158	-0.978	349/20.8	*8.5/1.8*	87.3/20.9	*18.7/8.5*	218.2/59.8	*18.7/1.8*	1.187	1.219	1.447	1.447	0.072	0.020
Gr21	Beaver	15	-0.973	-0.990	-1.036	-1.000	288.1/40.7	*46.3/19.1*	44.2/27.1	*46.3/27.4*	157.2/37.3	*27.9/18.6*	1.047	1.017	1.065	1.067	-0.463	0.475
Gr20	Beaver	10	-0.098	-0.993	-1.025	-0.705	234.3/14.5	*50.4/26.6*	87.9/72.8	*50.8/28.9*	326.7/9.1	*35.4/19.7*	1.032	1.011	1.043	1.045	-0.488	0.496
Gr19	Beaver	8	-0.096	-0.979	-1.061	-0.712	229.4/5.5	*50.5/13.5*	124.7/69.1	*50.3/16.1*	321.4/20.1	*18.9/11.9*	1.084	1.020	1.105	1.112	-0.609	0.625
Gr30	Beaver	7	0.186	0.137	0.106	0.143	115.6/44.4	*9.3/5.3*	13.3/12.2	*12.5/8.4*	271.6/43	*12.7/6.2*	1.362	1.287	1.753	1.754	-0.100	-0.237
Gr32	Beaver	7	-0.958	-0.983	-1.058	-1.000	251.9/1.6	*53.4/8.7*	159.9/50.8	*53.5/11.8*	343.2/39.1	*14.1/6.4*	1.076	1.026	1.104	1.108	-0.481	0.500
Gr25	Beaver	12	-0.955	-0.984	-1.062	-1.000	318.2/19.5	*67.3/45.2*	187/61.8	*67.3/45.2*	55.5/19.6	*49.1/29.7*	1.079	1.030	1.112	1.116	-0.438	0.459
Gr18	Beaver	11	-0.307	-0.431	-0.650	-0.463	128.3/1.5	*19.3/10*	260.2/87.8	*19.6/13.4*	38.3/1.6	*16.6/6.7*	1.508	1.402	2.114	2.116	-0.097	0.278
Gr17	Beaver	9	1.021	0.998	0.981	1.000	129.6/30.5	*21.3/15.5*	35.6/6.8	*46.3/20.1*	294.4/58.6	*46.5/15.5*	1.024	1.017	1.041	1.041	-0.163	-0.172
Gr15	Beaver	15	1.013	1.004	0.983	1.000	317.4/18.4	*40.1/11.7*	158.8/70.3	*40.7/14.9*	49.7/6.7	*17.5/11.7*	1.009	1.022	1.031	1.032	0.439	0.433

Lat/Long Data for Sawtooth Samples

WGS 84	Lat/Lon hddd−mm.mmm'		
Name	Position	Altitude	Date Modified
BGR1	N47 37.215 W112 42.233	1464 m	06/09/2012 17:22
BGR10	N47 36.994 W112 43.948	1369 m	6/19/2012 7:23:38 PM
BGR11	N47 36.996 W112 43.941	1371 m	6/19/2012 7:23:04 PM
BGR12	N47 37.026 W112 43.901	1373 m	6/19/2012 7:32:10 PM
BGR13	N47 36.998 W112 43.841	1379 m	6/20/2012 5:52:49 PM
BGR14	N47 36.825 W112 44.043	1384 m	6/20/2012 6:35:24 PM
BGR15	N47 36.832 W112 44.030	1382 m	6/20/2012 7:12:06 PM
BGR16	N47 36.867 W112 44.011	1382 m	6/20/2012 7:02:12 PM
BGR17	N47 36.542 W112 44.431	1380 m	6/20/2012 8:07:46 PM
BGR18	N47 36.529 W112 44.422	1385 m	6/20/2012 8:34:48 PM
BGR19	N47 36.397 W112 45.064	1388 m	6/20/2012 9:08:02 PM
BGR191	N47 36.394 W112 45.066	1386 m	6/20/2012 9:14:18 PM
BGR2	N47 37.223 W112 42.252	1443 m	06/09/2012 17:29
BGR20	N47 36.429 W112 45.017	1387 m	6/20/2012 9:24:27 PM
BGR21	N47 36.454 W112 45.185	1389 m	6/20/2012 9:46:18 PM
BGR3	N47 37.241 W112 42.292	1394 m	06/09/2012 18:10
BGR4	N47 37.236 W112 42.329	1426 m	06/09/2012 17:44
BGR5	N47 37.235 W112 42.364	1396 m	06/09/2012 18:08
BGR6	N47 37.112 W112 42.629	1371 m	06/09/2012 19:11
BGR7	N47 37.037 W112 42.648	1375 m	06/09/2012 19:25
BGR8	N47 36.998 W112 42.651	1369 m	06/09/2012 19:42
BGR81	N47 36.996 W112 42.652	1370 m	06/09/2012 20:14
BGR9	N47 36.986 W112 43.957	1371 m	6/19/2012 7:12:53 PM
GR10	N47 36.613 W112 44.305	1388 m	7/24/2011 9:04:14 PM
GR12	N47 36.608 W112 44.326	1393 m	7/24/2011 9:25:50 PM
GR13	N47 36.599 W112 44.343	1393 m	7/24/2011 9:17:42 PM
GR15	N47 36.210 W112 45.757	1470 m	7/25/2011 8:09:07 PM
GR17	N47 36.182 W112 45.746	1468 m	7/25/2011 8:54:45 PM
GR18	N47 36.148 W112 45.715	1470 m	7/25/2011 9:05:39 PM
GR19	N47 36.151 W112 45.706	1471 m	7/25/2011 9:15:19 PM
GR20	N47 36.160 W112 45.665	1467 m	7/25/2011 9:20:02 PM
GR21	N47 36.171 W112 45.639	1465 m	7/25/2011 9:32:43 PM
GR23	N47 36.186 W112 45.619	1465 m	7/25/2011 9:53:26 PM
GR24	N47 36.294 W112 45.572	1447 m	7/25/2011 10:18:10 PM
GR25	N47 36.246 W112 45.709	1546 m	7/26/2011 1:07:11 AM
GR3	N47 37.232 W112 42.365	1379 m	6/18/2011 10:18:49 PM
GR30	N47 36.301 W112 45.617	1523 m	7/26/2011 1:49:10 AM
GR32	N47 36.573 W112 45.600	1497 m	7/26/2011 2:11:23 AM
GR33	N47 36.538 W112 44.426	1383 m	7/26/2011 6:31:12 PM
GR34	N47 36.398 W112 45.066	1387 m	7/26/2011 6:51:03 PM
GR35	N47 36.429 W112 45.039	1391 m	7/26/2011 6:57:20 PM
GR36	N47 36.430 W112 45.012	1309 m	7/26/2011 7:02:55 PM
GR37	N47 36.445 W112 44.869	1355 m	7/26/2011 7:28:02 PM
GR38	N47 36.438 W112 45.162	1364 m	7/26/2011 8:37:58 PM
GR39	N47 36.489 W112 45.027	1378 m	7/26/2011 9:03:24 PM
GR5	N47 36.445 W112 44.901	1387 m	6/18/2011 11:47:23 PM
GR6	N47 37.198 W112 43.227	1400 m	7/24/2011 7:09:34 PM
GR8	N47 37.198 W112 43.223	1398 m	7/24/2011 7:41:33 PM

Appendix 3: AMS and strain data for Chapter 5; Eastern Thrust System, Wyoming Salient

The AMS data for the samples collected in the Wyoming Salient are presented here, with tables for both the individual specimen data and the mean sample data. The block sample data are split into two groups, depending on which transect they were collected on.

Individual Specimens

Name	S0 Strike	Dip		Km	L	F	P	Pj	T	U	K1dec	K1inc	K2dec	K2inc	K3dec	K3inc
WY1																
A1	179	34	w	417.7188	1.007	1.007	1.014	1.014	0.013	0.009	75.4	52.3	279.3	35.2	180.9	11.7
A2	179	34	w	430.1339	1.005	1.004	1.01	1.01	-0.112	-0.115	76.4	8.5	177.9	53.2	340.2	35.5
A3	179	34	w	433.243	1.008	1.01	1.018	1.018	0.114	0.11	85.9	75.8	269.5	14.1	179.3	0.9
B1	179	34	w	424.5644	1.007	1.005	1.012	1.012	-0.158	-0.161	142	51.5	239.3	5.8	333.9	37.9
B2	179	34	w	421.6973	1.003	1.008	1.011	1.012	0.413	0.411	53	43	227.4	46.8	320.4	2.8
C1	179	34	w	396.7401	1.012	1.005	1.017	1.017	-0.411	-0.415	155.4	63.6	271.5	12.3	6.8	22.9
C2	179	34	w	411.4654	1.002	1.008	1.01	1.011	0.594	0.593	51	22.2	193.9	62.9	314.9	14.8
D1	179	34	w	503.4958	1.008	1.003	1.011	1.012	-0.44	-0.443	261.1	20.1	28.4	58.9	162.3	22.7
D2	179	34	w	576.4928	1.003	1.009	1.012	1.012	0.516	0.514	93.8	62.5	241.3	23.7	337.2	13.1
D3	179	34	w	583.7744	1.005	1.013	1.019	1.019	0.415	0.412	263	2.6	161.7	76.9	353.6	12.8
E1	179	34	w	376.3712	1.004	1.012	1.016	1.016	0.494	0.491	112.3	10	212.4	44.7	12.7	43.5
E2	179	34	w	398.857	1.004	1.009	1.013	1.013	0.427	0.424	51.9	21.4	194.8	63.9	316.2	14.3
WY2																
A2	184	45	w	422.9868	1.009	1.006	1.014	1.014	-0.218	-0.222	100.5	5.4	205.5	69.9	8.6	19.3
A2	184	45	w	456.2567	1.005	1.006	1.01	1.01	0.1	0.097	86.1	5	346.7	61.6	178.7	27.9
A3	184	45	w	424.3455	1.006	1.005	1.011	1.011	-0.066	-0.069	63.1	20.6	200.5	62.9	326.6	16.8
B2	184	45	w	428.8141	1.008	1.007	1.014	1.014	-0.074	-0.078	109.3	32.3	245.9	49	4.2	22.4
B4	184	45	w	458.3911	1.006	1.006	1.013	1.013	0.015	0.012	91	14.3	216.9	66.5	356.2	18.2
C1	184	45	w	398.8918	1.002	1.004	1.006	1.006	0.3	0.299	79.4	25.4	325	40.9	191.6	38.4
D1	184	45	w	394.7468	1.004	1.005	1.009	1.009	0.117	0.115	85.1	23.7	293.3	63.6	180.1	11.1
E1	184	45	w	392.9064	1.003	1.004	1.007	1.007	0.082	0.08	80.6	76.2	212.2	9.3	303.9	10.2
F1	184	45	w	381.3786	1.003	1.005	1.008	1.008	0.195	0.193	95.4	3.3	336	83.3	185.7	5.9
F2	184	45	w	429.1897	1.005	1.003	1.008	1.008	-0.295	-0.297	92.2	57	279.1	32.9	187.1	3.2
G1	184	45	w	350.3172	1.007	1.008	1.015	1.015	0.06	0.057	64.9	25.2	296.5	52.9	167.8	25.3
H1	184	45	w	354.8731	1.001	1.007	1.008	1.009	0.754	0.753	88.5	56.5	269.9	33.5	179.4	0.6
H2	184	45	w	423.5747	1.006	1.003	1.008	1.008	-0.362	-0.364	86.6	18.5	334.5	48.3	190.5	35.8
H3	184	45	w	430.0731	1.002	1.008	1.011	1.011	0.565	0.563	311.9	22.6	72.9	51	208	29.9
WY3																
A1	180	30	w	50.13519	1.017	1.048	1.066	1.069	0.478	0.465	17.5	49.4	284.7	2.3	192.7	40.5
A2	180	30	w	52.03262	1.027	1.037	1.065	1.065	0.162	0.146	217.5	39.9	127.4	0.1	37.2	50.1
A3	180	30	w	57.59468	1.041	1.011	1.052	1.055	-0.554	-0.563	345.8	40.9	205.4	41.7	95.3	21.1

Name	S0 Strike	Dip		Km	L	F	P	Pj	T	U	K1dec	K1inc	K2dec	K2inc	K3dec	K3inc
B1	180	30	w	48.46657	1.035	1.018	1.053	1.054	-0.322	-0.334	220.4	50.9	2.9	32.8	105.6	18.8
B2	180	30	w	44.03396	1.02	1.061	1.082	1.086	0.504	0.489	3.3	31	100.9	12.4	210.1	56
B4	180	30	w	46.81468	1.03	1.02	1.051	1.052	-0.197	-0.209	233.3	16.4	35.6	72.8	141.9	5
B3	180	30	w	41.79092	1.027	1.052	1.08	1.082	0.314	0.297	64.7	24.9	256.3	64.6	156.8	4.4
C1	180	30	w	64.79936	1.016	1.02	1.036	1.036	0.132	0.123	269.3	21	160.8	39.7	20.2	43
C2	180	30	w	47.63832	1.021	1.021	1.043	1.043	-0.009	-0.019	259	44.3	11.4	21.4	119.2	38
C3	180	30	w	52.80416	1.039	1.004	1.042	1.047	-0.826	-0.829	225.8	19.1	323.5	21	97.2	61
C4	180	30	w	59.77638	1.018	1.016	1.035	1.035	-0.056	-0.065	235.9	26.6	26.1	60.1	139.3	12.8
D1	180	30	w	45.20975	1.027	1.04	1.068	1.069	0.186	0.17	215.7	0.6	125.1	47.3	306.3	42.7
D2	180	30	w	47.72909	1.047	1.057	1.107	1.107	0.092	0.066	217.1	58	50.9	31.2	317.1	6.2
D3	180	30	w	43.76007	1.028	1.028	1.056	1.056	0.004	-0.01	264.4	2.5	167	71.2	355.2	18.7
E1	180	30	w	64.21945	1.027	1.037	1.065	1.065	0.163	0.147	238.8	6.9	335.4	43.7	141.7	45.4
E2	180	30	w	45.13898	1.025	1.075	1.102	1.106	0.495	0.477	46	76.9	232.8	13	142.5	1.5
E4	180	30	w	56.40322	1.121	1.012	1.135	1.15	-0.807	-0.818	240.2	1.9	147.1	58.9	331.3	31
E5	180	30	w	61.99467	1.041	1.027	1.07	1.07	-0.196	-0.212	88.3	64	238.5	22.9	333.4	11.6
F1	180	30	w	43.93352	1.034	1.032	1.067	1.067	-0.035	-0.051	239.8	8.4	144	34.3	341.7	54.4
F2	180	30	w	38.31917	1.086	1.094	1.188	1.188	0.041	-0.002	245.2	14.5	357.3	55.5	146.4	30.6
WY4																
A1	176	40	w	109.7251	1.009	1.025	1.035	1.036	0.455	0.448	235.1	10.9	143.4	9	14.7	75.8
A2	176	40	w	79.64776	1.006	1.013	1.02	1.02	0.339	0.335	73.7	6	170.9	50.1	338.8	39.2
A3	176	40	w	73.6134	1.046	1.006	1.053	1.058	-0.763	-0.768	224.7	13.4	317.8	12.9	90.3	71.3
A4	176	40	w	98.15849	1.032	1.01	1.042	1.044	-0.535	-0.543	112	59.3	225.1	13.1	322	27.2
B1	176	40	w	124.1166	1.022	1.008	1.031	1.032	-0.441	-0.447	60.6	5.7	226.8	84.1	330.5	1.4
B2	176	40	w	84.8072	1.016	1.045	1.062	1.064	0.475	0.463	259.5	10.2	1.4	48.9	161.1	39.3
B3	176	40	w	72.69438	1.017	1.028	1.046	1.047	0.241	0.231	37.3	46.5	292	14	189.8	40.1
B4	176	40	w	95.92526	1.033	1.076	1.112	1.115	0.383	0.36	281.7	44.5	168.2	22.1	60.1	37.3
B5	176	40	w	127.7708	1.019	1.015	1.033	1.033	-0.12	-0.128	242.1	20.8	150.9	3.1	52.8	69
C1	176	40	w	94.23402	1.012	1.036	1.048	1.05	0.512	0.503	271.1	18.6	13.6	32.7	156.4	51.1
C2	176	40	w	91.79889	1.005	1.04	1.045	1.049	0.774	0.77	98	31	220.4	41.7	345.3	32.8
C3	176	40	w	75.45451	1.03	1.013	1.043	1.044	-0.402	-0.411	59	65.4	269.7	21.5	175.1	11.4
C4	176	40	w	74.31837	1.04	1.036	1.077	1.077	-0.053	-0.072	72.8	27.5	314.9	41.9	184.8	35.6

Name	S0 Strike	Dip		Km	L	F	P	Pj	T	U	K1dec	K1inc	K2dec	K2inc	K3dec	K3inc
C5	176	40	w	118.6586	1.025	1.049	1.075	1.076	0.308	0.292	229	43.7	332.7	13.9	76.1	43
C6	176	40	w	100.8155	1.01	1.049	1.059	1.063	0.661	0.653	214.1	34.2	46.8	55.1	308.2	6
WY6																
A1	160	20	w	303.0692	1.025	1.025	1.05	1.05	0.009	-0.003	190.4	18.3	315.9	60.3	92.5	22.5
A2	160	20	w	323.0049	1.018	1.013	1.031	1.031	-0.134	-0.142	204.4	25.4	331.5	51.8	100.8	26.4
B1	160	20	w	296.4121	1.018	1.02	1.038	1.038	0.068	0.058	202.9	40.9	330.1	34.9	83.4	29.6
B2	160	20	w	338.2731	1.024	1.024	1.049	1.049	0.009	-0.003	194.6	34.3	328.6	45.6	86.4	24.6
B2	160	20	w	252.1037	1.026	1.018	1.044	1.044	-0.189	-0.199	194.8	30.5	343.9	55.5	96	14.5
B3	160	20	w	337.7452	1.025	1.023	1.048	1.048	-0.044	-0.056	200.3	27.2	324.9	47.8	93.4	29.4
C1	160	20	w	250.1812	1.019	1.022	1.041	1.041	0.067	0.057	194.4	31.4	340.7	53.7	94.2	16.3
C2	160	20	w	315.351	1.024	1.026	1.051	1.051	0.049	0.037	190.2	25.9	331.7	58.2	91.6	17.1
D1	160	20	w	259.6632	1.023	1.028	1.052	1.052	0.086	0.074	194.6	28.2	330.6	53.2	92.4	21.5
D2	160	20	w	360.9501	1.023	1.016	1.039	1.039	-0.176	-0.185	186.3	9.9	290.5	54.5	89.7	33.7
E1	160	20	w	310.9207	1.022	1.019	1.041	1.041	-0.069	-0.079	151.4	36.9	295	47	46.5	18.9
E2	160	20	w	314.476	1.02	1.017	1.037	1.037	-0.099	-0.108	158.3	32.6	303.2	52	56.8	17.3
F1	160	20	w	298.3022	1.015	1.031	1.046	1.047	0.355	0.345	317.3	44	207.7	19.2	100.8	39.7
F2	160	20	w	338.9644	1.024	1.025	1.049	1.049	0.021	0.009	188.2	13.8	313.3	66.9	93.6	18.2
G1	160	20	w	315.8785	1.022	1.019	1.041	1.041	-0.088	-0.098	5.7	10.5	161.4	78.5	274.8	4.6
H1	160	20	w	297.9585	1.024	1.019	1.043	1.043	-0.1	-0.11	195.6	32.8	0.3	56.3	101	7
WY7																
A1	170	40	w	297.2086	1.006	1.007	1.014	1.014	0.073	0.069	250.8	49	148.9	10.2	50.5	39.2
A2	170	40	w	378.4789	1.012	1.007	1.019	1.019	-0.26	-0.264	302	51.9	191	15.7	90.2	33.6
A3	170	40	w	446.5373	1.012	1.009	1.02	1.021	-0.154	-0.159	293.2	51.6	182.7	15.6	81.8	34.1
A4	170	40	w	355.5309	1.005	1.011	1.016	1.017	0.411	0.408	254.9	53.2	27.6	26.9	130	23.1
B1	170	40	w	305.8737	1.01	1.009	1.019	1.019	-0.06	-0.064	264.9	3.4	168.4	62	356.7	27.8
B2	170	40	w	375.8705	1.012	1.015	1.026	1.026	0.115	0.109	219.6	48.7	356.5	32.7	101.8	22.3
B3	170	40	w	433.7891	1.01	1.009	1.019	1.019	-0.045	-0.05	209.2	37.1	324.4	29.4	81.4	39
C1	170	40	w	332.2943	1.015	1.003	1.018	1.019	-0.691	-0.694	239.5	37.2	45.2	51.9	144.2	7
C2	170	40	w	360.2563	1.009	1.015	1.024	1.024	0.254	0.248	255.3	48.5	0.5	13	101.1	38.6
C3	170	40	w	429.6137	1.017	1.007	1.024	1.025	-0.4	-0.405	245.2	59.4	4.6	16.2	102.5	25.2
D1	170	40	w	246.3812	1.008	1.022	1.03	1.032	0.477	0.472	300.8	22.4	201	22.4	70.9	57.4

Name	S0 Strike	Dip		Km	L	F	P	Pj	T	U	K1dec	K1inc	K2dec	K2inc	K3dec	K3inc
D2	170	40	w	353.8336	1.015	1.004	1.019	1.02	-0.576	-0.579	249.7	46.7	1.2	19.1	106.3	37.1
WY8																
A1	130	40	w	753.9278	1.001	1.03	1.031	1.036	0.914	0.913	293.3	8.8	190.5	55	29.3	33.5
A2	130	40	w	799.3813	1.01	1.015	1.026	1.026	0.193	0.187	260.4	36.4	140.8	33.8	22.2	35.5
A3	130	40	w	874.8649	1.016	1.009	1.025	1.025	-0.311	-0.317	237.5	42.6	103.2	37.2	352.6	24.8
B1	130	40	w	602.9286	1.012	1.024	1.036	1.037	0.331	0.323	130.9	9	239.5	63.6	36.7	24.6
B2	130	40	w	540.5831	1.007	1.029	1.036	1.039	0.601	0.595	228.7	37	129.8	11.5	25.4	50.7
C1	130	40	w	618.8452	1.007	1.033	1.04	1.043	0.636	0.63	223.6	38.3	317.1	4.3	52.5	51.3
C2	130	40	w	769.429	1.012	1.016	1.029	1.029	0.127	0.12	227.2	49.5	42.9	40.5	134.7	2.2
C3	130	40	w	903.2786	1.006	1.021	1.027	1.029	0.523	0.519	269	25.2	159.8	35	26.4	44.4
D1	130	40	w	691.3824	1.012	1.013	1.026	1.026	0.037	0.031	283.9	38.6	159.7	35.1	43.7	31.9
D2	130	40	w	723.4221	1.02	1.005	1.025	1.027	-0.6	-0.604	268.3	50.3	145.6	24.1	41	29.4
E1	130	40	w	731.2119	1.007	1.015	1.022	1.023	0.353	0.348	140.7	21.6	255.7	46.9	34.5	35.1
E2	130	40	w	555.7499	1.012	1.01	1.022	1.022	-0.096	-0.101	287.6	39.9	152.2	40.4	39.7	24.2
E3	130	40	w	723.9273	1.01	1.004	1.014	1.015	-0.428	-0.43	251.9	23	129.8	51.4	355.5	29.1
F2	130	40	w	702.0143	1.008	1.009	1.017	1.017	0.093	0.088	317.1	75.6	51.2	1.1	141.4	14.3
F1	130	40	w	731.4742	1.007	1.015	1.022	1.023	0.355	0.35	133.1	8.7	232.8	47.9	35.5	40.7
WY9																
A1	325	30	w	368.8488	1.013	1.01	1.023	1.023	-0.093	-0.098	179	85.4	24.2	4.1	294.1	1.9
A2	325	30	w	368.8034	1.01	1.012	1.022	1.022	0.079	0.074	172.2	64.6	23.2	22.1	288.3	11.8
B1	325	30	w	365.3404	1.007	1.012	1.019	1.019	0.239	0.234	346	67.2	212.4	16.2	117.7	15.6
C1	325	30	w	454.7401	1.025	1.014	1.039	1.039	-0.28	-0.289	219.7	39.4	86.8	39.6	333.1	25.8
B2	325	30	w	338.5505	1.005	1.016	1.021	1.022	0.54	0.536	41.3	20.7	174.2	60.9	303.6	19.5
Wy10																
A1	158	32	w	674.494	1.014	1.03	1.044	1.045	0.361	0.352	250.6	54.9	160.3	0.2	70.2	35.1
A2	158	32	w	752.78	1.011	1.028	1.04	1.041	0.428	0.42	273.2	57	168.1	9.6	72.2	31.3
A3	158	32	w	739.8346	1.01	1.03	1.041	1.043	0.49	0.482	262.8	57.1	163.7	5.9	69.9	32.3
B1	158	32	w	702.6679	1.017	1.024	1.042	1.042	0.173	0.163	243.9	56.6	345.3	7.4	80	32.4
B2	158	32	w	730.1422	1.012	1.029	1.041	1.042	0.395	0.387	223.1	52.5	334.2	15.4	74.6	33.2
C1	158	32	w	674.8691	1.014	1.032	1.047	1.048	0.379	0.369	253.2	57.2	163	0.1	72.9	32.8
C2	158	32	w	696.2649	1.014	1.028	1.042	1.043	0.323	0.314	255.2	57.4	346.4	0.7	76.8	32.6
C3	158	32	w	662.3826	1.012	1.038	1.05	1.052	0.51	0.501	240	55.8	337.8	5.2	71.2	33.6

Name	S0 Strike	Dip		Km	L	F	P	Pj	T	U	K1dec	K1inc	K2dec	K2inc	K3dec	K3inc
D1	158	32	w	692.3505	1.012	1.032	1.044	1.046	0.432	0.423	268.1	58	168.5	6	74.9	31.4
E1	158	32	w	734.1512	1.015	1.031	1.046	1.047	0.344	0.334	243.8	58.2	340.9	4.4	73.6	31.4
E2	158	32	w	703.3309	1.01	1.029	1.039	1.041	0.459	0.452	250	60	342	1.1	72.7	29.9
E3	158	32	w	750.6658	1.017	1.022	1.039	1.039	0.148	0.139	259	58.9	161.1	4.8	68.2	30.6
Wy11																
A1	140	10	w	10718.18	1.026	1.062	1.089	1.092	0.408	0.39	317.1	53.8	153.9	35	58.3	8
A2	140	10	w	12731.66	1.026	1.077	1.104	1.109	0.489	0.47	310.5	58.1	146.1	31	51.8	7
B1	140	10	w	11294.78	1.02	1.072	1.093	1.098	0.558	0.543	311	48.4	156.6	38.7	56	13
B2	140	10	w	10402.23	1.026	1.073	1.101	1.104	0.47	0.451	302	43.4	152.8	42.2	47.7	16
C1	140	10	w	13573.26	1.027	1.078	1.107	1.111	0.479	0.459	317.8	56.4	146.5	33.3	53.9	4
C2	140	10	w	10558.51	1.022	1.075	1.098	1.103	0.545	0.528	310.6	55.4	147.7	33.4	52.4	8
D1	140	10	w	11891.74	1.027	1.064	1.093	1.096	0.404	0.385	314.9	52.7	153.1	35.9	56.6	8.8
D2	140	10	w	9567.13	1.02	1.075	1.097	1.103	0.568	0.552	312	50.2	153.6	37.7	55.1	10.7
E1	140	10	w	11905.14	1.029	1.059	1.089	1.091	0.33	0.311	307.4	75.9	144.7	13.5	53.8	4
E2	140	10	w	12678.19	1.03	1.071	1.103	1.106	0.404	0.383	304.2	59	147.5	28.8	51.8	10.3
F1	140	10	w	12657.58	1.031	1.068	1.101	1.104	0.371	0.351	302.9	59.4	145.9	28.6	50.3	10.1
F2	140	10	w	11121.89	1.022	1.07	1.093	1.098	0.518	0.501	311.2	54.3	149.3	34.3	53.4	8.6
Wy12																
A1	90	10	w	1000.113	1.063	1.072	1.139	1.14	0.066	0.033	145.7	5.1	244.6	60.3	52.9	29.2
B2	90	10	w	760.1301	1.057	1.06	1.12	1.12	0.021	-0.007	314.8	3.3	220.1	54.4	47.1	35.4
A3	90	10	w	586.6854	1.067	1.055	1.126	1.126	-0.098	-0.127	116.7	3.5	217.4	71.9	25.6	17.8
B1	90	10	w	1109.35	1.059	1.097	1.161	1.163	0.235	0.199	124.7	27.9	259.7	53.2	22.4	22
A2	90	10	w	512.7671	1.066	1.03	1.099	1.101	-0.364	-0.384	121.8	27.7	248.2	48.5	15.4	28.2
B3	90	10	w	735.4818	1.104	1.109	1.224	1.224	0.022	-0.029	126.6	34.7	272.9	50.2	24.4	17
C1	90	10	w	1155.818	1.037	1.062	1.101	1.102	0.243	0.22	12.9	58.4	123.2	12	219.9	28.7
C3	90	10	w	497.3557	1.078	1.036	1.117	1.119	-0.359	-0.383	72.3	52.5	271	36	174.3	9.1
D1	90	10	w	1236.081	1.064	1.073	1.141	1.141	0.065	0.032	128.2	20.4	265.1	63	31.7	16.9
D2	90	10	w	476.819	1.056	1.071	1.131	1.131	0.108	0.077	119	6.5	224.8	67.3	26.4	21.7
D3	90	10	w	806.2901	1.107	1.077	1.193	1.193	-0.153	-0.195	113.4	4	218	74.5	22.4	15
WY13																
A1	166	32	w	747.4097	1.01	1.003	1.013	1.013	-0.497	-0.5	228.1	37.2	36.5	52.2	133.8	5.6
A2	166	32	w	731.9874	1.006	1.004	1.011	1.011	-0.205	-0.207	349.3	10.8	87.9	38	246.1	50

Name	S0 Strike	Dip		Km	L	F	P	Pj	T	U	K1dec	K1inc	K2dec	K2inc	K3dec	K3inc
B1	166	32	w	731.2331	1.009	1.005	1.013	1.013	-0.298	-0.301	349.6	20.2	94.8	35.6	236	47.4
B2	166	32	w	769.9993	1.006	1.003	1.009	1.01	-0.394	-0.396	347.2	33.4	81.3	6.3	180.7	55.9
B3	166	32	w	616.0053	1.006	1.002	1.008	1.008	-0.447	-0.448	359	1.7	267.6	39.5	91.1	50.5
C1	166	32	w	763.2806	1.006	1.003	1.009	1.009	-0.37	-0.372	222	55.5	33.7	34.2	126.4	3.8
C2	166	32	w	741.5153	1.006	1.006	1.012	1.012	0.004	0.001	241.3	51.4	24.3	32.5	126.6	18.4
D1	166	32	w	740.2382	1.007	1.004	1.011	1.011	-0.21	-0.212	246.1	77.5	102.7	10.1	11.4	7.3
D2	166	32	w	817.9493	1.007	1.005	1.012	1.012	-0.195	-0.198	217.9	59.1	100.5	15.4	2.7	26.1
E1	166	32	w	608.3309	1.006	1.004	1.01	1.01	-0.245	-0.247	211	15.9	12.2	73.2	119.5	5.1
F1	166	32	w	639.5343	1.007	1.004	1.011	1.011	-0.238	-0.24	167.4	15.2	76	5.3	327.4	73.9
G1	166	32	w	734.7776	1.008	1.005	1.012	1.013	-0.223	-0.226	245.9	45.2	30.8	39.1	136.4	18.4
G2	166	32	w	542.7434	1.008	1.002	1.01	1.011	-0.654	-0.655	246.5	39.5	10.6	34.2	125.6	31.9
WY14																
A1	180	30	w	72.79494	1.049	1.036	1.088	1.088	-0.147	-0.168	250.6	4	155.9	49.7	343.9	40
A2	180	30	w	164.4278	1.018	1.006	1.025	1.026	-0.507	-0.511	19.5	12	119.2	38.4	275.3	49.1
A3	180	30	w	145.8652	1.034	1.022	1.056	1.057	-0.21	-0.223	224.2	2.8	132.5	31.6	318.7	58.2
B1	180	30	w	103.315	1.006	1.06	1.066	1.073	0.812	0.807	266.9	5.4	2.5	45.9	171.7	43.6
B3	180	30	w	110.1119	1.028	1.027	1.056	1.056	-0.032	-0.045	158	16.7	67.7	0.9	334.7	73.3
B3	180	30	w	112.6465	1.027	1.051	1.08	1.081	0.296	0.278	12.6	17.4	106.1	11	226.9	69.2
C1	180	30	w	83.27904	1.022	1.058	1.082	1.084	0.435	0.419	94.9	37.6	356.7	10.4	253.8	50.4
C2	180	30	w	105.7199	1.026	1.022	1.048	1.048	-0.077	-0.088	33.4	16.9	131.7	25.4	273.3	58.8
C3	180	30	w	117.9642	1.019	1.037	1.057	1.058	0.317	0.305	43.5	8.3	148.8	61	309.1	27.6
D1	180	30	w	121.3239	1.02	1.018	1.039	1.039	-0.055	-0.065	183.1	1.3	90.7	62.5	273.7	27.5
D2	180	30	w	128.445	1.039	1.013	1.053	1.055	-0.488	-0.498	224.6	1.4	314.8	8	125.1	81.9
D3	180	30	w	106.8761	1.038	1.023	1.062	1.063	-0.242	-0.256	4.2	3.2	94.8	10.3	257.3	79.2
Wy15																
A1	158	66	w	62.62084	1.045	1.056	1.103	1.104	0.102	0.077	247.8	10.7	136.9	62.1	343	25.5
A2	158	66	w	69.45501	1.08	1.032	1.114	1.118	-0.413	-0.435	226.7	3.4	132.3	52.3	319.3	37.5
B1	158	66	w	54.46886	1.039	1.054	1.095	1.095	0.167	0.145	341.4	6.7	112.4	79.8	250.5	7.6
B2	158	66	w	76.00612	1.022	1.056	1.079	1.082	0.428	0.412	156.2	31.2	61.9	7	320.7	57.8
C1	158	66	w	50.55786	1.064	1.065	1.133	1.133	0.011	-0.02	51.8	14.3	169.8	61.4	315.3	24.2
D1	158	66	w	51.1741	1.053	1.057	1.113	1.113	0.029	0.003	105	71.1	319.4	15.8	226.5	10.2
D2	158	66	w	90.9127	1.016	1.051	1.067	1.07	0.528	0.516	23.4	55.6	256.9	22.2	156	24.9

Name	S0 Strike	Dip		Km	L	F	P	Pj	T	U	K1dec	K1inc	K2dec	K2inc	K3dec	K3inc
E1	158	66	w	56.94088	1.053	1.061	1.117	1.117	0.074	0.046	243.1	0.7	152.1	52.3	333.6	37.7
E2	158	66	w	61.50849	1.061	1.041	1.105	1.106	-0.187	-0.211	240.1	42.7	352.6	22.5	102.1	38.8
E3	158	66	w	88.97585	1.011	1.013	1.024	1.025	0.109	0.103	9.2	26.6	269.7	18.3	149.3	56.9
F1	158	66	w	58.21973	1.037	1.075	1.114	1.117	0.33	0.306	52.1	39.4	196	44.6	305.8	18.9
F2	158	66	w	58.44443	1.052	1.016	1.069	1.072	-0.52	-0.532	251.6	46.1	59.7	43.2	155.3	6
G1	158	66	w	48.06738	1.121	1.078	1.208	1.21	-0.209	-0.254	51.4	24.6	221.1	65.1	319.6	3.9
G2	158	66	w	60.33311	1.051	1.044	1.097	1.097	-0.065	-0.088	202.9	71.4	39.2	17.9	307.6	4.9
G3	158	66	w	89.05838	1.012	1.044	1.057	1.06	0.552	0.543	106.6	33.6	278.1	56.1	13.9	3.9
Wy16																
A1	148	78	w	801.1481	1.011	1.004	1.015	1.015	-0.505	-0.508	53.7	9.4	224.3	80.5	323.5	1.5
A2	148	78	w	1102.862	1.01	1.005	1.015	1.016	-0.294	-0.297	60	7.4	164.4	62.5	326.3	26.3
B1	148	78	w	675.5094	1.011	1.005	1.016	1.017	-0.377	-0.38	55.6	6.5	214.9	83	325.3	2.4
B2	148	78	w	1110.634	1.012	1.004	1.016	1.017	-0.508	-0.511	63.8	23	197.5	58.4	324.7	20.4
C1	148	78	w	887.8396	1.013	1.003	1.016	1.017	-0.636	-0.638	229.7	4.2	139.2	6.4	352.8	82.4
C2	148	78	w	973.301	1.012	1.003	1.015	1.016	-0.571	-0.573	232.8	8.3	323.1	2.4	68.9	81.4
D1	148	78	w	794.8141	1.013	1.005	1.019	1.019	-0.45	-0.454	59.2	9.9	197.1	76.8	327.7	8.7
D2	148	78	w	999.5809	1.011	1.001	1.013	1.014	-0.788	-0.789	64.7	14.3	210.7	72.9	332.4	9.2
E1	148	78	w	912.5336	1.013	1.004	1.017	1.017	-0.559	-0.562	64.6	21.3	230.4	68.1	332.7	4.9
E2	148	78	w	1034.86	1.01	1.005	1.014	1.015	-0.347	-0.35	54.1	18.3	229.7	71.6	323.6	1.3
F1	148	78	w	618.0577	1.01	1.007	1.017	1.017	-0.215	-0.219	52.7	3.2	150.5	68.1	321.4	21.6
F2	148	78	w	993.3121	1.011	1.004	1.015	1.016	-0.462	-0.465	48.9	7.8	249.4	81.7	139.3	2.9
WY18																
A1	164	20	w	61.3633	1.039	1.033	1.073	1.073	-0.078	-0.096	243	27.1	35.2	59.9	146.7	12
A2	164	20	w	205.7688	1.013	1.008	1.021	1.021	-0.201	-0.206	72	9.2	287.6	78.8	163.1	6.4
A4	164	20	w	59.79501	1.024	1.048	1.073	1.074	0.33	0.314	174.6	70.6	74.2	3.6	343	19.1
A4	164	20	w	69.00159	1.03	1.032	1.063	1.063	0.028	0.013	130.3	81.6	9.7	4.3	279.2	7.2
B1	164	20	w	64.29811	1.004	1.03	1.035	1.038	0.74	0.736	205.1	60.9	43.9	27.7	309.7	8
B2	164	20	w	61.1336	1.004	1.052	1.056	1.063	0.846	0.842	217.6	39.3	65.5	47.2	319.6	14.2
B3	164	20	w	60.56068	1.019	1.04	1.059	1.061	0.346	0.334	250.2	21.1	5.6	48.1	145	34.3
B4	164	20	w	70.22393	1.002	1.036	1.038	1.042	0.898	0.896	236.8	22.8	351.4	44.7	128.6	36.5
B5	164	20	w	73.36109	1.024	1.027	1.051	1.051	0.057	0.045	219.1	48.3	63.2	39.1	323.1	12.2
B6	164	20	w	73.05083	1.009	1.03	1.039	1.041	0.546	0.539	263.7	65.1	50	21.1	145	12.6

Name	S0 Strike	Dip		Km	L	F	P	Pj	T	U	K1dec	K1inc	K2dec	K2inc	K3dec	K3inc
B7	164	20	w	67.73775	1.006	1.029	1.035	1.037	0.668	0.663	204	41.7	58.8	42.6	311.1	18.3
B8	164	20	w	86.36004	1.018	1.014	1.032	1.033	-0.129	-0.137	215.2	76.5	103.9	5	12.8	12.5
C1	164	20	w	67.10691	1.038	1.03	1.07	1.07	-0.114	-0.131	185.8	46.4	359.4	43.4	92.4	3.2
C2	164	20	w	59.84058	1.016	1.036	1.052	1.053	0.385	0.374	72.6	5.4	327.5	70	164.4	19.2
C3	164	20	w	60.27801	1.035	1.034	1.07	1.07	-0.024	-0.041	219.1	54.2	26.6	35.2	120.8	5.9
C4	164	20	w	69.74893	1.002	1.042	1.044	1.05	0.903	0.901	85.7	83.8	210.4	3.6	300.7	5.1
C5	164	20	w	73.89298	1.011	1.035	1.047	1.049	0.509	0.5	22.1	3.5	124.4	74	291.2	15.6
Wy19																
A1	168	28	w	142.2617	1.025	1.025	1.051	1.051	0.014	0.002	334.9	41.6	173.8	46.8	73.5	9.5
A2	168	28	w	155.2115	1.033	1.037	1.071	1.071	0.063	0.046	238.9	86.2	134.5	1	44.4	3.7
A3	168	28	w	335.3554	1.012	1.006	1.018	1.019	-0.303	-0.307	289.9	51.5	151.8	30.6	48.7	21
A4	168	28	w	390.1615	1.013	1.004	1.017	1.018	-0.49	-0.493	166.2	64.1	18.8	22.2	283.5	12.6
A5	168	28	w	358.1854	1.017	1.008	1.025	1.026	-0.324	-0.329	145.9	47	289.1	36.7	34.1	19.1
B1	168	28	w	140.8371	1.022	1.013	1.036	1.036	-0.254	-0.263	172.6	69.1	280.1	6.6	12.5	19.8
B2	168	28	w	169.8048	1.017	1.008	1.026	1.026	-0.346	-0.352	228.4	40.9	340.9	23.8	92.4	39.7
B3	168	28	w	288.8326	1.006	1.01	1.017	1.017	0.254	0.25	153.2	59.2	290.4	23.6	28.8	18.6
C1	168	28	w	153.116	1.025	1.02	1.046	1.046	-0.122	-0.133	131.2	66.9	274.3	18.8	8.8	12.9
C2	168	28	w	310.0488	1.007	1.007	1.014	1.014	-0.002	-0.005	223.4	73.8	133.3	0	43.3	16.2
C4	168	28	w	304.1945	1.017	1.012	1.029	1.029	-0.2	-0.207	250.4	58	141.7	11.3	45.2	29.5
C3	168	28	w	328.4731	1.012	1.007	1.019	1.019	-0.262	-0.266	287.4	82.6	190	1	99.9	7.3
C5	168	28	w	358.3419	1.003	1.015	1.018	1.02	0.653	0.65	222.1	57.9	337.7	15.2	75.9	27.5
WY21																
A1	210	28	w	34.27467	1.085	1.259	1.366	1.381	0.477	0.416	275.6	21.7	156.1	51.1	19.2	30.5
A2	210	28	w	22.84453	1.062	1.166	1.238	1.247	0.434	0.39	287.8	23.4	111	66.6	18.3	1.2
A3	210	28	w	-8.79298	1.348	1.33	1.794	1.794	-0.023	0.168	301.7	2.6	191.2	82.5	32	7
B1	210	28	w	47.74824	1.02	1.04	1.06	1.061	0.337	0.324	268.7	26.1	71.1	62.8	175.2	7.1
B2	210	28	w	33.59471	1.081	1.096	1.185	1.185	0.085	0.043	132.3	28.5	232.6	18.1	350.7	55.2
C1	210	28	w	43.62613	1.043	1.071	1.116	1.117	0.242	0.216	314.5	50.2	57.1	10.2	155.2	37.9
C2	210	28	w	21.8874	1.097	1.155	1.267	1.269	0.216	0.159	132.5	1.2	41.9	29.6	224.6	60.4
C3	210	28	w	11.59796	1.121	1.239	1.39	1.397	0.304	0.229	132.6	6.9	15.2	75.4	224.2	12.9
C4	210	28	w	14.41042	1.087	1.457	1.585	1.633	0.636	0.564	322.9	13.6	95.2	70.2	229.4	14.1
D1	210	28	w	48.58082	1.049	1.081	1.133	1.134	0.241	0.212	115.3	13.6	229.3	59.3	18.2	27

Name	S0 Strike	Dip		Km	L	F	P	Pj	T	U	K1dec	K1inc	K2dec	K2inc	K3dec	K3inc
D2	210	28	w	23.41931	1.066	1.075	1.146	1.146	0.057	0.023	312.5	27.1	194.3	42.7	63.7	35.2
D3	210	28	w	15.87947	1.19	1.139	1.355	1.356	-0.145	-0.218	124.3	28.5	6.5	40.6	237.7	36.2
D4	210	28	w	17.07557	1.099	1.344	1.477	1.503	0.515	0.442	12.3	80	132.7	5.1	223.5	8.6
Wy23																
A1	212	24	w	227.9985	1.008	1.007	1.015	1.015	-0.043	-0.047	294.8	51.5	49.3	18.2	151.4	32.6
A2	212	24	w	236.2272	1.018	1.008	1.026	1.026	-0.394	-0.399	280.8	28.2	31	32.8	159.6	44
A3	212	24	w	249.0714	1.009	1.012	1.021	1.021	0.159	0.155	274.5	53	75.2	35.4	171.9	9.3
B1	212	24	w	270.7183	1.009	1.006	1.015	1.015	-0.236	-0.239	13.5	31.9	261.5	31	138.2	42.4
B2	212	24	w	240.1817	1.007	1.015	1.023	1.023	0.34	0.335	225.4	3.7	316.7	19.3	125	70.3
B3	212	24	w	253.9604	1.011	1.001	1.012	1.014	-0.837	-0.838	347.4	32.6	81.6	6.5	181.5	56.6
B4	212	24	w	238.9334	1.006	1.019	1.026	1.027	0.492	0.487	252.3	33.5	25.7	46.1	144.5	24.8
C1	212	24	w	277.8263	1.009	1.011	1.02	1.02	0.137	0.133	231.8	42.1	14.1	41.2	122.6	20
C2	212	24	w	246.1357	1.021	1.002	1.024	1.026	-0.811	-0.813	255.4	22.1	0.3	32.2	137.2	49.3
C3	212	24	w	195.4721	1.025	1.008	1.033	1.035	-0.487	-0.494	274.1	22.1	38.3	54.2	172.4	26.7
D1	212	24	w	265.7539	1.015	1.017	1.032	1.032	0.054	0.046	245.7	43.2	18.1	35.7	128.6	25.9
E1	212	24	w	278.6147	1.004	1.003	1.007	1.007	-0.135	-0.137	215.4	5	310.8	46.9	120.8	42.7
D2	212	24	w	240.3968	1.014	1.015	1.029	1.029	0.05	0.043	282.6	29.7	161.5	42.1	34.8	33.5
WY24																
A1	160	34	w	269.946	1.038	1.142	1.186	1.196	0.561	0.532	288.2	64.7	167.8	13.5	72.5	21
A2	160	34	w	192.0521	1.035	1.146	1.186	1.197	0.598	0.57	308.6	60.1	169.3	23.6	71.4	17.3
A3	160	34	w	245.7909	1.031	1.133	1.168	1.179	0.608	0.583	220.7	68.3	335.8	9.6	69.3	19.3
B1	160	34	w	273.4796	1.033	1.143	1.18	1.192	0.613	0.587	284.5	65.6	168.4	11.3	73.9	21.3
B2	160	34	w	201.7784	1.026	1.11	1.139	1.148	0.602	0.581	225.6	63.1	342.7	13	78.4	23.1
B3	160	34	w	244.4019	1.02	1.116	1.138	1.149	0.696	0.679	290.8	62.5	170.8	14.6	74.5	22.8
B4	160	34	w	256.7455	1.032	1.166	1.203	1.219	0.663	0.636	275.4	66	166.8	8.1	73.4	22.5
C1	160	34	w	261.1927	1.032	1.181	1.219	1.237	0.684	0.658	263.2	63.8	170	1.6	79.2	26.2
C2	160	34	w	184.6745	1.042	1.12	1.168	1.174	0.465	0.434	328.5	32.9	203.9	41.2	81.7	31.3
D1	160	34	w	253.3615	1.031	1.137	1.172	1.184	0.621	0.596	257.7	63.8	348.5	0.4	78.7	26.2
D2	160	34	w	210.6022	1.031	1.12	1.154	1.163	0.577	0.553	265.6	60.6	171.4	2.3	80.1	29.3
E1	160	34	w	275.1655	1.047	1.137	1.191	1.199	0.473	0.438	285.8	60.2	172.6	12.7	76.2	26.4
E2	160	34	w	217.8893	1.028	1.135	1.167	1.179	0.643	0.62	252.6	61.4	346.9	2.3	78.1	28.5
E3	160	34	w	233.5825	1.042	1.154	1.203	1.214	0.551	0.518	281.4	61.2	170.8	10.9	75.3	26.3

Name	S0 Strike	Dip		Km	L	F	P	Pj	T	U	K1dec	K1inc	K2dec	K2inc	K3dec	K3inc
Wy25																
A2	159	40	w	4.209728	2.834	1.696	4.807		-0.327	-0.634	39.7	31.3	156.5	36.6	281.6	37.8
B1	159	40	w	35.49287	1.067	1.092	1.165	1.166	0.154	0.117	30.5	34.8	283.2	23.2	166.7	46.1
B2	159	40	w	46.99791	1.065	1.047	1.115	1.116	-0.154	-0.18	99.8	20.6	0.4	23.5	226.6	57.9
B3	159	40	w	54.78189	1.049	1.095	1.149	1.152	0.311	0.28	42.7	49.7	304.7	6.8	209.1	39.5
C1	159	40	w	43.37339	1.103	1.043	1.151	1.155	-0.397	-0.426	119.1	3.9	28.2	12.8	225.9	76.6
C2	159	40	w	55.11795	1.07	1.039	1.112	1.113	-0.284	-0.309	110.7	7.7	18	18.8	222	69.5
C3	159	40	w	44.10938	1.092	1.089	1.19	1.19	-0.013	-0.056	110	22.8	3.5	34	226.9	47.1
C4	159	40	w	44.47904	1.05	1.075	1.129	1.13	0.196	0.167	129.7	7	38.4	10.5	252.8	77.4
C5	159	40	w	52.18145	1.017	1.12	1.139	1.152	0.741	0.726	331.5	12	71.2	38.3	227.2	49.2
D1	159	40	w	39.13154	1.093	1.11	1.213	1.213	0.084	0.036	116.5	13.2	12.1	46.4	218.1	40.6
D2	159	40	w	33.76532	1.133	1.092	1.238	1.239	-0.172	-0.224	98.5	4.4	1.8	56.1	191.4	33.5
D3	159	40	w	34.86291	1.108	1.091	1.208	1.208	-0.083	-0.13	28	51.8	132.6	11.3	230.9	35.9
D4	159	40	w	42.88226	1.094	1.059	1.159	1.16	-0.225	-0.26	70.6	26.6	335.9	9.2	228.5	61.6
Wy25b																
A1	159	40	w	129.1271	1.018	1.029	1.048	1.048	0.23	0.219	191.5	56.8	344.6	30.3	82	12.3
A2	159	40	w	119.9659	1.019	1.025	1.045	1.045	0.139	0.128	170.6	40.3	1.5	49.2	265.2	5.4
A3	159	40	w	119.2379	1.022	1.023	1.046	1.046	0.027	0.016	1	26.3	203.7	61.8	95.7	9.4
B1	159	40	w	130.392	1.022	1.014	1.036	1.036	-0.237	-0.245	273.1	69	55.3	16.9	149	12.1
B2	159	40	w	120.3382	1.014	1.011	1.025	1.025	-0.109	-0.115	208.9	3.1	303.2	53.5	116.6	36.4
B3	159	40	w	123.7723	1.007	1.029	1.036	1.038	0.599	0.593	244.2	45.4	3.9	26	112.5	33.2
C1	159	40	w	141.6706	1.021	1.013	1.034	1.035	-0.213	-0.221	101.3	83	230	4.4	320.5	5.4
C2	159	40	w	156.1325	1.017	1.026	1.044	1.044	0.208	0.198	189.5	61.1	4.8	28.8	95.9	2
C3	159	40	w	134.6529	1.005	1.019	1.023	1.025	0.605	0.601	247.5	62.8	15.6	17.6	112.3	20
D1	159	40	w	140.8235	1.006	1.012	1.018	1.019	0.352	0.348	335.1	82.1	205.7	5	115.1	6
C2	159	40	w	127.3833	1.02	1.015	1.035	1.035	-0.121	-0.129	177.7	55.8	77.8	6.7	343.4	33.4
D3	159	40	w	103.9332	1.02	1.022	1.043	1.043	0.054	0.043	219.9	2.9	129.5	6.8	332.8	82.6
WY26																
A1	120	30	w	270.081	1.029	1.042	1.072	1.073	0.182	0.165	299.4	3.4	199	71.6	30.6	18.1
A2	120	30	w	206.1092	1.019	1.031	1.05	1.051	0.246	0.235	102.7	38.8	302.3	49.5	200.6	9.8
B1	120	30	w	255.8317	1.018	1.01	1.028	1.028	-0.278	-0.284	193	55.2	286.5	2.4	18.2	34.6
B2	120	30	w	209.8101	1.034	1.033	1.068	1.068	-0.004	-0.021	233.9	73.7	28.3	14.7	120.1	6.7

Name	S0 Strike	Dip		Km	L	F	P	Pj	T	U	K1dec	K1inc	K2dec	K2inc	K3dec	K3inc
B3	120	30	w	233.1622	1.022	1.03	1.053	1.053	0.14	0.128	217.9	62.9	29	26.8	120.8	3.6
B4	120	30	w	198.7738	1.022	1.016	1.039	1.039	-0.161	-0.17	203.4	41.7	68.2	38.6	317.1	24.3
B5	120	30	w	188.5638	1.018	1.028	1.047	1.047	0.215	0.204	197.2	62.9	53.4	22.4	317.3	14.4
C1	120	30	w	238.0808	1.023	1.054	1.078	1.08	0.385	0.369	238.5	59.1	106.3	21.9	7.6	20.7
D1	120	30	w	238.5262	1.026	1.035	1.062	1.062	0.147	0.132	242.5	50.9	123.5	21.5	19.9	30.9
C2	120	30	w	202.5934	1.011	1.021	1.032	1.032	0.327	0.32	237.3	64.1	134.6	6.1	41.8	25.1
WY27																
A1	145	50	w	74.7322	1.045	1.121	1.172	1.178	0.44	0.407	171.7	55.9	70.4	7.6	335.4	33
A2	145	50	w	88.22958	1.038	1.04	1.079	1.079	0.026	0.007	252.2	35.8	156.4	7.9	55.7	53
B1	145	50	w	128.2812	1.013	1.03	1.044	1.045	0.385	0.376	63.4	24.5	301.4	49.3	168.8	30.2
B2	145	50	w	84.75356	1.026	1.02	1.047	1.047	-0.131	-0.142	245.7	52.8	349.8	10.5	87.3	35.2
C1	145	50	w	87.16881	1.034	1.035	1.07	1.07	0.007	-0.01	224.4	30.5	101.1	43	335.8	31.7
C2	145	50	w	130.4566	1.011	1.02	1.032	1.033	0.28	0.273	243.4	39	112.4	39	357.9	27.1
D1	145	50	w	93.85106	1.039	1.103	1.146	1.151	0.439	0.411	58.2	35.6	306.8	26.9	189.2	42.4
D2	145	50	w	64.14973	1.051	1.048	1.101	1.101	-0.032	-0.056	211.6	62.1	30	27.9	120.3	0.7
Wy28																
A1	150	50	w	400.8635	1.004	1.012	1.016	1.017	0.48	0.477	193.4	52.3	293.3	7.6	29	36.6
A2	150	50	w	358.4468	1.009	1.013	1.023	1.023	0.201	0.196	247.1	22.7	346.7	21.8	115.9	57.7
A3	150	50	w	343.2274	1.009	1.009	1.018	1.018	0.027	0.023	244.9	23.4	142.8	25.8	11.3	53.9
B1	150	50	w	444.4184	1.008	1.006	1.014	1.014	-0.169	-0.172	217.2	16.8	309.4	7	61.1	71.7
B2	150	50	w	361.5576	1.01	1.008	1.018	1.018	-0.146	-0.15	212.4	13.9	312.4	35.1	104.3	51.5
B3	150	50	w	327.3288	1.016	1.019	1.035	1.035	0.091	0.082	214.7	33.2	121.3	5.2	23.5	56.3
B4	150	50	w	347.1352	1.011	1.015	1.027	1.027	0.13	0.123	229.2	38	342.3	26.7	97.6	40.3
C1	150	50	w	450.3763	1.013	1.008	1.02	1.02	-0.25	-0.254	212.7	24.7	316.7	27.7	87.7	51.3
C2	150	50	w	366.7023	1.009	1.01	1.019	1.019	0.054	0.049	229.3	58.6	113.5	14.9	15.8	27
C3	150	50	w	434.7207	1.013	1.009	1.021	1.022	-0.173	-0.178	196.4	42.5	296.1	10.4	36.9	45.7
C4	150	50	w	348.1292	1.012	1.011	1.023	1.023	-0.026	-0.031	224.5	13.9	322.9	30.6	113.2	55.7
D2	150	50	w	328.7331	1.018	1.007	1.025	1.026	-0.47	-0.475	200.5	21.8	299.9	22.1	70.6	58
D1	150	50	w	434.6869	1.006	1.016	1.022	1.023	0.421	0.416	207.8	57.7	16	31.8	109.3	5.3
D3	150	50	w	321.2441	1.02	1.01	1.03	1.03	-0.334	-0.34	191.5	25.6	304.9	39.7	78.2	39.6

Name	S0 Strike	Dip		Km	L	F	P	Pj	T	U	K1dec	K1inc	K2dec	K2inc	K3dec	K3inc
Wy29																
A1	220	30	w	75.86481	1.038	1.015	1.054	1.055	-0.416	-0.426	352.7	6.6	260	21.7	98.7	67.2
A2	220	30	w	65.65037	1.051	1.06	1.114	1.114	0.075	0.048	7.9	75.3	243.1	8.5	151.3	11.9
A31	220	30	w	73.39439	1.051	1.031	1.084	1.084	-0.244	-0.263	206	25.1	78.4	52.5	309.1	25.9
B2	220	30	w	53.63769	1.03	1.046	1.078	1.079	0.207	0.189	333.3	73.4	189.5	13.5	97.2	9.4
B22	220	30	w	69.24392	1.027	1.049	1.077	1.078	0.286	0.269	202.8	59.8	335.8	21.7	74.1	20
B3	220	30	w	57.52927	1.022	1.156	1.182	1.199	0.735	0.715	32.5	18.4	264	61.9	129.6	20.5
C1	220	30	w	75.72079	1.037	1.033	1.071	1.071	-0.054	-0.071	231.2	49	335.5	12.1	75.2	38.4
C2	220	30	w	58.23813	1.064	1.067	1.135	1.135	0.026	-0.006	251.6	78.4	1.4	4	92.1	10.9
C3	220	30	w	56.18268	1.047	1.055	1.104	1.104	0.076	0.052	267.5	41.4	15.4	19.3	124	42.3
D1	220	30	w	84.68362	1.036	1.063	1.102	1.103	0.264	0.241	261	32.9	358	10.6	103.5	55
D2	220	30	w	55.09363	1.024	1.104	1.13	1.138	0.613	0.594	312.3	53.9	201.5	14.5	102.1	32.2
D3	220	30	w	60.79837	1.035	1.057	1.094	1.095	0.242	0.221	258.2	46.5	71.7	43.3	164.7	3.3
D4	220	30	w	51.48982	1.088	1.062	1.156	1.157	-0.169	-0.204	228.9	41.3	1.2	37.5	113.3	26.2
Wy30																
A1	170	22	w	198.2597	1.02	1.042	1.063	1.064	0.343	0.329	295.9	72.2	177.2	8.7	84.8	15.3
A2	170	22	w	205.4613	1.014	1.041	1.056	1.058	0.489	0.479	190.3	47.1	348.2	40.8	88	11.2
A3	170	22	w	193.7098	1.022	1.03	1.052	1.053	0.157	0.144	192.4	27.3	3.6	62.4	100.5	3.6
B1	170	22	w	212.3716	1.05	1.028	1.079	1.08	-0.271	-0.289	353.7	1.3	259.7	72.7	84.1	17.2
B2	170	22	w	188.1402	1.021	1.041	1.063	1.064	0.315	0.301	184.2	55.9	347.6	32.9	82.6	7.7
C1	170	22	w	197.8675	1.015	1.029	1.045	1.045	0.308	0.298	176.2	29.6	329.2	57.5	79.2	12.2
C2	170	22	w	184.1448	1.027	1.044	1.073	1.074	0.237	0.22	216.4	57.3	346.6	22.5	86.5	22.4
D1	170	22	w	215.7253	1.028	1.03	1.059	1.059	0.046	0.032	189	32.8	339.3	53.4	89.5	14.4
D2	170	22	w	182.1766	1.039	1.038	1.079	1.079	-0.01	-0.029	186.9	37.7	336.6	48.2	84.5	15.4
E1	170	22	w	203.8501	1.022	1.043	1.065	1.067	0.314	0.3	182.5	26.8	307.9	49	76.6	28.5
E2	170	22	w	245.3982	1.02	1.055	1.076	1.078	0.467	0.453	188.8	48.2	354.2	40.8	90.6	7.3
E3	170	22	w	216.639	1.029	1.048	1.078	1.079	0.254	0.236	192.8	45.9	340.2	39.2	84.5	16.9

Block Samples

Anisotropy of Magnetic Susceptibility Data from Wyoming Salient																				
SITE	Bulk sus	N	K1	K2	K3	Km	K1	*K1 95%*	K2	*K2 95%*	K3	*K3 95%*	L	F	P	Pj	T	U		
							Dec/Inc	*Error*	Dec/Inc	*Error*	Dec/Inc	*Error*								
WY1	4.48E-04	12	1.003	1.002	0.995	1.000	**92.4/49.3**	56.9/20.9	**241.9/36.6**	57/20.1	**343.7/15.4**	21.6/19.5	1.002	1.01	1.01	1.01	0.622	0.621		
WY2	4.10E-04	14	1.004	1	0.996	1.000	**87.6/23.2**	22.8/14.8	**286.6/65.6**	28.3/21.7	**180.6/7.1**	28.3/15.9	1.004	1	1.01	1.01	-0.02	-0.02		
WY4	9.48E-05	15	1.01	0.998	0.993	1.000	**248.4/16.9**	53.9/32.6	**19.3/65.1**	66.7/50.2	**152.8/17.7**	65.9/34.4	1.012	1.01	1.02	1.02	-0.42	-0.42		
WY3	5.06E-05	20	1.02	0.999	0.981	1.000	**238.4/10.6**	34.2/14.5	**17/76**	41.3/32.4	**146.7/9.1**	40.7/15.1	1.021	1.02	1.04	1.04	-0.07	-0.08		
WY6	3.07E-04	16	1.018	1.001	0.981	1.000	**190.4/25.8**	14.9/9.8	**324.3/55.1**	15.5/10.8	**89.3/21.8**	12.6/10.1	1.017	1.02	1.04	1.04	0.071	0.061		
WY7	3.60E-04	12	1.008	0.999	0.992	1.000	**250.3/48.1**	18.2/12.6	**352.1/10.4**	26.1/17.8	**91/40**	27/9.3	1.009	1.01	1.02	1.02	-0.15	-0.16		
WY10	7.09E-04	12	1.018	1.005	0.977	1.000	**251.3/57.7**	7/1.3	**342.6/.8**	7/2.3	**73.1/32.3**	2.4/1.4	1.013	1.03	1.04	1.04	0.385	0.376		
WY8	7.15E-04	15	1.009	1.002	0.989	1.000	**255.8/42.8**	27.6/10.3	**142.4/23.2**	27.3/13.2	**32.7/38.3**	13.9/10.8	1.007	1.01	1.02	1.02	0.344	0.339		
WY9	3.79E-04	5	1.008	1.002	0.99	1.000	**203.8/59**	38.1/10.8	**38.6/30.1**	40.9/8.1	**304.8/6.5**	21.5/11	1.007	1.01	1.02	1.02	0.29	0.286		
WY11	1.16E-02	12	1.039	1.014	0.948	1.000	**309.7/56.1**	8.1/3.2	**149.1/32.4**	8/2.1	**53.3/9**	3.7/2.5	1.024	1.07	1.1	1.1	0.479	0.461		
WY12	8.07E-04	11	1.051	1.001	0.948	1.000	**122.9/16.8**	20.7/11.6	**262.5/68.4**	21.9/17.9	**28.8/13.2**	21.3/12	1.05	1.06	1.11	1.11	0.043	0.017		
WY13	7.07E-04	13	1.002	1	0.998	1.000	**22.1/39.7**	54.6/17.1	**352.6/38.1**	56.2/25	**106.6/27.4**	34.8/16.4	1.002	1	1	1	0.089	0.088		
WY14	1.14E-04	12	1.018	1.001	0.981	1.000	**39/10.7**	38.2/19.5	**132.2/16.3**	38/29.2	**277.2/70.4**	29.9/20	1.016	1.02	1.04	1.04	0.118	0.109		
WY29	6.44E-05	13	1.031	1.006	0.963	1.000	246.4/55.3	34.9/15.8	13/22.5	35.1/26	114.2/25	26.6/16.3	1.025	1.05	1.07	1.07	0.279	0.263		
WY30	2.04E-04	12	1.025	1.007	0.967	1.000	187.4/37.3	26.4/3.8	338.3/48.9	26.4/7.7	85.8/14.7	7.8/3.7	1.018	1.04	1.06	1.06	0.391	0.378		
WY24	2.37E-04	14	1.062	1.032	0.906	1.000	280/63.5	15.9/3.2	170.3/9.9	15.9/3.8	75.8/24.3	4.9/1.2	1.029	1.14	1.17	1.18	0.645	0.621		
WY23	2.48E-04	13	1.008	0.999	0.993	1.000	265.5/34.6	21.2/16.6	20.7/31.8	26.2/19.2	141.2/39.2	25.1/17	1.008	1.01	1.02	1.02	-0.1	-0.1		
WY21	2.51E-05	13	0.932	0.858	0.749	0.846	125.5/4.8	26.6/13.2	335.3/84.4	28.6/24.6	215.7/2.8	28.4/7.7	1.087	1.15	1.25	1.25	0.24	0.188		
WY25	4.09E-05	13	1.097	0.998	0.904	1.000	52/34.4	37.3/7.5	320.2/2.6	41.8/12.3	226.5/55.4	27.6/7.1	1.099	1.1	1.21	1.21	0.023	-0.03		
WY25b	1.29E-04	12	1.009	1.003	0.988	1.000	205.9/52.5	52.8/21.5	7.9/36.1	52.8/19.7	104.3/8.7	22.8/18.4	1.006	1.02	1.02	1.02	0.404	0.4		
WY26	2.20E-04	10	1.018	0.988	0.984	0.997	217.1/65.5	15.3/11.6	102.9/10.6	38.6/13.4	8.6/21.8	38.5/12.5	1.02	1.01	1.03	1.03	-0.19	-0.2		
WY28	3.76E-04	14	1.009	0.998	0.992	1.000	215.8/31.4	17.6/14	315.9/16	33.7/17	69.0/53.9	33.7/13.7	1.011	1.01	1.02	1.02	-0.27	-0.28		
WY27	9.40E-05	8	1.016	1.003	0.981	1.000	235.9/34.9	59.6/16.7	86.6/50.9	59.6/37.1	336.9/15.3	43.2/18.9	1.013	1.02	1.04	1.04	0.255	0.247		
WY16	9.09E-04	12	1.009	0.997	0.994	1.000	56.6/8.4	11.6/3.7	177.5/74	15.7/10.1	324.6/13.5	14.9/3.8	1.011	1	1.02	1.02	-0.55	-0.55		
WY19	2.64E-04	13	1.011	0.999	0.99	1.000	213.2/75.8	25.3/15.3	317.6/3.6	37.8/15.6	48.5/13.7	34.2/15.4	1.012	1.01	1.02	1.02	-0.09	-0.1		
WY18	7.55E-05	17	1.014	1.005	0.981	1.000	223.3/54.9	42.4/16.2	47.6/35	41.2/21.8	316.2/2	23.9/18.7	1.009	1.02	1.03	1.04	0.445	0.438		
WY15	6.55E-05	16	1.019	1.008	0.973	1.000	54.1/11.8	60/18.1	184.8/72.3	60./25.9	321.3/13.1	26/19	1.011	1.04	1.05	1.05	0.509	0.5		

Strain Analysis Data

	I'cepts P			I'cepts T			SPO			DTNNM		MRL	
Site	R	Phi	Phi'	R	Phi	Phi'	R	Phi	Phi'	R	Phi	R	Phi
Bridger													
WY1													
WY2	1.031	101.2	-11.2	1.049	82.95	7.05	1.041	87.44	2.56	1.04323	8.10265	1.04946	2.47493
WY4													
WY3	1.037	23.32	66.68	1.1	83.57	6.43	1.04	65.85	24.15	1.12508	14.114	1.06334	19.1523
WY6													
WY7	1.03	144.49	-54.49	1.058	122.23	-32.23	1.051	121.44	-31.44	1.09399	132.442	1.06167	-40.4211
WY10	1.011	167.67	-77.67	1.174	96.94	-6.94	1.141	94.88	-4.88	1.11921	135.93	1.19688	-11.7182
WY8	1.045	78.78	11.22										
WY9													
WY11	1.009	155.79	-65.79	1.033	106.01	-16.01	1.113	102.89	-12.89	1.16032	17.283	1.0773	-10.6058
WY12	1.042	168.81	-78.81	1.104	109.22	-19.22	1.101	112.75	-22.75	1.1329	133.719	1.13565	-20.3758
WY13													
WY14													
Jackson													
WY29													
WY30	1.066	46.37	43.63	1.124	32.66	57.34	1.105	39.82	50.18	1.05324	58.453	1.11913	47.7652
WY24	1.049	84.54	5.46	1.053	61.25	28.75	1.091	77.68	12.32	1.13022	166.027	1.11853	2.16845
WY23													
WY21	1.022	173.57	83.57	1.058	6.25	83.75	1.048	0.04	89.96	1.04819	75.1023	1.05087	81.4585
WY25	1.018	44.97	45.03	1.057	17.16	72.84	1.054	17.73	72.27	1.18756	177.934	1.05798	67.6917
WY25b													
WY26	1.024	170.44	-80.44	1.107	160.49	-70.49	1.202	156.38	-66.38	1.42921	125.563	1.1026	114.0985
WY28	1.006	97.7	-7.7	1.028	44.8	45.2	1.056	79.09	10.91	1.06611	63.6711	1.02582	18.877
WY27	1.039	90.1	-0.1	1.085	85.41	4.59	1.16	96.07	-6.07	1.33701	#REF!	1.11564	179.8752
WY16													
WY19													
WY18	1.025	92.53	-2.53	1.055	78.19	11.81	1.154	92.68	-2.68	1.13161	176.846	1.06072	179.9354
WY15	1.025	70	20	1.058	57.97	32.03	1.054	112.56	-22.56	1.14603	26.7307	1.00874	125.874

Lat/Long Data for Sevier Samples

WGS 84	Lat/Lon hddd−mm.mmm'		
Name	Position	Altitude	Date Modified
WY1	N42 30.633 W110 30.510	2415 m	7/21/2012 3:31:23 AM
WY10	N42 33.983 W110 44.142	2676 m	7/21/2012 10:33:49 PM
WY11	N42 30.099 W110 47.312	2392 m	7/21/2012 10:57:16 PM
WY12	N42 29.409 W110 50.539	2322 m	7/21/2012 11:25:33 PM
WY13	N42 31.767 W110 53.823	2207 m	7/22/2012 12:30:54 AM
WY14	N42 31.651 W110 53.942	2200 m	7/22/2012 12:50:31 AM
WY15	N43 10.599 W110 59.690	1716 m	7/22/2012 2:58:00 AM
WY16	N43 12.370 W110 50.735	1769 m	7/22/2012 7:57:49 PM
WY18	N43 12.208 W110 51.676	1778 m	7/22/2012 9:20:55 PM
WY19	N43 12.232 W110 51.632	1777 m	7/22/2012 9:19:08 PM
WY2	N42 30.633 W110 30.513	2415 m	7/21/2012 3:43:07 AM
WY21	N43 20.802 W110 49.361	1931 m	7/23/2012 6:11:00 PM
WY23	N43 20.925 W110 49.611	1942 m	7/23/2012 6:35:54 PM
WY24	N43 17.881 W110 47.977	1820 m	7/23/2012 6:58:08 PM
WY241	N43 17.883 W110 47.974	1818 m	7/23/2012 7:06:23 PM
WY25	N43 14.105 W110 46.773	1791 m	7/23/2012 7:33:36 PM
WY251	N43 13.881 W110 46.856	1781 m	7/23/2012 7:42:55 PM
WY26	N43 13.971 W110 46.761	1784 m	7/23/2012 7:49:32 PM
WY27	N43 12.870 W110 47.201	1775 m	7/23/2012 8:05:03 PM
WY28	N43 12.900 W110 47.159	1775 m	7/23/2012 8:09:29 PM
WY29	N43 16.356 W110 31.581	1932 m	7/23/2012 9:58:15 PM
WY3	N42 30.010 W110 31.339	2423 m	7/21/2012 6:00:38 PM
WY30	N43 16.983 W110 32.018	1927 m	7/23/2012 10:14:14 PM
WY4	N42 30.463 W110 30.918	2412 m	7/21/2012 6:23:36 PM
WY6	N42 27.610 W110 35.083	2502 m	7/21/2012 8:02:19 PM
WY7	N42 27.198 W110 35.016	2459 m	7/21/2012 8:14:18 PM
WY8	N42 34.573 W110 44.056	2763 m	7/21/2012 10:01:53 PM
WY9	N42 34.727 W110 44.330	2749 m	7/21/2012 10:22:40 PM

Appendix 4: AMS and strain data for Chapter 6; Eastern Munster Basin, Southern Ireland

The AMS and strain data for the samples collected in the Eastern Munster Basin are presented here.

Individual Specimens

Name	Strike	Dip		Km		L	F	P	Pj	T	U	K1dec	K1inc	K2dec	K2inc	K3dec	K3inc
BB1																	
C1	060	15	s	624.6152	6.25E-04	1.002	1.021	1.023	1.026	0.86	0.859	28	20	293.4	12.5	173.4	66.1
B4	060	15	s	663.7663	6.64E-04	1.004	1.016	1.02	1.021	0.638	0.636	309.6	37.2	55.8	20.2	168.1	45.8
C3	060	15	s	684.2169	6.84E-04	1.005	1.024	1.029	1.032	0.659	0.655	41.7	9.6	308.5	18.4	157.9	69.1
D4	060	15	s	613.4778	6.13E-04	1.005	1.016	1.021	1.022	0.544	0.54	48.5	6.4	315.8	23.3	152.9	65.8
F3	060	15	s	446.1609	4.46E-04	1.021	1.01	1.031	1.032	-0.353	-0.36	199	67.3	25	22.6	294.1	2.1
A4	060	15	s	714.7488	7.15E-04	1.002	1.021	1.023	1.025	0.819	0.817	320	17.1	53.1	9.9	172	70
A3	060	15	s	543.0392	5.43E-04	1.007	1.019	1.026	1.027	0.442	0.436	290.7	15.6	23	8.2	139.9	72.3
B2	060	15	s	354.7134	3.55E-04	1.002	1.016	1.018	1.02	0.761	0.76	6.8	18.3	98.9	6.5	207.8	70.5
F4	060	15	s	716.6498	7.17E-04	1.003	1.024	1.027	1.029	0.762	0.759	43.9	8.6	310.6	20.8	155	67.3
D3	060	15	s	742.1351	7.42E-04	1.004	1.027	1.031	1.034	0.747	0.743	29.3	13.7	294.9	17.2	155.7	67.7
C2	060	15	s	430.3454	4.30E-04	1.007	1.021	1.028	1.029	0.522	0.517	120.7	7.1	29.7	7.8	252.6	79.4
D1	060	15	s	289.3835	2.89E-04	1.011	1.025	1.037	1.038	0.376	0.368	40.6	3.3	309.7	16.1	142	73.6
B3	060	15	s	497.0417	4.97E-04	1.009	1.01	1.019	1.019	0.064	0.059	279.9	0.4	10.1	30.8	189.3	59.2
D2	060	15	s	652.7183	6.53E-04	1.011	1.03	1.042	1.043	0.45	0.442	50.2	10.5	316.9	17.1	170.5	69.7
F1	060	15	s	323.5916	3.24E-04	1.157	1.05	1.216	1.225	-0.496	-0.532	157.8	14.3	11.9	73	250.2	9.2
BB2																	
B2	084	70	s	933.8539	9.34E-04	1.015	1.025	1.041	1.041	0.247	0.238	354.2	2.6	258.3	65.9	85.4	24
F1	084	70	s	853.9769	8.54E-04	1.014	1.016	1.03	1.03	0.047	0.04	173.3	6.1	271.3	52.4	78.8	36.9
C2	084	70	s	939.4805	9.39E-04	1.018	1.028	1.047	1.047	0.214	0.203	1.3	0.8	269	71.4	91.5	18.6
F2	084	70	s	894.2619	8.94E-04	1.023	1.027	1.05	1.05	0.077	0.065	177.5	3.3	278.5	73.4	86.5	16.3
G2	084	70	s	944.9767	9.45E-04	1.011	1.016	1.028	1.028	0.204	0.197	5.7	4.4	271.9	40.4	100.9	49.3
AY	084	70	s	790.2114	7.90E-04	1.02	1.015	1.036	1.036	-0.146	-0.155	183	2.7	279.3	66.9	91.9	22.9
F6	084	70	s	893.3929	8.93E-04	1.009	1.022	1.031	1.032	0.401	0.395	277.9	14.1	167.4	54.3	16.9	32
A3	084	70	s	857.4595	8.57E-04	1.012	1.024	1.036	1.037	0.32	0.312	109.5	8	216.6	64.5	15.9	24
X1	084	70	s	1039.433	1.04E-03	1.011	1.03	1.041	1.043	0.464	0.456	17.1	3.3	278.8	68.2	108.4	21.5
E12	084	70	s	888.461	8.88E-04	1.016	1.018	1.035	1.035	0.059	0.051	343.9	1.4	251.3	60.4	74.7	29.5
A3	084	70	s	904.7242	9.05E-04	1.015	1.022	1.037	1.038	0.187	0.178	2.1	2.7	265.3	68.7	93.2	21.1
AX	084	70	s	840.3334	8.40E-04	1.013	1.032	1.045	1.047	0.402	0.393	293.7	1.8	197.7	73.5	24.2	16.4
A1	084	70	s	985.5107	9.86E-04	1.022	1.011	1.034	1.034	-0.332	-0.339	276.7	8.4	178.3	44.8	14.8	43.9
A2	084	70	s	833.0176	8.33E-04	1.017	1.024	1.041	1.041	0.167	0.157	3.4	5	256.4	73.4	94.8	15.8
C1	084	70	s	895.4203	8.95E-04	1.016	1.024	1.041	1.041	0.21	0.2	182	3.4	278.6	62.5	90.3	27.3

Name	Strike	Dip		Km		L	F	P	Pj	T	U	K1dec	K1inc	K2dec	K2inc	K3dec	K3inc
G1	084	70	s	912.3546	9.12E-04	1.017	1.012	1.029	1.029	-0.169	-0.176	189	5	283.2	40.1	93.1	49.5
B1	084	70	s	846.5901	8.47E-04	1.016	1.023	1.039	1.04	0.167	0.158	353.6	0.7	262.5	57.6	84	32.4
F5	084	70	s	883.7181	8.84E-04	1.011	1.025	1.036	1.037	0.386	0.378	171	5.8	274.5	66.5	78.6	22.6
B3	084	70	s	954.7332	9.55E-04	1.017	1.024	1.041	1.042	0.182	0.172	175.5	8.9	289.8	69.1	82.4	18.7
H1	084	70	s	879.7899	8.80E-04	1.02	1.017	1.037	1.037	-0.073	-0.082	172.3	4	269.5	60.4	80.1	29.3
BB3																	
B2	082	52	s	133.5808	1.34E-04	1.1	1.136	1.249	1.25	0.144	0.09	182.4	63.5	88.1	2.1	357.1	26.4
C2	082	52	s	128.837	1.29E-04	1.014	1.055	1.07	1.074	0.582	0.571	126.3	4.1	33.3	36	221.9	53.7
F2	082	52	s	125.3315	1.25E-04	1.007	1.035	1.042	1.045	0.683	0.678	20	45.8	124.1	13.4	226.1	41.1
G1	082	52	s	266.897	2.67E-04	1.02	1.083	1.104	1.111	0.609	0.594	259.3	6.1	168.4	8.4	24.7	79.6
F1	082	52	s	127.4221	1.27E-04	1.035	1.037	1.073	1.073	0.016	-0.002	23.3	16.2	119.6	20.8	258.3	63.2
A2	082	52	s	221.9925	2.22E-04	1.001	1.009	1.01	1.011	0.749	0.748	225.3	38.7	329.7	17.2	78.6	46.2
D2	082	52	s	133.5926	1.34E-04	1.013	1.076	1.09	1.097	0.698	0.687	273.2	4.8	3.9	8.3	153.5	80.4
D1	082	52	s	156.6311	1.57E-04	1.024	1.015	1.039	1.04	-0.228	-0.237	129	12.9	35.9	13.4	261.5	71.3
A1	082	52	s	210.437	2.10E-04	1.005	1.018	1.023	1.024	0.575	0.571	19.7	7.2	118.8	51.4	284.1	37.7
B1	082	52	s	225.203	2.25E-04	1.032	1.062	1.096	1.097	0.319	0.298	81	58.4	244.5	30.6	338.9	7.4
C1	082	52	s	280.6768	2.81E-04	1.046	1.017	1.065	1.067	-0.448	-0.461	181.9	1.7	80.2	81.5	272.1	8.3
F3	082	52	s	187.8055	1.88E-04	1.007	1.031	1.038	1.04	0.642	0.637	334.1	5.2	242.8	13.7	84.5	75.3
BB4																	
A1	094	44	s	608.4869	6.08E-04	1.021	1.024	1.045	1.045	0.077	0.066	344.6	6.7	78.3	28.6	242.5	60.5
C2	094	44	s	334.1867	3.34E-04	1.001	1.033	1.034	1.039	0.916	0.915	327.9	5.9	60.7	24.9	225.6	64.3
B2	094	44	s	378.5818	3.79E-04	1.009	1.025	1.035	1.036	0.467	0.46	1.5	10.8	91.9	2	192	79
A3	094	44	s	279.2639	2.79E-04	1.004	1.016	1.019	1.021	0.616	0.613	103.7	29.4	2.2	19.5	243.5	53.6
B2	094	44	s	305.0193	3.05E-04	1.009	1.014	1.023	1.023	0.176	0.17	27.5	20.4	294.3	8.4	183.2	67.8
A2	094	44	s	342.7959	3.43E-04	1.021	1.013	1.034	1.035	-0.243	-0.251	26.1	17.5	121.5	16.7	252.6	65.4
B4	094	44	s	262.4803	2.62E-04	1.008	1.01	1.018	1.018	0.107	0.103	102.1	53.6	349.4	15.9	249.2	31.8
B4	094	44	s	219.1389	2.19E-04	1.01	1.014	1.025	1.025	0.174	0.168	156.7	30.5	19.4	51.3	260	21.4
B1	094	44	s	278.5435	2.79E-04	1.016	1.018	1.034	1.034	0.05	0.042	356.6	23.8	92.6	13.3	209.5	62.3
B1	094	44	s	594.4511	5.94E-04	1.01	1.04	1.051	1.054	0.584	0.576	348.3	8.4	78.7	2.5	184.8	81.2
C5	094	44	s	228.524	2.29E-04	1.005	1.009	1.014	1.014	0.246	0.243	174	17.3	345.4	72.5	83.2	2.5
B3	094	44	s	307.6792	3.08E-04	1.009	1.019	1.028	1.029	0.367	0.361	354.7	16.4	86.8	7	199	72.1
X1	094	44	s	295.2563	2.95E-04	1.01	1.019	1.029	1.03	0.322	0.316	346.1	17.1	86.9	31.4	231.7	53.3

Name	Strike	Dip		Km		L	F	P	Pj	T	U	K1dec	K1inc	K2dec	K2inc	K3dec	K3inc
C1	094	44	s	627.1447	6.27E-04	1.004	1.083	1.087	1.099	0.911	0.907	39.6	10.2	130.3	3.6	239.3	79.2
C2	094	44	s	621.0984	6.21E-04	1.002	1.014	1.015	1.017	0.786	0.785	102.3	1.9	11.9	12.7	200.5	77.2
C1	094	44	s	578.1221	5.78E-04	1.002	1.029	1.031	1.034	0.866	0.865	298.3	10.3	207.2	6.3	86.4	77.9
A2	094	44	s	575.824	5.76E-04	1.003	1.014	1.017	1.018	0.637	0.635	320.3	7	228.4	15	74.6	73.4
B3	094	44	s	612.269	6.12E-04	1.004	1.014	1.018	1.019	0.569	0.566	311	5.7	220.8	1.2	119.3	84.1
B2	094	44	s	596.2944	5.96E-04	1.007	1.014	1.021	1.021	0.329	0.324	188.8	2.1	279.1	8.9	85.5	80.8
D1	094	44	s	529.2285	5.29E-04	1.015	1.02	1.035	1.035	0.158	0.149	178.4	8.5	269	3.7	22	80.7
A1	094	44	s	578.5723	5.79E-04	1.003	1.018	1.02	1.022	0.736	0.734	325.7	7	235.4	3.1	121.9	82.4
BB5																	
C3	048	5	s	116.1201	1.16E-04	1.021	1.004	1.025	1.027	-0.703	-0.706	133.3	30.2	224.8	2.7	319.5	59.7
A2	048	5	s	104.7458	1.05E-04	1.022	1.041	1.064	1.065	0.286	0.271	150.6	46.6	19.1	32.1	271.4	25.8
B2	048	5	s	110.4745	1.10E-04	1.019	1.011	1.03	1.031	-0.271	-0.278	32.6	30.7	183.3	55.7	294.3	13.7
C2	048	5	s	85.71486	8.57E-05	1.036	1.01	1.047	1.049	-0.55	-0.558	159.5	66.9	339.2	23.1	69.2	0.1
D1	048	5	s	69.91884	6.99E-05	1.026	1.003	1.029	1.032	-0.804	-0.807	85.5	51.8	199.5	17.8	301.3	32.5
B3	048	5	s	89.7963	8.98E-05	1.018	1.007	1.026	1.026	-0.428	-0.433	283.6	54.3	117.7	34.9	23	6.7
E2	048	5	s	96.22992	9.62E-05	1.006	1.012	1.018	1.018	0.331	0.327	121.9	41.9	257.9	38.7	8.6	23.8
B1	048	5	s	167.5209	1.68E-04	1.119	1.184	1.325	1.328	0.201	0.133	160.8	36.9	5.4	50.5	260.1	12.3
C1	048	5	s	116.0728	1.16E-04	1.019	1.035	1.054	1.055	0.294	0.282	254.5	4.6	345.8	16.6	149.5	72.7
A3	048	5	s	89.06887	8.91E-05	1.037	1.012	1.05	1.052	-0.514	-0.523	119	43.8	219.3	10.6	319.8	44.3
C4	048	5	s	110.6099	1.11E-04	1.024	1.015	1.04	1.04	-0.23	-0.239	292.9	11.5	193.2	39.7	36	48
E1	048	5	s	145.6492	1.46E-04	1.138	1.342	1.527	1.543	0.391	0.299	293	12.5	113	77.5	23	0
BB6																	
D2	170	38	e	422.2632	4.22E-04	1.007	1.009	1.017	1.017	0.095	0.091	9.3	22.7	102.4	7.3	209.2	66
B6	170	38	e	322.3477	3.22E-04	1.009	1.01	1.019	1.019	0.031	0.027	353.5	12.3	84.3	3.5	189.7	77.2
E1	170	38	e	374.6118	3.75E-04	1.008	1.029	1.037	1.039	0.577	0.571	88.4	26.2	178.9	1	270.9	63.8
I2	170	38	e	376.7792	3.77E-04	1.003	1.013	1.016	1.017	0.573	0.57	100.9	9.1	7.6	19.9	214.2	68
F2	170	38	e	373.4799	3.73E-04	1.005	1.01	1.015	1.016	0.304	0.301	341.9	13.1	72.9	4.2	180.4	76.2
B2	170	38	e	386.5477	3.87E-04	1.005	1.014	1.019	1.02	0.48	0.477	111.2	8.9	15.7	31.4	215.3	57.1
D2	170	38	e	392.7376	3.93E-04	1.001	1.017	1.018	1.021	0.878	0.877	312	12.6	44.7	11.9	176.7	72.5
C2	170	38	e	375.9471	3.76E-04	1.002	1.01	1.012	1.013	0.68	0.678	118	5.6	25.8	21.5	221.9	67.8
C1	170	38	e	374.6041	3.75E-04	1.008	1.012	1.02	1.02	0.231	0.226	54.8	25.5	149.1	9.1	257.1	62.7
D3	170	38	e	363.223	3.63E-04	1.005	1.008	1.013	1.014	0.245	0.241	306.6	0.6	36.8	19.4	215	70.6

Name	Strike	Dip		Km		L	F	P	Pj	T	U	K1dec	K1inc	K2dec	K2inc	K3dec	K3inc
D1	170	38	e	363.0927	3.63E-04	1.002	1.023	1.025	1.028	0.84	0.838	21.5	18.6	115	10	231.9	68.6
F3	170	38	e	361.3459	3.61E-04	1.006	1.002	1.008	1.008	-0.532	-0.533	140.1	35.4	251.4	27.1	9.3	42.5
B3	170	38	e	358.3308	3.58E-04	1.006	1.005	1.011	1.011	-0.003	-0.006	307.5	20.6	44.4	17.7	171.9	62.3
H2	170	38	e	371.5454	3.72E-04	1.01	1.006	1.016	1.016	-0.26	-0.264	337.9	45.7	106.8	31.5	215.5	27.6
B1	170	38	e	372.5136	3.73E-04	1.008	1.03	1.038	1.04	0.586	0.579	150.3	1	60.2	7.1	248.3	82.9
BB7																	
E3	150	10	W	748.3964	7.48E-04	1.007	1.042	1.049	1.053	0.701	0.695	269.4	6.7	359.6	1.6	103.3	83.1
F3	150	10	W	647.6721	6.48E-04	1.013	1.032	1.045	1.047	0.401	0.391	264.7	6.6	355.6	7.9	135.2	79.6
D2	150	10	W	922.4034	9.22E-04	1.012	1.037	1.05	1.052	0.494	0.484	274.3	15.8	7.5	11.4	131.8	70.3
E3	150	10	W	770.8661	7.71E-04	1.005	1.047	1.052	1.058	0.809	0.805	269.8	11.4	1.6	9	129.1	75.4
DX	150	10	W	958.9119	9.59E-04	1.014	1.045	1.06	1.062	0.517	0.507	276.4	10.5	8.5	11.6	145.4	74.3
A3	150	10	W	1025.358	1.03E-03	1.015	1.058	1.074	1.078	0.587	0.576	282.6	8.2	13.9	9.1	151.5	77.7
E2	150	10	W	820.4029	8.20E-04	1.01	1.039	1.049	1.052	0.587	0.579	276.8	10.3	186.3	2.7	81.9	79.4
C1	150	10	W	795.9632	7.96E-04	1.012	1.043	1.056	1.059	0.555	0.545	251.9	7.8	342.8	6.7	113	79.7
F1	150	10	W	850.3525	8.50E-04	1.009	1.064	1.074	1.081	0.737	0.728	270.7	9.4	180.1	3.7	69.1	79.9
E2	150	10	W	914.2324	9.14E-04	1.011	1.046	1.057	1.06	0.62	0.611	269.1	12.5	1.5	10.8	131.2	73.3
E3	150	10	W	763.4915	7.63E-04	1.01	1.035	1.046	1.048	0.535	0.527	279.5	6.8	9.6	1	108.1	83.1
D2	150	10	W	865.0405	8.65E-04	1.015	1.039	1.054	1.056	0.454	0.443	287.4	11	18.9	7.4	142.3	76.7
F2	150	10	W	912.7615	9.13E-04	1.014	1.038	1.053	1.055	0.466	0.456	250.9	16.5	342.5	5.6	90.6	72.5
D1	150	10	W	762.2405	7.62E-04	1.013	1.064	1.078	1.084	0.654	0.644	321.3	9.8	230.6	3.8	120	79.4
C2	150	10	W	863.9484	8.64E-04	1.014	1.053	1.068	1.072	0.576	0.565	248.1	11.9	340.1	9	106.3	74.9
BB8																	
A2	230	44	n	893.2313	8.93E-04	1.008	1.011	1.019	1.019	0.13	0.125	179.2	47.1	277.9	8	15.2	41.8
CX	230	44	n	874.0671	8.74E-04	1.009	1.013	1.023	1.023	0.182	0.176	205.1	51.2	295.4	0.3	25.6	38.8
E4	230	44	n	936.5743	9.37E-04	1.009	1.009	1.018	1.018	0.021	0.017	207.9	51.9	113.3	3.6	20.5	37.9
X1	230	44	n	907.6378	9.08E-04	1.007	1.015	1.022	1.022	0.328	0.323	181.6	48.6	288.7	14.5	30.3	37.8
D3	230	44	n	884.2213	8.84E-04	1.011	1.014	1.025	1.025	0.106	0.1	224.7	47.9	131.9	2.5	39.6	41.9
A3	230	44	n	923.5255	9.24E-04	1.004	1.015	1.02	1.021	0.552	0.549	229.7	42	127.9	12.8	24.7	45.2
E3	230	44	n	936.8157	9.37E-04	1.008	1.014	1.022	1.022	0.269	0.264	200.1	48.2	295	4.4	28.9	41.5
D2	230	44	n	931.4727	9.31E-04	1.01	1.01	1.021	1.021	-0.001	-0.006	218.8	43.3	317.7	9.3	57.1	45.2
C2	230	44	n	934.5353	9.35E-04	1.005	1.018	1.023	1.024	0.536	0.532	199.7	47.8	292.5	2.6	24.8	42.1
E2	230	44	n	828.1445	8.28E-04	1.009	1.019	1.028	1.029	0.37	0.364	198.3	48	289.2	0.8	19.9	42

Name	Strike	Dip		Km		L	F	P	Pj	T	U	K1dec	K1inc	K2dec	K2inc	K3dec	K3inc
B1	230	44	n	876.8596	8.77E-04	1.01	1.015	1.025	1.025	0.181	0.175	205.2	50.8	113.6	1.3	22.5	39.2
B3	230	44	n	860.2162	8.60E-04	1.006	1.013	1.019	1.019	0.34	0.336	180.7	51.4	292.5	16.5	33.9	33.8
C1	230	44	n	821.9904	8.22E-04	1.018	1.009	1.027	1.028	-0.34	-0.345	209.1	51.9	85.7	23.4	342.3	28.2
D1	230	44	n	828.4901	8.28E-04	1.007	1.018	1.025	1.026	0.428	0.422	202.3	40.6	297.4	5.9	34.2	48.8
B2	230	44	n	912.6071	9.13E-04	1.008	1.012	1.02	1.02	0.227	0.222	206.6	45.8	111	5.4	15.9	43.7
BB9																	
BB10																	
A3	120	70	s	697.2626	6.97E-04	1.004	1.023	1.027	1.029	0.713	0.71	149.2	3.9	239.3	1.6	351.9	85.8
A2	120	70	s	691.6954	6.92E-04	1.007	1.029	1.036	1.038	0.594	0.589	123.4	4.3	213.6	2.1	330	85.2
B3	120	70	s	735.0358	7.35E-04	1.006	1.027	1.033	1.036	0.654	0.649	329.1	4.8	60.2	12.1	218.1	77
D1	120	70	s	833.5809	8.34E-04	1.005	1.026	1.032	1.034	0.675	0.67	243.5	0.1	153.5	11.1	334	78.9
B2	120	70	s	838.783	8.39E-04	1.011	1.026	1.037	1.038	0.411	0.404	343.1	8.8	75.2	12.9	219.8	74.3
CX	120	70	s	796.2066	7.96E-04	1.008	1.027	1.035	1.036	0.53	0.524	56.3	0.6	146.3	7.6	321.9	82.4
A1	120	70	s	840.2704	8.40E-04	1.002	1.018	1.019	1.022	0.843	0.841	340.5	12.8	250.4	0.6	157.7	77.2
B1	120	70	s	823.3661	8.23E-04	1.007	1.026	1.033	1.035	0.561	0.556	320.3	2.2	50.9	16	222.6	73.9
BB11																	
D3	090	5	s	460.1564	4.60E-04	1.004	1.016	1.021	1.022	0.577	0.574	117.9	2.9	27.6	6	234	83.4
C2	090	5	s	656.9138	6.57E-04	1.006	1.003	1.009	1.009	-0.365	-0.367	98.7	24.7	318.6	59	197.1	17.4
A2	090	5	s	678.4943	6.78E-04	1.008	1.005	1.013	1.013	-0.192	-0.195	80.3	23	173.8	8.2	282.1	65.5
A3	090	5	s	408.4391	4.08E-04	1.002	1.009	1.01	1.011	0.655	0.654	119.6	14	23.1	24.4	236.9	61.4
B2	090	5	s	475.3575	4.75E-04	1.007	1.007	1.014	1.014	0.036	0.033	121.2	2.1	30.5	17.3	218	72.6
B1	090	5	s	309.1342	3.09E-04	1.008	1.003	1.011	1.012	-0.425	-0.428	310.3	6.7	216.3	30.7	51.3	58.4
C3	090	5	s	618.2747	6.18E-04	1.001	1.004	1.005	1.005	0.568	0.567	98.5	14.7	279.3	75.3	188.5	0.2
C1	090	5	s	522.1618	5.22E-04	1.009	1.007	1.016	1.016	-0.075	-0.079	89	24.9	181.5	5.2	282.4	64.5
D2	090	5	s	482.1115	4.82E-04	1.002	1.01	1.012	1.013	0.681	0.679	65.2	29.6	330.6	8.1	226.9	59.1
D1	090	5	s	426.4669	4.26E-04	1.012	1.008	1.021	1.021	-0.181	-0.186	289.4	0.4	19.5	12.8	197.5	77.2
E1	090	5	s	554.8138	5.55E-04	1.01	1.052	1.063	1.068	0.673	0.665	167.6	62.4	352.8	27.5	261.7	2.1
E2	090	5	s	497.2755	4.97E-04	1.007	1.002	1.009	1.009	-0.569	-0.57	47.5	21.5	314.9	6.6	208.8	67.4
E3	090	5	s	420.7094	4.21E-04	1.01	1.005	1.015	1.015	-0.378	-0.381	120.2	22.8	26.8	8	278.6	65.6
BB12																	
B4	108	40	s	840.2451	8.40E-04	1.005	1.008	1.013	1.013	0.181	0.178	53.9	4.8	151	56.2	320.7	33.4
B2	108	40	s	820.5906	8.21E-04	1.005	1.01	1.015	1.015	0.279	0.275	106.3	12.3	14.4	8.4	250.8	75

Name	Strike	Dip		Km		L	F	P	Pj	T	U	K1dec	K1inc	K2dec	K2inc	K3dec	K3inc
B3	108	40	s	700.0523	7.00E-04	1.019	1.014	1.034	1.034	-0.15	-0.158	345.3	28.1	82	12.3	193.2	58.9
X	108	40	s	650.8606	6.51E-04	1.007	1.014	1.021	1.021	0.308	0.303	169.7	13.2	263.8	16.8	43.5	68.4
AX	108	40	s	796.6052	7.97E-04	1.024	1.028	1.053	1.053	0.062	0.049	107.9	14.4	199.2	5.2	308.5	74.6
B1	108	40	s	670.6227	6.71E-04	1.019	1.034	1.054	1.054	0.288	0.276	346.7	0.8	76.9	14	253.5	76
BB13																	
A1	180	24	e	683.5565	6.84E-04	1.027	1.027	1.054	1.054	0.01	-0.003	89.9	8.6	183.4	22	339.9	66.3
A2	180	24	e	644.187	6.44E-04	1.012	1.024	1.036	1.037	0.346	0.338	149.2	22.9	53.8	12.5	297.2	63.5
A2?	180	24	e	609.6984	6.10E-04	1.015	1.02	1.036	1.036	0.135	0.127	211.3	25.8	303.3	4	41.5	63.8
A3	180	24	e	664.5673	6.65E-04	1.014	1.024	1.038	1.039	0.278	0.27	135.3	27.3	42.7	5	303.1	62.2
A3?	180	24	e	619.5032	6.20E-04	1.012	1.026	1.038	1.039	0.353	0.345	210.7	26	304.8	8.5	51.4	62.4
A4	180	24	e	619.0685	6.19E-04	1.013	1.023	1.036	1.037	0.295	0.286	218.6	27.2	311	4.5	49.6	62.4
B1	180	24	e	623.1124	6.23E-04	1.018	1.015	1.034	1.034	-0.077	-0.085	176	19.8	272.8	18.2	42.2	62.5
X	180	24	e	557.7526	5.58E-04	1.015	1.028	1.043	1.043	0.303	0.294	210.1	7	300.3	0.9	37.7	82.9
B2	180	24	e	659.7955	6.60E-04	1.013	1.024	1.037	1.037	0.296	0.288	173.6	23.6	267	7.8	14.2	65
C1	180	24	e	626.9744	6.27E-04	1.014	1.032	1.047	1.048	0.389	0.379	175.8	25.1	271.4	11.7	24.2	62
B3	180	24	e	662.5305	6.63E-04	1.014	1.024	1.039	1.039	0.272	0.263	167.5	29	262.6	9.1	8.4	59.4
BQB1																	
C2	120	15	n	52.1353	5.21E-05	1.049	1.064	1.116	1.116	0.13	0.103	223.3	82	343.2	4	73.6	6.9
C1	120	15	n	95.46137	9.55E-05	1.108	1.124	1.245	1.245	0.069	0.014	249.8	14.9	66.6	75.1	159.6	0.8
B2	120	15	n	31.18018	3.12E-05	1.113	1.158	1.288	1.29	0.157	0.095	349	17.2	245.8	36.3	99.5	48.5
C3	120	15	n	42.4842	4.25E-05	1.073	1.035	1.111	1.113	-0.345	-0.368	168.7	10.8	66.6	47.8	268	40.1
	120	15	n														
E3	120	15	n	38.13776	3.81E-05	1.08	1.157	1.249	1.253	0.311	0.26	189.9	24.6	319.8	54.5	88.2	23.9
A1	120	15	n	48.54539	4.85E-05	1.018	1.082	1.102	1.109	0.629	0.615	358.1	38.1	159.5	50.4	260.8	9.2
A3	120	15	n	2.072649	2.07E-06	3.897	-0.389	-1.518	0	0	0.104	340.3	4.4	180	85.4	70.4	1.6
B3	120	15	n	33.87965	3.39E-05	1.033	1.07	1.106	1.108	0.355	0.333	2.2	23.1	131.6	56.1	261.5	23.3
E2	120	15	n	47.15303	4.72E-05	1.048	1.083	1.135	1.136	0.261	0.232	155.1	31.3	334.7	58.7	65	0.2
B1	120	15	n	95.97372	9.60E-05	1.282	1.291	1.655	1.655	0.014	-0.111	244.6	11.6	48.4	78	153.9	3.3
X	120	15	n	88.32413	8.83E-05	1.04	1.106	1.15	1.155	0.445	0.417	351.2	1.6	202	88.2	81.2	0.9
BQB2																	
C2	100	25	s	110.5986	1.11E-04	1.025	1.041	1.067	1.068	0.228	0.213	319	35.3	217.6	15.6	107.9	50.4
A2	100	25	s	112.7012	1.13E-04	1.02	1.036	1.057	1.058	0.284	0.272	89.2	10.3	217.3	73.5	356.8	12.7

Name	Strike	Dip		Km		L	F	P	Pj	T	U	K1dec	K1inc	K2dec	K2inc	K3dec	K3inc
A1	100	25	s	125.348	1.25E-04	1.016	1.019	1.035	1.035	0.106	0.098	266.9	8.3	41.7	78.3	175.7	8.2
C3	100	25	s	103.0838	1.03E-04	1.012	1.035	1.047	1.049	0.502	0.493	148.2	64.4	2.2	21.6	267	12.9
D1	100	25	s	127.2702	1.27E-04	1.018	1.024	1.042	1.043	0.164	0.154	283.1	66.6	162.7	12.3	68.2	19.6
D2	100	25	s	106.736	1.07E-04	1.03	1.016	1.046	1.047	-0.301	-0.311	191.8	5.2	328.3	82.9	101.4	4.9
D3	100	25	s	105.8636	1.06E-04	1.028	1.018	1.046	1.047	-0.203	-0.214	351	41.1	145.6	46	249.4	12.9
D4	100	25	s	90.07085	9.01E-05	1.009	1.037	1.046	1.049	0.614	0.607	163.1	38.5	5.4	49.3	262.1	11.2
F1	100	25	s	238.8759	2.39E-04	1.079	1.672	1.803	1.9	0.744	0.673	163.6	21.2	350.4	68.7	254.5	2.3
G2	100	25	s	121.3204	1.21E-04	1.084	1.013	1.098	1.107	-0.718	-0.73	3.3	33.8	266.5	10	162.2	54.3
G3	100	25	s	92.50342	9.25E-05	1.02	1.025	1.045	1.045	0.118	0.107	9.3	24.1	134.5	52.2	266	27.2
G4	100	25	s	87.48853	8.75E-05	1.01	1.049	1.06	1.064	0.667	0.659	175.9	44	348.8	45.8	82.5	3.5
G5	100	25	s	123.599	1.24E-04	1.042	1.024	1.067	1.068	-0.262	-0.277	187.9	40.9	42.6	43.5	294.5	18.2
X	100	25	s	106.3848	1.06E-04	1.02	1.024	1.045	1.045	0.073	0.063	338.6	46.3	149.4	43.3	243.8	4.6
X	100	25	s	121.5688	1.22E-04	1.026	1.068	1.096	1.099	0.441	0.422	38.8	78	192.5	10.8	283.5	5.2
W	100	25	s	93.1256	9.31E-05	1.052	1.022	1.075	1.077	-0.393	-0.408	340.6	33.5	231.6	26.2	112.1	45.1
WBB1																	
C2	080	20	s	665.4341	6.65E-04	1.014	1.02	1.033	1.034	0.177	0.169	184.2	3.5	354.9	86.5	94.1	0.6
A4	080	20	s	532.0334	5.32E-04	1.014	1.022	1.036	1.036	0.21	0.201	184.5	9.8	45.1	77.2	276	8.2
D1	080	20	s	687.4942	6.87E-04	1.011	1.02	1.031	1.032	0.304	0.298	10.3	3.3	112.6	74.9	279.4	14.7
B2	080	20	s	564.9269	5.65E-04	1.016	1.023	1.039	1.039	0.183	0.174	180.1	11.7	349.6	78.1	89.7	2.1
D2	080	20	s	618.0793	6.18E-04	1.012	1.012	1.024	1.024	-0.032	-0.038	2.5	3	104.5	75.8	271.8	13.9
FX	080	20	s	584.5453	5.85E-04	1.009	1.019	1.028	1.028	0.347	0.341	183.1	3	21.2	86.9	273.1	1
A3	080	20	s	582.7351	5.83E-04	1.02	1.013	1.034	1.034	-0.194	-0.202	9.7	9.1	208.5	80.4	100.2	3
F1	080	20	s	1606.738	1.61E-03	1.045	1.499	1.566	1.64	0.805	0.763	181.5	1.6	271.7	6.6	78	83.2
B1	080	20	s	664.5549	6.65E-04	1.012	1.02	1.032	1.032	0.255	0.248	180.5	24.6	358.8	65.4	90.2	0.6
C1	080	20	s	754.0935	7.54E-04	1.017	1.013	1.031	1.031	-0.135	-0.143	186.2	3.6	345.9	86.1	96.1	1.3
E1	080	20	s	614.6835	6.15E-04	1.015	1.011	1.026	1.026	-0.166	-0.172	186.2	3.5	33.6	86.1	276.3	1.8
F2	080	20	s	653.7712	6.54E-04	1.013	1.009	1.022	1.022	-0.175	-0.18	183.2	1.2	0.3	88.8	93.2	0.1
HHB1																	
A2	098	88	s	102.9671	1.03E-04	1.018	1.03	1.049	1.05	0.244	0.232	173.9	4.2	66.4	76.3	264.9	13.1
D1	098	88	s	104.6313	1.05E-04	1.026	1.039	1.066	1.066	0.193	0.177	308.5	15	204.1	42.6	53.2	43.5
B11	098	88	s	100.3624	1.00E-04	1.053	1.034	1.089	1.09	-0.219	-0.239	313	27.8	194.6	42.1	64.9	35.3
E1	098	88	s	136.047	1.36E-04	1.038	1.007	1.045	1.048	-0.668	-0.675	310.5	9.4	42.4	11.4	181.8	75.2

Name	Strike	Dip		Km		L	F	P	Pj	T	U	K1dec	K1inc	K2dec	K2inc	K3dec	K3inc
C1	098	88	s	129.2073	1.29E-04	1.038	1.018	1.057	1.058	-0.345	-0.357	326.4	6.8	193.6	80.1	57.3	7.2
E4	098	88	s	59.65144	5.97E-05	1.037	1.034	1.072	1.073	-0.039	-0.057	125.8	68.7	330.1	19.6	237.2	8.1
EX	098	88	s	137.2288	1.37E-04	1.021	1.033	1.054	1.055	0.213	0.2	330.9	28.1	203.5	48.6	77.1	27.6
1	098	88	s	243.4651	2.43E-04	1.029	1.109	1.141	1.149	0.566	0.543	3.2	2.5	93.4	5.6	249.3	83.9
B3	098	88	s	99.85158	9.99E-05	1.039	1.025	1.064	1.064	-0.219	-0.233	321.4	9	62.3	50.1	224.2	38.5
A4	098	88	s	98.89894	9.89E-05	1.009	1.06	1.069	1.075	0.736	0.728	209.2	37.5	312.7	17	62.2	47.5
B2	098	88	s	100.2294	1.00E-04	1.053	1.015	1.069	1.072	-0.559	-0.57	335.8	32.8	136.6	55.6	240	9
E1	098	88	s	115.8734	1.16E-04	1.009	1.043	1.052	1.056	0.634	0.626	313.5	15.7	44.9	5.3	153	73.3
C2	098	88	s	76.80359	7.68E-05	1.057	1.027	1.085	1.087	-0.348	-0.365	318.5	21.2	215	31.2	76.9	50.9
A3	098	88	s	121.9892	1.22E-04	1.003	1.07	1.074	1.083	0.906	0.903	350.2	14.1	195.3	74.5	81.8	6.3
BVB1																	
B2	120	80	s	829.0784	8.29E-04	1.004	1.029	1.033	1.036	0.742	0.738	254.2	5	344.9	7.3	130.2	81.2
B1	120	80	s	854.6217	8.55E-04	1.006	1.03	1.037	1.039	0.65	0.645	277	7.6	8.1	8.2	144.6	78.8
D2	120	80	s	739.6285	7.40E-04	1.006	1.032	1.038	1.041	0.688	0.683	297.3	5.2	27.9	6.7	169.9	81.5
F2	120	80	s	888.3503	8.88E-04	1.008	1.028	1.036	1.038	0.572	0.566	279.9	6.4	10.8	8.3	152.6	79.5
A2	120	80	s	765.7132	7.66E-04	1.007	1.027	1.034	1.036	0.594	0.588	281	4.8	11.3	3.8	139.4	83.9
D1	120	80	s	785.3524	7.85E-04	1.004	1.029	1.033	1.036	0.763	0.759	245.9	8.1	155.7	0.8	59.8	81.9
C1	120	80	s	868.6961	8.69E-04	1.006	1.03	1.036	1.038	0.683	0.678	286.8	8.9	17.2	2.7	124	80.7
F1	120	80	s	845.3331	8.45E-04	1.004	1.034	1.038	1.042	0.805	0.802	272.4	1.8	2.6	5.9	165.8	83.9
A1	120	80	s	791.7377	7.92E-04	1.001	1.033	1.034	1.039	0.928	0.927	281	7.3	11.5	3.8	129	81.8
E1	120	80	s	822.0428	8.22E-04	1.006	1.031	1.037	1.04	0.697	0.692	286.4	10.5	17	3.1	123.2	79

Block Samples

Name	N	Km	K1	K2	K3	K1dec	K1inc	K2dec	K2inc	K3dec	K3inc	L	F	P	Pj	T	U
BB1	15	5.53E-04	1.011	1.001	0.988	40.9	3.1	131.9	18.6	301.9	71.1	1.009	1.014	1.023	1.023	0.0193	0.187
BB2	20	8.99E-04	1.01	1.003	0.987	269.6	7.3	177.8	13.3	27	74	1.007	1.015	1.023	1.023	0.352	0.347
BB3	12	1.83E-04	1.008	1.004	0.988	197	68	102	2	11.7	21.7	1.004	1.016	1.021	1.022	0.5363	0.56
BB4	12	3.13E-04	1.01	1.001	0.989	81.3	9.8	205	73	349	14.1	1.008	1.013	1.021	1.021	0.199	0.194
BB5	12	1.08E-04	1.021	1.003	0.977	180.6	42	351	48	86	5	1.018	1.026	1.045	1.045	0.184	0.173
BB6	15	3.73E-04	1.005	1.004	0.991	140.6	15	32	50	242	36	1.001	1.013	1.015	1.016	0.797	0.796
BB7	15	9.70E-05	1.018	1.011	0.971	247	0.6	157	6.4	342	83.5	1.006	1.041	1.048	1.052	0.739	0.733
BB8	15	8.90E-04	1.01	1.001	0.989	100	20	353.3	38.6	211	44.6	1.009	1.013	1.022	1.022	0.198	0.193
BB9	9	5.90E-04	1.011	1.007	0.981	258.6	5	164	39	355	50	1.004	1.026	1.03	1.033	0.738	0.735
BB10	8	7.82E-04	1.01	1.008	0.982	285	37.3	135.3	48.5	27.2	15.4	1.002	1.026	1.028	1.031	0.831	0.829
BB11	13	5.01E-04	1.004	1.001	0.996	41.5	18.6	299.9	31	157.7	52.7	1.003	1.005	1.008	1.008	0.211	0.209
BB12	7	7.60E-04	1.008	1.004	0.989	249.6	35.7	132	32	13	37.5	1.004	1.015	1.019	1.02	0.55	0.546
BB13	11	6.34E-04	1.013	1.004	0.983	196	16	97	26	314	58	1.009	1.022	1.031	1.032	0.43	0.424
bqb1	12	3.25E-05	0.883	0.79	0.655	103.3	1.1	10	68	194	22	1.119	1.206	1.349	1.354	0.252	0.181
BQB2	17	1.15E-04	1.02	1.015	0.965	82	16	321	62	180	23	1.004	1.051	1.056	1.063	0.837	0.832
BVB1	10	8.19E-04	1.013	1.008	0.979	238	71	117	10	24	15	1.005	1.03	1.035	1.038	0.735	0.731
HHB1	14	1.16E-04	1.025	0.993	0.982	82.5	29	338.4	23.7	215.7	50.9	1.032	1.011	1.044	1.045	-0.482	0.49
WBB1	12	7.11E-04	1.026	0.995	0.979	264.7	0.8	174	10	359		1.031	1.017	1.048	1.049	-0.302	-0.313
DPG BQ	7	4.76E-05	1.019	1.005	0.977	85.4	23.9	306	59	183	17	1.014	1.029	1.043	1.044	0.352	0.343
DPG BM	5	1.16E-04	1.006	1.001	0.993	70.8	59.4	218	26.6	315.6	14	1.006	1.008	1.014	1.014	0.167	0.164

Strain Data A sections

Sample No		A Strike	Dip	Dip Direction	DD	DTNNM R	Phi	MRL R	MRL PHI
107013	bb5	094	85	004	N	1.10978	59.2008	1.36922	81.5255
107014	bb17	078	82	168	S	1.15672	86.5586	1.1775	-71.9478
107015	BB3	100	48	190	S	1.08414	63.8859	1.02762	75.578
107016	bb4	102	48	192	S	1.13626	11.2044	1.06927	16.0187
187021	bb14	056	82	326	N	1.10821	81.5617	1.03876	34.1629
187022	bb16/bv1	118	90	028	N	1.28695	17.7703	1.15312	-2.38367
187023	BB1	043	34	124	S	1.17703	65.6661	1.03565	84.9344
187024	BB2	090	76	180	S	1.15885	173.77	1.19068	-22.3816
187025	bb11	218	60	128	S	1.09393	64.6647	1.09738	50.9188
187026	bb15	094	85	004	N	1.18163	12.6336	1.34295	8.53276
26702a	bb6	134	16	224	S	1.13617	24.8581	1.12288	22.8097
26702b	bb7	124	24	214	S	1.15034	161.309	1.07708	86.1238
26702c	bb9	085	48	175	S	1.21965	15.0107	1.05409	-69.0332
257021	bb12	022	30	292	N	1.20825	79.2299	1.06226	-51.7325
257022	bb18	110	20	020	n	1.38078	32.5114	1.20052	-26.225
257024	bb10	104	90	014	N	1.19446	53.1393	1.05113	87.5485
257025	bb8	093	20	003	N	1.09521	16.0099	1.11248	20.6518
hh1		098	88	008	N	1.3961	170.5	1.28	-1.4
wb1		064	22	334	s	1.34	178.365	1.48	-3
bq1		078	20	348	s	1.1	146	1.148	-39
bq2		078	20	348	s	1.24	176	1.19	-2
bn1		098	48	008	s	1.02	162	1.02	42.142

Strain Data B sections

Sample No		B Strike	Dip	Dip Direction	DD	DTNNM R	Phi	MRL R	MRL PHI
107013	bb5	094	5.00	184	S	1.06995	66.2666	1.20502	79.4143
107014	bb17	078	8.00	348	N	1.06998	-22	1.07027	-84.016
107015	BB3	100	42.00	010	N	1.13507	-17.262	1.05004	-10.1381
107016	bb4	102	42.00	012	N	1.15376	-14.702	1.3209	-9.83705
187021	bb14	056	8.00	146	S	1.3244	-75	1.06686	-89.4302
187022	bb16/bv1	118	0.00	208	S	1.0573	18.9952	1.22811	-32.8881
187023	BB1	043	56.00	313	N	1.38246	87.8465	1.27518	73.4457
187024	BB2	090	14.00	360	N	1.08602	32.1135	1.17507	34.1476
187025	bb11	218	30.00	308	N	1.09993	-53	1.09445	1.86166
187026	bb15	094	5.00	184	S	1.06362	-22	1.2507	-31.0737
26702a	bb6	134	74.00	044	N	1.03216	65.4045	1.22252	74.5117
26702b	bb7	124	66.00	034	N	1.19612	22.684	1.12561	34.083
26702c	bb9	085	42.00	355	N	1.06752	-41.128	1.1843	-17.3403
257021	bb12	022	60.00	112	S	1.96601	-2.707	1.41189	-19.1755
257022	bb18	110	70.00			1.07518	30.0407	1.24802	-15.7646
257024	bb10	104	0.00	194	S	1.20833	66.9616	1.12856	72.4235
257025	bb8	093	70.00	183	S	1.18038	24.3032	1.11457	17.004

Strain Data C Sections

Sample No		Strike	Dip	DD	Dip Direction	DTNNM R	Phi	MRL R	MRL PHI
107013	bb5	004	90	094	N	1.06835	72.2572	1.2038	79.4011
107014	bb17	168	90	078	N	1.05394	120.246	1.04388	-66.8898
107015	BB3	190	90	100	N	1.13401	113.135	1.20678	-80.5811
107016	bb4	192	90	102	N	1.32184	17.9432	1.40367	12.6162
187021	bb14	326	90	056	N	1.10991	173.26	1.05563	-15.6661
187022	bb16/bv1	028	90	118	N	1.15199	148.498	1.31906	-38.0569
187023	BB1	124	90	043	N	1.13451	136.255	1.26515	-70.9832
187024	BB2	180	90	090	N	1.23719	25.6435	1.22595	19.7083
187025	bb11	128	90	218	N	1.23645	0.437742	1.09406	28.3983
187026	bb15	004	90	094	N	1.21517	6.22711	1.19971	13.1828
26702a	bb6	224	90	134	N	1.24865	82.4451	1.25649	73.6044
26702b	bb7	214	90	124	N	1.0331	35.3962	1.08209	-79.5756
26702c	bb9	175	90	085	N	1.26863	83.5825	1.17326	89.0328
257021	bb12	292	90	022	N	1.2559	141.101	1.25105	-11.6228
257022	bb18	020	90	110	N	1.3311	123.374	1.11258	-45.3354
257024	bb10	014	90	104	N	1.19305	18.4873	1.05909	-89.1065
257025	bb8	003	90	093	N	1.22172	34.0805	1.17173	42.2143
hh1		008	90	098	N	1.33	169	1.26	4.5
wb1		334	90	064	N	1.81906	73	1.6	74.8689
bq1		348	90	078	N	1.26	72.2	1.1	89.3498
bq2		348	90	078	N	1.14	56.4	1.155	73.25
bn1		008	90	098	N	1.06	58.9	1.1	87.536

Lat/Long Data for Munster Samples

WGS 84	Lat/Lon hddd−mm.mmm'		
Name	Position	Altitude	Date Modified
107013	N52 18.149 W7 43.700	327 m	05/05/2013 13:45
107015	N52 09.727 W7 50.552	66 m	05/04/2013 16:11
107016	N52 09.930 W7 56.173	52 m	05/04/2013 17:12
180723	N52 10.195 W7 35.333	273 m	05/04/2013 14:54
187024	N52 10.433 W7 37.657	248 m	05/04/2013 15:20
187025	N52 14.649 W7 27.649	230 m	05/06/2013 10:13
257024	N52 20.477 W7 27.601	57 m	05/05/2013 19:03
257025	N52 19.664 W7 38.575	230 m	05/05/2013 15:48
26702A	N52 16.806 W7 39.051	141 m	05/05/2013 14:25
26702B	N52 18.242 W7 37.931	406 m	05/05/2013 15:09
26702C	N52 24.469 W7 35.896	155 m	05/05/2013 17:41
BB12	N52 15.601 W7 30.507	407 m	05/06/2013 12:53
BB13	N52 15.627 W7 31.270	624 m	05/06/2013 14:17
BN1	N52 00.381 W7 34.790	2 m	03/02/2012 14:54
BQ1	N51 58.279 W7 42.161	4 m	03/02/2012 17:35
BQ2	N51 58.277 W7 42.162	4 m	03/02/2012 17:37
BQB1	N51 58.324 W7 42.147	13 m	05/04/2013 12:06
BQB2	N51 58.277 W7 42.191	6 m	05/04/2013 12:15
BV1	N52 06.346 W7 30.508	2 m	11/29/2012 1:14:16 PM
BVB1	N52 06.376 W7 30.578	10 m	05/04/2013 14:00
CS1	N52 15.191 W7 30.813	445 m	01/12/2013 12:34
CS2	N52 15.135 W7 30.927	427 m	01/12/2013 13:00
CS3	N52 14.915 W7 30.960	402 m	01/12/2013 13:30
HH1	N52 03.279 W7 32.593	5 m	03/02/2012 13:08
HHB1	N52 03.281 W7 32.620	6 m	05/04/2013 12:51
MB1	N52 01.213 W7 35.105	6 m	03/02/2012 16:29
MF1	N52 13.513 W7 32.658	760 m	12/14/2012 11:01:12 AM
MF2	N52 13.486 W7 32.664	773 m	12/14/2012 11:23:22 AM
MF3	N52 13.579 W7 32.664	760 m	12/14/2012 11:53:13 AM
MF4	N52 13.638 W7 32.723	766 m	12/14/2012 12:17:16 PM
MR11	N52 12.658 W7 30.432	105 m	01/12/2013 15:59
WB1	N51 56.901 W7 45.889	7 m	03/02/2012 18:05
WB2	N51 56.785 W7 45.917	8 m	03/02/2012 18:17
WBB1	N51 56.896 W7 45.880	9 m	05/04/2013 10:59